Turbulence-chemistry interaction models for numerical simulation of aeronautical propulsion systems

Nadezda Petrova

Thesis presented to obtain the degree of
DOCTOR OF THE ECOLE POLYTECHNIQUE
Specialization: Applied Mathematics
by
Nadezda PETROVA

Turbulence-chemistry interaction models for numerical simulation of aeronautical propulsion systems

Defended on 16 January 2015 in front of the jury:

Dr. Arnaud MURA	ISAE-ENSMA	Referee
Dr. Serge SIMOËNS	LMFA, École Centrale de Lyon	Referee
Prof. Gregoire ALLAIRE	CMAP, École Polytechnique	Examiner
Dr. Nicolas BERTIER	ONERA/DEFA	Examiner
Dr. Pascal BRUEL	LMA, Université de Pau	Examiner
Prof. Andrei LIPATNIKOV	Chalmers, Sweden	Examiner
Dr. Olivier SOULARD	CEA/DAM	Examiner
Prof. Vladimir SABELNIKOV	ONERA/DEFA	Supervisor

Thesis prepared at ONERA/DEFA

To my family

Acknowledgments

I wish to express my sincere gratitude to my thesis director Vladimir Sabelnikov for the honor he gave me by accepting my candidacy for the present work, sharing his expert knowledge of the combustion models and comprehensive guidance during my PhD project.

I express my special thanks to Nicolas Bertier for his invitation to participate in FTC project in a difficult situation where we had not yet obtained significant advances on the original Monte-Carlo topic, and for his subsequent help with the architecture of CEDRE code.

I remain indebted to Olivier Soulard for his great idea for solving SPDEs. I would like to thank him and Roland Duclous for the opportunity to take part in turbulence modeling project during CIRM summer school.

I would like to thank a lot Arnaud Mura and Serge Simoens, for accepting to take part in the jury as referees, and for their detailed and insightful reviews of my manuscript. Many thanks to Gregoire Allaire, Pascal Bruel, Andrei Lipatnikov for the careful examination of the present work. I would like to thank all the members of the jury for hard and interesting questions, resulted in a fruitful in-depth discussion following the defense.

I am very thankful to Philippe Grenard, Lionel Matuszewski, Thomas Le Pichon, Dmitry Davidenko, Aymeric Boucher and Yann Moule, and all the DEFA team for their readiness to help and professionalism. I would like to thank all my colleagues for all they gave me during these three years.

I thank Igor Favorskiy for useful advice on IT aspects.

Abstract

Modeling the turbulence-chemistry interaction is a key point in the numerical simulation of the combustion in the air-breathing engines. The present work is devoted to adaptation and integration of the different turbulent combustion models into the ONERA industrial code CFD package for diphasic reactive flows (CEDRE). The first part of the thesis is focused on the quasi-linear hyperbolic stochastic partial differential equations (SPDEs) which are statistically equivalent to a transport equation for the joint velocity-scalars probability density function (PDF). It is shown that in order to preserve the equivalence between the SPDEs and the transport equation for the joint velocity-scalars PDF, multivalued solutions of the SPDEs should be taken into account. A new stochastic method to solve the SPDEs, recently proposed by O. Soulard [Emako-Letizia2014], is considered and validated on one-dimensional test-cases. It is shown that this method is able to recover the multivalued solutions of the SPDEs in the statistical sense.

The numerical solution of the SPDEs is time consuming, therefore the second part of the thesis is concerned with a flamelet tabulated chemistry (FTC) and an extended partially stirred reactor (EPaSR) models. In the framework of CEDRE CFD software the FTC approach is updated, presuming that the distribution is given by a β-PDF. The adaptation of the LES/EPaSR model [SabelnikovFureby2013] to the RANS and its integration into CEDRE are done. The EPaSR and the FTC with the presumed β-PDF are validated against experimental data [MagreMoreau1988] on a configuration of a backward-facing step combustor. It is shown that the RANS/EPaSR calculation yields the best agreement with the experiment compared to other considered approaches.

Keywords: stochastic partial differential equations, probability density function, multivalued solution, extended partially stirred reactor, flamelet tabulated chemistry model

Résumé

La modélisation de l'interaction turbulence-chimie est un point clé dans la simulation numérique des écoulements réactifs turbulents. Cette thèse est consacrée à l'adaptation et l'intégration de différents modèles de combustion turbulente dans le code d'écoulements diphasiques réactifs pour l'énergétique (CEDRE) de l'ONERA. La première partie de la thèse est dédiée à l'étude des équations quasi-linéaires hyperboliques stochastiques aux dérivées partielles (SPDEs) qui sont statistiquement équivalentes à une équation de transport pour la fonction de densité de probabilité (PDF) jointe vitesse-scalaires. Il est démontré que pour préserver l'équivalence entre les SPDEs et l'équation de transport pour la PDF jointe vitesse-scalaires, les solutions multivaluées des SPDEs doivent être prises en compte. Une nouvelle méthode stochastique pour résoudre les SPDEs, récemment proposée par O. Soulard [EmakoLetizia2014], est étudiée et validée sur des cas-tests unidimensionnels. Il est montré que cette méthode permet de trouver les solutions multivaluées des SPDEs au sens statistique.

La résolution numérique des SPDEs étant particulièrement coûteuse, une seconde voie a été explorée au cours de cette thèse. Il s'agit, dans la deuxième partie de ce mémoire, de la mise en œuvre du modèle "flammelettes tabulées pour la chimie" (FTC) et du modèle "réacteur partiellement mélangé étendu" (EPaSR). Avec le code CEDRE, l'approche des FTC est mise à jour en supposant une distribution de type β-PDF. L'adaptation LES/EPaSR [SabelnikovFureby2013] pour le RANS et son intégration dans CEDRE ont été réalisées. Les modèles EPaSR et "FTC avec β-PDF présumée" ont été validés par rapport aux données expérimentales [MagreMoreau1988] sur une configuration de flamme stabilisée par une marche descendante. Il est montré que le calcul RANS/EPaSR donne un meilleur accord avec l'expérience que les autres approches évaluées.

Mots clés : équations aux dérivées partielles stochastiques, fonction de densité de probabilité, solutions multivaluées, réacteur partiellement mélangé étendu, flammelettes tabulées pour la chimie

Contents

Contents **7**

List of symbols **11**

List of dimensionless numbers **14**

List of abbreviations **15**

1 Introduction **19**

2 Background **23**
2.1 Turbulence characteristics 24
2.1.1 Homogeneous isotropic turbulence 25
The Kolmogorov hypothesis 28
2.2 Flame structure 28
2.2.1 Premixed flame 28
Regimes in premixed combustion 29
2.2.2 Non-premixed flame 32
2.3 Navier-Stokes equations for aerothermochemistry 34
2.3.1 Conservation of mass and species 34
2.3.2 Chemical kinetics 35
2.3.3 Conservation of momentum 35
2.3.4 Conservation of total energy 36
2.3.5 State law of an ideal gas 36
2.4 Reynolds averaged Navier-Stokes (RANS) approach 37
2.4.1 Definition of the ensemble average 37
2.4.2 Averaged Navier-Stokes equations 37
2.4.3 Closure of the RANS equations 38
2.4.4 Turbulence models 39
2.5 Large eddy simulation (LES) 40
2.5.1 Closure of the LES equations 40
2.6 General models of turbulent combustion 41
2.6.1 PDF approach 41
Eulerian PDFs 41
Presumed PDF 42
Transported Eulerian PDF 44

2.6.2 Partially stirred reactor models 51
Eddy dissipation concept 51
Partially stirred reactor model 53
Extended partially stirred reactor model 56
Unsteady partially stirred reactor model 58
2.6.3 Thickened flame model 59

I New approach to solve SPDEs statistically equivalent to a transport equation for velocity PDF 61

3 Eulerian (Field) Monte Carlo methods for solving the Favre one-time one-point velocity PDF transport equation 63
3.1 Description of the problem 65
3.1.1 One-dimensional model PDF equation 65
3.1.2 One-dimensional SPDEs 68
3.1.3 Equivalence between SPDEs and PDF equation 71
3.2 Stochastic numerical schemes 72
3.2.1 Schemes for partial differential equations 72
Numerical notations for stochastic schemes 74
Numerical stochastic schemes 75
Mean density conservation in stochastic schemes 80
3.2.2 Schemes for stochastic partial differential equations 80
General remarks 82
3.3 Numerical tests 83
3.3.1 Backward step velocity profile 83
Numerical solution 83
3.3.2 Scheme non-dissipativity test 96
PDF 96
PDEs 96
Numerical solution: test 1 97
3.3.3 Statistically homogeneous velocity fluctuations test 106
PDF 106
SPDEs 107
Numerical solution 110
3.3.4 Model PDF equation with non-zero RHS 127
PDF 127
SPDEs 127
Numerical solution 127
3.4 Conclusions 134
3.5 Perspectives 135

II Standard models of turbulent combustion 137

4 Flamelet tabulated chemistry (FTC) model 139
4.1 Original implementation of FTC beta-PDF model in CEDRE 139
4.1.1 Modeling of Favre-averaged progress variable 139
4.1.2 Modeling of Favre variance of progress variable 140
Transport equation 140
Algebraic expression 141
4.1.3 Modeling of Favre-averaged mixture fraction 142
4.1.4 Modeling of Favre variance of mixture fraction 142
Transport equation 142
Algebraic expression 142
4.1.5 Gradient of Favre-averaged progress variable 142
4.1.6 Coupling between tabulated chemistry and CEDRE 142
4.1.7 Presumed beta-PDF 143
4.1.8 Algorithm of beta-PDF integration 143
4.2 Updated FTC beta-PDF model 144
4.2.1 New models for dissipation and source terms 144
4.2.2 Gradient of Favre-averaged progress variable 144
4.2.3 Algorithm of beta-PDF integration 145
4.2.4 Numerical implementation of beta-PDF integration 147
Study of convergence of the semi-analytic beta integration method 148

5 Transported partially stirred reactor (TPaSR) model 151
5.1 Original EPaSR model 151
5.2 TPaSR model: EPaSR adaptation to CEDRE 152

6 Backward-facing step flow 155
6.1 A3C experimental setup 156
6.2 RANS nonreactive backward-facing step flow calculation 157
6.2.1 Computational domain and grid 157
6.2.2 Physical models 158
6.2.3 Boundary conditions 158
6.2.4 Numerical methods 159
6.2.5 Computational strategy 159
6.2.6 Results 162
Recirculation region 162
Favre-averaged velocity 163
RMS velocity fluctuations 165
Turbulent frequency 168
6.2.7 Conclusions 168
6.3 RANS reactive backward-facing step flow calculation 169
6.3.1 Numerical setup 169
6.3.2 Combustion modeling 170
6.3.3 Results 170

Quasi-laminar approaches 171
PFTC β-PDF models 178
TPaSR model 186
6.3.4 Conclusions 195
6.4 LES reactive backward-facing step flow calculation 195
6.4.1 Computational domain and grid 195
6.4.2 Physical models 196
6.4.3 Boundary conditions 196
6.4.4 Combustion modeling and numerical schemes 199
6.4.5 Computational strategy 199
6.4.6 Results 200
Mean temperature 200
Recirculation region 202
Mean streamwise velocity 203
Mean transverse velocity 204
Mean mass fractions 207
Velocity fluctuations 210
Impact of reflecting boundary conditions 213
6.4.7 Conclusions 216
6.5 Conclusions 216

7 Conclusions and future work 219
7.1 Conclusions 219
7.2 Future work 220
7.2.1 SPDEs 220
7.2.2 TPaSR model 220
7.2.3 FTC with presumed beta-PDF model 221

A Some aspects of SPDEs modelling 223
A.1 Random choice method (RCM) for solution satisfying entropy increase condition 223
A.2 Stochastic Runge-Kutta method 226
A.3 Schemes for SPDEs statistically equivalent to the joint velocity-scalar PDF equation 227
A.4 n dimensional space schemes for PDEs 228
A.5 Numerical tests 230
A.5.1 Step velocity profile 231
PDF 231
PDEs 231
Numerical solution 232
A.5.2 Ramp velocity profile 234
PDF 234
PDEs 235
Numerical solution 239
A.5.3 Triangle velocity profile 247
PDF 247

PDEs 248
Numerical solution 251
A.5.4 Hat velocity profile 254
PDEs 254
Numerical solution 254
A.5.5 Scheme non-dissipativity test 259
Numerical solution 259
A.6 Study of Langevin equation 269

B Dependence of solution on computational grid in reactive backward-facing step flow 273
B.1 Numerical setup 273
B.2 Results 275
B.2.1 RANS/PFTC beta-PDF 275
B.2.2 RANS/TPaSR 281

List of figures 287

List of tables 300

Bibliography 303

List of symbols

A, B, E_a	Arrhenius law parameters	
C_f	Friction coefficient	
C_p	Specific heat capacity at constant pressure of the mixture	J/(kg K)
C_s	Smagorinsky model constant	
C_μ	$k-\varepsilon$ model constant	
C_{p_k}	Specific heat capacity at constant pressure of species k	J/(kg K)
C	Progress variable	
D_k	Diffusion coefficient of species k	m^2/s
$F(Q)$	Fourier transformation of the quantity Q	
N_{br}	Number of different branches of multivalued solution	
N_r	Number of realizations	
N_{sp}	Number of species	
P	Pressure	Pa
R^0	Ideal gas constant	J/(mol K)
S_L	Laminar flame speed	m/s
T	Temperature	K
Y_k	Mass fraction of species k	
Z	Mixture fraction	
Δt	Time step	s
δ_L	Laminar flame thickness	m
$\dot{\omega}_k$	Rate of chemical reaction of species k	$kg/(m^3\ s)$
η_K	Kolmogorov length scale	m
γ^*_{eq}	Volume fraction of fine structures in equilibrium state	
γ^*	Volume fraction of fine structures	
λ_k	Thermal conductivity of species k	W/(m K)
λ	Thermal conductivity of the mixture	W/(m K)
μ_k	Dynamic viscosity of species k	kg/(m s)
μ	Dynamic viscosity of the mixture	kg/(m s)
ν	Kinematic viscosity	m^2/s
ω	Turbulent frequency	Hz
ρ	Density	kg/m^3
τ^*	Subgrid residence time scale	s
τ_K	Kolmogorov time scale	s

τ_{ch}	Chemical time scale	s
$\boldsymbol{S}$	Symmetric part of the strain tensor	
$\boldsymbol{V}$	Sample space of velocity	m/s
$\boldsymbol{u}''$	Favre velocity fluctuations	m/s
$\boldsymbol{u}'$	Reynolds velocity fluctuations	m/s
$\boldsymbol{u}^*$	Stochastic velocity	m/s
$\boldsymbol{u}^{RMS}$	RMS velocity fluctuations	m/s
$\boldsymbol{u}$	Velocity vector	m/s
ε	Turbulence dissipation rate	m^2/s^3
$\widetilde{Q}$	Favre average of the quantity Q	
$\widetilde{f}$	Favre PDF	
ξ	Stochastic noise	
e_t	Total energy	J/kg
f_β	β-PDF	
g	Fluctuating velocity PDF	
h_t	Total enthalpy	J/kg
i_{rea}	Realization index	
k	Kinetic energy of the turbulence	J/kg
l	Turbulent length scale	m
r^*	Stochastic density	kg/m^3
t	Time	s

List of dimensionless numbers

Da	Damkholer number
Ka	Karlovitz number
Pr	Prandtl number
Re_t	Turbulent Reynolds number
Re	Reynolds number
Sc	Schmidt number
cfl	Courant-Friedrich-Lewy number

List of abbreviations

BML	Bray–Moss–Libby model
BVM	Boussinesq viscosity model
CEDRE	CFD package for diphasic reactive flows (Code d'écoulements diphasiques réactifs pour l'énergétique)
CFD	computational fluid dynamics
CFL	Courant-Friedrich-Lewy condition
DNS	direct numerical simulation
EARSM	explicit algebraic Reynolds stress model
EBU	eddy break-up
EDC	eddy dissipation concept
EMC	Eulerian Monte Carlo
EPaSR	extended partially stirred reactor
FTC	flamelet tabulated chemistry model
GForce	generalized first order centered method
GLM	generalized Langevin model
ITNFS	intermittent turbulent net flame stretch
LAERTE	Reactive flow and research techniques laboratory (Laboratoire des ecoulements réactifs et de leurs techniques d'etudes)
LES	large eddy simulation
LFA	laminar flamelet assumption
LHS	left-hand side
LMC	Lagrangian Monte Carlo
MUSCL	monotonic upstream scheme for conservation laws

noTCI	chemistry model without turbulence-chemistry interaction
O-U	Ornstein-Uhlenbeck
ODE	ordinary differential equation
ODFI	Riemann invariants-based flow decentering operator (opérateur de décentrement sur les flux avec l'utilisation des invariants de Riemann)
PaSR	partially stirred reactor
PDE	partial differential equation
PDF	probability density function
PFTC	premixed flamelet tabulated chemistry model
PRECCINSTA	prediction and control of combustion instabilities in tubular and annular gas turbine combustion systems
PSR	perfectly stirred reactor
QL RCM	quasi-laminar model with reduced chemical mechanism
RANS	Reynolds-averaged Navier-Stokes equations
RCM	random choice method
RHS	right-hand side
RK2	explicit second order Runge-Kutta method in time
RMS	root mean square
SGF	stochastic GForce method
SGod	stochastic Godunov method
SL-F	stochastic Lax-Friedrichs method
SL-W	stochastic Lax-Wendroff method
SODE	stochastic ordinary differential equation
SPDE	stochastic partial differential equation
TCI	turbulence-chemistry interaction
TFLES	thickened flame large eddy simulation
TPaSR	transported partially stirred reactor
UPaSR	unsteady partially stirred reactor

Chapter 1

Introduction

The modern energy and environmental context motivate the improvement of combustion systems in air-breathing chambers. The structure of turbulent flames in industrial combustion chambers is complex: it is governed by turbulence, two-phase injection, chemical kinetics, acoustics and radiation. Once validated by comparison with experimental data, numerical simulations allow improving the understanding of the different physical mechanisms, in particular, analyzing combustion stability, and explaining formation of polluting emissions. The description of the turbulence-chemistry interaction (TCI) is a key point in the development of such numerical methods. Approaches based on probability density function (PDF) offer compelling advantages for modeling reacting turbulent flows [Pope2000]. They provide an effective resolution to the closure problems that arise from averaging or filtering of the highly nonlinear chemical source terms, from modeling the effects of convection, body forces. There are two different PDF-based methods: the first assumes a certain approximate shape of the PDF (*presumed PDF*) and the second consists in solving a transport equation for the PDF.

Over the past years, the use of the presumed PDFs for combustion progress variable or/and mixture fraction has been gaining popularity as an approach to average reaction rates in premixed and non-premixed turbulent flames. Commonly invoked for this purpose is a β-PDF, with the parameters determined by the values of its first and second moments. These moments are computed by integrating proper balance equations. The disadvantage of the presumed PDF method is the absence of an universality of the PDF. Therefore the results of each simulation should be validated case by case.

The approach based on the transport equation for the one-time one-point joint velocity-scalars PDF [Pope1985] is a natural and promising tool for the description of the TCI. It is nonetheless counterbalanced by a severe numerical constraint: the joint velocity-scalars PDF possesses a potentially high number of dimensions, which induces heavy computational cost. The finite difference methods cannot be used, as their cost increases exponentially with dimensionality. The common approach to circumvent this difficulty is to use the Monte Carlo methods, which yield a linearly growing effort and therefore are well suited to solve PDF equations.

In the field of turbulent combustion, Lagrangian Monte Carlo (LMC) methods [Pope1985] have become an essential component of the PDF approach. The LMC methods are based on stochastic particles, which evolve from prescribed stochastic ordinary differential equations (SODEs). Numerous publications document the convergence and accuracy of the LMC

methods. However, the development of new Eulerian Monte Carlo (EMC) methods are useful and stimulating, since the competition between the LMC and the EMC methods could push both approaches forward.

The EMC methods are based on stochastic Eulerian fields, which evolve according to the stochastic partial differential equations (SPDEs) statistically equivalent to the PDF equation. The EMC methods have already been proposed in [Valiño1998; SabelnikovSoulard2005; SabelnikovSoulard2006], in order to compute the one-time one-point PDF of turbulent reactive scalars. The methods discussed in these works are still numerically expensive, since their Courant-Friedrich-Lewy condition (CFL) criterion is similar to an advection/diffusion stability criterion.

Recently O. Soulard and V. Sabelnikov [SoulardSabelnikov2006; SabelnikovSoulard2010] have proposed SPDEs to solve a transport equation for the Favre joint PDF of velocity fields and turbulent reactive scalars. The Ornstein-Uhlenbeck (O-U) process for fluctuating velocity allows using the time step which is proportional to a grid size divided by total stochastic velocity. From this point of view the SPDEs are less expensive and allow more precise determination of PDF statistics.

The first part of the thesis is focused on the developing the EMC methods to solve the transported joint velocity-scalars PDF. They are time consuming therefore the second part of the thesis is concerned with a flamelet tabulated chemistry (FTC) with a presumed β-PDF and with an extended partially stirred reactor (EPaSR) models. These standard turbulence combustion approaches are less expensive.

The outline of this thesis is as follows. The fundamentals of the turbulence, the premixed and the non-premixed flames are recalled in the chapter 2. Then some background information on governing equations and various modeling approaches for turbulent combustion is given.

The chapter 3 presents the quasi-linear hyperbolic SPDEs which are statistically equivalent to the transport equation for the joint velocity-scalars PDF. It is shown that in order to preserve the equivalence between the SPDEs and the joint velocity-scalars PDF transport equation, the multivalued solutions of the SPDEs should be taken into account. Recently, the level set method [LiuOsher2006] has been developed to capture multivalued solutions of the deterministic hyperbolic PDEs. It should be noted that the level set method augments the problem dimension by one in the physical space, i.e $(t, \boldsymbol{x}) + 1$. However, the direct application of the level set method to the SPDEs needs a further development, because of a strong variation of the number of the branches of multivalued solutions of the SPDEs. Therefore, in the thesis a new stochastic method (proposed by O. Soulard [EmakoLetizia2014]) is applied to solve the SPDEs.

Validation of the new method is carried out on a series of one-dimensional test-cases. It is shown that the method is able to recover multivalued solution in the statistical sense. Velocity moments are compared with the analytical solutions of the PDF equation if they exist or with the numerical solutions of the PDF equation, and a good agreement is found. Numerical accuracy issues, such as spatial and statistical convergence rates, are investigated.

A FTC method is updated into the current version of CFD package for diphasic reactive flows (CEDRE) software, presuming that the distribution is given by a β-PDF. The chapter 4 describes the original algorithm [Savre2010] along with performed improvements. The semi-analytic β integration method [LienLiu2009] is extended from one variable (mixture fraction)

to two variables case (mixture fraction variable and progress variable). This modification permits to overcome boundary singularities in integration of the β-PDF over the mixture fraction and the progress variables.

The chapter 5 describes the adaptation of the large eddy simulation (LES)/EPaSR model [SabelnikovFureby2013] to the Reynolds-averaged Navier-Stokes equations (RANS) and its integration into CEDRE. This model is referred to as the transported partially stirred reactor (TPaSR) model.

RANS and LES simulations of a premixed methane/air flow in a backward-facing step combustor are presented in the chapter 6. The TPaSR, the FTC without TCI and the FTC with a presumed β-PDF models are considered, and the effects of various modeling assumptions are discussed. Validation of numerical results on experimental data [MagreMoreau1988] are done. It is demonstrated that the RANS/TPaSR with a $k-l$ turbulence model calculation yields the best agreement with the experiment compared to other considered methods.

The conclusions are summarized in the chapter 7 along with suggestions for future work.

Some results of the thesis are published in the following communications:

- C. Emako, V. Letizia, N. Petrova, R. Sainct, R. Duclous, and O. Soulard. "Diffusion limit of Langevin PDF models in weakly inhomogeneous turbulence". In: *CEMRACS* (2014)
- N. Petrova and V. Sabelnikov. "Simulation of turbulent combustion in air-breathing chambers: extension of Eulerian Monte Carlo methods". In: *13th Onera-DLR Aerospace Symposium ODAS* (2013)

Chapter 2

Background

Turbulent combustion is encountered in most practical combustion systems such as rockets, internal combustion or aircraft engines, industrial burners and furnaces; while laminar combustion applications are almost limited to candles, lighters and some domestic furnaces (examples can be found in [PoinsotCandel1995; Pope2000]). Studying and modeling turbulent combustion processes is therefore an important issue to develop and improve practical systems (i.e. to increase efficiency and reduce fuel consumption and pollutant formation). As combustion processes are difficult to handle using analytical techniques, numerical combustion for turbulent flames is a fast growing area.

There are three main numerical approaches used in turbulent combustion:

- **Direct numerical simulation (DNS):** Direct Numerical Simulation consists in solving the Navier-Stokes equations, resolving all the scales of motion without any turbulence model. The flow is described by the instantaneous fields from which all other information is determined. DNS is the simplest and unrivaled in accuracy approach. Yet its cost is extremely high and furthermore it increases very rapidly with Reynolds number. Consequently, today this method is not applicable to the simulation of practical engineering problems, in particular, to high-Reynolds-number flows.
- **LES:** Large Eddy Simulation explicitly computes structures which are larger than the computational mesh size of the flow field whereas the effects of the smallest ones are modeled. LES provide unsteady and spatially-filtered quantities. These instantaneous quantities cannot be directly compared to the experimental flow fields. Only the statistical quantities extracted from LES can be compared with the experimental data. Computationally LES is less expensive than DNS.
- **RANS:** Reynolds averaged Navier-Stokes equations describe mean flow fields and are adapted to practical industrial simulations. In this approach any instantaneous quantity is decomposed into a time or ensemble average and a fluctuating component. Unclosed quantities in the governing equations are modeled, using turbulence and combustion models.

In the present work we limit ourselves to model the turbulent reactive flow within computationally accessible RANS and LES approaches.

This chapter is organized as follows. First, we recall energy cascade and the Kolmogorov hypotheses, and introduce various scales of motion. Then the general description of the

flame structure is given. After that we formulate the governing equations describing the fundamental properties of turbulent reacting flows. Finally, we describe some general models of turbulent combustion.

2.1 Turbulence characteristics

Following the description of turbulent flows given in the book of [Peters2000], we mention the main characteristics of turbulent flow (for simplicity, a nonreactive density constant case is considered in this section).

Turbulent flow appears at sufficiently high Reynolds number

$$Re = \frac{UL}{\nu}, \tag{2.1}$$

where U is a characteristic velocity of the flow, L is a characteristic length scale of the geometry and ν is a kinematic viscosity of the fluid. It possesses several characteristic features

- **Irregularity.** Turbulent flow is irregular, random and chaotic, with a large number of eddies of different length scales.
- **Diffusivity.** In turbulent flow the diffusivity increases.
- **High Reynolds Numbers.** Turbulent flow occurs at high Reynolds number.
- **Three-Dimensional.** Turbulent flow is always three-dimensional.
- **Dissipation.** Turbulent flow is dissipative, which means that there is a steady transfer of kinetic energy from the large scales to the small scales and that this energy is then transformed into the internal energy at the small scales by viscous dissipation. Such the behavior is usually referred to as the eddy cascade hypothesis.
- **Continuum.** Even though we have small turbulent scales in the flow they are much larger than the molecular scale and we can treat the flow as a continuum.

An example of a turbulent jet is shown in fig. 2.1. It enters with a high velocity into initially quiescent surroundings. The large velocity difference between the jet and the surroundings generates shear layer instability, which after a transition region, becomes turbulent.

In order to characterize the distribution of eddy length scales at any position within the jet, the axial velocity u is simultaneously measured at time t at points $\boldsymbol{x}$ and $\boldsymbol{x}+\boldsymbol{r}$, where $\boldsymbol{r}$ is $\boldsymbol{r} = r\boldsymbol{e_r}$, r is a distance between two spatial points and $\boldsymbol{e_r}$ is a unit vector in the direction $\boldsymbol{r}$. The correlation between two axial velocities $u(t, \boldsymbol{x})$ and $u(t, \boldsymbol{x} + \boldsymbol{r})$ is defined by the average

$$R(t, \boldsymbol{x}, \boldsymbol{r}) = \overline{u'(t, \boldsymbol{x})u'(t, \boldsymbol{x} + \boldsymbol{r})}, \tag{2.2}$$

where $u' = u - \overline{u}$ is a fluctuating axial velocity and $\overline{u}$ is a mean axial velocity of the flow.

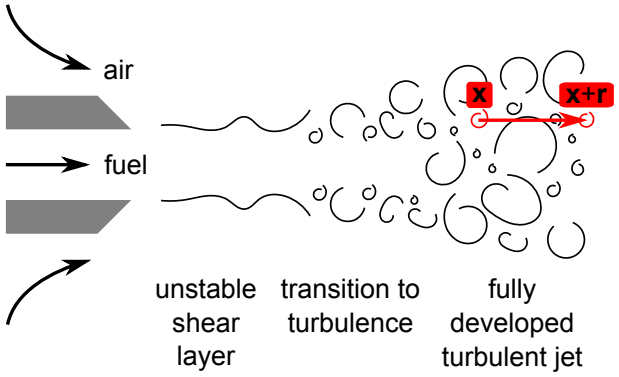

Figure 2.1: Schematic presentation of two-point correlation measurements in a turbulent jet

2.1.1 Homogeneous isotropic turbulence

For homogeneous isotropic turbulence the velocity field is invariant under translations, rotations and reflections of the coordinate system. For this case the normalized axial correlation is

$$f(t,r) = \frac{R(t,r)}{\overline{u'^2(t)}}, \tag{2.3}$$

where $R(t,r)$ is given by

$$R(t,r) = \overline{u'(t,\boldsymbol{x})u'(t,\boldsymbol{x}+r\boldsymbol{e_r})}. \tag{2.4}$$

The velocity fluctuations in the three coordinate directions are supposed to be equal. The turbulent kinetic energy which is defined in general case as

$$k = \frac{1}{2}\overline{\boldsymbol{u'u'}} \tag{2.5}$$

reads

$$k = \frac{3}{2}\overline{u'^2}. \tag{2.6}$$

According to [Kolmogorov1941], the normalized axial correlation is

$$f(t,r) = 1 - \frac{3}{4}\frac{C}{k}(\varepsilon r)^{2/3}, \ \eta_K \ll r \ll l_t, \tag{2.7}$$

where C is an universal Kolmogorov constant and ε is a viscous dissipation. l_t is the integral length scale defined by

$$l_t(t) = \int_0^{+\infty} f(t,r)dr. \tag{2.8}$$

and η_K is the Kolmogorov length scale

$$\eta_K = \left(\frac{\nu^3}{\varepsilon}\right)^{1/4}. \tag{2.9}$$

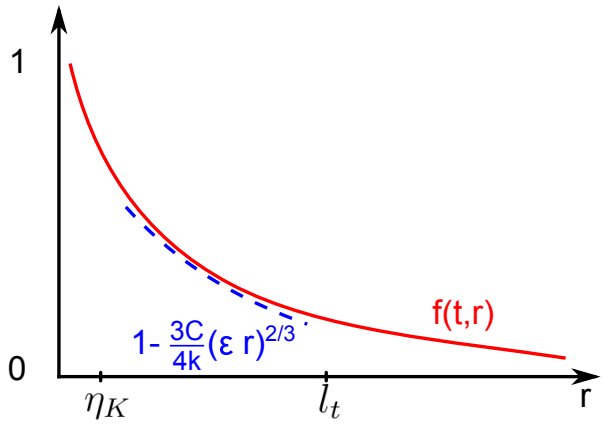

Figure 2.2: The normalized axial two-point velocity correlation for homogeneous isotropic turbulence as a function of the distance r between the two points

Figure 2.2 schematically represents $f(t,r)$. When $r \to 0$, $f(t,r)$ remains close to one, and then decays with increasing distance.

A Fourier transform of the isotropic two-point correlation function leads to a definition of the kinetic energy spectrum $E(\kappa)$, which is the density of kinetic energy per unit wavenumber κ. Integrating over the whole wave number space, we obtain that the total kinetic energy k:

$$k = \int_0^\infty E(\kappa) d\kappa, \tag{2.10}$$

where the wave number κ is inversely proportional to the eddy characteristic size l

$$\kappa = l^{-1}. \tag{2.11}$$

The spectrum of the energy density is schematically presented in logarithmic scale in fig. 2.3. There are three regions of the turbulent energy spectrum:

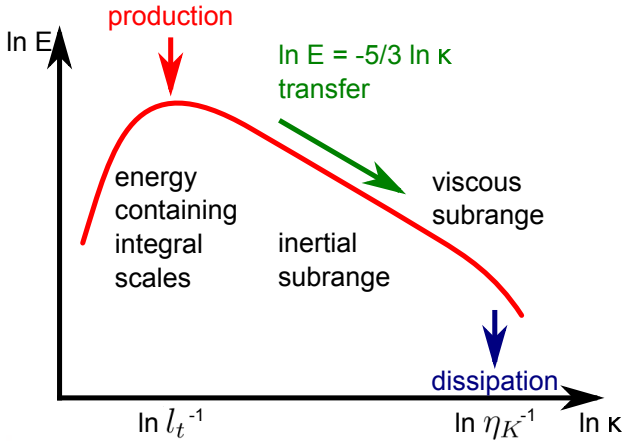

Figure 2.3: Density spectrum of kinetic energy in logarithmic scale

- **Energy-containing integral scales**
  In this subrange $E(\kappa)$ attains its maximal value, since eddies contain most of the kinetic energy. The integral scales are characterized by the integral length scale l_t (2.8). The root mean square (RMS) velocity fluctuation which is

$$v_t = \sqrt{\frac{2}{3}k} \tag{2.12}$$

  defines the integral velocity scale. One can deduce the turnover time l_t/v_t of these eddies. It is proportional to the integral time scale

$$\tau_t = \frac{k}{\varepsilon}. \tag{2.13}$$

- **Inertial subrange**
  The subrange of length scales between the integral scale and the Kolmogorov scale is called the inertial subrange. Length scales l_n such that $\eta_K \ll ... < l_n < ... < l_2 < l_1 \ll l_t$, $n = 1, ..$, velocity scales v_n, and timescales τ_n cannot be formed from ε alone. However, given an eddy size l_n, characteristic velocity scales and timescales for the eddy are those formed from ε and l_n [Pope2000]:

$$\begin{cases} \tau_n = \left(\frac{l_n^2}{\varepsilon}\right)^{1/3} \\ v_n = (\varepsilon l_n)^{1/3} \end{cases}$$

  The velocity scales and timescales v_n and τ_n decrease as l_n decreases. The kinetic energy v_n^2 at scale l_n is

$$v_n^2 \sim (\varepsilon l_n)^{2/3} = \varepsilon^{2/3}\kappa^{-2/3} \tag{2.14}$$

  and its density in wavenumber space is proportional to

$$E(\kappa) = \frac{dv_n^2}{d\kappa} \sim \varepsilon^{2/3}\kappa^{-5/3}. \tag{2.15}$$

  This is the $\kappa^{-5/3}$ law for the kinetic energy spectrum in the inertial subrange.
  In this area, $ln\ E(\kappa)$ decreases linearly with $ln(\kappa)$. The turbulence kinetic energy is neither dissipated nor produced, but only transferred to smaller scales by the breakup of large structures. The corresponding energy flux is imposed by the large structures.

- **Viscous subrange**
  For very small values of r only very small eddies fit into the distance between $\boldsymbol{x}$ and $\boldsymbol{x}+\boldsymbol{r}$. The motion of these small eddies is influenced by viscosity ν. Dimensional analysis yields the Kolmogorov length η_K (2.9), the Kolmogorov time τ_K and the Kolmogorov velocity v_K scales:

$$\begin{cases} \tau_K = \left(\frac{\nu}{\varepsilon}\right)^{1/2} \\ v_K = (\varepsilon\nu)^{1/4} \end{cases}$$

  Viscous subrange starts approximately from the Kolmogorov length scale η_K. $E(\kappa)$ decreases exponentially owing to viscous effects.

The Kolmogorov hypothesis

Let a quantity $\mathcal{T}(l)$ be the rate at which energy is transferred from eddies larger than l to those smaller than l. Accordingly to Kolmogorov's 1941 energy cascade concept, the rate of energy transfer from the large eddies of size l_t, determines the constant rate of energy transfer through the inertial subrange; hence the rate at which energy leaves the inertial subrange and enters the dissipation range; and hence the dissipation rate ε at the Kolmogorov scale η_K. We have

$$\mathcal{T}(l_t) \sim \mathcal{T}(l_n) \sim \mathcal{T}(\eta_K) \sim \varepsilon. \tag{2.16}$$

Accordingly to dimensional analysis we can write that

$$\frac{v_t^3}{l_t} \sim \frac{v_n^2}{\tau_n} \sim \frac{v_n^3}{l_n} \sim \frac{l_n^2}{\tau_n^3} \sim \frac{v_K^2}{\tau_K} \sim \frac{v_K^3}{\eta_K} \sim \varepsilon. \tag{2.17}$$

Consequently, the viscous dissipation ε can be related to the turnover velocity and the length scale of the integral scale eddies

$$\varepsilon \sim \frac{v_t^3}{l_t}. \tag{2.18}$$

2.2 Flame structure

2.2.1 Premixed flame

Premixed combustion regime corresponds to a limit case when fuel and oxidizer are completely mixed before combustion takes place. Once fuel and oxidizer are homogeneously mixed and a heat source is supplied it becomes possible for a flame front to propagate through the mixture. If we neglect the flame thickness then we can see that owing to the temperature sensitivity of the reaction rates the gas behind the flame front rapidly approaches the burnt gas state close to the chemical equilibrium, while the mixture in front of the flame typically remains in the unburnt state. Therefore, the combustion system on the whole contains two stable gas states: the unburnt and the burnt.

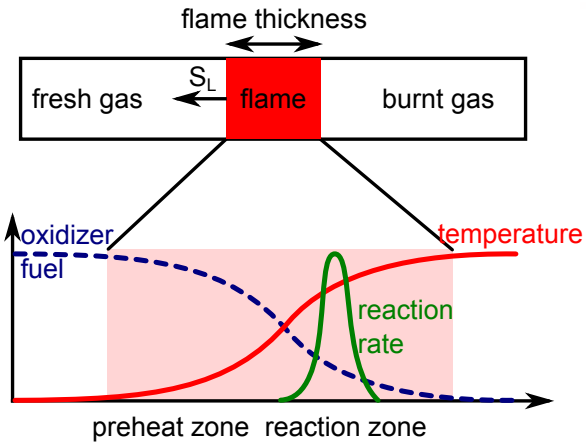

Figure 2.4: Structure of a laminar premixed flame

In a duct after the ignition these two states are presented in fig. 2.4. If we zoom the flame, then we can observe that both states exist in the system at the same time and are spatially separated by the flame front where the transition from one to the other takes place. The lower part of the fig. 2.4 is a close-up view of the structure of the flame. There are two zones: the preheat zone and the combustion reaction zone. In the preheat zone, the fresh gases mix and warm up due to molecular conductive effects. The temperature of the reactants increases gradually from the unburnt mixture temperature to an elevated temperature near the reaction zone. As the reactant temperature approaches the ignition temperature of the fuel, the chemical reactions accelerates, marking the front of the combustion reaction zone. Inside the flame, the reaction rate increases rapidly and then decreases as fuel and oxidizer are consumed and products are generated. Because of the species concentration gradient, the reactants diffuse toward the reaction zone and their concentration in the preheat zone decreases as they approach the reaction zone, which is quite thin. The temperature of the products is close to the adiabatic flame temperature.

Flame propagation through the unburnt mixture depends on two consecutive processes (more details can be found, for example, in [PoinsotVeynante2005]). First, the heat produced in the reaction zone is transferred upstream by molecular conductivity, heating the incoming unburnt mixture up to the ignition temperature. Second, the preheated components chemically react in the reaction zone.

The most important quantity in premixed combustion is the velocity at which the flame front propagates normal to itself and relative to the flow into the unburnt mixture. This velocity is called the laminar burning velocity S_L. It is a thermo-chemical transport property that depends on the fuel-to-oxidizer equivalence ratio, the temperature in the unburnt mixture, and the pressure.

The laminar premixed flame can be described using a reaction progress variable C, such as $C = 0$ in the fresh gases and $C = 1$ in the fully burnt ones. If we consider that all molecular diffusion coefficients for species are equal, this progress variable may be defined as a reduced temperature or a reduced mass fraction:

$$C = \frac{T - T_f}{T_b - T_f}, \qquad C = \frac{Y^F - Y_f^F}{Y_b^F - Y_f^F}, \tag{2.19}$$

where T, T_f, and T_b are respectively the local, the fresh gases and the burnt gases temperatures. Y^F, Y_f^F and Y_b^F are respectively the local, fresh gases and burnt gases fuel mass fractions. Y_b^F is non-zero for a rich combustion (fuel excess).

Regimes in premixed combustion

According to [Peters2000] diagrams defining regimes of premixed turbulent combustion in terms of velocity and lengths scale ratios have been proposed by [Peters1986; AbdelGayed-Bradley1989; BorghiDestriau1995]. For scaling purposes let us assume equal diffusivity D for all reactive scalars, take unity Schmidt number $\nu/D = 1$, and define flame thickness as

$$\delta_L = \frac{D}{S_L} \tag{2.20}$$

and flame transit time

$$\tau_F = \frac{D}{S_L^2} \tag{2.21}$$

with S_L being the front propagation speed.

The turbulent Reynolds number which is defined using turbulent intensity v_t (see definition (2.12)) and turbulent length scale l_t:

$$Re_t = \frac{v_t l_t}{\nu} \tag{2.22}$$

can be rewritten as

$$Re_t = \frac{v_t l_t}{S_L \delta_L}. \tag{2.23}$$

The turbulent Damkohler number reads

$$Da = \frac{S_L l_t}{v_t \delta_L}. \tag{2.24}$$

Using Kolmogorov time, length and velocity scales, denoted respectively by τ_K, l_K and v_K, let us introduce Karlovitz number as the measures the ratios of the flame scales in terms of the Kolmogorov scales:

$$Ka = \frac{\tau_F}{\tau_K} = \frac{\delta_L^2}{\eta_K^2} = \frac{v_K^2}{S_L^2}. \tag{2.25}$$

For homogeneous isotropic turbulence if we assume that $\nu = D$ and that the dissipation of energy relates to the turnover velocity and the length scale of the integral scale eddies as

$$\varepsilon \approx \frac{v_t^3}{l_t}, \tag{2.26}$$

then it can be shown that

$$Re_t = Da^2 Ka^2. \tag{2.27}$$

Given the appropriate reaction zone thickness l_δ in premixed flame

$$l_\delta = \delta \delta_L, \tag{2.28}$$

which is a fraction δ of the flame thickness, one can also introduce second Karlovitz number

$$Ka_\delta = \frac{l_\delta^2}{l_K^2} = \delta^2 Ka. \tag{2.29}$$

A diagram of Peters (1991) shows that δ varies from values of approximately $\delta = 0.1$ at atmospheric pressure to $\delta = 0.03$ at pressures around 30 atm.

The ratios v_t/S_L and l_t/δ_L may be expressed in terms of Reynolds and Karlovitz numbers as

$$\frac{v_t}{S_L} = Re_t \left(\frac{l_t}{\delta_L}\right)^{-1} = Ka^{2/3} \left(\frac{l_t}{\delta_L}\right)^{1/3}. \tag{2.30}$$

In fig. 2.5 the boundaries of different regimes of premixed turbulent are described by lines $Re_t = 1$ and $Ka = 1$. Another boundary of interest, namely $v_t/S_L = 1$ separates wrinkled

flamelets from the corrugated flamelets, and the line denoted by $Ka_\delta = 1$ separates thin reaction zones from broken reaction zones. The line $Re_t = 1$ separates turbulent and laminar flame regimes.

Several types of the premixed turbulent flame can be distinguished (fig. 2.5):

- **Flamelet regime** ($Re_t > 1$, $Ka < 1$)
  - Wrinkled flamelet regime ($v_t < S_L$). In this regime, the turnover velocity v_t of even the large eddies is smaller than the laminar burning velocity S_L. Laminar flame propagation therefore dominates over flame front corrugation by turbulence.
  - Corrugated flamelets regime. Here $\delta_L < \eta_K$, which implies that the entire flame structure is embedded within the eddies of the size of the Kolmogorov scale, where the flow is quasi-laminar. Therefore the flame structure is not perturbed by turbulent fluctuations and remains quasi-steady.
- **Thin reaction zone** ($Re_t > 1$, $Ka > 1$, $Ka_\delta < 1$)**.** In this regime the smallest eddies can enter into the diffusive-reactive flame structure since $\eta_K < \delta_L$. These small eddies are still larger than the inner reaction layer thickness l_δ and therefore cannot penetrate into that layer and modify the reaction zone.
- **Broken reaction zones** ($Re_t > 1$, $Ka_\delta > 1$). In this regime Kolmogorov eddies are smaller than the inner reaction layer thickness l_δ. These eddies may therefore enter into the inner layer and perturb it with the consequence that chemistry breaks down locally owing to enhanced heat loss to the preheat zone followed by temperature decrease and the loss of radicals.

This classification of combustion regimes by characteristics numbers is rough but useful approximation: in fact it allows choosing the appropriate turbulent combustion model prior to the numerical calculation. Furthermore, once the calculation is done, the predicted flame structure represents a first validation case for the obtained numerical results.

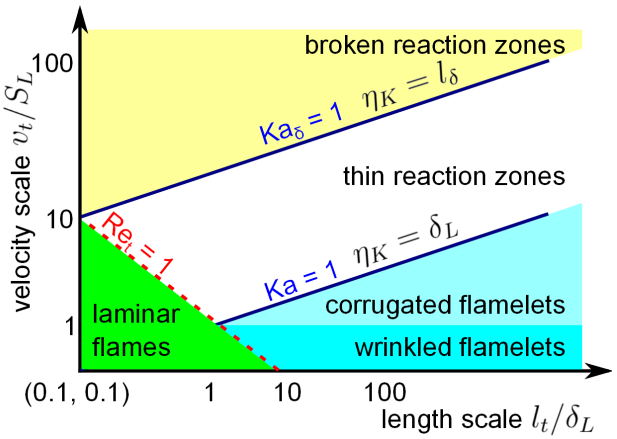

Figure 2.5: Regime diagram for premixed turbulent combustion [Peters2000]

2.2.2 Non-premixed flame

Detailed description of non-premixed flame can be found, for example, in [PoinsotVeynante2005]. We will give some details taken from this book.

Schematic structure of a laminar diffusion flame is represented in fig. 2.6. The fuel and oxidizer enter separately into the combustion chamber. There they diffuse towards the reaction zone, mix and burn during continuous interdiffusion generating heat. Temperature attains its maximum value in this zone and decreases away from the flame front towards fuel and oxidizer streams.

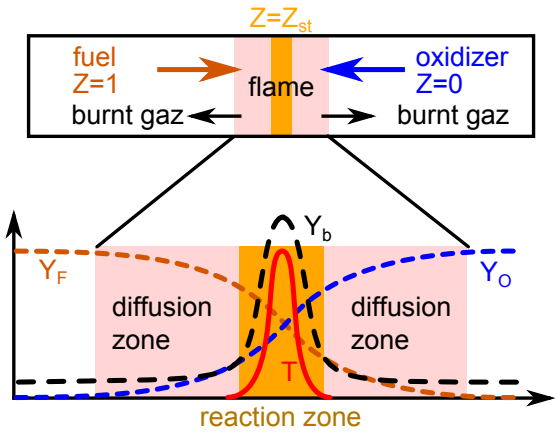

Figure 2.6: Structure of a laminar diffusion flame

The lower part of fig. 2.6 illustrates a number of important considerations:

- Away from the flame, the gas is too rich on the fuel side and too lean on the oxidizer side to burn. Chemical reactions can proceed only in a limited region, where fuel and oxidizer are sufficiently mixed. The most favorable mixing is obtained where fuel and oxidizer are in stoichiometric proportions: a diffusion flame usually lies on the surface where mixing produces a stoichiometric mixture.
- The flame structure plotted in fig. 2.6 is steady only when strain is applied to the flame, i.e. when fuel and oxidizer streams are pushed against each other at certain speeds.
- Diffusion flame does not propagate and, therefore, exhibits no intrinsic characteristic speed as premixed flame. In fact, the flame is unable to propagate towards fuel because of the lack of oxidizer and it cannot propagate towards oxidizer stream because of the lack of fuel. Accordingly, the reaction zone does not move significantly relatively to the flow field.
- There is no flame thickness defining a characteristic length scale, in contrast to premixed combustion.

In the diffusion flame, the chemical reaction rate is generally much faster than the diffusion rates of the gaseous reactants (i.e., the characteristic chemical reaction rime τ_{ch} is much smaller than the characteristic diffusion time τ_d). Consequently,

- Chemical reaction occurs in a narrow zone near the interface between the gaseous fuel and oxidizer

- Concentration of fuel and oxidizer are very low in the reaction zone (where most of the products are generated)
- Combustion rate is controlled by the rate at which fuel and oxidizer flow into the reaction zone.

The key parameter of non-premixed combustion is the mixture fraction Z. In the simple case, an infinitely fast one-step irreversible reaction equation can be written as

$$F + sO \rightarrow (1+s)P, \tag{2.31}$$

where F is a fuel, O is an oxidizer and P is a product of combustion. $s = (Y_F/Y_O)_{st}$ is the mass stoichiometric coefficient. Thus, the mixture fraction is defined as

$$Z = \frac{sY_F - Y_O + 1}{1+s}, \tag{2.32}$$

where Y_F is the fuel mass fraction and Y_O is the oxidizer mass fraction. The mixture fraction can be also interpreted as a normalized fuel-to-air equivalence ratio. In general way the mixture fraction can be defined as a quantity related to chemical elements.

The role of the mixture fraction Z is to describe the mixture state, i.e. to qualify the degree of inter-penetration of the fuel and the oxidizer. Z is usually taken as unity in the fuel stream and is zero in the oxidizer stream. For a diffusion flame, the reaction surface is located at the stoichiometric region $Z = Z_{st}$. For a premixed flame, Z is a constant anywhere in the flow.

There is no fixed reference length scale which can be easily identified for the diffusion flame. Nevertheless, we can construct dimensionless numbers and make a similar classification as for turbulent premixed flame.

Let us introduce a diffusive time which is the inverse of scalar dissipation rate of the mixture fraction Z:

$$\tau_\chi \approx \chi_Z^{-1} = \left(D|\bigtriangledown Z|^2\right)^{-1}, \tag{2.33}$$

where D is a molecular diffusion coefficient. The Damkholer number is defined as:

$$Da = \frac{\tau_\chi}{\tau_c} \approx (\tau_c \chi_Z)^{-1} \tag{2.34}$$

This number is used to characterize the reaction zone. DNS calculations of the flame-vortex interaction evidence two limit Damkholer numbers, Da_{LFA} (laminar flamelet assumption (LFA)) and Da_{ext}. As shown in fig. 2.7, three regimes can then be distinguished for non-premixed turbulent combustion:

- If $Da > Da_{LFA}$, the flame front has a structure of a stationary laminar flame.
- When $Da_{ext} < Da < Da_{LFA}$: highly unsteady effects take place.
- When $Da < Da_{ext}$, local extinction appears.

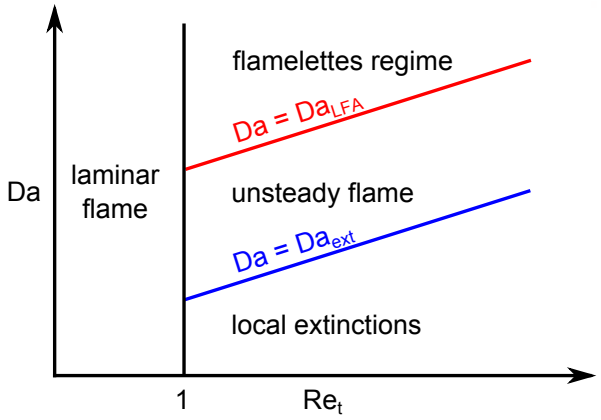

Figure 2.7: Regimes of non-premixed turbulent combustion

2.3 Navier-Stokes equations for aerothermochemistry

Navier-Stokes equations for aerothermochemistry can be found, for example, in [PoinsotVeynante2005]. They can be written as follows.

2.3.1 Conservation of mass and species

The total mass conservation equation is

$$\frac{\partial \rho}{\partial t} + \frac{\partial \rho u_i}{\partial x_i} = 0. \tag{2.35}$$

Here ρ is a density and u_i is the i^{th} component of the velocity vector.

For a gas mixture consisting of N_{sp} species, the principle of mass conservation can be expressed in the form of N_{sp} equations for each of species whose sum allows finding the relationship (2.35):

$$\frac{\partial \rho Y_k}{\partial t} + \frac{\partial \rho (u_i + V_{k,i}) Y_k}{\partial x_i} = \dot{\omega}_k(\boldsymbol{Y}, T), \qquad k = 1, .., N_{sp}, \tag{2.36}$$

where Y_k and $\dot{\omega}_k$ correspond respectively to the mass fraction and the rate of formation/extinction of the species k (in the units of $[\dot{\omega}_k] = [\text{kg m}^{-3}\ \text{s}^{-1}]$ detailed in "chemical kinetics". $\boldsymbol{Y}$ is a vector of the mass fractions and T represents temperature. $V_{k,i}$ is the i-component of the diffusion velocity V_k of species k. By definition:

$$\sum_{k=1}^{N_{sp}} Y_k V_{k,i} = 0, \qquad \sum_{k=1}^{N_{sp}} \dot{\omega}_k = 0. \tag{2.37}$$

According to Fick's law [Fick1855], one can define $V_{k,i} Y_k$ as

$$V_{k,i} Y_k = -D_k \frac{\partial Y_k}{\partial x_i}, \tag{2.38}$$

where D_k is a diffusion coefficient of the species k in the mixture.

2.3.2 Chemical kinetics

Consider a chemical system of N_{sp} species reacting through M reactions

$$\sum_{k=1}^{N_{sp}} \nu'_{k,j} \mathcal{M}_k \rightleftharpoons \sum_{k=1}^{N_{sp}} \nu''_{k,j} \mathcal{M}_k, \ j = 1, .., M, \tag{2.39}$$

where $\mathcal{M}_k$ is a symbol for species k, $\nu'_{k,j}$ and $\nu''_{k,j}$ are the molar stoichiometric coefficients of species k in reaction j. Mass conservation enforces

$$\sum_{k=1}^{N_{sp}} \nu'_{k,j} W_k = \sum_{k=1}^{N_{sp}} \nu''_{k,j} W_k, \qquad \sum_{k=1}^{N_{sp}} \nu_{kj} W_k = 0, j = 1, .., M, \tag{2.40}$$

where W_k is the atomic weight of species k and

$$\nu_{kj} = \nu''_{kj} - \nu'_{kj}. \tag{2.41}$$

The mass reaction rate $\dot{\omega}_k$ for species k is the sum of rates $\dot{\omega}_{kj}$ produced by all M reactions

$$\dot{\omega}_k = \sum_{j=1}^{M} \dot{\omega}_{kj} = W_k \sum_{j=1}^{M} \nu_{kj} \left(K_{fj} \prod_{k=1}^{N_{sp}} \left(\frac{\rho Y_k}{W_k} \right)^{\nu'_{kj}} - K_{rj} \prod_{k=1}^{N_{sp}} \left(\frac{\rho Y_k}{W_k} \right)^{\nu''_{kj}} \right), \tag{2.42}$$

where K_{fj} and K_{rj} are the forward and reverse rates of reaction j.

The rate constants K_{fj} and K_{rj} are usually modeled using the empirical Arrhenius law

$$K_{fj} = A_{fj} T^{\beta_j} \exp\left(-\frac{T_{aj}}{T} \right), \tag{2.43}$$

here A_{fj} is the pre-exponential constant, β_j is the temperature exponent and T_{aj} is the activation temperature. The backward rates K_{rj} are computed from the forward rates through the equilibrium constants.

2.3.3 Conservation of momentum

Applying the fundamental law of dynamics to a fluid particle, we obtain the following equation of momentum

$$\frac{\partial \rho u_i}{\partial t} + \frac{\partial \rho u_j u_i}{\partial x_i} = -\frac{\partial P}{\partial x_j} + \frac{\partial \tau_{ji}}{\partial x_j} + \rho \sum_{k=1}^{N_{sp}} Y_k f_{k,i} = \frac{\partial \sigma_{ji}}{\partial x_j} + \rho \sum_{k=1}^{N_{sp}} Y_k f_{k,i}, \tag{2.44}$$

where P is the pressure, $f_{k,i}$ is the volume force acting on species k in direction i. The viscous tensor τ_{ji} is defined by

$$\tau_{ij} = \mu \left(\frac{\partial u_i}{\partial x_j} + \frac{\partial u_j}{\partial x_i} \right) - \frac{2}{3} \mu \frac{\partial u_i}{\partial x_j} \delta_{ij} \tag{2.45}$$

where δ_{ij} denotes the Kronecker symbol, μ is the dynamic viscosity. The tensor σ_{ij} is defined as the sum of the viscous stress tensor and pressure tensor:

$$\sigma_{ij} = -P\delta_{ij} + \tau_{ij}. \tag{2.46}$$

Equation (2.44) is the same in reacting and non-reacting flows. Even though this equation does not include any explicit reaction terms, the flow is modified by combustion: the dynamic viscosity μ strongly changes because of a temperature variation. As a consequence, the local Reynolds number varies much more than in a non-reacting flow: even though the momentum equations are the same with and without combustion, the flow behavior is very different.

2.3.4 Conservation of total energy

The conservation equation for total energy e_t is

$$\frac{\partial \rho e_t}{\partial t} + \frac{\partial \rho e_t u_i}{\partial x_i} = -\frac{\partial q_i}{\partial x_i} + \frac{\partial \left(\sigma_{ij} u_i\right)}{\partial x_j} + \dot{Q} + \rho \sum_{k=1}^{N_{sp}} Y_k f_{k,i} \left(u_i + V_{k,i}\right), \tag{2.47}$$

where $\dot{Q}$ is the heat source term (due for example to an electric spark, a laser or a radiative flux). $\rho \sum_{k=1}^{N_{sp}} Y_k f_{k,i} \left(u_i + V_{k,i}\right)$ is the power produced by volume forces f_k on species k. The energy flux q_i is

$$q_i = -\lambda \frac{\partial T}{\partial x_i} + \rho \sum_{k=1}^{N_{sp}} h_k Y_k V_{k,i}. \tag{2.48}$$

This flux includes a heat diffusion term expressed bu Fourier's Law $\lambda \frac{\partial T}{\partial x_i}$ (λ is the heat diffusion coefficient) and a second term associated with the diffusion of species with the different enthalpies h_k which is specific of multi-species gas.

We recall that the total energy is defined by the relation

$$e_t = \sum_{k=1}^{N_{sp}} \left(\int_{T_0}^{T} Y_k C_{p,k}(T^*) dT^* + Y_k h_k^0 \right) - \frac{P}{\rho} + \frac{u_i u_i}{2}, \tag{2.49}$$

where h_k^0 is the enthalpy of formation of the species k at the reference temperature T_0 and $C_{p,k}$ represents the mass specific heat at a constant pressure of the species k.

2.3.5 State law of an ideal gas

A state law for the mixture of a perfect gas is also added to this system of equations:

$$P = \rho R^0 \sum_{i=1}^{N_{sp}} \frac{Y_k}{W_k} T, \tag{2.50}$$

where R^0 is the gas constant ($R^0 = 8.314\,\mathrm{J\ mol^{-1}K^{-1}}$) and W_k is the atomic weight of species k.

2.4 Reynolds averaged Navier-Stokes (RANS) approach

2.4.1 Definition of the ensemble average

The RANS approach consists in solving the Navier-Stokes equations to which a statistical ensemble average with some closure hypothesis is applied. For constant density flows, the averaging consists in splitting any quantity $Q(t,\boldsymbol{x})$ into a Reynolds mean component $\overline{Q}(t,\boldsymbol{x})$ and a fluctuating component $Q'(t,\boldsymbol{x})$

$$Q(t,\boldsymbol{x}) = \overline{Q}(t,\boldsymbol{x}) + Q'(t,\boldsymbol{x}). \tag{2.51}$$

For variable density flows mass-weighted averages (Favre averages) are usually preferred.

$$\widetilde{Q} = \frac{\overline{\rho Q}}{\overline{\rho}}. \tag{2.52}$$

(2.51) is replaced by a new decomposition

$$Q = \widetilde{Q} + Q'', \tag{2.53}$$

where Q'' are the fluctuations relative to the Favre averages.

2.4.2 Averaged Navier-Stokes equations

Using the formalism proposed by Favre, the following RANS system is obtained:

- **Mass**

$$\frac{\partial \overline{\rho}}{\partial t} + \frac{\partial \overline{\rho}\widetilde{u}_i}{\partial x_i} = 0, \tag{2.54}$$

- **Chemical species**

$$\frac{\partial \overline{\rho}\widetilde{Y}_k}{\partial t} + \frac{\partial \overline{\rho}\widetilde{Y}_k\widetilde{u}_i}{\partial x_i} = -\frac{\partial(\overline{\rho V_{k,i} Y_k} + \overline{\rho}\widetilde{u_i'' Y_k''})}{\partial x_i} + \overline{\dot{\omega}}_k,\ k = 1,..,N_{sp}. \tag{2.55}$$

- **Momentum**

$$\frac{\partial \overline{\rho}\widetilde{u}_i}{\partial t} + \frac{\partial \overline{\rho}\widetilde{u}_i\widetilde{u}_j}{\partial x_j} + \frac{\partial \overline{P}}{\partial x_i} = \frac{\partial(\overline{\tau}_{ij} - \overline{\rho}\widetilde{u_i'' u_j''})}{\partial x_j}, \tag{2.56}$$

- **Total energy**

$$\frac{\partial \overline{\rho}\widetilde{e}_t}{\partial t} + \frac{\partial(\overline{\rho}\widetilde{e}_t + \overline{P})\widetilde{u}_i}{\partial x_i} =$$

$$\frac{\partial\left(-\left(\overline{\rho u_i e_t} - \overline{\rho}\widetilde{u}_i\widetilde{e}_t\right) + \left(\overline{\tau_{ji}u_j} - \overline{\tau}_{ji}\widetilde{u}_j\right) - \overline{q}_i + \overline{\tau}_{ji}\widetilde{u}_j\right)}{\partial x_i} + \overline{\dot{Q}} + \overline{\rho\sum_{k=1}^{N_{sp}} Y_k f_{k,i}\left(u_i + V_{k,i}\right)}. \tag{2.57}$$

- **Averaged thermodynamics law**

$$\overline{P} = \overline{\rho} R^0 \widetilde{T} \sum_{i=1}^{N_{sp}} \frac{\widetilde{Y}_k}{W_k}. \tag{2.58}$$

2.4.3 Closure of the RANS equations

The averaged Navier-Stokes eqs. (2.55) to (2.58) for the compressible flows involve terms that are not closed. They should be modeled.

- **Averaged diffusive fluxes for species $\overline{\rho V_{k,i} Y_k}$ and total energy $\overline{q}_i$**: According to Boussinesq hypothesis these terms can be modeled as

$$\overline{\rho V_{k,i} Y_k} = -\overline{\rho D_k \frac{\partial Y_k}{\partial x_i}} \approx \overline{\rho} \overline{D}_k \frac{\partial \widetilde{Y}_k}{\partial x_i}, \tag{2.59}$$

  where $\overline{D}_k$ is a mean species molecular diffusion coefficient.

$$\overline{q}_i = -\overline{\lambda} \frac{\partial \widetilde{T}}{\partial x_i} + \overline{\rho} \sum_{k=1}^{N_{sp}} \widetilde{h}_k \overline{D}_k \frac{\partial \widetilde{Y}_k}{\partial x_i}, \tag{2.60}$$

  where $\overline{\lambda}$ denotes a mean thermal diffusivity.

- **Averaged viscous stress tensor $\overline{\tau}_{ij}$**: from (2.61) we deduce

$$\overline{\tau}_{ij} = \overline{\mu} \left(\frac{\partial \widetilde{u}_i}{\partial x_j} + \frac{\partial \widetilde{u}_j}{\partial x_i} \right) - \frac{2}{3} \overline{\mu} \frac{\partial \widetilde{u}_i}{\partial x_j} \delta_{ij}, \tag{2.61}$$

  $\overline{\mu}$ is a mean dynamic viscosity.

- **Reynolds stress tensor $\overline{\rho} \widetilde{u_i'' u_j''}$**: this term represents the turbulent flux of the momentum. Following the turbulence viscosity assumption proposed by Boussinesq, it can be modeled as

$$\overline{\rho} \widetilde{u_i'' u_j''} = -\tau_{ij}^t = -\mu_t \left(\frac{\partial \widetilde{u}_i}{\partial x_j} + \frac{\partial \widetilde{u}_j}{\partial x_i} - \frac{2}{3} \frac{\partial \widetilde{u}_k}{\partial x_k} \delta_{ij} \right) + \frac{2}{3} \overline{\rho} k \delta_{ij}, \tag{2.62}$$

  where k is the kinetic energy of turbulence and μ_t is the turbulent dynamic viscosity.

- **Species turbulent fluxes $\overline{\rho} \widetilde{u_i'' Y_k''}$**: it is usually closed using a classical gradient assumption

$$\overline{\rho} \widetilde{u_i'' Y_k''} = -\frac{\mu_t}{Sc_{kt}} \frac{\partial \widetilde{Y}_k}{\partial x_i} = -\overline{\rho} D_k^t \frac{\partial \widetilde{Y}_k}{\partial x_i}, \tag{2.63}$$

  where Sc_{kt} is a turbulent Schmidt number and D_k^t is a turbulent diffusion coefficient for species k.

- **Turbulent fluxes of total energy**: using a gradient assumption we obtain

$$(\overline{\rho u_i e_t} - \overline{\rho}\widetilde{u}_i\widetilde{e}_t) - (\overline{\tau_{ji}u_j} - \overline{\tau_{ji}}\widetilde{u}_j) = -\lambda_t\frac{\partial\widetilde{T}}{\partial x_i} + \overline{\rho}\sum_{k=1}^{N_{sp}} D_k^t\widetilde{h}_k\frac{\partial\widetilde{Y}_k}{\partial x_i} + \tau_{ji}^t\widetilde{u}_i. \tag{2.64}$$

  The coefficient of turbulent thermal conductivity is estimated from the turbulent Prandtl number constant $\lambda_t = \frac{\mu_t C_\mu}{Pr_t}$.

- **Mean reaction rate $\overline{\dot{\omega}}_k$:** The most difficult task is to model the mean reaction rate. In the following section 2.6 this problem will be discussed in details. Here we mention a most simple approach, named quasi-laminar approach, to evaluate mean reaction rate. If we consider a reaction at an irreversible stage, we can write the rate of fuel consumption using the Arrhenius law:

$$F + sO \rightarrow (1+s)P, \tag{2.65}$$

  where F is a fuel and O is an oxidizer. The fuel mass reaction rate $\dot{\omega}_F$ is

$$\dot{\omega}_F = -A_1\rho^2 T^{\beta_1} Y_F Y_O \exp\left(-T_A/T\right), \tag{2.66}$$

  where A_1 is the pre-exponential constant and T_A the activation temperature. This expression, related to the rate of reaction, is difficult to average. The nonlinearity of the exponential term implies a significant error if one "distributes" the operator of the temperature averaging. Thus, the average reaction rate in the quasi-laminar approach is written

$$\overline{\dot{\omega}}_F = -A_1\overline{\rho^2}\widetilde{T}^{\beta_1}\widetilde{Y}_F\widetilde{Y}_O \exp\left(-T_A/\widetilde{T}\right) \tag{2.67}$$

  The approximated expression (2.67) is a very coarse approximation because even small fluctuations in the reaction region can cause important fluctuations of the chemical source.

2.4.4 Turbulence models

In the framework of RANS, the use of a turbulence model allows closing the Reynolds stresses and the turbulent dynamic viscosity [Pope2000]. The parameter μ_t is often obtained from algebraic equations (e.g. Prandtl mixing length model) which do not require any additional balance equation, one-equation closure (e.g. Prandtl-Kolmogorov), and two-equation closure (e.g. $k-\varepsilon$ model). The Reynolds stresses $\widetilde{u_i''u_j''}$ are also unclosed. Their closure may be done directly or by deriving balance equations for the Reynolds stresses. Classical turbulence models such $k-\varepsilon$, $k-\omega$ or $k-l$ are generally used. All of these are the first order models designed to calculate the turbulent viscosity using, e.g., a Boussinesq hypothesis. Recall that:

$$k = \frac{1}{2}\widetilde{u_i''u_i''}, \qquad \varepsilon = \nu_t\widetilde{\frac{\partial u_i''}{\partial x_j}\frac{\partial u_i''}{\partial x_j}} \qquad l = C_\varepsilon\frac{k^{3/2}}{\varepsilon}, \qquad \omega = \frac{\varepsilon}{k}. \tag{2.68}$$

where $\nu_t = C_\mu\frac{k^2}{\varepsilon}$, where $C_\mu = 0.09$, $C_\varepsilon = C_\mu^{3/4}$ are model constants obtained from the experiment. Transport equations of k and ε (l or ω) are then derived from the momentum conservation equation.

2.5 Large eddy simulation (LES)

The essential idea of the LES is that the spatial distribution of the grid nodes implicitly generates a scale separation, since scales smaller than a typical scale associated to the grid spacing cannot be captured. The LES problem makes several subranges of scales appearing:

- Resolved scales which are large enough to be accurately captured on the grid with a given numerical method;
- Unresolved scales which are too small to be represented on the computational grid.

Mathematically, scales are separated using a scale high-pass filter which is also a low-pass filter in a frequency. The filtering corresponds to a convolution product in physical space. In density constant flows, the resolved part $\overline{Q}(t,\boldsymbol{x})$ of a space-time variable $Q(t,\boldsymbol{x})$ is defined formally by the relation

$$\overline{Q}(t,\boldsymbol{x}) = \frac{1}{\Delta}\int_{-\infty}^{\infty}\int_{-\infty}^{\infty} G\left(t-t', \frac{\boldsymbol{x}-\boldsymbol{x'}}{\Delta}\right)(t',\boldsymbol{x'})dt'd\boldsymbol{x'} = G * Q, \tag{2.69}$$

where the convolution kernel G is characteristic of the used filter, and is associated with the cut-off scale in space and time, Δ and τ_{cut}, respectively. The non-resolved part of $Q(t,\boldsymbol{x})$, denoted $Q'(t,\boldsymbol{x})$ is defined as

$$Q'(t,\boldsymbol{x}) = Q(t,\boldsymbol{x}) - \overline{Q}(t,\boldsymbol{x}). \tag{2.70}$$

Frequently, for variable density flows a change of variables in which filtered variables are weighted by the density is used. This change of variables is written as

$$\overline{\rho Q} = \overline{\rho}\widetilde{Q}. \tag{2.71}$$

The operator $\widetilde{()}$ is linear but does not commute with the derivative operators neither in space nor in time in comparison with the Favre-averaged operator in the RANS approach.

2.5.1 Closure of the LES equations

The filtering Navier-Stokes equations read as eqs. (2.55) to (2.58). The closure should be added. The closure of the LES equations as the calculation of the turbulent viscosity differs from that of the RANS equations.

- **The averaged diffusive fluxes for species $\overline{\rho V_{k,i} Y_k}$ and total energy** $\overline{q}_i$ are exactly the same that in the RANS equations and given by eq. (2.60) and eq. (2.60). In the LES modeling the diffusion of the kinetic turbulent energy is neglected because the turbulent kinetic energy of subgrid is negligible in comparison with other terms in the eq. (2.57).
- **The Reynolds stress tensor** for the Favre-filtered momentum field is given by

$$(\overline{\rho u_i u_j} - \overline{\rho}\widetilde{u}_i\widetilde{u}_j) = -\left(\overline{\rho\widetilde{u}_i\widetilde{u}_j} - \overline{\rho}\widetilde{u}_i\widetilde{u}_j\right) - \left(\overline{\rho\widetilde{u}_i u''_j} - \overline{\rho}u''_i\widetilde{u}_j\right) - \overline{\rho u''_i u''_j}. \tag{2.72}$$

The first term in eq. (2.72) is the Leonard tensor, representing interactions among resolved scales; the second term is the Clark tensor, representing interactions between resolved and unresolved scales; and the last is the Reynolds tensor, which represents interactions among unresolved scales. The last two terms cannot be closed and thus should be modeled. By analogy with the molecular viscosity for the instantaneous equations, the Boussinesq hypothesis is used in order to explicit the turbulent stress tensor. In LES it presents also by eq. (2.62).

- **The turbulent viscosity** of a subgrid can be calculated with different models, for example, Smagorinsky-Lilly model [Smagorinsky1963], Wall-Adapting Local Eddy-Viscosity model, Germano dynamic model [GermanoPiomelli1991], [MoinSquires1991] and so on. For example, the Smagorinsky approach models the eddy viscosity as

$$\mu_t = \overline{\rho}(C_s\Delta)^2\sqrt{2\widetilde{S}_{ij}\widetilde{S}_{ij}}, \tag{2.73}$$

where Δ is the grid size and C_s is a Smagorinsky constant, usually equals to 0.18. $\boldsymbol{S}$ is a symmetric part of the filtered stress tensor of deformation, i.e.

$$\widetilde{S}_{ij} = \frac{1}{2}\left(\frac{\partial\widetilde{u}_j}{\partial x_i} + \frac{\partial\widetilde{u}_i}{\partial x_j}\right). \tag{2.74}$$

The turbulent energy is calculated as

$$k = \frac{2}{\sqrt{C_\mu}}(C_s\Delta)^2\widetilde{S}_{ij}\widetilde{S}_{ij}. \tag{2.75}$$

C_μ is a modeled constant.

2.6 General models of turbulent combustion

2.6.1 PDF approach

Probability density function (PDF) methods are well-suited for studying turbulent reacting flow problems, as they take into account the interaction between the chemistry and the turbulence. We present various PDF methods following the work of [Pope1994].

Eulerian PDFs

Let consider a set of N composition variables $\boldsymbol{\phi}(t,\boldsymbol{x})$, where $\boldsymbol{\phi} = (\phi_1, ..., \phi_N)$ which describe the flow. The joint PDF $f_{\boldsymbol{\phi}}(\boldsymbol{\Psi}; t, \boldsymbol{x})$ measures the probability of the random variable being in any specified interval. Here $\boldsymbol{\Psi} = (\Psi_1, ..., \Psi_N)$ denote the sample space variables. For example, for $\boldsymbol{\Psi}^* + \frac{\Delta\boldsymbol{\Psi}^*}{2} > \boldsymbol{\Psi}^* - \frac{\Delta\boldsymbol{\Psi}^*}{2}$, the probability that at given time and position, the quantities $\boldsymbol{\phi}(t,\boldsymbol{x})$ take values in the range $[\boldsymbol{\Psi}^* - \frac{\Delta\boldsymbol{\Psi}^*}{2}, \boldsymbol{\Psi}^* + \frac{\Delta\boldsymbol{\Psi}^*}{2}]$ is

$$Prob\left\{\boldsymbol{\Psi}^* - \frac{\Delta\boldsymbol{\Psi}^*}{2} \le \boldsymbol{\phi}(t,\boldsymbol{x}) \le \boldsymbol{\Psi}^* + \frac{\Delta\boldsymbol{\Psi}^*}{2}\right\} = \int\limits_{\boldsymbol{\Psi}^* - \frac{\Delta\boldsymbol{\Psi}^*}{2}}^{\boldsymbol{\Psi}^* + \frac{\Delta\boldsymbol{\Psi}^*}{2}} f_{\boldsymbol{\phi}}(\boldsymbol{\Psi}; t, \boldsymbol{x})d\boldsymbol{\Psi}. \tag{2.76}$$

Given that the reactive flows are usually characterized by a varying density, the quantities are often mass-weighed prior to averaging. Such the procedure is called Favre averaging. The corresponding PDF $\widetilde{f}_{\boldsymbol{\phi}}$ is defined by:

$$\widetilde{f}_{\boldsymbol{\phi}}(\boldsymbol{\Psi};t,\boldsymbol{x}) = \frac{\overline{\rho f_{\boldsymbol{\phi}}(\boldsymbol{\Psi};t,\boldsymbol{x})}}{\overline{\rho}}. \tag{2.77}$$

If $\boldsymbol{u}(t,\boldsymbol{x})$ is the Eulerian velocity of the fluid, we can introduce sample space velocity variables $\boldsymbol{V} = (V_1, V_2, V_3)$ and denote the one-time one-point Eulerian joint PDF of velocity by $f_{\boldsymbol{u}}(\boldsymbol{V};t,\boldsymbol{x})$. The velocity-composition joint PDF is $f_{\boldsymbol{u\phi}}(\boldsymbol{V},\boldsymbol{\Psi};t,\boldsymbol{x})$.

The PDF contains all the statistical information of the random variable at a given point of space and time. For example, if we consider the Favre joint composition PDF $\widetilde{f}_{\boldsymbol{\phi}}(\boldsymbol{\Psi};t,\boldsymbol{x})$, the Favre nth order moment of the quantity $Q(\boldsymbol{\phi})$ can be calculated as follows

$$\widetilde{Q^n}(\boldsymbol{\phi}) = \int_{-\infty}^{\infty} Q^n(\boldsymbol{\Psi})\, \widetilde{f}_{\boldsymbol{\phi}}(\boldsymbol{\Psi};t,\boldsymbol{x}) d\boldsymbol{\Psi}. \tag{2.78}$$

The fundamental interest of the Favre composition or velocity-composition joint PDF resides in an exact resolution of chemistry. The Favre-averaged source term is

$$\widetilde{\dot{\omega}}(t,\boldsymbol{x}) = \int \dot{\omega}(\boldsymbol{\Psi}) \widetilde{f}_{\boldsymbol{\phi}}(\boldsymbol{\Psi};t,\boldsymbol{x}) d\boldsymbol{\Psi}. \tag{2.79}$$

According to the definition given in [Pope1994], in a PDF method the probability density function in a turbulent flow is determined as the solution of a modeled evolution equation.

Presumed PDF

Strictly speaking, the presumed PDF methods are not PDF methods in the sense of the definition given above. It assumes that the PDF has a particular shape that is usually parameterized by its first and second moments and is not determined from a modeled evolution equation. The moments of presumed PDF are found from modeled transport equations. Different mathematical functions can be employed to model the shape of the scalar PDF (different profiles of PDF can be found for example in [WarnatzMaas2006]).

Uni-dimensional beta function First, one can employ uni-dimensional β function defined on the interval $[0,1]$ in order to write the PDF:

$$\widetilde{f}(\Psi;t,\boldsymbol{x}) = \frac{\Gamma(a+b)}{\Gamma(a)\Gamma(b)} \Psi^{a-1} |1-\Psi|^{b-1}, \tag{2.80}$$

where Γ function is defined by:

$$\Gamma(\alpha) = \int_0^{+\infty} s^{\alpha-1} e^{-s} ds,\ \alpha > 0. \tag{2.81}$$

The first two moments $\widetilde{\Psi}$ and $\widetilde{\Psi''^2}$ are expressed in terms of two parameters a and b:

$$\begin{cases} \widetilde{\Psi} = \dfrac{a}{a+b}, \\ \widetilde{\Psi''^2} = \dfrac{ab}{(a+b)^2(a+b+1)}. \end{cases}$$

By reversing these expressions, a and b can be expressed as function of moments of Ψ:

$$\begin{cases} a = \widetilde{\Psi}\left(\dfrac{\widetilde{\Psi}(1-\widetilde{\Psi})}{\widetilde{\Psi''^2}} - 1\right), \\ b = (1-\widetilde{\Psi})\left(\dfrac{\widetilde{\Psi}(1-\widetilde{\Psi})}{\widetilde{\Psi''^2}} - 1\right). \end{cases}$$

Thus, the form taken by the β-PDF is determined by the first two statistical moments. Assuming that the production rate of species k depends on Ψ and using the expression (2.80), the averaged production rate is

$$\widetilde{\dot{\omega}}_k(t,\boldsymbol{x}) = \int_{-\infty}^{+\infty} \dot{\omega}_k(\Psi)\widetilde{f}(\Psi)d\Psi = \int_{-\infty}^{+\infty} \dot{\omega}_k(\Psi)\frac{\Gamma(a+b)}{\Gamma(a)\Gamma(b)}\Psi(t,\boldsymbol{x})^{a-1}\left|1-\Psi(t,\boldsymbol{x})\right|^{b-1}. \tag{2.82}$$

Figure 2.8 presents the evolution of the β-PDF for variables a and b. When $\widetilde{\Psi''^2}$ tends to 0, the β-PDF tends to a single Dirac delta peak centered at $\widetilde{\Psi}$. On the other hand, when $\widetilde{\Psi''^2}$ approaches its maximum value, the β-PDF approaches a bimodal shape represented by two Dirac delta peaks localized at 0 and 1 (the latter limit is characterized by an infinitely thin flame front).

[Girimaji1991] extends one-dimensional β-PDF approach towards multidimensional β-functions. The latter enable the modelling of the joint PDF, such as for example PDF for the mixture fraction Z and the progress variable C [LandenfeldSadiki2002].

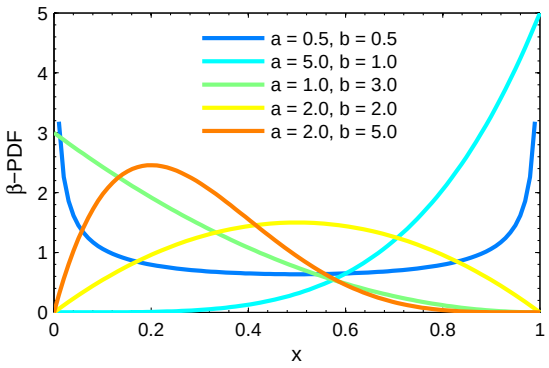

Figure 2.8: β-PDF for different parameters a and b, defined in eq. (2.80)

Truncated Gaussian function For a second approach, as an example, we can cite the truncated Gaussian function for analytical approximation to the one-dimensional PDFs. The analytical representation of this PDF is given by [Warnatz1984]

$$\widetilde{f}(\Psi; t, \boldsymbol{x}) = \alpha\delta(\Psi) + \beta\delta(1-\Psi) + \gamma \exp\left(-\frac{(\Psi-\zeta)^2}{2\sigma^2}\right). \tag{2.83}$$

Here ζ and σ characterize the position and the width of the Gaussian distribution, respectively, Ψ can be a progress variable c, a temperature T and so on. The normalization constant γ is obtained (for given α and β) from the relation

$$\gamma = \frac{(1-\alpha-\beta)\sqrt{\frac{2\sigma}{\pi}}}{erf\left(\frac{1-\zeta}{\sqrt{2\sigma}}\right) + erf\left(\frac{\zeta}{\sqrt{2\sigma}}\right)}, \tag{2.84}$$

where "erf" denotes the error function.

In conclusion, the β-function, Gaussian function and so on are an arbitrary choice for the presumed PDFs, which is difficult to justify with solid physical reasoning. The flexibility of the shape of a β function or a Gaussian function is not sufficient to justify its use, because PDF, calculated for a physical processes, often possess a shape very different from β and Gaussian PDFs and may not be successfully approximated by the latter. Consequently, the validity of any presumed PDF must be checked case by case. In addition, no account is taken of the influence of the dynamics (e.g. reaction) on the shape of the PDF. Another disadvantage is that presumed PDF methods are computationally more expensive for the general case of many compositions compared to the exact PDF methods.

Transported Eulerian PDF

The transported Eulerian PDF method consists of solving a model transport equation for the PDF: a velocity PDF, a composition PDF and a velocity-composition joint PDF for reacting ideal-gas mixtures. In Eulerian PDF methods, the quantities that have to be modeled are one-time one-point conditional expectations. It presents an effective resolution to the closure problems that arise from averaging or filtering chemical source terms, from modeling the effects of convection, body forces and the mean pressure gradient (details can be found for instance in [Haworth2010]). These terms appear exactly in the PDF transport equation and so do not have to be modeled.

As reviewed in [KuznetsovSabelnikov1986], the first attempt to obtain an equation for PDF in turbulent flow was performed by [Frost1960] when considering the turbulent combustion of a homogeneous mixture of combustible gases. An equation for the temperature PDF was derived in this work. A similar equation, this time entitled Langevin model, appeared later in [Chung1969]. Later, this approach was developed further by Kuznetsov and Frost [Frost1973; KuznetsovFrost1973; Frost1977].

Exact non-closed equations for n-point probability distribution densities of various fluid dynamic characteristics, obtained from the Navier-Stokes equation, were introduced into the theory of turbulence almost simultaneously by [Kuznetsov1967; Lundgren1967; Monin1967a; Monin1967b; Novikov1968; Ulinich1968; UlinichLyubimov1968]. Subsequently, the equations

for PDF were extended to the case of the Lagrangian motion description of a medium in [Lyubimov1969; LyubimovUlinich1970]. The general method of deriving the equations for PDF in an arbitrary continuum is given in [Ievlev1972; Fox1975; Ievlev1975; Hill1976]. These methods are also reviewed in [Hoffmeister1980; Sabelnikov1985; Sabelnikov1986; BorghiDestriau1995].

Joint velocity PDF

The first works are based on the solution of a modeled transport equation for the joint PDF of the velocity components $\overline{f}_{\boldsymbol{u}}$ (e.g. [Lundgren1969]). The obtained $\overline{f}_{\boldsymbol{u}}$ allows having statistics about velocity fields and in particular, Reynolds stresses. However, despite the statistical description of the velocity in the turbulent flow this PDF does not give a sufficiently detailed description of underlying physics.

Joint scalars PDF

Later, a modeled equation for the PDF of a set of scalar variables $\boldsymbol{\phi} = (Y_1, .., Y_{N_{sp}}, h_t)$ (e.g. mass fractions and enthalpy) was considered. It describes the thermochemical state of a reacting medium (a composition joint PDF $\overline{f}_{\boldsymbol{\phi}}$) to model mixing and chemical reaction. In this approach any complicated reactions can be treated exactly. There were many researchers [JanickaKolbe1978; Pope1981; Bradbury1982; GiviSirignano1984; NguyenPope1984; Soulard2005; Ourliac2009] who demonstrated the ability of $\overline{f}_{\boldsymbol{\phi}}$ to handle nonlinear reactions.

The transport equation for the Favre averaging PDF of $\widetilde{f}_{\boldsymbol{\phi}}$ governing the one-point statistics of a turbulent reactive scalars $\boldsymbol{\phi}$ is as follows [Pope1985]:

$$\frac{\partial \overline{\rho}\widetilde{f}_{\boldsymbol{\phi}}}{\partial t}+\frac{\partial}{\partial x_j}(\overline{\rho}\widetilde{u}_j\widetilde{f}_{\boldsymbol{\phi}}) = -\frac{\partial}{\partial x_j}\left(\overline{\rho}\langle u_j''|\boldsymbol{\Psi}\rangle\widetilde{f}_{\boldsymbol{\phi}}\right)-\frac{\partial}{\partial \Psi_\alpha}\left(\overline{\rho}\left\langle -\frac{\partial}{\partial x_j}D_\alpha\frac{\partial \boldsymbol{\phi}_\alpha}{\partial x_j}|\boldsymbol{\Psi}\right\rangle\widetilde{f}_{\boldsymbol{\phi}}\right)-\frac{\partial}{\partial \Psi_\alpha}\left(\overline{\rho}S_\alpha(\boldsymbol{\Psi})\widetilde{f}_{\boldsymbol{\phi}}\right). \tag{2.85}$$

Here, $\alpha = 1, .., N_{sp}+1$, $\langle\ |\boldsymbol{\Psi}\rangle$ is a conditional mean given scalars variables $\boldsymbol{\Psi}$ from scalar space. S_α is a chemical source term for species α. The first term on the left-hand side (LHS) of the eq. (2.85) is the temporal change of $\overline{\rho}\widetilde{f}_{\boldsymbol{\phi}}$. The second term on the LHS represents the advection of $\widetilde{f}_{\boldsymbol{\phi}}$ in the physical space by the Favre-averaged velocity. The first term on the right-hand side (RHS) of the equation (2.85) is the turbulent advection, which is the transport by the fluctuating velocity in physical space. The second term on the right represents the effects of molecular mixing, it is called "micro-mixing term". The last term is the chemical source.

The turbulent advection term is modeled with a gradient diffusion hypothesis with coefficient Γ_t:

$$\langle u_j''|\boldsymbol{\Psi}\rangle\widetilde{f}_{\boldsymbol{\phi}} = -\Gamma_t\frac{\partial \widetilde{f}_{\boldsymbol{\phi}}}{\partial x_j} \tag{2.86}$$

with $\Gamma_t = \frac{\nu_t}{\sigma_t}$, σ_t is a turbulent Schmidt number for the mass fraction components of $\widetilde{f}_{\boldsymbol{\phi}}$, and turbulent Prandtl number for the last component of $\widetilde{f}_{\boldsymbol{\phi}}$, which is in fact the total enthalpy.

The micromixing is usually modeled using the Interaction by Exchange with the Mean model [VillermauxDevillon1972]:

$$\left\langle -\frac{\partial}{\partial x_j}D_\alpha\frac{\partial \boldsymbol{\phi}_\alpha}{\partial x_j}|\boldsymbol{\Psi}\right\rangle\widetilde{f}_{\boldsymbol{\phi}} = -\omega_{\boldsymbol{\phi}}\left(\Psi_\alpha - \widetilde{\boldsymbol{\phi}}_\alpha\right)\widetilde{f}_{\boldsymbol{\phi}} \tag{2.87}$$

with $\omega_{\boldsymbol{\phi}}$ is a characteristic pulsation of the small scales of turbulence. In the end, we obtain the following equation:

$$\frac{\partial \overline{\rho}\widetilde{f}_{\boldsymbol{\phi}}}{\partial t} + \frac{\partial}{\partial x_j}\left(\overline{\rho}\widetilde{u}_j \widetilde{f}_{\boldsymbol{\phi}}\right) = \frac{\partial}{\partial x_j}\left(\overline{\rho}\Gamma_t \frac{\partial \widetilde{f}_{\boldsymbol{\phi}}}{\partial x_j}\right) + \frac{\partial}{\partial \Psi_\alpha}\left(\overline{\rho}\omega_{\boldsymbol{\phi}}\left(\Psi_\alpha - \widetilde{\boldsymbol{\phi}}_\alpha\right)\widetilde{f}_{\boldsymbol{\phi}}\right) - \frac{\partial}{\partial \Psi_\alpha}\left(\overline{\rho}S_\alpha(\boldsymbol{\Psi})\widetilde{f}_{\boldsymbol{\phi}}\right). \tag{2.88}$$

For the inhomogeneous three dimensional flows, analytical solution to the PDF transport equation (2.88) does not exist, so numerical methods are required. Standard techniques such as finite differences are severely limited because of the large dimensionality of the joint PDF $\widetilde{f}_{\boldsymbol{\phi}}$. They cannot be employed as their cost increases exponentially with dimensionality. Monte Carlo methods, on the other hand, yield a linearly growing effort and are more adapted to solve the PDF equations, but in the same time they are less accurate than the latter one. In the field of the numerical turbulent combustion, LMC methods [Pope1985] have become an essential component of the PDF approach since the 1980's. LMC methods are based on stochastic particles, which evolve from prescribed SODEs. The particles are randomly distributed in the computational domain and are associated with the cell they are located in at a given instant of time. They are used to compute the one-point statistics of the quantities describing the state of a turbulent reactive flow. Due to the statistical nature of the method, computed mean fields have inherent noise. The error scales as $N_p^{-1/2}$ for a domain with N_p particles, which increases the computational expense hyperlinearly. Numerous publications document algorithms, convergence and accuracy of LMC methods [MuradogluJenny1999; Pope2000; MuradogluPope2001; ViswanathanWang2011].

However, LMC methods have inherent difficulties for controlling statistical convergence. In particular, the sampling error is not always controlled with precision, as it depends on the particle distribution in the physical domain. Furthermore, to improve convergence rates, it is often necessary to couple the LMC method to an Eulerian RANS (LES) solver [JennyPope2001; RemboldJenny2006; WangPope2008]; this can quickly result in a heavy tool to manipulate, due to the different nature (Lagrangian/Eulerian) of the solvers. All of the mentioned shortcomings arise from the Lagrangian nature of the LMC method.

Contrariwise, Eulerian Monte Carlo (EMC) methods are based on stochastic Eulerian fields that evolve from stochastic partial differential equations (SPDEs). EMC methods have been extensively used in several domains [WernerDrummond1997; OsnesLangtangen1998]. However, their application to the simulation of turbulent reactive flows only seems to be dating back from the work by Valino [Valiño1998]. Valino derives the SPDEs statistical equivalent to the joint composition PDF with several restrictive hypotheses: the stochastic fields are required to be smooth and twice differentiable in space. V. Sabelnikov and O. Soulard [SabelnikovSoulard2005; SabelnikovSoulard2006] developed a new path to derive the SPDEs for solving equations of the PDF in the context of the EMC methods. The principal idea is based on the rapidly decorrelating velocity field model first proposed in [Kazantsev1968; Kraichnan2003]. The Kraichnan-Kazantsev model describes the advection of a scalar by a solenoidal white-in-time Gaussian velocity field and leads to a Fokker-Planck composition PDF equation with a diffusion term in physical space. V. Sabelnikov and O. Soulard established the connection between the LMC and the EMC methods for the general case of compressible, inhomogeneous, low-Mach-number turbulent flame with molecular diffusion effects.

The RANS/EMC solver was validated against experimental data taken from [Magre-Moreau1988] on a configuration consisting in the turbulent combustion of a premixed stoichiometric methane-air mixture [Soulard2005; Ourliac2009]. The flame was stabilized by a recirculation zone in a plane channel with a sudden expansion (backward facing step). It was also successfully applied to the ignition by a laser of a chamber filled by a co-axial $H_2 - O_2$ injector [Ourliac2009]. The RANS/EMC solver was implemented into CEDRE software platform developed at ONERA. It was validated in terms of convergence and statistical precision over the cited above configurations.

Let us briefly recall the system of the SPDEs statistically equivalent to the transport equation of the Favre joint PDF of mass fractions and total enthalpy. Details with proof of statements can be found in [SoulardSabelnikov2006]. The system of conservative SPDEs is written as follows

$$\frac{\partial rY_k}{\partial t} + \frac{\partial \left((\widetilde{u}_j + u_j'') \circ rY_k \right)}{\partial x_j} = -r\omega(Y_k - \widetilde{Y}_k) + rS_k(\boldsymbol{Y}, T),\ k = 1, .., N_{sp}, \tag{2.89}$$

$$\frac{\partial rh_t}{\partial t} + \frac{\partial \left((\widetilde{u}_j + u_j'') \circ rh_t \right)}{\partial x_j} = -r\omega(h_t - \widetilde{h}_t) + \frac{\partial \overline{P}}{\partial t}, \tag{2.90}$$

$$u_j'' = -\Gamma_t \frac{1}{\overline{\rho}} \frac{\partial \overline{\rho}}{\partial x_j} + \frac{1}{2} \frac{\partial \Gamma_t}{\partial x_j} + \sqrt{2\Gamma_t}\dot{\xi}_j,\ j = 1, .., 3, \tag{2.91}$$

where $r(t, \boldsymbol{x})$ is the stochastic density which is different from the physical density $\rho(t, \boldsymbol{x})$, ω is a mean turbulent frequency. $\circ$ is a symbol in the Stratonovich interpretation. The velocity contains the stochastic term $\sqrt{2\Gamma_t}\dot{\xi}$, which represents the derivative of a Brownian motion: it is not differentiable in the sense of classical functions since infinite, which in the numerical calculation results in overly high velocities.

The statistical equivalence between the stochastic fields and the model Reynolds and Favre PDFs from eq. (2.88) is achieved by making use the stochastic density $r(t, \boldsymbol{x})$. To explicit this equivalence, we introduce the average operator $\langle\ \rangle_s$ of a stochastic quantity Q as

$$\langle Q \rangle_S = \frac{1}{N_r} \sum_{irea=1}^{N_r} Q_{irea}(t, \boldsymbol{x}), \tag{2.92}$$

where N_r is a number of stochastic fields. The Favre-averaged stochastic quantity Q, noted as $\langle Q \rangle_r$, is

$$\langle Q \rangle_r = \frac{\langle rQ \rangle_S}{\langle r \rangle_S}. \tag{2.93}$$

The corresponding unweighted f_s and weighted f_r PDFs are related by

$$f_r(\boldsymbol{u''}, \boldsymbol{Y}, h_t; t, \boldsymbol{x}) = \frac{\langle r(t, \boldsymbol{x}) | \boldsymbol{u''}, \boldsymbol{Y}, h_t \rangle_S}{\langle r(t, \boldsymbol{x}) \rangle_S} f_S(\boldsymbol{u''}, \boldsymbol{Y}, h_t; t, x). \tag{2.94}$$

If the following consistency condition is verified

$$\langle r(t, \boldsymbol{x}) \rangle_S = \frac{1}{N_r} \sum_{irea=1}^{N_r} r_{irea}(t, \boldsymbol{x}) \underset{N_r \to +\infty}{\to} \overline{\rho}(t, \boldsymbol{x}), \tag{2.95}$$

and initial and boundary conditions are the same for the Favre joint fluctuating velocity-composition PDF $\widetilde{f}_{\boldsymbol{u''},\boldsymbol{Y},h_t}$ and the Favre stochastic PDF f_r, then their transport equations are identical.

$$f_r \underset{N_r\to+\infty}{\to} \widetilde{f}_{\boldsymbol{u''},\boldsymbol{\phi}}, \qquad \langle Q\rangle_r \underset{N_r\to+\infty}{\to} \widetilde{Q}. \tag{2.96}$$

It should be noted that we use the same notation for stochastic fields of velocity $\boldsymbol{u''}$, mass fractions $\boldsymbol{Y}$ and total enthalpy h_t in SPDEs and Eulerian variables in PDF equation.

Equations (2.89) and (2.90) are hyperbolic differential equations. They can be solved by any hyperbolic scheme in space like Godunov, Lax-Wendroff or Lax-Friedrich scheme, other examples can be found in [Toro1999], and a special stochastic scheme in time [BurrageBurrage1996] because of the Stratonovich interpretation of them. According to the analytical results of V. Sabelnikov and O. Soulard any proposed numerical scheme is stable if and only if

$$\frac{|du_j|}{\Delta x_j} < 1.$$

Since the velocity du_j is proportional to $\sqrt{\Delta t}$, the stability condition reads

$$\Delta t < \frac{\Delta x_j^2}{2\Gamma_t}. \tag{2.97}$$

The dependence of Δt in Δx_j^2, due to the diffusive nature of the Brownian motion, plays a negative role for fine meshes. Thus it is advisable to return to a time step with a conventional Courant-Friedrichs-Lewy (CFL) condition. Other inconvenience of the composition PDF equation (which is true for both LMC and EMC techniques) that it overcomes only the closure problem of nonlinear chemical terms and it does not address to the problem of the turbulent flow field. That is why it is important to consider the joint velocity-composition PDF $f_{\boldsymbol{u},\boldsymbol{\phi}}$.

Joint velocity-scalars PDF

Let us introduce the Favre joint velocity-composition PDF $\widetilde{f}_{\boldsymbol{u},\boldsymbol{\phi}}(\boldsymbol{V},\boldsymbol{\Psi};t,\boldsymbol{x})$, where $\boldsymbol{V}$ and $\boldsymbol{\Psi}$ are independent variables from the velocity space and composition space. It allows finding all one-point statistics of velocity $\boldsymbol{u}$ and compositions $\boldsymbol{\phi}$. For example, in the framework of the RANS, the mean velocity, the Reynolds stresses, the flux of velocity and scalar fluctuations and finally chemical source are treated exactly. We will work not only with statistics of the velocity, but also with those of its fluctuations:

$$\boldsymbol{u''} = \boldsymbol{u} - \widetilde{\boldsymbol{u}}. \tag{2.98}$$

Let be $\widetilde{g}_{\boldsymbol{u''\phi}}(\boldsymbol{V''},\boldsymbol{\phi};t,\boldsymbol{x})$ - the Favre joint fluctuating velocity $\boldsymbol{u''}(t,\boldsymbol{x})$ - composition $\boldsymbol{\phi}(t,\boldsymbol{x})$ PDF in the turbulent reactive gas flows (here $\boldsymbol{V''}$ is the fluctuating velocity space). This PDF is related with the Favre joint velocity-composition PDF and with the Reynolds PDF as:

$$\widetilde{g}_{\boldsymbol{u''},\boldsymbol{\phi}}(\boldsymbol{V''},\boldsymbol{\Psi};t,\boldsymbol{x}) = \widetilde{f}_{\widetilde{\boldsymbol{u}}+\boldsymbol{u''},\boldsymbol{\phi}}(\widetilde{\boldsymbol{V}}+\boldsymbol{V''},\boldsymbol{\Psi};t,\boldsymbol{x}) = \widetilde{f}_{\boldsymbol{u\phi}}(\boldsymbol{V},\boldsymbol{\Psi};t,\boldsymbol{x}) = \frac{\langle\rho|\boldsymbol{V},\boldsymbol{\Psi}\rangle}{\overline{\rho}}\overline{f}_{\boldsymbol{u\phi}}(\boldsymbol{V},\boldsymbol{\Psi};t,\boldsymbol{x}), \tag{2.99}$$

where $\langle\ |\boldsymbol{V},\boldsymbol{\Psi}\rangle$ is a conditional mean. Pope and his colleagues propose to model the evolution equation for $\widetilde{g} = \widetilde{g}_{\boldsymbol{u''\phi}}$ as follows [Pope2000]:

$$\frac{\partial \overline{\rho}\widetilde{g}}{\partial t} + \frac{\partial}{\partial x_j}\left(\overline{\rho}\left(\widetilde{u}_j + V_j''\right)\widetilde{g}\right) =$$

$$-\frac{\partial}{\partial V_j''}\left(\frac{\partial}{\partial x_k}\left(\overline{\rho}\widetilde{u_j''u_k''}\right)\widetilde{g}\right) + \frac{\partial}{\partial V_j''}\left(\overline{\rho}\left(-C_1\omega + \frac{\partial \widetilde{u}_k}{\partial x_k}\right)V_j''\widetilde{g}\right)$$

$$+\frac{1}{2}\overline{\rho}C_0\varepsilon\frac{\partial^2\widetilde{g}}{\partial V_j''\partial V_j''} + \frac{\partial}{\partial \Psi_\alpha}\left(\overline{\rho}C_{\boldsymbol{\phi}}\omega(\Psi_\alpha - \widetilde{\boldsymbol{\phi}}_\alpha)\widetilde{g}\right) - \frac{\partial}{\partial \Psi_\alpha}\left(\overline{\rho}S_\alpha(\boldsymbol{\Psi})\widetilde{g}\right);\ j,k = 1,..,3. \quad (2.100)$$

In this equation ε is the mean turbulent energy dissipation rate, ω is the mean turbulent frequency, C_0, C_1 and $C_{\boldsymbol{\phi}}$ are model constants.

The LHS of eq. (2.100) represents the temporal change and the advection of $\widetilde{g}$ by the total velocity. The first term on the RHS is the Reynolds stress tensor. The second is the sum of the generalized Langevin model (GLM) [HaworthPope1986] which is used to model the influence of molecular velocity diffusion and fluctuating pressure and the term of turbulence production. The third term has its origin in the stochastic force, the fourth term describes the effects of molecular mixing of the scalar $\boldsymbol{\phi}(t,\boldsymbol{x})$, and the last - the effects of chemical reaction. Chemical reactions are treated exactly and do not require any particular model. The eq. (2.100) need be completed by the mean continuity equation and the momentum equation. As well as for the joint composition PDF $f_{\boldsymbol{\phi}}$, the finite differences are not useful to solve the eq. (2.100) because of their high computational cost. The classical methods are replaced by Monte Carlo Methods such as LMC and EMC techniques.

There are many works which validated the RANS (LES)/LMC methods or the stand-alone LMC method for the joint velocity (fluctuation of the velocity)-composition PDF. For example one can cite works of Pope and his colleagues. RANS/LMC method was applied to an axisymmetric non-premixed piloted jet methane-air flame [MuradogluPope2001] studied experimentally by [MasriDibble1996]. Results were shown to be in good agreement with available experimental data. The stand-alone particle method was used to calculate a bluff-body stabilized flow [JennyPope2001]. [WangPope2008] investigated the hybrid solver on calculations of the Sandia piloted flame E [BarlowFrank1998] and on the Cabra H_2/N_2 lifted flame [CabraMyhrvold2002].

Following [SoulardSabelnikov2006] let us present the conservative form of the SPDEs statistically equivalent to the equation of the Favre joint fluctuating velocity-turbulent scalars PDF. The evolution equation for stochastic fluctuating velocity is given by (2.101). Equation (2.102) represents the equation for stochastic mass fractions and eq. (2.103) is the equation for stochastic total enthalpy.

$$\frac{\partial r u_i''}{\partial t} + \frac{\partial r(\widetilde{u}_k + u_k'')u_i''}{\partial x_k} = \frac{r}{\overline{\rho}}\frac{\partial \overline{r u_k'' u_i''}}{\partial x_k} - rC_1\omega u_i'' - \frac{\partial \widetilde{u}_i}{\partial x_k} r u_k''$$

$$+ r\sqrt{C_0\varepsilon}\dot{\xi}_i(t);\ k,i = 1,..,3. \quad (2.101)$$

$$\frac{\partial r Y_j}{\partial t} + \frac{\partial r\left(\widetilde{u}_k + u_k''\right)Y_j}{\partial x_k} = -rC_Y\omega\left(Y_j - \widetilde{Y}_j\right) + rS_j(\boldsymbol{Y},T); j = 1,..,N_{sp}. \quad (2.102)$$

$$\frac{\partial r h_t}{\partial t} + \frac{\partial r\left(\widetilde{u}_k + u_k''\right)h_t}{\partial x_k} = -rC_h\omega\left(h_t - \widetilde{h}_t\right) + \frac{r}{\rho}\frac{\partial \overline{P}}{\partial t}. \quad (2.103)$$

Here, r is a stochastic density (different from the physical density, i.e. $r \neq \rho$), T_L is a characteristic time of turbulence, $\dot{\xi}_i$ are time derivatives of standard independent Wiener noises, Y_j are stochastic mass fractions, h_t is a stochastic total enthalpy, $\boldsymbol{u}''$ is a stochastic velocity. C_h, C_Y and C_0 are model constants. Mean pressure is defined by the eq. (2.106).

As for the SPDEs statistically equivalent to the joint composition PDF equation, this set of SPDEs is statistically equivalent to PDF eq. (2.100), if the stochastic density $r(t, \boldsymbol{x})$ is used. The equivalence is achieved if following two consistency conditions are verified

$$\langle r \rangle_S \underset{N_r \to +\infty}{\to} \overline{\rho}, \qquad \left\langle \frac{r}{\rho} \right\rangle_S \underset{N_r \to +\infty}{\to} 1. \tag{2.104}$$

The first condition guarantees consistency at the level of Favre statistics, while the second guarantees consistency at the level of Reynolds statistics. To ensure the first condition, it is sufficient to take the same initial and boundary conditions for $\langle r \rangle_s$ and $\overline{\rho}$. The second condition is unconditionally verified by the definition of the physical density

$$\rho = \frac{P}{R^0 T \sum\limits_{k=1}^{N_{sp}} \frac{Y_k}{W_k}}. \tag{2.105}$$

As a consequence, the mean pressure can be found by

$$\left\langle r R^0 T \sum_{k=1}^{N_{sp}} \frac{Y_k}{W_k} \right\rangle_S \underset{N_r \to +\infty}{\to} \overline{P}. \tag{2.106}$$

The transport equation for fluctuating velocity $\boldsymbol{u''}(t, \boldsymbol{x})$ is a Langevin equation. It introduces the differentiable noise instead of non-differentiable white noise. As a result, the stochastic velocity yielded by the Langevin equation tends to finite values and the time step Δt is proportional to Δx. This is the main advantage of stochastic equations in comparison with the SPDEs (2.89) - (2.91) which are statistically equivalent to the joint composition PDF equation. In order to solve the SPDEs (2.101) - (2.103), V. Sabelnikov and O. Soulard considered classical spatial schemes which satisfy the entropy increase condition and validated the proposed numerical schemes in 1D case [SoulardSabelnikov2006]. But in fact, as we will see in section 3.1, these schemes are not suitable in finding solutions of the SPDEs which are statistically equivalent to the joint velocity-scalars PDF equation. The SPDEs (2.101) - (2.103) have the following properties:

- The SPDEs can have the multivalued solutions. Only the multivalued solutions are statistically equivalent to the solutions of the PDF equation.
- There is no pressure term. The SPDEs are similar to equations of pressureless gas dynamics for which vacuum states and delta - shocks are present.

The resolution of the SPDEs (2.101)-(2.103) represents a challenge for numerical mathematics. It exists only level set methods in computation of multivalued solutions (see for instance [LiuOsher2006]), which rely on a local increase in problem dimensionality. In the present work we are interested in resolution of the SPDEs (2.101) - (2.103) without increasing their dimensionality. We propose efficient numerical schemes for their resolution in statistical sense and validate them in one-dimensional case. The details are given in appendix A.

2.6.2 Partially stirred reactor models

Eddy dissipation concept

The eddy dissipation concept (EDC) gives an empirical expression for the mean reaction rate based on the assumption that chemical reactions occur in the regions where the dissipation of the turbulence energy takes places. Each computational cell is divided into two subzones: the reacting "fine structure" and "the surrounding fluid" as shown in fig. 2.9. In the mode expressions, subscripts $()^*$ and $()^0$ refer to the fine structures and surrounding fluid respectively. Micromixture areas are treated as adiabatic, isobaric, perfectly stirred reactors (PSRs), where the chemical source terms are potentially high due to favorable mixing of final products with fresh reactants in the volume. The surrounding regions are chemically inert. According to the EDC, the reaction rates of all species can be calculated using only variables of the fine structure regions $\boldsymbol{\psi^*} = [\boldsymbol{Y^*}, T^*]^T$, where $\boldsymbol{Y^*} = (Y_1^*, ..., Y_{N_{sp}}^*)$ is a mass fractions vector and T^* is a temperature in the fine structure region. As

$$\widetilde{\boldsymbol{\psi}}_k = \gamma^* \boldsymbol{\psi^*} + (1 - \gamma^*)\boldsymbol{\psi^0}, \tag{2.107}$$

therefore

$$\overline{\dot{\omega}}_k \approx \gamma^* \dot{\omega}_k(\boldsymbol{\psi^*}) + (1 - \gamma^*)\dot{\omega}_k(\boldsymbol{\psi^0}) \approx \gamma^* \dot{\omega}_k(\boldsymbol{\psi^*}), \tag{2.108}$$

where γ^* is the volume fraction of each calculation cell wherein the process is conducted on a small scale mixing.

The assumption of quasi-equilibrium between micromixing and chemical production, which supposes the equilibrium of the mass transfer between two regions: the fine structure region and its surrounding, allows writing the algebraic relation between the mean chemical source and the mean mass fraction:

$$\frac{\overline{\rho}}{\tau^*}\left(Y_k^* - Y_k^0\right) = \dot{\omega}_k(T^*, \boldsymbol{Y^*}) \tag{2.109}$$

and the energy conservation is given by

$$\frac{\overline{\rho}}{\tau^*}\sum_{k=1}^{N_{sp}}\left(Y_k^* h_k^* - Y_k^0 h_k^0\right) = \sum_{k=1}^{N_{sp}} h_{k,f}^{\theta}\dot{\omega}_k\left(T^*, \boldsymbol{Y^*}\right), \tag{2.110}$$

in which τ^* is the micromixing time during which the variable Y_k^* is reached from Y_k^0 by action of the applied chemical reaction mechanism, h_k is the enthalpy and h_k^{θ} is the enthalpy of the formation of the species k.

If $\gamma^* < 1$ it is possible to exclude $\boldsymbol{Y^0}$, T^0 from eqs. (2.109) and (2.110) with aid of eq. (2.107). The eqs. (2.109) and (2.110) become

$$\frac{\overline{\rho}}{\tau^*(1 - \gamma^*)}\left(Y_k^* - \widetilde{Y}_k\right) = \dot{\omega}_k(T^*, \boldsymbol{Y^*}) \tag{2.111}$$

and

$$\frac{\overline{\rho}}{\tau^*(1 - \gamma^*)}\sum_{k=1}^{N_{sp}}\left(Y_k^* h_k^*(T^*) - \widetilde{Y}_k\widetilde{h}_k(\widetilde{T})\right) = \sum_{k=1}^{N_{sp}} h_{k,f}^{\theta}\dot{\omega}_k\left(T^*, \boldsymbol{Y^*}\right). \tag{2.112}$$

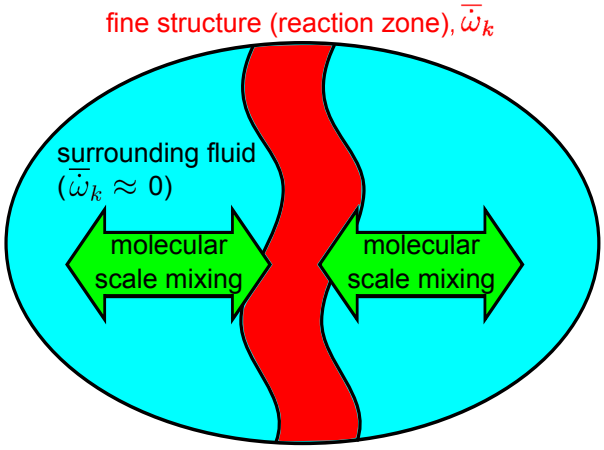

Figure 2.9: Schematic computation cell based on EDC model [Magnussen1981]

Different expressions are proposed in the literature for the micromixing time and the volume fraction. One of them states that the volume fraction of the fine structure is [Magnussen1981]:

$$\gamma^* = \gamma^3 \chi = 2.13^3 \left(\nu^* \varepsilon / k\right)^{3/4} \chi, \tag{2.113}$$

where χ is a parameter that expresses the probability that the conditions are suitable for reactions to occur in the fine structures, and ν^* represents the kinetic viscosity in the fine structures. Within [Magnussen1981] approach, the mass exchange between the fine structure is $\frac{\gamma^{*3}\chi}{\tau^*}$ with the time scale for the mass transferring between the fine structure and the surroundings

$$\tau^* = 0.41 \sqrt{\frac{\nu^*}{\varepsilon}}. \tag{2.114}$$

Furthermore, Magnussen [Magnussen1981; Magnussen2005] assumed that only a χ part of sheet-formed structures filled the necessary conditions for combustion.

Alternatively, the definition for the mass exchange between the fine structure and surroundings used in [GranMagnussen1996; MagelSchnell1996] is $\frac{\gamma^{*2}\chi}{\tau^*}$.

Works of Batchelor and Townsend show that at high Reynolds number, the turbulent fine structures responsible for mixing phenomena and small-scale dissipation are concentrated in isolated regions [BatchelorTownsend1949]. The velocity gradients (in the case of nonreactive flows) are intermittent. The fine structures, which are composed mainly of the fine scale turbulence, are distributed non-uniformly.

Chomiak proposes a hypothesis that the chemical reactions take place mainly in these dissipative and mixed at the molecular level zones [Chomiak1970]. Based on this assumption, he describes a possible mechanism of propagation of premixed flame at high Reynolds number.

Kuo and Corrsin [KuoCorrsin1971; KuoCorrsin1972] further suggest the mechanisms of vortices stretching and show that these intermittent fine structures are topologically complex and may appear as vortex sheets, ribbons and tubes folded in specific regions of the flow. They also associate γ^* to the intermittency factor γ, which corresponds to the probability to have turbulent flow at a given time-space point.

The recent direct simulations of combustion [WoodwardPorter2000; TanahashiSato2008], have numerically confirmed this flow structure, specifically that

- Vortex tubes of high intensity are indeed concentrated into filaments, immersed in sheets of low-intensity vorticity
- Volume of such the fine structures is small
- This volume is inversely proportional to the Reynolds number

Kuo and Corrsin show that the fraction of fine structures in a volume Δ^3 of sheet-like structures, as well as in a surface Δ^2 and the characteristic thickness of Kolmogorov scale η_K is estimated by [KuoCorrsin1972]:

$$\gamma_S^* \approx \frac{\eta_K \Delta^2}{\Delta^3 + \eta_K \Delta^2} \approx \frac{\eta_K}{\Delta + \eta_K} \approx Re_\Delta^{-3/4} \tag{2.115}$$

given that $\eta_K = \Delta Re_\Delta^{-3/4}$, and $Re_\Delta^{-3/4} = u'\Delta/\nu$. In eq. (2.115), S refers to the sheet-like form adopted by thin structures.

Tennekes considers tube-like fine structures, with length comparable to Taylor scale l_T and diameter on the order of magnitude of the Kolmogorov scale η_K [Tennekes2003]. In this case, the fraction of fine structure is estimated as:

$$\delta_T \approx \frac{(\eta_K^2 l_T)(\Delta/l_T)^3}{\Delta^3} \approx \frac{\eta_K}{\Delta + \eta_K} \approx \frac{\eta_K}{\Delta} \approx Re_\Delta^{-3/4}, \tag{2.116}$$

where the subscript T refers to tube like shape.

Figure 2.10 shows results in terms of vorticity and heat-release structures from DNS of planar flame propagation in homogeneous isotropic turbulence. This direct simulation confirms that structures of both forms coexist.

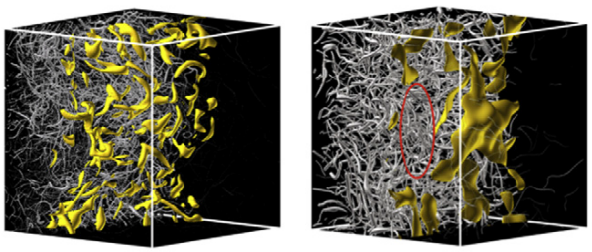

Figure 2.10: Results from recent DNS of combustion at moderate Re_t and Da numbers from [TanahashiSato2008]. Figures show iso-surfaces of the heat-release (yellow) and vorticity (gray) from a planar flame in homogeneous isotropic turbulence at $Re_t \approx 515$ and 141, $Da \approx 21$ and 5, and $Ka \approx 1.3$ and 2.8, respectively.

Partially stirred reactor model

The difference between the EDC and the partially stirred reactor (PaSR) combustion models consists in the choice of the reacting volume fraction and the residence time τ^*. Among

different choices of the reacting volume fraction we mention here the following one [Vulis1950]:

$$\gamma^* = \frac{\tau_{ch}}{\tau_{ch} + \tau^*}, \tag{2.117}$$

where τ_{ch} is the characteristic chemical time. The same notations and the formulas (2.111) and (2.112) are used. It is well-known that the solution of the algebraic equations (2.111) and (2.112) is in general not unique. It raises some problems when applying the EDC or the PaSR combustion models.

For more clarity let us consider just one equation for the temperature T, namely $h = C_p T$, $N = 1$. Then the RHS of the eq. (2.112) can be seen as a heat generation term. The LHS can be considered as a heat transfer term that represents how much energy leaves the reactor per unit time. The two terms schematically are shown in figs. 2.11 and 2.12. Curve HR presents the RHS of the eq. (2.112) and is the heat generation. It starts at practically negligible values at low temperatures, peaks close to the adiabatic flame temperature, and drops to zero at T_b, because at least one of the reactants mass fractions becomes zero there. It is very important to note that the peak occurs close to T_b, but is not situated exactly at the latter. Curve HR is determined by the nature of the fuel, the inlet conditions, and the pressure.

The LHS of the eq. (2.112) is a straight line with slope equal to

$$\frac{1}{\tau_{res}} = \frac{1}{\tau^*(1-\gamma^*)}, \quad \tau_{res} = \tau^*(1-\gamma^*), \tag{2.118}$$

i.e. it is steep when the residence time τ_{res} is short. Such lines are drawn as HT_{high} to HT_{low} in fig. 2.11 or as HT in fig. 2.12. The reactor will operate at the intersection of such a line with curve HR. Let us describe the various possibilities.

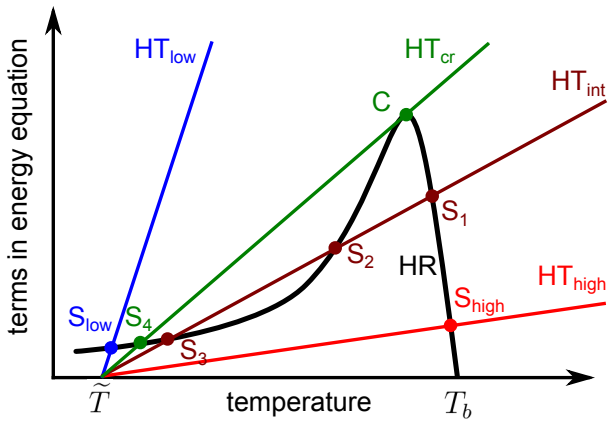

Figure 2.11: The dependence of the rates of heat release HR and of heat loses HT_{low}, HT_{cr}, HT_{int} and HT_{high} on the temperature for various heat transfer conditions

1. Long residence time τ_{res}
   This situation is denoted by HT_{high} curve. The reactor can operate only at point S_{high} practically at the thermodynamic equilibrium, at a temperature very close to T_b. Hence, the amount of unburnt fuel escaping the reactor is very small and we achieve almost complete combustion.

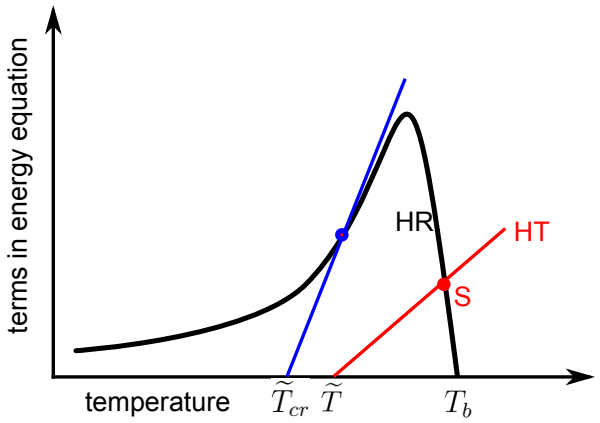

Figure 2.12: The dependence of the rates of heat release HR and of heat loses HT on the temperature; the case of self-ignition

2. Intermediate residence time τ_{res}
   This situation is shown by HT_{int} curve. Three intersections can be distinguished:
   (a) The point at low temperatures (point S_3) corresponds to negligibly small reaction rates and temperature increments. It represents an un-ignited flow through the reactor.
   (b) The point S_1 corresponds to a burning reactor, operating at high temperatures (practically at the thermodynamic equilibrium). However, the reactor temperature is now lower than the temperature point S_{high}. Decreasing the residence time lowers the temperature and increases the amount of unburnt fuel leaving the reactor.
   (c) Point S_2 is not physically realizable, as any small excursion (e.g. due to fuel supply unsteadiness) will make the system go to S_1 or to S_3.
3. Short residence time τ_{res} This situation corresponds to HT_{low} curve. The reactor can only operate at the low-temperature solution (S_{low}). No high-temperature operation is possible, the reactor has been quenched. At short residence time, the flame extinguishes completely. The reactants just pass through the reactor without interaction.
4. Critical conditions: HT_{cr} curve shows the critical condition. For a given type of fuel, fuel and oxygen mass fractions, pressure, and inlet temperature (i.e. for a given HR curve), if the mass flow rate increases beyond this point, the reactor will extinguish and will shift to the low-temperature intersection (cold, unreacted flow through the reactor). Hence, point C corresponds to the blow-off limit of the reactor. Any point between C and S_4 (such as S_2) is unstable (i.e. not physically realizable). Any point to the right (such as S_{high} or S_1) is stable, but can occur only at small flow rates.
5. Figure 2.12 shows a self-ignition in the reactor. It corresponds to the situation when the heat transfer HT is less than the heat generation for any case discussed above, i.e. when $\widetilde{T} > \widetilde{T}_{cr}$, where $\widetilde{T}_{cr}$ is the intersection point of the tangent at the heat release curve (HR) at the inflection point and of the temperature axis.

The numerical problem consists in choosing of a correct solution in the EDC or PaSR combustion models during the computation of the system (2.109) and (2.110) or (2.111) and (2.112). The difficulty can be explained by the fact that we have to do the choice between two stable solutions ("cold" - small temperature, and "hot" - large temperature). From the physical point of view the choice of the solution is determined by the whole history of the fluid particles arriving to the cell.

Y. Moule shows in his PhD thesis [Moule2013] that according to different initial conditions for iterative Newton-Raphson method for the eqs. (2.111) and (2.112), the solution of this system can converge and diverge. Other authors do not detail their approach to resolution of this problem.

The possible solutions consist in using the extended partially stirred reactor model (EPaSR) or unsteady partially stirred reactor model (UPaSR).

Extended partially stirred reactor model

V. Sabelnikov and C. Fureby developed a new model named Extended PaSR model for simulation of turbulent combustion [SabelnikovFureby2013] in the framework of the LES approach. This model, more complete than previous one, takes into account the unsteady convective and diffusive terms in balance equations for $\boldsymbol{\psi}^*$. It makes use of the similarities between the mathematical treatment of multiphase flows and the knowledge of fine-scale turbulence and chemistry obtained by DNS and experiments. Following [SabelnikovFureby2013] let us summarize the main principles of this model.

The concept of the EPaSR model is based on the idea that at high Re numbers the turbulent fine structures are not uniformly distributed but concentrated in small isolated regions, whose volume is a small fraction of the total volume. This has recently been verified by DNS in nonreactive and reactive flows [WoodwardPorter2000]. Turbulent reacting flows may be viewed as a muddle of vortex structures of different topological character, sheets, ribbons, and tubes, in which the tubes and ribbons carry most of the high-intensity vorticity and dissipation. This implies that the fine-structure regions, denoted by $(^*)$ as above, are embedded in a surrounding fluid, here denoted by $(^0)$, will be responsible for most of the molecular mixing, chemical reactions, and heat release.

For the derivation of the EPaSR model, let

$$\boldsymbol{\psi} = [\boldsymbol{Y}, h_s] \tag{2.119}$$

be the composition space, where h_s is the sensible enthalpy. The evolution of $\boldsymbol{\psi}$ is governed by the local balance equations of mass fractions and total energy describing convection, diffusion, and chemical reactions. Fine structures and surroundings are related with the averaged space by the expression

$$\widetilde{\boldsymbol{\psi}} = \gamma^* \boldsymbol{\psi}^* + (1 - \gamma^0)\boldsymbol{\psi}^0, \tag{2.120}$$

where $\gamma^* = \frac{Vol^*}{Vol}$ is a fine-structure volume fraction, i.e. the fraction of each computation cell in which the mixing process takes place on a small scale. $\boldsymbol{\psi}^*$, $\boldsymbol{\psi}^0$ is composition space in fine structure and its surrounding, respectively.

According to theoretical [Chomiak1970; Chomiak1979], experimental [Fureby2007] and computational [TanahashiFujimura2000; TanahashiSato2008] observations, most exothermic

reactions mainly occur in the fine structures and so, it follows that the source term of the species and energy is evaluated at the fine-structure conditions $\boldsymbol{\psi}^*$:

$$\overline{\dot{\omega}}_k \approx \gamma^* \overline{\dot{\omega}}_k(\boldsymbol{\psi}^*). \tag{2.121}$$

Assuming that the fine structure density ρ^* and velocity fields $\boldsymbol{u}^*$ coincide with mean values, i.e.

$$\rho^* \approx \overline{\rho}, \qquad \widetilde{\boldsymbol{u}}^* \approx \widetilde{\boldsymbol{u}}^{\boldsymbol{0}} \approx \widetilde{\boldsymbol{u}}, \tag{2.122}$$

and using (2.120), the set of balance equations for the fine structure fractions $\boldsymbol{\psi}^*$ together with the LES balance equations for $\widetilde{\boldsymbol{\psi}}$ is

$$\frac{\partial}{\partial t}\left(\overline{\rho}\widetilde{\psi}_i\right) + \boldsymbol{\nabla}\cdot\left(\overline{\rho}\widetilde{\boldsymbol{u}}\widetilde{\psi}_i\right) = \boldsymbol{\nabla}\cdot\left(\overline{\boldsymbol{k}}_i - \boldsymbol{b}_i\right) + \overline{\dot{\omega}}_i,\ i = 1,..,N_{sp}+1, \tag{2.123}$$

$$\frac{\partial}{\partial t}\left(\overline{\rho}\gamma^*\psi_i^*\right) + \boldsymbol{\nabla}\cdot\left(\overline{\rho}\gamma^*\psi_i^*\widetilde{\boldsymbol{u}}\right) = \boldsymbol{\nabla}\cdot\left(\gamma^*\left(\overline{\boldsymbol{k}}_i - \boldsymbol{b}_i\right)\right) + \gamma^*\overline{\dot{\omega}}_i^* + \overline{M}_i^*, \tag{2.124}$$

$$\frac{\partial}{\partial t}\left(\overline{\rho}\gamma^*\right) + \boldsymbol{\nabla}\cdot\left(\overline{\rho}\gamma^*\widetilde{\boldsymbol{u}}\right) = -\frac{\overline{\rho}(\gamma^* - \gamma_{eq}^*)}{\tau^*}, \tag{2.125}$$

where $\boldsymbol{k}_i \approx \frac{\overline{\mu}}{Sc_i}\boldsymbol{\nabla}\widetilde{Y}_i$ for $i = 1,..,N_{sp}$ is the species mass flux; $\boldsymbol{k}_{N_{sp}+1} \approx \overline{\lambda}\boldsymbol{\nabla}\widetilde{T}$ is the heat flux vector. $\boldsymbol{b}$ is flux vectors:

$$\boldsymbol{b}_i = \overline{\rho}\left(\widetilde{\boldsymbol{u}Y_i} - \widetilde{\boldsymbol{u}}\widetilde{Y}_i\right), i = 1,..,N_{sp}; \qquad \boldsymbol{b}_{N_{sp}+1} = \overline{\rho}\left(\widetilde{\boldsymbol{u}h_s} - \widetilde{\boldsymbol{u}}\widetilde{h}_s\right). \tag{2.126}$$

The reaction rates are defined as

$$\overline{\dot{\omega}}_i = \gamma^*\overline{\dot{\omega}}_i^*, i = 1,..,N_{sp}; \qquad \overline{\dot{\omega}}_{N_{sp}+1} = \overline{\boldsymbol{\tau}}\cdot\boldsymbol{\nabla}\widetilde{\boldsymbol{u}} + \frac{\partial\overline{P}}{\partial t} + \boldsymbol{\nabla}\overline{P}\cdot\widetilde{\boldsymbol{u}} - \gamma^*\sum_{i=1}^{N_{sp}}\left(\overline{\dot{\omega}}_i h_{f,i}^{\theta}\right), \tag{2.127}$$

where $\boldsymbol{\tau}$ is the viscous stress tensor, P is the pressure, $h_{f,i}^{\theta}$ are the species formation enthalpies.

The RHS of the balance equations for the fine structure contains an additional term, denoted $\overline{\boldsymbol{M}}^*$. This is the exchange terms at the immaterial interface between the fine-structure volume and the surrounding fluid. The sum of the exchange terms in fine structure and its surroundings is equal to zero: $\overline{\boldsymbol{M}}^* + \overline{\boldsymbol{M}}^0 = \boldsymbol{0}$. As follows from the core physical considerations, $\overline{\boldsymbol{M}}^*$ and $\overline{\boldsymbol{M}}^0 = -\overline{\boldsymbol{M}}^*$ contain two kinds of terms:

$$\overline{\boldsymbol{M}}^* = \overline{\boldsymbol{\Theta}}^* + \overline{\boldsymbol{\Omega}}^*, \tag{2.128}$$

$$\overline{\boldsymbol{\Theta}}^* = \frac{1}{2}\left(\dot{m} + |\dot{m}|\right)\boldsymbol{\psi}^0 + \frac{1}{2}\left(\dot{m} - |\dot{m}|\right)\boldsymbol{\psi}^*, \tag{2.129}$$

$$\overline{\boldsymbol{\Omega}}^* = -\frac{\gamma^*\overline{\rho}}{\tau^*}\left(\boldsymbol{\psi}^* - \boldsymbol{\psi}^0\right). \tag{2.130}$$

The first type of term, here denoted by $\overline{\boldsymbol{\Theta}}$, is due to the exchange rate of mass between the fine structures and the surroundings. If the exchange rate of mass is absent, as in the dynamic equilibrium state, the mass transport rate $\dot{m} = 0$, and these two terms become zero. We recall that

$$\dot{m} = -\frac{\overline{\rho}(\gamma^* - \gamma_{eq}^*)}{\tau^*}, \tag{2.131}$$

where γ^*_{eq} is the equilibrium fine structure volume fraction and τ^* is the fine structure residence time.

The required closure models for τ^* and γ^*_{eq} are based on the cartoon of turbulent combustion (for example, illustrated in fig. 2.10). V. Sabelnikov and C. Fureby proposed following submodels for these quantities at high Re and moderate Da numbers:

$$\tau^* = \sqrt{\tau_K \tau_\Delta}, \tag{2.132}$$

where $\tau_\Delta = \frac{\Delta}{u'}$ is the subgrid velocity stretch time. The fine-structure residence time represents the geometrical mean of the Kolmogorov time τ_K and the time scale associated with the subgrid velocity stretch.

The equilibrium reacting fine-structure fraction is defined as

$$\gamma^*_{eq} = \frac{\tau_{ch}}{\tau_{ch} + \tau^*}. \tag{2.133}$$

The chemical time scale is representative of the overall chemical reaction and is assumed to be for example

$$\tau_{ch} \approx \frac{\delta_L}{S_L}, \tag{2.134}$$

where δ_L and S_L are the laminar flame thickness and flame speeds, respectively

It can be concluded that if $\dot{m} > 0$, $\gamma^* < \gamma^*_{eq}$, the exchange rate of mass is driven by the surroundings to the fine structures. Otherwise, if $\dot{m} < 0$, $\gamma^* > \gamma^*_{eq}$, then the exchange rate of mass is directed from the fine structures to the surroundings. As we can see, $0 < \gamma^*_{eq} < 1$, and γ^* tends to its equilibrium state with the characteristic time τ^*.

The second type of term in the expression (2.128), denoted by $\mathbf{\Omega}$ is due to molecular diffusion through the interface between the fine structures and surroundings. Indeed, even if the exchange rate of mass is absent (i.e. in the dynamic equilibrium), there is exchange through the interface due to molecular diffusion.

It should be noted that if subgrid convection can be neglected, the EPaSR model simplifies to the PaSR model.

The LES/EPaSR model was evaluated against other LES turbulence-chemistry interaction models for a high Reynolds number turbulent lean premixed bluff-body stabilized flame [SabelnikovFureby2013]. Experimental data were used to provide the reference with which the considered models are compared. For this combustor, the overall best performing model is the LES/EPaSR model, closely followed by the LES/PaSR model.

Unsteady partially stirred reactor model

The abridged version of the EPaSR model, which is named unsteady partially stirred reactor (UPaSR) model was used by Y. Moule, V. Sabelnikov and A. Mura [Moule2013; MouleSabelnikov2014]. It is obtained from eq. (2.124) by neglecting of convective and diffusive terms. The system of equations of UPaSR model in the fine-structure regions reads

$$\frac{\partial \overline{\rho} Y^*_k}{\partial t} + \frac{\overline{\rho}\,(Y^*_k - Y^0_k)}{\tau^*} = \dot{\omega}(T^*, \boldsymbol{Y}^*). \tag{2.135}$$

and the energy conservation stays the same that in eq. (2.110).

Y. Moule, V. Sabelnikov and A. Mura validated LES/UPaSR model on the configuration of the non-premixed supersonic co-flowing jets of hydrogen and vitiated air. The comparisons performed between computational results and experimental data established that the physical processes were well-described by the LES/UPaSR simulation [Moule2013; MouleSabelnikov2014].

2.6.3 Thickened flame model

The objective of a thickened flame large eddy simulation (TFLES) is to artificially thicken the flame front structure so it can be resolved on a LES mesh, but such that the laminar flame speed remains unaltered. For laminar flame, Butler and O'Rourke [ButlerORourke1977] propose to thicken the flame directly by altering the diffusion term. In such the approach, it is important to ensure that the flame spreads at a proper speed, which is achieved by artificially adjusting chemical production rates.

All quantities (flame thickness and velocity, diffusion coefficients and chemical production rates) are related via simple relationships as shown via asymptotic analysis by Zel'dovich and Frank Kamenetskii [ZeldovichFrankKamenetskii1938]:

$$\begin{cases} S_L \propto \sqrt{D\dot{\omega}_c} & \text{(2.136a)} \\ \delta_L \propto \dfrac{D}{S_L} & \text{(2.136b)} \end{cases}$$

where D represents a characteristic diffusion coefficient of the flame and $\dot{\omega}_c$ is the chemical production rate of a progress variable. According to eq. (2.136), an increase in flame thickness by a factor F with a constant flame speed S_L, can be achieved by multiplying the molecular diffusivity D by F, and the reaction rate $\dot{\omega}$ by $1/F$.

In a turbulent environment, the flame propagates at $S_t \neq S_L$. A well-designed turbulent combustion model should preserve the flame properties, and, in particular, its propagation speed. For this reason, when the turbulent flame is thickened via TFLES model, the effects of turbulence on the flame speed are to be accounted for by means of correction of chemical sources. Colin and al. introduce an efficiency factor E defined as the ratio between the folding factor of non-thickened flame Ξ and thickened flame Ξ^* [ColinDucros2000]:

$$E = \frac{\Xi(\delta_L)}{\Xi^*(F\delta_L)}. \tag{2.137}$$

A detailed expression for E, which accounts for the local stretching and quenching of flame, was proposed in [ColinDucros2000; CharletteMeneveau2002].

When the thickening coefficient is fixed so that the turbulent flame front is solved on a given mesh the chemical sources can be evaluated directly using the filtered quantities. Finally, the transport equation of the progress variable according to the TFLES model writes:

$$\frac{\partial \overline{\rho}\widetilde{C}}{\partial t} + \boldsymbol{\nabla} \cdot (\overline{\rho}\widetilde{\boldsymbol{u}}\widetilde{C} - \overline{\rho}EFD_c\boldsymbol{\nabla}\widetilde{C}) = \frac{E}{F}\overline{\rho} \cdot \omega_c(\widetilde{C}, \overline{T}), \tag{2.138}$$

where D_c is a diffusion coefficient of the progress variable C. In general, E and F can be evaluated dynamically, so that the thickening of the flame depends directly on the local mesh size. In this context, the thickening factor can be calculated according to

$$F = 1 + (F_{max} - 1)\alpha_1, \tag{2.139}$$

where α_1 is the flame sensor which allows locating the flame front in the flow and F_{max} is the maximum value of the thickening defined by

$$F_{max} = \frac{n_f \Delta}{\delta_L}, \tag{2.140}$$

where n_f is the number of items needed to solve the laminar flame. The folding factor Ξ can be evaluated using the expression:

$$\Xi(\delta_L) = 1 + \alpha\Gamma\left(\frac{\Delta}{\delta_L}, \frac{u'_\Delta}{S_L}\right)\frac{u'_\Delta}{S_L}, \tag{2.141}$$

where α is the coefficient introduced by Charlette and al. [ColinDucros2000] and Γ is the modified intermittent turbulent net flame stretch (ITNFS) function proposed by Meneveau and Poinsot [MeneveauPoinsot1991]:

$$\Gamma = 0.75 \exp\left(-\frac{1.2}{(u'_\Delta/S_L)^{0.3}}\right)\left(\frac{\Delta}{\delta_L}\right)^{2/3}. \tag{2.142}$$

Δ is evaluated from the volume to surface ratio of each cell. The subgrid speed fluctuations u'_Δ are evaluated following Smagorinsky model:

$$u'_\Delta = C_S^2 \Delta \sqrt{\widetilde{S}_{ij}\widetilde{S}_{ij}}, \tag{2.143}$$

where C_S is the constant of Smagorinsky model and $\boldsymbol{S}$ is the symmetric part of the filtered stress tensor of deformation.

TFLES is used with simple chemical mechanisms model, typically consisting of two equations. The extension of TFLES towards detailed chemistry (such as FTC tables) is complex due to the nonlinear dependence between species, in this case the use of scalar thickening factor is no longer justified.

Part I

New approach to solve SPDEs statistically equivalent to a transport equation for velocity PDF

Chapter 3

Eulerian (Field) Monte Carlo methods for solving the Favre one-time one-point velocity PDF transport equation

In turbulent reactive flows, the prediction of interesting phenomena (such as pollutant production, soot formation or extinctions/ignitions) requires a precise knowledge of the one-time one-point joint velocity-scalars PDF, satisfying the transport eq. (2.100). The advantage of this PDF method is that both convection and reaction terms are represented exactly without modeling assumptions. It is nonetheless counterbalanced by a severe numerical constraint: the joint velocity-scalars PDF possesses a potentially high number of dimensions, which induces heavy computational costs. In particular, finite difference methods cannot be used, as their cost increases exponentially with dimensionality.

Due to the aforementioned problem, the PDF equations are often resolved by Monte Carlo methods. In the field of turbulent combustion, Monte Carlo methods are mostly considered under their Lagrangian form [Pope1985]. In LMC methods SODEs are statistically equivalent to the transport equation for the joint velocity-scalars PDF. In each realization of the SODEs characteristics do not intersect in joint sample space. As a result, there are no numerical difficulties to establish the solutions of the SODEs. Numerous publications document the convergence and accuracy for the LMC methods. Nevertheless, the projection of solution of the particles located at grid nodes into physical space and achievement of a decent convergence are delicate in the LMC approach.

Therefore, the development and evaluation of an alternative EMC method is of interest. EMC methods are based on stochastic Eulerian fields, which evolve from stochastic partial differential eqs. (2.101) to (2.103) statistically equivalent to the joint velocity-scalars PDF transport eq. (2.100). These SPDEs, similarly to the SPDE (2.101) statistically equivalent to the velocity PDF transport equation[1], belong to quasi-linear hyperbolic equations. Characteristic curves of the SPDEs can cross, which results in a multivalued solution for the velocity $\boldsymbol{u}(t, \boldsymbol{x})$. At points where solution of the velocity is multivalued, the corresponding density

[1]This transport equation is a particular case of eq. (2.100).

$r(t, \boldsymbol{x})$ also becomes a multivalued function. In addition, when the velocity becomes multivalued, the density becomes unbounded (i.e. given for instance by a Dirac delta function). Points of singularity where the velocity solution is multivalued develop in finite time even for a large class of smooth initial values. Indeed, considering the characteristics equations as a system of ordinary differential equations (ODEs) in its configuration space, one can see crossing characteristics correspond to a multivalued solution.

If we want to preserve the equivalence between eqs. (2.101) to (2.103) and the underlying joint velocity-scalars PDF transport eq. (2.100), we should take into account multivalued solutions of the SPDEs, not considered in previous work [SoulardSabelnikov2006]. Numerical schemes which satisfy entropy increase condition are not appropriate for the description of the solution behavior beyond the singularity, where multivalued solutions in physical space need to be accounted for.

Furthermore, the so called entropy or viscosity solution, which defines a unique weak solution, is not the appropriate one for a large class of problems. Examples include dispersive waves [FlaschkaForest1980; LaxDavid Levermore1983; Whitham2011], optical waves [EngquistRunborg1999; EngquistRunborg2003], seismic waves [TrierSymes1991; FomelSethian2002; SymesQian2003], semi-classical limits of Schrodinger equations [ChengLiu2003; JinLi2003; SparberMarkowich2003], electron beam modulation in vacuum electronic devices [LiWöhlbier2004]. For example, while resolving linear wave equation by a widely used WKB method[2], the class of weak solutions is not adequate for treating dispersive wave propagation problems because crossing wave fronts and superposition of solutions are important [LiuOsher2006].

Capturing multivalued solutions of the SPDEs by efficient algorithms is an important issue. There exist only level set methods for computing multivalued solutions to a class of nonlinear first order partial differential equations. These methods are described for instance in [LiuOsher2006]. In such methods the multivalued solutions are embedded as the zeroes of a set of scalar functions that solve the initial value problems of a time-dependent partial differential equation in an augmented space.

In this work we are interested in Eulerian method for solving the SPDEs statistically equivalent to the velocity PDF transport equation without increasing space dimension. If we are able to solve correctly these equations, then we can solve eqs. (2.101) to (2.103) corresponding to the joint velocity-scalars PDF transport equation. Recently, O. Soulard proposed a new approach to solve the SPDEs which allows taking into account the multivalued solutions in a statistical sense [EmakoLetizia2014]. We develop and study these stochastic schemes for the SPDEs eqs. (2.101) to (2.103) and show that these numerical methods yield good agreement with theoretical solutions in the statistic sense for one-dimensional test-cases.

The chapter is organized as follows. Firstly, we describe a problem and recall a transport equation for the velocity PDF with zero RHS. Secondly, we write the partial differential equations (PDEs) equivalent to the PDF equation. Then we explain numerical schemes which allow finding multivalued solutions in the statistical sense and give details of numerical modeling of the SPDEs which are statistically equivalent to the velocity PDF equation. In the third part the proposed numerical stochastic schemes are validated in one-dimensional case on tests of progressively increasing complexity. Finally, the conclusion about this new

[2]This classical method, named after physicists Wentzel, Kramers, and Brillouin, yields an approximate nonlinear models for the original linear wave equation.

numerical approach is given.

3.1 Description of the problem

Section 3.1 is organized as follows. Section 3.1.1 is devoted to a description of the model transport equation for the one-time one-point velocity PDF in one dimensional case. Afterwards a presentation of the SPDEs which are statistically equivalent to the PDF transport equation is developed (section 3.1.2). Finally, the equivalence between the PDF transport equation and the SPDEs are discussed (section 3.1.3).

3.1.1 One-dimensional model PDF equation

Let us consider the turbulent flow which is statistically homogeneous in the perpenducular planes (x_2, x_3) and inhomogeneous in x-direction $(x = x_1)$. Model equation for the one-time one-point velocity PDF $\widetilde{f}_u(V;t,x)$ reads (see eq. (2.100))

$$\frac{\partial \overline{\rho}\widetilde{f}_u}{\partial t} + \frac{\partial \overline{\rho} V \widetilde{f}_u}{\partial x} = -\frac{\partial}{\partial V}\left(\overline{\rho}\left[-\frac{1}{\rho}\frac{\partial \overline{P}}{\partial x} + C_1\omega\left(V - \widetilde{u}\right)\right]\widetilde{f}_u\right) + \frac{1}{2}\overline{\rho}C_0\varepsilon\frac{\partial^2 \widetilde{f}_u}{\partial V^2}, \tag{3.1}$$

Here, $t \in \mathbb{R}^+ = [0; +\infty)$ is a time variable, $x \in \mathbb{R} = (-\infty; +\infty)$ is a spatial variable, $V \in \mathbb{R}$ is a sample space for velocity $u(t,x)$. The variables $V,\ t,\ x$ are independent. $\overline{\rho}(t,x)$ is a mean density in a flow. We recall that ε is the mean turbulent energy dissipation rate, ω is the mean turbulent frequency, C_0 and C_1 are model constants.

For illustration purposes we assume zero RHS of eq. (3.1) hereafter. Equation (3.1) becomes

$$\frac{\partial \overline{\rho}\widetilde{f}_u}{\partial t} + \frac{\partial \overline{\rho} V \widetilde{f}_u}{\partial x} = 0 \tag{3.2}$$

with initial conditions

$$\overline{\rho}(t=0,x) = \overline{\rho}_0(x), \qquad \widetilde{f}_u(V;t=0,x) = \widetilde{f}_0(V;x). \tag{3.3}$$

This equation allows finding all Favre moments of the velocity. Indeed, multiplying eq. (3.2) by V^n, $n \geq 0$, integrating it over $-\infty < V < +\infty$, one can deduce the evolution equation for $\widetilde{u^n}$,

$$\frac{\partial \overline{\rho}\widetilde{u^n}}{\partial t} + \frac{\partial \overline{\rho}\widetilde{u^{n+1}}}{\partial x} = 0, \tag{3.4}$$

where

$$\widetilde{u^n}(t,x) = \int\limits_{-\infty}^{+\infty} V^n \widetilde{f}_u(V;t,x)dV. \tag{3.5}$$

In particular, using a normalization condition

$$\int\limits_{-\infty}^{+\infty} \widetilde{f}_u(V;t,x)dV = 1 \tag{3.6}$$

for $n = 0$ the first moment equation reads

$$\frac{\partial \overline{\rho}}{\partial t} + \frac{\partial \overline{\rho}\widetilde{u}}{\partial x} = 0 \tag{3.7}$$

and the second is

$$\frac{\partial \overline{\rho}\widetilde{u}}{\partial t} + \frac{\partial \overline{\rho}\widetilde{u^2}}{\partial x} = 0. \tag{3.8}$$

Equation (3.2) is a first order PDE. It can be solved using the method of characteristics along which the PDE becomes ordinary differential equations. The equations of the characteristic curves are

$$\begin{cases} \dot{t} = 1, \\ \dot{x} = V, \\ \dot{V} = 0, \\ \dot{F} = 0, \end{cases} \tag{3.9}$$

where $F = \overline{\rho}\widetilde{f}_u$, $\dot{(\,)} = \frac{d}{ds}$, s is a particular parameterization of the curves and $(0,\ y,\ V_0(y))$ is a point from which characteristic curve emanates. Initial conditions for eq. (3.9) read

$$\begin{cases} x(0) = y, \\ V(0) = V_0(y), \\ F(V; 0, x) = \overline{\rho}_0(x(0))\widetilde{f}_0(V(0); x(0)). \end{cases} \tag{3.10}$$

The solution of eq. (3.9) with the initial conditions (3.10) is given by

$$\begin{cases} x = y + Vs = y + V_0(y)t, \\ F = \overline{\rho}_0(y)\widetilde{f}_0(V_0(y); y). \end{cases} \tag{3.11}$$

It should be noted that the characteristics of the PDF eq. (3.2) do not cross.

Let us consider a backward step velocity profile which leads to analytical solution of the PDF transport eq. (3.2). The initial conditions for eq. (3.2) read

$$\widetilde{f}_u(V; t = 0, x) = H(-(x - x_c))\delta(V - V_0) + H(x - x_c)\delta(V), \tag{3.12}$$

$$\overline{\rho}(t = 0, x) = \overline{\rho}_0, \tag{3.13}$$

where H is a Heaviside function and $x_c \in \mathbb{R}$, $V_0 \in \mathbb{R}^+$, $\overline{\rho}_0 \in \mathbb{R}^+$.

Applying (3.11), the solution of the Cauchy problem (3.2), (3.12) and (3.13) results in

$$\overline{\rho}\widetilde{f}_u(V; t, x) = \overline{\rho}_0 H(V_0 t - (x - x_c))\delta(V - V_0) + \overline{\rho}_0 H(x - x_c)\delta(V),\ t > 0, \tag{3.14}$$

where the mean density is

$$\overline{\rho}(t, x) = \overline{\rho}_0 H(V_0 t - (x - x_c)) + \overline{\rho}_0 H(x - x_c) = \begin{cases} \overline{\rho}_0, & \text{if } x < x_c \text{ and } x > V_0 t + x_c, \\ 2\overline{\rho}_0, & \text{if } x \in [x_c; x_c + V_0 t]. \end{cases} \tag{3.15}$$

(3.12) and (3.14) show that at the initial time $t = 0$ each point in space is associated with one Dirac delta function $\delta(V - V_0)$, if $x < x_c$ and $\delta(V)$, if $x \geq x_c$. After the time $t > 0$, the

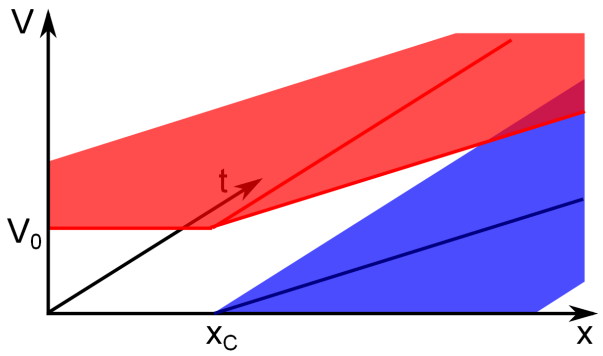

Figure 3.1: Backward step: solution of eqs. (3.2), (3.12) and (3.13)

interval $x_c \leq x \leq x_c + V_0 t$ contains two Dirac delta functions $\delta(V - V_0)$ and $\delta(V)$ (see in fig. 3.1). Figure 3.1 illustrates the solution of the eqs. (3.2), (3.12) and (3.13). There are two planes V_0 and 0 in the phase space which do not intersect.

We are interested now in the transport equation for the Reynolds one-time one-point fluctuating velocity PDF $\overline{g}_{u'}$ denoted as $\overline{g}$ in one dimensional case. At the initial time the density is set to one and considered to be homogeneous in time and in space: $\overline{\rho}(t,x) = 1\,\mathrm{kg/m^3}$. The mean velocity is assumed equal to zero. $V = V' = V''$ is a sample space of velocity $u(t,x) = u'(t,x) = u''(t,x)$. Using eq. (2.100) and eq. (3.1), the model transport equation reads

$$\frac{\partial \overline{g}}{\partial t} + \frac{\partial V' \overline{g}}{\partial x} = -\frac{\partial}{\partial V'}\left(\frac{\partial}{\partial x}\left(\overline{u'^2}\right)\overline{g}\right) - C_1 \frac{\partial}{\partial V'}\left(\omega V' \overline{g}\right) + \frac{C_0}{2}\varepsilon \frac{\partial^2 \overline{g}}{\partial V'^2}. \tag{3.16}$$

At initial time the PDF is

$$\overline{g}(V'; t = 0, x) = \overline{g}_0(V'; x). \tag{3.17}$$

Equation (3.16) is a parabolic equation because of the second derivative with respect to V'. In order to write the stochastic characteristic curves, the function g' is considered. It satisfies the following transport equation

$$\frac{\partial g'}{\partial t} + \frac{\partial V' g'}{\partial x} = -\frac{\partial}{\partial V'}\left(\frac{\partial}{\partial x}\left(\overline{u'^2}\right) g'\right) - C_1 \frac{\partial}{\partial V'}\left(\omega V' g'\right) + \sqrt{C_0 \varepsilon}\frac{\partial g'}{\partial V'} \circ \dot{\xi}. \tag{3.18}$$

Here $\circ$ is a symbol in the Stratonovich interpretation. Equation (3.18) contains the stochastic term $\dot{\xi}$, which represents the derivative of a Brownian motion. The Reynolds PDF $\overline{g}$ is the mean of the g' over ξ. Equation (3.18) is a hyperbolic equation. The system of the equations

for the stochastic characteristics of eq. (3.18) reads

$$\begin{cases} \dot{t} = 1, \\ \dot{x} = V', \\ \dot{V'} = \frac{\partial}{\partial x}\left(\overline{u'^2}\right) + \omega V' + \sqrt{C_0 \varepsilon}\dot{\xi}, \\ \dot{g'} = -C_1 \omega. \end{cases} \tag{3.19}$$

For each realization of white noise ξ the characteristics of eq. (3.19) do not cross in phase space.

3.1.2 One-dimensional SPDEs

The first three characteristic equations of (3.9) in physical space are the characteristics eq. of the following PDE of velocity field

$$\frac{\partial u}{\partial t} + u\frac{\partial u}{\partial x} = 0 \tag{3.20}$$

with initial condition

$$u(t = 0, x) = u_0(x). \tag{3.21}$$

Equation (3.20) is a Burger equation. Introducing the density field $r(t, x)$ by the equation (details can be found in [SoulardSabelnikov2006; SabelnikovSoulard2010])

$$\frac{\partial r}{\partial t} + \frac{\partial ru}{\partial x} = 0, \tag{3.22}$$

we can rewrite eq. (3.20) in conservative form

$$\frac{\partial ru}{\partial t} + \frac{\partial ru^2}{\partial x} = 0 \tag{3.23}$$

with initial conditions:

$$r(t = 0, x) = r_0(x), \qquad u(t = 0, x) = u_0(x). \tag{3.24}$$

Equations (3.22) and (3.23) are nothing more than a system of pressureless gas dynamics equations [BouchutJin2003]: eq. (3.23) does not contain pressure. The time evolution of the density (eq. (3.22)) can be also represented as

$$\frac{dln(r)}{dt} = -\frac{\partial u}{\partial x}, \tag{3.25}$$

where $\frac{d}{dt} = \frac{\partial}{\partial t} + u\frac{\partial}{\partial x}$ is a total derivative. As we can see from eq. (3.25), the density is strictly positive.

The characteristics of eq. (3.20), contrary to the characteristics of eq. (3.9) in phase space, cross in the general case. Indeed, let $\Gamma = \{(0,\ x)\}$ be the curve in $\mathbb{R}^2$, where $\mathbb{R} = (-\infty; +\infty)$. $(\Gamma,\ u_0)$ is the curve in $\mathbb{R}^3$ given by $\{(0,\ x,\ u_0(x))\}$. To construct a solution of eq. (3.20) we start by picking a point $(0,\ y,\ u_0(y))$ on $(\Gamma,\ u_0)$ and then construct a characteristic curve

emanating from $(0,\ y,\ u_0(y))$. Characteristics equations of the first order quasi-linear PDE (3.20) read

$$\begin{cases} \dot{t} = 1, \\ \dot{x} = u, \\ \dot{u} = 0. \end{cases} \tag{3.26}$$

Initial conditions for eq. (3.26) are

$$\begin{cases} x(0) = y, \\ u(0) = u_0(y). \end{cases} \tag{3.27}$$

where $\dot{()} = \frac{d}{ds}$, s is a particular parameterization of the curves. The solution of eq. (3.26) is given by

$$\begin{cases} t = s, \\ x = y + u_0(y)s, \\ u = u_0(y) \end{cases} \tag{3.28}$$

or

$$\begin{cases} x = y + u_0(y)t, \\ u = u_0(y). \end{cases} \tag{3.29}$$

The inverse function theorem states that if the function $y+u_0(y)t : \mathbb{R}^2 \to \mathbb{R}$ is a continuously differentiable function of two variables with non-zero derivatives at the point $(t^*,\ y^*)$, then $y+u_0(y)t$ is invertible in a neighborhood of $(t^*,\ y^*)$ and the inverse is a continuously differentiable function. If the function $y + u_0(y)t$ has zero derivatives at the point y^*, i.e. if

$$u_0(y^*) = 0, \qquad t^* \frac{\partial u_0(y^*)}{\partial y} + 1 = 0, \tag{3.30}$$

or

$$\frac{\partial u_0(y^*)}{\partial y} < 0, \qquad u^0(y^*) = 0, \qquad t^* = \frac{-1}{\frac{\partial u_0(y^*)}{\partial y}}, \tag{3.31}$$

then the point $(t^*,\ y^*)$ is singular. Multiplicity of the function $y+u_0(y)t$ at the singular point $(t^*,\ y^*)$ is the order of tangency of the graphs $x = y+u_0(y)t$ and $x = y^*+u_0(y^*)t^*$ at $(t^*,\ y^*)$, if $y+u_0(y)t$ is a smooth function (details can be found, for instance, in [ChechkinGoritsky2009]). A solution satisfying the entropy increase condition after $t > t^*$ contains shock waves. In other words kinetic energy is dissipated [RojdestvenskiiYanenko1978].

To illustrate a multivalued solution of eqs. (3.20) and (3.22), let us consider the same initial profile that is given in section 3.1.1. The initial conditions for velocity and density are set according to the (3.12) and (3.13)

$$u(t = 0, x) = u_0(x) = V_0 H(-(x - x_c)), \qquad r(t = 0, x) = \overline{\rho}_0. \tag{3.32}$$

For time $t > 0$ there are two velocity values $u(t, x)$ in the interval $x \in [x_c; x_c + V_0 t]$

$$u_1(t, x) = V_0, \qquad u_2(t, x) = 0. \tag{3.33}$$

The corresponding density is

$$r_1(t,x) = \overline{\rho}_0, \qquad r_2(t,x) = \overline{\rho}_0. \tag{3.34}$$

Outside of this interval the solution of velocity and density is single-valued and is given by

$$u(t,x) = V_0, \qquad r(t,x) = \overline{\rho}_0, \qquad x < x_c \tag{3.35}$$

and

$$u(t,x) = 0, \qquad r(t,x) = \overline{\rho}_0, \qquad x > x_c + V_0 t. \tag{3.36}$$

The correspondence between PDF $\widetilde{f}_u(V;t,x)$ of eq. (3.3) and eqs. (3.20) and (3.22) is defined by the following relation

$$\widetilde{f}_u(V;t,x) = \begin{cases} \delta(V - V_0), & \text{if } x < x_c, \\ \frac{\delta(V-V_0)+\delta(V)}{2}, & \text{if } x \in [x_c; x_c + V_0 t], \\ \delta(V), & \text{if } x > x_c + V_0 t. \end{cases} \tag{3.37}$$

The mean density is

$$\overline{r} = \begin{cases} \overline{\rho}_0, & \text{if } x < x_c, \\ 2\overline{\rho}_0, & \text{if } x \in [x_c; x_c + V_0 t], \\ \overline{\rho}_0, & \text{if } x > x_c + V_0 t. \end{cases} \tag{3.38}$$

One can deduce immediately the equivalence between the solution of the PDF equation and the PDEs.

Figure 3.2 shows two different solutions of the PDEs (3.20), (3.22) and (3.32). The first one takes into account a multivalued solution and the second one is calculated with the entropy increase condition on the discontinuity shocks.

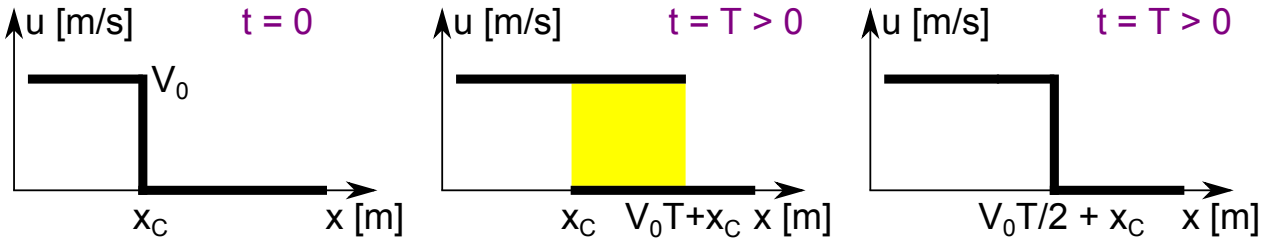

Figure 3.2: Backward step: initial profile of the velocity (left); solution of the PDF (3.2), (3.12) and (3.13) at $t = T$ (center); solution of the PDEs (3.20), (3.22) and (3.32) by any scheme with entropy increase condition at $t = T$ (right).

The solution of the PDEs (3.22), (3.20) and (3.32) with entropy increase condition can be written as

$$u(t,x) = V_0 H\left(-V_0\frac{t}{2} + x\right), \ t > 0. \tag{3.39}$$

The Favre PDF corresponding to the eq. (3.39) is

$$\widetilde{f}_u(V;t,x) = H\left(V_0\frac{t}{2} - x\right)\delta(V - V_0) + H\left(-V_0\frac{t}{2} + x\right)\delta(V). \tag{3.40}$$

We can see that each point in space is associated with one Dirac delta function: $\delta(V-V_0)$, if $x < V_0\frac{t}{2}$ and $\delta(V)$, if $x \geq V_0\frac{t}{2}$. The solution (3.40) is different from the solution (3.14), (3.15). Thus, methods satisfying the entropy increase condition cannot predict a correct solution of the PDF equation (3.2) with initial conditions (3.12) and (3.13).

The first three characteristic equations of (3.19) in physical space are the characteristics eq. of the following SPDE of velocity field

$$\frac{\partial u''}{\partial t} + u''\frac{\partial u''}{\partial x} = \frac{\partial \overline{u''^2}}{\partial x} + C_1\omega u'' + \sqrt{C_0\varepsilon}\dot{\xi}. \tag{3.41}$$

As a Favre-averaged velocity is zero and a mean density is equal to one, we write $u''(t,x) = u(t,x)$. Introducing the stochastic density r as for eq. (3.20), the conservation form of eq. (3.41) reads

$$\frac{\partial r}{\partial t} + \frac{\partial r u''}{\partial x} = 0, \tag{3.42}$$

$$\frac{\partial r u''}{\partial t} + \frac{\partial r u''^2}{\partial x} = \frac{r}{\overline{r}}\frac{\partial \overline{r u''^2}}{\partial x} + rC_1\omega u'' + r\sqrt{C_0\varepsilon}\dot{\xi}. \tag{3.43}$$

The SPDEs (3.42) and (3.43) are statistically equivalent to the PDF eq. (3.18).

3.1.3 Equivalence between SPDEs and PDF equation

At the first time we consider the PDF eq. (3.2). The PDEs (3.22)-(3.24) are equivalent to the PDF equations (3.2) and (3.3). If the solution of velocity $u(t,x)$ is single-valued, the equivalence can readily be proven. For example, the proof can be written as follows. The PDF of the velocity can be defined in terms of Dirac delta functions by

$$\widetilde{f}_u(V;t,x) = \langle f'(V;t,x)\rangle, \tag{3.44}$$

where the angular brackets indicate an ensemble mean and

$$f'(V;t,x) = \delta\left(V - u(t,x)\right) \tag{3.45}$$

is a fine-grained PDF. Differentiating eq. (3.45), we have

$$\frac{\partial f'}{\partial t} = -\frac{\partial f'}{\partial V}\frac{\partial u}{\partial t}, \tag{3.46}$$

$$\frac{\partial f'}{\partial x} = -\frac{\partial f'}{\partial V}\frac{\partial u}{\partial x}. \tag{3.47}$$

Equations (3.46) and (3.47) imply

$$\frac{\partial f'}{\partial t} + u(t,x)\frac{\partial f'}{\partial x} = -\frac{\partial f'}{\partial V}\frac{\partial u}{\partial t} - u(t,x)\frac{\partial f'}{\partial V}\frac{\partial u}{\partial x}. \tag{3.48}$$

Multiplying eq. (3.48) by $r(t,x)$ and taking into account that

$$r(t,x)\frac{\partial f'}{\partial t} = \frac{\partial r f'}{\partial t} - f'\frac{\partial r}{\partial t}$$

and

$$r(t,x)u(t,x)\frac{\partial f'}{\partial x} = \frac{\partial ruf'}{\partial x} - f'\frac{\partial ru}{\partial x},$$

we obtain

$$\frac{\partial rf'}{\partial t} - f'\frac{\partial r}{\partial t} + \frac{\partial ruf'}{\partial x} - f'\frac{\partial ru}{\partial x} = -r\frac{\partial f'}{\partial V}\left(\frac{\partial u}{\partial t} - u\frac{\partial u}{\partial x}\right). \tag{3.49}$$

It follows from eqs. (3.20), (3.23) and (3.49) that the transport equation for $r(t,x)f'(V;t,x)$ is

$$\frac{\partial rf'}{\partial t} + \frac{\partial ruf'}{\partial x} = 0. \tag{3.50}$$

Averaging eq. (3.50), we obtain the eq. (3.2) for $\overline{\rho}(t,x)\widetilde{f}(V;t,x)$ (more details can be found in [Pope1981]).

When the PDEs possess a multivalued solution, i.e. when the characteristics cross in eq. (3.29), we should take into account multivalued solutions of the density $r(t,x)$ and the velocity $u(t,x)$. The proof of this statement is based on the coincidence of three first characteristics (see eq. (3.9) for the PDF transport equation and eq. (3.26) for the PDEs). Examples given in appendix A.5.2, appendix A.5.3 demonstrate the equivalence between the multivalued solutions and the PDF solutions, when the solutions of the PDF eq. (3.2) and the PDEs (3.22)-(3.24) are analytical.

Let us consider now the model transport equation for the fluctuating velocity PDF eq. (3.16) and the SPDEs eqs. (3.42) and (3.43). In the case of the single-valued solution of eq. (3.41), the proof can be found in [SoulardSabelnikov2006]. When the multivalued solution of eq. (3.41) appears, the proof of the equivalence between the eqs. (3.42) and (3.43) and eq. (3.16) can be based on the stochastic characteristic for the function g' and the characteristics of eq. (3.41). Three fist characteristics of eq. (3.19) are the characteristics for eq. (3.41). As we can see from eq. (3.19) the function g' changes on all branches of the multivalued solution of eq. (3.41).

3.2 Stochastic numerical schemes

This section is devoted to modeling stochastic processes for the SPDEs. Section 3.2.1 described stochastic schemes for the PDEs (3.22)-(3.23) which are statistically equivalent to the PDF model transport eq. (3.2) with zero RHS. Stochastic Lax-Friedrichs, Lax-Wendroff, GForce and Godunov schemes are formulated. In section 3.2.2, stochastic schemes are proposed for the SPDEs (3.42)-(3.43).

3.2.1 Schemes for partial differential equations

In order to calculate the multivalued solutions of the PDEs (3.22)-(3.24) in the statistical sense O. Soulard inspired from the method of Glimm [Glimm1965], where the choice of solution depends on stochastic noise. The starting point of Glimm's method is identical to that of Godunov [Godunov1959]. It assumes the existence of a discontinuity between each two cells of grid. A Riemann problem is then solved to advance the solution in time. In the original formulation, Glimm's method finds the entropic solutions (see details in appendix A.1).

As it was explained above, if we want to preserve the equivalence between the solution of the PDF equation and the solution of the PDEs after the appearance of shock waves, we should avoid the dissipativity in the numerical schemes taking into account the multivalued solutions of the PDEs. Glimm's method and other methods with entropy increase condition are not suited to solve the PDEs (3.22)-(3.24) because they are dissipative. We propose a new stochastic method to capture the multivalued solutions of the PDEs (3.22)-(3.24) only in a statistical sense. The idea of a new method is following:

1. The numerical schemes for the PDEs are based on stochastic processes which are deduced from classical schemes for the PDF transport equation.
2. The choice of the velocity does not depend any more only on the length of the interval as in the random choice method (RCM) method, but also on a weight proportional to the stochastic density which is added in the probability.
   The same procedure is applied for each velocity field realization. Each particular realization of velocity and density always has a single solution.
3. In comparison with the RCM method, we do not solve the Riemann problem in the classical sense. One realization of the density and the velocity has no physical interpretation.

Let us provide a detailed description of the method. Consider one realization among the ensemble of all realizations defined by the initial conditions. Thus the profiles of velocity $u(0,x)$ and density $r(0,x)$ are deterministic. For this initial data, using the statement of equivalence, we can write the formula relating the solution of the PDEs (3.22)-(3.24) and the solution of the PDF equation (3.2)-(3.3):

$$\overline{\rho}(t,x)\widetilde{f}(t,x) = \sum_{s=1}^{N_{br}(t)} r_s(t,x)\delta\left(V - u_s(t,x)\right), \tag{3.51}$$

where $N_{br}(t)$ is a number of different branches of the multivalued solution of the PDEs at time t.

We construct an inner stochastic process which allow approximating the solution (3.51) of the PDEs in statistical sense by the following formula

$$\sum_{s=1}^{N_{br}(t)} r_s(t,x)\delta\left(V - u_s(t,x)\right) \approx \frac{1}{N_r}\sum_{irea=1}^{N_r} r^*_{irea}(t,x)\delta\left(V - u^*_{irea}(t,x)\right), \tag{3.52}$$

where N_r tends to infinity. Here, $(r^*_{irea}(t,x), u^*_{irea}(t,x))$, $irea = 1,..,N_r$ is some inner stochastic realization such that at initial time

$$r^*_{irea}(0,x) = r(0,x), \qquad u^*_{irea}(0,x) = u(0,x). \tag{3.53}$$

During the time $t > 0$, the realization $(r^*_{irea}(t,x), u^*_{irea}(t,x))$ evolves accordingly to some process and remains single-valued. The inner stochastic process must be such that all Favre moments of velocity and mean density coincide with the statistics of the multivalued solution (3.51) of the PDEs starting from the single initial condition $(r(0,x), u(0,x))$ at time 0.

In the general case the solution of the PDF equation is related with the solution of the PDEs (or SPDEs) as

$$\overline{\rho}(t,x)\widetilde{f}(t,x) = \left\langle \sum_{s=1}^{N_{br}(t)} r_s(t,x)\delta\left(V - u_s(t,x)\right) \right\rangle, \tag{3.54}$$

where angular brackets signify ensemble average. At initial time the mass-weighted PDF multiplied by mean density can be written as

$$\overline{\rho}(t_0,x)\widetilde{f}(t_0,x) = \left\langle r(t_0,x)\delta\left(V - u(t_0,x)\right)\right\rangle. \tag{3.55}$$

At time t the solution (3.56) is approximated by

$$\left\langle \sum_{s=1}^{N_{br}(t)} r_s(t,x)\delta\left(V - u_s(t,x)\right) \right\rangle \approx \left\langle \frac{1}{N_r}\sum_{irea=1}^{N_r} r^*_{irea}(t,x)\delta\left(V - u^*_{irea}(t,x)\right) \right\rangle, \tag{3.56}$$

where $N_r \to +\infty$. We will denote

$$\frac{1}{N_r}\sum_{irea=1}^{N_r} r^*_{irea}(t,x)\delta\left(V - u^*_{irea}(t,x)\right)) = \left\langle r^*(t,x)\delta\left(V - u^*(t,x)\right)\right\rangle_S. \tag{3.57}$$

There exists obviously a large choice of inner stochastic process such that the Favre statistics of velocity and mean density coincide with statistics of the multivalued solutions of the PDEs (SPDEs).

Numerical notations for stochastic schemes

Let us describe the proposed numerical approach to solve multivalued problems in one-dimensional case. Calculations are performed on domain $D = [a - \frac{h}{2}; b + \frac{h}{2}]$. N_x is a number of points in x including boundary points a and b. The spatial step is uniform, so $\Delta x = h = \frac{b-a}{N_x - 1}$, points of the grid are $x_j = a + (j-1)\Delta x$, $j = 1, .., N_x$.

At left and right boundaries, either Neumann condition is imposed, i.e. $r(t, x_1 = a) = r(t, x_2)$, $u(t, x_1 = a) = u(t, x_2)$, $r(t, x_{N_x} = b) = r(t, x_{N_x - 1})$ and $u(t, x_{N_x} = b) = u(t, x_{N_x - 1})$ or periodic condition is used: $r(t, x_1 = a) = r(t, x_{N_x} = b)$, $u(t, x_1 = a) = u(t, x_{N_x} = b)$.

We define some stochastic process (r^*_{irea}, u^*_{irea}), $irea = 1, .., N_r$, where N_r is a number of stochastic realizations.

$$\Delta t^n = cfl \frac{\Delta x}{\max\limits_{j=1,..,N_x,\ irea=1,..,N_r}(|u^{*n}_{irea,j}|)}, \text{ with constant } cfl < 1. \tag{3.58}$$

At the initial time all realizations are the same, i.e.

$$r^{*0}_{irea,j} = r^0(x_j), \qquad u^{*0}_{irea,j} = u^0(x_j). \tag{3.59}$$

If at initial time the velocity profile depends also on the external stochastic process $\xi_1, ..., \xi_N$, we should associate with each realization ξ_{ir}, $ir = 1, .., N$ some inner stochastic process $\left(r^{*,ir}_{irea}, u^{*,ir}_{irea}\right)$. Numerically, each external realization ξ_{ir} is associated with one inner realization. It can be used, when $N_r \gg 1$ and $t \gg t_0$.

The following notation is used for the PDF: $\widetilde{f}_u(t^n, x_j) = \widetilde{f}^n_j$.

Numerical stochastic schemes

PDF Let us deduce a stochastic numerical scheme for the PDEs (3.22) and (3.23). We suppose that the PDEs (3.22) is solved by the first order temporal and spatial schemes. For example, the discretized PDEs (3.22) can be written as

$$\overline{\rho}_j^{n+1}\widetilde{f}_j^{n+1} = \sum_{k=-l}^{k=l}\left(\alpha_k + \frac{\Delta t^n}{\Delta x}\beta_k V_k\right)\overline{\rho}_{j+k}^{n}\widetilde{f}_{j+k}^{n}, \tag{3.60}$$

where α_k, β_k are some coefficients, $k = -l, .., l$ and V_k is a sample space of velocity.

Stochastic process Numerical stochastic scheme is deduced from the eq. (3.60). Accordingly to the stochastic approximation (3.57) at the point (t^n, x_j), we can write that

$$\overline{\rho}_j^{n}\widetilde{f}_j^{n} \approx \left\langle \left\langle r_j^{n*}\delta\left(V - u_j^{n*}\right)\right\rangle_S \right\rangle. \tag{3.61}$$

Using the definition (3.61), the finite difference scheme of eq. (3.60) can be transformed to

$$\left\langle \left\langle r_j^{*n+1}\delta\left(V - u_j^{*n+1}\right)\right\rangle_S \right\rangle = \sum_{k=-l}^{k=l}\left\langle \left\langle r_{j+k}^{*n}\left(\alpha_k + \frac{\Delta t^n}{\Delta x}\beta_k V_k\right)\delta(V - u_{j+k}^{*n})\right\rangle_S \right\rangle. \tag{3.62}$$

The ensemble averaged fine-grained PDF possess the following property [Pope1985]:

$$\langle r^* V\delta(V - u^*)\rangle = \langle r^* u^*\delta(V - u^*)\rangle. \tag{3.63}$$

Thus taking into account eq. (3.63), the eq. (3.62) yields

$$\left\langle \left\langle r_j^{*n+1}\delta\left(V - u_j^{*n+1}\right)\right\rangle_S \right\rangle = \sum_{k=-l}^{k=l}\left\langle \left\langle r_{j+k}^{*n}\left(\alpha_k + \frac{\Delta t^n}{\Delta x}\beta_k u_{j+k}^{*n}\right)\delta(V - u_{j+k}^{*n})\right\rangle_S \right\rangle. \tag{3.64}$$

Equation (3.64) is

$$\left\langle \left\langle r_j^{*n+1}\delta\left(V - u_j^{*n+1}\right)\right\rangle_S \right\rangle = \left\langle \left\langle \sum_{k=-l}^{k=l} r_j^{*n+1}\frac{r_{j+k}^{*n}}{r_{j+k}^{*n+1}}\left(\alpha_k + \frac{\Delta t^n}{\Delta x}\beta_k u_{j+k}^{*n}\right)\delta(V - u_{j+k}^{*n})\right\rangle_S \right\rangle. \tag{3.65}$$

Let us introduce the following definition

$$r_j^{*n+1}P_j^k = r_{j+k}^{*n}\left(\alpha_k + \frac{\Delta t^n}{\Delta x}\beta_k u_{j+k}^{*n}\right), \tag{3.66}$$

where P_j^k is the probability to expect the sample value of velocity to be equal to u_{j+k}^{*n}. It follows from eq. (3.67) that

$$\left\langle \left\langle r_j^{*n+1}\delta\left(V - u_j^{*n+1}\right)\right\rangle_S \right\rangle = \left\langle \left\langle \sum_{k=-l}^{k=l} r_j^{*n+1}P_j^k\delta(V - u_{j+k}^{*n})\right\rangle_S \right\rangle. \tag{3.67}$$

We impose that the stochastic velocity at the following time step t^{n+1} is equal to

$$u_j^{*n+1} = \begin{cases} u_{j-l}^{*n}, & \text{with probability } P_j^{-l}, \\ \dots & \\ u_{j+l}^{*n}, & \text{with probability } P_j^{l}. \end{cases} \tag{3.68}$$

The stochastic density is

$$r_j^{*n+1} = \sum_{k=-l}^{k=l} r_{j+k}^{*n} \left(\alpha_k + \frac{\Delta t^n}{\Delta x} \beta_k u_{j+k}^{*n} \right), \tag{3.69}$$

where the probability is defined as

$$P_j^k = \frac{r_{j+k}^{*n}}{r_j^{*n+1}} \left(\alpha_k + \frac{\Delta t^n}{\Delta x} \beta_k u_{j+k}^{*n} \right). \tag{3.70}$$

Stochastic Lax-Friedrichs method Let us write a stochastic Lax-Friedrichs method for the PDEs (3.22) and (3.23). The PDF equation (3.2) is discretized with a Lax-Friedrichs scheme in space and a forward Euler scheme in time. Thus, we have

$$\overline{\rho}_j^{n+1} \widetilde{f}_j^{n+1} = \frac{\overline{\rho}_{j-1}^n \widetilde{f}_{j-1}^n + \overline{\rho}_{j+1}^n \widetilde{f}_{j+1}^n}{2} - \frac{\Delta t^n}{2\Delta x} V \left(\overline{\rho}_{j+1}^n \widetilde{f}_{j+1}^n - \overline{\rho}_{j-1}^n \widetilde{f}_{j-1}^n \right). \tag{3.71}$$

Accordingly to eq. (3.60) $l = 1$ and

α_{-1}	α_0	α_1	β_{-1}	β_0	β_1	V_{-1}	V_0	V_1
$\frac{1}{2}$	0	$\frac{1}{2}$	$\frac{1}{2}$	0	$-\frac{1}{2}$	V	V	V

Table 3.1: Coefficients in eq. (3.60) discretized with Lax-Friedrichs scheme

Using (3.68), (3.69) and (3.70) we obtain that the stochastic velocity at the following time step t^{n+1} is equal to

$$u_j^{*n+1} = \begin{cases} u_{j+1}^{*n}, & \text{with probability } P_j^{+1}, \\ u_{j-1}^{*n}, & \text{with probability } P_j^{-1} = 1 - P_j^{+1}. \end{cases} \tag{3.72}$$

The stochastic density is

$$r_j^{*n+1} = r_j^{*n} - \frac{\Delta t^n}{\Delta x} \left(F_{j+1/2}^n - F_{j-1/2}^n \right), \tag{3.73}$$

where the probability is defined as

$$P_j^{+1} = \frac{1}{2} \frac{r_{j+1}^{*n}}{r_j^{*n+1}} \left(1 - \frac{\Delta t^n}{\Delta x} u_{j+1}^{*n} \right), \qquad P_j^{-1} = 1 - P_j^{+1}, \tag{3.74}$$

and the flux is

$$F^n_{j+1/2} = \frac{r^{*n}_j u^{*n}_j + r^{*n}_{j+1} u^{*n}_{j+1}}{2} - \frac{\Delta x}{2\Delta t^n}\left(r^{*n}_{j+1} - r^{*n}_j\right). \tag{3.75}$$

It is known that the classical Lax-Friedrichs scheme in space with the Euler scheme in time has the first order of the point-wise convergence. The stochastic scheme, given by (3.72) and (3.73), has only a weak convergence for the mean density and for all Favre moments of velocity. The expected order of convergence is one.

Stochastic GForce method The GForce scheme is a combination of the Lax-Friedrichs and the Lax-Wendroff schemes. It is still first order accurate. If the problem consists in a linear advection, the GForce method behaves similarly to the Godunov method. The GForce scheme is defined by the following expression

$$\overline{\rho}^{n+1}_j \widetilde{f}^{n+1}_j = \overline{\rho}^n_j \widetilde{f}^n_j + \frac{V\Delta t^n}{\Delta x}\left(-\overline{\rho}^n_{j+1/2}\widetilde{f}^n_{j+1/2} + \overline{\rho}^n_{j-1/2}\widetilde{f}^n_{j-1/2}\right), \tag{3.76}$$

where

$$\overline{\rho}^n_{j+1/2}\widetilde{f}^n_{j+1/2} = \frac{1}{2}\frac{\Delta x}{\Delta t^n}(1+c)\left[1-(1-c)\omega\right]\overline{\rho}^n_j\widetilde{f}^n_j - \frac{1}{2}\frac{\Delta x}{\Delta t^n}(1-c)\left[1-(1+c)\omega\right]\overline{\rho}^n_j\widetilde{f}^n_j = -\beta_0\overline{\rho}^n_j\widetilde{f}^n_j, \tag{3.77}$$

$$c = V\frac{\Delta t^n}{\Delta x}, \qquad \omega = \frac{1}{1+cfl}. \tag{3.78}$$

The definitions of c and ω from eq. (3.78) imply that

$$1-(1-c)\omega > 0, \qquad 1-(1+c)\omega > 0. \tag{3.79}$$

where CFL constant is given by (3.58).

In terms of the stochastic process (3.68), (3.69) and (3.70), the stochastic GForce scheme reads

$$u^{*n+1}_j = \begin{cases} u^{*n}_{j+1}, & \text{with probability } P^{+1}_j, \\ u^{*n}_{j-1}, & \text{with probability } P^{-1}_j, \\ u^{*n}_j, & \text{with probability } P^0_j = 1 - P^{+1}_j - P^{-1}_j. \end{cases} \tag{3.80}$$

$$r^{*n+1}_j = r^{*n}_j - \frac{\Delta t^n}{\Delta x}(F^n_{j+1/2} - F^n_{j-1/2}), \tag{3.81}$$

$$P^{+1}_j = \frac{1}{2}\frac{r^{*n}_{j+1}}{r^{*n+1}_j}(1-c_{j+1})[1-\omega(1+c_{j+1})],\ P^{-1}_j = \frac{1}{2}\frac{r^{*n}_{j-1}}{r^{*n+1}_j}(1-c_{j-1})[1-\omega(1-c_{j-1})],$$

$$P^0_j = 1 - P^{+1}_j - P^{-1}_j, \tag{3.82}$$

where $c_j = u^{*n}_j\frac{\Delta t^n}{\Delta x}$.

$$F^n_{j+1/2} = \frac{r^{*n}_j u^{*n}_j + r^{*n}_{j+1}u^{*n}_{j+1}}{2} - \frac{\Delta x}{2\Delta t^n}\left(\frac{cfl + c^2_{j+1}}{1+cfl}r^{*n}_{j+1} - \frac{cfl+c^2_j}{1+cfl}r^{*n}_j\right). \tag{3.83}$$

Here again, the numerical stochastic process weakly converges to the PDF statistics with first order of convergence.

Stochastic Godunov method Godunov's scheme is a conservative numerical scheme. It is first order accurate in both space, and time. Discretized the PDF eq. (3.2) with this scheme, we obtain

$$\overline{\rho}_j^{n+1}\widetilde{f}_j^{n+1} = \overline{\rho}_j^n\widetilde{f}_j^n - \frac{\Delta t^n}{\Delta x}\left(|V|\overline{\rho}_j^n\widetilde{f}_j^n + V^-\overline{\rho}_{j+1}^n\widetilde{f}_{j+1}^n - V^+\overline{\rho}_{j-1}^n\widetilde{f}_{j-1}^n\right), \tag{3.84}$$

where

$$V^+ = \max(V,0), \qquad V^- = \min(V,0). \tag{3.85}$$

Accordingly to eq. (3.60) $l = 1$ and

α_{-1}	α_0	α_1	β_{-1}	β_0	β_1	V_{-1}	V_0	V_1
0	1	1	1	-1	-1	V^+	$\lvert V\rvert$	V^-

Table 3.2: Coefficients in eq. (3.60) discretized with Godunov scheme

The numerical stochastic scheme for (3.84) reads

$$r_j^{*n+1} = r_j^{*n} - \frac{\Delta t^n}{\Delta x}\left(|u_j^{*n}|r_j^{*n} + u_{j+1}^- r_{j+1}^{*n} - u_{j-1}^+ r_{j-1}^{*n}\right), \tag{3.86}$$

where

$$u_{j-1}^+ = \max(u_{j-1}^{*n},0), \qquad u_{j+1}^- = \min(u_{j+1}^{*n},0). \tag{3.87}$$

The associated stochastic process for velocity is given by

$$u_j^{*n+1} = \begin{cases} u_{j+1}^{*n}, & \text{with probability } P_j^{+1}, \\ u_{j-1}^{*n}, & \text{with probability } P_j^{-1}, \\ u_j^{*n}, & \text{with probability } P_j^0 = 1 - P_j^{+1} - P_j^{-1} \end{cases} \tag{3.88}$$

with probabilities defined as

$$P_j^{+1} = \frac{r_{j+1}^{*n}}{r_j^{*n+1}} u_{j+1}^- \frac{\Delta t^n}{\Delta x}, \tag{3.89}$$

$$P_j^{-1} = \frac{r_{j-1}^{*n}}{r_j^{*n+1}} u_{j-1}^+ \frac{\Delta t^n}{\Delta x}, \tag{3.90}$$

$$P_j^0 = \frac{r_j^{*n}}{r_j^{*n+1}}\left(1 - |u_j^{*n}|\frac{\Delta t^n}{\Delta x}\right). \tag{3.91}$$

This stochastic scheme also converges weakly to the PDF statistics with first order of convergence in space and in time.

Stochastic Lax-Wendroff method In order to obtain the stochastic Lax-Wendroff method in space the same procedure is used that for the stochastic Lax-Friedrichs method.

PDF. The classical Lax-Wendroff method is a two-step approach. It is second-order accurate in both space and time for smooth function. The first step in the Lax-Wendroff method calculates values for $\widetilde{f}$ at half time steps, $t^n + 1/2$ and half grid points, $x_j + 1/2$. In the second step values at $t^n + 1$ are calculated using the data for t^n and $t^n + 1/2$. Consequently, at the first step the discretized equation for the PDF eq. (3.2) is

$$\overline{\rho}_j^{n+1/2}\widetilde{f}_j^{n+1/2} = \frac{\overline{\rho}_j^n\widetilde{f}_j^n + \overline{\rho}_{j+1}^n\widetilde{f}_{j+1}^n}{2} - \frac{\Delta t^n}{2\Delta x}V\left(\overline{\rho}_{j+1}^n\widetilde{f}_{j+1}^n - \overline{\rho}_j^n\widetilde{f}_j^n\right) \tag{3.92}$$

and at the second step

$$\overline{\rho}_j^{n+1}\widetilde{f}_j^{n+1} = \overline{\rho}_j^n\widetilde{f}_j^n - \frac{\Delta t^n}{\Delta x}V\left(\overline{\rho}_{j+1/2}^{n+1/2}\widetilde{f}_{j+1/2}^{n+1/2} - \overline{\rho}_{j-1/2}^{n+1/2}\widetilde{f}_{j-1/2}^{n-1/2}\right). \tag{3.93}$$

Stochastic process. Replacing $\widetilde{f}$ in eq. (3.92) by the stochastic approximation (3.57), at time $n + 1/2$ the probability to stay in the same cell with the velocity u_j^{*n} is written as

$$P_j^0 = \frac{\frac{1}{2}r_j^{*n}\left(1 + u_j^{*n}\frac{\Delta t^n}{\Delta x}\right)}{\overline{r^*}}, \tag{3.94}$$

where

$$\overline{r^*} = \frac{1}{2}(r_j^{*n} + r_{j+1}^{*n}) + \frac{1}{2}\frac{\Delta t^n}{\Delta x}\left(r_j^{*n}u_j^{*n} - r_{j+1}^{*n}u_{j+1}^{*n}\right). \tag{3.95}$$

Here, $\overline{r^*}$ is a mean density. The evolution of the velocity on interface is

$$u_{j+1/2}^{*n+1/2} = \begin{cases} u_j^{*n}, & \text{with probability } P_j^0\left(r_j^{*n}, u_j^{*n}; r_{j+1}^{*n}, u_{j+1}^{*n}\right), \\ u_{j+1}^{*n}, & \text{with probability } 1 - P_j^0\left(r_j^{*n}, u_j^{*n}; r_{j+1}^{*n}, u_{j+1}^{*n}\right), \end{cases} \tag{3.96}$$

$$r_{j+1/2}^{*n+1/2} = \overline{r^*}\left(r_j^{*n}, u_j^{*n}; r_{j+1}^{*n}, u_{j+1}^{*n}\right). \tag{3.97}$$

The evolution of the velocity at the center of cell at time t^{n+1} is

$$u_j^{*n+1} = \begin{cases} u_{j-1/2}^{*n+1/2}, & \text{with probability } P_j^0\left(r_{j-1/2}^{*n+1/2}, u_{j-1/2}^{*n+1/2}, r_{j+1/2}^{*n+1/2}, u_{j+1/2}^{*n+1/2}\right), \\ u_{j+1/2}^{*n+1/2}, & \text{with probability } 1 - P_j^0\left(r_{j-1/2}^{*n+1/2}, u_{j-1/2}^{*n+1/2}, r_{j+1/2}^{*n+1/2}, u_{j+1/2}^{*n+1/2}\right), \end{cases} \tag{3.98}$$

$$r_j^{*n+1} = \overline{r^*}\left(r_{j-1/2}^{*n+1/2}, u_{j-1/2}^{*n+1/2}, r_{j+1/2}^{*n+1/2}, u_{j+1/2}^{*n+1/2}\right). \tag{3.99}$$

The construction of eqs. (3.96) to (3.99) can be rigorously justified in the manner similar to that detailed in section 3.2.1. As the classical Lax-Wendroff is a second order accurate scheme in time and in space for smooth functions, the numerical stochastic process should also weakly converge to smooth PDF statistics with the second order of convergence in time and in space.

Mean density conservation in stochastic schemes

The proposed numerical schemes such as Lax-Friedrichs, Lax-Wendroff, GForce and Godunov do not preserve the mean density $\overline{\rho}$ exactly, so some fluctuations may appear in numerical tests. For illustration purposes we assume, without loss of generality, that if the mean density is homogeneous in space and in time: $\overline{\rho} = 1$ then the integration, e.g. of the discretized eq. (3.84) in case of Godunov scheme, gives

$$\int_{-\infty}^{\infty} \widetilde{f}_j^{n+1} dV = 1 - \frac{\Delta t^n}{\Delta x} \left[\int_{-\infty}^{\infty} |V| \widetilde{f}_j^n dV - \int_{-\infty}^{0} V \widetilde{f}_{j+1}^n dV - \int_{0}^{\infty} V \widetilde{f}_{j-1}^n dV \right] \neq 1. \tag{3.100}$$

This signifies that the mean density $\overline{\rho} = 1$ is not preserved. As a consequence, the mean of the stochastic density is not constant:

$$\left\langle \frac{1}{N_r} \sum_{irea=1}^{N_r} r_{irea,j}^{*n+1} \right\rangle = 1 - ... \neq 1. \tag{3.101}$$

It means that the stochastic density will fluctuate.

3.2.2 Schemes for stochastic partial differential equations

In order to recover numerical solution of the SPDEs (3.42)-(3.43) we use a physical (or differential) splitting method, the forward Euler scheme in time and the deduced above stochastic schemes in space. The procedure can be written in four steps:

1. We start to solve the following PDEs:

$$\frac{\partial r u''}{\partial t} + \frac{\partial r u''^2}{\partial x} = 0, \tag{3.102}$$

$$\frac{\partial r}{\partial t} + \frac{\partial r u''}{\partial x} = 0 \tag{3.103}$$

with initial conditions at time t^n:

$$IC : r(t^n, x), u''(t^n, x). \tag{3.104}$$

Stochastic schemes, proposed above for the PDEs (3.102) and (3.103) construct stochastic process of density $r^*(t, x)$ and velocity $u''^*(t, x)$ at time $t^{n+1/4}$ in such the manner that their statistics coincide with statistics of eqs. (3.102) and (3.103). The eq. (3.103) for the density is completely solved at this time step. Consequently, the obtained value of stochastic density is the same for the following sub-temporal steps, i.e. $r^*(t^{n+1/4}, x) = r^*(t^{n+2/4}, x) = r^*(t^{n+3/4}, x) = r^*(t^{n+1}, x)$.

2. At the second step of differential splitting equation for stochastic velocity is considered

$$\frac{\partial u''}{\partial t} = \frac{1}{\overline{r}} \frac{\partial \overline{r u''^2}}{\partial x}, \tag{3.105}$$

$$IC : r^*(t^{n+1/4}, x), u''^*(t^{n+1/4}, x). \tag{3.106}$$

Numerically, the solution at $t^{n+2/4}$ for stochastic velocity realization is

$$u''^{*n+2/4} = u''^{*n+1/4} - \frac{\overline{r^{*n+1/4}}}{\overline{r^{*n}}}\widetilde{u''^{*n+1/4}} + \widetilde{u''^{*n}}. \tag{3.107}$$

The idea behind the correction (3.107) can be understood if we consider the continuous equation for the fluctuating velocity when the averaging operator is applied:

$$\frac{\overline{\partial r u''}}{\partial t} + \frac{\overline{\partial r u''^2}}{\partial x} = \frac{\partial \overline{r u''^2}}{\partial x} \tag{3.108}$$

using one of the proposed above stochastic schemes the value of velocity is known at time $t^{n+1/4}$. On the other hand, the eq. (3.102) for velocity fluctuations discretized with a forward Euler scheme reads

$$(ru'')^{n+1/4} - (ru'')^n = -\Delta t \frac{r^n}{\overline{r^n}} \frac{\partial r u''^2}{\partial x}. \tag{3.109}$$

Applying averaging to eq. (3.109), it yields

$$\overline{(ru'')^{*n+1/4}} - \overline{(ru'')^{*n}} = \overline{r^{*n+1/4}}\widetilde{u''^{*n+1/4}} - \overline{r^{*n}}\widetilde{u''^{*n}} = -\overline{\Delta t \frac{\partial r u''^2}{\partial x}}. \tag{3.110}$$

Thus, the term $-\frac{1}{\overline{r}}\overline{\Delta t \frac{\partial r u''^2}{\partial x}}$ at time t^n can be approximated by

$$\frac{\overline{r^{n+1/4}}}{\overline{r^{*n}}}\widetilde{u''^{*n+1/4}} - \widetilde{u''^{*n}}, \tag{3.111}$$

whence the formula (3.107) follows.

3. The Langevin term of eq. (3.43) is now added to the calculated variable. Equation yields

$$\frac{\partial u''}{\partial t} = -C_1 \omega u'' + \sqrt{C_0 \varepsilon}\dot{\xi}(t), \tag{3.112}$$

$$IC : r^*(t^{n+2/4}, x) = r^*(t^{n+1/4}, x), u''^*(t^{n+2/4}, x). \tag{3.113}$$

Numerical scheme reads

$$u''^{*n+3/4} = u''^{*n+2/4} - C_1 \omega^n (u''^{*n+2/4} - \widetilde{u''^{*n+2/4}})dt + \sqrt{C_0 \varepsilon^{*n+2/4}}\xi^{n+2/4}\sqrt{\Delta t}. \tag{3.114}$$

4. Due to the finite number of realizations of stochastic fields: $\overline{\xi} \neq 0$ and $\overline{\xi^2} \neq 1$. In addition, we are interested in the Favre statistics and first of all we want to conserve the Favre-averaged fluctuating velocity. There are two possible solutions: either to adjust the noise such that

$$\overline{r^*\xi} = 0 \tag{3.115}$$

(using for example the Gram-Schmidt process which allow constructing an orthogonal vector ξ to r) or to correct the Favre-averaged velocity after step 3 [Ourliac2009]:

$$u''^{*n+1} = u''^{*n+3/4} - \widetilde{u''^{*n+3/4}}. \tag{3.116}$$

If a second moment $\widetilde{u''^2}$ calculated from stochastic fields is used in the definition of ε and a first moment $\widetilde{u''}$ is not corrected after each time step, the finite sample noise of an Ornstein-Uhlenbeck process can drive a numerical instability, which causes quantities that should be conserved not only to fluctuate around a constant value but even to grow or decay away from it [LemonsLackman1995]. In order to avoid a noise-induced instability in self-consistent Monte-Carlo calculations Lemons proposes to linearly shift the stochastic variables so as to return the "conserved" quantities back to their desired values, for instance by applying a correction to the Favre-averaged velocity (eq. (3.116)).

General remarks

The SPDEs have the multivalued solutions, whereas the proposed numerical stochastic process in each realization has only a single solution which is discontinuous and takes values from different branches of multiplicity of velocity and density. This process converges to the PDF statistics only weakly but not in the sense of point-wise spatial convergence for each velocity field. In fact, the stochastic velocity "chooses" one branch of multivalued velocity solution. The probability of such a choice of the branch depends on the uniformly distributed noise and the density.

Spatial convergence for statistical moments can be considered only on intervals where these statistics are continuous functions. One would expect that the spatial convergence should be the same for the PDF statistics, i.e. if the PDF equation is discretized by the first order scheme, then deduced stochastic scheme is a first accurate.

The separation of statistical error and spatial error in the SPDEs (3.42)-(3.43) is difficult because of the presence of two stochastic errors: one from uniformly distributed noise, which allows calculating velocity transport equation and another from Gaussian noise which takes into account a stochastic force.

3.3 Numerical tests

In this section several numerical tests are performed using the derived above numerical stochastic schemes. In some tests we consider also a spatial scheme of Osher (details are given in [Toro1999]) and a kinetic scheme for one-dimensional pressureless gas taken from [BouchutJin2003]. These two schemes satisfy the entropy increase condition. The scheme, which satisfy the entropy increase condition, will be called classical scheme. In order to minimize the numerical diffusion, we set the Courant-Friedrichs-Lewy constant close to one, but still meeting the eq. (3.58): $cfl = 0.99$. Backward and direct step, ramp, triangle and hat initial velocity profiles in one-dimensional case are considered for Riemann problem. Averaged numerical solutions are compared with analytical solutions (if the latter exist) or numerical solution of corresponding PDF equation. Further, the SPDEs (3.42)-(3.43) are solved for the considered initial profiles of velocity, and solutions are compared to numerical solution of the transport equation (3.16) for the velocity PDF.

Following abbreviations are used in the legends of figures:

- Stochastic Godunov method (SGod)
- Stochastic Lax-Friedrichs method (SL-F)
- Stochastic Lax-Wendroff method (SL-W)
- Stochastic GForce method (SGF)
- Exact solution, used as reference (Ex sol)

A logarithmic scale is used for spatial and statistical convergence.

3.3.1 Backward step velocity profile

In this test we investigate the ability of stochastic numerical scheme to recover a multivalued solution for a Riemann problem described in section 3.1.1. The problem consists in the transfer of the backward step velocity pattern centered at the middle of the domain. The center of the strip is denoted by x_c and is situated at $x_c = 0.5\,\mathrm{m}$. The velocity V_0 is set to $V_0 = 1\,\mathrm{m/s}$ and the density $\overline{\rho_0}$ is $1\,\mathrm{kg/m^3}$. The length of the computational domain is $L = 1\,\mathrm{m}$. The investigated PDEs are given by eqs. (3.22) and (3.23).

Numerical solution

We consider a stochastic process (r^*_{irea}, u^*_{irea}), $irea = 1, .., N_r$ satisfying following initial conditions. At time $t = 0$ the stochastic density and velocity are defined as

$$r^{*n=0}_{irea,j} = 1\,\mathrm{kg/m^3}, \qquad u^{*n=0}_{irea,j} = \begin{cases} 1\,\mathrm{m/s}, & \text{if } j \leq [\frac{N_x}{2}], \\ 0, & \text{if } j > [\frac{N_x}{2}]. \end{cases} \; j = 1, .., N_x, \; irea = 1, .., N_r. \quad (3.117)$$

The process (r^*_{irea}, u^*_{irea}) evaluates accordingly to stochastic schemes (Lax-Friedrichs, Lax-Wendroff, GForce or Godunov) described above.

Spatial profiles. To trace the mean profile of the density, the Favre moments of the velocity and the distribution of the density and the velocity, the stochastic fields are fixed to $N_r = 10^4$ and the domain D is discretized with $N_x = 10^3$ cells (figs. 3.3 to 3.16).

Figure 3.3 shows spatial profiles of the mean density and its variance at time $t = 0.1\,\mathrm{s}$. The mean density is compared to the exact solution (3.15). Due to the numerical diffusion at the left limit situated at 0.5 m where a multivalued solution appears the mean density is blurred, and then stochastic fluctuations of density are presented up to the right limit situated at 0.6 m of the multivalued solution.

The appearance of density fluctuations in the region of multivalued solution $x \in [0.5\,\mathrm{m}; 0.6\,\mathrm{m}]$ can be explained by the nature of numerical stochastic schemes. The density takes the largest values in this interval, because its calculation is based on the gradient of velocity. In fact, the formula for density can be seen as a classical scheme for the density transport equation. The numerical velocity derivative is proportional to $O\left(\frac{1}{\Delta x}\right)$, which results in large density fluctuations. In the right panel of fig. 3.3 one can observe that the stochastic Godunov method yields higher stochastic density fluctuations compared to other methods.

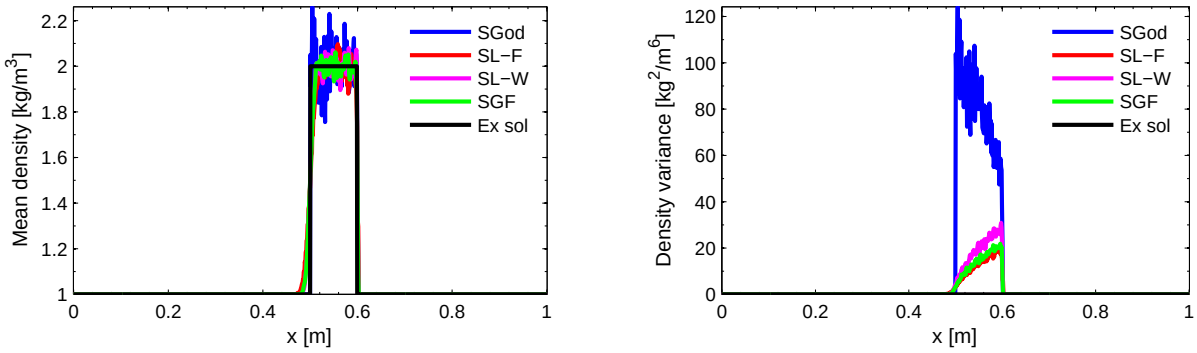

Figure 3.3: Backward step: spatial profiles of mean density (left) and density variance (right) at time $t = 0.1\,\mathrm{s}$. $N_r = 10^4$, $N_x = 10^3$.

The Favre average, variance, flatness and hyperflatness of the velocity field are illustrated in figs. 3.4 and 3.5 at the time $t = 0.1\,\mathrm{s}$. We observe that the Favre moments of the velocity remain continuous all along the regions of the single-valued solution of the PDEs. In the region of the multivalued solution fluctuations appear, but even here the comparison of the spatial profiles of the Favre moments of the velocity with the theoretical solution gives good result. The skewness and the flatness of the velocity have two peaks at $x = 0.5\,\mathrm{m}$ and $x = 0.6\,\mathrm{m}$, because of the stochastic nature of numerical schemes. One concludes that as expected the greater the order of moments is, the more realizations are required to predict it.

To understand the nature of fluctuations of density and, as a consequence, the velocity statistics let us consider the sample space of density and velocity at time 0.1 s from which statistics above are calculated (figs. 3.6 to 3.8).

Figure 3.6 illustrates one sample space of the density and the velocity obtained with the stochastic Lax-Friedrichs scheme. It can be seen that the velocity alternates between one and zero at each numerical point of space in the region $[0.585\,\mathrm{m}; 0.595\,\mathrm{m}]$. Such a behavior of the velocity realization can be justified by the nature of the stochastic Lax-Friedrichs scheme, in which at the following time step the velocity at point x_j can take either the value x_{j-1} or the value x_{j+1}. As a consequence, there are two possible realizations of the velocity. The first is

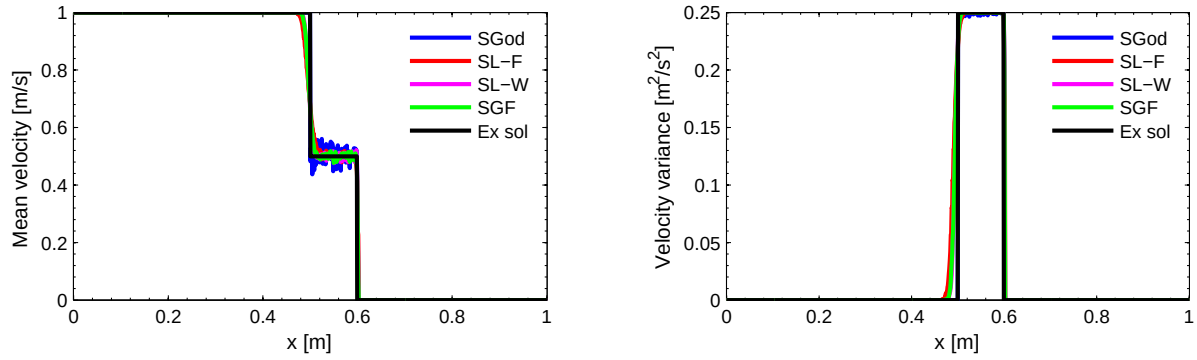

Figure 3.4: Backward step: spatial profiles of Favre average (left) and Favre variance (right) of velocity at time $t = 0.1\,\mathrm{s}$. $N_r = 10^4$, $N_x = 10^3$.

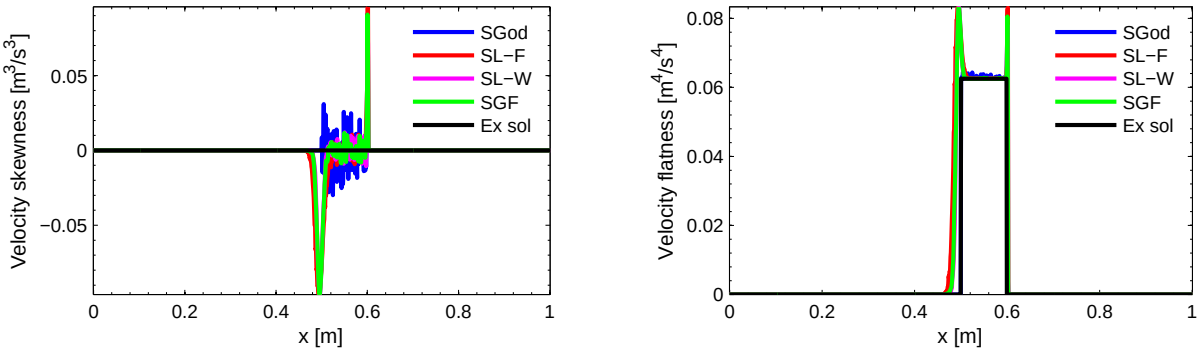

Figure 3.5: Backward step: spatial profiles of Favre skewness (left) and flatness (right) of velocity at time $t = 0.1\,\mathrm{s}$. $N_r = 10^4$, $N_x = 10^3$.

similar to the realization presented in fig. 3.6, but the region where the velocity alternated between one and zero is different from $[0.585\,\mathrm{m}; 0.595\,\mathrm{m}]$. The second possible realization of the velocity is similar to the realization demonstrated on the right panel of fig. 3.7. The corresponding stochastic density takes large values at points where the stochastic velocity changes values. One can note in fig. 3.6 that even the velocity is equal to one in the interval $[0.575\,\mathrm{m}; 0.585\,\mathrm{m}]$, the density takes substantial values. It can be explicated by the fact that on the previous time step the velocity alternated between one and zero on this interval.

Figures 3.7 and 3.8 show sample spaces of density and velocity obtained with stochastic Lax-Wendroff, GForce and Godunov schemes. There are two possible velocity realizations for three stochastic schemes. The first is when there is only one point where the velocity jumps from one to zero. The density increases to the left limit of this point and decreases from this point. Another possible realization is when the velocity is equal to one or to zero in the intervals larger than Δx.

Figures 3.9 to 3.11 demonstrate the mean profile of the density, the Favre moments of

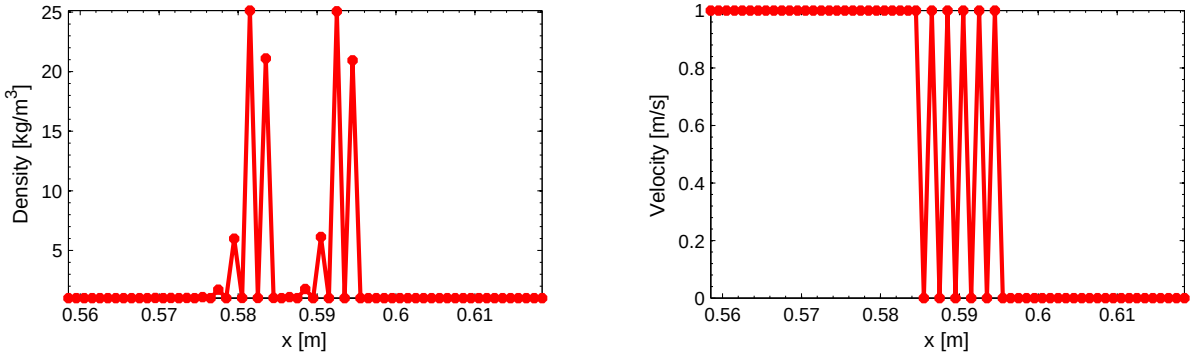

Figure 3.6: Backward step: spatial profiles of one realization of density and velocity at time $t = 0.1\,\mathrm{s}$ obtained by stochastic Lax-Friedrichs method. $N_r = 10^4$, $N_x = 10^3$.

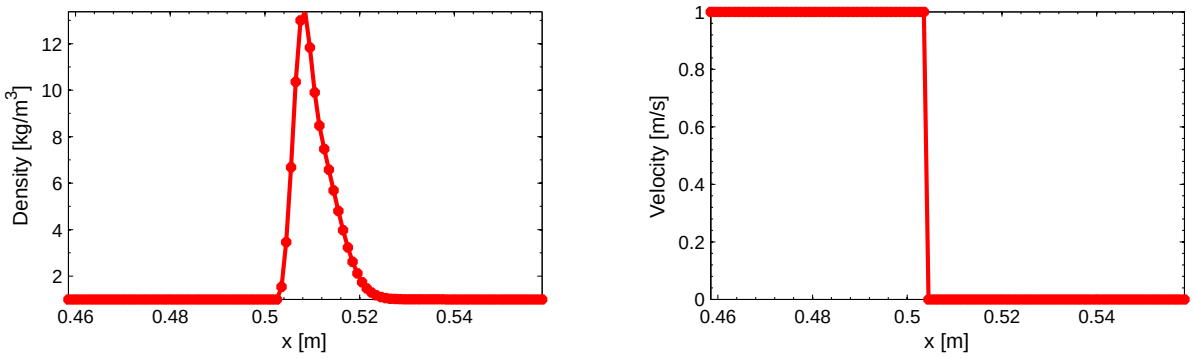

Figure 3.7: Backward step: spatial profiles of one realization of density and velocity at time $t = 0.1\,\mathrm{s}$ obtained by stochastic Lax-Wendroff method. $N_r = 10^4$, $N_x = 10^3$.

the velocity when the following mean density correction is applied:

$$r^{*n+1}_{irea,j} = \overline{\rho}^{n+1}_j \frac{r^{*n+1}_{irea,j}}{\overline{r^{*n+1}_j}}. \tag{3.118}$$

The same stochastic noise is used both in the construction of spatial profiles without mean density correction (figs. 3.3 to 3.5) and with mean density correction (3.118) (figs. 3.9 to 3.11). One can note that the proposed mean correction of density does not improve spatial profiles; in particular, the Favre moments of velocity are more fluctuation-polluted than those without correction. Consequently this correction will not be considered in following tests.

The PDF of the velocity is given by two Dirac delta functions concentrated at $u_1 = 0\,\mathrm{m/s}$ and $u_2 = 1\,\mathrm{m/s}$ with the probability $\frac{1}{2}$. Numerical Favre-averaged PDF is defined by the expression (2.94). Figures 3.12 to 3.15 show the calculated Favre-averaged PDF and the distribution of the velocity at $x = 0.5505\,\mathrm{m}$, $t = 0.1\,\mathrm{s}$ non normalized. These diagrams detail the ability of four stochastic schemes to predict the PDF. Numerical values of probability to have $u_1 = 0\,\mathrm{m/s}$ and $u_2 = 1\,\mathrm{m/s}$ are close to $\frac{1}{2}$ for four stochastic schemes. One can note that

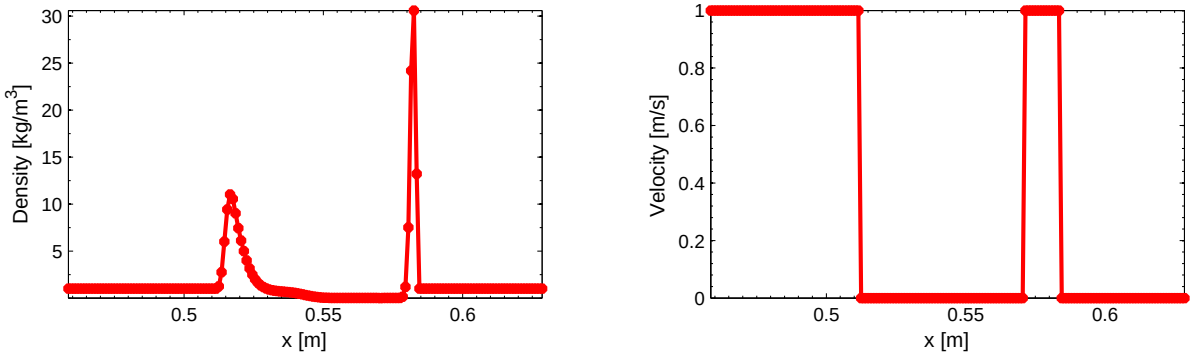

Figure 3.8: Backward step: spatial profiles of one realization of density and velocity at time $t = 0.1\,\mathrm{s}$ obtained by stochastic GForce method. $N_r = 10^4$, $N_x = 10^3$.

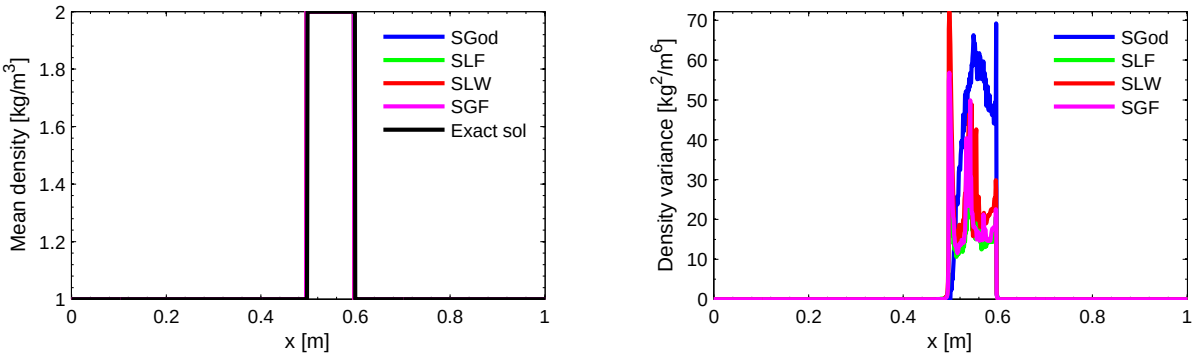

Figure 3.9: Backward step: spatial profiles of mean density (left) and density variance (right) at time $t = 0.1\,\mathrm{s}$ with mean correction of density (3.118). $N_r = 10^4$, $N_x = 10^3$.

the distribution of values $0\,\mathrm{m/s}$ and $1\,\mathrm{m/s}$ are not uniform, especially for stochastic GForce scheme. But the weighted PDF is close to the theoretical PDF thanks to the correction made by the conditional expectation of the density for given velocities which is plotted in right panel of fig. 3.16.

The distribution of the density is presented in fig. 3.16. We can see that the values of the stochastic density vary approximately from $0.5\,\mathrm{kg/m^3}$ to $100\,\mathrm{kg/m^3}$ for the given Δx and Δt.

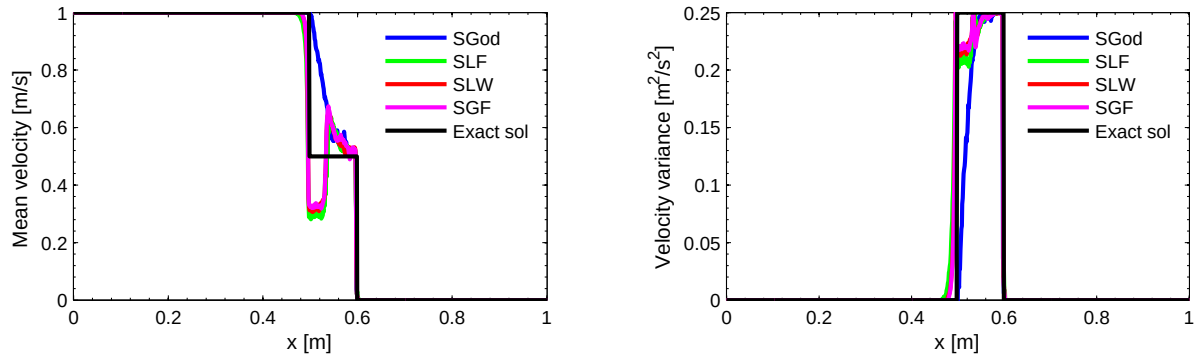

Figure 3.10: Backward step: spatial profiles of Favre average (left) and Favre variance (right) of velocity at time $t = 0.1\,\mathrm{s}$ with mean correction of density (3.118). $N_r = 10^4$, $N_x = 10^3$.

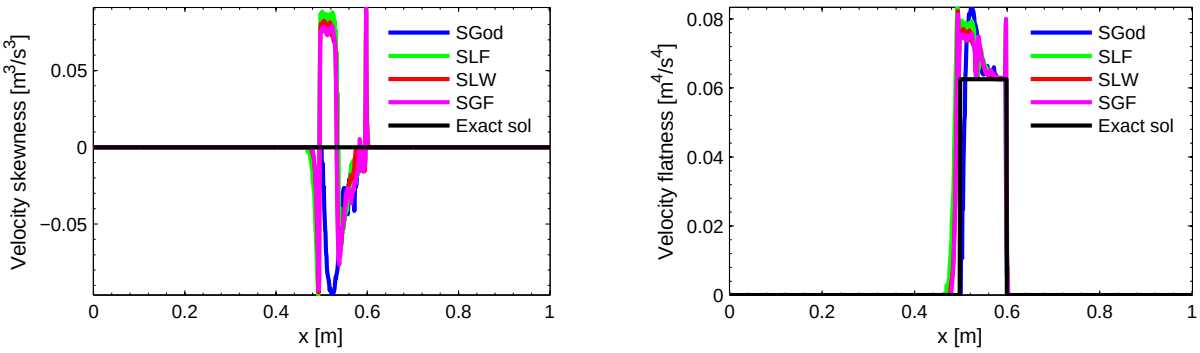

Figure 3.11: Backward step: spatial profiles of Favre skewness (left) and flatness (right) of velocity at time $t = 0.1\,\mathrm{s}$ with mean correction of density (3.118). $N_r = 10^4$, $N_x = 10^3$.

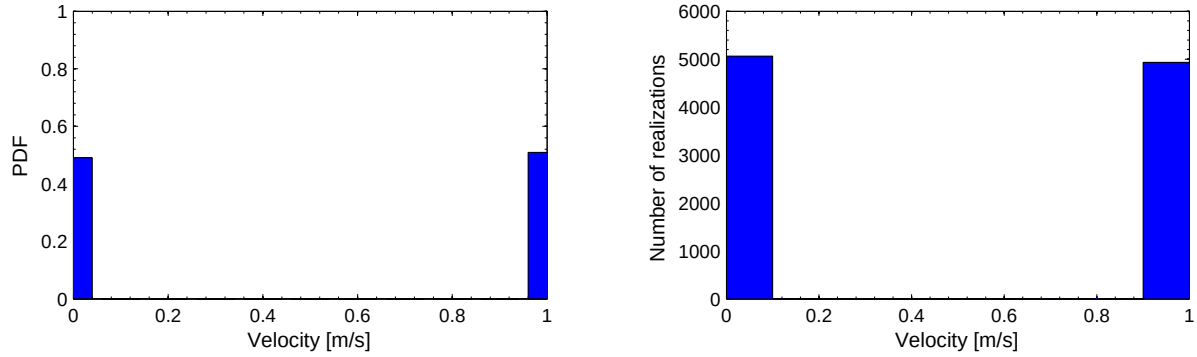

Figure 3.12: Backward step: Favre-averaged PDF (left) and distribution of velocity (right) at $x = 0.5505\,\mathrm{m}$, $t = 0.1\,\mathrm{s}$. Stochastic Godunov method, $N_r = 10^4$, $N_x = 10^3$.

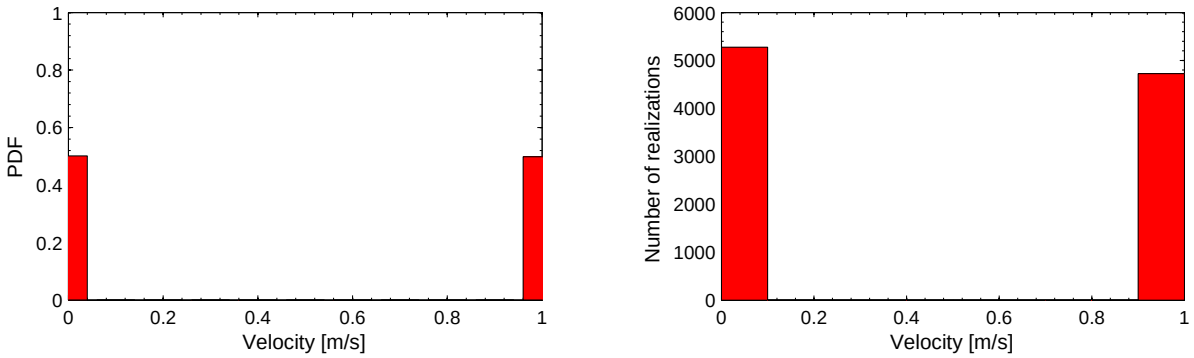

Figure 3.13: Backward step: Favre-averaged PDF (left) and distribution of velocity (right) at $x = 0.5505\,\mathrm{m}$, $t = 0.1\,\mathrm{s}$. Stochastic Lax-Friedrichs method, $N_r = 10^4$, $N_x = 10^3$.

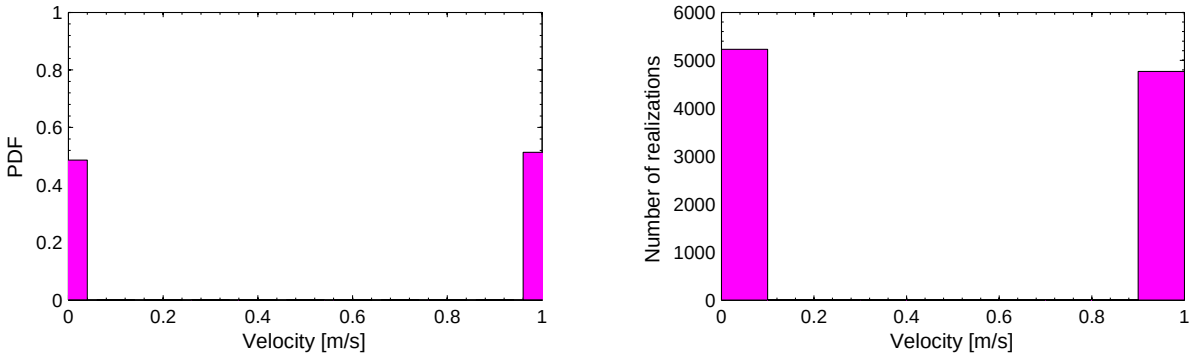

Figure 3.14: Backward step: Favre-averaged PDF (left) and distribution of velocity (right) at $x = 0.5505\,\mathrm{m}$, $t = 0.1\,\mathrm{s}$. Stochastic Lax-Wendroff method, $N_r = 10^4$, $N_x = 10^3$.

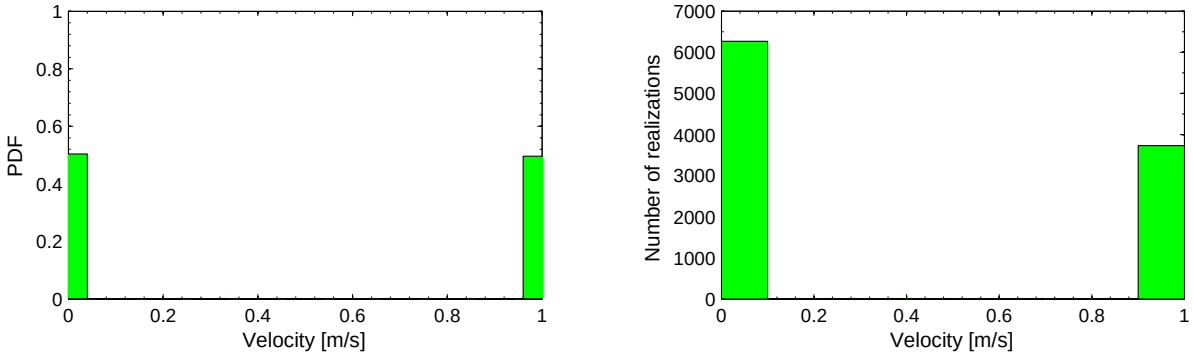

Figure 3.15: Backward step: Favre-averaged PDF (left) and distribution of velocity (right) at $x = 0.5505\,\mathrm{m}$, $t = 0.1\,\mathrm{s}$. Stochastic GForce method, $N_r = 10^4$, $N_x = 10^3$.

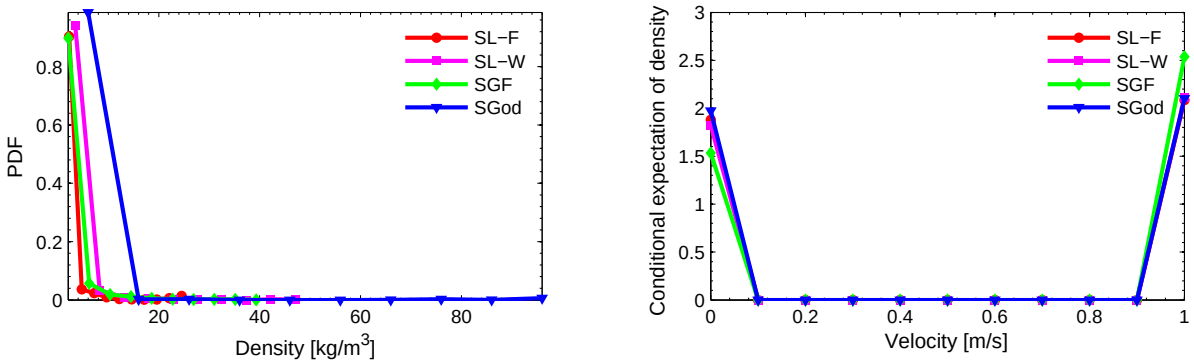

Figure 3.16: Backward step: PDF of density (left) and conditional expectation of density for given velocities (right) at $x = 0.5505\,\mathrm{m}$, $t = 0.1\,\mathrm{s}$. $N_r = 10^4$, $N_x = 10^3$.

Convergence. To assess the convergence of the stochastic methods, the domain of calculation at a given time $t > 0$ is divided on three parts where each solution is continuous, i.e.

$$D = \begin{cases} D_1 = \{x \in [0\,\mathrm{m}; x_c)\}, \\ D_2 = \{x \in [x_c; x_c + V_0 t]\}, \\ D_3 = \{x \in (x_c + V_0 t; 1\,\mathrm{m}]\}, V_0 = 1\,\mathrm{m/s}. \end{cases} \tag{3.119}$$

The error is defined for each interval of D as

$$Error_i = \frac{1}{D_i} \int\limits_{D_i} |Q^{num} - Q^{ref}| dx, \;\; i = 1, 2, 3, \tag{3.120}$$

where Q^{num} is a numerical solution and Q^{ref} is the analytical solution. In the case of statistical errors, calculations are performed for a fixed number of cells: $N_x = 10^5$. The number of stochastic fields varies from $N_r = 10$ to $N_r = 1200$ fields ($N_r = [10,\ 100,\ 500,\ 900,\ 1200]$). The calculated points are best-fitted with the function $f(N_r) = \exp(\alpha) N_r^{\beta}$. This operation is repeated at different time steps.

Figures 3.17 to 3.20 show the evolution of the convergence rates β and coefficients α for the mean density and the Favre moments of the velocity plotted in the region where the multivalued solution appears. We observe that the convergence rates are noised by the spatial error, but they still fluctuate around the expected $N^{-0.5}$. For stochastic Lax-Wendroff method the statistical convergence of the Favre flatness of velocity in the given numerical conditions is not observed. The convergence coefficients fluctuate between -10 and 2 for different stochastic schemes.

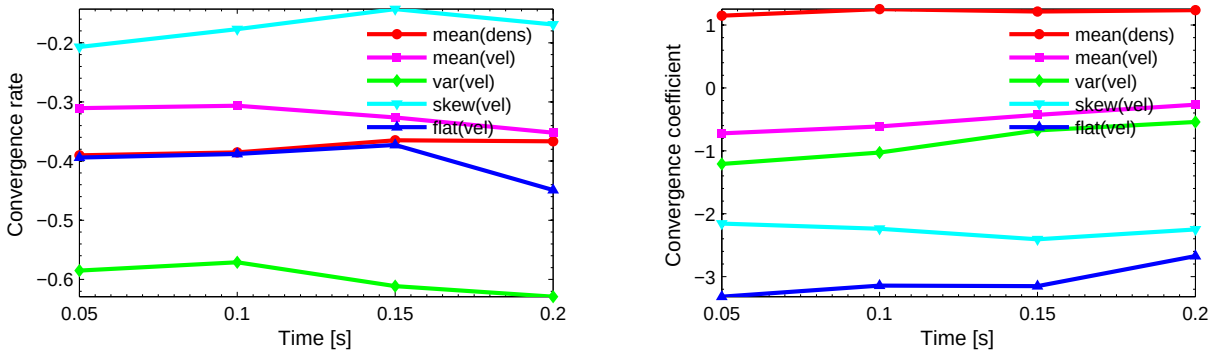

Figure 3.17: Backward step: time evolution of statistical convergence rates (left) and coefficients (right) for $0.5\,\mathrm{m} \leq x \leq 0.5\,\mathrm{m} + V_0 t$, $V_0 = 1\,\mathrm{m/s}$ (stochastic Lax-Friedrichs method). $N_x = 10^5$.

Figure 3.21 illustrates the convergence rates and coefficients for $x \leq 0.5\,\mathrm{m}$ in the interval where only single-valued solution is defined. The first moments of the density and the velocity converge. Higher velocity moments are dominated by spatial error and therefore no statistical convergence can be observed for the chosen spatial discretization. One can explain it also by numerical diffusion near the point $x = 0.5\,\mathrm{m}$.

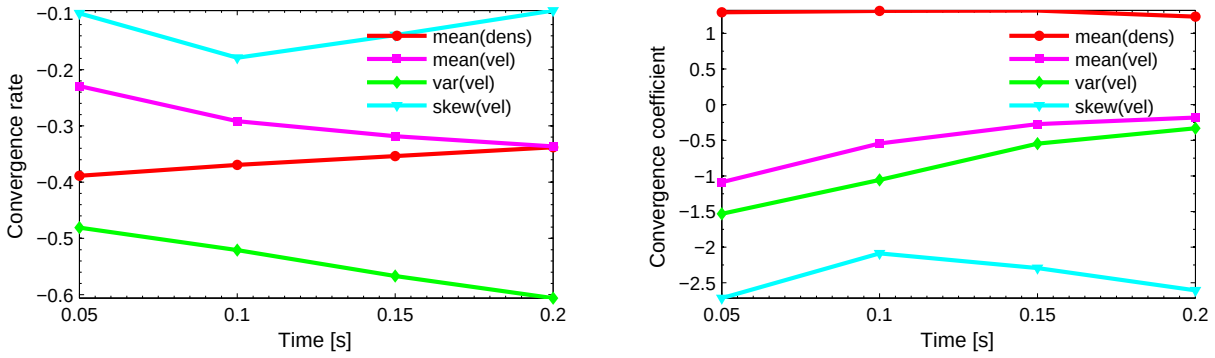

Figure 3.18: Backward step: time evolution of statistical convergence rates (left) and coefficients (right) for $0.5\,\mathrm{m} \leq x \leq 0.5\,\mathrm{m} + V_0 t$, $V_0 = 1\,\mathrm{m/s}$ (stochastic Lax-Wendroff method). $N_x = 10^5$.

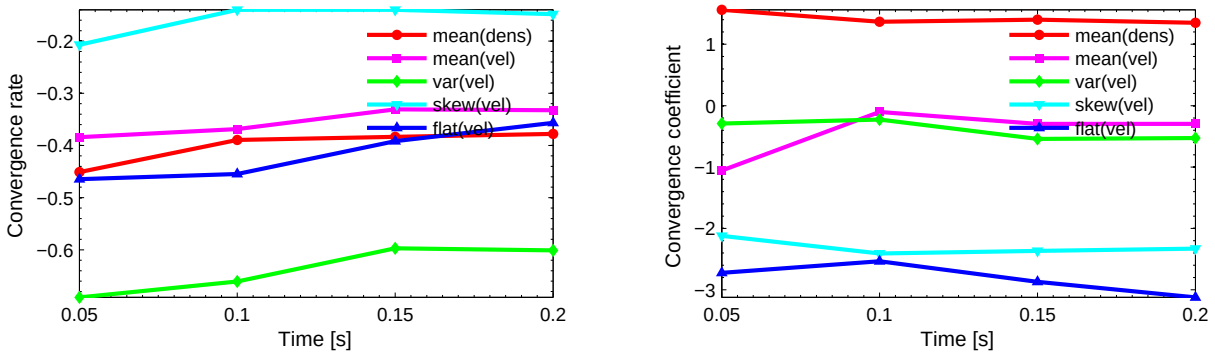

Figure 3.19: Backward step: time evolution of statistical convergence rates (left) and coefficients (right) for $0.5\,\mathrm{m} \leq x \leq 0.5\,\mathrm{m} + V_0 t$, $V_0 = 1\,\mathrm{m/s}$ (stochastic GForce method). $N_x = 10^5$.

The spatial convergence calculations are performed with a fixed number of stochastic fields $N_r = 10^7$. The number of a grid cells is varied from 20 to 100. We recall that CFL constant is 0.99. Indeed we failed to observe spatial convergence in a similar test with $cfl = 0.5$. This latter result can be explained either by the statistical error which dominates on the spatial error for the chosen N_r or by significant diffusion of the numerical solution.

The separation of statistical and spatial errors is a complicated problem. In order to observe the spatial convergence it is necessary to consider a number of stochastic realizations $N_r \gg 1$. The statistical error should be much smaller than spatial: $O(\frac{1}{N_r}) \ll O(\Delta x)$. Figures 3.17 to 3.19 show statistical errors at $t = 0.2\,\mathrm{s}$ for stochastic Lax-Friedrichs, Lax-Wendroff and GForce schemes.

We inject $N_r = 10^7$ into the interpolated formula for statistical error, which allows us to estimate the latter for this large number of realization. From this estimation we deduce that value 10^7 is situated on the verge of validity for spatial convergence estimation for the mean density, Favre-averaged velocity and velocity variance. For higher moments 10^7 realizations are simply not sufficient. For stochastic Godunov scheme (fig. 3.20), the sepa-

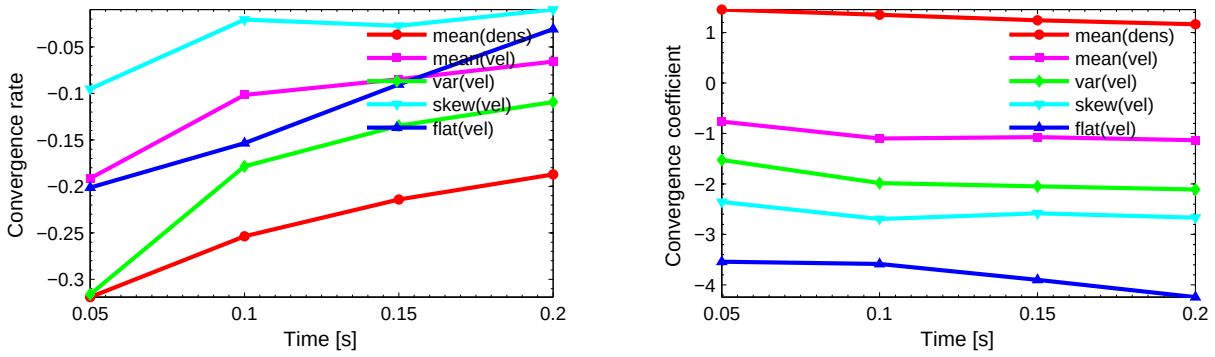

Figure 3.20: Backward step: time evolution of statistical convergence rates (left) and coefficients (right) for $0.5\,\mathrm{m} \leq x \leq 0.5\,\mathrm{m} + V_0 t$, $V_0 = 1\,\mathrm{m/s}$ (stochastic Godunov method). $N_x = 10^5$.

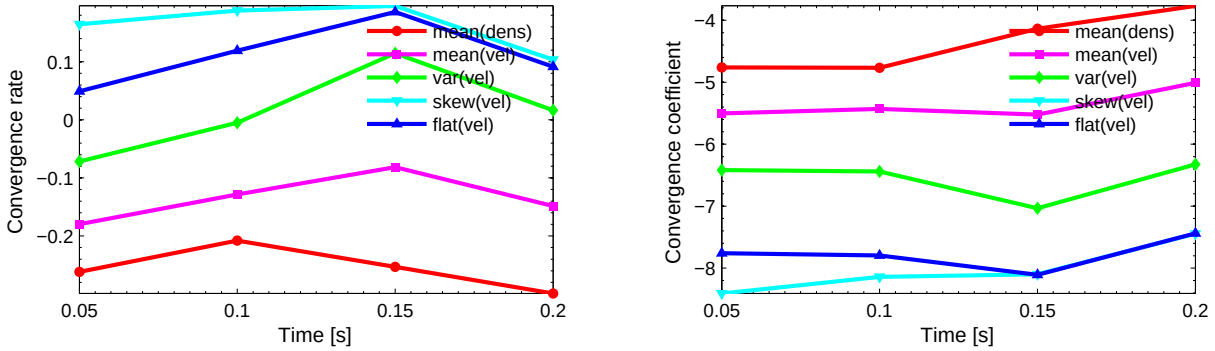

Figure 3.21: Backward step: time evolution of statistical convergence rates (left) and coefficients (right) for $0 \leq x \leq 0.5$ (stochastic Lax-Friedrichs method). $N_x = 10^5$.

ration of stochastic error from spatial error is even more complicated because the statistical convergence rate is close to 0.

The spatial convergence in logarithmic scale $A_i log(N_x) + B_i$ for $t = 0.2\,\mathrm{s}$ is presented in table 3.3. Convergence coefficients (A_1, B_1) stand for the numerical solution in the interval D_1, (A_2, B_2) are the convergence coefficients in the domain D_2 and (A_3, B_3) correspond to D_3. In the intervals D_1 and D_2 a $\frac{1}{2}$-order spatial convergence is indeed observed for the mean density, the Favre-averaged velocity and the Favre variance of velocity (error in Δx). There is first order of spatial convergence in the domain D_3 for any proposed stochastic scheme.

As we can note there is no spatial convergence for the stochastic Godunov method. One can justify it by the dominating influence of the statistical error.

One important point that the Lax-Wendroff method in its classical formulation, which is a second order-precise for smooth functions, possess only a first order convergence rate when it is applied to discontinuous functions. The adapted Lax-Wendroff method to stochastic process gives also in the best case the first order of convergence.

Figures 3.22 and 3.23 show the spatial errors for the first and second moments for the

Moments	A_1	A_2	A_3	B_1	B_2	B_3
Stochastic Lax-Friedrichs						
Mean density	-0.56	-0.54	-0.95	-0.74	0.13	1.04
Mean velocity	-0.54	-0.49	-0.97	-1.04	-1.29	0.71
Velocity variance	-0.53	-0.64	-0.99	-1.33	-2.96	0.35
Stochastic Lax-Wendroff						
Mean density	-0.54	-0.52	-0.97	-1.17	-0.33	1.12
Mean velocity	-0.55	-0.5	-0.98	-1.4	-1.62	0.7
Velocity variance	-0.55	-0.51	-0.98	-1.62	-4.01	0.26
Stochastic GForce						
Mean density	-0.53	-0.51	-0.98	-1.24	-0.35	1.13
Mean velocity	-0.53	-0.51	-0.97	-1.47	-1.6	0.66
Velocity variance	-0.53	-0.5	-0.98	-1.7	-4.03	0.23
Stochastic Godunov						
Mean density	-	-	-0.99	-	-	1.18
Mean velocity	-	-	-0.92	-	-	0.32
Velocity variance	-	-	-0.84	-	-	-0.53

Table 3.3: Backward step: spatial convergence of different methods. $N_r = 10^7$. The error on the interval i (as defined in eq. (3.120)) is approximated with $A_i log(N_x) + B_i$, with $i = 1, 2, 3$.

density and the velocity as a function of N_x, at time $t = 0.2\,\mathrm{s}$, calculated with the stochastic GForce method. Its convergence rate is -0.5 in the region of multivalued solution .

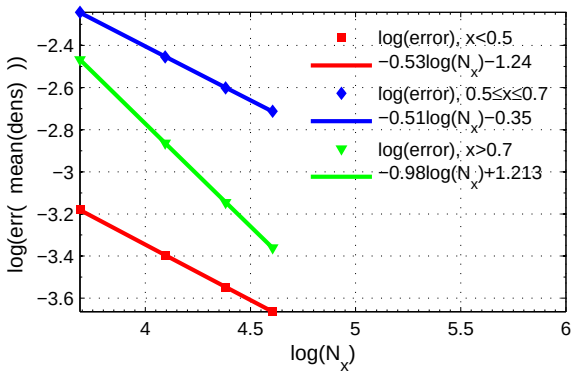

Figure 3.22: Backward step: spatial error for mean density at $t = 0.2\,\mathrm{s}$ calculated by stochastic GForce method. $N_r = 10^7$.

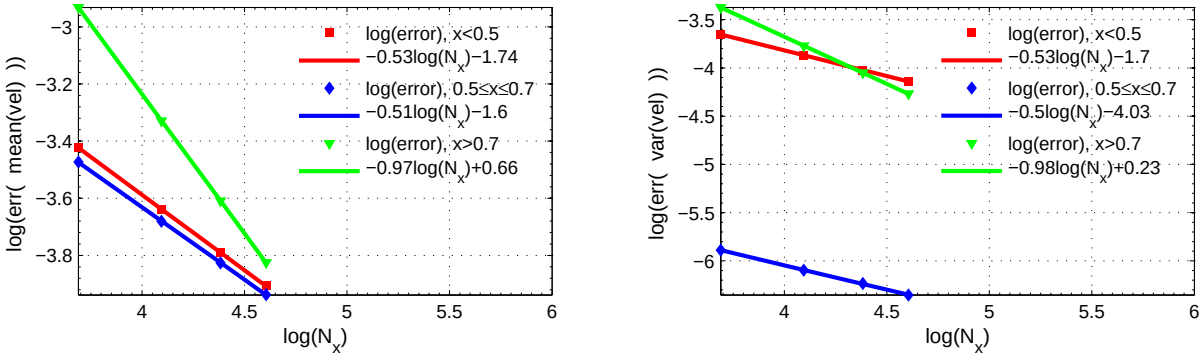

Figure 3.23: Backward step: spatial error for the mean (left panel) and variance (right panel) of velocity at $t = 0.2\,\mathrm{s}$ calculated by stochastic GForce method. $N_r = 10^7$.

3.3.2 Scheme non-dissipativity test

In this test we verify that the numerical stochastic schemes are non-dissipative.

PDF

The mean density identically equals to one in time and in space. The PDF satisfies the following transport equation:

$$\frac{\partial \overline{g}}{\partial t} + \frac{\partial V' \overline{g}}{\partial x} = -\frac{\partial}{\partial V'} \left(\frac{\partial}{\partial x} \left(\overline{u'^2} \right) \overline{g} \right), \tag{3.121}$$

where $u'(t,x)$ denotes fluctuating velocity, and V' stands for the sample space of velocity u'. At the initial time the mean velocity is zero: $\overline{u}(t=0,x) = \overline{u'}(t=0,x) = 0$. The Favre statistics coincide with the Reynolds statistics, $u(t,x) = u'(t,x) = u''(t,x)$. Multiplying the eq. (3.121) by V' (V'^2), and integrating the result over V' it can be shown that the first and the second velocity moments satisfy

$$\frac{\partial \overline{u'}}{\partial t} + \frac{\partial \overline{u'^2}}{\partial x} = \frac{\partial \overline{u'^2}}{\partial x} \tag{3.122}$$

and

$$\frac{\partial \overline{u'^2}}{\partial t} + \frac{\partial \overline{u'^3}}{\partial x} = 0. \tag{3.123}$$

According to (3.122) the first moment is constant in time

$$\frac{\partial \overline{u'}}{\partial t} = 0, \tag{3.124}$$

$$\overline{u'} \equiv 0. \tag{3.125}$$

Integrating the eq. (3.123) over space we deduce that the integral in space of the second moment of velocity is constant:

$$\frac{\partial I}{\partial t} = 0, \qquad I = \int_{-\infty}^{+\infty} \overline{u'^2} dx = const. \tag{3.126}$$

PDEs

The PDEs equivalent to the transported PDF (3.121) read

$$\frac{\partial r}{\partial t} + \frac{\partial r u''}{\partial x} = 0, \tag{3.127}$$

$$\frac{\partial r u''}{\partial t} + \frac{\partial r u''^2}{\partial x} = \frac{r}{\overline{r}} \frac{\partial \overline{r u''^2}}{\partial x}. \tag{3.128}$$

where the mean density $\overline{r}(t,x)$ is equal to one. Multivalued solution of eqs. (3.127) and (3.128) has to conserve the integral I defined in (3.126).

Numerical solution: test 1

Calculations are performed on the domain $D = [0\,\mathrm{m}; 10\,\mathrm{m}]$. The initial fields of the velocity are

$$u'' = \begin{cases} 0, & \text{if } x < 4.75\,\mathrm{m}, \\ \sigma\xi \exp\left(-\frac{(x-x_c)^2}{L^2}\right), & \text{if } 4.75\,\mathrm{m} \leq x \leq 5.25\,\mathrm{m},\ \xi = N(0,1), \\ 0, & \text{if } x > 5.25\,\mathrm{m}, \end{cases} \tag{3.129}$$

ξ is a normal Gaussian noise, $x_c = 5\,\mathrm{m}$, $L = 0.1\,\mathrm{m}$ is a characteristic width of velocity domain and $\sigma = 1\,\mathrm{m/s}$ is a maximum standard deviation. The initial profile of the velocity variance is presented in fig. 3.24. The initial value of the integral is

$$I(t=0) = 0.1253\,\mathrm{m}^3/\mathrm{s}^2. \tag{3.130}$$

We check here the convergence of the integral (3.126) calculated from the PDEs. The

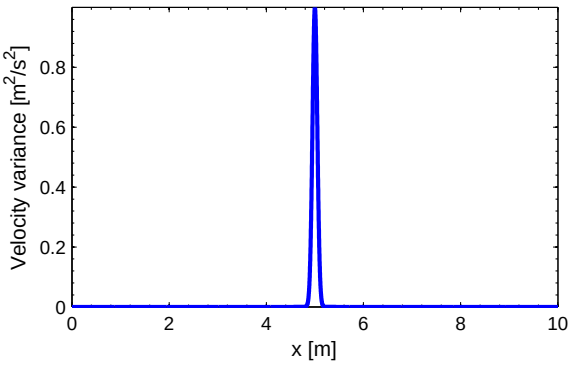

Figure 3.24: Scheme non-dissipativity test: initial spatial profile of velocity variance. $N_r = 10^4$, $N_x = 10^4$.

convergence for velocity moments are investigated in appendix A.5.5.

Spatial profiles. To illustrate spatial profiles of statistics, the computational domain D is discretized with $N_x = 10^4$ points and the number of stochastic fields is set to $N_r = 10^4$. We suppose that the characteristic time t_c is defined as

$$t_c = \frac{L}{\sigma}. \tag{3.131}$$

The evolution of the velocity variance integrated over space is shown in the left panel of fig. 3.25. The time $t = 1\,\mathrm{s}$ corresponds to 10 characteristics times. Thus, the obtained results from different stochastic schemes prove that the integral is indeed conserved at least during ten characteristic times. The deviation of numerical integral from theoretical value of I which is $0.1253\,\mathrm{m}^3/\mathrm{s}^2$ is a consequence of diffusion in time. For example, at $10t_c$, the value of the integral calculated by stochastic Lax-Friedrichs scheme is $0.1174\,\mathrm{m}^3/\mathrm{s}^2$ that is about 6.3% of error from theoretical value. $I^{SGod}(t = 10t_c) = 0.094\,64\,\mathrm{m}^3/\mathrm{s}^2$, that is 24.48%.

Errors for other methods are $Err^{SL-W}(10t_c) = 10.7\%$ and $Err^{SGF}(10t_c) = 13.6\%$, where the error is defined as

$$Err = \frac{|I^{theoret} - I^{num}|}{I^{theoret}}. \tag{3.132}$$

For the time $t \geq 3t_c$ stochastic Godunov method gives the error two times greater than other methods. The error for stochastic Lax-Friedrichs method is minimal in comparison with other approaches.

The right panel of fig. 3.25 shows evolution of spatial profile of velocity variance calculated with stochastic Lax-Friedrichs method. One can note that the velocity variance is diffused in space. At $2t_c$ the non-zero velocity variance is located in $(4.5\,\mathrm{m}; 5.5\,\mathrm{m})$. The value of the maximum peak is approximately $0.25\,\mathrm{m}^2/\mathrm{s}^2$. At $8t_c$ the non-zero velocity variance propagated from $3.7\,\mathrm{m}$ to $6.7\,\mathrm{m}$ and its maximum peak is about $0.8\,\mathrm{m}^2/\mathrm{s}^2$. In addition, one concludes that the fluctuations accumulate with time.

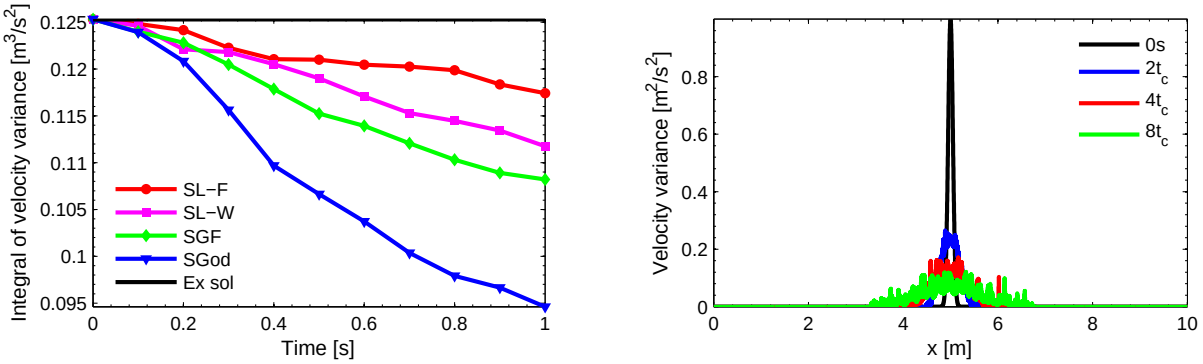

Figure 3.25: Scheme non-dissipativity test: evolution of integral on space of velocity variance (left) and spatial profile of velocity variance at different time calculated with stochastic Lax-Friedrichs scheme (right). $N_r = 10^4$, $N_x = 10^4$.

Figure 3.26 illustrates spatial profiles of velocity variance at time $t = 1\,\mathrm{s} = 10t_c$ calculated with different numerical schemes from which the integrals I at this time were calculated. As it is shown, the velocity variance obtained by stochastic Godunov method is less diffused in space than other variances and therefore the integral of velocity variance (right panel of fig. 3.25) is lower compared to other methods.

The same test was also performed with a kinetic scheme taken from [BouchutJin2003]. We considered first and second order schemes in space and in time. There was no conservation of the integral (3.126). In fact, when the PDEs (3.127), (3.128) equivalent to the PDF equation (3.121) are solved with entropy increase condition, we necessarily obtain the energy dissipation. A fluctuating velocity tends to zero, because when the kinetic scheme treats jumps, the energy dissipates.

The evolution of spatial profiles of velocity variance calculated with kinetic scheme are shown in left panel of fig. 3.27. One can note that the velocity variance diffuses slowly in space and dissipates faster when stochastic profiles. At $2t_c$ (right panel offig. 3.27) the velocity variance calculated with kinetic scheme remains close to the velocity variance calculated with stochastic Lax-Friedrichs scheme. At $4t_c$ it is two times lower than it is in stochastic schemes

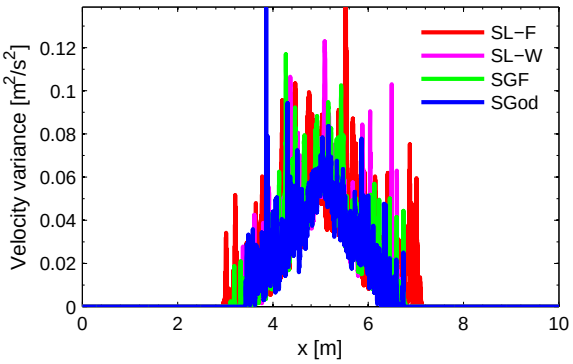

Figure 3.26: Scheme non-dissipativity test: spatial profile of velocity variance at $10t_c$. $N_r = 10^4$, $N_x = 10^4$.

(left panel of fig. 3.28) and at $10t_c$ it finally vanishes compared to the theoretical value (right panel of fig. 3.28). This test demonstrates that classical scheme which satisfies the entropy increase condition is not suited to solve the SPDEs if equivalence between the PDF equation and the SPDEs need to be preserved.

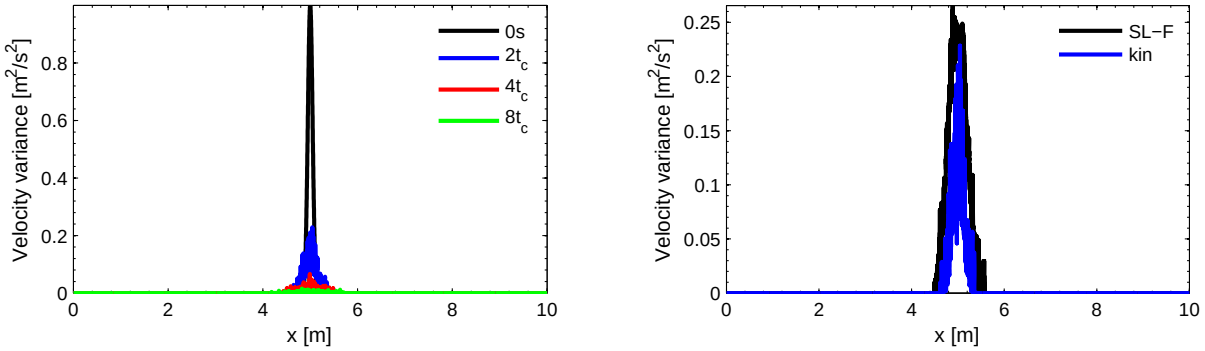

Figure 3.27: Scheme non-dissipativity test: evolution of velocity variance at different time calculated with kinetic scheme (left), spatial profile of velocity variance at $2t_c$ (right). $N_r = 10^4$, $N_x = 10^4$.

In order to understand better the process of the energy dissipation we compare the evolution of sample space in time for two schemes: stochastic Lax-Friedrichs and kinetic scheme.

Figures 3.29 to 3.31 demonstrate the evolution of three realizations of density and velocity at $2t_c$, $4t_c$ and $6t_c$ respectively obtained with kinetic scheme. At $2t_c$ each realization contains a peak of density at different space point, where the velocity has a large jump. One can note that sample space of velocity oscillates due the RHS of the velocity transport equation containing the term $\frac{1}{\bar{r}}\frac{\partial \overline{ru''^2}}{\partial x}$. The latter depends on x and modifies profiles of velocity at each point in time and in space. As a consequence, at next time step the velocity modifies the density and vice versa. The same fluctuating profiles of velocity fields were obtained for kinetic scheme with $cfl = 0.5$ and for Osher scheme with $cfl = 0.99$.

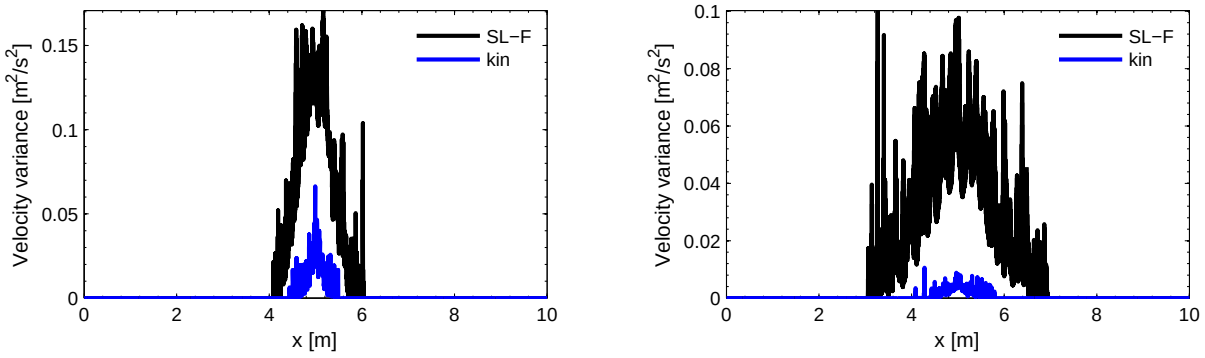

Figure 3.28: Scheme non-dissipativity test: spatial profile of velocity variance at $4t_c$ (left) and at $10t_c$ (right). $N_r = 10^4$, $N_x = 10^4$.

The same test was conducted with zero RHS in the velocity transport equation. There were then no oscillations in velocity fields. Thus we can conclude that the nature of oscillations is related to the term $\frac{1}{\bar{r}}\frac{\partial \overline{ru''^2}}{\partial x}$.

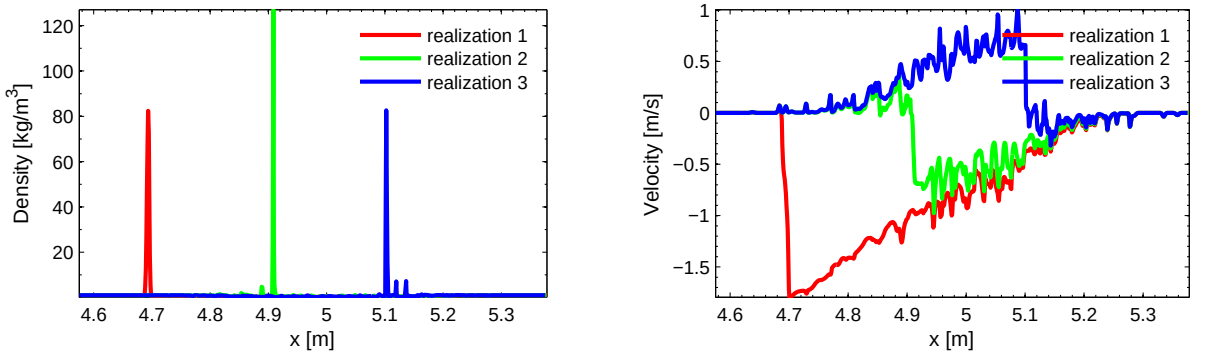

Figure 3.29: Scheme non-dissipativity test: examples of stochastic density (left) and velocity (right) fields at $2t_c$ calculated with kinetic scheme. $N_r = 10^4$, $N_x = 10^4$.

At time $4t_c = 0.4\,\mathrm{s}$ one can see that peaks of density and points of gradient catastrophe for corresponding velocities move to the left boundary or to the right boundary accordingly the sign of velocity. For example, the density peak for 1st realization, located at point $x = 4.7\,\mathrm{m}$, at $6t_c = 0.6\,\mathrm{s}$, moves to $x = 4.6\,\mathrm{m}$. The velocity at this point is lower than $-1\,\mathrm{m/s}$.

The absolute values of stochastic velocity fields decrease in time. At time $6t_c$ the absolute value of velocity is three times lower that at $2t_c$ for all the realizations. The propagation in space of density Dirac delta function is slower than in previous time. The breakdown of the velocity profile explains the energy dissipation observed in this test. In kinetic scheme the velocity profiles usually have the same sign in space for each considered realization. Accordingly the density contains multiple Dirac delta functions corresponding to these velocity jumps.

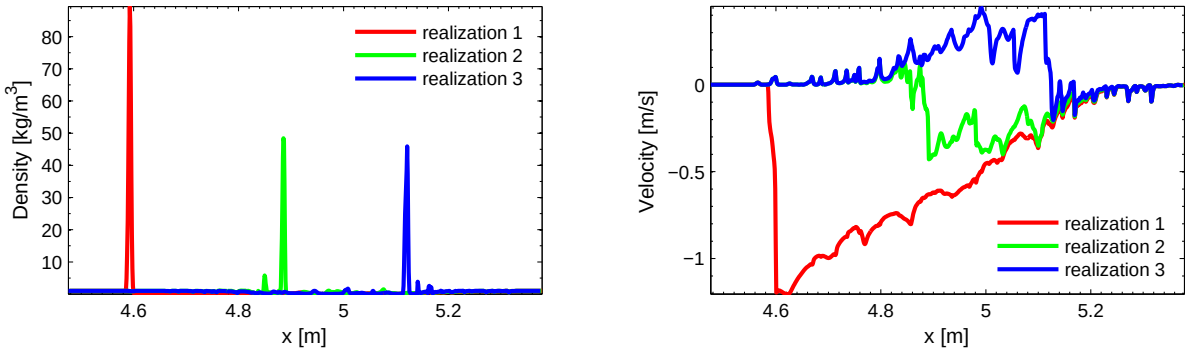

Figure 3.30: Scheme non-dissipativity test: examples of stochastic density (left) and velocity (right) fields at $4t_c$ calculated with kinetic scheme. $N_r = 10^4$, $N_x = 10^4$.

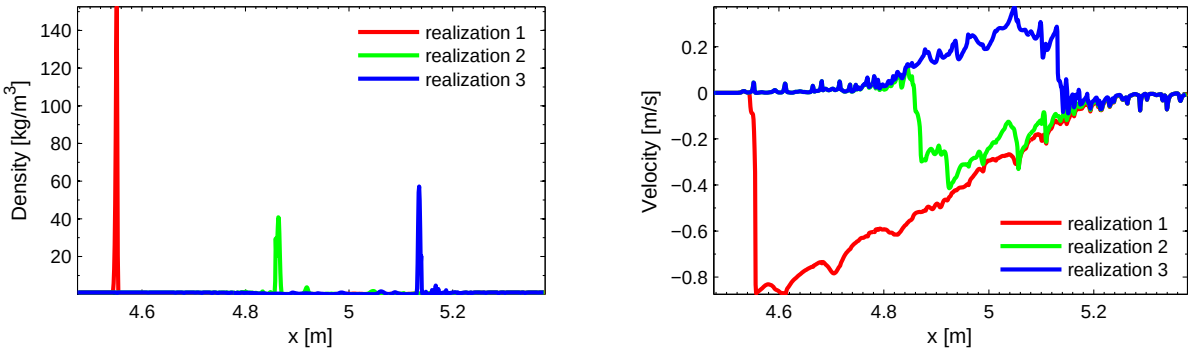

Figure 3.31: Scheme non-dissipativity test: examples of stochastic density (left) and velocity (right) fields at $6t_c$ calculated with kinetic scheme. $N_r = 10^4$, $N_x = 10^4$.

Figures 3.32 and 3.33 show the evolution of stochastic density and velocity fields obtained with stochastic Lax-Friedrichs scheme. The behavior of the scheme is completely different from that of kinetic scheme. At time $2t_c$ a zoom in of the velocity profiles clearly oscillate. In fact, such the profiles consist of multiple jumps between negative, zero and positive values.

At times $4t_c$ and $6t_c$ the maximum absolute value of velocity remains the same as for $2t_c$. The amplitude of velocity jumps increases with simulation time. The density and velocity profiles propagate in space faster than in kinetic scheme. In the mean this scheme give the correct velocity variance while kinetic scheme dissipates the energy which tends finally to zero and does not properly propagate in space.

Let us consider statistics at $t = 1\,\mathrm{s} = 10t_c$ for studied stochastic schemes. During the calculations the mean velocity remains equal to zero (fig. 3.34).

Contrariwise, in fig. 3.35, the mean density fluctuates. The largest fluctuations of the density are observed in the solution obtained with the stochastic Godunov method. One can note that at the time 1 s the maximum deviation from the theoretical value 1 is about 20%. The right panel of the fig. 3.35 shows a zoom in of the mean density. As we can see, the mean density calculated with stochastic Lax-Friedrichs, stochastic Lax-Wendroff and

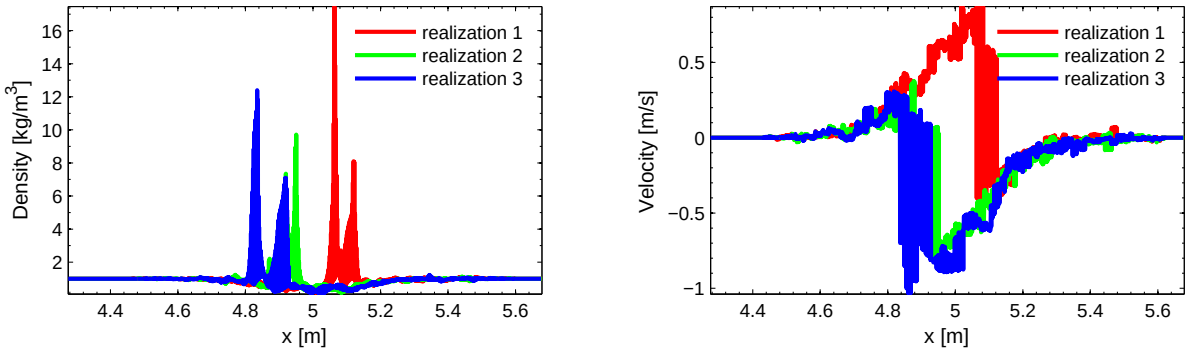

Figure 3.32: Scheme non-dissipativity test: examples of stochastic density (left) and velocity (right) fields at $2t_c$ calculated with stochastic Lax-Friedrichs scheme. $N_r = 10^4$, $N_x = 10^4$.

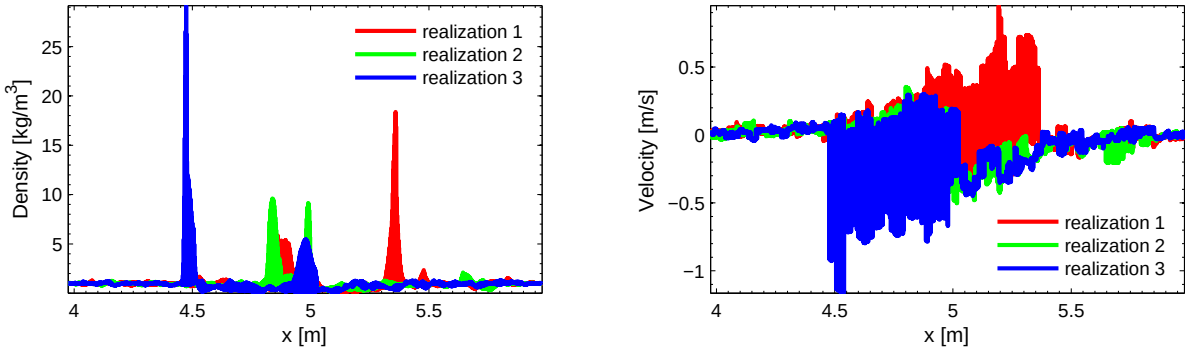

Figure 3.33: Scheme non-dissipativity test: examples of stochastic density (left) and velocity (right) fields at $6t_c$ calculated with stochastic Lax-Friedrichs scheme. $N_r = 10^4$, $N_x = 10^4$.

stochastic GForce methods is in a good agreement with the theoretical value (the error is below 5×10^{-5}).

Figure 3.36 illustrates the density variance. Its values are significant in stochastic Godunov scheme. High density fluctuations have impact on the velocity statistics. That is why the integral I calculated by stochastic Godunov scheme contains the largest error in comparison with other schemes.

Figure 3.37 shows spatial profiles of skewness and flatness of velocity. We can observe that these profiles are close for four stochastic schemes despite of some fluctuations of each method.

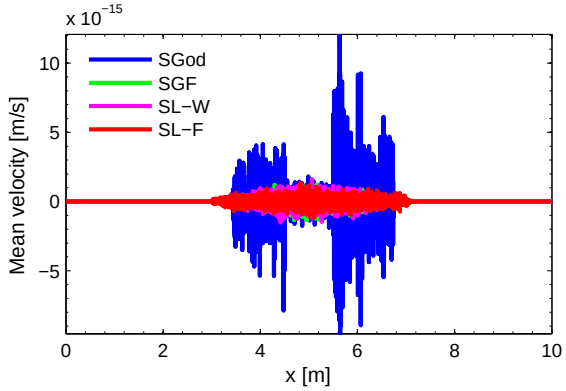

Figure 3.34: Scheme non-dissipativity test: spatial profile of mean velocity at time $t = 1\,\mathrm{s}$. $N_r = 10^4$, $N_x = 10^4$.

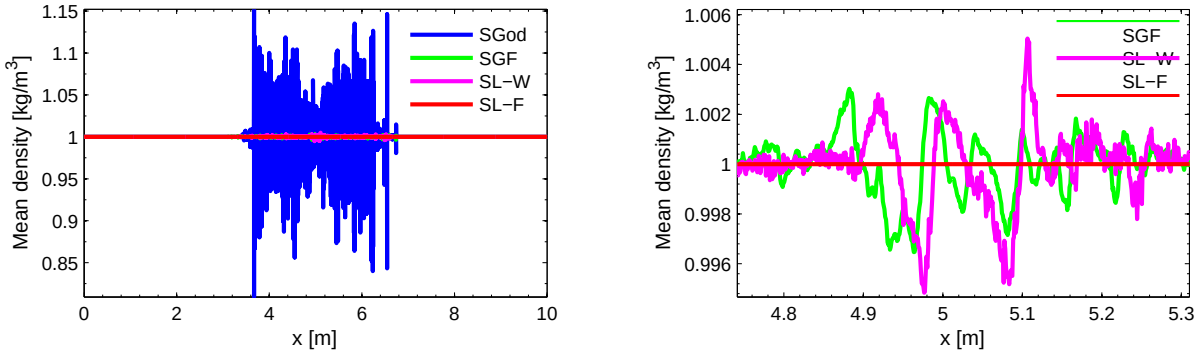

Figure 3.35: Scheme non-dissipativity test: spatial profiles of mean density at time $t = 1\,\mathrm{s}$. $N_r = 10^4$, $N_x = 10^4$.

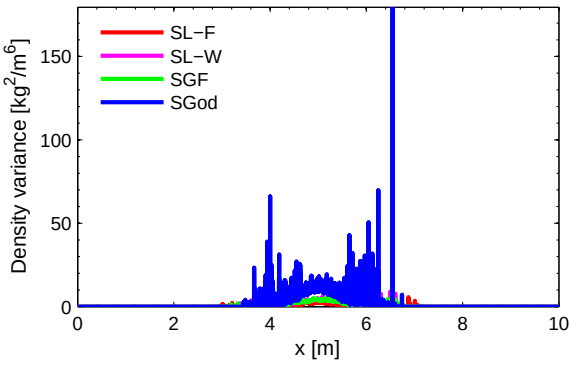

Figure 3.36: Scheme non-dissipativity test: spatial profile of the variance of density at time $t = 1\,\mathrm{s}$. $N_r = 10^4$, $N_x = 10^4$.

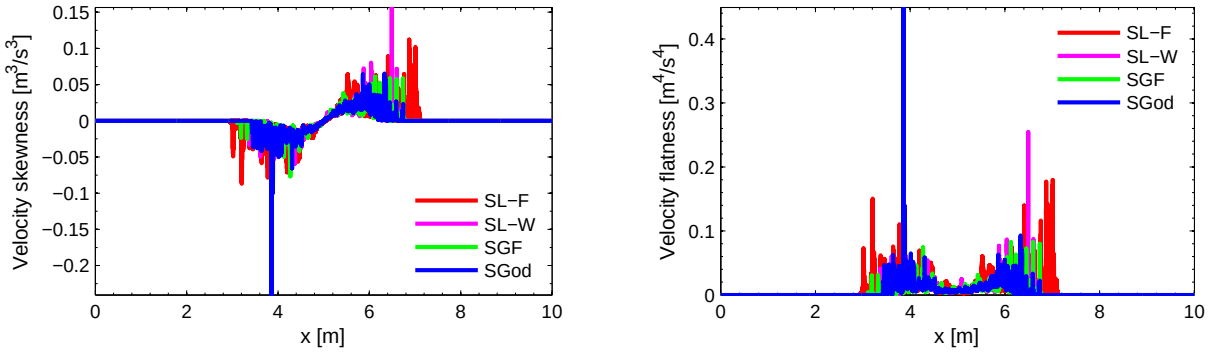

Figure 3.37: Scheme non-dissipativity test: spatial profiles of skewness and flatness of velocity at time $t = 1\,\mathrm{s}$. $N_r = 10^4$, $N_x = 10^4$.

Convergence. We consider the statistical convergence for the integral I. The number of cells is fixed to $N_x = 10^5$ and the number of stochastic fields varies from 100 to 1700. As above, the finite time, where statistical convergence is considered, is $t = 10t_c = 1\,\mathrm{s}$. The integral $I = 0.1253\,\mathrm{m}^3/\mathrm{s}^2$ calculated from the initial velocity variance profile (fig. 3.24) is taken as a reference solution with which other integrals are compared during the time t. Figure 3.38 shows the time evolution of the convergence rates and coefficients of the integral I in logarithmic scale (see the definition of I in (3.126)). In the left panel of fig. 3.38 we can observe that the convergence rate deteriorates for long calculation time. At the same time the convergence coefficient decreases, which partially compensates the statistical error. For example, at time $t = 0.2\,\mathrm{s}$, the statistical convergence to the integral I for the stochastic Lax-Friedrichs method is $err_1 = 6.2339N_r^{-0.48}$ and at time $t = 1\,\mathrm{s}$ $err_2 = 1.05N_r^{-0.08}$. If $N_r < 100$, then $err_2 < err_1$. When $N_r > 3000$, then $err_2 \approx 5err_1$.

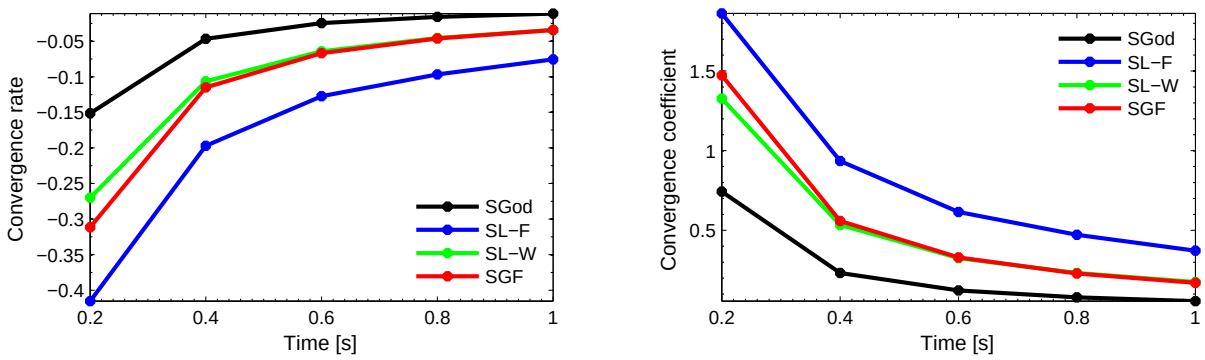

Figure 3.38: Scheme non-dissipativity test: time evolution of the statistical convergence rates (left) and coefficients (right) for integral over space of velocity variance. $N_x = 10^5$.

3.3.3 Statistically homogeneous velocity fluctuations test

In this test, we consider the model PDF eq. (3.16) with all the terms in RHS. We want to check that the solution still tends to the solution of the statistically homogeneous equation.

PDF

The PDF transport eq. (3.16) is investigated. It is assumed that a turbulent frequency is constant and constants C_0 and C_1 are following

$$C_0 = 2C_1, \qquad \omega = const. \tag{3.133}$$

The mean density is supposed to be a constant

$$\overline{\rho}(t,x) = 1\,\mathrm{kg/m^3}. \tag{3.134}$$

In this case Favre and Reynolds PDFs coincide. We consider statistically homogeneous case

$$\widetilde{g}_{u'}(V';t) = \overline{g}_{u'}(V';t) = g(V';t). \tag{3.135}$$

with mean velocity equaled to zero at the initial time.

$$\overline{u'}(t=0) = 0 \tag{3.136}$$

The variance of the velocity is

$$\overline{u'^2}(t=0) = \sigma_0^2 = const, \tag{3.137}$$

Equation (3.16) becomes

$$\frac{\partial g}{\partial t} = C_1\omega\frac{\partial V' g}{\partial V'} + \frac{C_0}{2}\omega\overline{u'^2}\frac{\partial^2 g}{\partial V'^2}. \tag{3.138}$$

The asymptotic solution of the PDF equation (3.138) with conditions (3.136) and (3.137) at $t \to \infty$ is a stationary Gaussian function

$$g(V';t\to\infty) = g_G(V') = \frac{\exp(-\frac{V'^2}{2\sigma_0^2})}{\sqrt{2\pi\sigma_0^2}}. \tag{3.139}$$

It can be easily established because (3.138) is a parabolic equation. This asymptotic solution does not depend on initial profile of the PDF. It is sufficient that two first moments were 0 and σ_0^2.

Multiplying eq. (3.138) by V' and integrating it over V', one can deduce the equation for the first moment of velocity

$$\frac{\partial\overline{u'}}{\partial t} = -\overline{u'}C_1\omega. \tag{3.140}$$

The equation for the second moment of velocity is obtained from eq. (3.138) which is multiplied by V'^2 and integrated over V'. It reads

$$\frac{\partial\overline{u'^2}}{\partial t} = -2\overline{u'^2}C_1\omega + C_0\omega\overline{u'^2} = 0. \tag{3.141}$$

It follows from eq. (3.140) and (3.136) that at any time the mean velocity is zero

$$\overline{u'}(t) = 0 \tag{3.142}$$

and

$$\overline{u'^2} = \sigma_0^2. \tag{3.143}$$

The equation for the nth order velocity moment $\overline{u'^n}(t,x)$, obtained by multiplication of eq. (3.138) by V'^n and integration of that over V', reads

$$\frac{\partial \overline{u'^n}}{\partial t} = -n\overline{u'^n}C_1\omega + n(n-1)\overline{u'^{n-2}}\frac{C_0}{2}\omega\overline{u'^2},\ n \geq 1. \tag{3.144}$$

SPDEs

The SPDEs statistically equivalent to the PDF eq. (3.16) are given by eqs. (3.42) and (3.43). We supplement eqs. (3.42) and (3.43) with the following initial conditions

$$r_0 = r(t=0,x) = \overline{\rho}_0 h(x) \exp\left(-\frac{\eta^2}{2}\left(h(x)^2 - 1\right)\right), \qquad h(x) > 1,\ \overline{\rho}_0 = 1\,\mathrm{kg/m^3}, \tag{3.145}$$

$$u_0''(x) = \eta\sigma_0 h(x). \tag{3.146}$$

where η is a standard normally distributed random variable, i.e. the distribution of η is given by

$$f_\eta = \frac{\exp(-\frac{\eta^2}{2})}{\sqrt{2\pi}}. \tag{3.147}$$

The function $h(x)$ is strictly greater than 1. Below $h(x)$ is taken as

$$h(x) = 2 + H\left(-\frac{x}{L}\right) + \left(1 - \frac{x}{L}\right) H\left(\frac{x}{L}\right) H\left(1 - \frac{x}{L}\right), \tag{3.148}$$

where $L > 0$ is arbitrary length of interval. Figure 3.39 shows the spatial profile of the function $h(x)$. Obviously $\frac{\partial h}{\partial x} \leq 0$ and multivalued solutions are expected.

For statistically homogeneous case

$$\frac{\partial \overline{ru''^2}}{\partial x} = 0. \tag{3.149}$$

Taking into account (3.149), the explicit solution can be obtained from eqs. (3.42) and (3.43) and initial conditions (3.145) and (3.146). It reads

$$u''(t,x) = \eta\sigma_0 w(t,x), \tag{3.150}$$

where

$$w(t,x) = 3H\left(3\eta\sigma_0 T_t - (x - Q_t)\right) + 2H\left(x - Q_t - (L + 2\eta\sigma_0 T_t)\right) + H\left(x - Q_t - 3\eta\sigma_0 T_t\right) H\left(L + 2\eta\sigma_0 T_t - (x - Q_t)\right) \frac{3 - (x - Q_t)}{1 - \eta\frac{\sigma_0 T_t}{L}}, \tag{3.151}$$

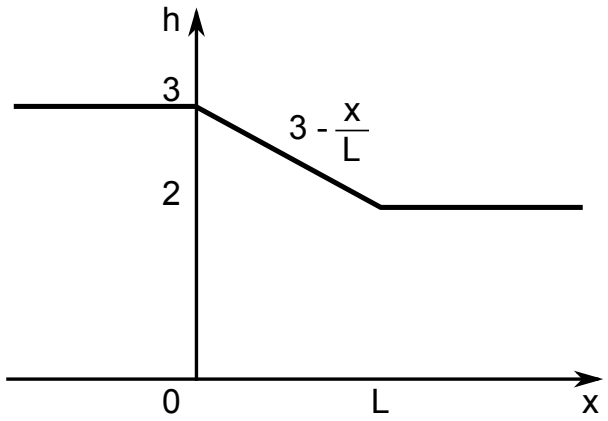

Figure 3.39: Statistically homogeneous velocity fluctuations test: an example of $h(x)$

where

$$T_t = \frac{1 - \exp\left(-2C_1\omega t\right)}{2C_1\omega} \tag{3.152}$$

and

$$Q_t = \sqrt{C_0\omega\sigma_0^2} \int_0^t \int_0^s \exp\left(-2C_1\omega(s-z)\right) dW_z ds. \tag{3.153}$$

As it is seen from (3.151) a gradient catastrophe appears if $\eta > 0$ and

$$\eta\sigma_0 > 2C_1\omega L. \tag{3.154}$$

The moment when the gradient catastrophe takes place is given by

$$t_* = \frac{1}{2C_1\omega} ln\left(\frac{1}{1 - \frac{2C_1\omega L}{\eta\sigma_0}}\right). \tag{3.155}$$

Using (3.151), we deduce that

$$T_t^* = \frac{L}{\eta\sigma_0}. \tag{3.156}$$

Injecting (3.156) in (3.152) we obtain the critical time t^*. The spatial position where the gradient catastrophe appears is

$$x = Q_{t_*} + 3L. \tag{3.157}$$

When the time t exceeds t_*, multivalued solutions should be taken into account.

In conclusion, even if the Langevin term is present in the SPDEs (3.42)-(3.43) and initial conditions (3.145)-(3.146) are regular, velocity discontinuity still appears. The dissipation term $-\frac{2C_1}{2}\omega u$ controls the time when discontinuity occurs and the Brownian term changes the position where the shocks appear. $\eta < 0$ corresponds to the rarefication wave.

Using the equivalence between the PDF eq. and the PDEs we obtain

$$\overline{u'^n} = \overline{r_0 u''^n}. \tag{3.158}$$

The mean stochastic density is one

$$\overline{r}(t,x) = \overline{\rho}(t,x) = 1\,\mathrm{kg/m^3}. \tag{3.159}$$

At the initial time it can be directly shown from the definition of r_0 (3.145) that

$$\overline{r}_0 = \frac{h}{\sqrt{2\pi}} \int_{-\infty}^{\infty} \exp\left(-\frac{\eta^2}{2}(h^2-1)\right) \exp\left(-\frac{\eta^2}{2}\right) d\eta = \frac{h}{\sqrt{2\pi}} \int_{-\infty}^{\infty} \exp\left(-\frac{\eta^2}{2}\right) h^2 d\eta = 1. \tag{3.160}$$

For the nth moment we deduce that

$$\overline{r_0 u_0''^n} = \frac{1}{\sqrt{2\pi}} \int_{-\infty}^{\infty} h(x) \exp\left(-\frac{\eta^2}{2}(h^2-1)\right) \eta^n \sigma_0^n \left(h(x)\right)^n \exp\left(-\frac{\eta^2}{2}\right) d\eta =$$

$$\frac{\sigma_0^n}{\sqrt{2\pi}} \int_{-\infty}^{\infty} \eta^n \left(h(x)\right)^{n+1} \exp\left(-\frac{\eta^2 h^2}{2}\right) d\eta = \frac{\sigma_0^n}{\sqrt{2\pi}} \int_{-\infty}^{\infty} \xi^n \exp\left(-\frac{\xi^2}{2}\right) d\xi. \tag{3.161}$$

The first moment is

$$\overline{r_0 u_0''} = \frac{\sigma_0}{\sqrt{2\pi}} \int_{-\infty}^{\infty} \xi \exp\left(-\frac{\xi^2}{2}\right) d\xi = 0. \tag{3.162}$$

The second is

$$\overline{r_0 u_0''^2} = \frac{\sigma_0^2}{\sqrt{2\pi}} \int_{-\infty}^{\infty} \xi^2 \exp\left(-\frac{\xi^2}{2}\right) d\xi = \sigma_0^2. \tag{3.163}$$

Equations (3.42) and (3.43) can be written in dimensionless variables r, $v = \frac{u''}{\sigma_0}$, $\tau = \omega t$, $\zeta = \frac{x}{l}$, $l = \frac{\sigma_0}{\omega}$ and $L_0 = \frac{L}{l}$, where l is a length scale, ω^{-1} is a time scale and σ_0 is a velocity scale.

$$\frac{\partial r}{\partial t} + \frac{\partial r v''}{\partial \zeta} = 0, \tag{3.164}$$

$$\frac{\partial v''}{\partial \tau} + v'' \frac{\partial v''}{\partial \zeta} = \frac{1}{\overline{r}} \frac{\partial \overline{r v''^2}}{\partial \zeta} - C_1 v'' + \sqrt{C_0 \widetilde{v''^2}}\dot{\xi}. \tag{3.165}$$

The dimensionless profile of $h(x)$ (3.148) is

$$h(\zeta) = 2 + H\left(-\frac{\zeta}{L_0}\right) + \left(1 - \frac{\zeta}{L_0}\right) H\left(\frac{\zeta}{L_0}\right) H\left(1 - \frac{\zeta}{L_0}\right). \tag{3.166}$$

The term $\frac{1}{\overline{r}} \frac{\partial \overline{r v''^2}}{\partial \zeta}$ is left in eq. (3.165) for the numerical algorithm, while it is theoretically zero.

Numerical solution

Stochastic numerical schemes are applied to solve eqs. (3.164) and (3.165). The parameters of simulations are following: $L_0 = 0.25$, the modeled constants are $C_0 = 2C_1 = 1$. Calculations are performed on the domain $D = [-150; 150]$. Periodic boundary conditions are used at both boundary points. The initial profiles of density and velocity are given by eqs. (3.145) and (3.146) respectively. Numerically we impose that the mean density strictly equals to one, the Favre-averaged velocity is zero and the Favre velocity variance is one at the initial time. Other stochastic moments are not strictly equal to their theoretical values. At $\tau = \omega t = 10$ the influence of boundary conditions are not observed and the density and velocity changes are present only inside the interval $(-40, 40)$. At $\tau = 2$ the domain of prolongation on initial conditions is $(-10; 10)$. The stochastic Lax-Friedrichs scheme diverges from $\tau > 7$. Consequently, it is only considered for $\tau < 7$.

Spatial profiles. Figures 3.40 to 3.42 illustrate spatial profiles of mean density, density variance, Favre velocity variance, skewness and flatness calculated with $N_x = 3 \times 10^4$ and $N_r = 4800$ at $\tau = \omega t = 2$. Only small deviations from the initial values are observed for four stochastic schemes.

The mean density is close to its theoretical value. Stochastic Godunov scheme gives the largest fluctuations among all the schemes. The maximum error of this method is about 3×10^{-3}. The stochastic Lax-Friedrichs method is exact. For other schemes the error is approximately 10^{-4}.

The density variance, which follows a ramp-shaped profile, is the same for three stochastic schemes: Lax-Friedrichs, Lax-Wendroff and GForce. The ramp-shaped profile of the density variance can be justified by initial data. Indeed, each realization of the density is positive and given by (3.145). For $\zeta < 0$ its values are large than for $\zeta \geq 0$, but strictly less than one and greater than zero. The mean density is one. As a result, the density variance follows the profile of $h(\zeta)$. The stochastic Godunov scheme yields a fluctuating profile of the density variance in the interval $(0; 1)$. Outside of this interval the behavior of the density variance is identical to profiles calculated by other schemes.

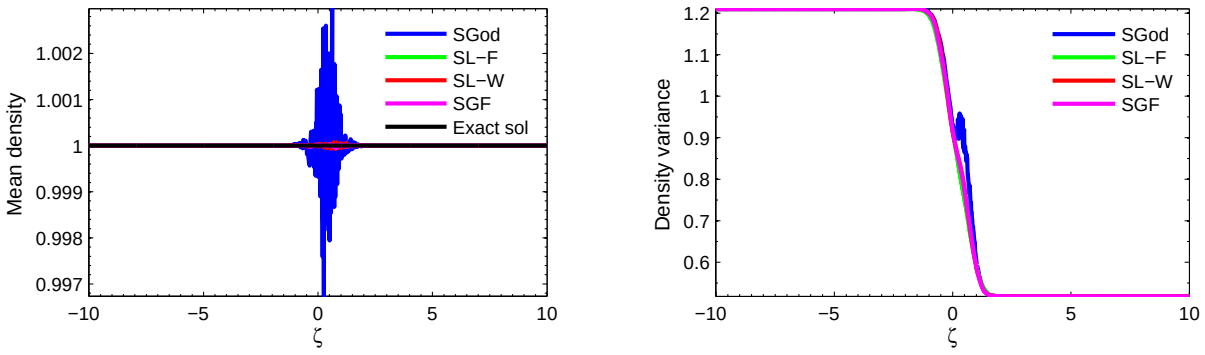

Figure 3.40: Statistically homogeneous velocity fluctuations test: spatial profiles of mean density (left) and variance density (right) at $\tau = 2$. $N_r = 4800$, $N_x = 3 \times 10^4$ on $D = [-150; 150]$.

The mean velocity is not presented here because it is equal to zero as a result of correction at each time step:

$$v'' = v'' - \widetilde{v''}. \tag{3.167}$$

The velocity variance (left panel of fig. 3.41) is in good agreement with the theoretical value 1. The maximum error is approximately five times greater than that for the mean density in the calculation by stochastic Godunov and 30 times greater for other schemes, but it remains compatible with the theoretical error which is: $O\left(\frac{1}{\sqrt{N_r}}\right) = 0.0144\ O(1)$. As for the mean density, the stochastic Godunov method gives the maximum error of 5%.

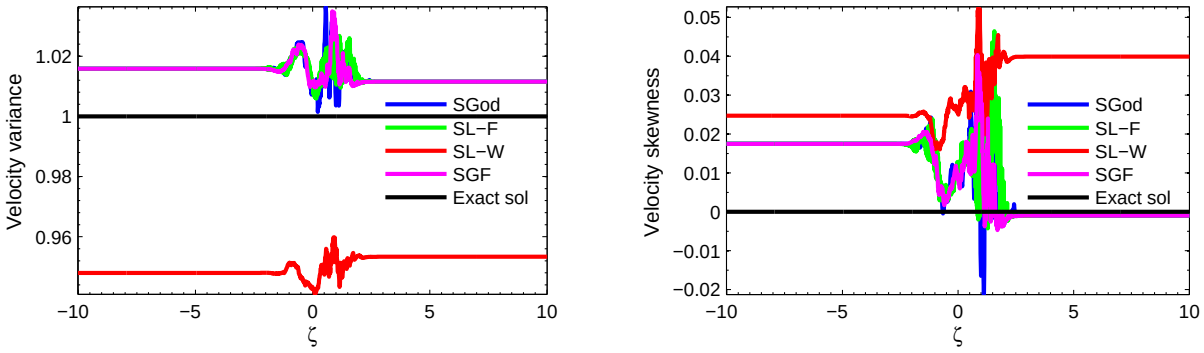

Figure 3.41: Statistically homogeneous velocity fluctuations test: spatial profiles of Favre velocity variance (left) and Favre velocity skewness (right) at $\tau = 2$. $N_r = 4800$, $N_x = 3 \times 10^4$ on $D = [-150; 150]$.

The error on the velocity skewness is on the same order of magnitude as that of velocity variance. It fluctuates around the zero. Contrariwise, the velocity flatness is 10% different from the theoretical value of 3 (fig. 3.42).

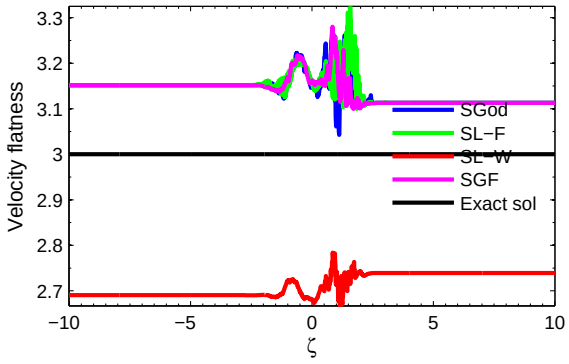

Figure 3.42: Statistically homogeneous velocity fluctuations test: spatial profiles of Favre velocity flatness at $\tau = 2$. $N_r = 4800$, $N_x = 3 \times 10^4$ on $D = [-150; 150]$.

At $\tau = 2$ the dissipation in kinetic scheme which satisfies the entropy increase condition is not yet observed (fig. is not presented here), even if the probability to have multivalued

solution is not zero at this characteristic time for some realizations of velocity. It can be explained by two causes:

- Stochastic term $\sqrt{\widetilde{v''^2}}\eta$ alters the values of velocity and therefore forces the velocity variance to fluctuate around its theoretical value.
- According to [LemonsLackman1995] $\sqrt{\widetilde{v''^2}}\eta$ can destabilize the stochastic process and velocity variance can decrease or increase regardless of the selected scheme.

The time which is necessary to see the energy dissipation in kinetic scheme is larger than in example given in section 3.3.2. Theoretically, even if the velocity variance differs from one, the PDF for kinetic scheme remains a Gaussian function, if the normalization by velocity variance for velocity statistics are used, i.e. the n-th moment of velocity is

$$\frac{\overline{rv''^n}}{\overline{r}(\sqrt{\widetilde{v''^2}})^n}. \tag{3.168}$$

The energy dissipation for kinetic scheme is observed after $\tau > 8$, if the number of fields is $N_r = 4800$ and the number of cells is $N_x = 3 \times 10^4$. Before this time the velocity variance fluctuates around its theoretical value of one.

Figures 3.43 and 3.44 show spatial profiles of mean density at different times $\tau = [8.5;\ 9;\ 9.5;\ 10]$, obtained with different schemes: stochastic Lax-Wendroff, Lax-Friedrichs, Godunov and kinetic. One can note that stochastic Lax-Wendroff and GForce approaches give the lowest error (around 10^{-4} according to fig. 3.43) in comparison with other schemes. As in previous tests the mean density fluctuates more in stochastic Godunov scheme, for this test the error is 1.5×10^{-2} (left panel in fig. 3.44). It corresponds to the theoretical error which is $O\left(\frac{1}{\sqrt{4800}}\right) = 1.4 \times 10^{-2}\ O(1)$. The kinetic scheme gives 4×10^{-4} error (right panel in fig. 3.44).

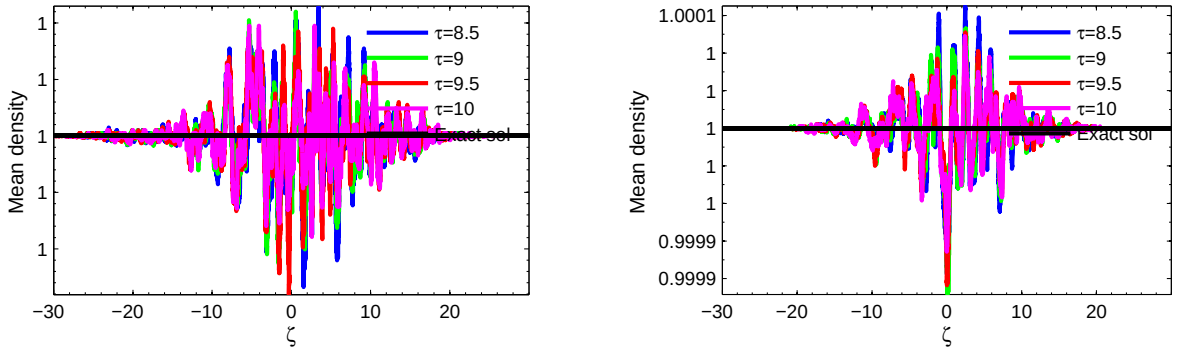

Figure 3.43: Statistically homogeneous velocity fluctuations test: spatial profiles of mean density at $\tau \geq 8.5$. Left: stochastic Lax-Wendroff method; right: stochastic GForce method. $N_r = 4800$, $N_x = 3 \times 10^4$ on $D = [-150; 150]$.

Figures 3.45 and 3.46 illustrate spatial profiles of density variance. In stochastic Lax-Wendroff and GForce schemes the profile is the same and does not vary in time. It can be explained by the fact that GForce scheme is a combination of Lax-Wendroff and Lax-Friedrichs schemes. The stochastic Godunov scheme gives a peak of density variance near

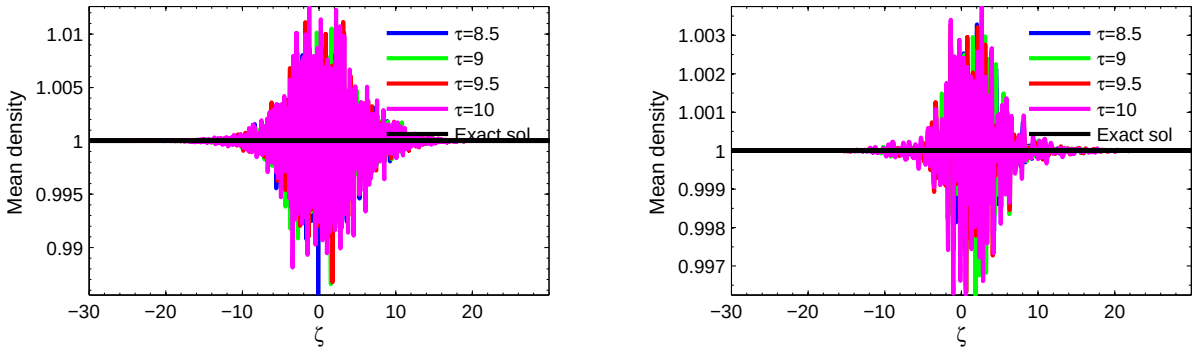

Figure 3.44: Statistically homogeneous velocity fluctuations test: spatial profiles of mean density at $\tau \geq 8.5$. Left: stochastic Godunov method; right: kinetic scheme. $N_r = 4800$, $N_x = 3 \times 10^4$ on $D = [-150; 150]$.

$\zeta = 0$ (left fig. 3.45). In the neighborhood of this point the profile fluctuates. The density variance also fluctuates around $\zeta = 0$ in kinetic scheme (right fig. 3.45) but less significantly compared to the stochastic Godunov scheme.

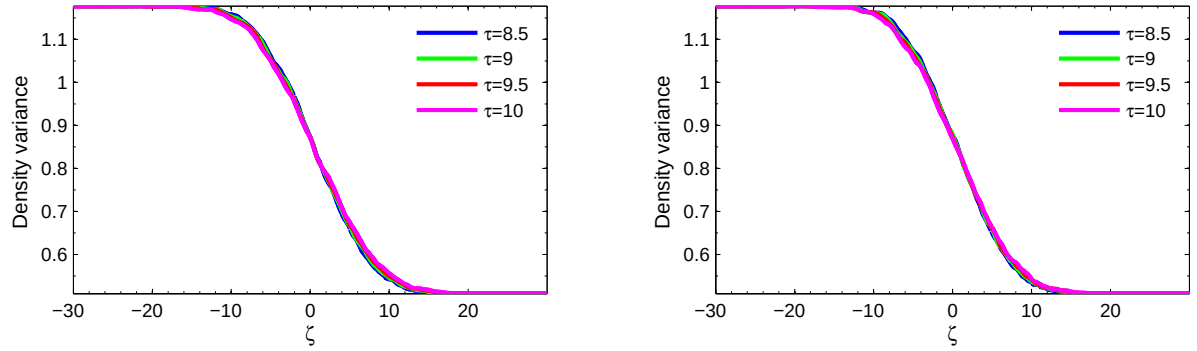

Figure 3.45: Statistically homogeneous velocity fluctuations test: spatial profiles of density variance at $\tau \geq 8.5$. Left: stochastic Lax-Wendroff method; right: stochastic GForce method. $N_r = 4800$, $N_x = 3 \times 10^4$ on $D = [-150; 150]$.

The velocity variance is presented in figs. 3.47 and 3.48. In stochastic GForce and Godunov methods it fluctuates around the theoretical value of one at different time. One can note that it somewhat decreases in kinetic scheme. In fact it is not so obvious to observe the energy dissipation in kinetic scheme due the presence of the stochastic term. For example, stochastic Lax-Wendroff scheme yields velocity variance bigger than one at $\tau \geq 8.5$. The maximum error for this scheme is 17.5% at $\tau = 10$, while for kinetic scheme it is 24.75% at the same time.

Figures 3.49 to 3.51 show spatial profiles of velocity skewness. It fluctuates around zero for three stochastic schemes (fig. 3.49 and left panel of fig. 3.50), while it remains negative for kinetic scheme for $\tau \geq 8.5$ (right panel of fig. 3.50). One can also note that the velocity

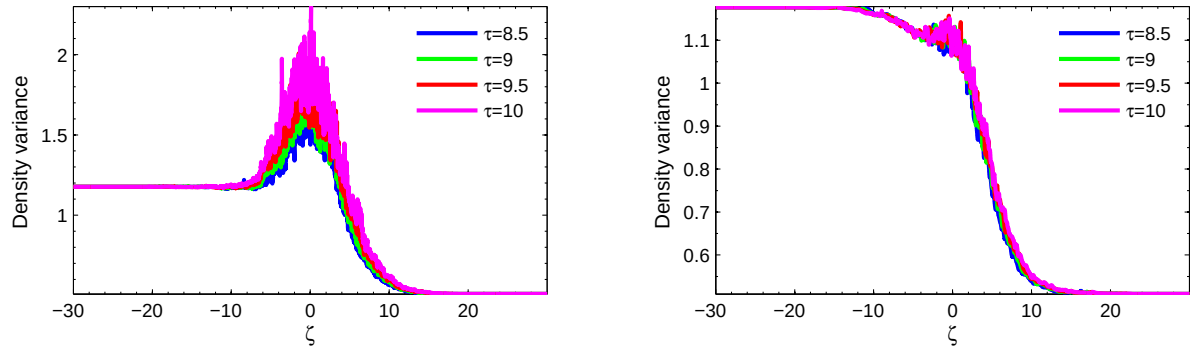

Figure 3.46: Statistically homogeneous velocity fluctuations test: spatial profiles of density variance at $\tau \geq 8.5$. Left: stochastic Godunov method; right: kinetic scheme. $N_r = 4800$, $N_x = 3 \times 10^4$ on $D = [-150; 150]$.

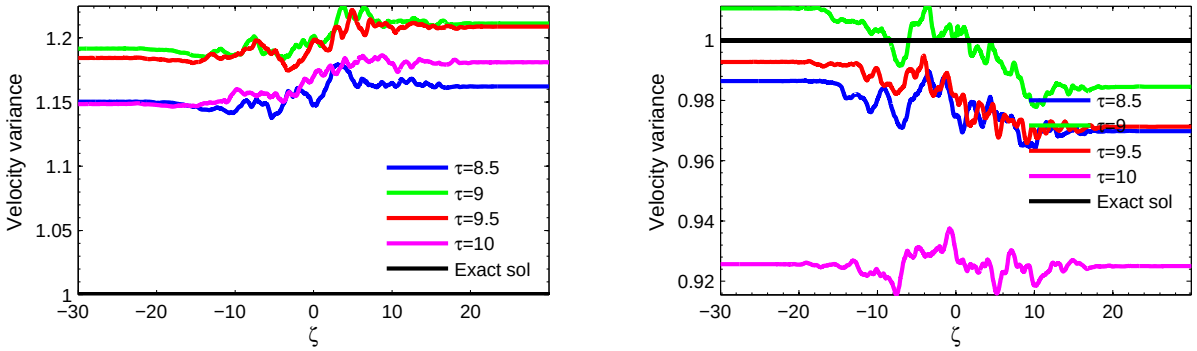

Figure 3.47: Statistically homogeneous velocity fluctuations test: spatial profiles of velocity variance at $\tau \geq 8.5$. Left: stochastic Lax-Wendroff method; right: stochastic GForce method. $N_r = 4800$, $N_x = 3 \times 10^4$ on $D = [-150; 150]$.

skewness contains the minimal deviation from the theoretical error at $\tau = 10$ for kinetic scheme in comparison with other time step $\tau \geq 8.5$. The corrected velocity skewness with (3.168) for kinetic scheme is presented in fig. 3.51. The correction does not result in a decreased error value and even increases the error between the theoretical value and calculated statistics.

The theoretical and numerical velocity flatness are illustrated in figs. 3.52 to 3.54. The tendency in kinetic scheme is the same that for previous considered moments (right fig. 3.53). The velocity flatness is lower than the theoretical value of 3 for any $\tau \geq 8.5$. The correction (3.168) improves its value (fig. 3.54). At time $\tau = 10$ the error for kinetic scheme is approximately 13% while before the correction it is 40%. Stochastic Lax-Wendroff scheme contains also 40% of error, while other schemes 20% at $\tau = 10$.

Figures 3.55 to 3.57 show spatial profiles of velocity hyperskewness. In theory it should equal zero. One can note that $N_r = 4800$ stochastic fields are not sufficient to predict the theoretical value. The stochastic methods give the error of about 60%. Nevertheless their

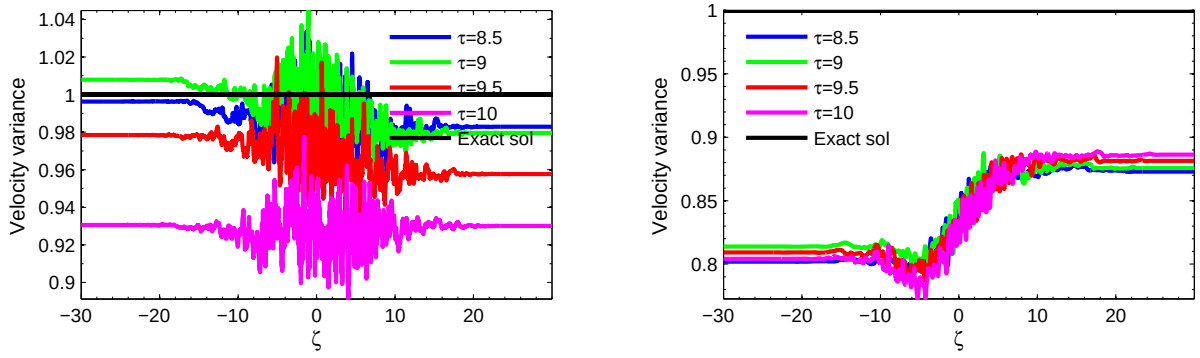

Figure 3.48: Statistically homogeneous velocity fluctuations test: spatial profiles of velocity variance at $\tau \geq 8.5$. Left: stochastic Godunov method; right: kinetic scheme. $N_r = 4800$, $N_x = 3 \times 10^4$ on $D = [-150; 150]$.

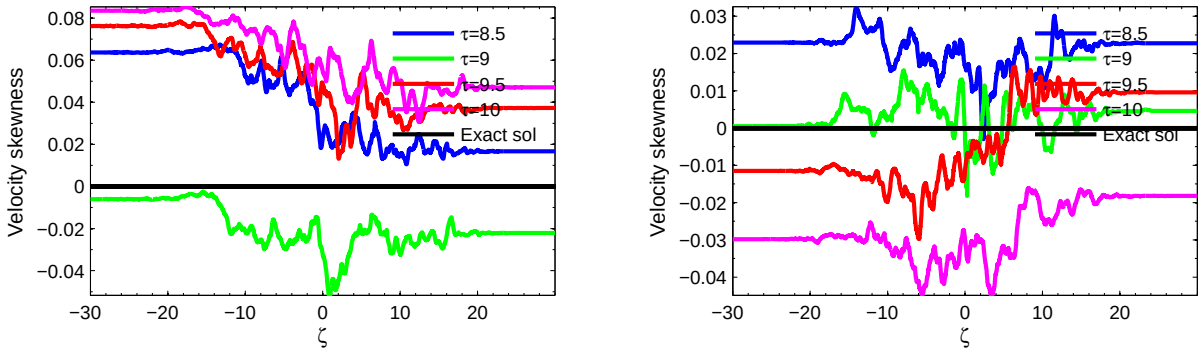

Figure 3.49: Statistically homogeneous velocity fluctuations test: spatial profiles of velocity skewness at $\tau \geq 8.5$. Left: stochastic Lax-Wendroff method; right: stochastic GForce method. $N_r = 4800$, $N_x = 3 \times 10^4$ on $D = [-150; 150]$.

velocity hyperskewness fluctuate around zero at the considered moments of time. Kinetic scheme gives negative values for hyperskewness for $\tau \geq 8.5$ (right fig. 3.56). The corrected statistics for this scheme are presented in fig. 3.57. As for skewness it does not improve result.

Finally, we consider hyperflatness for four schemes (figs. 3.58 to 3.60). At time $\tau = 10$ the maximum error for stochastic GForce and Godunov schemes is approximately 30%, for other schemes it is 45%. The correction for kinetic scheme gives 60% of error.

In order to compare stochastic and classical approaches let us consider the evolution of stochastic density and velocity fields in two schemes: stochastic Godunov and kinetic. Figures 3.61 and 3.62 illustrate the evolution of three realizations of density and velocity at $\tau = 0.5$. For stochastic scheme velocity fields fluctuate (right panel in fig. 3.61). We observe that the velocity jumps from one value to another at the neighbor points.

In the case of the scheme satisfying the entropy increase condition there are no jumps in velocity fields, which remain continuous functions. At this moment there is no gradient catastrophe. The density oscillates more in stochastic scheme rather than in deterministic

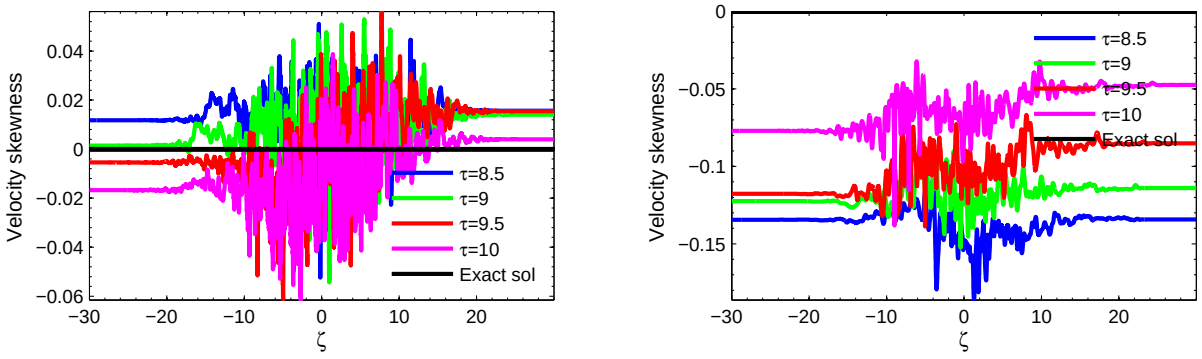

Figure 3.50: Statistically homogeneous velocity fluctuations test: spatial profiles of velocity skewness at $\tau \geq 8.5$. Left: stochastic Godunov method; right: kinetic scheme. $N_r = 4800$, $N_x = 3 \times 10^4$ on $D = [-150; 150]$.

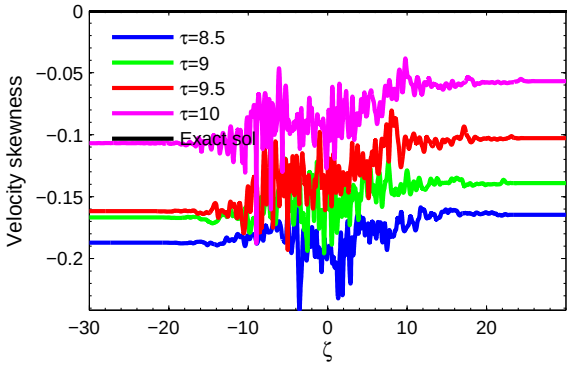

Figure 3.51: Statistically homogeneous velocity fluctuations test: spatial profiles of velocity skewness at $\tau \geq 8.5$ calculated by kinetic scheme after normalization (3.168). $N_r = 4800$, $N_x = 3 \times 10^4$ on $D = [-150; 150]$.

scheme as a result of numerical derivative of velocity. If the velocity is positive, the density accumulates; if it is negative, the density decrease in the region of varying velocity gradient.

At time $\tau = 1$ two terms $\frac{1}{\overline{r}} \frac{\partial \overline{r v''^2}}{\partial \zeta}$ and $v'' = v'' - \widetilde{v''}$ depending on ζ start influencing the solution of kinetic scheme (fig. 3.64). 1st and 2nd realizations begin to oscillate in the interval $(0; 3)$. The region where the stochastic scheme fluctuates $(-2; 4)$ is larger than in the scheme satisfying the entropy increase condition. In addition the stochastic term which is added to each realization changes the value of velocity fields. For example, the 3rd velocity realization in stochastic Godunov scheme is -1 at $\zeta = -1$, $\tau = 0.5$, while at $\zeta = -1$, $\tau = 1$ it is -1.2. The 2nd velocity realization in kinetic scheme changes the sign.

At times $\tau = 1.5$ and $\tau = 2$ (figs. 3.65 and 3.66) the behavior of schemes is identical to that at $\tau = 1$. Stochastic schemes completely transform the ramp velocity profiles into fluctuations, while in kinetic scheme the imprint of the initial ramp can still be observed. That said, solution calculated with the scheme satisfying the entropy increase condition ceases

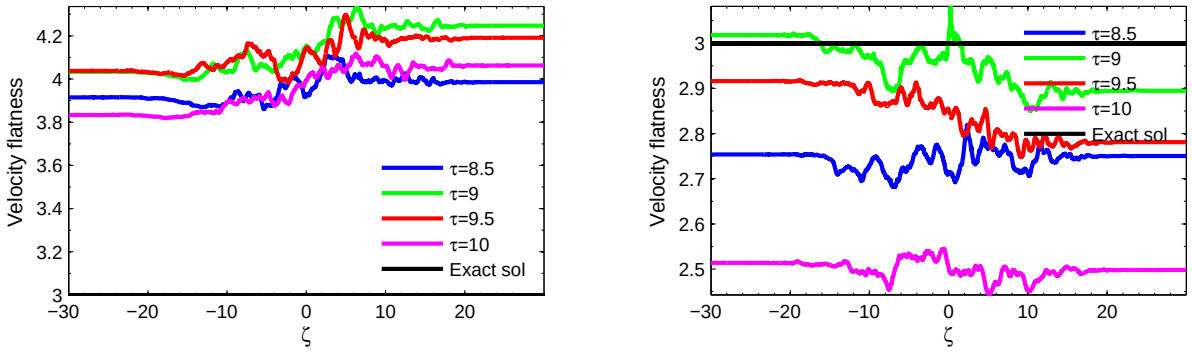

Figure 3.52: Statistically homogeneous velocity fluctuations test: spatial profiles of velocity flatness at $\tau \geq 8.5$. Left: stochastic Lax-Wendroff method; right: stochastic GForce method. $N_r = 4800$, $N_x = 3 \times 10^4$ on $D = [-150; 150]$.

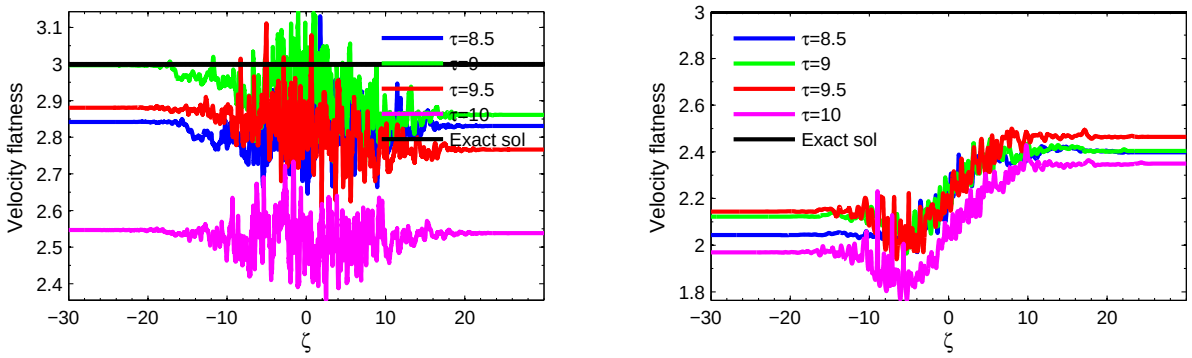

Figure 3.53: Statistically homogeneous velocity fluctuations test: spatial profiles of velocity flatness at $\tau \geq 8.5$. Left: stochastic Godunov method; right: kinetic scheme. $N_r = 4800$, $N_x = 3 \times 10^4$ on $D = [-150; 150]$.

to be valid once it starts to oscillate.

At time $\tau = 2.5$ the profiles of velocity in stochastic Godunov scheme takes different values at each point where the initial solution spread. The density consists of multiple numerical Dirac delta functions (fig. 3.67). In kinetic scheme the velocity ramp profile for the 3rd realization moves to the left boundary of computational domain and fluctuates only in the neighborhood of zero (fig. 3.68). Finally, two schemes will give fluctuating profiles of velocity at any point in space.

The behavior of classical schemes is unclear when the transported profiles takes different values at each interval Δx in space. For example, if we consider deterministic Oscher scheme, the solution diverges for $\tau > 5$ and statistics tend to infinity. It can be justified by the deterministic nature of this scheme or also by stochastic term in the velocity transport equation.

Let us consider some sample space of density and velocity for stochastic schemes at time $\tau = 2$. In previous tests, velocity and density fields have large jumps between two neighborly

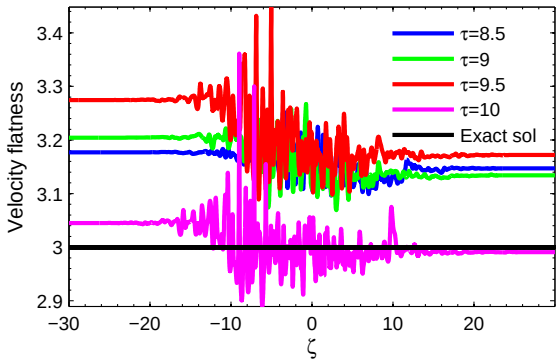

Figure 3.54: Statistically homogeneous velocity fluctuations test: spatial profiles of velocity flatness at $\tau \geq 8.5$ calculated by kinetic scheme after normalization (3.168). $N_r = 4800$, $N_x = 3 \times 10^4$ on $D = [-150; 150]$.

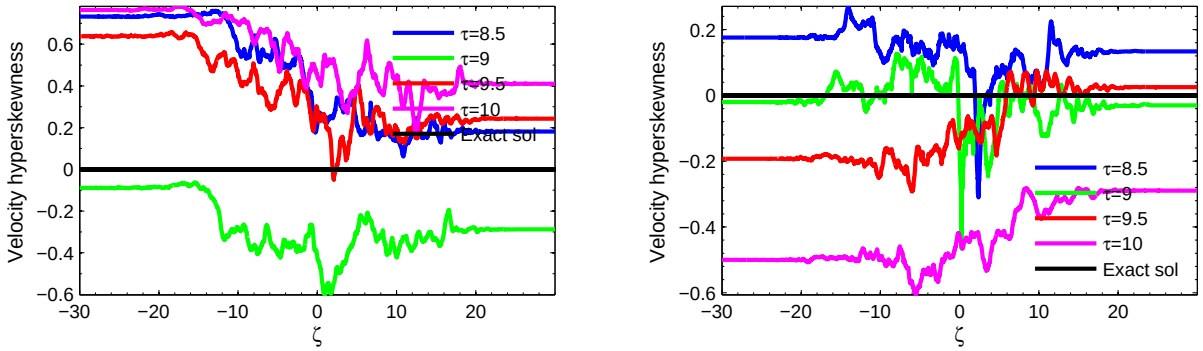

Figure 3.55: Statistically homogeneous velocity fluctuations test: spatial profiles of velocity hyperskewness at $\tau \geq 8.5$. Left: stochastic Lax-Wendroff method; right: stochastic GForce method. $N_r = 4800$, $N_x = 3 \times 10^4$ on $D = [-150; 150]$.

numerical intervals Δx. This is especially well demonstrated by the samples calculated with the stochastic Lax-Friedrichs method. For example, figs. 3.69 and 3.70 illustrate respectively the density and the velocity fields for the same realization. The velocity is negative in the computational domain D. Consequently, the initial profile of corresponding ramp moves to the left boundary of D. If we zoom the profiles in the interval $(-0.3, 0.3)$, we observe the jumps of density and velocity at each point in space. One can also note that the interval $(-5; -3)$ contains the largest jumps of density and velocity. For instance, the density varies from 0.05 to 0.5, while the velocity changes from -1.21 to -0.3. Analysis of different realizations of density and velocity for other schemes allows concluding that profiles calculated with stochastic Lax-Friedrichs method contain more frequently large jumps of density and velocity than other schemes.

Let us consider the numerical weighted PDF. Its profile depends on the number of realizations and velocity regions in which we search the distribution. Figure 3.71 compares

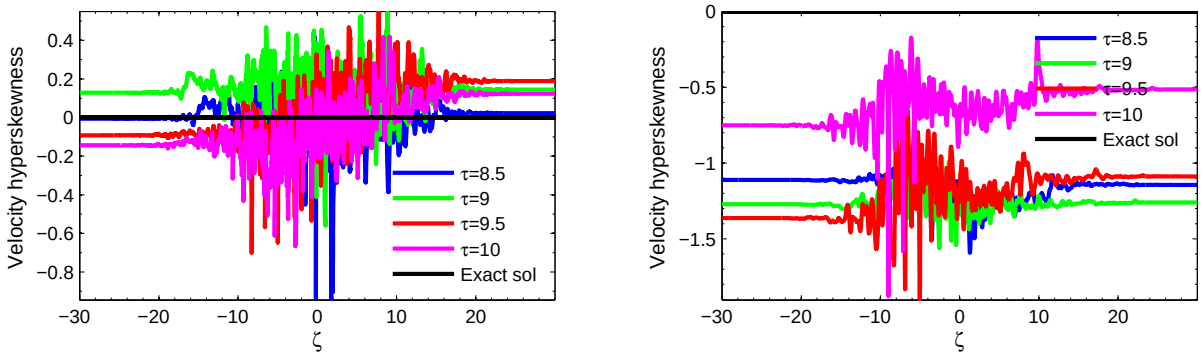

Figure 3.56: Statistically homogeneous velocity fluctuations test: spatial profiles of velocity hyperskewness at $\tau \geq 8.5$. Left: stochastic Godunov method; right: kinetic scheme. $N_r = 4800$, $N_x = 3 \times 10^4$ on $D = [-150; 150]$.

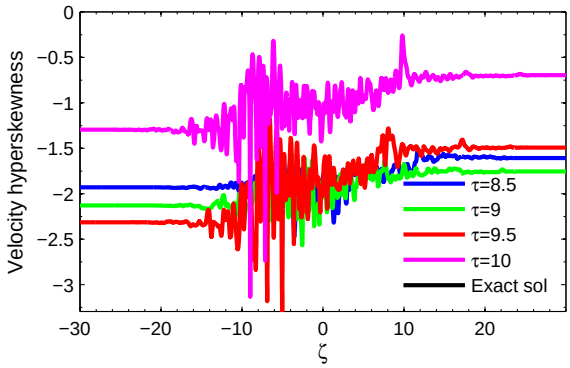

Figure 3.57: Statistically homogeneous velocity fluctuations test: spatial profiles of velocity hyperskewness at $\tau \geq 8.5$ calculated by kinetic scheme after normalization (3.168). $N_r = 4800$, $N_x = 3 \times 10^4$ on $D = [-150; 150]$.

analytical profile and numerical profile of the PDF at $\zeta = 0.005$ at different time calculated with stochastic Godunov method. We search the velocity in the interval $[-4.5; 4.5]$, which is divided into 9 uniformly distributed bins. One can conclude that the numerical PDF stays close to the theoretical normal Gaussian PDF independently on the considered time. Obviously increasing the number of bins decreases the maximal peak of the numerical PDF.

Figure 3.72 illustrates the conditional expectation of density for given velocities at $\zeta = 0.005$ and at different time moments. One can note that its profiles vary in time, but the maximal peak does not exceed the value 1.35.

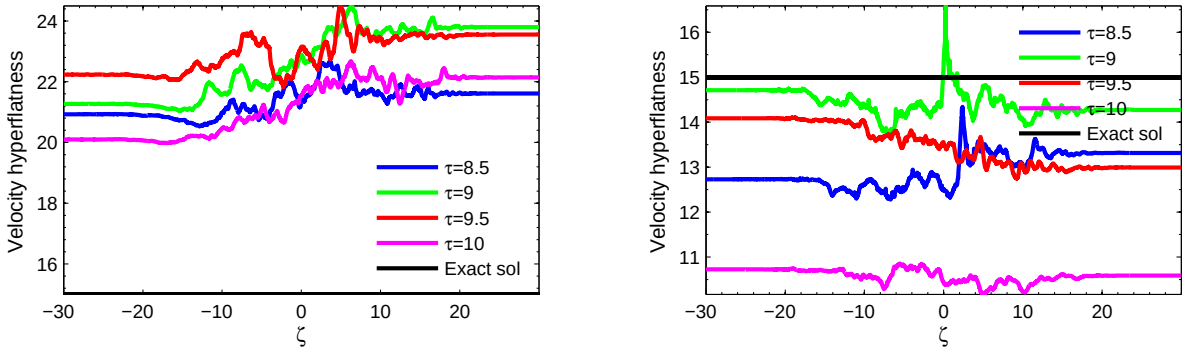

Figure 3.58: Statistically homogeneous velocity fluctuations test: spatial profiles of velocity hyperflatness at $\tau \geq 8.5$. Left: stochastic Lax-Wendroff method; right: stochastic GForce method. $N_r = 4800$, $N_x = 3 \times 10^4$ on $D = [-150; 150]$.

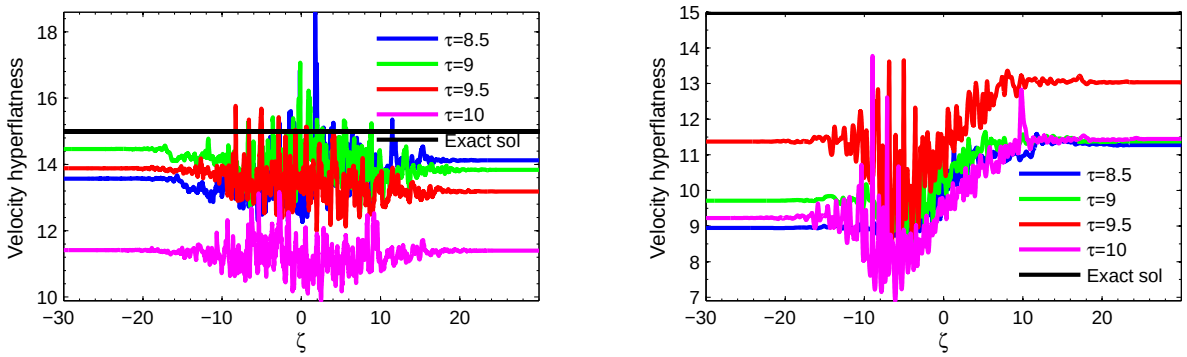

Figure 3.59: Statistically homogeneous velocity fluctuations test: spatial profiles of velocity hyperflatness at $\tau \geq 8.5$. Left: stochastic Godunov method; right: kinetic scheme. $N_r = 4800$, $N_x = 3 \times 10^4$ on $D = [-150; 150]$.

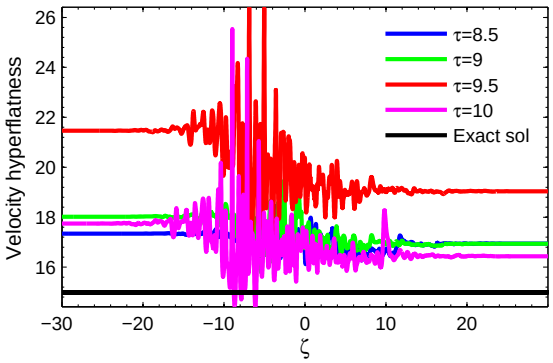

Figure 3.60: Statistically homogeneous velocity fluctuations test: spatial profiles of velocity hyperflatness at $\tau \geq 8.5$ calculated by kinetic scheme after normalization (3.168). $N_r = 4800$, $N_x = 3 \times 10^4$ on $D = [-150; 150]$.

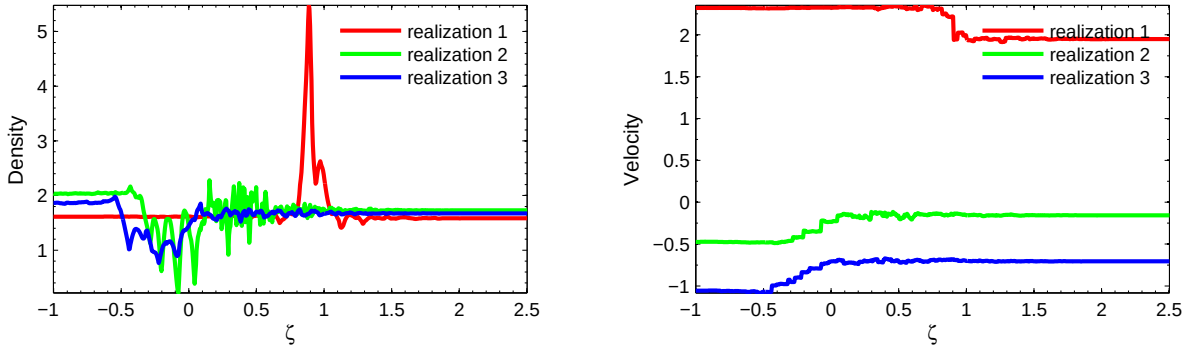

Figure 3.61: Statistically homogeneous velocity fluctuations test: examples of stochastic density (left) and velocity (right) fields at $\tau = 0.5$ calculated with stochastic Godunov scheme. $N_r = 4800$, $N_x = 3 \times 10^4$ on $D = [-150; 150]$.

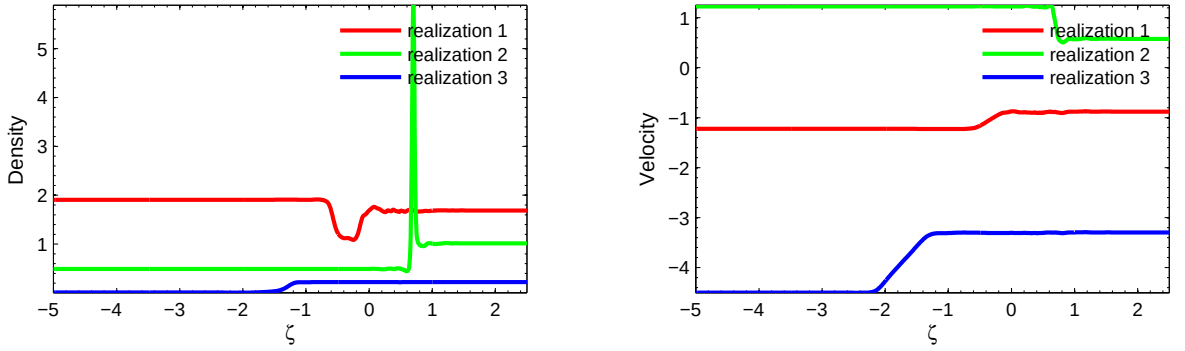

Figure 3.62: Statistically homogeneous velocity fluctuations test: examples of stochastic density (left) and velocity (right) fields at $\tau = 0.5$ calculated with kinetic scheme. $N_r = 4800$, $N_x = 3 \times 10^4$ on $D = [-150; 150]$.

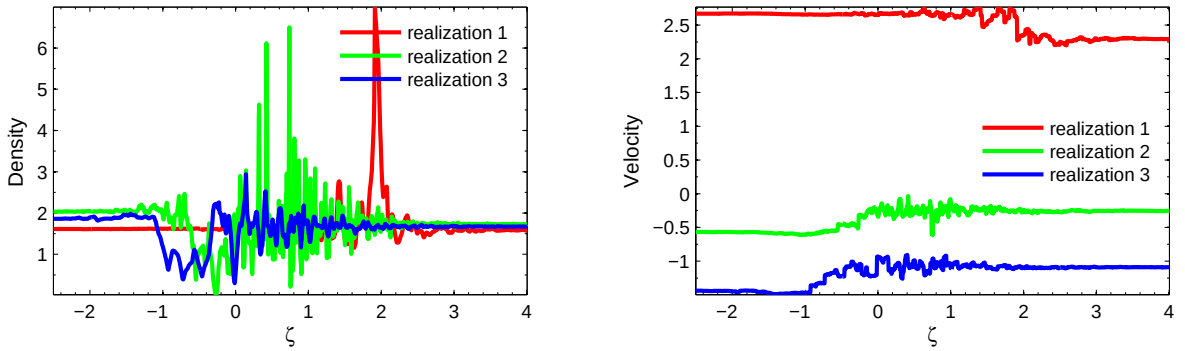

Figure 3.63: Statistically homogeneous velocity fluctuations test: examples of stochastic density (left) and velocity (right) fields at $\tau = 1$ calculated with stochastic Godunov scheme. $N_r = 4800$, $N_x = 3 \times 10^4$ on $D = [-150; 150]$.

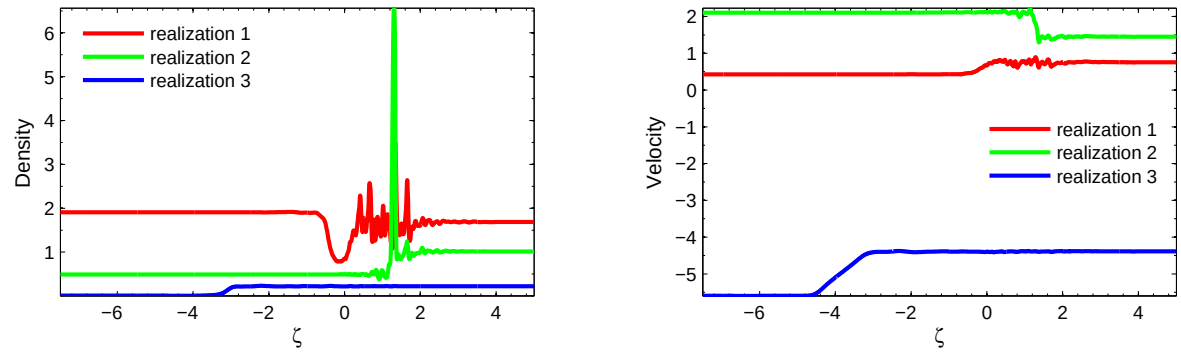

Figure 3.64: Statistically homogeneous velocity fluctuations test: examples of stochastic density (left) and velocity (right) fields at $\tau = 1$ calculated with kinetic scheme. $N_r = 4800$, $N_x = 3 \times 10^4$ on $D = [-150; 150]$.

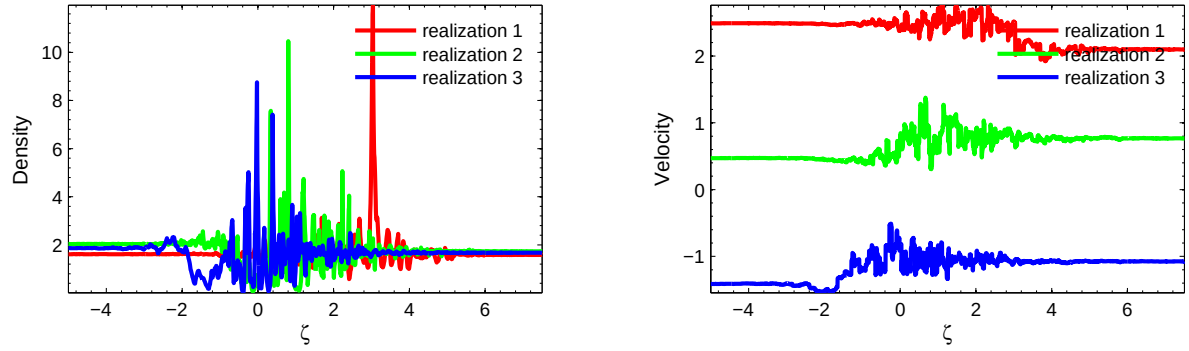

Figure 3.65: Statistically homogeneous velocity fluctuations test: examples of stochastic density (left) and velocity (right) fields at $\tau = 1.5$ calculated with stochastic Godunov scheme. $N_r = 4800$, $N_x = 3 \times 10^4$ on $D = [-150; 150]$.

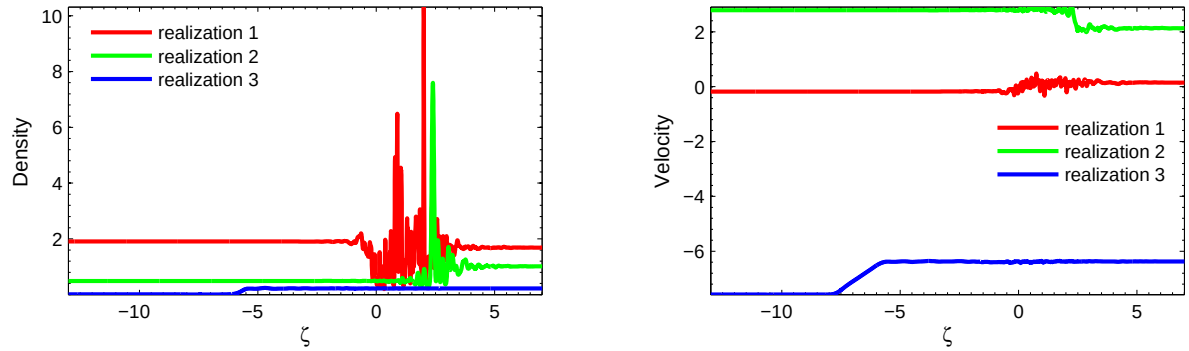

Figure 3.66: Statistically homogeneous velocity fluctuations test: examples of stochastic density (left) and velocity (right) fields at $\tau = 1.5$ calculated with kinetic scheme. $N_r = 4800$, $N_x = 3 \times 10^4$ on $D = [-150; 150]$.

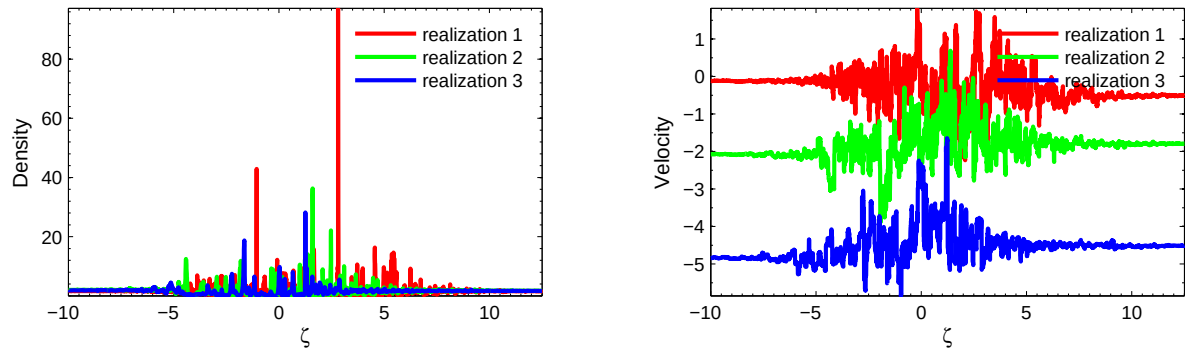

Figure 3.67: Statistically homogeneous velocity fluctuations test: examples of stochastic density (left) and velocity (right) fields at $\tau = 2.5$ calculated with stochastic Godunov scheme. $N_r = 4800$, $N_x = 3 \times 10^4$ on $D = [-150; 150]$.

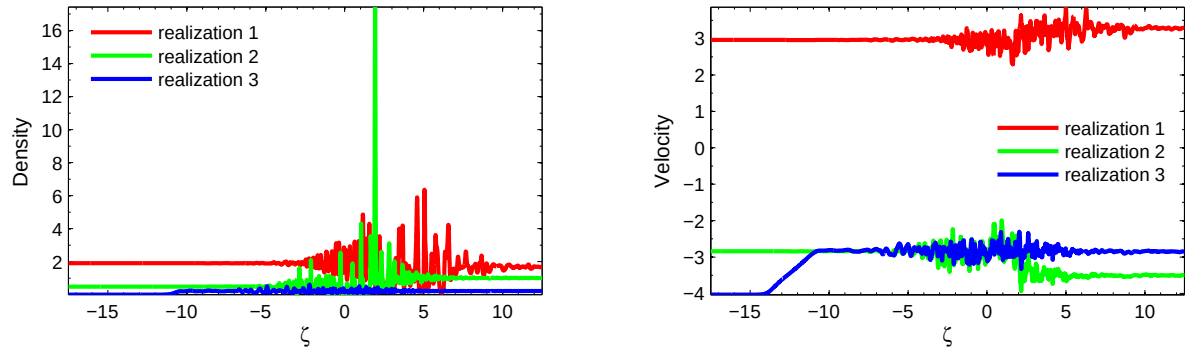

Figure 3.68: Statistically homogeneous velocity fluctuations test: examples of stochastic density (left) and velocity (right) fields at $\tau = 2.5$ calculated with kinetic scheme. $N_r = 4800$, $N_x = 3 \times 10^4$ on $D = [-150; 150]$.

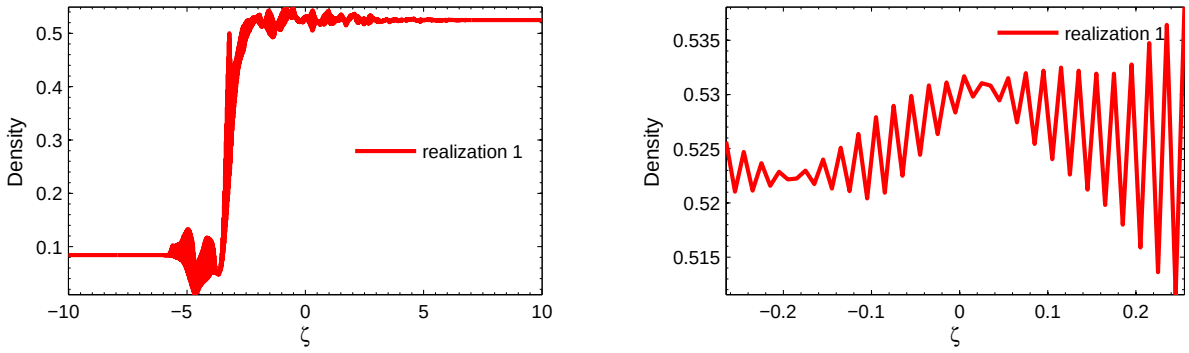

Figure 3.69: Statistically homogeneous velocity fluctuations test: spatial profile of one realization of density (left) and its zoom (right) at $\tau = 2$; stochastic Lax-Friedrichs method. $N_r = 4800$, $N_x = 3 \times 10^4$ on $D = [-150; 150]$.

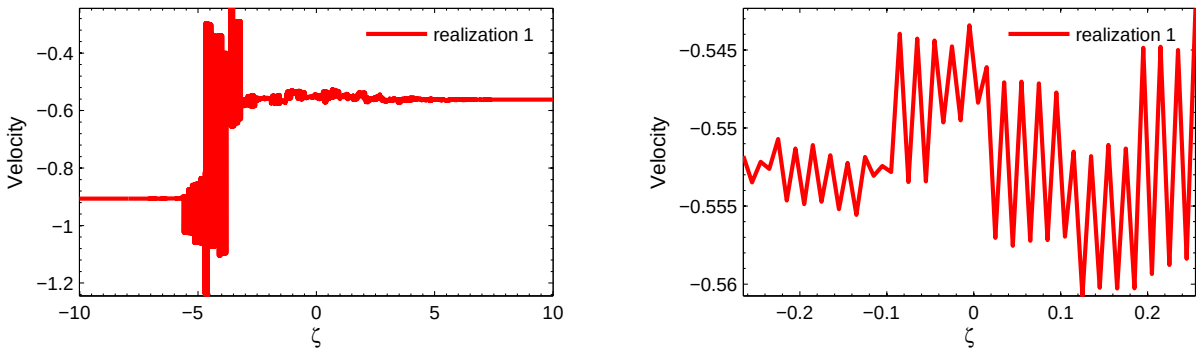

Figure 3.70: Statistically homogeneous velocity fluctuations test: spatial profile of one realization of velocity (left) and its zoom (right) at $\tau = 2$; stochastic Lax-Friedrichs method. $N_r = 4800$, $N_x = 3 \times 10^4$ on $D = [-150; 150]$.

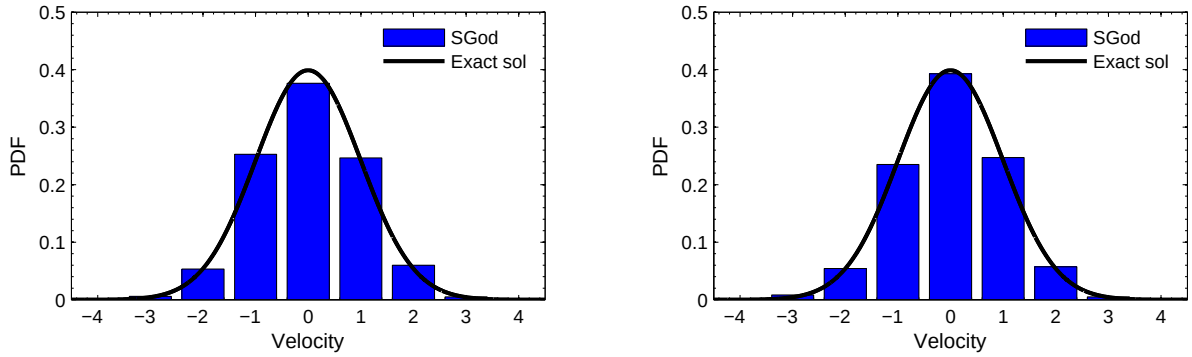

Figure 3.71: Statistically homogeneous velocity fluctuations test: Favre PDF of velocity at time $\tau = 2$ (left) and $\tau = 8$ (right), $\zeta = 0.005$; stochastic Godunov method. $N_r = 4800$, $N_x = 3 \times 10^4$ on $D = [-150; 150]$.

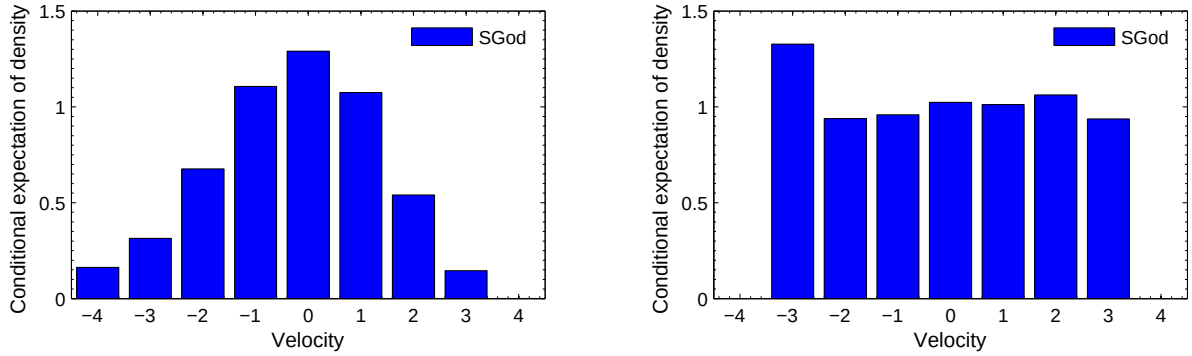

Figure 3.72: Statistically homogeneous velocity fluctuations test: conditional expectations of density for given velocities at time $\tau = 2$ (left) and $\tau = 8$ (right), $\zeta = 0.005$; stochastic Godunov method. $N_r = 4800$, $N_x = 3 \times 10^4$ on $D = [-150; 150]$.

Convergence. In order to check the statistical convergence the number of cells is fixed to $N_x = 10^5$ and the number of stochastic fields varies from $N_r = 72$ to 480. The reference solution is given by the PDF solution (3.139) which is a Gaussian function: the Favre-averaged velocity is zero, the Favre velocity variance, skewness and flatness are respectively one, zero and three. In this test the stochastic Lax-Friedrichs scheme does not diverge from theoretical values for $\tau < 2$. Therefore we again consider all the four schemes.

The time evolution of statistical convergence rate and coefficient for different moments and schemes are shown in figs. 3.73 to 3.76 . The Favre velocity skewness does not converge to its theoretical value in any of four schemes. It can be seen from the convergence coefficient for the third velocity moment that the coefficient takes a very small value and is about 0.0067. Such the behavior can be explained by the fact that at the initial time this moment was not zero and the time that it is necessary for this moment to tend to its theoretical value is longer than the considered time $\omega t = 2$. Other statistical convergence rates fluctuate around their theoretical value -0.5. The mean density is equal to one in the case of the stochastic Lax-Friedrichs method, i.e. this scheme is exact for the mean density, because this scheme is linear.

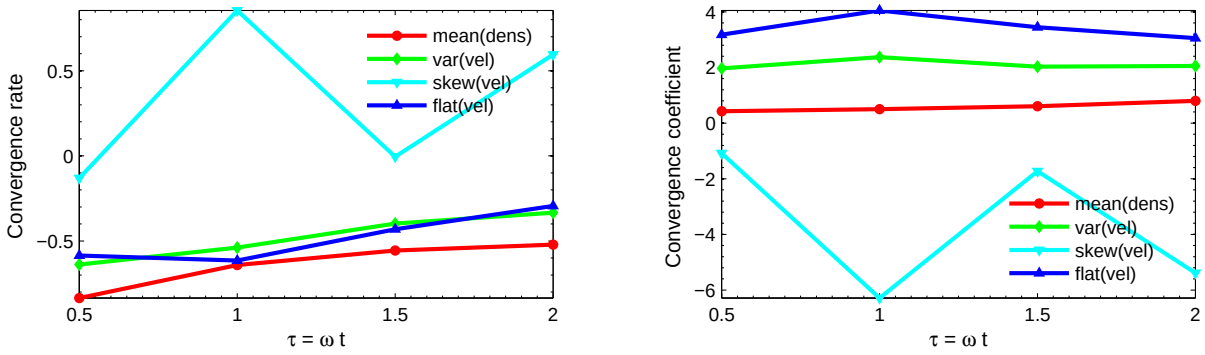

Figure 3.73: Statistically homogeneous velocity fluctuations test: time evolution of statistical convergence rate (left) and coefficient (right) of stochastic Godunov scheme. $N_x = 10^5$.

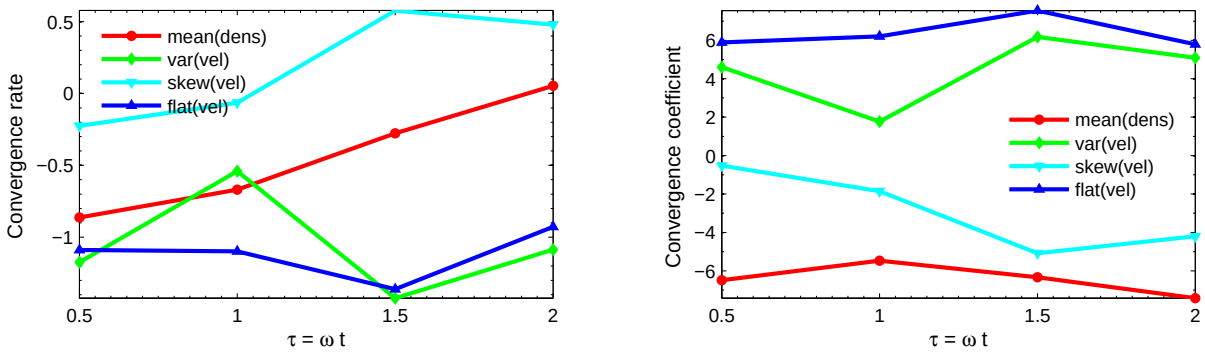

Figure 3.74: Statistically homogeneous velocity fluctuations test: time evolution of statistical convergence rate (left) and coefficient (right) of stochastic Lax-Wendroff scheme. $N_x = 10^5$.

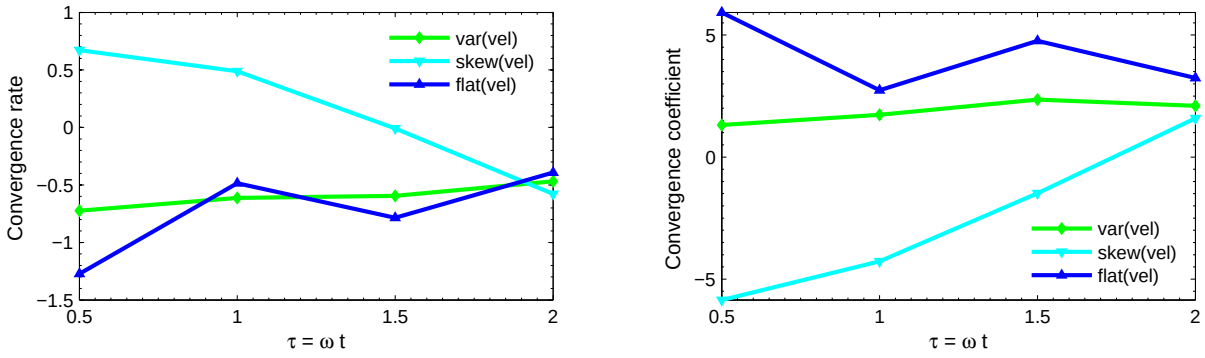

Figure 3.75: Statistically homogeneous velocity fluctuations test: time evolution of statistical convergence rate (left) and coefficient (right) of stochastic Lax-Friedrichs scheme. $N_x = 10^5$.

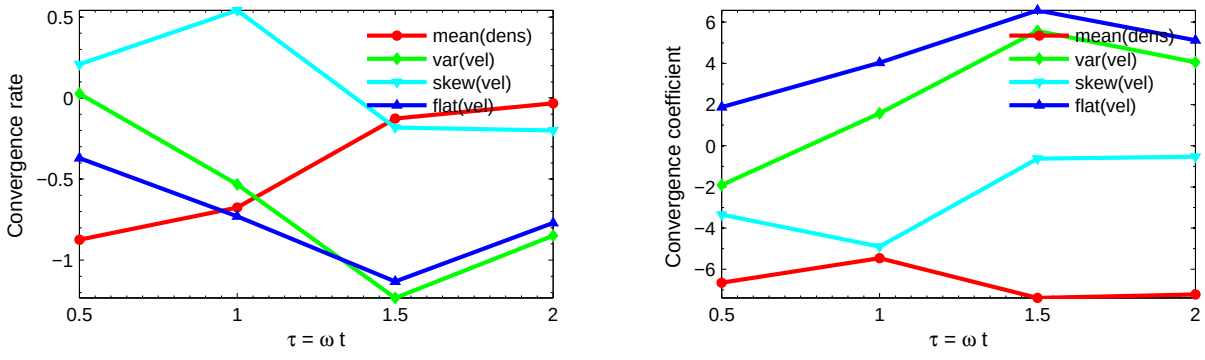

Figure 3.76: Statistically homogeneous velocity fluctuations test: time evolution of statistical convergence rate (left) and coefficient (right) of stochastic GForce scheme. $N_x = 10^5$.

3.3.4 Model PDF equation with non-zero RHS

PDF

We consider the PDF transport eq. (3.16). At the initial time the density is set to one and considered to be homogeneous in time and in space: $\overline{\rho}(t,x) = 1\,\mathrm{kg/m^3}$. The mean velocity is assumed equal to zero. $V = V' = V''$ is a sample space of velocity $u(t,x) = u'(t,x) = u''(t,x)$.

At the initial time the velocity variance is

$$\widetilde{u^2}(x) = \widetilde{u'^2}(x) = \sigma^2 \max\left(\exp\left(-\frac{x^2}{L^2}\right),\ 0.01\right), \tag{3.169}$$

where $L = 0.1\,\mathrm{m}$ is a width of Gaussian velocity profile and $\sigma = 1\,\mathrm{m/s}$ is a maximum standard deviation. The turbulent frequency satisfies the equation

$$\frac{d\omega}{dt} = -C_\omega \omega^2, \quad \omega(t=0) = \omega_0 = 1\,\mathrm{Hz}. \tag{3.170}$$

We suppose that it is homogeneous in space. Modeled constants are set to $C_\omega = 0.8$, $C_1 = 3.6$ and $C_0 = \frac{C_1}{2} - 1$. Analytical solution of the eq. (3.170) with imposed initial condition is

$$\omega(t) = \frac{1}{\omega_0^{-1} + C_\omega t}. \tag{3.171}$$

Turbulent energy k is calculated from fluctuations of velocity and turbulent dissipation is defined as

$$\varepsilon = \omega k = \omega \widetilde{u''^2} = \omega \overline{u'^2}. \tag{3.172}$$

One can show that when the time tends to infinity, the transfer coefficient of the third moment of velocity $\overline{u''^3}$ can be written as

$$\nu_{\overline{u'^3}} = -\frac{\overline{u'^3}\omega}{\overline{u'^2}\frac{\partial \overline{u'^2}}{\partial x}}. \tag{3.173}$$

Detailed proof of the statement (3.173) is given in [EmakoLetizia2014].

SPDEs

The SPDEs which are statistically equivalent to the PDF from eq. (3.16) read eqs. (3.42) and (3.43) The velocity variance is given by (A.103). The turbulent dissipation is calculated as

$$\varepsilon = \omega \widetilde{u''^2}. \tag{3.174}$$

Numerical solution

The purpose of this test is to check the ability of the numerical stochastic schemes to predict correctly statistics and a transfer coefficient of the third velocity moment. As we can see, the eq. (3.43) contains a stochastic term $r\sqrt{C_0\varepsilon}\dot{\xi}$ and as it was noted before it can change a Favre-averaged velocity. The secondary objective of this test is to check a correction method of the Favre-averaged fluctuating velocity:

$$u'' = u'' - \widetilde{u''}. \tag{3.175}$$

The solution obtained via the numerical resolution of eq. (3.16) is taken as a reference solution with which statistics from the SPDEs (3.42), (3.43) and (A.103) are compared. The space discretization parameters for the PDF transport equation are taken from appendix A.5.5.

We observe that the stochastic Lax-Friedrichs method diverges at $t = 1\,\mathrm{s}$, whereas other numerical schemes remain very close to the PDF solution. As a consequence, the stochastic Lax-Friedrichs scheme is not suited to solve the SPDEs when the turbulent frequency varies in time. At the same time, in the case when the turbulent frequency is zero, this method yields the lowest density fluctuations and recovers solution.

Spatial profiles. In order to illustrate spatial profiles of statistics calculated by the SPDEs, the number of cells is set to 612 and the number of stochastic fields is imposed to be 2000. The computational domain is $D = [-6\,\mathrm{m}; 6\,\mathrm{m}]$.

Figure 3.77 shows a spatial profile of the transfer coefficient $\nu_{\overline{u'^3}}$ calculated with the PDF solution at different moments in time. As stochastic statistics fluctuate significantly, the calculation of $\nu_{\overline{u'^3}}$ cannot be direct and requires the use of some filter to smooth numerical solutions at the initial time and then the application of a space derivative of the second velocity moment.

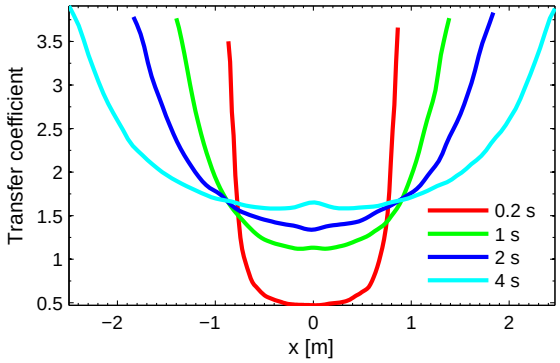

Figure 3.77: Model PDF eq. with non-zero RHS: transfer coefficient calculated with PDF

Figures 3.78 and 3.79 represent the value of third moment transfer coefficient $\nu_{\overline{u'^3}}$ defined in eq. (3.173). The values of $\overline{u'^2} = \widetilde{u''^2}$ and $\overline{u'^3} = \widetilde{u''^3}$ are calculated using different stochastic methods. The quantity $\partial\widetilde{u''^2}/\partial x$ is derived from $\widetilde{u''^2}$ via 2nd order Savitzky-Golay filter [SavitzkyGolay1964] of window $x = 1.2\,\mathrm{m}$.

One concludes that the transfer coefficient calculated with stochastic schemes follows the same behavior that it obtained from deterministic equation, except the neighborhood of $x = 0\,\mathrm{m}$. This is a particular point where the derivative of velocity variance is equal to zero and where the velocity skewness is also zero in deterministic case, while for stochastic schemes these moments fluctuate significantly for given number of fields $N_r = 2000$ (right panels of figs. 3.82 and 3.83).

Figures 3.80-3.84 show different spatial profiles of density and velocity statistics at time $3\,\mathrm{s}$ obtained without and with Favre-averaged velocity correction. The same sequence of Gaussian noise is used in two tests: with mean correction and without it. This allows precisely

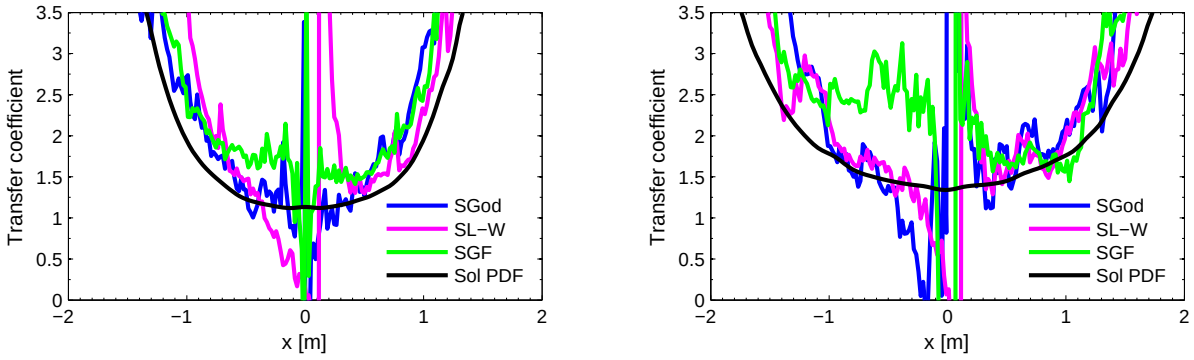

Figure 3.78: Comparison of transfer coefficient calculated using PDF (black line) and stochastic methods (colored lines). Left: $t = 1\,\mathrm{s}$, right: $t = 2\,\mathrm{s}$. $N_r = 2000$, $N_x = 612$.

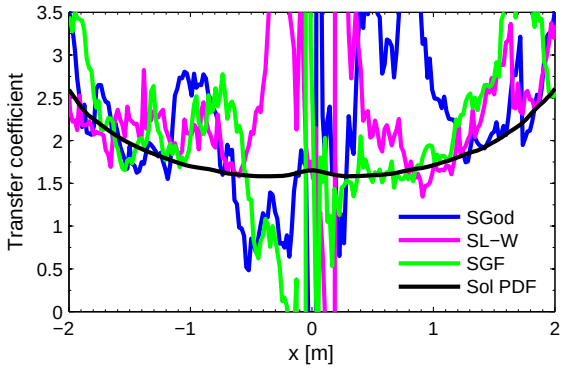

Figure 3.79: Comparison of transfer coefficient calculated using PDF (black line) and stochastic methods (colored lines) for $t = 4\,\mathrm{s}$. $N_r = 2000$, $N_x = 612$.

evaluating the influence of the mean velocity correction. All the profiles are compared with the PDF solution.

Figure 3.80 shows spatial profiles of the mean density. The Favre-averaged velocity correction results in drastically decreasing density fluctuations for three numerical stochastic schemes: Lax-Wendroff, GForce and Godunov. Without the Favre-averaged velocity correction the stochastic For example Lax-Wendroff scheme gives about 20% of density fluctuations (left panel of fig. 3.80), while with velocity correction the density fluctuations for the same scheme are only about 2% (right panel of fig. 3.80).

Figure 3.81 illustrates the Favre-averaged velocity when no correction is used. For all methods the Favre-averaged velocity is different from zero. As a consequence, Favre velocity statistics contain more noise than the same statistics with mean velocity correction (figs. 3.82 to 3.84). It should be noted that even if the Favre-averaged velocity correction is not used, the calculated statistics approximate exact solution and do not diverge.

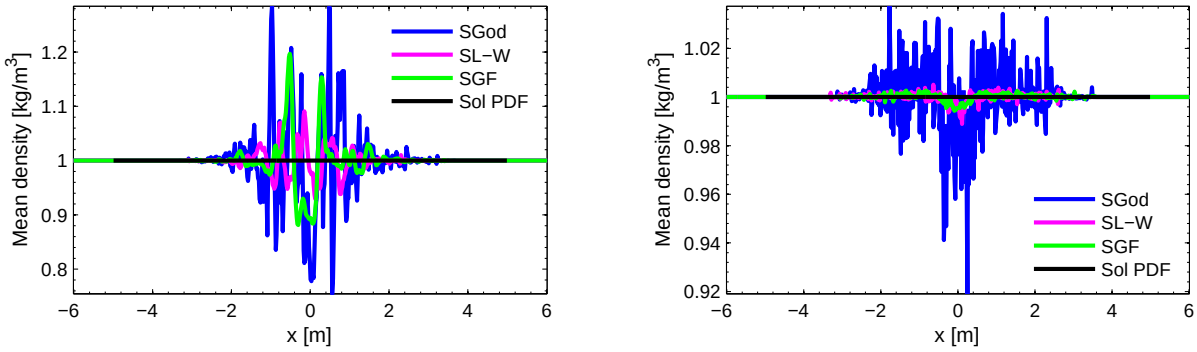

Figure 3.80: Model PDF eq. with non-zero RHS: spatial profile of mean density at time 3 s; left: without mean velocity correction, right: with mean velocity correction. $N_r = 2000$, $N_x = 612$.

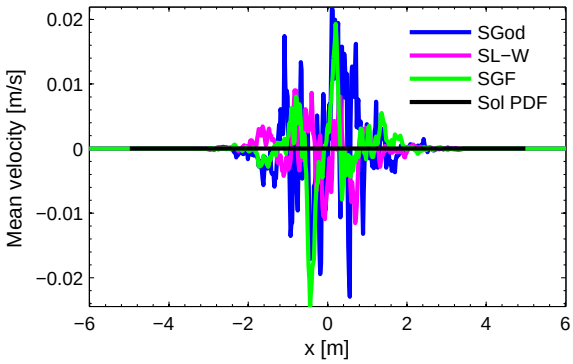

Figure 3.81: Model PDF eq. with non-zero RHS: spatial profile of Favre-averaged velocity at time 3 s; left: without mean velocity correction, right: with mean velocity correction. $N_r = 2000$, $N_x = 612$.

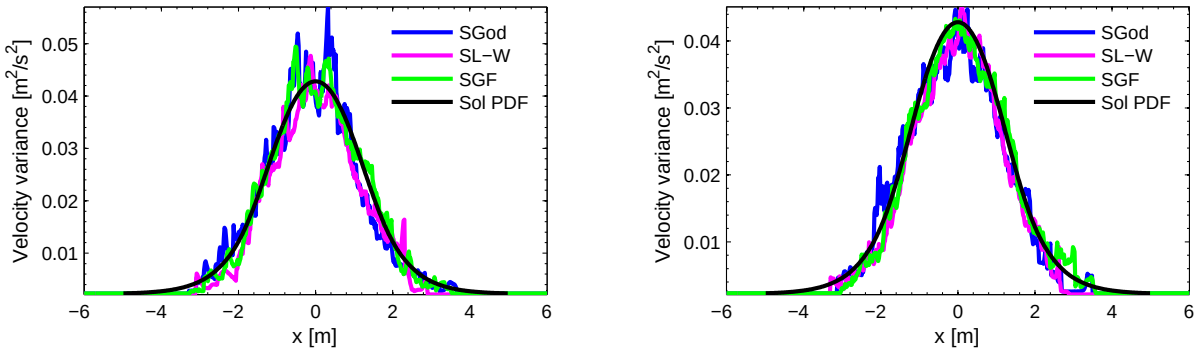

Figure 3.82: Model PDF eq. with non-zero RHS: spatial profile of Favre velocity variance at time 3 s; left: without mean velocity correction, right: with mean velocity correction. $N_r = 2000$, $N_x = 612$.

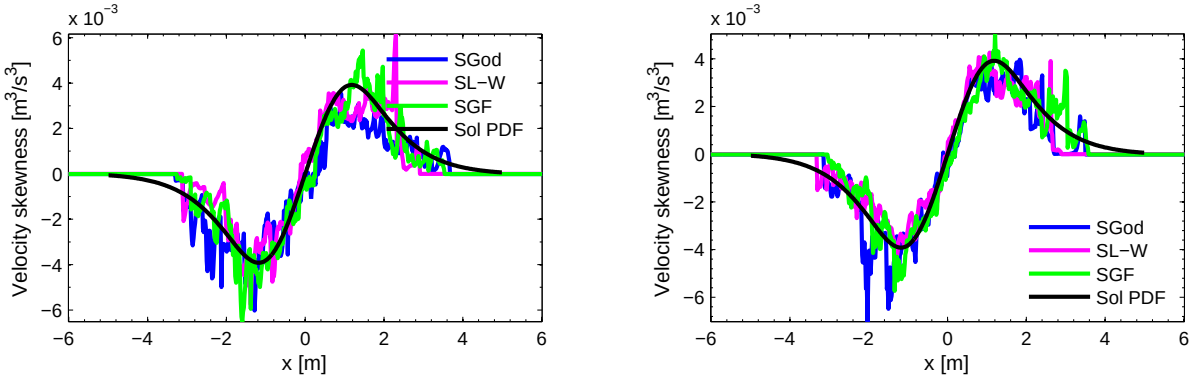

Figure 3.83: Model PDF eq. with non-zero RHS: spatial profile of Favre velocity skewness at time 3 s; left: without mean velocity correction, right: with mean velocity correction. $N_r = 2000$, $N_x = 612$.

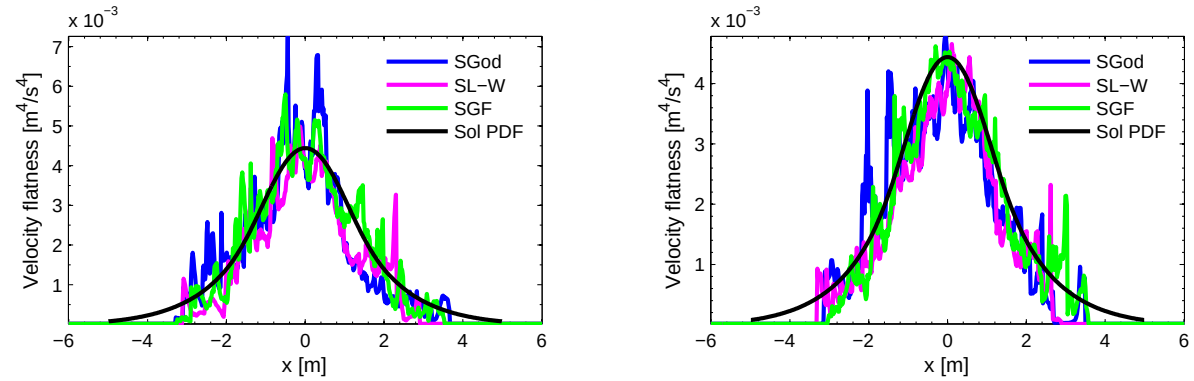

Figure 3.84: Model PDF eq. with non-zero RHS: spatial profile of Favre velocity flatness at time 3 s; left: without mean velocity correction, right: with mean velocity correction. $N_r = 2000$, $N_x = 612$.

Convergence. Let us consider a spatial convergence at time 0.2 s when a correction of fluctuating velocity is applied to the stochastic process. The number of realizations is fixed to $N_r = 10^6$ and the number of grid cells is varied from $N_x = 40$ to $N_x = 100$. The numerical domain of calculation is $[-1\,\mathrm{m}; 1\,\mathrm{m}]$. The solution obtained from numerical resolution of the PDF is taken as a reference solution.

Spatial convergence of stochastic schemes for the mean density and first four moments of velocity are shown in figs. 3.85 and 3.86. Due to the applied correction, the Favre average of the velocity is identically zero. The rate of spatial convergence is very close to the theoretical value, and it is about -1 for all the considered moments. Statistics calculated from the PDF are continuous functions and therefore one can suppose that the stochastic Lax-Wendroff method should weakly converge as N_x^{-2}. However such the rate has been never observed in practice.

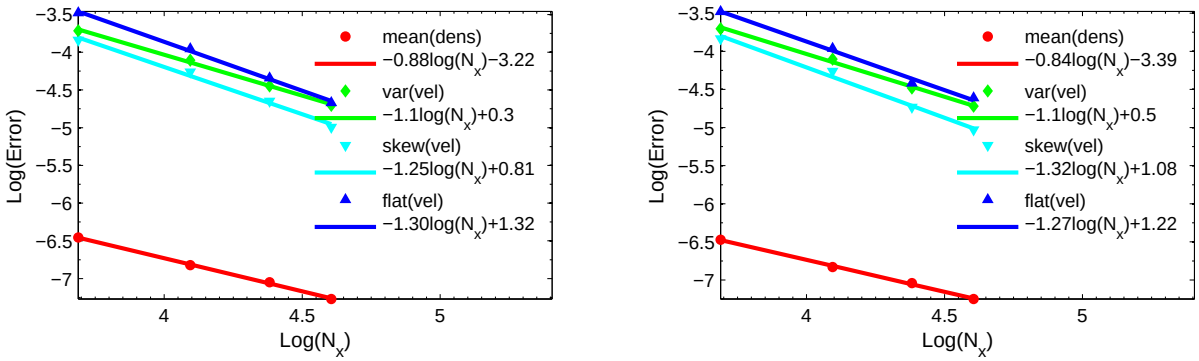

Figure 3.85: Model PDF eq. with non-zero RHS: spatial convergence of stochastic GForce (left) and stochastic Lax-Wendroff (right). $N_r = 10^6$.

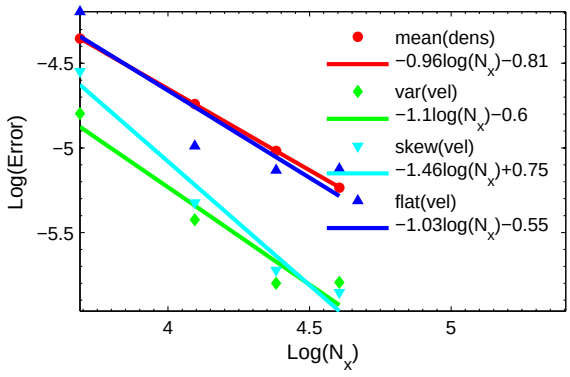

Figure 3.86: Model PDF eq. with non-zero RHS: spatial convergence of stochastic Godunov method. $N_r = 10^6$.

The determination of statistical error is complex in this test, because the solution of the SPDEs depends on statistics of $\widetilde{u''^2}$ which is used in resolution of eq. (3.43). If the Favre

velocity variance is heavily noised, after some time the solution of the SPDEs diverges. For example, is one takes $N_r = 8$, the solution existence time is about $t = 0.02\,\mathrm{s}$. If the number of fields N_r is increased, the time of existence of solution also increases. Consequently, the observation of statistical error is limited in our case by the available numerical resources.

3.4 Conclusions

The quasi-linear hyperbolic SPDEs which are statistically equivalent to the transport equation for the velocity PDF (or for the joint velocity-scalars PDF) are studied. It is shown that in order to preserve the equivalence between the SPDEs and the PDF transport equation, the multivalued solutions of the SPDEs should be taken into account. The entropy solutions of the SPDEs are dissipative and single-valued. They are not equivalent to the transported PDF solutions. It is demonstrated on several tests (see figs. 3.2 and 3.28).

The new stochastic method, recently proposed by O. Soulard, which capture the multivalued solutions is applied to solve the SPDEs in one-dimensional case. It is generalized to the resolution of the SPDEs in the three-dimensional case (see appendix A.3, appendix A.4).

The stochastic Godunov, Lax-Friedrichs, Lax-Wendroff and GForce are used to solve the SPDEs. The results of the numerical simulation are compared with the reference solutions, which are found from direct numerical solution of the PDF equation (finite-volume method) or which are analytical. In general, there is good agreement between the present stochastic simulations and the reference solutions. It is shown that the stochastic Godunov, Lax-Wendroff and GForce schemes give approximately the same results, while the stochastic Lax-Friedrichs scheme is less accurate for some tests and can diverge (see section 3.3.3 and section 3.3.4).

The accuracy of the EMC solver is quantified through a detailed study of numerical errors. It is found that the statistical error depends on the time where singularities in the derivatives of solutions develop. Before this time the statistical convergence rates are -0.5 (see fig. A.22) for the mean stochastic density, the Favre-averaged velocity and velocity variance. After the occurrence of the singularities the statistical error is scales as $N_r^{-0.3}$ (see, e.g., fig. 3.20). The Favre velocity skewness and flatness converge statistically slower than velocity variance. The greater the moment, the more stochastic fields are required to observe the convergence. It is observed that the spatial error of the stochastic schemes depends on the smoothness of the solutions. If the mean density and the velocity moments are smooth functions, the spatial order of convergence scales as Δx, otherwise $\Delta x^{0.5}$.

Overall, the present results give a satisfactory indication on the adequacy of the new stochastic method. However, more validation is necessary before its further application for numerical simulations of turbulent combustion.

3.5 Perspectives

Further research for the new stochastic method could be aimed at the formulation and validation of second order spatial schemes. Indeed, the Lax-Wendroff method applied to the PDF transport equation is a second-order accurate both in both space and time for problems having smooth solutions. From the numerical viewpoint, a first order spatial convergence of the stochastic Lax-Wendroff method with respect to Δx is observed. At the moment, we have undertaken a currently unsuccessful attempt of constructing such scheme using limiters.

An optimal way of correcting the mean density has to be investigated. Indeed the simple correction $r_j^{*n} = \overline{\rho}_j^n \frac{r_j^{*n}}{\overline{r_j^n}}$ has undesirable secondary effect of influencing higher Favre velocity moments. The decorrelation between the Wiener noise and the stochastic fields (see, e.g., eq. (3.115)) should be used to improve the velocity statistics.

Finally, the development of a hybrid algorithm for the joint velocity-scalars PDF equation should be investigated. This method is a combination of a finite-volume scheme which is used to solve the RANS equations and the EMC method to solve the joint velocity-scalars PDF equation. The motivation is to reduce the bias and the statistical error and to have an algorithm which is more efficient than stand-alone method.

Part II

Standard models of turbulent combustion

Chapter 4

Flamelet tabulated chemistry (FTC) model

During his PhD work J. Savre implemented FTC models in CEDRE for premixed and non-premixed flames. He validated these models on two configurations. The first validation test was the turbulent premixed flame of Nandula [NandulaPitz1996] and the second was the turbulent premixed flame of prediction and control of combustion instabilities in tubular and annular gas turbine combustion systems (PRECCINSTA) [MeierWeigand2007].

The aim of this work is to revise existing FTC models in CEDRE and validate them on different representative configurations of turbulent flames. The development effort of restoring of the described in this section FTC models from an old CEDRE version into the current one, as well as some numerical corrections for a β-PDF integration are parts of the present work.

4.1 Original implementation of FTC beta-PDF model in CEDRE

The details of FTC β-PDF models in CEDRE can be found in [Savre2010]. Let us recall here only the key moments.

4.1.1 Modeling of Favre-averaged progress variable

Assuming that all molecular diffusion coefficients for species are equal

$$D_k = D,\ k = 1, .., N_{sp} \tag{4.1}$$

and that all turbulent diffusion coefficient for species are also equal

$$D_k^t = D^t, \tag{4.2}$$

the Favre-averaged progress variable $\widetilde{C}$ is calculated from an algebraic equation, e.g.

$$\widetilde{C} = \frac{\widetilde{Y}_{\mathrm{CO}} + \widetilde{Y}_{\mathrm{CO_2}}}{\widetilde{Y}^{eq}_{\mathrm{CO}} + \widetilde{Y}^{eq}_{\mathrm{CO_2}}}, \tag{4.3}$$

where $\widetilde{Y}^{eq}_{\mathrm{CO}}$ and $\widetilde{Y}^{eq}_{\mathrm{CO}_2}$ are equilibrium values of Y_{CO} and Y_{CO_2}. Using the linear interpolation, one can obtain that

$$\widetilde{Y}^{eq}_{\mathrm{CO}} = Y^{eq}_{\mathrm{CO}}(\widetilde{Z}), \qquad \widetilde{Y}^{eq}_{\mathrm{CO}_2} = Y^{eq}_{\mathrm{CO}_2}(\widetilde{Z}). \tag{4.4}$$

4.1.2 Modeling of Favre variance of progress variable

Transport equation

The second moment of the progress variable $\widetilde{C''^2}$ is found from the transport equation

$$\frac{\partial}{\partial t}\left(\overline{\rho}\widetilde{C''^2}\right) + \frac{\partial}{\partial x_j}\left(\overline{\rho}\widetilde{u}_j\widetilde{C''^2}\right) = \frac{\partial}{\partial x_j}\left(\overline{\rho}\left(D + D^t\right)\frac{\partial}{\partial x_j}\left(\widetilde{C''^2}\right)\right) + 2\overline{\rho}D^t|\boldsymbol{\nabla}\widetilde{C}|^2 - 2\overline{\rho}\widetilde{s}_{\chi_c} + 2S_c, \tag{4.5}$$

where D and D^t are molecular and turbulent diffusion coefficients, respectively. They are taken the same that for species. $2\overline{\rho}\widetilde{s}_{\chi_c}$ is a dissipation term and S_c is a source.

CEDRE provides many options for modeling dissipation and source terms. The source S_c can be calculated as shown in table 4.1.

	S_c
1	$\overline{\rho}\left(\widetilde{C\dot{\omega}_c} - \widetilde{C}\widetilde{\dot{\omega}_c}\right)$
2	$\overline{\rho}(0.75 - \widetilde{C})\widetilde{\dot{\omega}}_c s^{0.25}$
3	$0.3(c_m - \widetilde{C})\rho_0 S_L \Xi^{Pet}\|\boldsymbol{\nabla}\widetilde{C}\|s^{0.25}$
4	$0.3(0.75 - \widetilde{C})\rho_0 S_L \Xi^{Pet}\|\boldsymbol{\nabla}\widetilde{C}\|s^{0.25}$
5	$0.5\overline{\rho}(0.75 - \widetilde{C})\widetilde{\dot{\omega}}_c s^{0.25}$
6	$1.5(0.75 - \widetilde{C})\rho_0 S_L\|\boldsymbol{\nabla}\widetilde{C}\|s^{0.25}$
7	$0.3(c_m - \widetilde{C})\rho_0 S_L \Xi^{Zim}\|\boldsymbol{\nabla}\widetilde{C}\|s^{0.25}$
8	$0.3(0.75 - \widetilde{C})\rho_0 S_L \Xi^{Zim}\|\boldsymbol{\nabla}\widetilde{C}\|s^{0.25}$
9	$3(0.75 - \widetilde{C})\rho_0 S_L\|\boldsymbol{\nabla}\widetilde{C}\|s^{0.25}$

Table 4.1: Source S_c in the transport equation of the Favre variance of progress variable $\widetilde{C''^2}$

In table 4.1 ρ_0 denotes the laminar flame density, S_L is the laminar flame speed, $\dot{\omega}_c$ is a chemical production rate of the progress variable and Ξ is wrinkling factor: Ξ^{Pet} is proposed by [Peters1999] for the RANS and by [Pitsch2005] for LES; Ξ^{Zim} is proposed by [KarpovLipatnikov1994] for two approaches. The value c_m is defined as

$$c_m = \frac{\widetilde{C\dot{\omega}_c}}{\widetilde{\dot{\omega}_c}} \tag{4.6}$$

and s is

$$s = \frac{\widetilde{C''^2}}{\widetilde{C}(1 - \widetilde{C})}. \tag{4.7}$$

The available options for modeling of the dissipation term $2\overline{\rho}\widetilde{s}_{\chi_c}$ are given in table 4.2.

	$2\overline{\rho}\widetilde{s_{\chi_c}}$
10	$2c_d\overline{\rho}\omega\widetilde{C''^2}$
20	$2c_d\overline{\rho}\omega\gamma^{ITNFS}\widetilde{C''^2}$
30	$c_d(2c_m-1)\rho_0 S_L\Xi^{Pet}\sqrt{\lvert\boldsymbol{\nabla}\widetilde{C}\rvert^2 s}$
40	$c_d(1.5-1)\rho_0 S_L\Xi^{Pet}\sqrt{\lvert\boldsymbol{\nabla}\widetilde{C}\rvert^2 s}$
50	$2c_d\overline{\rho}\omega\widetilde{C}(1-\widetilde{C})$
60	$5c_d(2c_m-1)\rho_0 S_L\sqrt{\lvert\boldsymbol{\nabla}\widetilde{C}\rvert^2 s}$
70	$c_d(2c_m-1)\rho_0 S_L\Xi^{Zim}\sqrt{\lvert\boldsymbol{\nabla}\widetilde{C}\rvert^2 s}$
80	$c_d(1.5-1)\rho_0 S_L\Xi^{Zim}\sqrt{\lvert\boldsymbol{\nabla}\widetilde{C}\rvert^2 s}$
90	$10c_d(2c_m-1)\rho_0 S_L\sqrt{\lvert\boldsymbol{\nabla}\widetilde{C}\rvert^2 s}$

Table 4.2: Dissipation term $2\overline{\rho}\widetilde{s_{\chi_c}}$ in the transport equation of the Favre variance of progress variable $\widetilde{C''^2}$

In table 4.2 ω is a turbulent frequency, γ^{ITNFS} is an ITNFS function proposed by [MeneveauPoinsot1991] in order to take into account the interaction between chemistry and turbulence. The constant c_d in the term of production of the mixture fraction variance is set to 1.

Algebraic expression

Instead of solving the transport equation (4.5) the Favre progress variable variance can be directly calculated from algebraic expression (table 4.3).

	$\widetilde{C''^2}$
10	$c_d\left(\frac{\mu_t}{Sc_t\overline{\rho}\omega}\lvert\boldsymbol{\nabla}\widetilde{C}\rvert^2+\frac{S_c}{\overline{\rho}\omega}\right)$
20	$c_d\gamma^{ITNFS}\left(\frac{\mu_t}{\overline{\rho}\omega}\lvert\boldsymbol{\nabla}\widetilde{C}\rvert^2+\frac{S_c}{\overline{\rho}\omega}\right)$
30	$2c_d(2c_m-1)\widetilde{C}(1-\widetilde{C})\frac{1}{\rho S_L\Xi^{Pet}\lvert\boldsymbol{\nabla}\widetilde{C}\rvert}\left(\frac{\mu_t}{Sc_t}\lvert\boldsymbol{\nabla}\widetilde{C}\rvert^2+S_c\right)$
50	$2c_d(1.5-1)\widetilde{C}(1-\widetilde{C})\frac{1}{\rho_0 S_L\Xi^{Pet}\lvert\boldsymbol{\nabla}\widetilde{C}\rvert}\left(\frac{\mu_t}{Sc_t}\lvert\boldsymbol{\nabla}\widetilde{C}\rvert^2+S_c\right)$
70	$2c_d(2c_m-1)\widetilde{C}(1-\widetilde{C})\frac{1}{\rho_0 S_L\Xi^{Zim}\lvert\boldsymbol{\nabla}\widetilde{C}\rvert}\left(\frac{\mu_t}{Sc_t}\lvert\boldsymbol{\nabla}\widetilde{C}\rvert^2+S_c\right)$
80	$2c_d(1.5-1)\widetilde{C}(1-\widetilde{C})\frac{1}{\rho_0 S_L\Xi^{Zim}\lvert\boldsymbol{\nabla}\widetilde{C}\rvert}\left(\frac{\mu_t}{Sc_t}\lvert\boldsymbol{\nabla}\widetilde{C}\rvert^2+S_c\right)$

Table 4.3: Algebraic expressions for Favre progress variable variance

4.1.3 Modeling of Favre-averaged mixture fraction

In order to ensure the conservation of mass the first moment of the mixture fraction satisfies the transport equation

$$\frac{\partial}{\partial t}\left(\overline{\rho}\widetilde{Z}\right)+\frac{\partial}{\partial x_j}\left(\overline{\rho}\widetilde{u}_j\widetilde{Z}\right)=\frac{\partial}{\partial x_j}\left(\overline{\rho}\left(D+D^t\right)\frac{\partial}{\partial x_j}\left(\widetilde{Z}\right)\right). \tag{4.8}$$

4.1.4 Modeling of Favre variance of mixture fraction

Transport equation

The variance of the mixture fraction $\widetilde{Z''^2}$ is found from the transport equation

$$\frac{\partial}{\partial t}\left(\overline{\rho}\widetilde{Z''^2}\right)+\frac{\partial}{\partial x_j}\left(\overline{\rho}\widetilde{u}_j\widetilde{Z''^2}\right)=\frac{\partial}{\partial x_j}\left(\overline{\rho}\left(D+D^t\right)\frac{\partial}{\partial x_j}\left(\widetilde{Z''^2}\right)\right)+2\overline{\rho}D^t|\boldsymbol{\nabla}\widetilde{Z}|^2-2\overline{\rho}c_d\frac{\widetilde{Z''^2}}{\tau_t}, \tag{4.9}$$

where τ_t is a characteristic time of the turbulence-chemistry interaction.

Algebraic expression

To avoid solving the transport equation, the mixture fraction variance is calculated from an algebraic expression

$$\widetilde{Z''^2}=\frac{\mu_t}{Sc_t\overline{\rho}\omega}|\boldsymbol{\nabla}\widetilde{Z}|^2. \tag{4.10}$$

4.1.5 Gradient of Favre-averaged progress variable

Using the definition (4.3) for the Favre-averaged progress variable and assuming that $\widetilde{Z}=const$, the gradient is

$$\boldsymbol{\nabla}\widetilde{C}=\frac{\boldsymbol{\nabla}\widetilde{Y}_{\mathrm{CO}}+\boldsymbol{\nabla}\widetilde{Y}_{CO2}}{\widetilde{Y}^{eq}_{\mathrm{CO}}+\widetilde{Y}^{eq}_{\mathrm{CO_2}}}. \tag{4.11}$$

The formula (4.11) is exact for premixed flames.

4.1.6 Coupling between tabulated chemistry and CEDRE

In CEDRE only the major species are transported, whereas other species are found from the table, which is constructed using [CANTERA] solver. The table contains the detailed chemical sources, mass fractions, etc. The access to the table is done with two entry parameters: mixture fraction Z and progress variable C. The chemical sources for the transported species in CEDRE are interpolated from the table. In order to preserve the sum of chemical sources, the source of nitrogen is adjusted in order to satisfy

$$\overline{\dot{\omega}}^{CEDRE}_{N_2}=-\sum_{k=1}^{N_{sp}-1}\overline{\dot{\omega}}^{table}_{k}, \tag{4.12}$$

where N_{sp} is a number of transported species in CEDRE.

4.1.7 Presumed beta-PDF

The presumed β-PDF $\widetilde{f}_\beta(Z, C; t, \boldsymbol{x})$, expressing at each spatial location in terms of the mean values of $\widetilde{Z}(t, \boldsymbol{x})$ and $\widetilde{C}(t, \boldsymbol{x})$ and also their variances $\widetilde{Z''^2}(t, \boldsymbol{x})$ and $\widetilde{C''^2}(t, \boldsymbol{x})$, is defined as

$$\widetilde{f}_\beta(Z, C; t, \boldsymbol{x}) = \frac{1}{B(p_1, q_1)B(p_2, q_2)} Z^{p_1-1}(1-Z)^{q_1-1} C^{p_2-1}(1-C)^{q_2-1}, \tag{4.13}$$

where the β-functions $B(p_1, q_1)$ and $B(p_2, q_2)$ appear to be the normalization constants which ensure that the total probability integrates to 1, i.e.

$$B(p_i, q_i) = \int_0^1 Z^{p_i-1}(1-Z)^{q_i-1} dZ, \quad i \in \{1, 2\}. \tag{4.14}$$

Here the so-called shape parameters p_1, q_1, p_2 and q_2 are some functions of the position $\boldsymbol{x}$ and time t. The properties of the β-distribution leads to the following expressions for these shape parameters:

$$p_1 = \widetilde{z}\left(\frac{\widetilde{Z}(1-\widetilde{Z})}{\widetilde{Z''^2}} - 1\right) \qquad q_1 = \left(1-\widetilde{Z}\right)\left(\frac{\widetilde{Z}(1-\widetilde{Z})}{\widetilde{Z''^2}} - 1\right) \tag{4.15}$$

and

$$p_2 = \widetilde{C}\left(\frac{\widetilde{C}(1-\widetilde{C})}{\widetilde{C''^2}} - 1\right) \qquad q_2 = \left(1-\widetilde{C}\right)\left(\frac{\widetilde{C}(1-\widetilde{C})}{\widetilde{C''^2}} - 1\right). \tag{4.16}$$

Note that in the case of infinitely fast chemistry, e.g. when at least one limit of $\widetilde{Z''^2} \to \widetilde{Z}(1-\widetilde{Z})$ or $\widetilde{C''^2} \to \widetilde{C}(1-\widetilde{C})$ holds, the parameters p_1, q_1 or respectively p_2, q_2 approach zero.

4.1.8 Algorithm of beta-PDF integration

The approximate integration method of the β-PDF (4.13) consists in replacing the β-PDF by the linear combination of two Dirac δ functions at singular points 0 and 1 and the β-PDF in the inner interval $(0; 1)$. The new PDF for one variable Ψ is

$$\widetilde{f}(\Psi; t, \boldsymbol{x}) = \alpha(t, \boldsymbol{x})\delta(0) + \gamma(t, \boldsymbol{x})\delta(\Psi - 1) + \widetilde{f}_\beta(\Psi; t, \boldsymbol{x}) H(\Psi) H(1-\Psi), \tag{4.17}$$

where δ is Dirac function and H is a Heaviside function of the following form

$$H(\Psi) = \begin{cases} 1 & \text{if } \Psi > 0, \\ 0 & \text{if } \Psi \le 0. \end{cases} \tag{4.18}$$

Let $0 < \epsilon < 10^{-6}$ be an arbitrary parameter. Integral of the PDF $\widetilde{f}(\Psi; t, \boldsymbol{x})$ on the interval $[0; 1]$ is

$$\int_0^1 \widetilde{f}(\Psi; t, \boldsymbol{x}) d\Psi = \alpha(t, \boldsymbol{x}) + \gamma(t, \boldsymbol{x}) + \int_\epsilon^{1-\epsilon} \widetilde{f}_\beta(\Psi; t, \boldsymbol{x}) d\Psi = 1. \tag{4.19}$$

On the other hand

$$\int_0^1 \widetilde{f}(\Psi;t,\boldsymbol{x})\Psi d\Psi = \gamma(t,\boldsymbol{x}) + \int_\epsilon^{1-\epsilon} \widetilde{f}_\beta(\Psi;t,\boldsymbol{x})\Psi d\Psi = \widetilde{\Psi}. \tag{4.20}$$

Therefore, the parameters $\alpha(t,\boldsymbol{x})$ and $\beta(t,\boldsymbol{x})$ can be determined from formulas:

$$\gamma(t,\boldsymbol{x}) = \widetilde{\Psi} - \int_\epsilon^{1-\epsilon} \widetilde{f}_\beta(\Psi;t,\boldsymbol{x})\Psi d\Psi, \tag{4.21}$$

$$\alpha(t,\boldsymbol{x}) = 1 - \int_\epsilon^{1-\epsilon} \widetilde{f}_\beta(\Psi;t,\boldsymbol{x})d\Psi - \widetilde{\Psi} + \int_\epsilon^{1-\epsilon} \widetilde{f}_\beta(\Psi;t,\boldsymbol{x})\Psi d\Psi. \tag{4.22}$$

One can note that the β-PDF $\widetilde{f}_\beta(\Psi;t,\boldsymbol{x})$ and the function $\Psi\widetilde{f}_\beta(\Psi;t,\boldsymbol{x})$ can be easily integrated in the interval $(\epsilon;1-\epsilon)$, because this interval does not contain any singular points of the β-distribution.

An important part of the algorithm is the numerical integration of the β-PDF $\widetilde{f}_\beta(Z,C;t,\boldsymbol{x})$. It is observed that it may encounter singularity difficulties at mixture fraction values $Z=0$ or $Z=1$ and at progress variable values $C=0$ or $C=1$. Another drawback of the existing β-integration method is that for some combinations of shape parameters q_1, q_2, p_1, p_2 the PDF can take numerically negative values due to the strong dependence on the grid of the mixture fraction and the progress variable and on ϵ.

In order to overcome these two numerical difficulties, we implement a piece-wise integration method, which was described in mono-dimensional case in [LienLiu2009], extending it to the two-dimensional case (see section 4.2.3).

4.2 Updated FTC beta-PDF model

4.2.1 New models for dissipation and source terms

The options 6 and 9 from table 4.1 and options 60 and 90 from table 4.2 were added during the present work in order to investigate the influence of model constants on the solution. The wrinkling factor is approximated, for simplicity, by constants $\Xi=5$ and $\Xi=10$.

4.2.2 Gradient of Favre-averaged progress variable

Equation (4.11) for the calculation of Favre-averaged progress variable gradient is valid only for the premixed flames (i.e. $\widetilde{Z}\equiv const$). We propose following possibilities to approximate this gradient for other flame types. Three cases should be distinguished:

- Premixed flame: $\widetilde{Z}\equiv const$.
  The sum of equilibrium mass fractions is constant:

$$\widetilde{Y}^{eq} = \widetilde{Y}^{eq}_{\mathrm{CO}} + \widetilde{Y}^{eq}_{\mathrm{CO_2}} = const. \tag{4.23}$$

Three components of the gradient $\nabla\widetilde{C}$ are

$$\frac{\partial\widetilde{C}}{\partial x_j} = \frac{1}{\widetilde{Y}^{eq}}\left[\frac{\partial\widetilde{Y}_{\mathrm{CO}}}{\partial x_j} + \frac{\partial\widetilde{Y}_{\mathrm{CO_2}}}{\partial x_j}\right],\ j = 1,2,3. \tag{4.24}$$

- Laminar non-premixed flame: $\widetilde{Z} \neq const,\ \widetilde{Z''^2} \equiv 0$.
  The sum of equilibrium mass fractions depends only on $\widetilde{Z}$:

$$\widetilde{Y}^{eq} = \widetilde{Y}^{eq}\left(\widetilde{Z}\right) = Y^{eq}_{\mathrm{CO}}\left(\widetilde{Z}\right) + Y^{eq}_{\mathrm{CO_2}}\left(\widetilde{Z}\right). \tag{4.25}$$

  Therefore, the components of the Favre-averaged progress variable gradient are

$$\frac{\partial\widetilde{C}}{\partial x_j} = \frac{1}{\left(\widetilde{Y}^{eq}\right)^2}\left(\widetilde{Y}^{eq}\left[\frac{\partial\widetilde{Y}_{\mathrm{CO}}}{\partial x_j} + \frac{\partial\widetilde{Y}_{\mathrm{CO_2}}}{\partial x_j}\right] - \left[\widetilde{Y}_{\mathrm{CO}} + \widetilde{Y}_{\mathrm{CO_2}}\right]\frac{\partial\widetilde{Z}}{\partial x_j}\frac{\partial\widetilde{Y}^{eq}}{\partial\widetilde{Z}}\right). \tag{4.26}$$

- Turbulent non-premixed flame: $\widetilde{Z} \neq const,\ \widetilde{Z''^2} \neq 0$.
  The sum of equilibrium mass fractions depends on $\widetilde{Z}$ and $\widetilde{Z''^2}$:

$$\widetilde{Y}^{eq} = \widetilde{Y}^{eq}\left(\widetilde{Z}, \widetilde{Z''^2}\right) = Y^{eq}_{\mathrm{CO}}\left(\widetilde{Z}, \widetilde{Z''^2}\right) + Y^{eq}_{\mathrm{CO_2}}\left(\widetilde{Z}, \widetilde{Z''^2}\right). \tag{4.27}$$

  Thus,

$$\frac{\partial\widetilde{C}}{\partial x_j} = \frac{1}{\widetilde{Y}^{eq}}\left[\frac{\partial\widetilde{Y}_{\mathrm{CO}}}{\partial x_j} + \frac{\partial\widetilde{Y}_{\mathrm{CO_2}}}{\partial x_j}\right] - \frac{\widetilde{Y}_{\mathrm{CO}} + \widetilde{Y}_{\mathrm{CO_2}}}{\left(\widetilde{Y}^{eq}\right)^2}\left(\frac{\partial\widetilde{Z}}{\partial x_j}\frac{\partial\widetilde{Y}^{eq}}{\partial\widetilde{Z}} + \frac{\partial\widetilde{Z''^2}}{\partial x_j}\frac{\partial\widetilde{Y}^{eq}}{\partial\widetilde{Z''^2}}\right). \tag{4.28}$$

As the mixture fraction is obtained from the transport equation, the value $\frac{\partial\widetilde{Z}}{\partial x_j}$ is exact in the given above expressions. The derivative of $\frac{\partial\widetilde{Y}^{eq}(\Psi)}{\partial\Psi}$ can be found for example using the first order numerical approximation of the derivative:

$$\frac{\partial\widetilde{Y}^{eq}(\Psi)}{\partial\Psi} = \frac{\partial\widetilde{Y}^{eq}(\Psi_2) - \partial\widetilde{Y}^{eq}(\Psi_1)}{(\Psi_2 - \Psi_1)}, \tag{4.29}$$

where $\Psi \in (\Psi_1; \Psi_2)$.

4.2.3 Algorithm of beta-PDF integration

Let us consider two independent variables: a mixture fraction Z and a progress variable C. The function $g(Z, C)$ is defined on the set of points (Z_k, C_n) such that

$$Z_1 = 0 < Z_2 < .. < Z_k < .. < Z_{N_z} = 1$$

and

$$C_1 = 0 < C_2 < .. < C_n < .. < C_{N_c} = 1,$$

where N_z and N_c are numbers of discretization points of Z and C, respectively. Using the bi-linear interpolation on a regular two-dimensional grid $[Z_{k-1}; Z_k] \times [C_{n-1}; C_n]$ the function $g(Z, C)$ can be presented as

$$g(Z, C) = \alpha_{1kn} Z + \alpha_{2kn} C + \alpha_{3kn} ZC + \alpha_{4kn}. \tag{4.30}$$

Since $g(Z, C)$ is

$$g(Z,C) = \frac{1}{(Z_k - Z_{k-1})(C_n - C_{n-1})}[g(Z_{k-1}, C_{n-1})(Z_k - Z)(C_n - C) + g(Z_k, C_{n-1})(Z - Z_{k-1})(C_n - C)$$
$$+ g(Z_{k-1}, C_n)(Z_k - Z)(C - C_{n-1}) + g(Z_k, C_n)(Z - Z_{k-1})(C - C_{n-1})] \tag{4.31}$$

The volume of $[Z_{k-1}; Z_k] \times [C_{n-1}; C_n]$ is

$$Vol = (Z_k - Z_{k-1})(C_n - C_{n-1}) \tag{4.32}$$

The coefficients α_{ikn}, $i = 1, .., 4$, $k = 1, .., N_z$, $n = 1, .., N_c$ of the eq. (4.30) can be found from the expression (4.31), they are given by the following formulas:

$$\alpha_{1kn} = Vol^{-1} \left[(g(Z_k, C_{n-1}) - g(Z_{k-1}, C_{n-1}))C_n + (g(Z_{k-1}, C_n) - g(Z_k, C_n))C_{n-1} \right] \tag{4.33}$$

$$\alpha_{2kn} = Vol^{-1} \left[(g(Z_{k-1}, C_n) - g(Z_{k-1}, C_{n-1}))Z_k + (g(Z_k, C_{n-1}) - g(Z_k, C_n))Z_{k-1} \right] \tag{4.34}$$

$$\alpha_{3kn} = Vol^{-1} \left[g(Z_{k-1}, C_{n-1}) - g(Z_k, C_{n-1}) - g(Z_{k-1}, C_n) + g(Z_k, C_n) \right] \tag{4.35}$$

$$\alpha_{4kn} = Vol^{-1} \left[g(Z_{k-1}, C_{n-1}) Z_k C_n - g(Z_k, C_{n-1}) Z_{k-1} C_n - g(Z_{k-1}, C_n) Z_k C_{n-1} + g(Z_k, C_n) Z_{k-1} C_{n-1} \right] \tag{4.36}$$

It can be shown that the integral of the function $g(Z, C)$ defined in (4.31) with the β-PDF $\widetilde{f}_\beta$ given by (4.13) on the domain $[Z_{k-1}; Z_k] \times [C_{n-1}; C_n]$ for $2 \le k \le N_z$ and $2 \le n \le N_c$ is

$$\int_{Z_{k-1}}^{Z_k} \int_{C_{n-1}}^{C_n} (\alpha_{1kn} Z + \alpha_{2kn} C + \alpha_{3kn} ZC + \alpha_{4kn}) \widetilde{f}_\beta(Z, C) dC dZ =$$

$$\int_0^{Z_k} \int_0^{C_n} (\alpha_{1kn} Z + \alpha_{2kn} C + \alpha_{3kn} ZC + \alpha_{4kn}) \widetilde{f}_\beta(Z, C) dC dZ$$

$$- \int_0^{Z_{k-1}} \int_0^{C_n} (\alpha_{1kn} Z + \alpha_{2kn} C + \alpha_{3kn} ZC + \alpha_{4kn}) \widetilde{f}_\beta(Z, c) dC dZ$$

$$- \int_0^{Z_k} \int_0^{C_{n-1}} (\alpha_{1kn} Z + \alpha_{2kn} C + \alpha_{3kn} ZC + \alpha_{4kn}) \widetilde{f}_\beta(Z, C) dC dZ$$

$$+\int_0^{Z_{k-1}}\int_0^{C_{n-1}}(\alpha_{1kn}Z+\alpha_{2kn}C+\alpha_{3kn}ZC+\alpha_{4kn})\widetilde{f}_\beta(Z,C)dCdZ=$$

$$\alpha_{1kn}\frac{B(p_1+1,q_1)}{B(p_1,q_1)}[I_{Z_k}(p_1+1,q_1)(I_{C_n}(p_2,q_2)-I_{C_{n-1}}(p_2,q_2))$$

$$+I_{Z_{k-1}}(p_1+1,q_1)(-I_{C_n}(p_2,q_2)+I_{C_{n-1}}(p_2,q_2)]$$

$$+\alpha_{2kn}\frac{B(p_2+1,q_2)}{B(p_2,q_2)}[I_{Z_k}(p_1,q_1)(I_{C_n}(p_2+1,q_2)-I_{C_{n-1}}(p_2+1,q_2))$$

$$+I_{Z_{k-1}}(p_1,q_1)(-I_{C_n}(p_2+1,q_2)+I_{C_{n-1}}(p_2+1,q_2))]$$

$$+\alpha_{3kn}\frac{B(p_1+1,q_1)}{B(p_1,q_1)}\frac{B(p_2+1,q_2)}{B(p_2,q_2)}[I_{Z_k}(p_1+1,q_1)(I_{C_n}(p_2+1,q_2)-I_{C_{n-1}}(p_2+1,q_2))+$$

$$I_{Z_{k-1}}(p_1+1,q_1)(-I_{C_n}(p_2+1,q_2)+I_{C_{n-1}}(p_2+1,q_2))]$$

$$+\alpha_{4kn}[I_{Z_k}(p_1,q_1)(I_{C_n}(p_2,q_2)-I_{C_{n-1}}(p_2,q_2))+I_{Z_{k-1}}(p_1,q_1)(-I_{C_n}(p_2,q_2)+I_{C_{n-1}}(p_2,q_2)], \quad (4.37)$$

where, $I_Z(p_1,q_1)$ ($I_C(p_2,q_2)$), $0<Z<1$ ($0<C<1$) is regularized incomplete β-function, i.e.

$$I_Z(p_1,q_1)=\frac{1}{B(p_1,q_1)}\int_0^Z z^{p_1-1}(1-z)^{q_1-1}dz. \quad (4.38)$$

The averaged value $\widetilde{g}$ is simply the sum of sub-integrals from (4.37):

$$\widetilde{g}=\int_0^1\int_0^1 g(Z,C)\widetilde{f}_\beta(Z,c)dCdZ=\sum_{k=2}^{N_z}\sum_{n=2}^{N_c}\int_{Z_{k-1}}^{Z_k}\int_{C_{n-1}}^{C_n}(\alpha_{1kn}Z+\alpha_{2kn}C+\alpha_{3kn}ZC+\alpha_{4kn})\widetilde{f}_\beta(Z,C)dCdZ \quad (4.39)$$

4.2.4 Numerical implementation of beta-PDF integration

We consider the following grid for the variances of mixture fraction and progress variable: $VarZ_i=0,..,\widetilde{Z}(1-\widetilde{Z})$ and $VarC_j=0,..,\widetilde{C}(1-\widetilde{C})$ for each $\widetilde{Z}$ and $\widetilde{C}$, $i=1,..,N_{VarZ}$, $j=1,..,N_{VarC}$ There are 8 particular cases which should be calculated differently.

1. $\widetilde{Z''^2}=0$, $\widetilde{C''^2}\neq\{0,\widetilde{C}(1-\widetilde{C})\}$

$$\widetilde{g}=\int_0^1\int_0^1 g(Z,C)\widetilde{f}_\beta(Z,C)dCdZ=\int_0^1 g(\widetilde{Z},C)\widetilde{f}_\beta(C)dC. \quad (4.40)$$

2. $\widetilde{Z''^2}=\widetilde{Z}(1-\widetilde{Z})$, $\widetilde{C''^2}\neq\{0,\widetilde{C}(1-\widetilde{C})\}$

$$\widetilde{g}=\int_0^1\int_0^1 g(Z,C)\widetilde{f}_\beta(Z,C)dCdZ=\widetilde{Z}\int_0^1 g(1,C)\widetilde{f}_\beta dC+(1-\widetilde{Z})\int_0^1 g(0,C)\widetilde{f}_\beta dC. \quad (4.41)$$

3. $\widetilde{C''^2} = 0$, $\widetilde{Z''^2} \neq \{0, \widetilde{Z}(1-\widetilde{Z})\}$

$$\widetilde{g} = \int_0^1 \int_0^1 g(Z,C)\widetilde{f}_\beta dC dZ = \int_0^1 g(Z,\widetilde{C})\widetilde{f}_\beta(Z) dZ. \tag{4.42}$$

4. $\widetilde{C''^2} = \widetilde{C}(1-\widetilde{C})$, $\widetilde{Z''^2} \neq \{0, \widetilde{Z}(1-\widetilde{Z})\}$

$$\widetilde{g} = \int_0^1 \int_0^1 g(Z,C)\widetilde{f}_\beta(Z,C) dC dZ = \widetilde{C} \int_0^1 g(Z,1)\widetilde{f}_\beta(Z) dZ + (1-\widetilde{C}) \int_0^1 g(Z,0)\widetilde{f}_\beta(Z) dZ. \tag{4.43}$$

5. $\widetilde{Z''^2} = 0$, $\widetilde{C''^2} = 0$

$$\widetilde{g} = \int_0^1 \int_0^1 g(Z,C)\widetilde{f}_\beta(Z,C) dC dZ = g(\widetilde{Z},\widetilde{C}) \tag{4.44}$$

6. $\widetilde{Z''^2} = 0$, $\widetilde{C''^2} = \widetilde{C}(1-\widetilde{C})$

$$\widetilde{g} = \int_0^1 \int_0^1 g(Z,C)\widetilde{f}_\beta(Z,C) dC dZ = \widetilde{C} g(\widetilde{Z},1) + (1-\widetilde{C}) g(\widetilde{Z},0) \tag{4.45}$$

7. $\widetilde{Z''^2} = \widetilde{Z}(1-\widetilde{Z})$, $\widetilde{C''^2} = 0$

$$\widetilde{g} = \int_0^1 \int_0^1 g(Z,C)\widetilde{f}_\beta(Z,C) dC dZ = \widetilde{Z} g(1,\widetilde{C}) + (1-\widetilde{Z}) g(0,\widetilde{C}) \tag{4.46}$$

8. $\widetilde{Z''^2} = \widetilde{Z}(1-\widetilde{Z})$, $\widetilde{C''^2} = \widetilde{C}(1-\widetilde{C})$

$$\widetilde{g} = \int_0^1 \int_0^1 g(Z,C)\widetilde{f}_\beta(Z,C) dC dZ = \widetilde{Z}\widetilde{C} g(1,1) + (1-\widetilde{Z})\widetilde{C} g(0,1) + \widetilde{Z}(1-\widetilde{C}) g(1,0) + (1-\widetilde{Z})(1-\widetilde{C}) g(0,0) \tag{4.47}$$

We emphasize the importance of calculating the volume according to

$$Vol = Z(k)C(n) - Z(k-1)C(n) - Z(k)C(n-1) + Z(k-1)C(n-1)$$

in order to properly preserve the normalization of the β-PDF.

Study of convergence of the semi-analytic beta integration method

In this section we study the numerical convergence. As the solver does not distinguish the variables Z and C in the β-integration function, we consider only two different cases: firstly,

when the function $g(Z,C)$ depends on C and Z is constant, and secondly, when the function $g(Z,C)$ depends on Z and C at the same time.

The first validation test is performed on the analytic function $g(C) = C^{20}$. The number of points of the progress variable is varied from $N_c = 5$ to $N_c = 5000$. Different values of parameters p and q are chosen. The second test function is taken as $g(Z,C) = Z^5C^2$. The number of points of the progress variable is varied from $N_c = 5$ to $N_c = 55$. The same set of points is considered for the mixture fraction. The total number of points in the $2D$ grid is given by $N = N_c \times N_z$ and varies from $N = 25$ to $N = 3025$. Different shape parameters p_k and q_k, $k = 1, 2$ are considered. The solutions obtained from Matlab function $\frac{beta(p+20,q)}{beta(p,q)}$ (the first case) and $\frac{beta(p_1+5,q_1)beta(p_2+2,q_2)}{beta(p_1,q_1)beta(p_2,q_2)}$ (the second case) are taken as the reference solutions to which results from our solver are compared. The errors with respect to the reference solutions are defined as

$$E_{N_c}(p,q) = \frac{|\widetilde{g}_{N_c}(p,q) - \widetilde{g}_{ref}(p,q)|}{\widetilde{g}_{ref}(p,q)}, \tag{4.48}$$

$$E_N(p_1,q_1,p_2,q_2) = \frac{|\widetilde{g}_N(p_1,q_1,p_2,q_2) - \widetilde{g}_{ref}(p_1,q_1,p_2,q_2)|}{\widetilde{g}_{ref}(p_1,q_1,p_2,q_2)}. \tag{4.49}$$

Figure 4.1 represents the evolution of $E_{N_c}(p,q)$ and $E_N(p_1,q_1,p_2,q_2)$ for the polynomial functions C^{20} and Z^5C^2 as functions of N_z and N_c. A second order convergence is observed for the different shape parameters in the first test and the first order of convergence in the second $2D$ test.

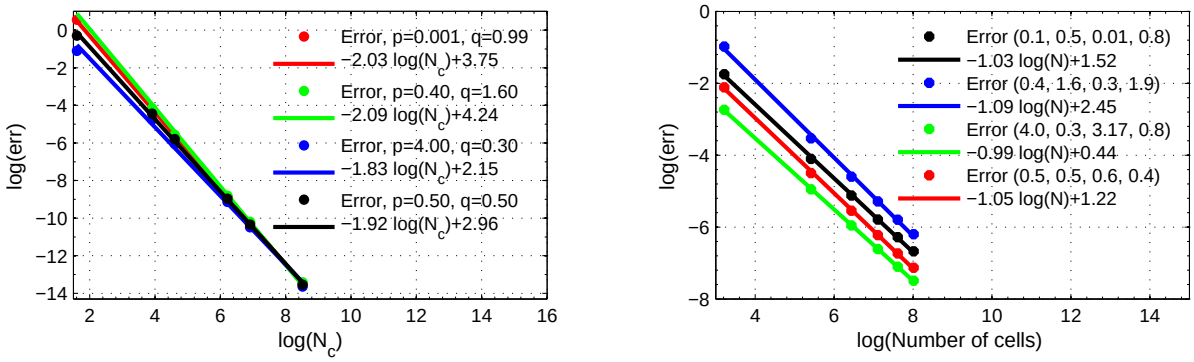

Figure 4.1: Logarithmic spatial convergence of the semi-analytical method of the integration with the β-PDF. Left: convergence rate for $g(C) = C^{20}$, right: convergence rate for $g(Z,C) = Z^5C^2$. The vector of 4 numbers corresponds to (p_1, q_1, p_2, q_2).

Figure 4.2 illustrates production rates and mass fractions of CO_2 obtained from the PFTC β-PDF table of the premixed flame CH_4/O_2, $\widetilde{Z} = 0.0455$, $\widetilde{Z''^2} = 0$, which is constructed with the described piecewise integration method. The integration of PFTC table was done over C and Z.

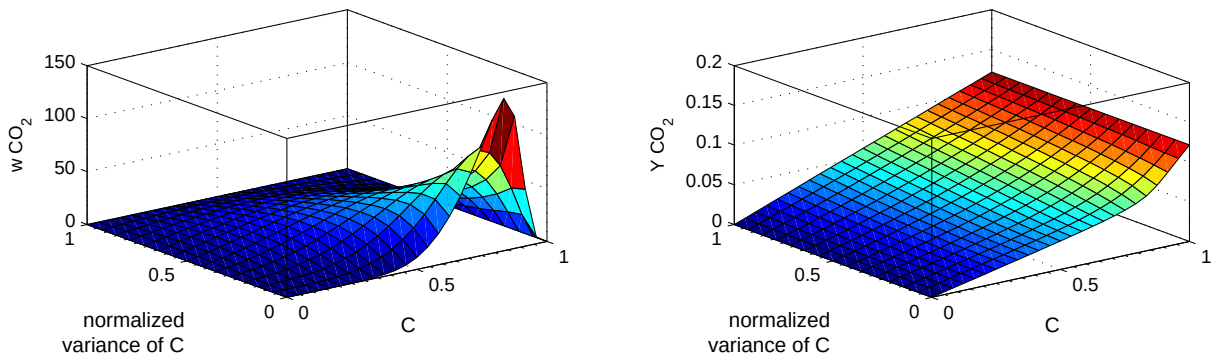

Figure 4.2: Production rate (left) and mass fraction (right) of CO_2; obtained from PFTC β-PDF table of the premixed flame CH_4/O_2, $\widetilde{Z} = 0.0455$, $\widetilde{Z''^2} = 0$, $N_c = 25$, $N_{VarC} = 15$

Chapter 5

Transported partially stirred reactor (TPaSR) model

EPaSR model was developed by V. Sabelnikov and C. Fureby and presented in section 2.6.2. The summarized equations are given by eqs. (2.123) to (2.125), where the composition space is defined in (2.119). The main idea of the EPaSR as well as the PaSR models is that at high turbulent Reynolds numbers the most of the molecular mixing, chemical reactions, and heat release take place in the fine structure regions. The fine-structure regions, embedded in a surrounding fluid, are not uniformly distributed but concentrated in small isolated regions, whose volume is a small fraction of the total volume. The advantage of the EPaSR model compared with the PaSR model that it takes into account the whole history of the fluid particles arriving to the cell. We adapt the original EPaSR model to CEDRE software platform, naming it by TPaSR model.

5.1 Original EPaSR model

Let us consider a subsonic reactive flow, when acoustic instability is absent. In this case the temporal variation of the mean pressure can be neglected:

$$\frac{\partial \overline{P}}{\partial t} \approx 0. \tag{5.1}$$

We assume also that all mean molecular $\overline{D}_k$ and turbulent D_k^t diffusion coefficients for species $k = 1, .., N_{sp}$ are equal to each other, i.e.

$$D = \overline{D}_k = \frac{\overline{\mu}}{Sc_k \overline{\rho}}, \qquad D^t = D_k^t = \frac{\mu_t}{Sc_k^t \overline{\rho}},\ k = 1, .., N_{sp}. \tag{5.2}$$

$\overline{\mu}$ is the mean viscosity, μ_t is the turbulent viscosity, Sc_k is the Schmidt number of species k. The turbulent number of Schmidt is equal to the turbulent number of Prandtl

$$Sc_t = Pr_t. \tag{5.3}$$

In the framework of the RANS using the Boussinesq hypothesis, (5.1), (5.2) and (5.3), eq. (2.123) of the EPaSR model for the variables of the mean composition space $\widetilde{\psi} = [\widetilde{\boldsymbol{Y}}, \widetilde{h}_s]$

are

$$\frac{\partial}{\partial t}\left(\overline{\rho}\widetilde{Y_k}\right)+\frac{\partial}{\partial x_j}\left(\overline{\rho}\widetilde{u_j}\widetilde{Y_k}\right)=\frac{\partial}{\partial x_j}\left[\overline{\rho}\left(D+D^t\right)\frac{\partial\widetilde{Y_k}}{\partial x_j}\right]+\gamma^*\overline{\dot{\omega}}_k^*\left(\boldsymbol{Y^*},T^*\right),\ k=1,..,N_{sp}. \quad (5.4)$$

$$\frac{\partial}{\partial t}\left(\overline{\rho}\widetilde{h_s}\right)+\frac{\partial}{\partial x_j}\left(\overline{\rho}\widetilde{u_j}\widetilde{h_s}\right)=\frac{\partial}{\partial x_j}\left[\left(\overline{\lambda}\frac{\partial\widetilde{T}}{\partial x_j}+\overline{\rho}D^t\frac{\partial\widetilde{h_s}}{\partial x_j}+\overline{\rho}D\sum_{k=1}^{N_{sp}}\widetilde{h}_{s,k}\frac{\partial\widetilde{Y_k}}{\partial x_j}\right)\right]$$
$$+\left[\overline{\tau}_{ij}\frac{\partial\widetilde{u_i}}{\partial x_j}+\frac{\partial\overline{P}}{\partial x_j}\widetilde{u}_j-\sum_{k=1}^{N_{sp}}\overline{\dot{\omega}}_k\left(\widetilde{\boldsymbol{Y}},\widetilde{T}\right)h_{k,f}^{\theta}\right]. \quad (5.5)$$

Here $\widetilde{h}_{s,k}$ is the sensible enthalpy of species k, $h_{f,k}^{\theta}$ are the species formation enthalpy, $\boldsymbol{\tau}$ is the viscous stress tensor, $\overline{\lambda}$ is the heat diffusion coefficient, $\overline{\dot{\omega}}_k$ is the mean reaction rate of species k.

Equation (2.124) of the EPaSR model for the variables of the composition space in the fine-structure regions are following. The equation for the mass fraction Y_k^* is

$$\frac{\partial}{\partial t}\left(\overline{\rho}\gamma^*Y_k^*\right)+\frac{\partial}{\partial x_j}\left(\overline{\rho}\widetilde{u_j}\gamma^*Y_k^*\right)=\frac{\partial}{\partial x_j}\left[\gamma^*\overline{\rho}\left(D+D^t\right)\frac{\partial\widetilde{Y_k}}{\partial x_j}\right]+\overline{M}_k^*+\gamma^*\overline{\dot{\omega}}_k^*\left(\boldsymbol{Y^*},T^*\right),\ k=1,..,N_{sp}. \quad (5.6)$$

The equation for the sensible enthalpy h_s^* reads

$$\frac{\partial}{\partial t}\left(\overline{\rho}\gamma^*h_s^*\right)+\frac{\partial}{\partial x_j}\left(\overline{\rho}\widetilde{u_j}\gamma^*h_s^*\right)=\frac{\partial}{\partial x_j}\left[\gamma^*\left(\overline{\lambda}\frac{\partial\widetilde{T}}{\partial x_j}+\overline{\rho}D^t\frac{\partial\widetilde{h_s}}{\partial x_j}+\overline{\rho}D\sum_{k=1}^{N_{sp}}\widetilde{h}_{s,k}\frac{\partial\widetilde{Y_k}}{\partial x_j}\right)\right]+\overline{M}_{N_{sp+1}}^*$$
$$+\gamma^*\left[\overline{\tau}_{ij}\frac{\partial\widetilde{u_i}}{\partial x_j}+\frac{\partial\overline{P}}{\partial x_j}\widetilde{u}_j-\sum_{k=1}^{N_{sp}}\overline{\dot{\omega}}_k\left(\widetilde{\boldsymbol{Y}},\widetilde{T}\right)h_{k,f}^{\theta}\right]. \quad (5.7)$$

$\overline{M}_k^*$ is the exchange terms at the immaterial interface between the fine-structure volume and the surrounding fluid defined in (2.128).

5.2 TPaSR model: EPaSR adaptation to CEDRE

The structure of CEDRE does not allow implementing directly the eqs. (5.5) to (5.7) for the Favre-averaged sensible enthalpy and variables of the fine-structure regions and therefore requires for the original EPaSR model to be modified. We will denominate this modified EPaSR model by the TPaSR model.

In CEDRE the conservative quantities: mass fractions $\overline{\rho}\widetilde{\boldsymbol{Y}}$, momentum $\overline{\rho}\widetilde{\boldsymbol{u}}$, total energy $\overline{\rho}\widetilde{e_t}$ and scalars $\overline{\rho}\boldsymbol{z}=(\overline{\rho}k,\overline{\rho}\omega,\overline{\rho}z_1,...,\overline{\rho}z_{n_z})$ in RANS (or $\overline{\rho}\boldsymbol{z}=(\overline{\rho}z_1,...,\overline{\rho}z_{n_z})$ in LES) satisfy transport equations described in section 2.4.2 (see eqs. (2.55) to (2.57)). The evolution equation for additional scalars $\overline{\rho}z_m$, $m=1,..,n_z$ with assumptions above is the following:

$$\frac{\partial}{\partial t}\left(\overline{\rho}z_m\right)+\frac{\partial}{\partial x_j}\left(\overline{\rho}\widetilde{u_j}z_m\right)=\frac{\partial}{\partial x_j}\left[\overline{\rho}\left(D+D^t\right)\frac{\partial}{\partial x_j}\left(z_m\right)\right]+\overline{\rho}S_{z_m},\ j=1,..,3,\ m=1,..,n_z, \quad (5.8)$$

where $\overline{\rho} S_{z_m}$ is a source for m-th scalar z_m.

Consequently, we can define the mean composition space as

$$\widetilde{\boldsymbol{\psi}} = [\widetilde{\boldsymbol{Y}}, \widetilde{e}_t]. \tag{5.9}$$

Equation (5.4) is the same in the TPaSR model. Instead of eq. (5.5) for the Favre-averaged sensible enthalpy the transport eq. (2.57) for the Favre-averaged total energy is used. Both equations are equivalent.

As we can see from the evolution equation (5.8), there is no possibility to transport $\overline{\rho}\gamma^* e_t^*$, because the exact equation for the conservative variable $\overline{\rho}\gamma^* e_t^*$ should contain the mean pressure $\overline{P}$ in the flux. As a result, the composition space in the fine-structure regions is given by

$$\boldsymbol{\psi}^* = [\boldsymbol{Y}^*, h_t^*], \tag{5.10}$$

where h_t^* is a total enthalpy. The Favre-averaged total enthalpy $\widetilde{h}_t$ can be calculated from the Favre-averaged total energy $\widetilde{e}_t$ by the formula

$$\widetilde{h}_t = \widetilde{e}_t + \frac{\overline{P}}{\overline{\rho}}. \tag{5.11}$$

The first terms on the RHS of the eqs. (5.6) and (5.7) consisting of the species, enthalpy and heat fluxes for the mean quantity is replaced by the fluxes for the quantities in the fine-structure regions multiplied by γ^*. In eq. (5.7) the term

$$\gamma^* \overline{\tau}_{ij} \frac{\partial \widetilde{u}_i}{\partial x_j}, \tag{5.12}$$

which represents the heating associated with the friction of particles against each other, is neglected in the RANS. Thus, the new equation for the mass fraction $\boldsymbol{Y}^*$ in the fine-structure regions reads

$$\frac{\partial}{\partial t}\left(\overline{\rho}\gamma^* Y_k^*\right) + \frac{\partial}{\partial x_j}\left(\overline{\rho}\widetilde{u}_j \gamma^* Y_k^*\right) = \frac{\partial}{\partial x_j}\left[\overline{\rho}\left(D + D^t\right)\frac{\partial}{\partial x_j}\left(\gamma^* Y_k^*\right)\right] + \overline{M}_k^* + \gamma^* \overline{\dot{\omega}}_k^*,\ k = 1, .., N_{sp} \tag{5.13}$$

and the new equation for the total enthalpy h_t^* becomes

$$\frac{\partial}{\partial t}\left(\overline{\rho}\gamma^* h_t^*\right) + \frac{\partial}{\partial x_j}\left(\overline{\rho}\widetilde{u}_j \gamma^* h_t^*\right) = \frac{\partial}{\partial x_j}\left[\overline{\rho}\left(D + D^t\right)\frac{\partial}{\partial x_j}\left(\gamma^* h_t^*\right)\right] + \overline{M}_{h_t}^*,\ j = 1, .., 3. \tag{5.14}$$

Let us rewrite the exchange terms given in 2.128 for the variables $\boldsymbol{Y^*}$ and h_t^*. The exchange terms at the immaterial interface between the fine-structure volume and the surrounding fluid are calculated as follows:

$$\overline{\boldsymbol{M}}^* = \overline{\boldsymbol{\Theta}}^* + \overline{\boldsymbol{\Omega}}^*. \tag{5.15}$$

The first term $\overline{\boldsymbol{\Theta}}$ is

$$\overline{\Theta}_k^* = \frac{1}{2}\left(\dot{m} + |\dot{m}|\right) Y_k^0 + \frac{1}{2}\left(\dot{m} - |\dot{m}|\right) Y_k^*,\ k = 1, .., N_{sp}, \tag{5.16}$$

and

$$\overline{\Theta}^*_{N_{sp}+1} = \frac{1}{2}\left(\dot{m} + |\dot{m}|\right) h_t^0 + \frac{1}{2}\left(\dot{m} - |\dot{m}|\right) h_t^* \tag{5.17}$$

for the total enthalpy. The expression for $\dot{m}$ is given by (2.131). Supposing that $1-\gamma^*$ is strictly positive, the mass fractions Y_k^0 and the total enthalpy h_t^0 in a surrounding fluid can be calculated as

$$Y_k^0 = \frac{\widetilde{Y}_k - \gamma^* Y_k^*}{1-\gamma^*}, \qquad h_t^0 = \frac{\widetilde{h}_t - \gamma^* h_t^*}{1-\gamma^*}, \tag{5.18}$$

where $\widetilde{h}_t$ is given by eq. (5.11). If $\gamma^* = 1$ or $\gamma^* = 0$, we impose

$$Y_k^0 = Y_k^* = \widetilde{Y}_k, \qquad h_t^0 = h_t^* = \widetilde{h}_t. \tag{5.19}$$

The second term $\overline{\mathbf{\Omega}}^*$ in the framework of the LES approach is

$$\overline{\Omega}_k^* = -\overline{\rho}\frac{\gamma^*}{\tau^*}\left(Y_k^* - Y_k^0\right), \qquad \overline{\Omega}^*_{N_{sp}+1} = -\overline{\rho}\frac{\gamma^*}{\tau^*}\left(h_t^* - h_t^0\right). \tag{5.20}$$

It coincides with the definition (2.130) proposed by V. Sabelnikov and C. Fureby in [SabelnikovFureby2013]. In the RANS approach $\overline{\mathbf{\Omega}}^*$ was modified.

$$\overline{\Omega}_k^* = -\overline{\rho} C_\omega \omega \left(Y_k^* - Y_k^0\right), \qquad \overline{\Omega}^*_{N_{sp}+1} = -\overline{\rho} C_\omega \omega \left(h_t^* - h_t^0\right). \tag{5.21}$$

The constant C_ω is set to 10.5. The comparison of eq. (2.130) and eq. (5.21) shows that the last expression does not include γ^*. In fact, when the same definition of $\overline{\mathbf{\Omega}}^*$ that in the LES/EPaSR model is used for the RANS/TPaSR model, there is insufficient exchange between a cold gas and a hot gas in the case of premixed flames. Based on works of Magnussen [MagnussenHjertager1977], V. Sabelnikov has proposed to modify and adapt $\overline{\mathbf{\Omega}}^*$ to the RANS modeling.

Instead of solving the transport eq. (2.125) for the volume fraction γ^* of the fine structures and $N_{sp}-1$ eq. (5.4) for the mass fractions Y_k^*, we solve N_{sp} eq. (5.4) and find γ^* from the relation

$$\gamma^* = \sum_{k=1}^{N_{sp}} \gamma^* Y_k^*, \tag{5.22}$$

because the sum of the mass fractions Y_k^* in the fine-structure regions are equal to one.

There are several possibilities to model the fine structure residence time τ^* in the framework of the RANS approach. The first choice represents the geometrical mean of the Kolmogorov time and the integral time scale.

$$\tau^* = \sqrt{\tau_K \tau_t}. \tag{5.23}$$

The second choice is

$$\tau^* = C\tau_K, \tag{5.24}$$

where C is a free constant. If $C=1$, (5.24) is the Kolmogorov time and if $C=0.41$, it is the Magnussen time. In the LES model the subgrid residence time τ^* is defined as in eq. (2.132).

Chapter 6

Backward-facing step flow

In this thesis, the configuration of the backward-facing step, presented in figs. 6.2 and 6.3, is chosen to validate premixed flamelet tabulated chemistry (PFTC) with presumed β-PDF and TPaSR approaches against the experimental data [MagreMoreau1988] which was carried out at ONERA. The backward-facing step configuration is a widespread mean to stabilize the combustion at high velocities and is generally used to evaluate the performance of turbulence models in the prediction of separated flows.

This configuration is interesting for several reasons:

1. Simple $2D$ geometry allows performing many calculations in a reasonable time. This property is particularly relevant in the context of model validation, where many tests are necessary. In particular, the turbulent flow is bi-dimensional.

2. The existence of experimental measurements in both nonreactive and reactive flows. In addition, this flow was extensively studied numerically in the past. There are many databases that can be used for validation of results. For instance, numerous investigations with different approaches were carried out on this topic at ONERA. R. Courtois calculated a turbulent combustion on this configuration with a LES approach [Courtois2005]. B. Sainte-Rose improved the results of R. Courtois using a hybrid RANS/LES (DDES) model [SainteRose2010]. Hereafter, O. Soulard and M. Ourliac investigated reactive flow with a hybrid RANS/EMC solver, which was based on solving stochastic partial differential equations statistically equivalent to the joint turbulent scalars PDF equation [Soulard2005; Ourliac2009]. We will discuss and compare their results with our simulations in this chapter.

3. The extensive study on the backward-facing step is due to the fact that it gives rise to a large number of distinctly different flow patterns, including boundary layers, mixing layer, separation layer, reattachment, flow reversal.

This chapter deals with two- and three-dimensional simulations of backward-facing step flows and provides results obtained by numerical computations for nonreactive and reactive cases. We analyze numerical results comparing them with the experimental data and results

of previous numerical simulations at ONERA.

6.1 A3C experimental setup

The combustion chamber used in [MagreMoreau1988] was mounted on the A3C test bench. Its geometry is shown in fig. 6.1. The channel incorporates a backward-facing step of 0.1 m width, playing a flame holder role. The channel upstream of the step has a length of 1.5 m and a height of 6.5 cm. Downstream the step a larger channel of length 1.4 m and a height of 0.1 m is located. Burnt gases are evacuated at outlet of this tunnel. The sonic nozzles are installed at inlet and outlet of the main chamber in order to better control mass flow rate and acoustics and enable experiments in a pressurized regime. The level of turbulence is controlled by a honeycomb placed in the upstream pipe. Worthwhile characteristic of the device is the high level of turbulence in the flow, even without combustion.

Air preheated to 520 K passes through a long duct upstream of the step. The methane is injected at about 1 m upstream of the step. Then, it mixes with high temperature air from clean air heater. Finally, air/methane mixture is injected in the chamber entrance. The equivalence air-fuel ratio can vary in the range $[0.8; 1]$, but usually the ratio of 1:0.8 is used. The injected velocity of the gas is typically around 50 m/s. The level of velocity fluctuations measured at 0.15 m upstream of the step is 11 % of the flow velocity in the case of the honeycomb (in general, velocity fluctuations of $4\,\mathrm{m/s} - 8\,\mathrm{m/s}$ are observed).

The experimental studies consisted in shadowgraphic visualizations and wall pressure measurements followed by gas sampling and analysis by chromatography in order to find the mean concentration profile inside the flame. The velocity profile and turbulence level was also studied in detail by laser Doppler anemometry. The measurement of the temperature profiles was made also by means of a pneumatic probe and emission absorption spectroscopy. A program of measurements by CARS (coherent anti-stokes Raman spectroscopy) led to measurements of the fluctuating temperature.

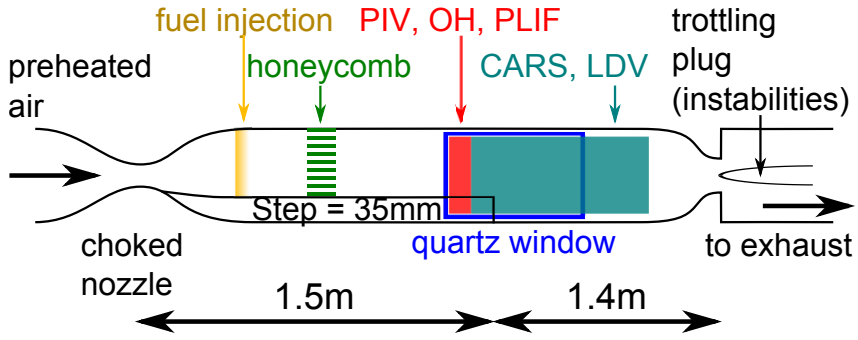

Figure 6.1: Scheme of A3C test bench along with optimal diagnostics

6.2 RANS nonreactive backward-facing step flow calculation

6.2.1 Computational domain and grid

The configuration is a backward-facing step (figs. 6.2 and 6.3). Given the size the rig A3C, the computational domain consists only in the combustion chamber. Indeed, the simulation of entire experimental domain would be computationally expensive and at the same time unnecessary to describe the physical phenomena of interest. As shown in fig. 6.2, the physical domain is $L_x = 1.1\,\mathrm{m}$ horizontally and $H = 0.1\,\mathrm{m}$ vertically. The height of the step, placed at the lower wall, is $h = 0.035\,\mathrm{m}$ and its extremity is located at 0.1 m inside the computational domain. Positions will hereafter be given using the step extremity as the origin. Figure 6.3 represents the main parts of the considered flow. In particular, the experimentally predicted characteristic size of the recirculation zone is found to be $4.3h$ in nonreactive flow [MoreauLabbe1985]. The streamwise position of the reattachment point is denoted by X_r.

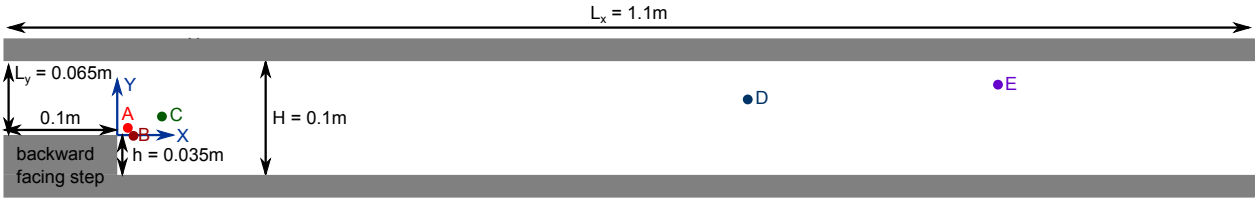

Figure 6.2: Backward-facing step dimensions (the aspect ratio is preserved in this figure) and sensor point locations for convergence studies

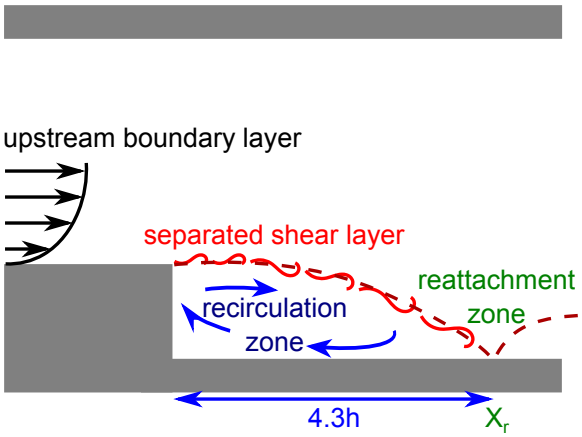

Figure 6.3: Principal features of a backward step flow

Figure 6.4 shows a close-up view of the step extremity of a 2D grid. The grid is refined in the X and Y directions at the corner of the step and in the recirculation region. It is made of 36956 rectangular cells.

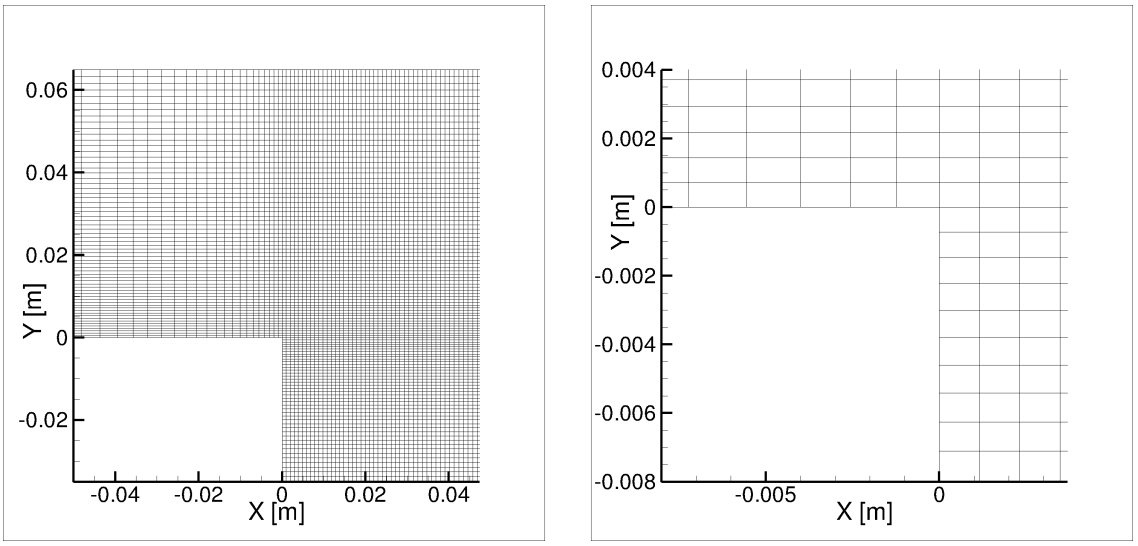

Figure 6.4: 2D grid for backward-facing step flow

6.2.2 Physical models

For nonreactive backward-facing step flow calculations, we consider $k-l$ and $k-\omega$ RANS turbulence models. Boussinesq viscosity model (BVM) or explicit algebraic Reynolds stress model (EARSM) is used. Turbulent Prandtl and Schmidt numbers are constant: $Pr_t = Sc_t = 0.9$. The used wall law allows recovering a skin friction of attached boundary layer. The thermal conductivity is modeled with the Eucken law. The mixture viscosity is calculated from the average of viscosities of species (obtained with the Sutherland law). The Schmidt numbers for all species are constants and equal to unity. (Detailed model description can be found in CEDRE documentation [ChevalierCourbet2005]).

6.2.3 Boundary conditions

- **Inlet:**
  A methane/air mixture ($\widetilde{Y}_{\mathrm{CH_4}} = 0.0446557$, $\widetilde{Y}_{\mathrm{N_2}} = 0.7326543$, $\widetilde{Y}_{\mathrm{O_2}} = 0.22269$) is injected at $\widetilde{T} = 525\,\mathrm{K}$ with a equivalent ration being equal to 0.8 (therefore, the mean mixture fraction $\widetilde{Z} \approx 0.0446$ is constant).
  There are two types of inlet conditions for the velocity $\widetilde{u}_x$, the turbulent energy k and the turbulent length scale l:
  - **Homogeneous profiles:** The inflow velocity is $\widetilde{u}_x = 58\,\mathrm{m/s}$. The inlet values of the turbulent quantities are $k = 60\,\mathrm{m^2/s^2}$ and $l = 0.01\,\mathrm{m}$.
  - **Nonhomogeneous profiles:** Figure 6.5 shows vertical profiles of the Favre-averaged streamwise velocity $\widetilde{u}_x$, the RMS velocity fluctuations $\sqrt{2/3k}$ normalized by a maximal value of $\widetilde{u}_x$ and the turbulent length scale l normalized by L_y at inlet of the backward step. These profiles were obtained after numerical simulation of a 2D channel of height $L_y = 0.065\,\mathrm{m}$, and length $L_x^{ch} = 30L_y = 1.95\,\mathrm{m}$. The grid was uniform, consisting of 89401 cells, each of them has a size of $6.5\,\mathrm{mm} \times 0.2\,\mathrm{mm}$.

The calculation of this channel was performed with inlet velocity $\widetilde{u}_x = 53\,\mathrm{m/s}$, which yielded maximum outlet velocity of approximately 58 m/s.

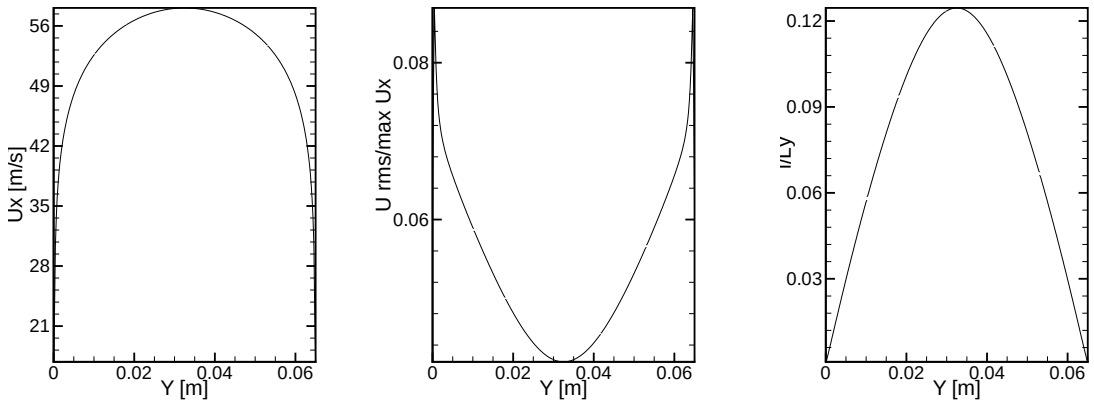

Figure 6.5: Vertical profiles of Favre-averaged streamwise velocity $\widetilde{u}_x$ (left), $\frac{\sqrt{2/3k}}{\max(\widetilde{u}_x)}$ (center) and $\frac{l}{L_y}$ (right) at the inlet of A3C chamber

- **Outlet:**
  At outlet, the pressure is set to $\overline{P} = 1\,\mathrm{bar}$.
- **Walls:**
  During numerical simulation the walls are assumed to be adiabatic. In the A3C experiment, the walls are cooled by water, but the wall temperature was not measured. Assumption of adiabatic walls overestimates the temperature near walls in case of reactive flow.

In the outlet and inlet sections reflecting boundary conditions are applied.

6.2.4 Numerical methods

The backward Euler temporal integration scheme along with the second order monotonic upstream scheme for conservation laws (MUSCL) scheme in space are applied. The time step is fixed to $\Delta t = 1 \times 10^{-4}\,\mathrm{s}$.

6.2.5 Computational strategy

The current version of CEDRE enables grid parallelization by dynamically dividing physical domain based on the number of available processors. Therefore, the physical domain was divided into 72 or 128 parts distributed on 72 or 128 Nehalem nodes consisting of two 2.80 GHz quad-core processors. 30 minutes were sufficient to obtain a converged solution in nonreactive case.

There are three main tools that are used in CEDRE to determine whether reasonable convergence is achieved within a RANS simulation.

- Mass and energy flow balances

- Residual behavior
- Mean values integrated over a computational domain; maximum, minimum values

Mass and energy flow balances

Mass and energy flow balances should give a low discrepancy between the positive and negative sums. The force balance considered to be achieved if this discrepancy is lower than 0.1%. For example, for the converged solution obtained with a $k-l$ (BVM) model with nonhomogeneous inlet profiles the inlet of mass flow is equal to the outlet of mass flow at the order 10^{-5}. Figure 6.6 shows the level of fluctuations of the mass flow at inlet and outlet, which is defined as the difference between mass flow at inlet and mass flow at outlet divided by mass flow at inlet. We recall that the residence time in the chamber is

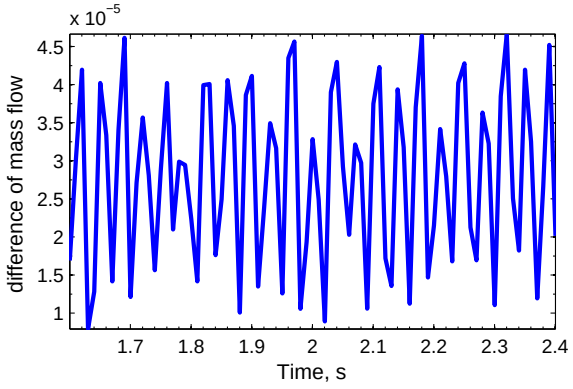

Figure 6.6: Discrepancy between the positive and negative sums of mass flow during 40 characteristic time in A3C chamber (converged solution); $k-l$ (BVM) model with nonhomogeneous inlet profiles

$$\tau = \frac{L_x}{\widetilde{u}_x} \approx 0.019\,\mathrm{s}. \tag{6.1}$$

Residual behavior

The residuals of the calculated quantities $\boldsymbol{Q}$ should decrease by some amount from the initial value. They reach a certain value and then remain almost constant for longer computational time, oscillating about this value with small amplitude. There are many definitions of residual of the quantity Q such as maximum, mean or global residuals. The criterion requires in general that the normalized unscaled residuals drop by three orders of magnitude (drop to 10^{-3}).

Mean values integrated over a computational domain; maximum, minimum values

From some point of computational time mean values of all the transported quantities integrated over the computational domain should be constant in time in the sense that their fluctuations are negligible compared to the maximal value of the mean considered quantities. Figure 6.7 demonstrates the error $Error(\overline{P})$ and $Error(\widetilde{T})$ for the converged solution obtained by the $k-l$ (BVM) model with nonhomogeneous inlet conditions. The

error of the quantity Q integrated over the computational domain is defined as

$$Error(Q) = \frac{\left| \frac{1}{Vol} \int\limits_{Vol} Q d\boldsymbol{x} - \max\limits_{time} \left| \frac{1}{Vol} \int\limits_{Vol} Q d\boldsymbol{x} \right| \right|}{\max\limits_{time} \left| \frac{1}{Vol} \int\limits_{Vol} Q d\boldsymbol{x} \right|}. \tag{6.2}$$

One can see that the fluctuations of $Error(\overline{P})$ and $Error(\widetilde{T})$ are on the order of 10^{-6}. Let us denote

$$Diff(\overline{P}) = \frac{\max\limits_{time,\boldsymbol{x}} \overline{P} - \min\limits_{time,\boldsymbol{x}} \overline{P}}{\max\limits_{time,\boldsymbol{x}} \overline{P}}, \tag{6.3}$$

where $\max\limits_{time,\boldsymbol{x}} \overline{P}$ is a maximum pressure and $\min\limits_{time,\boldsymbol{x}} \overline{P}$ is a minimum pressure in the chamber from some point of computational time. It is found that $Diff(\overline{P}) \approx 10^{-3}$. Normalized fluctuations of the mean pressure $Error(\overline{P}) \approx 10^{-6}$ are negligible in comparison with the normalized difference between the maximum and minimum pressure $Diff(\overline{P}) \approx 10^{-3}$. These quantities have the same behavior during about 40τ. It means that the solution is converged.

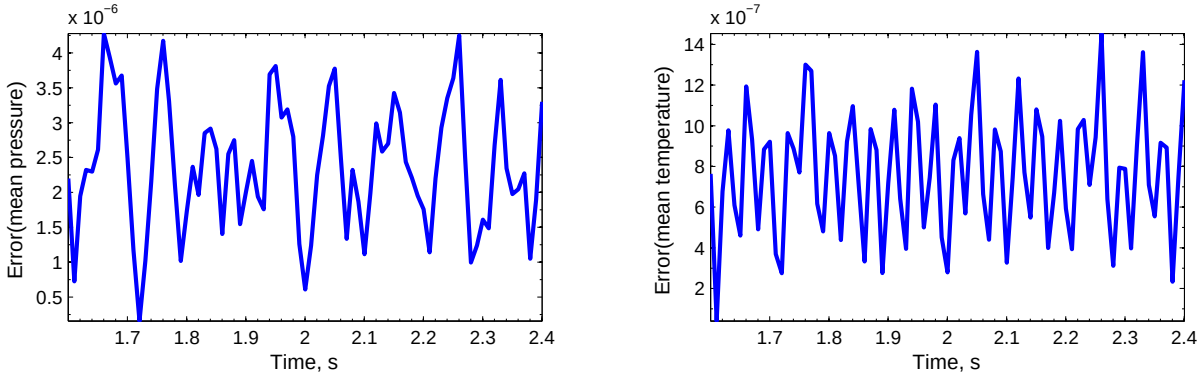

Figure 6.7: Errors of mean pressure $\overline{P}$ (left) and Favre-averaged temperature $\widetilde{T}$ (right) integrated over the computational domain of converged solution during 40 characteristic time in A3C chamber. $k-l$ (BVM) model with the nonhomogeneous inlet profiles

Maximum and minimum quantities are constant in the same sense that in previous criterion of convergence.

Quantities $\overline{P}$, $\widetilde{u}_x$, $\widetilde{u}_y$, $\widetilde{T}$, k and l integrated over the computational domain remain constant in time at five points placed in the chamber at coordinates represented in table 6.1 in the sense that their fluctuations can be neglected compared to the maximum value of considered quantity. The same criterion is used for maximum and minimum values.

Point	X	Y	Z	X/h	Y/h	Z/h in RANS	Z/h in LES
A	0.005	0.02	0.035	0.14	0.57	0	1
B	0.01	-0.005	0.035	0.29	-0.14	0	1
C	0.035	0.012	0.035	1	0.34	0	1
D	0.55	0.027	0.035	15.7	0.77	0	1
E	0.77	0.04	0.035	22	1.14	0	1

Table 6.1: Position of sensor points in backward-facing step flow. Schematic distribution of these points is given in fig. 6.2.

6.2.6 Results

The main interest of this calculation is an initialization of fields for the backward-facing step reactive flow and a validation of turbulence models.

Recirculation region

The study of $k-\varepsilon$ (BVM) turbulence model was performed in [Ourliac2009]. During his work M. Ourliac showed that in the given homogeneous boundary conditions cited in the previous subsection, the $k-\varepsilon$ model underestimated the recirculation region, i.e. a fresh gas and a burnt gas were too rapidly mixed. Therefore, we consider in this work only $k-l$ and $k-\omega$ turbulence models. As we can see in fig. 6.8 the numerical results are significantly different depending on the turbulence model. A slight separation of the boundary layer occurs at the upper wall (fig. 6.8). The transverse velocity $\widetilde{u}_y$ is low throughout the flow, except in the recirculation region where it is the same order of magnitude that the longitudinal velocity $\widetilde{u}_x$.

A region of recirculating flow is clearly visible in all simulations (see fig. 6.8) No secondary vortex is captured with the $k-l$ and $k-\omega$ turbulence models on the opposite side wall of the step. It is known that the recirculation region is important for the flame stabilization. However, the influence of the secondary recirculation region on the flame stabilization is minor, so it is not necessary to further refine the grid for the RANS simulation in order to properly capture this effect.

The table 6.2 summarizes the comparison of the ratio between the mean reattachment length and the size of the step X_r/h. The exact determination of X_r is difficult due to fuzzy character of the eddy edge. The error of estimation of X_r is about $\pm 0.2h$. The mean experimental reattachment length is 4.3 [MoreauLabbe1985]. One can notice that independently on inlet boundary conditions considered in section 6.2.3 the mean reattachment length is in a better agreement with the experiment for the $k-l$ turbulence model. In this case, the relative error of the numerical results with the experimental value is 12.3%, which is significantly lower than other errors obtained with the $k-\omega$ turbulence models. Note that in all the RANS simulations discussed here the reattachment length X_r is overestimated. We recall that $X_r/h = 7.8$ in the PhD work of B. Saint-Rose (RANS, $k-\omega$ (BVM) model with nonhomogeneous inlet profiles) [SainteRose2010].
The analysis of the recirculation region length shows that the fresh and burnt gas intermix slowly, especially in the case of the $k-\omega$ model where the error exceeds 32%. As the flame

	$k-l$ (BVM)	$k-\omega$ (BVM)	$k-\omega$ (EARSM)	Exp
X_r/h	4.83	6.34	5.77	4.3
Error	12.3%	47.4%	31.86%	–

Table 6.2: Mean reattachment location X_r in nonreactive backward-facing step flow rescaled by the step height h. The last column shows the relative error of the numerical results with respect to the experimental value.

angle decreases with increasing X_r, it will be underestimated by the $k-\omega$ model in the reactive flow.

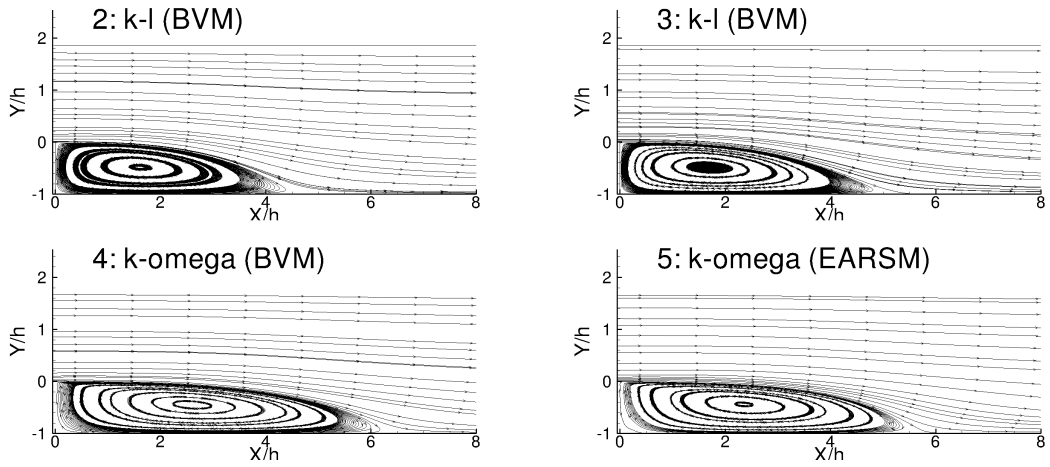

Figure 6.8: Recirculation regions in nonreactive backward-facing step flow; 2: $k-l$ (BVM) model with homogeneous inlet profiles, 3: $k-l$ (BVM) model with nonhomogeneous inlet profiles, 4: $k-\omega$ (BVM) model with homogeneous inlet profiles, 5: $k-\omega$ (EARSM) model with homogeneous inlet profiles

Favre-averaged velocity

Vertical profiles of the Favre-averaged streamwise and transverse velocities are compared with experimental data in figs. 6.9 and 6.10. According to the reference frame introduced in fig. 6.2, X denotes the distance from the step extremity. The solutions obtained with the $k-\omega$ turbulence model using either BVM or EARSM almost coincide.

The comparison of mean streamwise velocity $\widetilde{u}_x$ shows a satisfactory agreement between the experimental and simulation data. Largest differences with the experimental measurements are observed in the lower part of the chamber ($Y < 0\,\mathrm{m}$). Nevertheless, in this part of the chamber the results of the $k-\omega$ turbulence model calculation are in good agreement with the experimental data when $X \leq 0.02\,\mathrm{m}$. The absolute value of the mean streamwise velocity $\widetilde{u}_x$ is overestimated by the $k-l$ turbulence model when $X < 0.1\,\mathrm{m}$. However, one should take into account that this area is difficult to cover experimentally because of a complicated

particle seeding. Near the inlet, the profiles of the longitudinal velocity $\widetilde{u}_x$ are overestimated in all the simulations where the homogeneous boundary conditions are applied.

In the upstream area, $\widetilde{u}_x$ is in good agreement with experimental measurements, in particular for the $k-l$ turbulence model with nonhomogeneous inlet conditions.

Unlike to $\widetilde{u}_x$, the profiles of transverse velocity $\widetilde{u}_y$ show very pronounced differences with the experimental data. When $X < 0.12\,\mathrm{m}$, the transverse velocity is largely overestimated by the $k-\omega$ turbulence model for $Y < 0\,\mathrm{m}$. The $k-l$ turbulence model seems to yield better agreement in the recirculation region except near the step extremity ($X \leq 0.02\,\mathrm{m}$, $Y < 0\,\mathrm{m}$). The absence of the secondary counter rotation vortex in the simulation can explain this difference. The fluid rises along the wall without undergoing inverse influence. For $Y \in [0.02\,\mathrm{m}; 0.06\,\mathrm{m}]$, the simulation predicts the flow deflected downwardly whereas experimentally the flow is directed upwards. In particular, there is an important gradient of the mean transverse velocity near the upper wall in the Y direction. The presence of such the gradient confirms the existence of a detachment of the boundary layer along the upper wall.

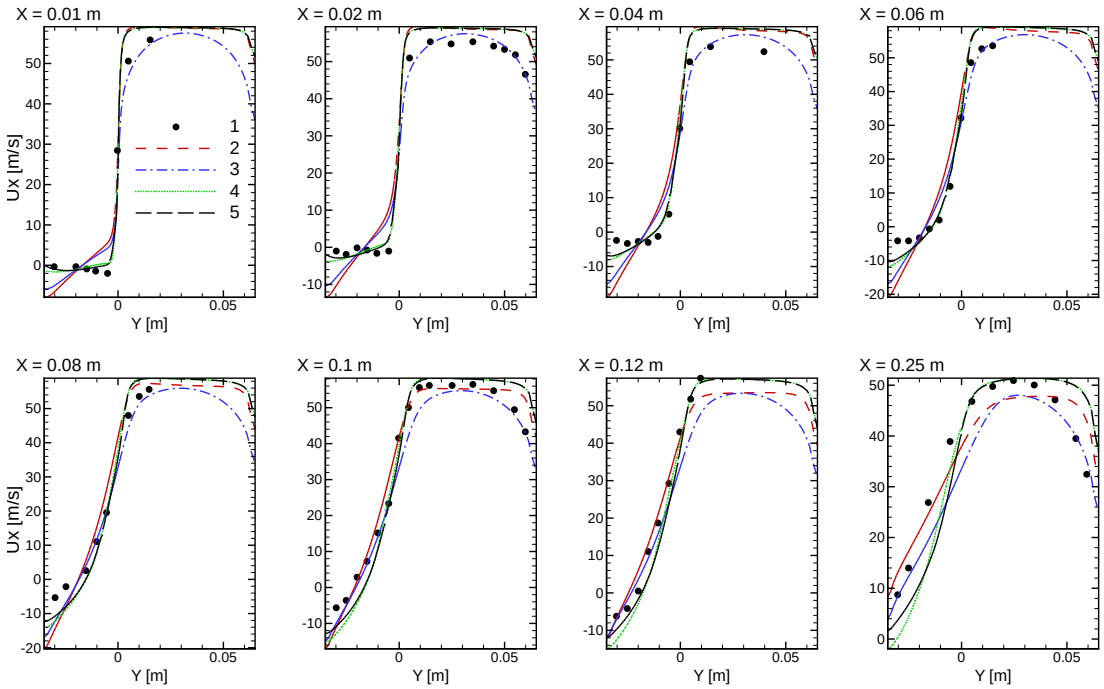

Figure 6.9: Vertical profiles of Favre-averaged streamwise velocity $\widetilde{u}_x$ in nonreactive backward-facing step flow; 1: experimental data, 2: $k-l$ (BVM) model with homogeneous inlet profiles, 3: $k-l$ (BVM) model with nonhomogeneous inlet profiles, 4: $k-\omega$ (BVM) model with homogeneous inlet profiles, 5: $k-\omega$ (EARSM) model with homogeneous inlet profiles

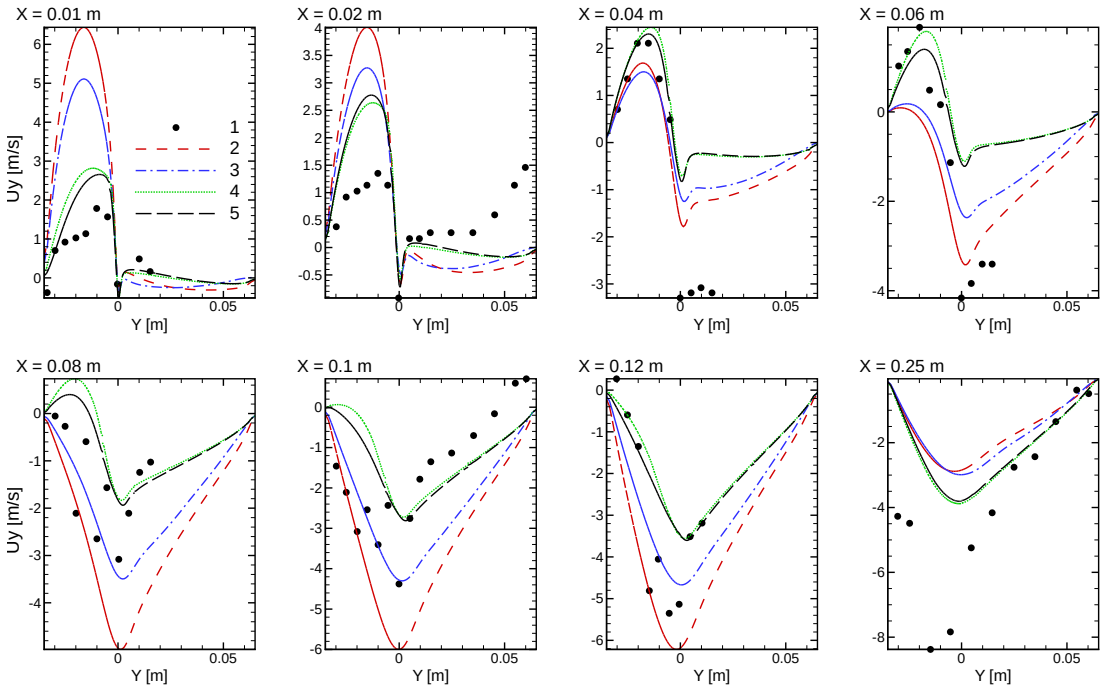

Figure 6.10: Vertical profiles of Favre-averaged transverse velocity $\widetilde{u}_y$ in nonreactive backward-facing step flow; 1: experimental data, 2: $k-l$ (BVM) model with homogeneous inlet profiles, 3: $k-l$ (BVM) model with nonhomogeneous inlet profiles, 4: $k-\omega$ (BVM) model with homogeneous inlet profiles, 5: $k-\omega$ (EARSM) model with homogeneous inlet profiles

RMS velocity fluctuations

Within the RANS approach we consider that the fluctuating velocity is isotropic. Each component is equal and calculated as

$$u_x^{RMS} = u_y^{RMS} = \sqrt{\frac{2}{3}k}. \tag{6.4}$$

Vertical profiles of RMS velocity fluctuations compared with experimental data are presented in figs. 6.11 and 6.12. u_x^{RMS} and u_y^{RMS} calculated by the $k-l$ turbulence model with nonhomogeneous initial conditions has good agreement with experimental RMS velocity fluctuations in the upper part of the chamber. u_x^{RMS} and u_y^{RMS} obtained with homogeneous inlet profiles independently on the turbulence model overestimate approximately twice the experimental velocity fluctuations for $X > 0\,\mathrm{m}$. Independently on the turbulence model and inlet profiles, numerical u_x^{RMS} and u_y^{RMS} overestimate the experimental velocity fluctuations in the lower part of the chamber ($X \leq 0\,\mathrm{m}$). Thus, for example, the maximal calculated value of u_y^{RMS} is approximately $12\,\mathrm{m/s}$, while it is $5\,\mathrm{m/s}$ in the experiment.

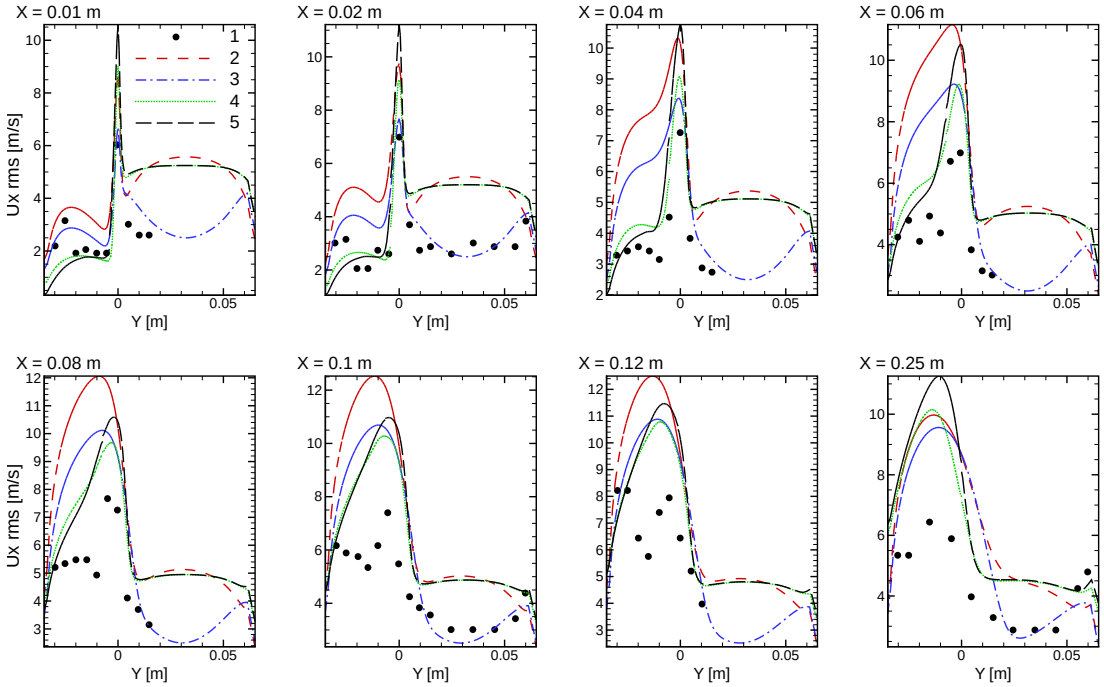

Figure 6.11: Vertical profiles of u_x^{RMS} in nonreactive backward-facing step flow; 1: experimental data, 2: $k-l$ (BVM) model with homogeneous inlet profiles, 3: $k-l$ (BVM) model with nonhomogeneous inlet profiles, 4: $k-\omega$ (BVM) model with homogeneous inlet profiles, 5: $k-\omega$ (EARSM) model with homogeneous inlet profiles

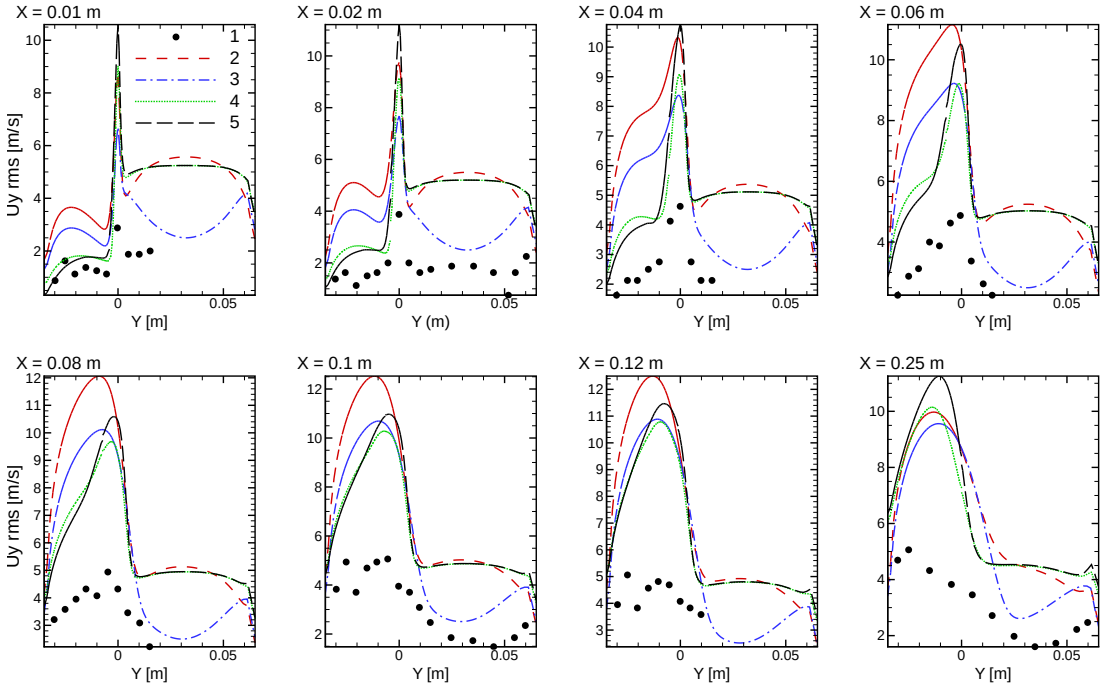

Figure 6.12: Vertical profiles of u_y^{RMS} in nonreactive backward-facing step flow; 1: experimental data, 2: $k-l$ (BVM) model with homogeneous inlet profiles, 3: $k-l$ (BVM) model with nonhomogeneous inlet profiles, 4: $k-\omega$ (BVM) model with homogeneous inlet profiles, 5: $k-\omega$ (EARSM) model with homogeneous inlet profiles

Turbulent frequency

The vertical profiles of turbulent frequency ω calculated with different turbulence models are plotted in fig. 6.13. Near the walls, the turbulent frequency calculated with the $k-\omega$ model is about 10 times greater than the turbulent frequency obtained with the $k-l$ approach. An important difference of ω takes place within 1 cm from the wall. Inside the chamber the turbulent frequency is similar for turbulence models. The high values of the turbulent frequency in the $k-\omega$ model imply that the equilibrium reacting fine-structure fraction γ^*_{eq} will be close to one in the RANS/TPaSR approach when reactive flow will be considered. It means that the behavior of the turbulent flame will be the same that in RANS/quasi-laminar approach.

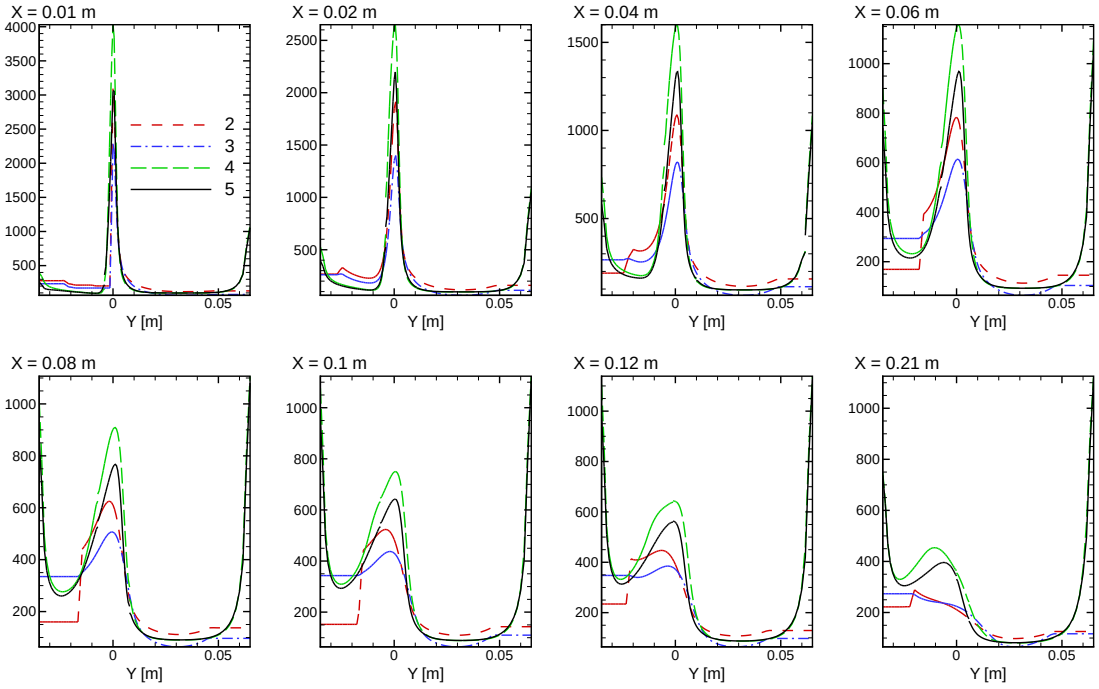

Figure 6.13: Vertical profiles of turbulent frequency ω [Hz] in nonreactive backward-facing step flow; 2: $k-l$ (BVM) model with homogeneous inlet profiles, 3: $k-l$ (BVM) model with nonhomogeneous inlet profiles, 4: $k-\omega$ (BVM) model with homogeneous inlet profiles, 5: $k-\omega$ (EARSM) model with homogeneous inlet profiles

6.2.7 Conclusions

The $k-l$ and $k-\omega$ turbulence models are used to simulate the nonreactive flow behind the backward-facing step. The Reynolds stress tensor is modeled either with the BVM or with the EARSM. The homogeneous and nonhomogeneous inlet profiles of the Favre-averaged streamwise velocity, the turbulent energy and the turbulent length scale are considered. Steady results are obtained and compared with the available experimental measurements.

It is found that the $k-l$ (BVM) turbulence model yields a more accurate estimation of the recirculation region length, than the $k-\omega$ turbulence model (BVM or EARSM). The

nonhomogeneous inlet profiles improve agreement between calculations and experimental profiles in the upper part of the chamber.

6.3 RANS reactive backward-facing step flow calculation

At $\widetilde{T} = 525\,\mathrm{K}$, the kinematic viscosity of the mixture is $4 \times 10^{-5}\,\mathrm{m}^2/\mathrm{s}$. It implies that the turbulent Reynolds number (2.22) is

$$Re_t = 5 \times 10^4 \tag{6.5}$$

and the Kolmogorov length scale (2.9) is

$$\eta_K = 0.1\,\mathrm{mm}. \tag{6.6}$$

In our conditions for reactive backward-facing step flow, the laminar flame speed is $S_L = 0.9\,\mathrm{m/s}$ and the flame thickness is $\delta_L = 5.483\,54 \times 10^{-4}\,\mathrm{m}$. From the chemical time scale of $\tau_{ch} = 6.092\,82 \times 10^{-4}\,\mathrm{s}$, we deduce that the turbulent Damkohler number (2.24) and the Karlovitz number (2.25) are

$$Da \approx 9.5, \qquad Ka \approx 30.069. \tag{6.7}$$

Consequently, one can conclude that this is a regime of thickened flame, where small eddies of the turbulence disturb the internal structure of the flame, causing its thickening.

6.3.1 Numerical setup

In reactive case, we use the same computational domain, grid, boundary conditions and physical models as in the calculation of nonreactive flow described above in section 6.2.2. The $k - l$ turbulence model with BVM is only considered.

The measurements of the temperature in [MagreMoreau1988] were done in a water-cooled combustion facility. Thus, in the experiment wall heat fluxes and the redistribution of the heat through metal walls by means of thermal diffusion took place. Since [MagreMoreau1988] does not contain a detailed description of temperature balance of walls being simultaneously cooled by water and heated by flame, during numerical simulation the walls are assumed to be adiabatic. These boundary conditions obviously correspond to a simplified representation of the experiment. As a consequence, the approximation of the adiabatic walls overestimates temperature at the lower wall and underestimates the temperature in the upstream part of upper wall (i.e. there no reaction takes place).

The physical domain was divided into 64 or 128 parts distributed on 64 or 128 Nehalem nodes consisting of two 2.80 GHz quad-core processors. 15 hours were sufficient to obtain a converged solution in reactive case, if the flame was lit and calculation started from a previous converged solution obtained by another model.

6.3.2 Combustion modeling

In the case of the RANS/quasi-laminar with reduced chemical mechanism (QL RCM) and the RANS/TPaSR model the methane combustion in air is modeled by a global two-step chemical reaction, which describes a complete combustion of methane, the resultant products being CO, CO_2 and H_2O [WestbrookDryer1981]:

$$CH_4 + 1.5O_2 \rightarrow 2H_2O + CO \qquad 0.5O_2 + CO \leftrightarrow CO_2 \tag{6.8}$$

The two-step reaction offers only an approximate description of methane oxidation and, in particular, overestimates the Favre-averaged temperature $\widetilde{T}$. The implementation of a detailed kinetic mechanism in a computational fluid dynamics (CFD) code is still prohibitive due to the high associated computational costs. In order to overcome this difficulty, the FTC approaches are also used:

- RANS/PFTC β-PDF
- RANS/PFTC without turbulence-chemistry interaction (noTCI)

These approaches allow accurate description of the main thermo-chemical phenomena with a relatively low computational cost of methane combustion modeling. It aims to describe the detailed chemistry by a reduced transported number of mass fractions in CEDRE such as: $\widetilde{Y}_{CH_4}$, $\widetilde{Y}_{O_2}$, $\widetilde{Y}_{N_2}$, $\widetilde{Y}_{CO}$, $\widetilde{Y}_{CO_2}$ and $\widetilde{Y}_{H_2O}$.

The quasi-laminar table is done with two entry parameters: mixture fraction $\widetilde{Z}$ and progress variable $\widetilde{C}$. In order to generate laminar premixed FTC table, one-dimensional laminar unstretched premixed flames are first solved in physical space, for different values of the mixture fraction. Then, the obtained solutions are stored in the FTC table, using index variables Z and C (considering that the variable C is evaluated from the species mass fractions). The Favre-averaged progress variable $\widetilde{C}$ is defined as

$$\widetilde{C} = \frac{\widetilde{Y}_{CO} + \widetilde{Y}_{CO_2}}{Y^{eq}_{CO} + Y^{eq}_{CO_2}}. \tag{6.9}$$

The quasi-laminar table containing 60 species has 200 points in $\widetilde{C}$ and 20 points in $\widetilde{Z}$ concentrated around $\widetilde{Z} = 0.0446$. β-PDF integration is performed. The turbulent table have the same size as quasi-laminar, but in addition it possess 25 points in the variance progress variable space $\widetilde{C''^2}$ uniformly distributed between 0 and $\widetilde{C}\left(1-\widetilde{C}\right)$.

In previous PhD works on related subjects at ONERA [Courtois2005; Soulard2005; Ourliac2009; SainteRose2010], the chemistry is taken into account only by one irreversible global methane-air reaction.

6.3.3 Results

The first idea was to validate PFTC β-PDF and TPaSR models performing calculations with the backward Euler and the second order Riemann invariants-based flow decentering operator (ODFI) spatial schemes. Unfortunately, only the PFTC noTCI model converges in this configuration. With other chemical mechanisms solutions do not converge, which

could be possibly explained by numerical acoustic waves generated by reflecting boundary conditions used at inlet and outlet of the computational domain.

The second step to achieve the convergence for other chemical models with the backward Euler scheme and the second order MUSCL scheme consists in attaching a box at the outlet boundary of the combustion chamber. Two different computational domains are presented in fig. 6.14. The mesh is refined in the combustion chamber ($X < 1\,\mathrm{m}$) as it is shown in fig. 6.4, while the cell size progressively increases at the outlet of the box. In the domain of the combustion chamber, the 2nd order spatial scheme was used and in the box the 1st order or the 2nd order spatial scheme was applied. The reattachment boundary condition was imposed between two domains in the case of using different orders of numerical spatial scheme . For the box presented in the right part of the left panel of fig. 6.14 we considered slip boundary conditions instead of adiabatic walls. For the right domain in fig. 6.14 the regular grid was used everywhere. On these configurations with the reflecting boundary conditions at inlet and outlet solutions calculated with chemical models described in section 6.3.2 did not converge due to traveling numerical waves in the channel. That was why we considered only the 1st order ODFI scheme in space.

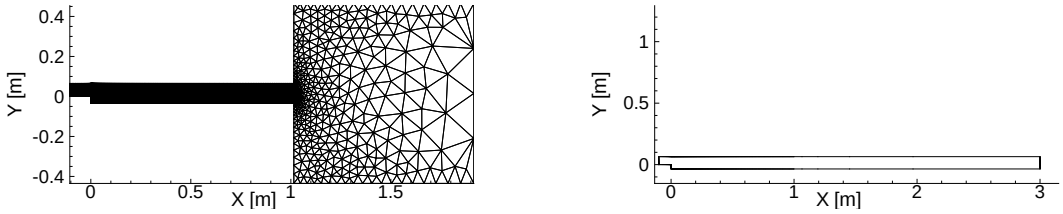

Figure 6.14: Two computational domains to evacuate acoustic waves; left: sudden enlargement, right: prolongation of domain

Quasi-laminar approaches

Table 6.3 presents some simulation details for quasi-laminar approaches.

	Method	Boundary condition	Time step Δt
PFTC noTCI	backward Euler with MUSCL scheme	nonhomogeneous	$3 \times 10^{-5}\,\mathrm{s}$
PFTC noTCI	RK2 with 1st order ODFI scheme	nonhomogeneous	$4 \times 10^{-7}\,\mathrm{s}$
QL RCM	RK2 with 1st order ODFI scheme	nonhomogeneous	$4 \times 10^{-7}\,\mathrm{s}$

Table 6.3: Considered test-cases for RANS/quasi-laminar models for reactive backward-facing step flow. Explicit second-order Runge Kutta method in time is denoted by RK2.

Favre-averaged temperature In fig. 6.15, isolines of $\widetilde{T} = 1500\,\mathrm{K}$ are displayed for three quasi-laminar computations and compared to the measurements. In the recirculation region ($0.1\,\mathrm{m} < X < 0.3\,\mathrm{m}$) the PFTC noTCI model gives satisfying value of the flame angle. In the main part of the combustion chamber ($0.3\,\mathrm{m} < X < 0.7\,\mathrm{m}$) the flame angle is overestimated, whereas it is underestimated near the upper wall. In the case of reduced chemistry, the flame angle is overestimated in the entire domain.

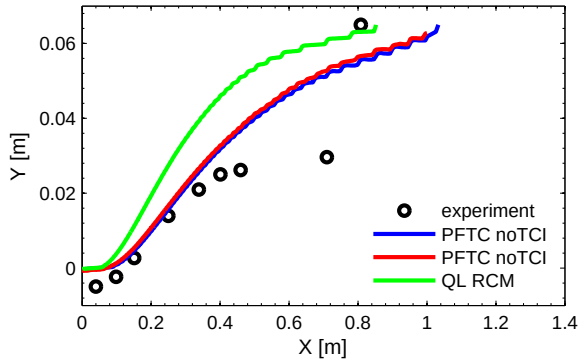

Figure 6.15: 1500 K temperature isolines in reactive backward-facing step flow; RANS/quasi-laminar approaches; blue curve: PFTC noTCI with 2nd order spatial scheme; red curve: PFTC noTCI with 1st order spatial scheme

Figure 6.16 shows the vertical temperature profiles of $\widetilde{T}$ calculated with quasi-laminar approaches: tabulated detailed chemistry and reduced chemistry as presented in table 6.3. They are compared with the experimental results obtained by [MagreMoreau1988]. In lower part of the chamber ($Y < 0\,\mathrm{m}$) for $X \leq 0.15\,\mathrm{m}$ of the chamber the numerical temperature is overestimated due to the adiabatic boundary conditions. For $X \geq 0.25\,\mathrm{m}$ the detailed chemical mechanism of methane/air combustion describes better the experiment than the global two-step chemical reaction. In the two cases it is necessary to take into account the turbulence-chemistry interaction in order to spread the temperature profiles. One can also note that the temperature profiles calculated with the 1st order ODFI scheme is close to the temperature profiles obtained with the MUSCL scheme of the second order.

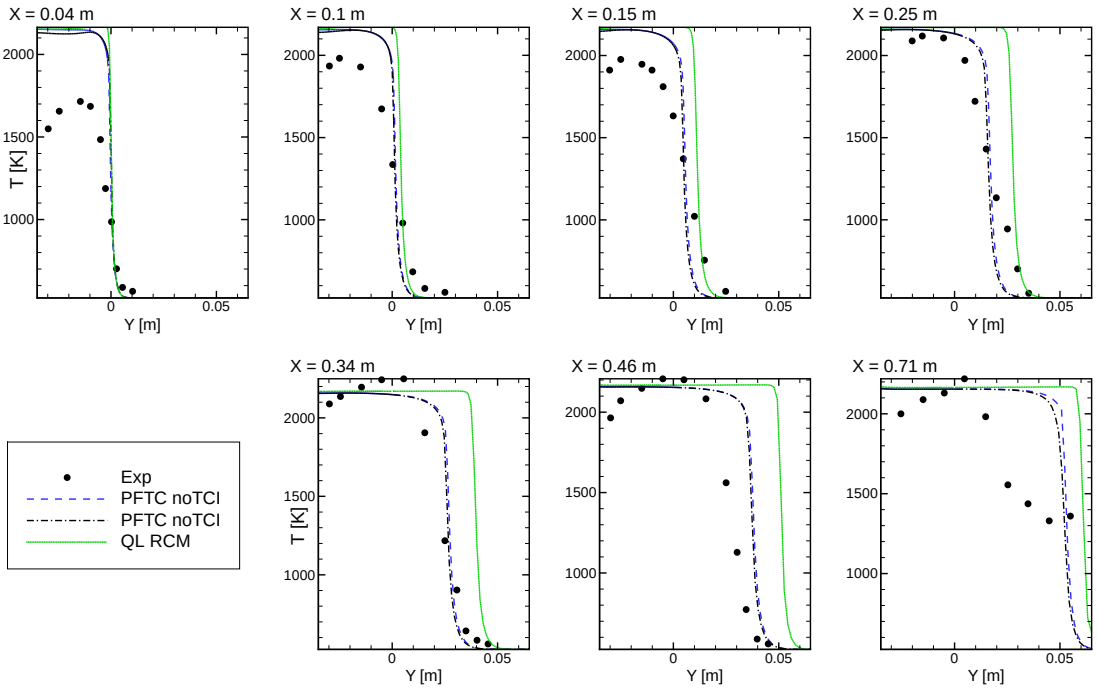

Figure 6.16: Vertical profiles of Favre-averaged temperature $\widetilde{T}$ in reactive backward-facing step flow; RANS/quasi-laminar approaches; blue curve: PFTC noTCI with 2nd order spatial scheme; black curve: PFTC noTCI with 1st order spatial scheme

Favre-averaged streamwise velocity The profiles of Favre-averaged streamwise velocity $\widetilde{u}_x$ are demonstrated in fig. 6.17. One can note that the use of the detailed chemistry clearly improves the results. The quasi-laminar approach with the reduced chemical mechanism overestimates the velocity, especially in the low part of the chamber, where it is almost two times greater than the experimentally observed velocity.

Favre-averaged transverse velocity Transverse velocity $\widetilde{u}_y$ is presented in fig. 6.18. As for streamwise velocity $\widetilde{u}_x$ the detailed chemistry improves the results in case of quasi-laminar model.

RMS velocity fluctuations The used $k-l$ turbulence model is based on isotropic velocity fluctuations. Each component of RMS velocity fluctuation is calculated as

$$u_x^{RMS} = u_y^{RMS} = \sqrt{\frac{2}{3}k}. \tag{6.10}$$

Figures 6.19 and 6.20 show the RMS values of velocity. They are underestimated for u_x^{RMS} and overestimated for u_y^{RMS}, whereas both of these quantities are overestimated in the nonreactive flow.

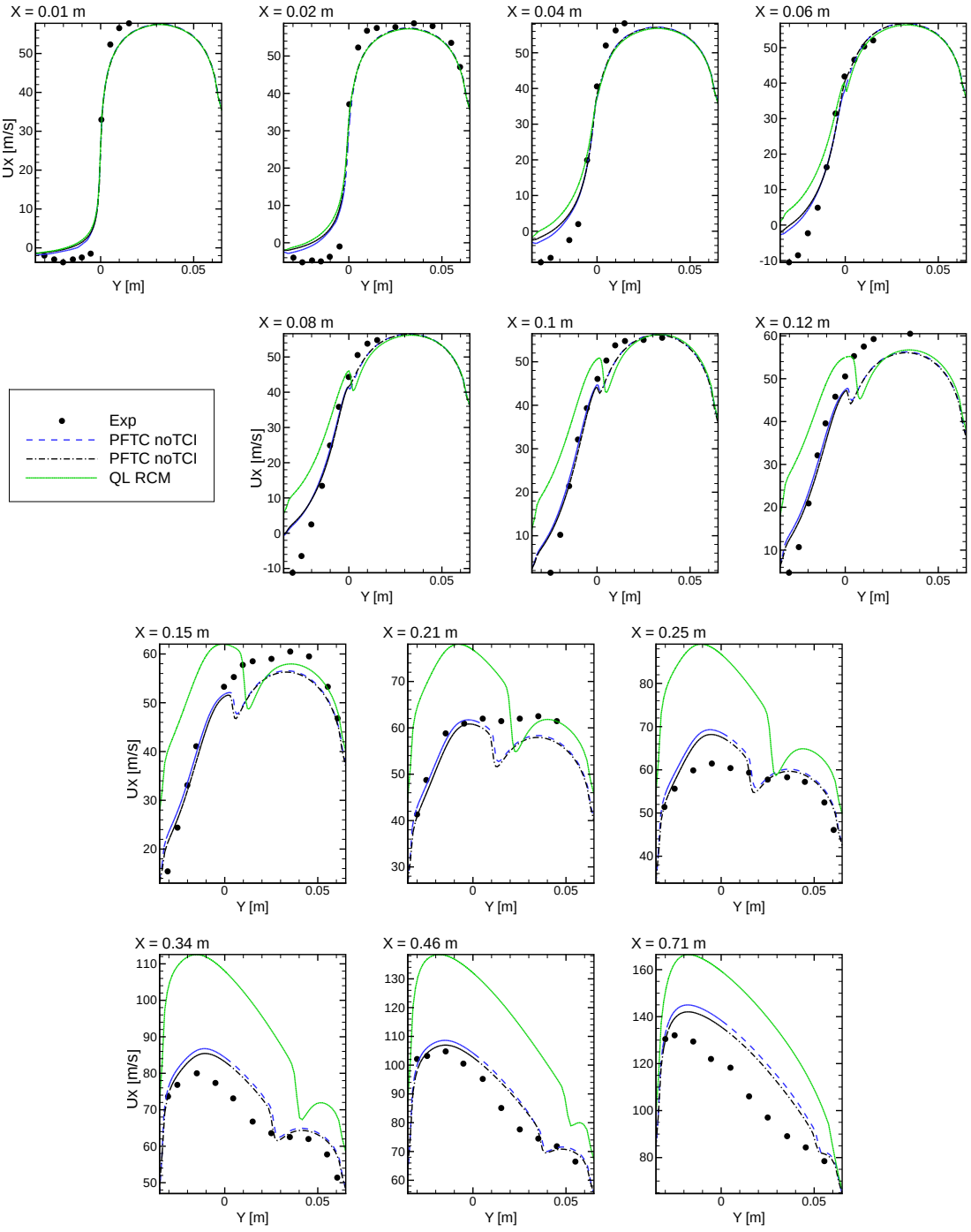

Figure 6.17: Vertical profiles of Favre-averaged streamwise velocity $\widetilde{u}_x$ in reactive backward-facing step flow; RANS/quasi-laminar approaches; blue curve: PFTC noTCI with 2nd order spatial scheme; black curve: PFTC noTCI with 1st order spatial scheme

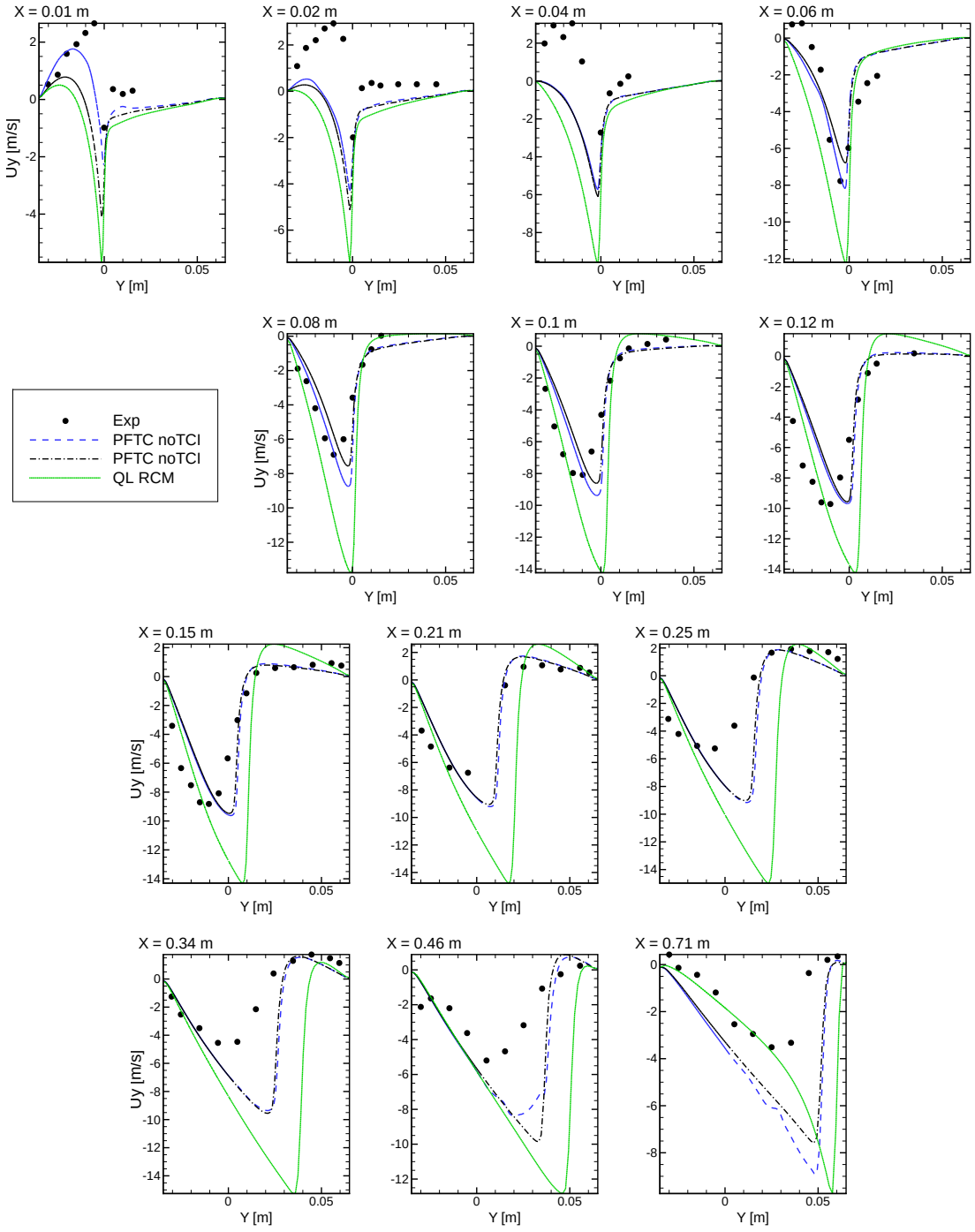

Figure 6.18: Vertical profiles of Favre-averaged transverse velocity $\widetilde{u}_y$ in reactive backward-facing step flow; RANS/quasi-laminar approaches; blue curve: PFTC noTCI with 2nd order spatial scheme; black curve: PFTC noTCI with 1st order spatial scheme

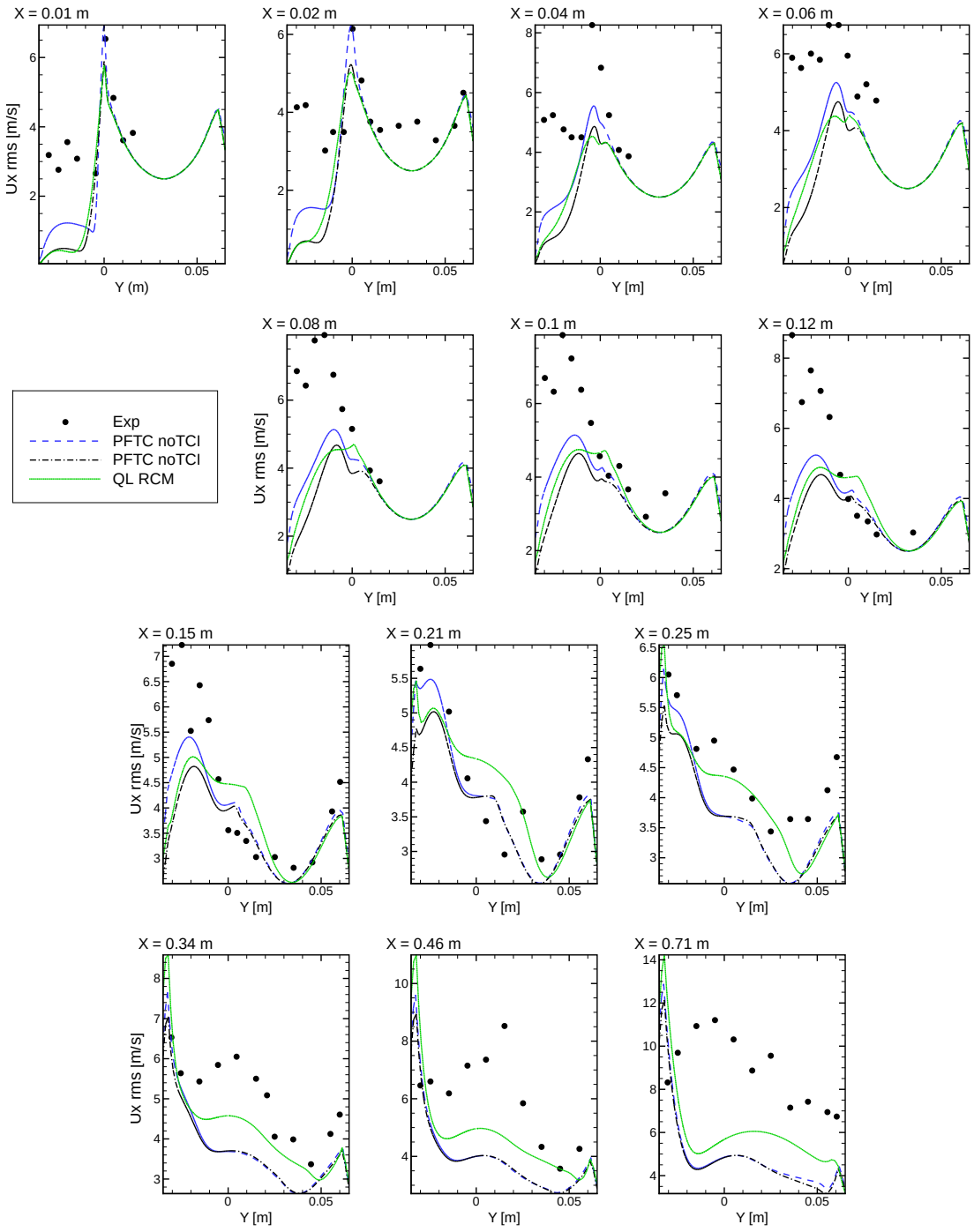

Figure 6.19: Vertical profiles of u_x^{RMS} in reactive backward-facing step flow; RANS/quasi-laminar approaches; blue curve: PFTC noTCI with 2nd order spatial scheme; black curve: PFTC noTCI with 1st order spatial scheme

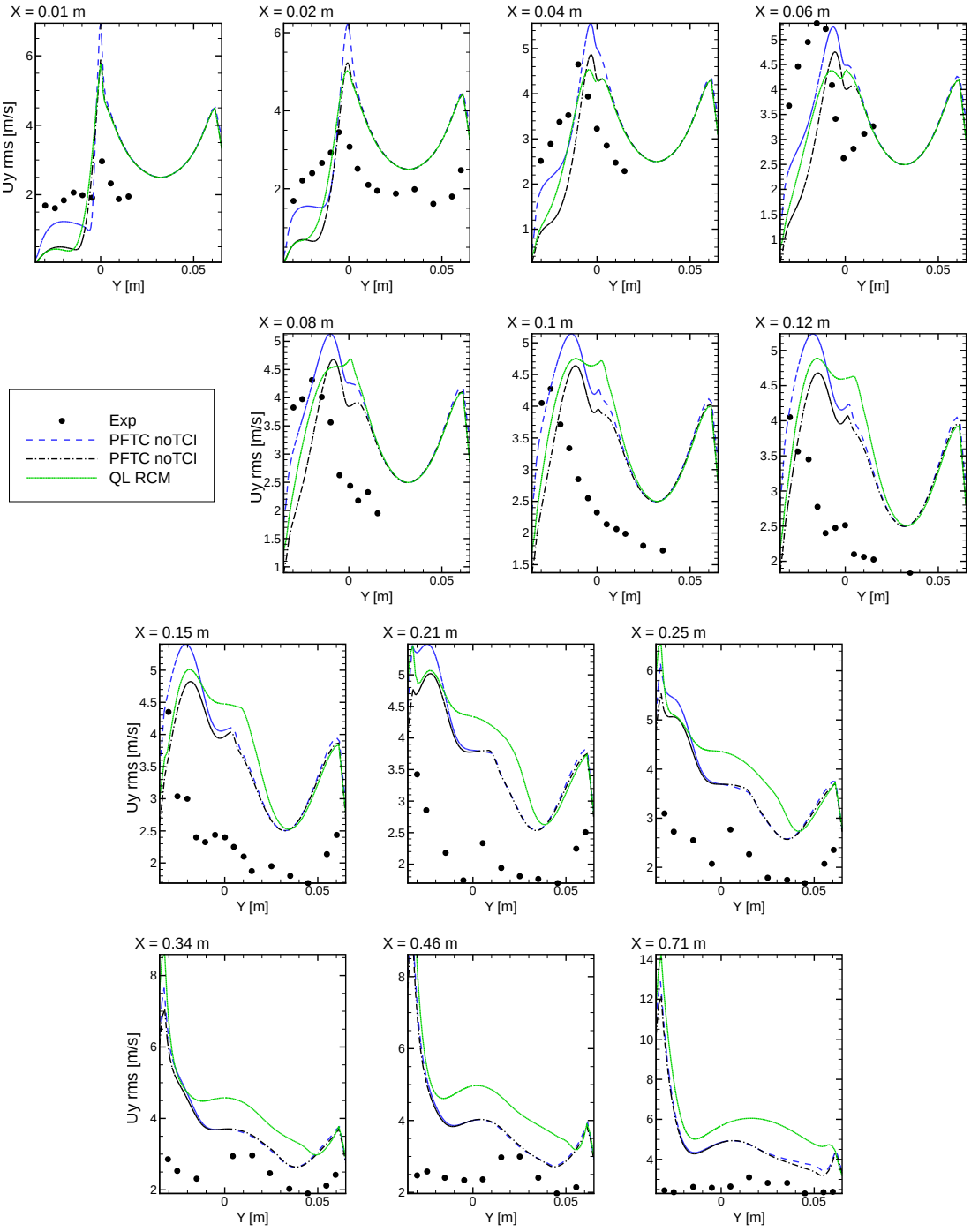

Figure 6.20: Vertical profiles of u_y^{RMS} in reactive backward-facing step flow; RANS/quasi-laminar approaches; blue curve: PFTC noTCI with 2nd order spatial scheme; black curve: PFTC noTCI with 1st order spatial scheme

PFTC β-PDF models

Table 6.4 represents different test-cases which we investigate for the PFTC β-PDF model, denoted as PFTC β-PDF $N_1 - N_2$. The first number N_1 signifies the model used for modeling of dissipation term in the transport equation of the Favre variance of progress variable $\widetilde{C''^2}$ (see table 4.2). The second number N_2 denotes the choice of modeling of source in the transport equation of $\widetilde{C''^2}$ (see table 4.1). The transport equation for $\widetilde{C''^2}$ is considered.

	Method	Boundary condition	Time step Δt
PFTC β-PDF 20-2	RK2 with 1st order ODFI sch.	nonhomogeneous	4×10^{-7} s
PFTC β-PDF 30-3	RK2 with 1st order ODFI sch.	nonhomogeneous	4×10^{-7} s
PFTC β-PDF 40-4	RK2 with 1st order ODFI sch.	nonhomogeneous	4×10^{-7} s
PFTC β-PDF 60-1	RK2 with 1st order ODFI sch.	nonhomogeneous	4×10^{-7} s
PFTC β-PDF 60-6	RK2 with 1st order ODFI sch.	nonhomogeneous	4×10^{-7} s
PFTC β-PDF 70-7	RK2 with 1st order ODFI sch.	nonhomogeneous	4×10^{-7} s
PFTC β-PDF 80-8	RK2 with 1st order ODFI sch.	nonhomogeneous	4×10^{-7} s
PFTC β-PDF 90-9	RK2 with 1st order ODFI sch.	nonhomogeneous	4×10^{-7} s

Table 6.4: Considered test-cases for RANS/PFTC β-PDF models in reactive backward-facing step flow

The models PFTC β-PDF 10-1 and PFTC β-PDF 10-2 are not presented, because the flame is narrowed in these cases.

Favre-averaged temperature Similarly to the quasi-laminar approach, the Favre-averaged temperature is overestimated within the PFTC β-PDF method at the lower wall due to simplified boundary conditions, see fig. 6.21. In the entire domain, all models except of the PFTC β-PDF 60-1 and 20-2 give similar profiles of Favre-averaged temperature. Both models remain in good agreement with the experimental data in comparison with other considered PFTC β-PDF models.

The temperature fields for two models: PFTC β-PDF 20-2 and 60-1 are presented in figs. 6.22 and 6.23. The option 20 corresponds to the ITNFS model for modeling of dissipation term in the transport equation of $\widetilde{C''^2}$. In the option 60 for modeling of dissipation term the wrinkling factor is approximated by constant of 5. ITNFS model (PFTC β-PDF 20-2) underestimates the values of temperature, while PFTC β-PDF 60-1 overestimates them. Close to the outlet boundary $X = 0.71\,\mathrm{m}$ $\widetilde{T}$ obtained with the ITNFS model follows the experimental data that is not the case for others models. In PFTC β-PDF 20-2 the temperature diffuses more than in PFTC β-PDF 60-1 model.

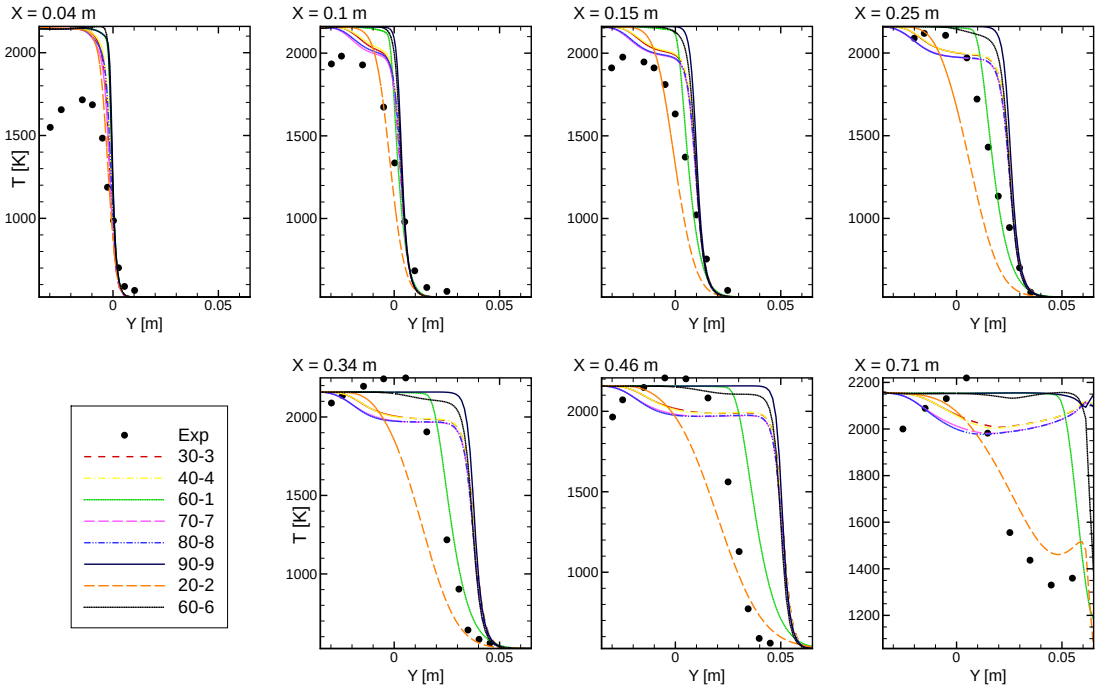

Figure 6.21: Vertical profiles of Favre-averaged temperature $\widetilde{T}$ in reactive backward-facing step flow; RANS/PFTC β-PDF

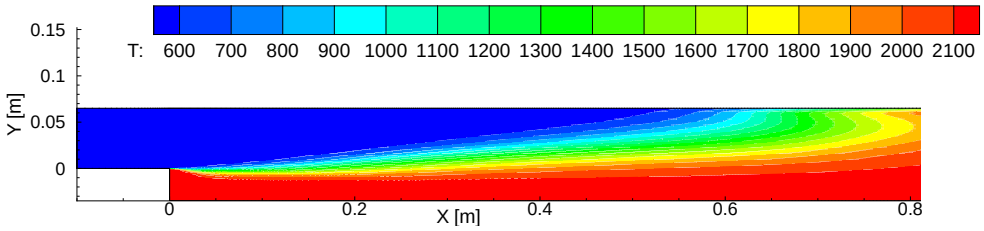

Figure 6.22: Field of Favre-averaged temperature $\widetilde{T}$ [K] in reactive backward-facing step flow; RANS/PFTC β-PDF 20-2

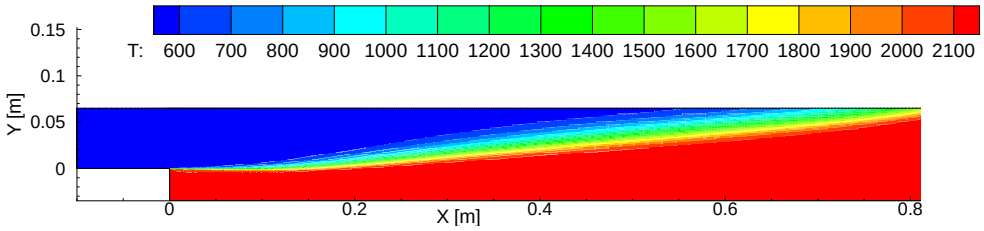

Figure 6.23: Field of Favre-averaged temperature $\widetilde{T}$ [K] in reactive backward-facing step flow; RANS/PFTC β-PDF 60-1

Favre variance of progress variable in PFTC β-PDF approach Figure 6.24 represents a comparison of vertical profiles of progress variable variances $\widetilde{C''^2}$ for four models: 20-2, 40-4, 60-1 and 80-8 at the same locations as the temperature profiles. The values of progress variable variance calculated with 40-4 and 80-8 models are similar (the difference between them is less than 20%).

Since the progress variable variance influences the temperature field, we can conclude that the maximum value of $\widetilde{C''^2} = 0.12$ is not sufficient to diffuse the flame near the isoline $\widetilde{T} = 1500\,\mathrm{K}$. The PFTC β-PDF 20-2 which underestimates the temperature has a peak at $\widetilde{C''^2} = 0.23$, while the PFTC β-PDF 60-1 model has a maximal peak at $\widetilde{C''^2} = 0.19$ for $X \leq 0.46\,\mathrm{m}$. As the experimental data for the temperature are located between two numerical profiles calculated with PFTC β-PDF 20-2 and PFTC β-PDF 60-1 models, we can conclude that the peaks of $\widetilde{C''^2}$ and its maximal values should be located between two profiles calculated with PFTC β-PDF 20-2 and PFTC β-PDF 60-1 models.

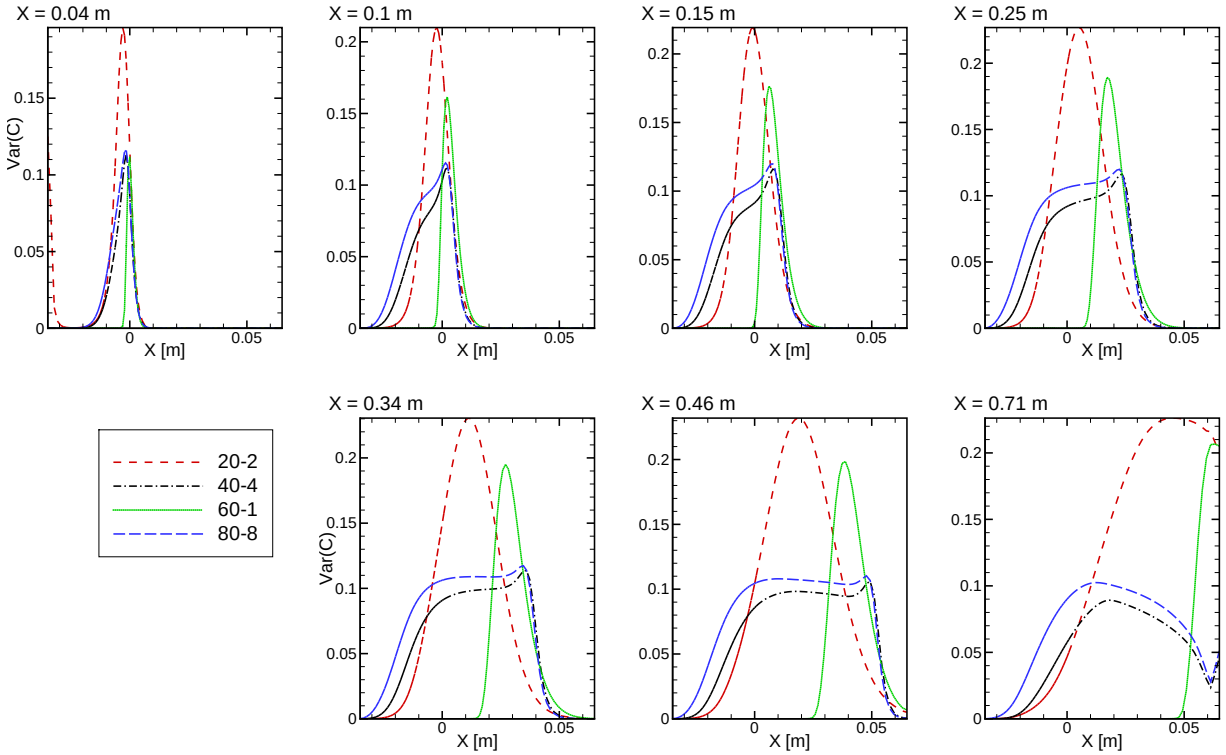

Figure 6.24: Vertical profiles of Favre variance of progress variable $\widetilde{C''^2}$ in reactive backward-facing step flow; RANS/PFTC β-PDF

Favre-averaged streamwise velocity The streamwise velocity $\widetilde{u}_x$ is shown in fig. 6.25. PFTC noTCI model approximates the profiles better than PFTC β-PDF series of models. Among PFTC β-PDF, the best results were obtained using PFTC β-PDF 20-2. All models in this series overestimate the Favre-averaged streamwise velocity, except PFTC β-PDF 20-2, which underestimates the velocity $\widetilde{u}_x$ for $X \geq 0.12\,\mathrm{m}$.

Favre-averaged transverse velocity The Favre-averaged transverse velocity $\widetilde{u}_y$ is presented in fig. 6.26. The PFTC β-PDF 20-2 model gives satisfying agreement of the numerical profiles of mean transverse velocity with the experimental data. For other PFTC β-PDF models, the absolute values of velocity are overestimated. PFTC β-PDF models improve the velocity values in comparison with PFTC noTCI approach near the lower part of the step nose region.

RMS velocity fluctuations The vertical profiles of RMS velocity fluctuations at different locations are shown in figs. 6.27 and 6.28. The main point of the comparison of these profiles with the experimental results is that nonhomogeneous inlet profiles allow decreasing fluctuations in the upper step nose region approximating better the experimental data. We also observe that the overestimation of u_x^{RMS} is compensated by the underestimation of u_y^{RMS}.

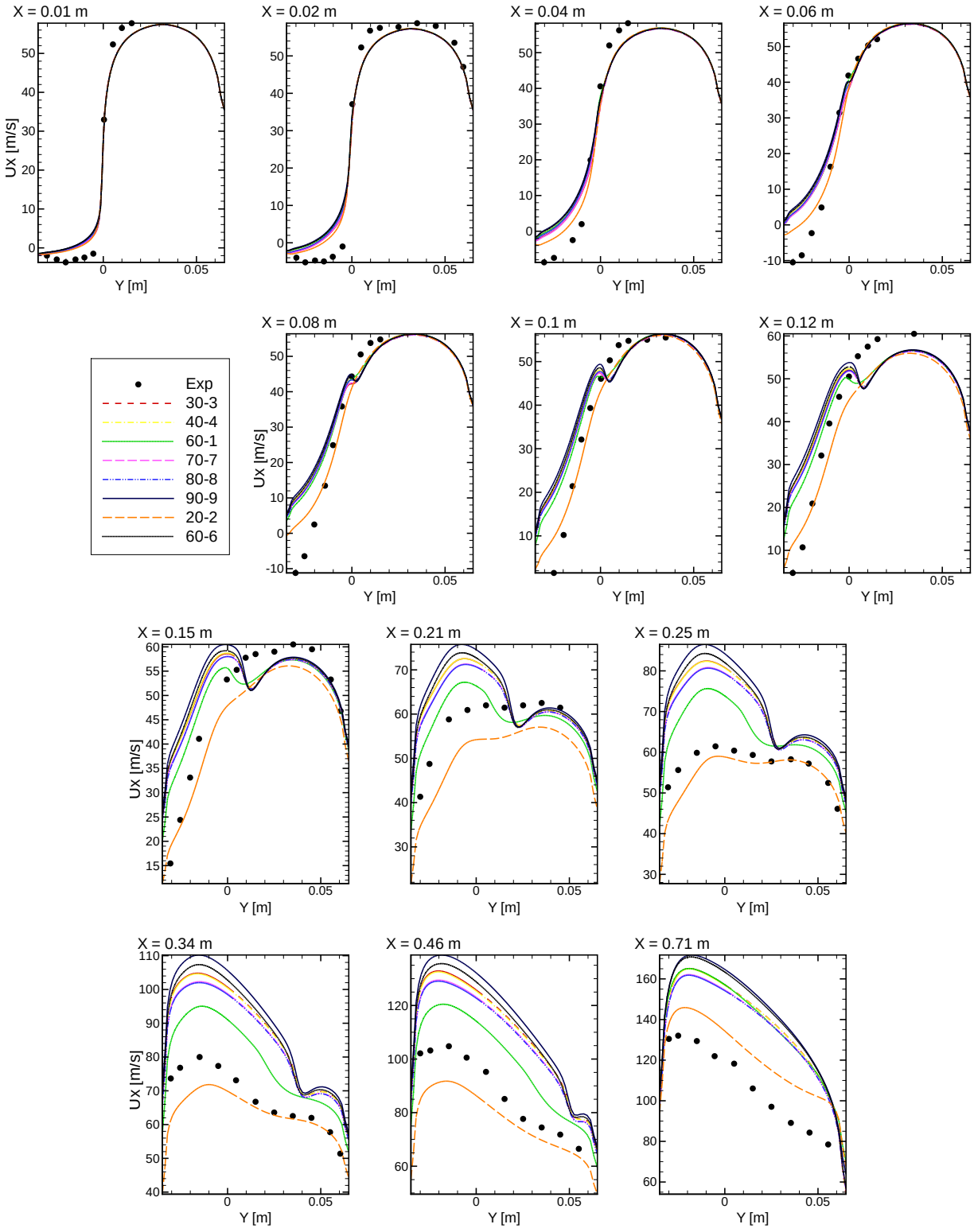

Figure 6.25: Vertical profiles of Favre-averaged streamwise velocity $\widetilde{u}_x$ in reactive backward-facing step flow; RANS/PFTC β-PDF

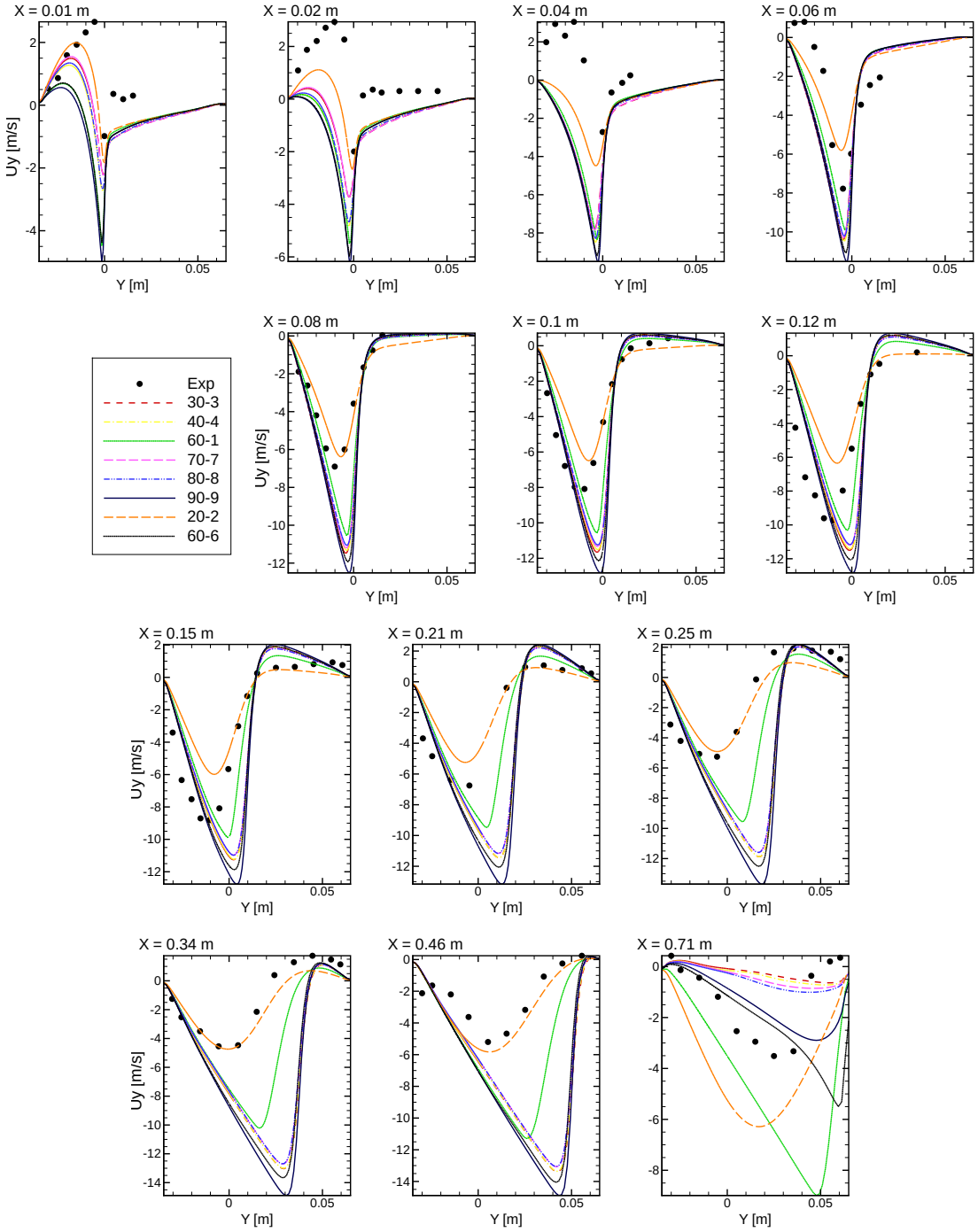

Figure 6.26: Vertical profiles of Favre-averaged transverse velocity $\widetilde{u}_y$ in reactive backward-facing step flow; RANS/PFTC β-PDF

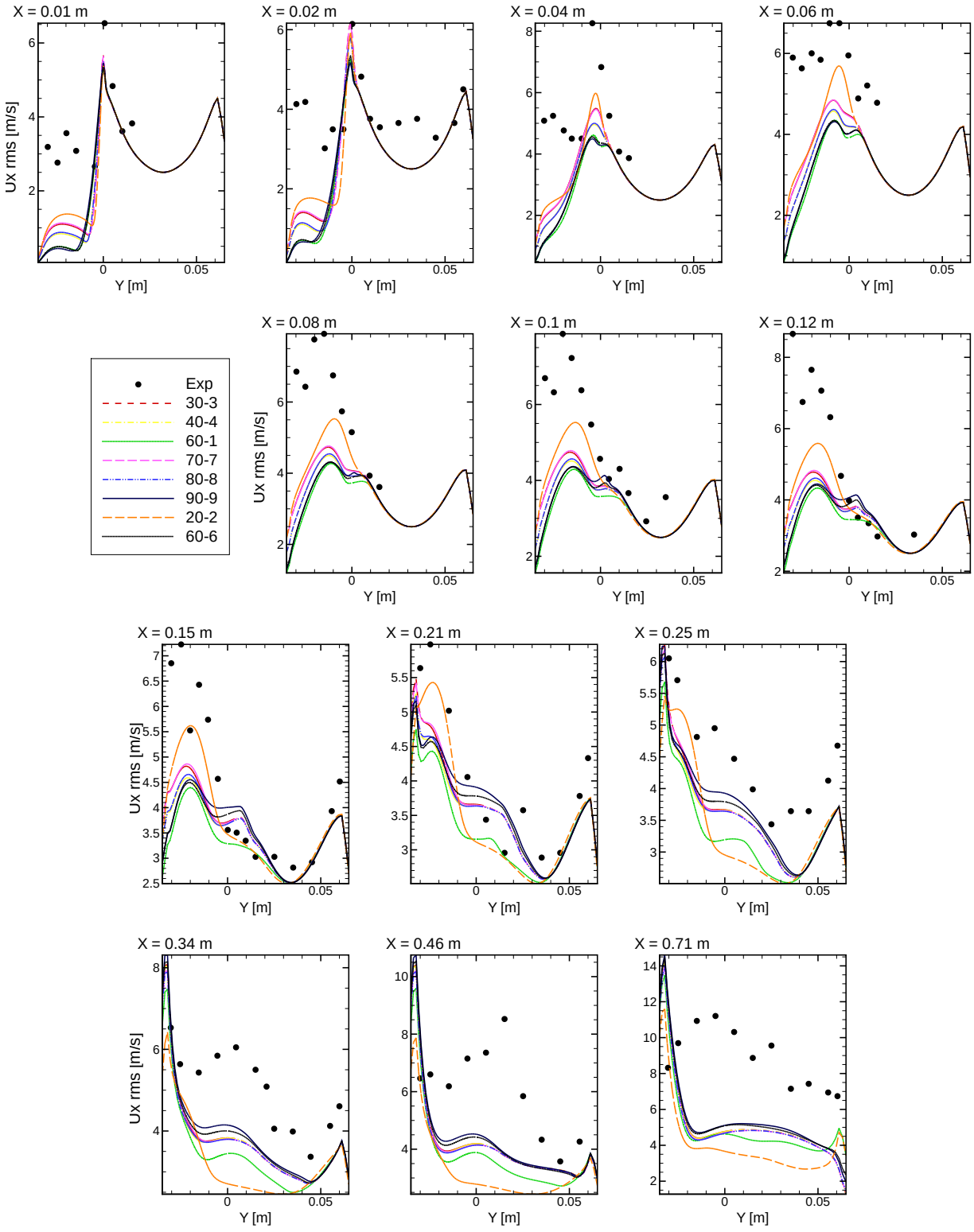

Figure 6.27: Vertical profiles of u_x^{RMS} in reactive backward-facing step flow; RANS/PFTC β-PDF

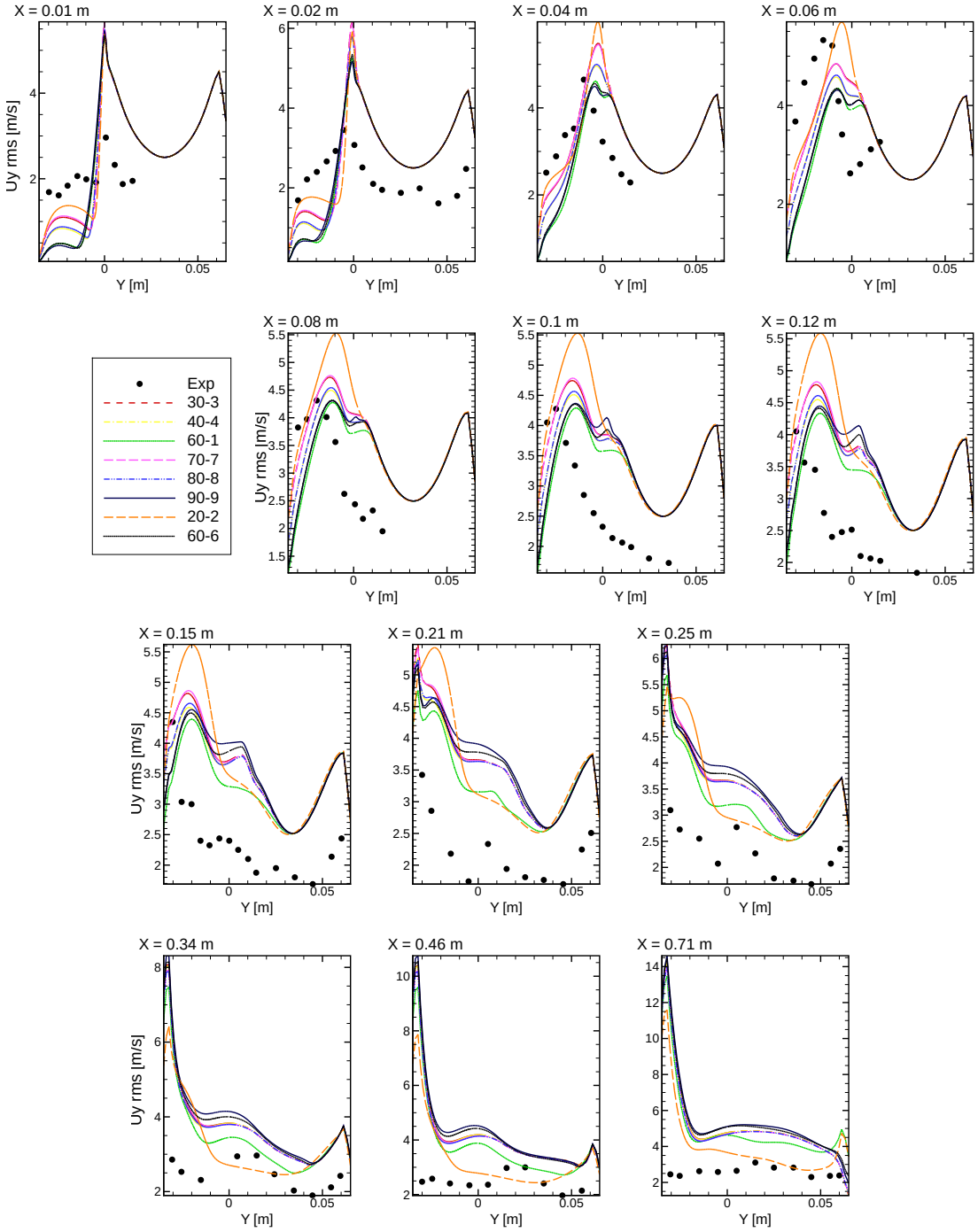

Figure 6.28: Vertical profiles of u_y^{RMS} in reactive backward-facing step flow; RANS/PFTC β-PDF

TPaSR model

Table 6.5 shows the test cases considered in the simulation with the RANS/TPaSR model.

Residence time	C_ω	Method	Boundary condition	Time step Δt
geom.	10.5	RK2 with 1st order ODFI sch.	nonhomogeneous	4×10^{-7} s
geom.	5	RK2 with 1st order ODFI sch.	nonhomogeneous	4×10^{-7} s
geom.	15	RK2 with 1st order ODFI sch.	nonhomogeneous	4×10^{-7} s
kol.	10.5	RK2 with 1st order ODFI sch.	nonhomogeneous	4×10^{-7} s
magn.	10.5	RK2 with 1st order ODFI sch.	nonhomogeneous	1×10^{-7} s

Table 6.5: Considered test-cases for RANS/TPaSR approach in reactive backward-facing step flow. Following abbreviations are used: "geom." - geometrical fine structure residence time, "kol." - Kolmogorov fine structure residence time and "magn." - Magnussen fine structure residence time.

Favre-averaged temperature Figure 6.29 shows the vertical profiles of mean temperature $\widetilde{T}$ at different locations X calculated with the RANS/TPaSR model. Different definitions of subgrid residence time τ^* with variation of C_ω constant are considered. Profiles are compared with the experimental points. The comparison shows that the TPaSR model with the geometrical subgrid residence time $\tau^* = \sqrt{\tau_K \tau_L}$ yields the best agreement between the calculation and the experiment. The variation of the constant C_ω for geometrical subgrid residence time proves that the dependence of solution on C_ω is continuous.

When C_ω is less than 10.5, the fresh gas goes in the cell and the temperature decreases. On the contrary, if C_ω exceed 10.5, the burned gas enters in the cell and the temperature increases in the region of the chemical reactions. In order to preserve the model stability, the influence of C_ω should be relatively weak, which is indeed fulfilled for the results described here. This signifies that a small change of C_ω does not change a global solution of system. Furthermore, according to our expectations, the best result is indeed obtained with theoretically predicted value of $C_\omega = 10.5$.

To understand the difference between the TPaSR solutions obtained with the Kolmogorov τ_K, the Magnussen $0.41\tau_K$ and the geometrical $\sqrt{\tau_K \tau_L}$ subgrid residence times, let us consider the vertical profiles of the volume fraction of the fine structure region γ^* and its equilibrium state γ^*_{eq}, which are presented in fig. 6.30. The constant 0.41 in the definition of the Magnussen time allows increasing the values of γ^* and γ^*_{eq}. Indeed γ^* and γ^*_{eq} calculated with Magnussen time is approximately 1.3 larger than γ^* and γ^*_{eq} obtained with the Kolmogorov subgrid residence time. In the lower region of the step nose the values of γ^* and γ^*_{eq} are lower than 0.5. Then, it continuously increases, thus for $X = 0.71$ m, at the lower wall $\gamma^*_{eq} = \gamma^* = 0.82$ for geometrical time and close to $\gamma^*_{eq} = \gamma^* = 0.92$ for the Magnussen and the Kolmogorov times. In the vertical middle region the values of the volume fraction of the fine-structure region in equilibrium state for $\sqrt{\tau_K \tau_L}$ are approximately 0.2, the volume fraction of the fine-structure region is slightly overestimated compared to its equilibrium value. The large variation of γ^*_{eq} (from 0.2 to 0.8) along the vertical cross-section with mean value 0.2 attained

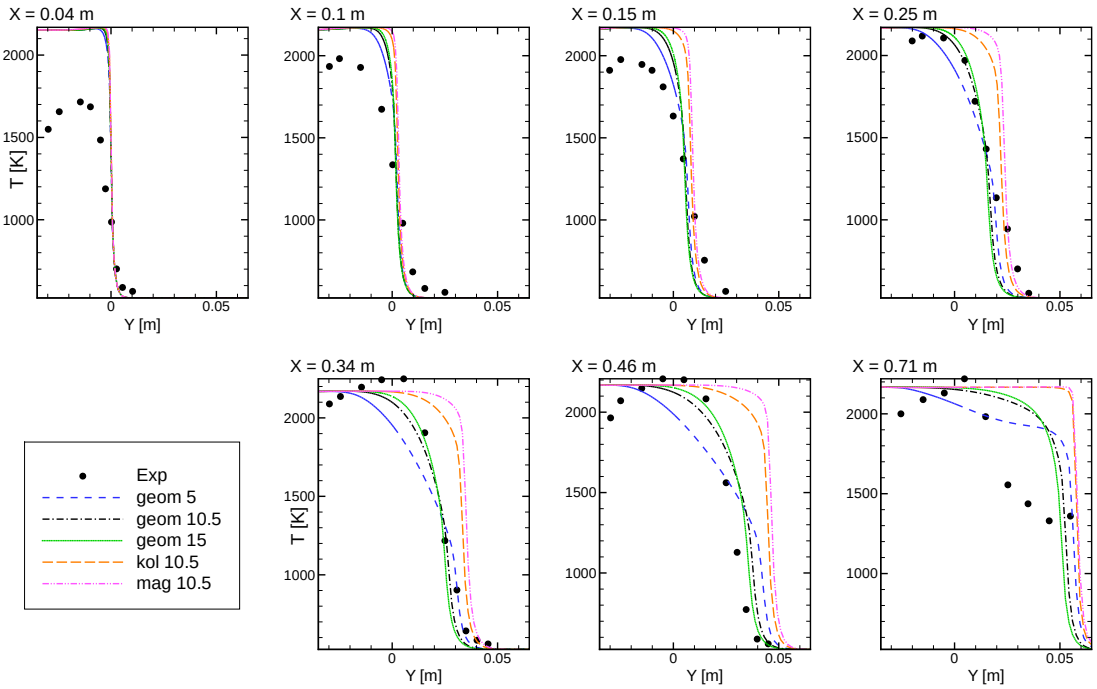

Figure 6.29: Vertical profiles of Favre-averaged temperature $\widetilde{T}$ in reactive backward-facing step flow; RANS/TPaSR

in the middle of the cross-section allows a more precise calculation of the flame than in the case of the Kolmogorov and the Magnussen subgrid residence time. The adaptation of the TPaSR model to the RANS simulation allows increasing γ^* in comparison with γ^*_{eq}, that improves the mixture between the burnt and fresh gases.

In order to provide the details of operation of the TPaSR model, let us consider the vertical profiles of the mean temperature $\widetilde{T}$ and the temperature T^* in the fine structure region. Figure 6.31 evidences that the temperature in the fine-structure regions T^* is greater than the mean temperature $\widetilde{T}$ according to the following theoretical prediction:

$$\widetilde{T} = \gamma^* T^* + (1 - \gamma^*) T^0 \leq \gamma^* T^*. \tag{6.11}$$

The gradient observed in T^* temperature profile is larger than the gradient in the profile of $\widetilde{T}$. The similar behavior is observed for mass fractions.

Figure 6.32 shows the distribution of the Favre-averaged temperature $\widetilde{T}$ in the combustion chamber, obtained with the geometrical fine structure residence time.

The temperature calculated with TPaSR model using the geometrical subgrid residence time better approaches the experimental data than other considered models (i.e. quasi-laminar and PFTC β-PDF models). Isolines of temperature $\widetilde{T} = 1500\,\mathrm{K}$ in reactive backward-facing step flow calculated with the TPaSR and the PFTC β-PDF 20-2, 60-1 are presented in fig. 6.33. The PFTC β-PDF 60-1 model overestimates the flame angle, while the PFTC β-PDF 20-2 model underestimates it in the entire domain except the region where the flame impacts the upper wall. The flame angle reconstructed with the TPaSR model stays close to the experimental values for $X \leq 0.4\,\mathrm{m}$. The angle is overestimated for $0.4\,\mathrm{m} < X < 0.7\,\mathrm{m}$

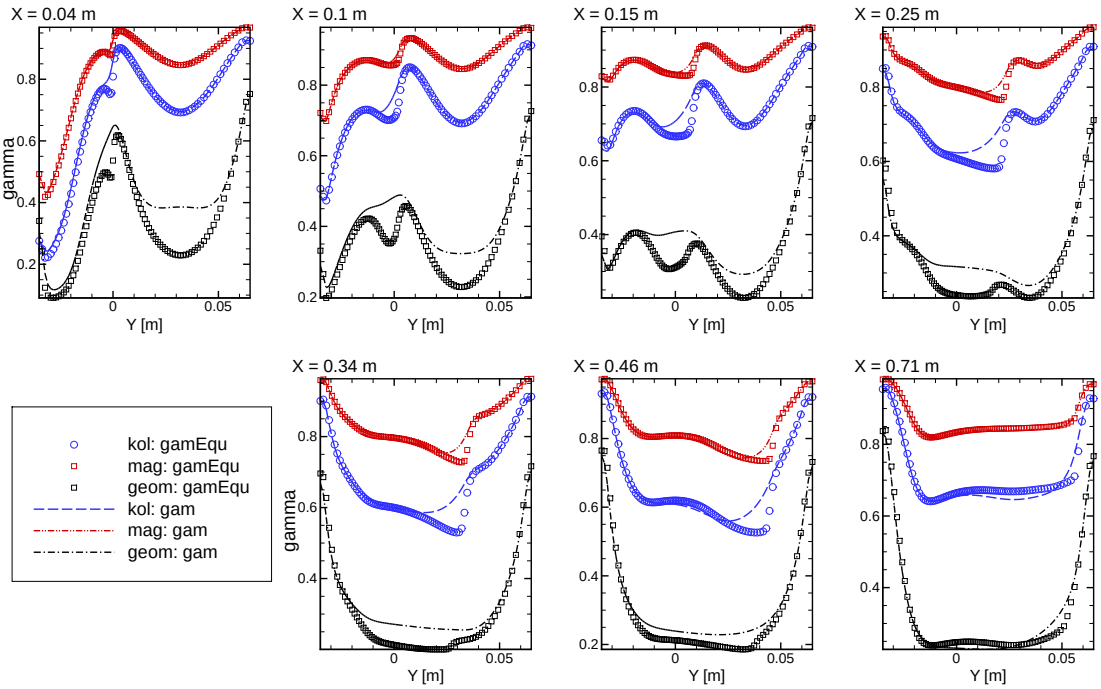

Figure 6.30: Vertical profiles of volume fraction γ^* of the fine structure and its equilibrium state γ^*_{eq} in reactive backward-facing step flow; RANS/TPaSR

and underestimated at the point $X = 0.8\,\mathrm{m}$. Calculation using the PFTC noTCI model on the same grid with the same inlet and outlet boundary conditions overestimates the flame angle for $X \geq 0.25\,\mathrm{m}$ and underestimates it at $X = 0.8\,\mathrm{m}$ (see fig. 6.15).

The chemical source calculated with variables of fine-structure region and then multiplied by γ^* is used in the transport equation for the Favre-averaged mass fractions. It is significantly lower than in the RANS/QL RCM approach. Consequently, as represented in figs. 6.15 and 6.33, the angle of the flame front decreases.

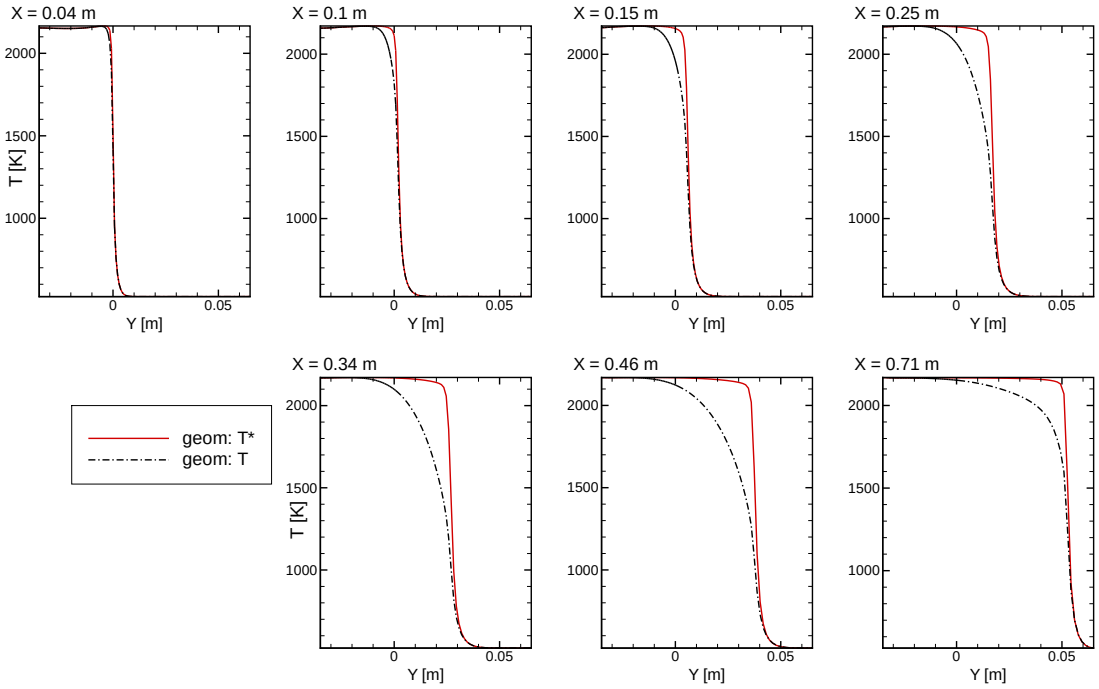

Figure 6.31: Comparison of vertical profiles of Favre-averaged temperature $\widetilde{T}$ and temperature in fine structure region T^* in reactive backward-facing step flow; RANS/TPaSR

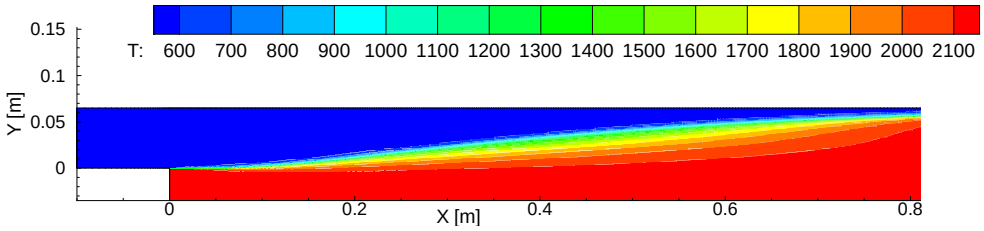

Figure 6.32: Field of Favre-averaged temperature $\widetilde{T}$ [K] in reactive backward-facing step flow; RANS/TPaSR

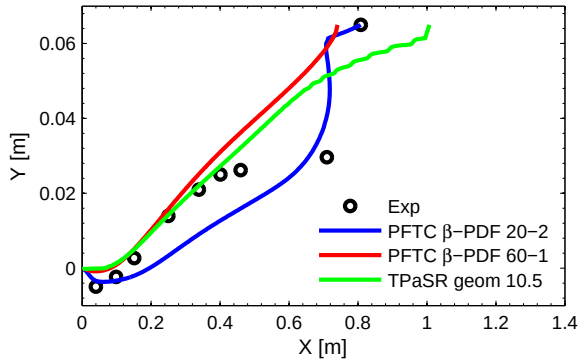

Figure 6.33: Isolines of temperature $\widetilde{T} = 1500\,\mathrm{K}$ in reactive backward-facing step flow; RANS

Favre-averaged streamwise velocity The vertical profiles of Favre-averaged streamwise velocity $\widetilde{u}_x$ at different X locations are presented in fig. 6.34. They are obtained according different subgrid residence times τ^*: geometrical, Kolmogorov and Magnussen. The best result is observed for the geometrical subgrid residence time. The variation of C_ω constant for the geometrical subgrid residence time gives approximately the same results. The curves remain close to each other for $X \leq 0.15\,\mathrm{m}$. The profiles for $C_\omega = 10.5$ are located between the profiles obtained with $C_\omega = 5$ and $C_\omega = 15$. That signifies that the TPaSR model depends continuously on C_ω.

Favre-averaged transverse velocity Figure 6.35 shows vertical profiles of the Favre-averaged transverse velocity $\widetilde{u}_y$. In the step nose region the numerical transverse velocity is negative while in the experiment it is positive. In the middle part of the combustion chamber the velocity has a satisfactory agreement with the experimental data for the TPaSR model with the geometrical subgrid residence time τ^*. The minimal peaks of the transverse velocity are shifted to the upper wall. For $X \geq 0.25\,\mathrm{m}$ the absolute values of $\widetilde{u}_y$ are overestimated. The model with Kolmogorov subgrid residence time better approximates the experimental results than the model with Magnussen subgrid residence time. The variation of C_ω constant does not induce a global change in the solution.

RMS velocity fluctuations The RMS velocity fluctuations are presented in figs. 6.36 and 6.37. One can note that the RMS velocity fluctuations for three subgrid residence time formulas follows approximately the same curve for $X \leq 0.1\,\mathrm{m}$. For $X > 0.1\,\mathrm{m}$ the Kolmogorov and the Magnussen approaches gives larger values of the RMS than the geometrical modeling of the subgrid time. As for other models, the underestimation of the fluctuations in the case of RMS streamwise velocity is compensated by their overestimation for RMS vertical velocity.

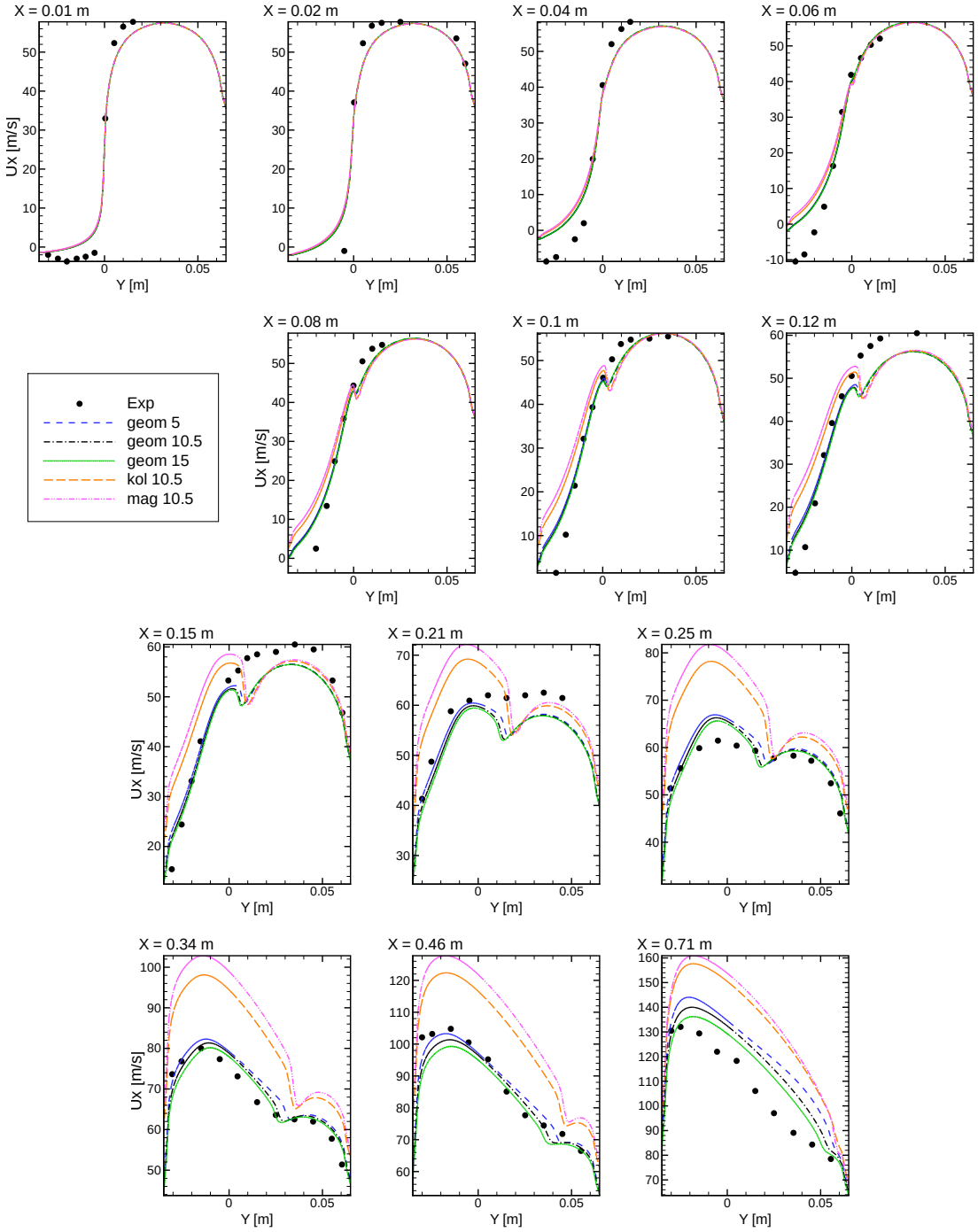

Figure 6.34: Vertical profiles of Favre-averaged streamwise velocity $\widetilde{u}_x$ in reactive backward-facing step flow; RANS/TPaSR

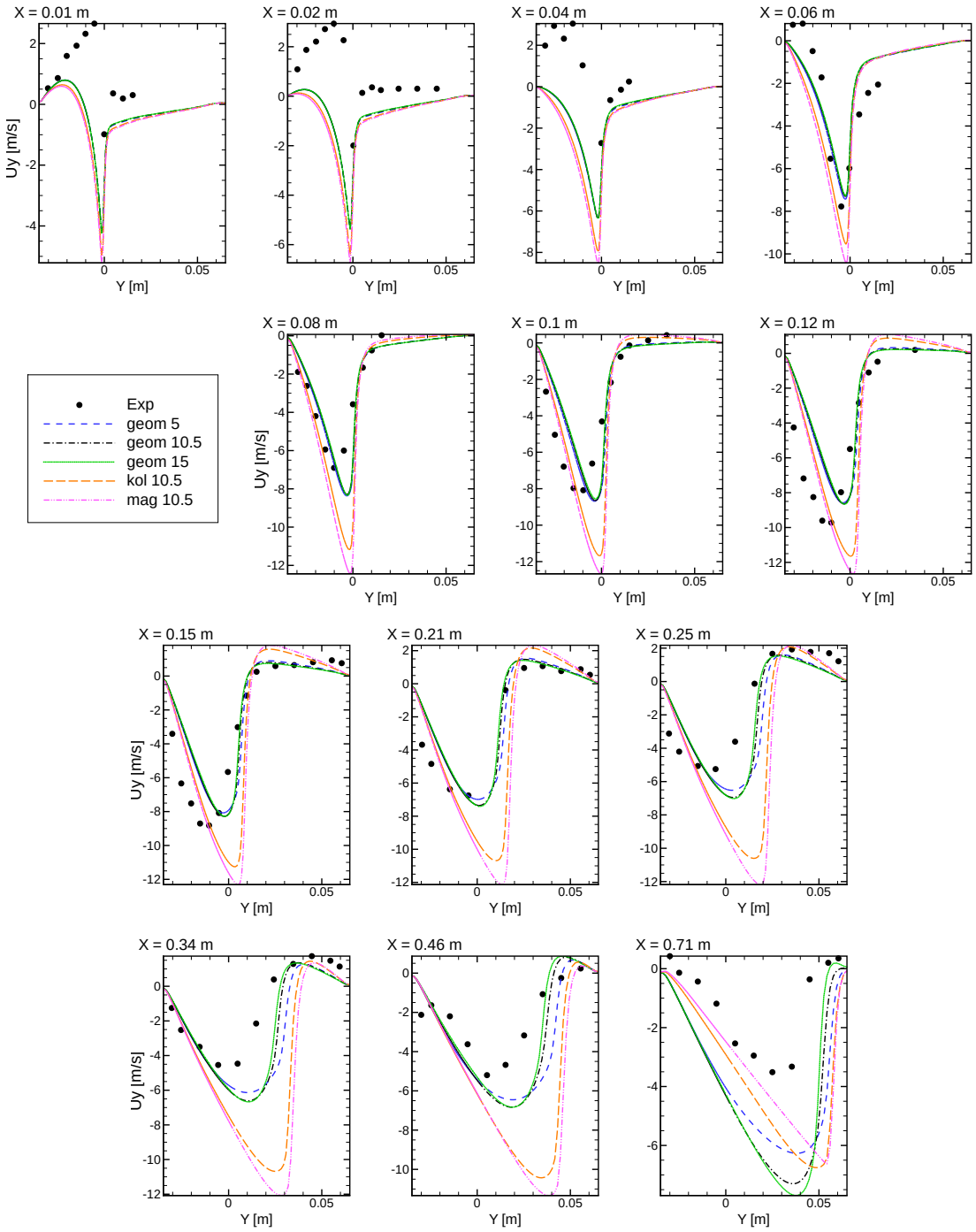

Figure 6.35: Vertical profiles of Favre-averaged transverse velocity $\widetilde{u}_y$ in reactive backward-facing step flow with homogeneous inlet profiles; RANS/TPaSR

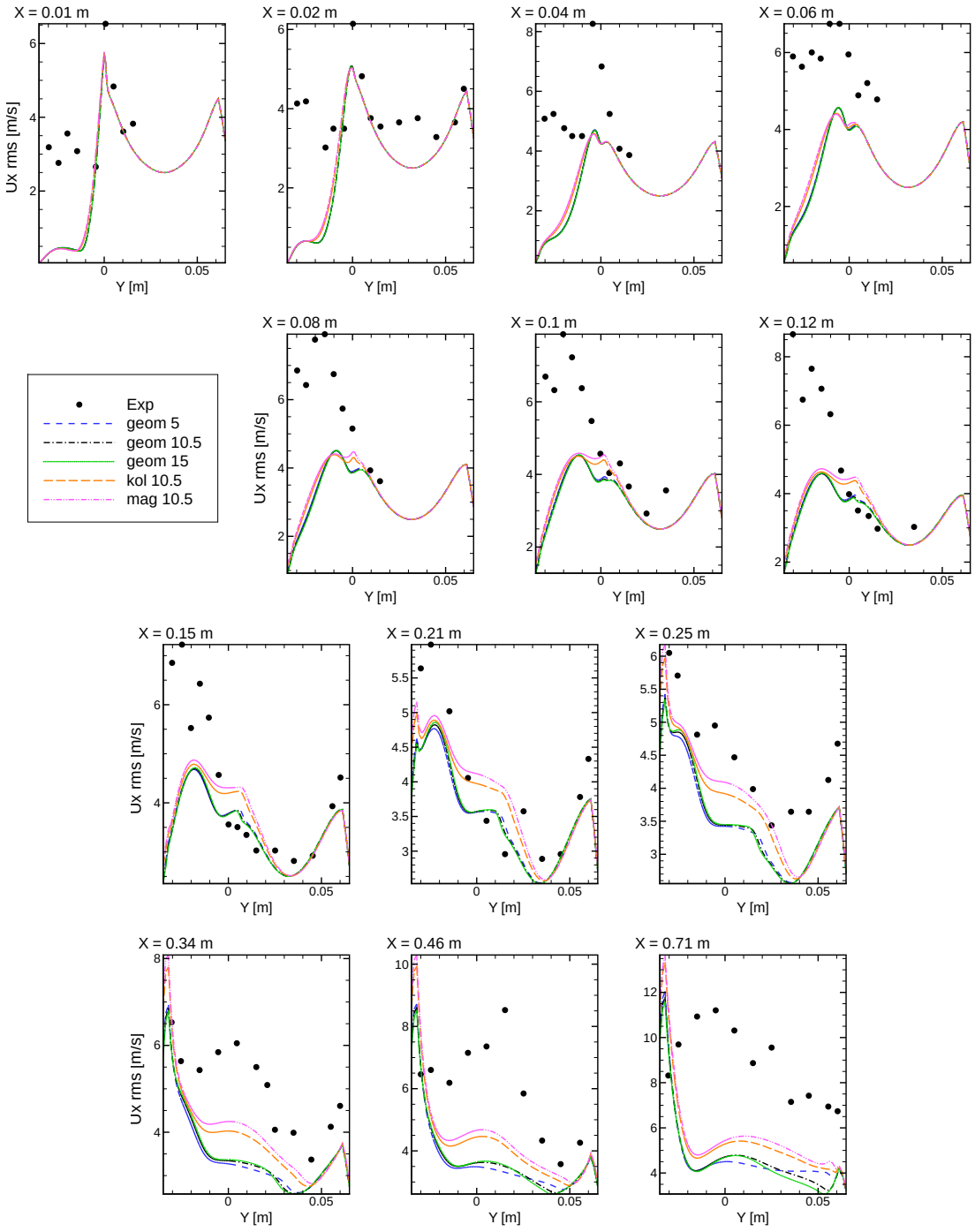

Figure 6.36: Vertical profiles of u_x^{RMS} in reactive backward-facing step flow; RANS/TPaSR

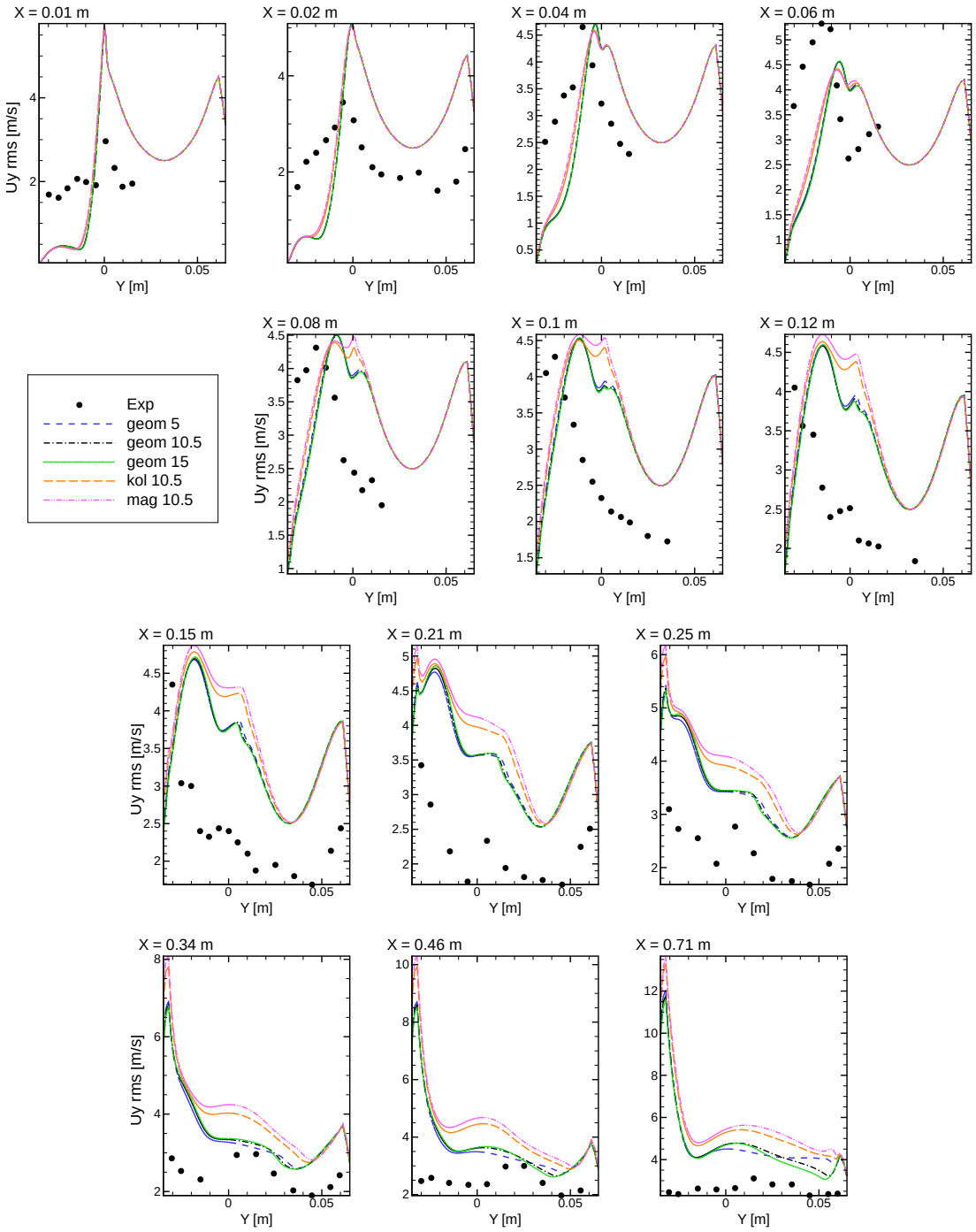

Figure 6.37: Vertical profiles of Favre average of u_y^{RMS} in reactive backward-facing step flow; RANS/TPaSR

6.3.4 Conclusions

The quasi-laminar approach with reduced chemical mechanism (QL RCM) and the premixed flamelet chemistry without turbulence-chemistry interaction (PFTC noTCI) are used in the RANS calculations of the premixed turbulent flame on the configuration of the backward-facing step. The analysis of the Favre-averaged temperature and velocity fields demonstrates the need to take into account the turbulence-chemistry interaction.

The TPaSR model adapted to the RANS is implemented into the industrial code CEDRE of ONERA. The PFTC β-PDF model is integrated into the current version of CEDRE with the modifications proposed in chapter 4. The reactive flow behind the step is calculated and analyzed with different options of the PFTC β-PDF and the TPaSR models. The obtained results are compared with the experimental data. It is shown that the most close to experimental data temperature and velocity [MagreMoreau1988] predictions are obtained with the TPaSR model with the subgrid residence time defined as the geometrical mean of the Kolmogorov time and the integral time scale (5.23). It is found (results are not given here) that in the case of the TPaSR model (reduced chemistry) the match between the calculated and the experimental flame angle is observed for the grid of 8000 cells. The QL RCM, the PFTC noTCI and the PFTC β-PDF approaches on the same grid are not able to predict the flame.

6.4 LES reactive backward-facing step flow calculation

6.4.1 Computational domain and grid

In order to perform the LES calculation, we have to extend the 2D domain used for the RANS calculation (described in section 6.2.1) into a three-dimensional one. Given the computational cost of the resolution of the lateral boundary layers, we add only a width of $2h$ in the third direction Z. B. Sainte-Rose has shown that due to the use of periodic boundary conditions at the walls $Z \equiv const$ the choice of computational domain depth does not influence the solution [SainteRose2010]. In the Z direction the grid is uniform and consists in 30 cells, thus ΔZ is about 0.0023 m. As for 2D case, the grid is refined in the X and Y directions at the corner of the step, in the recirculation region and in near the lower wall of the chamber. At the corner of the step a grid resolution ΔX is equal to ΔY and is 1×10^{-4} m. Figure 6.39 illustrates a slice of the 3D grid at $Z = h$. The total number of inner cells is 4 106 010.

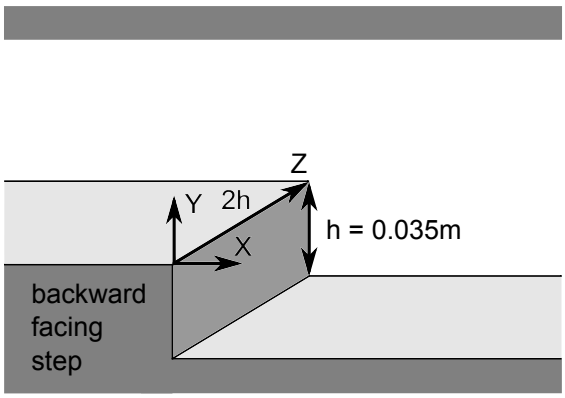

Figure 6.38: Extrusion of the bidimensional domain used for RANS calculations into a three-dimensional domain for LES

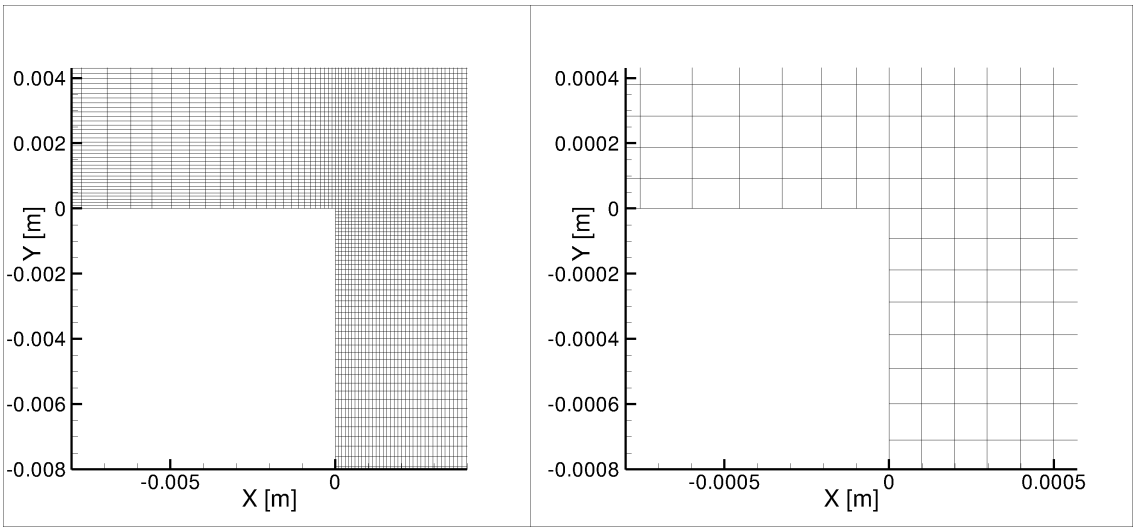

Figure 6.39: Slice of 3D grid at $Z = h$ for backward-facing step flow

6.4.2 Physical models

The same physical models are used that in section 6.2.2. Modeling of turbulence is performed with Smagorinsky model.

6.4.3 Boundary conditions

In this following work the symbol $\widetilde{Q}$ signifies a filtering of the variable Q in the sense of Favre in transport equations of the LES. The symbol $\langle\rangle$ is used to describe the temporal mean in the sense of Reynolds.

- **Inlet:**
  There are two different types of inlet streamwise velocity.
  - Nonhomogeneous steady-state profile of streamwise velocity $\widetilde{u}_x$ (left panel of fig. 6.5)

– Synthesized inlet velocity fluctuations, which are added to the nonhomogeneous steady-state profiles of $\widetilde{u}_x$, $\widetilde{u}_y$ and $\widetilde{u}_z$, are used to generate incoming turbulence. In order to generate the unsteady synthesized profiles of velocity u_x, u_y and u_z, we use the Ornstein-Uhlenbeck process for velocity fluctuations $\boldsymbol{v'}$, which allows constructing time-correlated velocity fluctuations. We suppose that the distribution of the velocity fluctuations is isotropic in the three directions:

$$v'_x \approx v'_y \approx v'_z \approx \sqrt{\frac{2}{3}k}. \tag{6.12}$$

This statement is not exact because the velocity fluctuations are not isotropic. Due to the absence of the experimental data for each component of velocity fluctuations at inlet of the combustion chamber, we use a simplified hypothesis taking isotropic velocity fluctuations $\boldsymbol{v'}$. The data for the turbulent energy and the turbulent frequency are obtained from the calculation of the 2D channel explained in section 6.2.3. Applying the formula (A.116) detailed in appendix A.6 to each component of the velocity fluctuations, we obtain

$$\boldsymbol{v}'(t+\Delta t, y) = \exp\left[-\omega(y)\Delta t\right]\boldsymbol{v}'(t,y) + \sigma(y)\sqrt{1-\exp\left[-2\omega(y)\Delta t\right]}\boldsymbol{\xi}(t+\Delta t), \tag{6.13}$$

where $\sigma = \sqrt{\frac{2}{3}k}$, $\boldsymbol{\xi}$ is a normal Gaussian vector which does not depend on space and $\Delta t = 1\times10^{-6}\,\mathrm{s}$. At the initial time t_0 the fluctuation velocity $\boldsymbol{v}'(t_0)$ is supposed to be a normal Gaussian vector $\boldsymbol{\xi}(t_0)$. The total velocity at time $t+\Delta t$ is

$$\boldsymbol{u}(t+\Delta t, y) = \widetilde{\boldsymbol{u}}(y) + \boldsymbol{v}'(t+\Delta t, y). \tag{6.14}$$

The profiles of $\widetilde{\boldsymbol{u}}$ are taken from 2D channel (see section 6.2.3), $\widetilde{u}_z = 0$. In order to guarantee that the inlet does not become the outlet, the cutting by zero of the total velocity is used at some points. Figure 6.41 illustrates the temporal profiles of total velocity u_x and u_y at points $X = 0\,\mathrm{m}$, $X = 0.0046\,\mathrm{m}$ and $X = 0.0325\,\mathrm{m}$. As we can see the transverse velocities are close to each other, because $\widetilde{u}_y$ is almost zero.

The time-averaged profiles of streamwise velocity and σ^2, calculated by the following formula

$$\langle Q\rangle = \frac{1}{T}\int_{t_0}^{T} Q(\tau)d\tau, \tag{6.15}$$

where Q is any quantity, are plotted in fig. 6.40, t_0 is the initial time. The total averaged time is

$$T - t_0 = 0.21\,\mathrm{s}. \tag{6.16}$$

It corresponds to about 11 characteristic residence time in the combustion chamber.

After all corrections used to ensure the positive sign of inlet velocity and the velocity fluctuations corrections (such as the centralization and the normalization), the total deviation of the time-averaged velocity from the initial velocity profiles

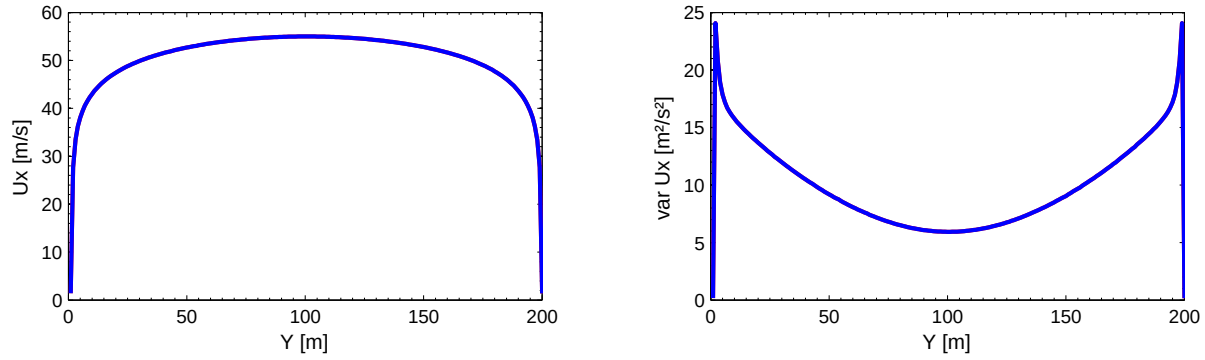

Figure 6.40: Time-averaged profiles of streamwise velocity (left) and $\frac{2}{3}k$ (right); the averaged time is 0.21 s

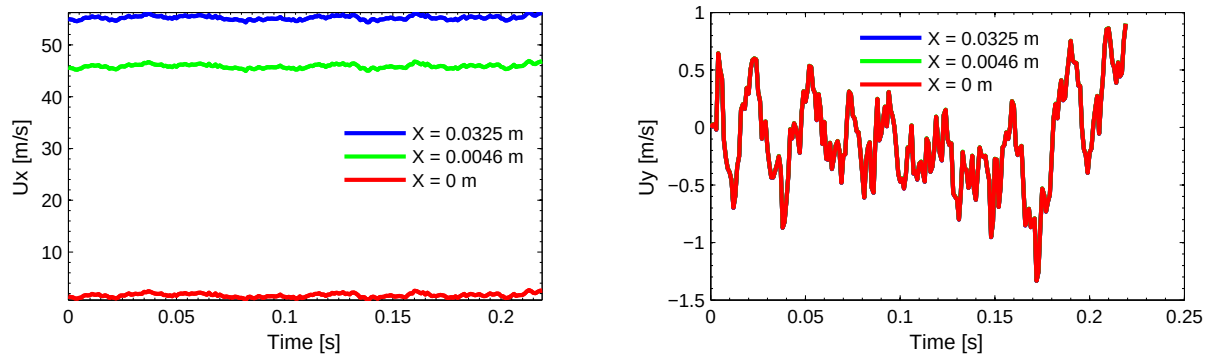

Figure 6.41: Time evolution of inlet longitudinal and transverse velocity at different points

Error (%)	$\widetilde{u}_x$	$\widetilde{u}_y$	$\widetilde{u}_z$
L_∞ norm	0.0001	10.5	0.0001
L_2 norm	0.01	5.96	0.0001
	$\widetilde{u''^2}_x$	$\widetilde{u''^2}_y$	$\widetilde{u''^2}_z$
L_∞ norm	6.1	3.31	3.23
L_2 norm	1.15	5.2	1.17

Table 6.6: Deviation of time-averaged velocity and velocity variance profiles from initial velocity profile in different norm; the averaged time is 0.21 s

and the initial variance $\sigma^2 = \frac{2}{3}k$ of each velocity components are presented in different norms in table 6.6.

Other inlet parameters are described in section 6.2.3.

- **Lateral boundary:**
  Periodic boundary conditions are imposed at the lateral boundaries to get the accurate

development of the 3D shear layer.

- **Walls:**
  Adiabatic walls are supposed.

6.4.4 Combustion modeling and numerical schemes

Four types of simulations were considered in the framework of LES. They are presented in table 6.7.

	Method	Boundary condition	Time step Δt
QL RCM	backward Euler with MUSCL scheme	steady nonhomogeneous	1×10^{-6} s
QL RCM (OU)	backward Euler with MUSCL scheme	unsteady nonhomogeneous	1×10^{-6} s
PFTC TFLES	backward Euler with MUSCL scheme	steady nonhomogeneous	1×10^{-6} s
PFTC β-PDF of Peters	backward Euler with MUSCL scheme	steady nonhomogeneous	1×10^{-6} s

Table 6.7: Considered test-cases within LES for reactive backward-facing step flow

The details of the chemical reduced mechanism and the construction of the FTC tables are described in section 6.3.2. The LES/TPaSR model is not considered, because it is very sensitive to the grid size. As the grid is not sufficiently refined, the volume fraction of the fine-structure region γ^*_{eq} responsible for the combustion in the chamber is less than 0.01 for the considered 3D grid. As a result, the combustion does not take place. In order to have the combustion, the order of γ^*_{eq} must be greater than 0.3.

6.4.5 Computational strategy

The physical domain was divided into 256 parts distributed on 256 Nehalem nodes consisting of two 2.80 GHz quad-core processors. In order to obtain time-averaged fields for one considered model starting from a solution calculated by another model, around 210 hours were necessary.

After a transition time which corresponds to 3 residence times in the combustion chamber (6.1), unsteady fields are averaged. The averaged time for the LES in all four cases is approximately 0.21 s, that corresponds to 11 residence times in the chamber. The time-averaged vertical profiles at 10 residence times are compared with the time-averaged profiles at 11 residence times at X points where the experimental data at $Z = h$ are available (see, e.g. fig. 6.46). The obtained numerical profiles of $\langle \widetilde{T} \rangle$, $\langle \widetilde{u}_x \rangle$, $\langle \widetilde{u}_y \rangle$, $\langle u_x^{RMS} \rangle$, $\langle u_y^{RMS} \rangle$ at 10 characteristic times superimpose visually to the respective profiles at 11 characteristic times.

6.4.6 Results

Mean temperature

Vertical profile of $\langle\widetilde{T}\rangle$ compared with experimental data We compare the calculated vertical mean temperature profiles with the results of experimental measurement (see fig. 6.42). In the recirculation region, the experimentally obtained temperature is significantly below than the adiabatic temperature at the end of the combustion process. This is due to a significant cooling of the fluid particles along the bottom wall (which is non-adiabatic) due to their long residence time in this region. Despite this, the average thickness of the flame is well reproduced by the numerical simulations because the temperature gradient is correctly modeled. In the experiment, behind the reattachment region (which distance from the step in the experiment is between 0.1 m and 0.12 m), the acceleration of the flow considerably reduces the residence time of the particles flowing along the wall. This results in lower thermal losses and a gradual temperature rise, which therefore becomes closer to the calculated temperature field. The area $X > 0.25\,\mathrm{m}$ is characterized by a good agreement between the experimental and numerical profiles. However, for much higher values of X a discrepancy in temperature re-appears due to the fact that the calculated flame front impacts the upper wall earlier than in the experiment.

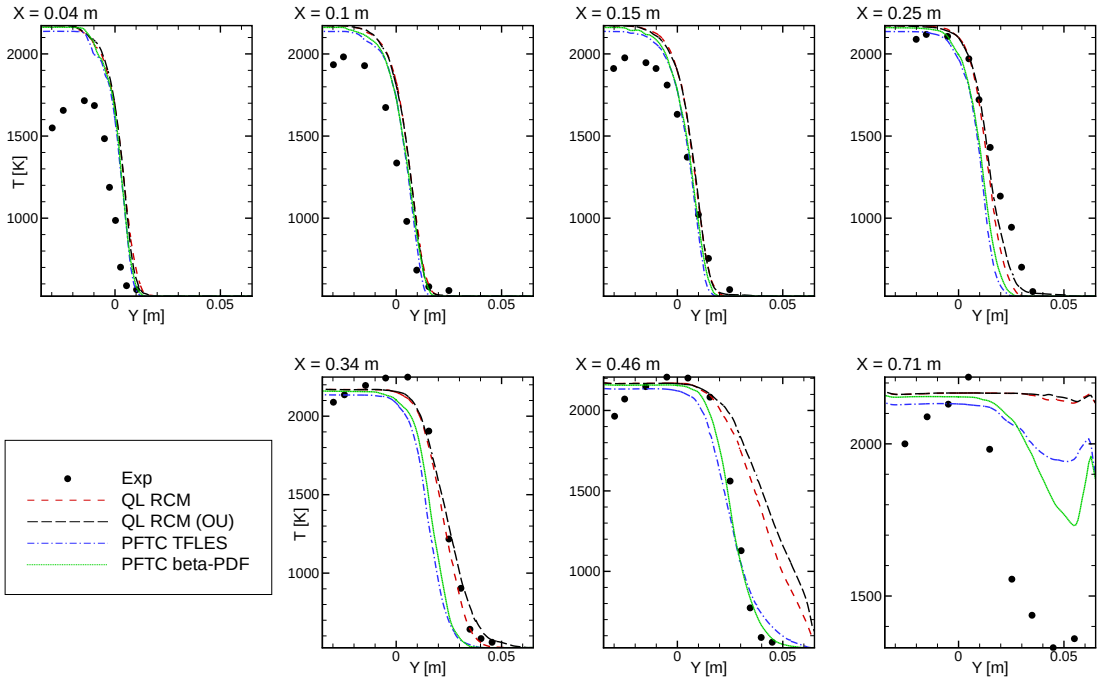

Figure 6.42: Vertical profiles of mean temperature $\langle\widetilde{T}\rangle$ in reactive backward-facing step flow; LES

Isolines of mean temperature $\langle\widetilde{T}\rangle = 1500\,\mathrm{K}$ In order to better understand the flame front position, let us consider the isolines of $\langle\widetilde{T}\rangle = 1500\,\mathrm{K}$, compared with the experimental

isoline in fig. 6.43. Even if all the performed simulations generally underestimate the horizontal position of the point where the flame impacts the upper wall, the choice of model still has an influence. For $0\,\text{m} < X < 0.45\,\text{m}$ the quasi-laminar models better reproduce the flame front positions whereas the PFTC β-PDF and the quasi-laminar PFTC TFLES overestimate it. By contrast, for $X > 0.55\,\text{m}$, all the models underestimate the flame angle, but the PFTC TFLES and the PFTC β-PDF profiles better estimate the point of flame contact with the upper wall (6.8). Such an underestimation for large values of X may be due to excessively large recirculation zone. Indeed, a larger recirculation zone induces lean mixing and therefore a slower burning than in the experiment. In the experiment, the flame front clearly flattens

Case	X [m]	Error [%]
Experiment	0.8	
LES/QL RCM	0.6	25
LES/QL RCM (OU)	0.58	27.5
PFTC TFLES	0.65	18.7
LES/PFTC β-PDF	0.65	18.7

Table 6.8: Flame contact point with the upper wall and its relative error in reactive backward-facing step flow

before raising near the contact with the upper wall ($0.6\,\text{m} < X < 0.8\,\text{m}$), which is due to the acceleration of the fresh gas. If such the raising can be also seen in the numerical profiles, the flattening is not reproduced numerically. This will be explained in section 6.4.6 devoted to the description of streamwise velocity.

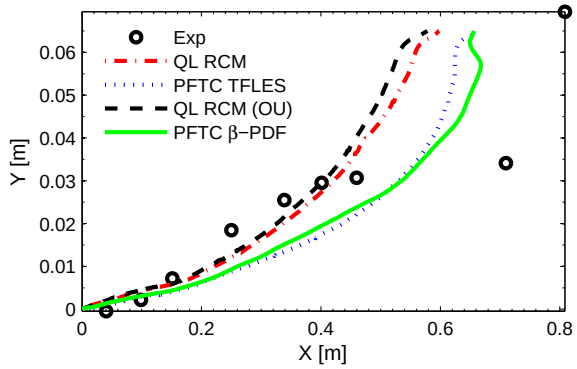

Figure 6.43: Isolines of mean temperature $\langle\widetilde{T}\rangle = 1500\,\text{K}$ in reactive backward-facing step flow; LES

Fields of $\langle\widetilde{T}\rangle$ The mean temperature field for $Z = 0.035\,\text{m}$ is presented in fig. 6.44. This temperature distribution is obtained with the LES/QL RCM mechanism and unsteady synthesized inlet velocity profiles. Approximately the same temperature fields are obtained with other combustion models.

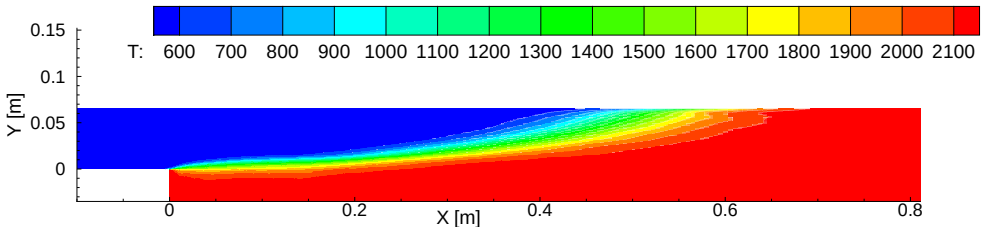

Figure 6.44: Field of mean temperature $\langle \widetilde{T} \rangle$ [K] in reactive backward-facing step flow calculated with LES/QL RCM (OU); $Z = 0.035\,\mathrm{m}$

Comparison of LES and RANS approaches In the framework of RANS approach the TPaSR model gives the best profiles of Favre-averaged temperature in comparison with other RANS models. As a consequence, we consider only the RANS/TPaSR model with the geometrical subgrid residence time. It should be noted the quantities that we compare with the same experimental profiles have slightly different signification in RANS and LES approaches. Nevertheless, the comparison of fig. 6.29 and fig. 6.42 shows that the temperature gradient near the upper wall is better predicted by the LES/QL RCM mechanism than by the RANS/TPaSR model. At $X = 0.71\,\mathrm{m}$ the LES models overestimate more the mean temperature than the RANS/TPaSR model, because the point where the flame front impacts the upper wall for the LES calculations is about 0.6 m, for the RANS/TPaSR it is about 1 m, while in the experiment the location of this point is approximately 0.8 m. In general, the isoline of $\widetilde{T} = 1500\,\mathrm{K}$ calculated with the RANS/TPaSR model is closer to the experience than LES approaches.

Recirculation region

Before investigating the flow structure through its velocity profiles, it is necessary to examine the structure of the recirculation region. Figure 6.45 shows the recirculation zones for four considered models. The numerical fields, downstream of the step, present a main vortex rotating clockwise. In the simulation this recirculation region is longer than in the experiment. The reattachment length is $X_r = 0.168\,\mathrm{m}$ to $0.195\,\mathrm{m}$ depending on the combustion models (see table 6.9), while the experimental value is located in the interval $[0.1\,\mathrm{m}; 0.12\,\mathrm{m}]$. Such the difference can be due to the fact that the grid used in the current simulation is not sufficiently refined. The increase of the reattachment length is caused by the absence of the turbulent longitudinal vortices associated with the inflow boundary layer.

Figure 6.45 highlights the presence of a secondary recirculation region close to the upper wall of the step. This vortex rotates counter-clockwise. Although this small structure was not experimentally observed by laser velocimetry, its existence cannot be excluded to the extent that the measurement technique did not correctly follow the particles near the wall step region[1].

[1]In fact, only a small proportion of particles used for flow visualization penetrates into this region.

	X_r	X_r/h	Error X_r/X_r^{exp}
Experiment	$0.1\,\mathrm{m} - 0.12\,\mathrm{m}$	$2.8571 - 3.4286$	
QL RCM	$0.168\,\mathrm{m}$	4.8	1.4 - 1.68
QL RCM (OU)	$0.167\,\mathrm{cm}$	4.7714	1.3916 - 1.67
PFTC TFLES	$0.195\,\mathrm{m}$	5.5714	1.625 - 1.95
PFTC β-PDF	$0.188\,\mathrm{m}$	5.3714	1.5666 - 1.88

Table 6.9: The mean reattachment location X_r in reactive backward-facing step flow. The last column shows the error of the numerical results with respect to the experimental value. LES.

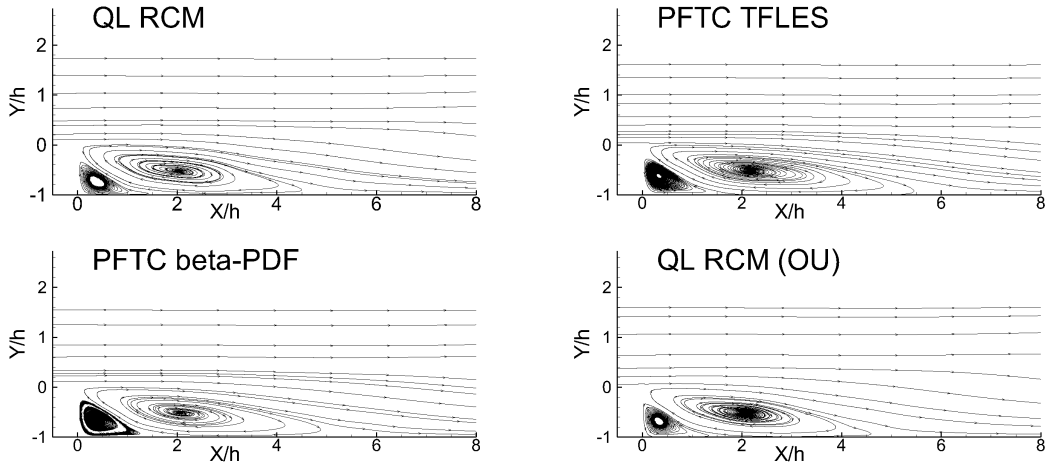

Figure 6.45: Recirculation regions in reactive backward-facing step flow; LES

Mean streamwise velocity

The mean longitudinal velocity obtained with four different models follow the same trend as the experimental measurements (fig. 6.46). The upper part of the chamber ($Y > 0\,\mathrm{m}$) and particularly the recirculation region ($0.01\,\mathrm{m} < X < 0.12\,\mathrm{m}$) is characterized by a good agreement between numerical and experimental data. At the flame front, flow gradually accelerates due to the injection of the fresh gas between the upper wall and the flame. However, in the region behind the reattachment point the longitudinal velocity is underestimated. As discussed in section 6.4.6, this underestimation may be due to excessively large recirculation zone which yields to an inefficient mixture. In the downstream region ($0.45\,\mathrm{m} < X < 0.71\,\mathrm{m}$) the calculations overestimate velocity profiles. Here, PFTC TFLES and the PFTC β-PDF models yield the best agreement with the experimental values; in particular they reproduce better the position of the flame contact point with the upper wall. With increasing X the velocity progressively increases in order to discharge the burnt gas, and the velocity gradient between lower and upper parts of the chamber vanishes. In the lower part of the chamber ($Y < 0\,\mathrm{m}$), the velocities up to $-11\,\mathrm{m/s}$ are measured. Despite of a slight underestimation of this value, the simulation reasonably reproduces the experimental profiles. On the profiles

$0.01\,\mathrm{m} < X < 0.04\,\mathrm{m}$, a velocity maximum is observed along the bottom wall, which corresponds to the previously identified secondary vortex. It is not experimentally observed for the reasons discussed in section 6.4.6.

Comparison of LES and RANS approaches The comparison of mean streamwise velocity plotted in figs. 6.34 and 6.46 shows that LES approaches predict better the velocity for $X \leq 0.12\,\mathrm{m}$ than the RANS/TPaSR model. Contrariwise, for $0.25\,\mathrm{m} \leq X \leq 0.46\,\mathrm{m}$ and $Y < 0\,\mathrm{m}$ the RANS/TPaSR model leads to a good agreement with the experimental data, because the $k - l$ turbulence model reproduces correctly the recirculation region with the mean reattachment location $X_r = 0.107\,\mathrm{m}$. Contrariwise to the results of LES calculation, it locates exactly in the experimental interval of X_r. For $X \geq 0.25m$ we observe that $\widetilde{u}_x$ calculated with the RANS/TPaSR model coincides with experimental profiles.

Mean transverse velocity

Vertical profiles of the mean transverse velocity calculated in the framework of the LES and the experimental measurements are compared in fig. 6.47. As we can see, numerical $\langle \widetilde{u}_y \rangle$ depends on the model and there are two different class of solutions: obtained with the tabulated chemistry and with the reduced chemical mechanism. For $X = 0.01\,\mathrm{m}$ the general trend of down-deflected flow is reproduced in the numerical profiles, but the absolute values are two to four times overestimated, especially by PFTC TFLES and PFTC β-PDF models. The simulations predict also transverse velocity minimum near the lower wall, which corresponds to the already discussed secondary vortex. In the experiment, the flow deviation decreases for $X \geq 0.15\,\mathrm{m}$ but remains maintained by the flame front in the upper part of the chamber. The same behavior is reproduced numerically, yet with overestimation. For instance, the quasi-laminar models with the reduced chemical mechanism predict a minimum velocity of $\langle \widetilde{u}_y \rangle = -14\,\mathrm{m/s}$ in $X = 0.46\,\mathrm{m}$ cross-section, whereas it should be only $\langle \widetilde{u}_y \rangle = -5\,\mathrm{m/s}$ according to the measurement. In the next profile at $X = 0.71\,\mathrm{m}$ $\langle \widetilde{u}_y \rangle$ drastically decreases for these models. In fact, $X = 0.71\,\mathrm{m}$ is behind the flame contact point with the upper wall. The flow deflection disappears, since it is no longer maintained by the flame front. Such the phenomenon is not yet observed for PFTC TFLES and the PFTC β-PDF profiles since in these latter cases the contact point is situated at larger X.

Comparison of LES and RANS approaches From figs. 6.35 and 6.47 we can see that the RANS modeling does not predict the secondary vortex placed near the step corner, because the grid is not sufficiently refined. For $X \geq 0.06\,\mathrm{m}$ the $k - l$ turbulence model approximates better the experimental profiles than LES, due the correct length of the main recirculation region.

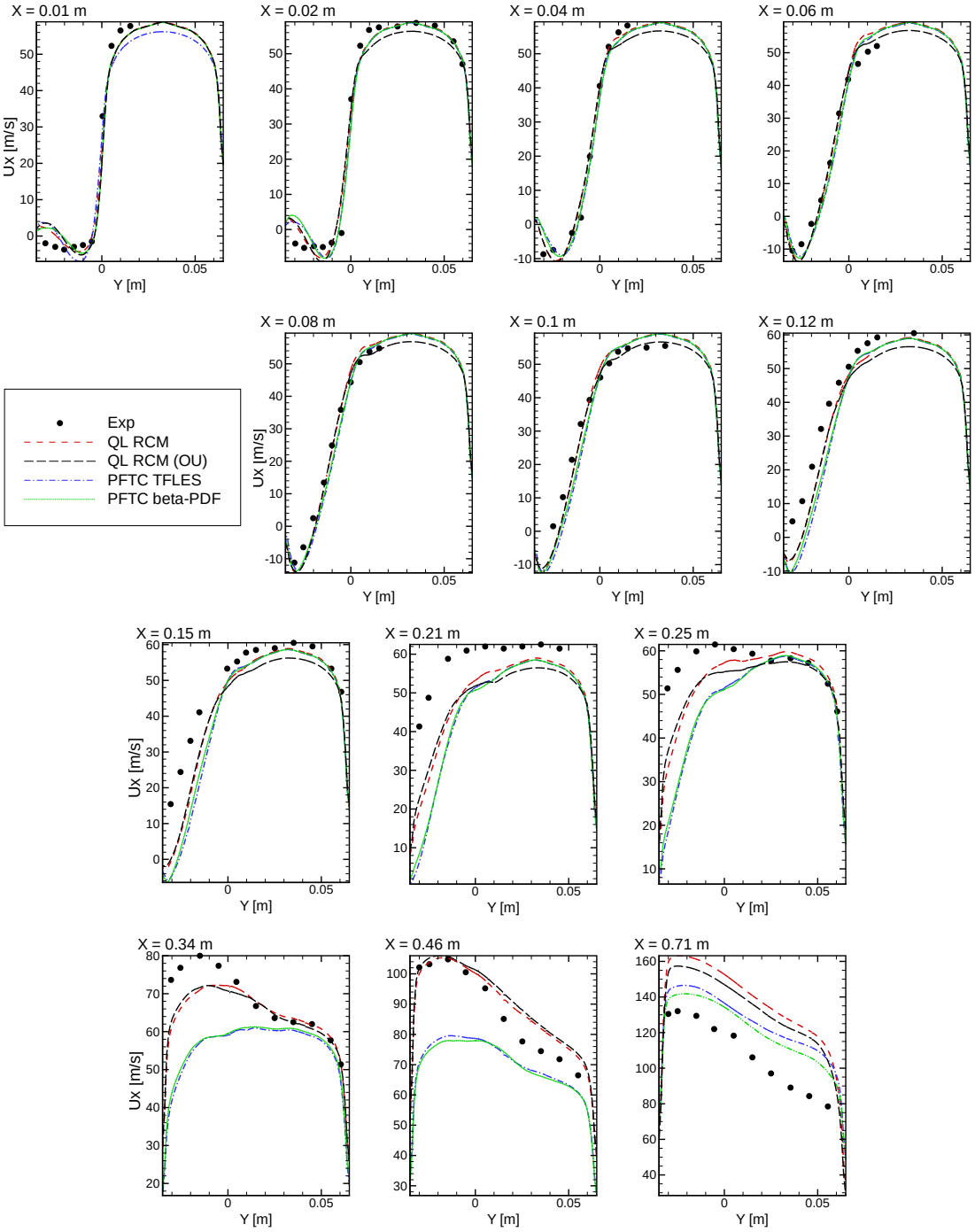

Figure 6.46: Vertical profiles of mean streamwise velocity $\langle \widetilde{u}_x \rangle$ in reactive backward-facing step flow; LES

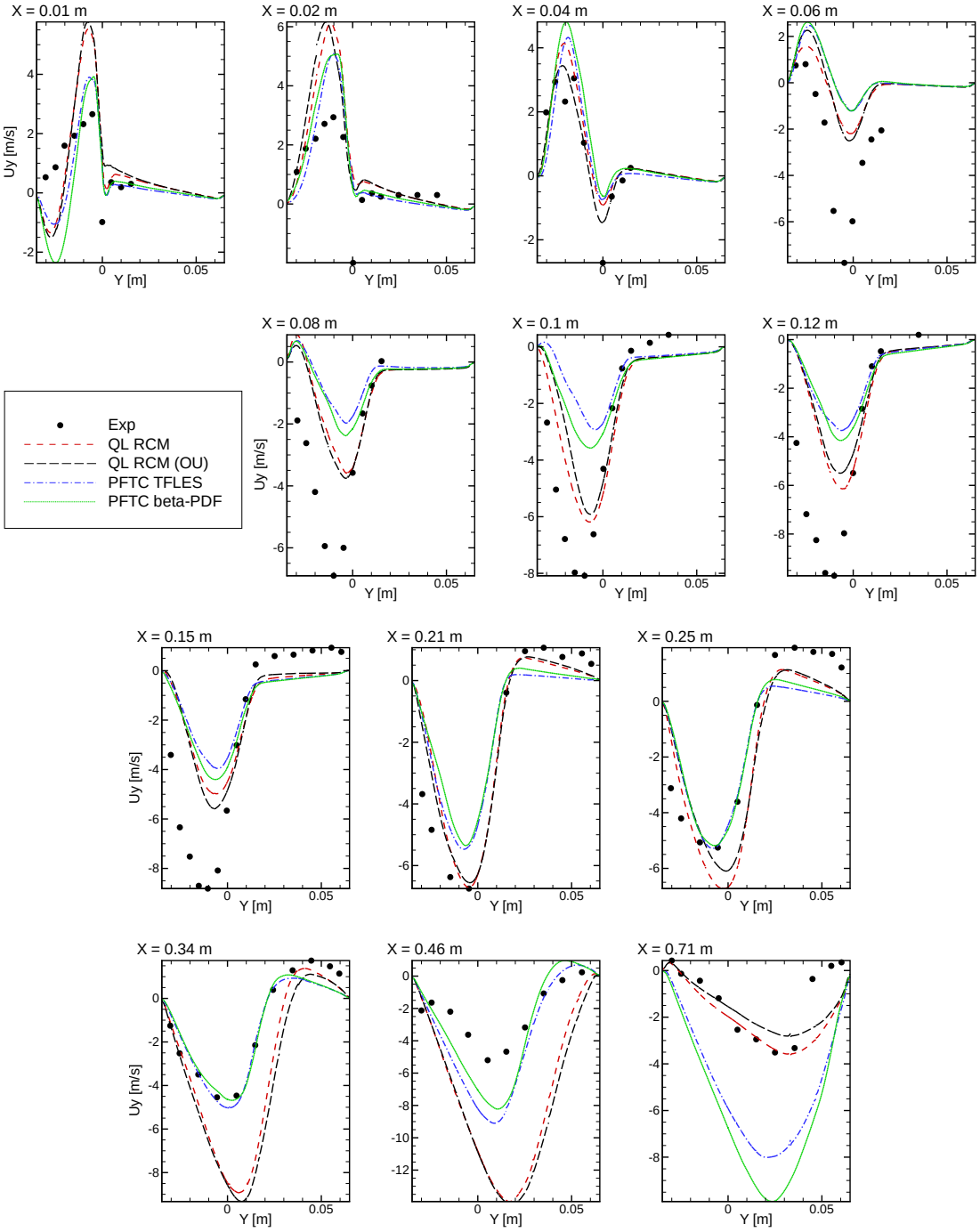

Figure 6.47: Vertical profiles of mean transverse velocity $\langle \widetilde{u}_y \rangle$ in reactive backward-facing step flow; LES

Mean mass fractions

To evaluate the influence of the tabulated chemistry let us consider vertical profiles of mean mass fractions of N_2, CO_2 and CO which can change the density, which in its turn affects the velocity profiles.

The mean mass fraction of the nitrogen obtained with the tabulated detailed chemistry remains close to the mean mass fraction of the nitrogen obtained with the quasi-laminar approach with the reduced chemical mechanism ($\langle\widetilde{Y}_{N_2}\rangle = 0.732\,65$). As we can see from fig. 6.48 the difference is less than 1%. The vertical profiles of the mean mass fractions of CO_2 in all the models are similar to each other for $X \leq 0.15\,\mathrm{m}$, while for $X > 0.15\,\mathrm{m}$ the tabulated detailed chemistry overestimate them by a factor of two in comparison with the reduced chemistry.

However, the vertical profiles of the mean mass fraction of CO calculated with PFTC noTCI and PFTC β-PDF are very different from each other and from the reduced chemical mechanism. Figure 6.49 shows the vertical profiles of $\langle\widetilde{Y}_{CO}\rangle$. We observe that in the lower part of the chamber PFTC β-PDF profiles of $\langle\widetilde{Y}_{CO}\rangle$ are close to those calculated with the reduced chemical mechanism, while PFTC TFLES model yields an overestimation by a factor of two. In the combustion region (i.e. close to the temperature isoline $\langle\widetilde{T}\rangle = 1500\,\mathrm{K}$), $\langle\widetilde{Y}_{CO}\rangle$ is three-four times overestimated by PFTC TFLES and twice by the PFTC β-PDF.

Such a behavior of the detailed chemistry model is expected. As the progress variable is based on mass fractions $\langle\widetilde{Y}_{CO}\rangle$ and $\langle\widetilde{Y}_{CO_2}\rangle$, the chemical source differs from the chemical source of the reduced chemistry and as a result, the fields of velocity are different as well.

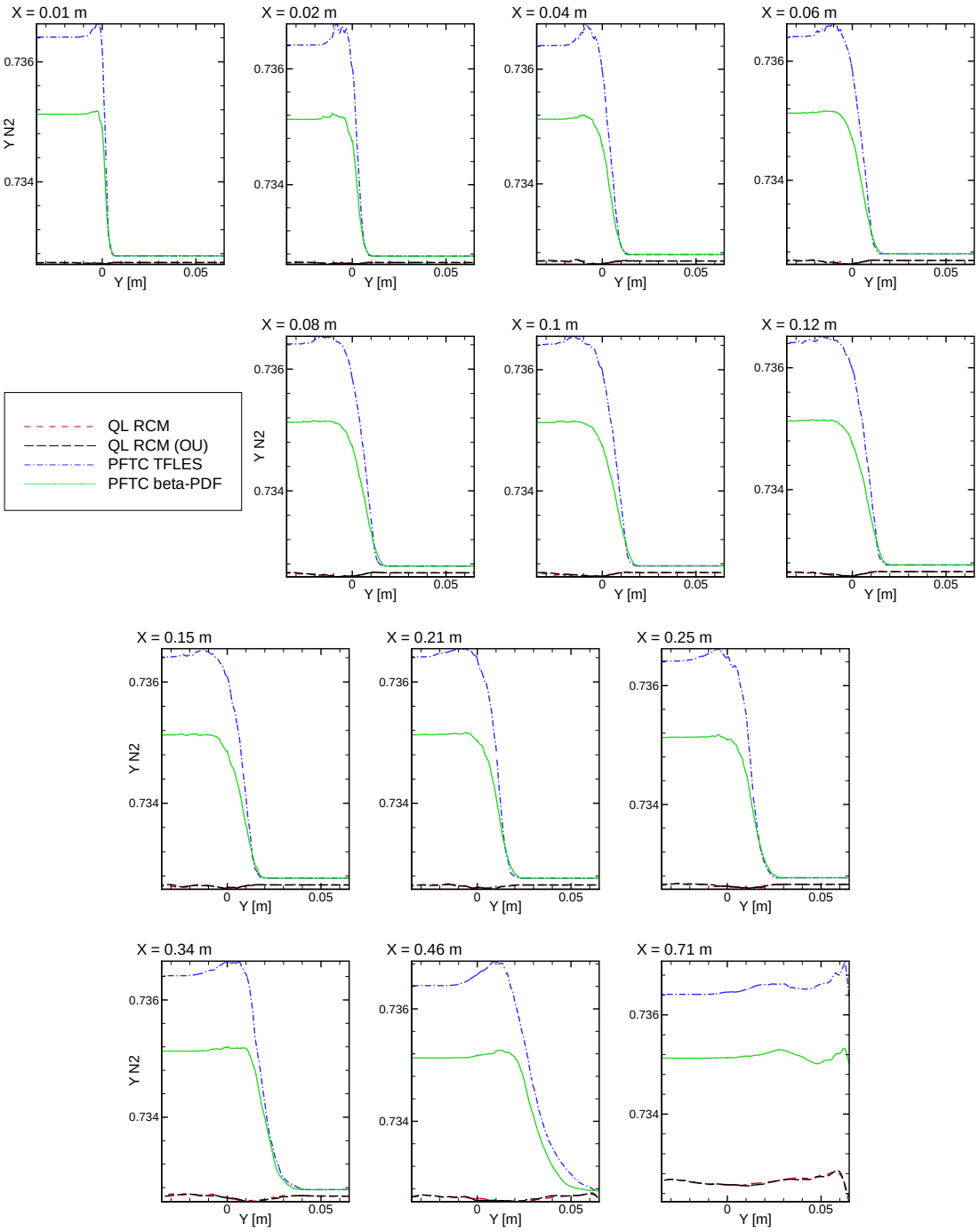

Figure 6.48: Vertical profiles of $\langle \widetilde{Y}_{N_2} \rangle$ in reactive backward-facing step flow; LES

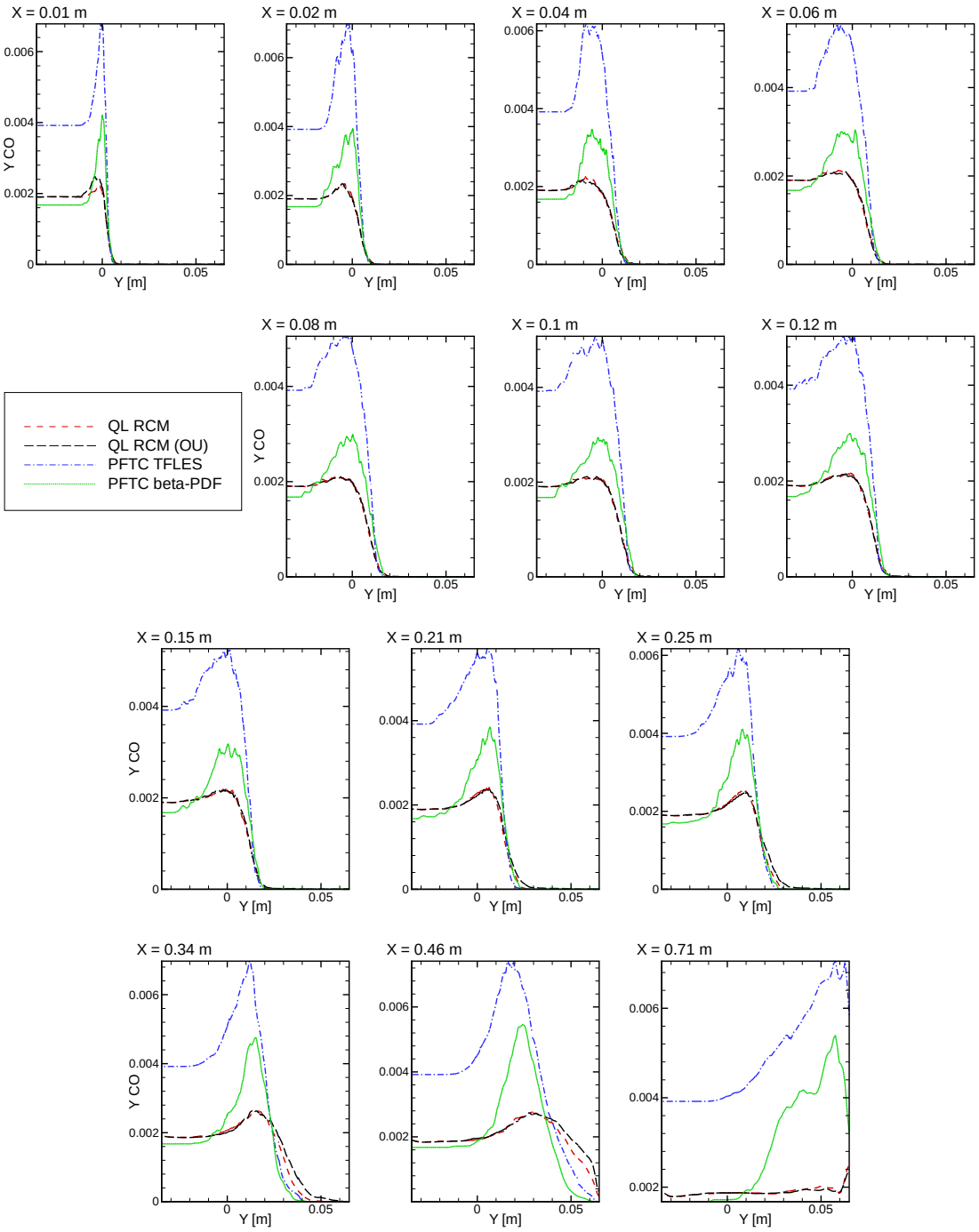

Figure 6.49: Vertical profiles of $\langle \widetilde{Y}_{\mathrm{CO}} \rangle$ in reactive backward-facing step flow; LES

Velocity fluctuations

Figures 6.50 and 6.51 show that the levels of numerical velocity fluctuations do not match those of the experiment. For example, in the lower part of the combustion chamber the longitudinal numerical velocity fluctuations are approximately three to four times overestimated with respect to the experimental profiles. Such the fluctuations are caused by intense eddies that are present in this region. Concerning the transverse velocity fluctuations, the numerical results are again four times greater than experimental data in the lower part of the chamber. The possible reason to justify such the discrepancy between the experiment and simulations is that the flow is controlled by numerical acoustics, and not by the turbulence.

The presence of numerical acoustic modes may cause a significant increase of velocity in the recirculation region, thus causing a strong flow deflection downwards. Therefore the negative velocities behind the step are high and vortices are intense. The resulting fluctuation levels of velocity are well above levels detected by the experiment, sometimes with an overestimation by a factor of 3. This trend progressively fades outside the recirculation zone.

Comparison of LES and RANS approaches The comparison of the RANS/TPaSR RMS velocity plotted in figs. 6.36 and 6.37 and the LES velocity fluctuations presented in figs. 6.50 and 6.51 shows that in the framework of the RANS due to the first order spatial scheme and coarse grid, the RMS velocity fluctuations follow the experimental data. This is not the case for the LES models.

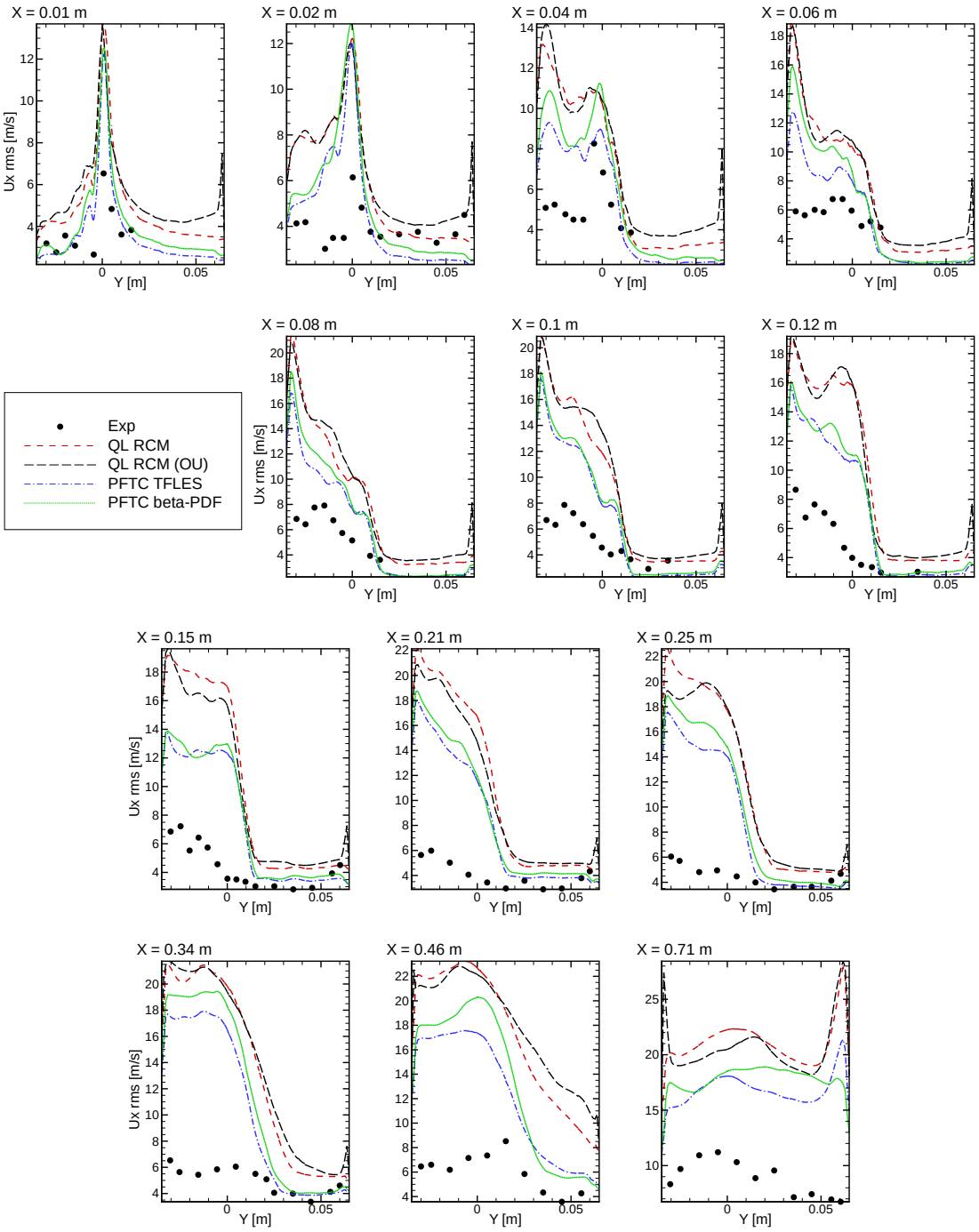

Figure 6.50: Vertical profiles of $\langle u_x^{RMS} \rangle$ in reactive backward-facing step flow; LES

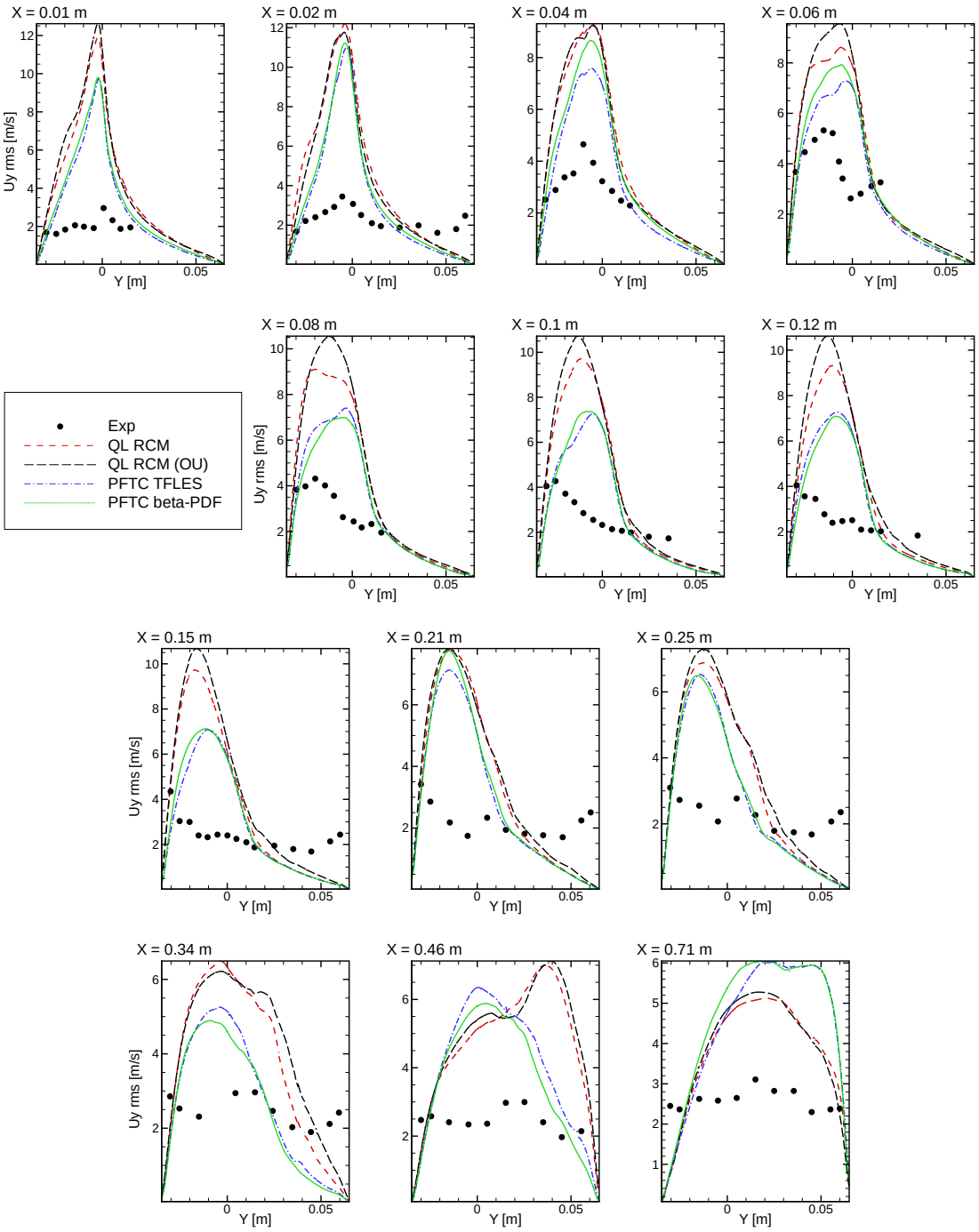

Figure 6.51: Vertical profiles of $\langle u_y^{RMS} \rangle$ in reactive backward-facing step flow; LES

Impact of reflecting boundary conditions

Currently the non-reflecting boundary conditions, which would allow evacuating numerical acoustic pressure waves from the computational domain, are not available in CEDRE. In the present work we use reflecting boundary conditions at inlet and outlet of the chamber. The inlet experimental condition enables the existence of the quarter wave acoustic mode. We emphasize that the numerical acoustic pressure waves induced by non-ideal reflecting conditions are different from physical acoustic waves. In addition, the computational domain represents only a part of the experimental setup. Furthermore, the acoustic characterization of experimental bench, required to impose the proper impedance conditions at inlet and outlet of the simulation domain, is not provided within the description of the experimental results.

In order to observe numerical acoustic pressure waves for four simulations, spectra of pressure, velocity and temperature at different positions in the chamber (see table 6.1) are considered. For instance, the temporal spectra of pressure and temperature for the LES/PFTC β-PDF model are plotted in figs. 6.52 to 6.56. The symbol F in figures means a Fourier transformation.

The development of large vortices in the shear layer is most likely related to the numerical longitudinal acoustic modes. The spectral analysis of signals of pressure and temperature at the point A seems to confirm this: the fundamental frequency is predominant. This result shows that near the step, the flame heat and flapping are indeed controlled by numerical acoustics. The fact that the spectra of temperature and pressure have a similar shape at the point A reflects a substantial coupling between the flame and the numerical acoustics.

One can note from figs. 6.52 to 6.56 that the pressure spectra evidence an important contribution of the fundamental frequency. The contribution of higher harmonics increase while moving downstream the flow. Such the observation confirms the presence of several numerical acoustic modes in the chamber, namely the quarter wave mode and its satellites (for example, the fundamental frequency of 180 Hz, and higher harmonics of 400 Hz and 650 Hz are visible on fig. 6.56). These frequencies can be reasonably compared to those given by the analytical expression:

$$f_n = \frac{nc}{4L_x} \tag{6.17}$$

where n is an integer number, c is the speed of sound in the chamber and L_x is the chamber length. The speed of sound in fresh gas is about 461 m/s and in burnt gas is about 909 m/s. The average speed of sound in the chamber is roughly 830 m/s. As a consequence, one can deduce from eq. (6.17) that

$$f_1 = 188\,\text{Hz},\ \ f_2 = 376\,\text{Hz},\ \ f_3 = 564\,\text{Hz}. \tag{6.18}$$

In all the figures (some of them are omitted here) the peaks representing numerical quarter-wave harmonics are visible. However, it may happen that the energy is mainly condensed in higher harmonics (see for instance fig. 6.53). These results are similar to those obtained in [SainteRose2010].

The spectra of temperature and transverse velocity (not presented here) are similar at D and E points, which indicates that the downstream flow is likely to be controlled by turbulence. On the temperature spectra at B, C, D and E points, we see that the spectrum

remains non-zero in a rather long frequency interval, i.e. that eddies of different sizes are generated. Furthermore, the amplitude of spectra decreases in the downstream, which reflects reduction in eddies energy.

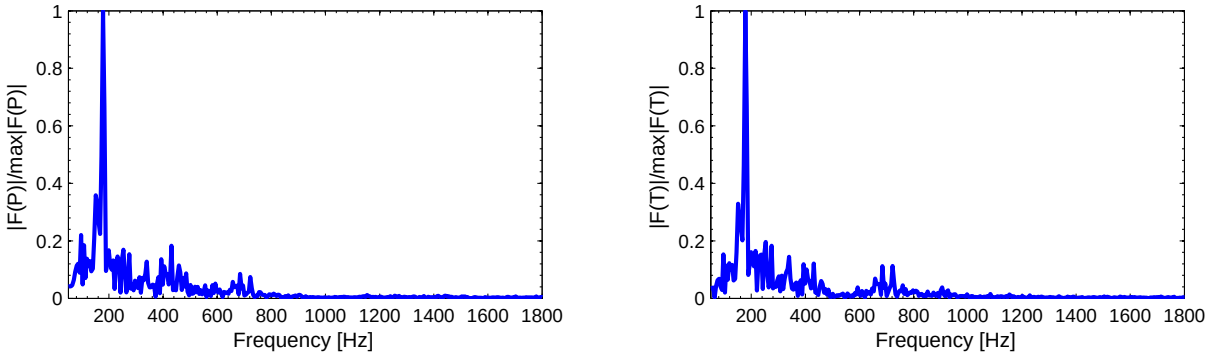

Figure 6.52: Spectra of pressure (left) and temperature (right) at point A in reactive backward-facing step flow; LES/PFTC β-PDF

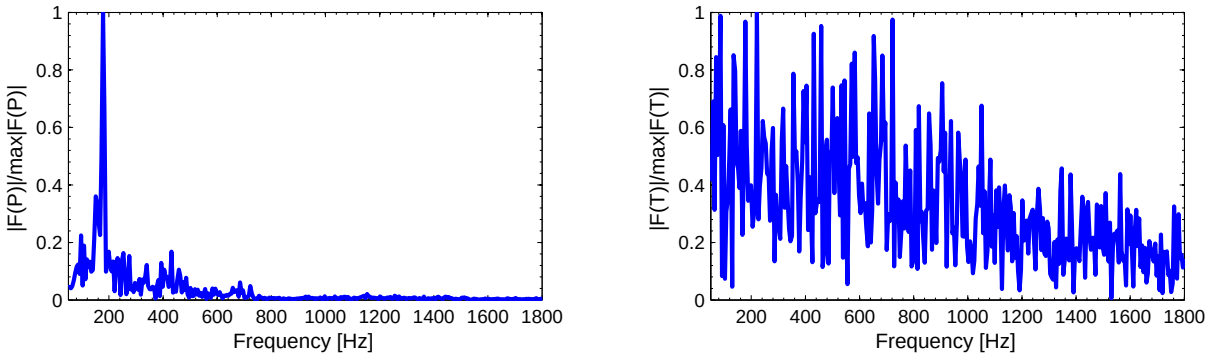

Figure 6.53: Spectra of pressure (left) and temperature (right) at point B in reactive backward-facing step flow; LES/PFTC β-PDF

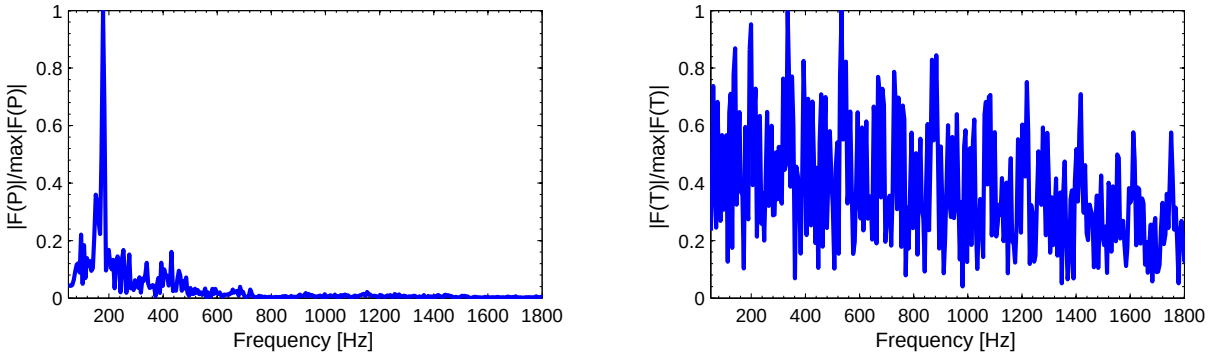

Figure 6.54: Spectra of pressure (left) and temperature (right) at point C in reactive backward-facing step flow; LES/PFTC β-PDF

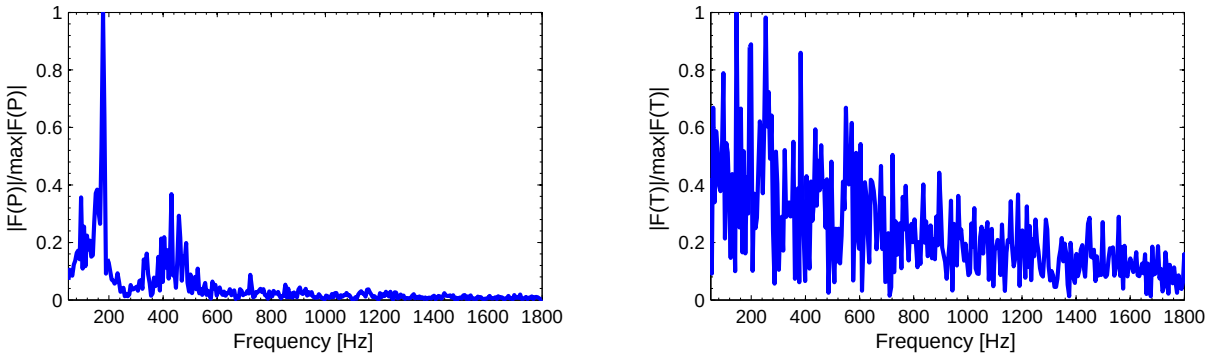

Figure 6.55: Spectra of pressure (left) and temperature (right) at point D in reactive backward-facing step flow; LES/PFTC β-PDF

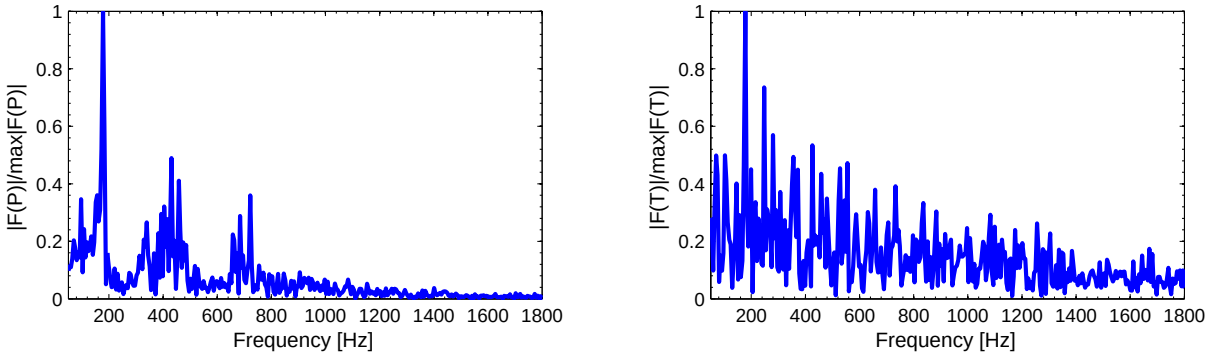

Figure 6.56: Spectra of pressure (left) and temperature (right) at point E in reactive backward-facing step flow; LES/PFTC β-PDF

6.4.7 Conclusions

Different combustion models, namely the quasi-laminar approach with the reduced chemical mechanism (QL RCM), the PFTC β-PDF model, the PFTC TFLES are applied for LES of the turbulent methane/air combustion behind the backward-facing step. Synthesized inlet velocity fluctuations are used to generate incoming turbulence.

Analysis of numerical results shows that the reflecting boundary conditions used in CEDRE for inlet and outlet of the chamber significantly impact the obtained solutions independently on the QL RCM, the PFTC β-PDF and the PFTC TFLES models. The numerical pressure fluctuations dominate over the velocity fluctuations and alter the averaged fields of the velocity and the temperature. In addition, the unsteady synthesized inlet velocity profiles do not improve results. These results confirm the conclusion of the previous work [Courtois2005]. R. Courtois showed that in the code AVBP CERFACS the use of reflecting boundary conditions generated numerical acoustic pressure waves, while the use of non-reflecting boundary conditions (not yet implemented into CEDRE) allowed evacuating the numerical acoustic waves and obtaining the mean temperature, velocity and velocity fluctuations fields in satisfactory agreement with the experiment data.

The comparison of the obtained numerical results with the experimental measurements shows that the divergence between numerical and experimental velocity profiles is mainly due to the recirculation region overestimation which is 40% in the QL RCM approach and 60% in the PFTC β-PDF and the PFTC TFLES models. The QL RCM, the PFTC β-PDF and the PFTC TFLES models give practically the same results for the mean temperature. For example (see fig. 6.42), at $X = 0.34\,\mathrm{m}$, the mean experimental temperature is better approximated by the QL RCM approach, while at $X = 0.46\,\mathrm{m}$ by the PFTC β-PDF and the PFTC TFLES models.

6.5 Conclusions

The $k - l$ and $k - \omega$ turbulence models are used in RANS calculations of turbulent non-reactive backward-facing step flow. The results are compared with the experimental data [MagreMoreau1988]. It is shown that the $k - l$ turbulence model with nonhomogeneous inlet profiles yields the most accurate recirculation region estimation for the nonreactive flow.

The quasi-laminar approach with the reduced chemical mechanism (QL RCM), the premixed flamelet chemistry model without turbulence-chemistry interaction (PFTC noTCI), the PFTC model with a presumed β-PDF (PFTC β-PDF) and the transported partially stirred reactor with the reduced chemical mechanism (TPaSR) in the framework of RANS are applied to simulate the reactive flow behind the step combustor. In LES the QL RCM, the PFTC β-PDF and the PFTC TFLES are used. Obtained results are analyzed and compared with the available experimental data [MagreMoreau1988].

The RANS/TPaSR model with the subgrid residence time defined as the geometrical mean of the Kolmogorov time and the integral time scale (5.23) gives the best result among all the considered models and has good agreement with experimental measurements.

The LES/QL RCM, the LES/PFTC β-PDF and the PFTC TFLES give practically the same results. It is found that reflecting boundary conditions do not allow evacuating numerical acoustic waves in the LES. As a consequence they impact the calculated solutions

independently on the considered model. Therefore, it is difficult to evaluate a behavior of the LES/QL RCM, the LES/PFTC β-PDF and the PFTC TFLES models.

A further study of these models should be performed with non-reflecting boundary conditions. It will allow clearly seeing advantages and disadvantages of the LES/PFTC β-PDF and the PFTC TFLES approaches.

Chapter 7

Conclusions and future work

7.1 Conclusions

In the present work we studied different approaches for modeling the TCI. The first part of the thesis is devoted to the presentation of the numerical method to solve the SPDEs statistically equivalent to the one-time one-point joint velocity-scalars PDF transport equation. These SPDEs are quasi-linear hyperbolic PDEs, therefore they can have multivalued solutions. It is shown that in order to preserve the equivalence between the SPDEs and the PDF equation, it is necessary to take into account the multivalued solutions. The classical numerical schemes satisfying the entropy increase condition are not appropriated to solve the SPDEs because they are dissipative and do not capture the multivalued solutions.

A new stochastic method proposed by O. Soulard [EmakoLetizia2014] is applied to solve the SPDEs. It permits to recover the multivalued solutions of the SPDEs in the statistical sense. Numerical schemes for the SPDEs statistically equivalent to the transport equation for the one-time one-point velocity PDF are implemented and several validation tests are performed in one-dimensional case. Velocity moments and PDF are compared with analytical or numerical solutions of the PDF equation, and good agreement is found.

Numerical accuracy issues are investigated, and in particular statistical and spatial errors are studied. Depending on a test-case, the spatial discretization order of convergence varies from -0.5 to -1 with respect to the number of cells, the number of stochastic fields and considered time interval, while the expected theoretical order of convergence is -1. The statistical order of convergence is also found to be dependent on the spatial discretization, time interval and test-case. In general, the order of convergence fluctuates around -0.5 and decreases with time to -0.3.

Since the solution of the SPDEs remains time consuming, in the second part of the thesis we consider standard turbulent combustion approaches such as the FTC model with a presumed β-PDF and the TPaSR model in the framework of RANS and LES. The TPaSR model is adapted to a low Mach number combustion and implemented into the ONERA industrial code CEDRE. In parallel, the FTC model based on the presumed β-PDF is modified from its original version implemented by J. Savre [Savre2010]. The semi-analytic β integration method [LienLiu2009] is extended from one variable (mixture fraction) to two variables case (mixture fraction variable and progress variable). This modification permits to overcome boundary singularities in integration of the β-PDF over the mixture fraction

and the progress variables.

Different models, including the TPaSR, the quasi-laminar with reduced chemical mechanism, the FTC without TCI and the FTC with the presumed β-PDF models are applied to the reactive backward-facing step flow, experimentally studied by [MagreMoreau1988]. The RANS/TPaSR with a $k-l$ turbulence model has a good agreement with experimental data and is closer to the experimental profiles of Favre-averaged temperature and velocity than other considered models. Due to the difficulties linked with numerical convergence towards a stationary field, only the first order spatial scheme is used in the framework of the RANS.

Within the LES, numerical acoustic pressure waves do not dissipate and impact averaged fields of temperature, velocity and velocity fluctuations. We can conclude that reflecting boundary conditions which are only currently available in CEDRE have to be improved. Because of this difficulty it was impossible to validate the flame front calculated by the LES/PFTC with the presumed β-PDF, the PFTC noTCI/TFLES and the quasi-laminar with reduced chemical mechanism models. Concerning the LES/TPaSR model, it is shown that the numerical solution depends strongly on the mesh size. We expect that using non-reflecting boundary conditions and a fine mesh would allow a more precise flame calculation.

7.2 Future work

7.2.1 SPDEs

It would be of interest to explore the capabilities of the proposed EMC method of solving reactive flows in complex real-life geometries defined by multi-block grids (both structured and non-structured). The Eulerian character of EMC methods makes it more suited (than LMC methods) for tackling these issues. One can expect that the development of more efficient algorithms LES/EMC may become a powerful instrument for gas turbine industry.

7.2.2 TPaSR model

The adaptation and the integration into CEDRE of the TPaSR model opens new perspectives. Firstly it should be extended to the general case of subsonic and supersonic flows. This can be performed by resolving the set of transport equations for the fine structure regions and its surrounding with a multiphase flow solver.

Numerical simulations show that the LES/TPaSR model is sensible to the computational mesh size due to the definition of the fine structure residence time based on the cell size. It would be interesting to continue the research of the fine structure residence time in the framework of the LES and validate the TPaSR model on the configuration of the backward-facing step combustor.

These approaches should be evaluated in the frameworks of the RANS and the LES against existing combustion models for high Reynolds number turbulent premixed flames and compared with experimental data.

The extension of the model to non-premixed flames should also be considered. Different methods to calculate the chemical characteristic time must be appropriated. It can be the tabulated chemical time widely used in the field of the turbulent combustion, such as in the non-premixed turbulent combustion in high-speed flows [IzardLehnasch2009].

7.2.3 FTC with presumed beta-PDF model

It should be noted that the large choice of modeling sources in the transport equation for a progress variable variance, does not allow determining the best closure using only a configuration of the backward-facing step. Therefore, it is necessary to continue studying behavior of the presumed β-PDF for premixed flames on other configurations. In addition, it will be interesting to recalculate the reactive backward-facing step flow with non-reflecting boundary conditions at inlet and outlet of the chamber.

It would be interesting to investigate different non-premixed flames where it is possible to use the presumed β-PDF for two variables: mixture fraction and progress variable in order to validate a semi-analytical method of the β-function integration for two variables. Moreover, the idea of piece-wise reconstruction method can be extended for other presumed PDFs.

Appendix A

Some aspects of SPDEs modelling

A.1 Random choice method (RCM) for solution satisfying entropy increase condition

According to the book [Toro1999] the initial problem for hyperbolic conservation laws in one space variable is

$$\frac{\partial \boldsymbol{q}}{\partial t} + \frac{\partial \boldsymbol{F}(\boldsymbol{q})}{\partial x} = 0, \tag{A.1}$$

$$\boldsymbol{q}(t,x) = \boldsymbol{q} : \mathbb{R}^+ \times \mathbb{R} \to \mathbb{R}^N, \tag{A.2}$$

$$\boldsymbol{q}(0,x) = \boldsymbol{q}_0(x), \tag{A.3}$$

where the flux function $\boldsymbol{F} : \mathbb{R}^N \to \mathbb{R}^N$ is a continuous function with its two fist derivatives satisfying the condition that the Jacobian matrix

$$D_q \boldsymbol{F} = A(\boldsymbol{q}) \tag{A.4}$$

has N real distinct right eigenvalues

$$\lambda_1(\boldsymbol{q}) < \lambda_2(\boldsymbol{q}) ... < \lambda_N(\boldsymbol{q}) \tag{A.5}$$

known as the characteristic velocities. The function $\boldsymbol{q}_0 : \mathbb{R} \to \mathbb{R}^N$ is the given initial data. For example, Euler's equations for the one-dimensional motion of an ideal compressible gas are a system of hyperbolic conservation laws.

A domain $[0,T] \times [0,L]$ in the $t-x$ plane is discretized as shown in fig. A.1. The spatial domain of length L is subdivided into N_x finite volumes, called computing cells $I_i = [x_{i-1/2}, x_{i+1/2}]$ of size $\Delta x = x_{i+1/2} - x_{i-1/2}$, with $i = 1, ..., N_x$. For simplicity we assume regular meshes.

We suppose also that at any time the solution has a piece-wise constant distribution illustrated in fig. A.2. The solution may be locally seen as a pair of constant states $(\boldsymbol{q}_i^n, \boldsymbol{q}_{i+1}^n)$ separated by a discontinuity situated at the intercell boundary $x_{i+1/2}$. A local Riemann problem $RP(\boldsymbol{q}_i^n, \boldsymbol{q}_{i+1}^n)$ can be written as

$$\frac{\partial \boldsymbol{q}}{\partial t} + \frac{\partial \boldsymbol{F}(\boldsymbol{q})}{\partial x} = 0 \tag{A.6}$$

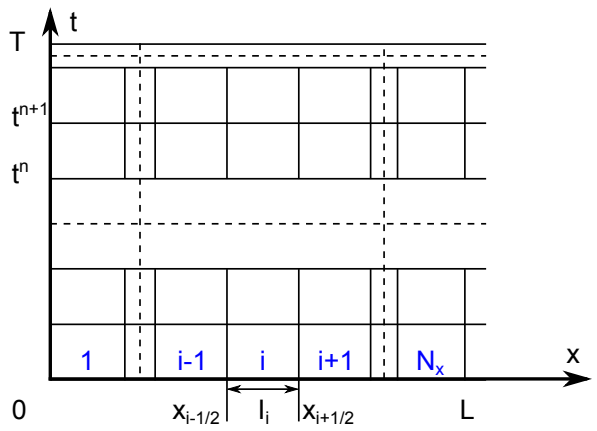

Figure A.1: Discretization of $[0, L]$ interval into N_x finite volumes

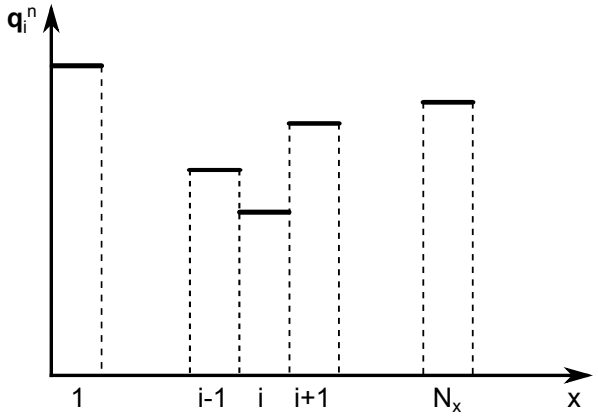

Figure A.2: Piece-wise constant distribution of the solution at time t^n

with the initial condition

$$\boldsymbol{q}(x,0) = \boldsymbol{q}_0(x) = \begin{cases} \boldsymbol{q}_i^n & \text{if } x < 0, \\ \boldsymbol{q}_{i+1}^n & \text{if } x > 0. \end{cases} \tag{A.7}$$

At each given time step t^n and each intercell boundary $x_{i+1/2}$ eqs. (A.6) and (A.7) define a local Riemann problem, which can be solved either numerically or analytically. Based on that, a solution of the global problem for time index $n+1$ can be constructed.

The RCM updates the solution from the data value $\boldsymbol{q}_i^n$ in cell I_i at time level n, to the value $\boldsymbol{q}_i^{n+1}$ at time level $n+1$, in two steps as follows:

1. Solve the Riemann problems $RP(\boldsymbol{q}_{i-1}^n, \boldsymbol{q}_i^n)$ and $RP(\boldsymbol{q}_i^n, \boldsymbol{q}_{i+1}^n)$ to find their respective solutions $\boldsymbol{q}_{i-1/2}(x/t)$ and $\boldsymbol{q}_{i+1/2}(x/t)$. Figure A.3 shows typical wave patterns emerging from intercell boundaries $x_{i-1/2}$ and $x_{i+1/2}$.

2. Random sample the obtained solutions at time Δt within cell I_i to pick up a state and

assign to cell I_i:

$$\boldsymbol{q}_i^{n+1} = \begin{cases} \boldsymbol{q}_{i-1/2}(\theta^n \Delta x/\Delta t), & \text{if } 0 \le \theta^n \le \frac{1}{2}, \\ \boldsymbol{q}_{i+1/2}((\theta^n - 1)\Delta x/\Delta t), & \text{if } \frac{1}{2} < \theta^n \le 1. \end{cases} \tag{A.8}$$

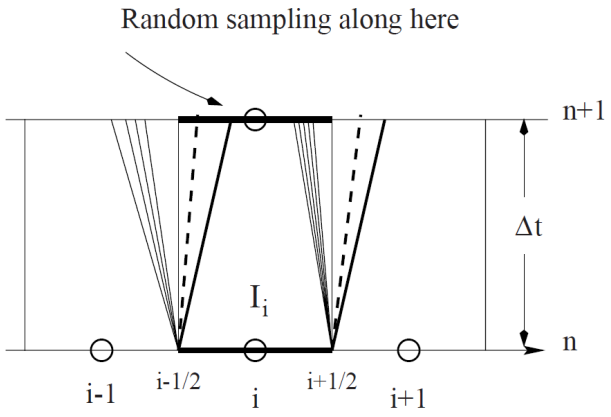

Figure A.3: Random choice method: solution is updated to t^n by random sampling of Riemann problem solution at I_i cell. The random sampling is represented by thick horizontal line.

The case in which $0 \le \theta^n \le \frac{1}{2}$ is detailed in fig. A.4. The updated solution depends on the random sampling procedure applied to the right side of the left Riemann problem solution $\boldsymbol{q}_{i-1/2}(x/t)$.

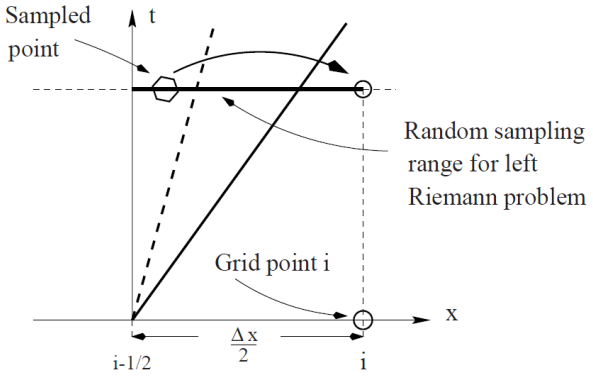

Figure A.4: RCM sampling of the RHS of the left Riemann problem solution with $0 \le \theta^n \le \frac{1}{2}$. Sampled state is assigned to the center of I_i cell.

The RCM is not strictly conservative, but only conservative in a statistical sense. In such a method no spreading of a discontinuity is possible. The Godunov method takes an integral average of local solutions of Riemann problems, while the RCM randomly picks a single state, contained in the local solutions. The main property of these methods is that the solution satisfies the entropy increase condition and the solution is unique in space and in time.

A.2 Stochastic Runge-Kutta method

We adapt here the second order Runge-Kutta scheme to solve numerically the PDEs (3.22) and (3.23).

PDF. At the midpoint $t^{n+1/2}$ of a time interval the discretized PDF equation (3.2) is

$$\overline{\rho}_j^{n+1/2}\widetilde{f}_j^{n+1/2} = \overline{\rho}_j^n \widetilde{f}_j^n - \Delta t^n \left[\frac{\partial \overline{\rho} V \widetilde{f}}{\partial x}\right]^n . \tag{A.9}$$

At time t^{n+1} we deduce that

$$\overline{\rho}_j^{n+1}\widetilde{f}_j^{n+1} = \alpha \overline{\rho}_j^n \widetilde{f}_j^n + \beta \left(\overline{\rho}_j^{n+1/2}\widetilde{f}_j^{n+1/2} - \Delta t^n \left[\frac{\partial \overline{\rho} V \widetilde{f}}{\partial x}\right]^{n+1/2} \right), \tag{A.10}$$

where α and β are some positive coefficients such as $\alpha + \beta = 1$.

Stochastic process. The stochastic process (r^*, u^*) given by (3.57) can be interpreted in two-steps scheme: at the midpoint $t^{n+1/2}$ the stochastic process $(r^{*n+1/2}, u^{*n+1/2})$ is found by any of the space schemes proposed in sections 3.2.1 to 3.2.1. At time t^{n+1} with probability α the stochastic process (r^{*n+1}, u^{*n+1}) is calculated using (r^{*n}, u^{*n}) and with probability β using the data of $(r^{*n+1/2}, u^{*n+1/2})$. For example, if we consider a stochastic Lax-Friedrichs method the stochastic process (r^*, u^*) can be written at time $t^{n+1/2}$ as

$$u_j^{*n+1/2} = \begin{cases} u_{j+1}^{*n}, & \text{with probability } P_j^{+1}, \\ u_{j-1}^{*n}, & \text{with probability } P_j^{-1} = 1 - P_j^{+1}. \end{cases} \tag{A.11}$$

$$P_j^{+1} = \frac{1}{2}\frac{r_{j+1}^{*n}}{r_j^{*n+1/2}}\left(1 - \frac{\Delta t^n}{\Delta x} u_{j+1}^{*n}\right), \qquad P_j^{-1} = 1 - P_j^{+1}, \tag{A.12}$$

$$r_j^{*n+1/2} = r_j^{*n} - \frac{\Delta t^n}{\Delta x}\left(F_{j+1/2}^n - F_{j-1/2}^n\right), \tag{A.13}$$

where

$$F_{j+1/2}^n = \frac{r_j^{*n}u_j^{*n} + r_{j+1}^{*n}u_{j+1}^{*n}}{2} - \frac{\Delta x}{2\Delta t^n}\left(r_{j+1}^{*n} - r_j^{*n}\right). \tag{A.14}$$

After the step $n+1/2$ a random number η uniformly distributed on interval $(0, 1)$ is generated. Let us suppose that $\alpha \leq \beta = 1 - \alpha$. If $\eta < \alpha$ then (r_j^{*n+1}, u_j^{*n+1}) is calculated using $(r^{n^*}, u^{n^*}) = (r^{*n}, u^{*n})$ or with $(r^{n^*}, u^{n^*}) = (r^{*n+1/2}, u^{*n+1/2})$:

$$u_j^{*n+1} = \begin{cases} u_{j+1}^{n^*}, & \text{with probability } P_j^{+1}, \\ u_{j-1}^{n^*}, & \text{with probability } P_j^{-1} = 1 - P_{irea,j}^{+1}. \end{cases} \tag{A.15}$$

$$P_j^{+1} = \frac{1}{2}\frac{r_{j+1}^{n^*}}{r_j^{*n+1}}\left(1 - \frac{\Delta t^n}{\Delta x} u_{j+1}^{n^*}\right), \qquad P_{irea,j}^{-1} = 1 - P_j^{+1}, \tag{A.16}$$

$$r_j^{*n+1} = r_j^{n^*} - \frac{\Delta t^n}{\Delta x}\left(F_{j+1/2}^{n^*} - F_{j-1/2}^{n^*}\right), \tag{A.17}$$

where

$$F_{j+1/2}^n = \frac{r_j^{n^*}u_j^{n^*} + r_{j+1}^{n^*}u_{j+1}^{n^*}}{2} - \frac{\Delta x}{2\Delta t^n}\left(r_{j+1}^{n^*} - r_j^{n^*}\right). \tag{A.18}$$

Numerical definitions of stochastic density and velocity should be applied to each external realization $ir = 1, .., N_\eta$ and each inner realization $irea = 1, .., N_r$.

A.3 Schemes for SPDEs statistically equivalent to the joint velocity-scalar PDF equation

Let us consider a transport equation for the Favre joint fluctuating velocity $u = u''$ - scalar ϕ PDF $\widetilde{g}(V, \psi; t, x)$ in one-dimensional case. For simplification we assume that Favre-averaged velocity is identically zero $\widetilde{u} \equiv 0$:

$$\frac{\partial \overline{\rho}\widetilde{g}}{\partial t} + \frac{\partial \overline{\rho}V''\widetilde{g}}{\partial x} = -\frac{\partial}{\partial V''}\left(\frac{\partial}{\partial x}\left(\overline{\rho}\widetilde{u''^2}\right)\widetilde{g}\right) - \frac{\partial \overline{\rho}C_1\omega V''^2}{\partial V''} + \frac{1}{2}\overline{\rho}C_0\varepsilon\frac{\partial^2\widetilde{g}}{\partial V''^2} + \frac{\partial}{\partial \psi}\left(\overline{\rho}C_\psi\omega(\psi - \widetilde{\phi})\widetilde{g}\right), \tag{A.19}$$

where ψ and V'' are respectively the sample space of scalar $c(t, x)$ and fluctuating velocity $u''(t, x)$. The SPDEs which are statistically equivalent to the joint fluctuating velocity-scalar PDF $\widetilde{g}$ from eq. (A.19) are

$$\frac{\partial ru''}{\partial t} + \frac{\partial ru''^2}{\partial x} = \frac{r}{\overline{r}}\frac{\partial \overline{ru''^2}}{\partial x} - rC_1\omega u'' + r\sqrt{C_0\varepsilon}\dot{\xi}(t), \tag{A.20}$$

$$\frac{\partial rc}{\partial t} + \frac{\partial ru''c}{\partial x} = -rC_c\omega\left(c - \widetilde{c}\right), \tag{A.21}$$

$$\frac{\partial r}{\partial t} + \frac{\partial ru''}{\partial x} = 0, \tag{A.22}$$

where $\varepsilon = \omega\widetilde{u''^2}$, c and u'' are stochastic scalar and fluctuating velocity.

The stochastic process for eqs. (A.20) and (A.22) is given in section 3.2.2. Using also a physical (or differential) splitting method, Euler scheme in time, we can add the following resolutions allowing establishing the concentration for the global step defined in section 3.2.2.

1. We start to solve the following PDE:

$$\frac{\partial rc}{\partial t} + \frac{\partial ru''c}{\partial x} = 0, \tag{A.23}$$

with initial conditions at time t^n:

$$IC : c(t^n, x). \tag{A.24}$$

The stochastic scalar $c^*(t, x)$ is calculated by the same procedure that the stochastic velocity $u''^*(t, x)$ at time $t^{n+1/4}$.

3. The micromixing and Langevin terms of eqs. (A.20) and (A.21) are now added to the calculated variables. Equation for the concentration yields

$$\frac{\partial c}{\partial t} = -C_c \omega \left(c - \widetilde{c}\right), \tag{A.25}$$

$$IC : c^*(t^{n+2/4}, x) = c^*(t^{n+1/4}, x). \tag{A.26}$$

Numerical scheme reads

$$c^{*n+3/4} = c^{*n+2/4} - C_0 \omega^n (c^{*n+2/4} - \widetilde{c^{*n+2/4}}) \Delta t. \tag{A.27}$$

Obtained solution for scalar $c^*(t^{n+3/4}, x)$ is a finite value for the time t^{n+1}, i.e. $c^*(t^{n+1}, x) = c^*(t^{n+3/4}, x)$.

A.4 n dimensional space schemes for PDEs

The idea of the numerical scheme in n dimensions space is the same that in one-dimensional case.

PDF. Let us consider, for example, Godunov scheme in three-dimensional space. Let be $\boldsymbol{V} = (V_1, V_2, V_3) \in \mathbb{R}^3$ is a sample space for velocity $\boldsymbol{u}(t, \boldsymbol{x}) = (u_1(t, \boldsymbol{x}), u_2(t, \boldsymbol{x}), u_3(t, \boldsymbol{x})) \in \mathbb{R}^3$, where $\boldsymbol{x} = (x_1, x_2, x_3) \in \mathbb{R}^3$ is a space variable. The transport equation for the PDF $\widetilde{f}_{\boldsymbol{u}}(\boldsymbol{V}; t, \boldsymbol{x})$ denoted as $\widetilde{f}$ is

$$\frac{\partial \overline{\rho} \widetilde{f}}{\partial t} + V_1 \frac{\partial \overline{\rho} \widetilde{f}}{\partial x_1} + V_2 \frac{\partial \overline{\rho} \widetilde{f}}{\partial x_2} + V_3 \frac{\partial \overline{\rho} \widetilde{f}}{\partial x_3} = 0. \tag{A.28}$$

The eq. (A.28) can be solved directly or with coordinate splitting method. To be specific, let us consider here the second option. In this approach one applies one-dimensional Godunov methods in each coordinate direction, which yields first order temporal and spatial accuracy. The sweep in the x_1 direction of eq. (A.28) gives

$$\frac{\partial \overline{\rho} \widetilde{f}}{\partial t} + V_1 \frac{\partial \overline{\rho} \widetilde{f}}{\partial x_1} = 0. \tag{A.29}$$

The initial condition (IC) for this problem (A.29) is the initial data for the original full problem (A.28)

$$IC : \overline{\rho}^n, \widetilde{f}^n, \tag{A.30}$$

where the index n signifies n-temporal step, i.e. $\overline{\rho}^n = \overline{\rho}(t^n, \boldsymbol{x})$ and $\widetilde{f}^n = \widetilde{f}(t^n, \boldsymbol{x})$.

In order to solve numerically eq. (A.29), we introduce the following parameters of the simulation. The computational domain $[x_1^{\min}; x_1^{\max}] \times [x_2^{\min}; x_2^{\max}] \times [x_3^{\min}; x_3^{\max}]$ is discretized with $N_{x_1} \times N_{x_2} \times N_{x_3}$ points. Spatial steps Δx_i is uniform in each direction x_i, $i = 1, 2, 3$, points of the grid are $x_{j,k,l} = (x_1^{\min} + (j-1)\Delta x_1;\ x_2^{\min} + (k-1)\Delta x_2;\ x_3^{\min} + (l-1)\Delta x_3)$, where $j = 1, .., N_{x_1}$, $k = 1, .., N_{x_2}$ and $l = 1, .., N_{x_3}$.

Applying Godunov scheme to the eq. (A.29), we deduce

$$\overline{\rho}_{j,k,l}^{n+1/3}\widetilde{f}_{j,k,l}^{n+1/3} = \overline{\rho}_{j,k,l}^{n}\widetilde{f}_{j,k,l}^{n} + \frac{\Delta t^n}{\Delta x_1}\left(|V_1|\overline{\rho}_{j,k,l}^{n}\widetilde{f}_{j,k,l}^{n} + V_1^{-}\overline{\rho}_{j+1,k,l}^{n}\widetilde{f}_{j+1,k,l}^{n} - V_1^{+}\overline{\rho}_{j-1,k,l}^{n}\widetilde{f}_{j-1,k,l}^{n}\right), \tag{A.31}$$

$$IC : \overline{\rho}^n, \widetilde{f}^n, \tag{A.32}$$

V_1^- and V_1^+ are defined as in (3.85). The solution of eqs. (A.31) and (A.32) after a time Δt^n is denoted by $\overline{\rho}^{n+1/3}, f^{n+1/3}$.

The sweep in x_2 direction of eq. (A.28) is given by

$$\frac{\partial \overline{\rho}\widetilde{f}}{\partial t} + V_2\frac{\partial \overline{\rho}\widetilde{f}}{\partial x_2} = 0, \tag{A.33}$$

$$IC : \overline{\rho}^{n+1/3}, \widetilde{f}^{n+1/3}. \tag{A.34}$$

With Godunov scheme eq. (A.33) can be formulated as

$$\overline{\rho}_{j,k,l}^{n+2/3}\widetilde{f}_{j,k,l}^{n+2/3} = \frac{\Delta t^n}{\Delta x_2}\left(|V_2|\overline{\rho}_{j,k,l}^{n+1/3}\widetilde{f}_{j,k,l}^{n+1/3} + V_2^{-}\overline{\rho}_{j,k+1,l}^{n+1/3}\widetilde{f}_{j,k+1,l}^{n+1/3} - V_2^{+}\overline{\rho}_{j,k-1,l}^{n+1/3}\widetilde{f}_{j,k-1,l}^{n+1/3}\right). \tag{A.35}$$

The solution of eqs. (A.33) and (A.34) after a time Δt^n is denoted by $\overline{\rho}^{n+2/3}, \widetilde{f}^{n+2/3}$.

The sweep in x_3 direction of eq. (A.28) is

$$\frac{\partial \overline{\rho}\widetilde{f}}{\partial t} + V_3\frac{\partial \overline{\rho}\widetilde{f}}{\partial x_3} = 0, \tag{A.36}$$

$$IC : \overline{\rho}^{n+2/3}, \widetilde{f}^{n+2/3}. \tag{A.37}$$

Numerically, it reads

$$\overline{\rho}_{j,k,l}^{n+1}\widetilde{f}_{j,k,l}^{n+1} = \frac{\Delta t^n}{\Delta x_3}\left(|V_3|\overline{\rho}_{j,k,l}^{n+2/3}\widetilde{f}_{j,k,l}^{n+2/3} + V_3^{-}\overline{\rho}_{j,k,l+1}^{n+2/3}\widetilde{f}_{j,k,l+1}^{n+2/3} - V_3^{+}\overline{\rho}_{j,k,l-1}^{n+2/3}\widetilde{f}_{j,k,l-1}^{n+2/3}\right). \tag{A.38}$$

The solution of eqs. (A.36) and (A.37) after a time Δt^n is denoted by $\overline{\rho}^{n+1}, \widetilde{f}^{n+1}$, which is then regarded as the solution to the full problem (A.28) at time t^{n+1}.

Stochastic process. Let note (r^*, u^*, v^*, w^*) a stochastic process in 3-dimensional space. Thus the sweep in the x_1 direction in terms of stochastic numerical scheme for the PDEs, accordingly to eq. (A.31) is

$$u_{j,k,l}^{*n+1/3} = \begin{cases} u_{j,k,l}^{*n}, & \text{with probability } P_j^{+1}, \\ u_{j+1,k,l}^{*n}, & \text{with probability } P_j^{-1}, \\ u_{j-1,k,l}^{*n}, & \text{with probability } P_j^{0} = 1 - P_j^{+1} - P_j^{-1}. \end{cases} \tag{A.39}$$

Probabilities are calculated using formulas:

$$P_j^{+1} = \frac{r_{j+1,k,l}^{*n}}{r_{j,k,l}^{*n+1/3}}u_{j+1,k,l}^{-}\frac{\Delta t^n}{\Delta x_1}, \tag{A.40}$$

$$P_j^{-1} = \frac{r^{*n}_{j-1,k,l}}{r^{*n+1/3}_{j,k,l}} u^{+}_{j-1,k,l} \frac{\Delta t^n}{\Delta x_1}, \tag{A.41}$$

$$P_j^{0} = \frac{r^{*n}_{j,k,l}}{r^{*n+1/3}_{j,k,l}} \left(1 - |u^{*}_{j,k,l}| \frac{\Delta t^n}{\Delta x_1}\right). \tag{A.42}$$

At this step, other unknown terms stay the same.

The sweep in the x_2 direction, accordingly to eq. (A.35), is

$$v^{*n+2/3}_{j,k,l} = \begin{cases} v^{*n}_{j,k,l}, & \text{with probability } P_k^{+1}, \\ v^{*n}_{j,k+1,l}, & \text{with probability } P_k^{-1}, \\ v^{*n}_{j,k-1,l}, & \text{with probability } P_k^{0} = 1 - P_k^{+1} - P_k^{-1}. \end{cases} \tag{A.43}$$

where the probability is calculated as in eqs. (A.40) to (A.42), but instead of r^{*n} and u^*, the stochastic density $r^{*n+1/3}$ and velocity v^* are used respectively, Δx_1 is replaced by Δx_2.

Finally we deduce from eq. (A.38) that

$$w^{*n+1}_{j,k,l} = \begin{cases} w^{*n}_{j,k,l}, & \text{with probability } P_l^{+1}, \\ w^{*n}_{j,k,l+1}, & \text{with probability } P_l^{-1}, \\ w^{*n}_{j,k,l-1}, & \text{with probability } P_l^{0} = 1 - P_l^{+1} - P_l^{-1}. \end{cases} \tag{A.44}$$

Here the probabilities are calculated with $r^{*n+2/3}$ and with velocity w.

The proposed 3-dimensional stochastic Godunov process should weakly converge to the PDF statistics with first order of convergence in space and in time.

A.5 Numerical tests

A.5.1 Step velocity profile

As there is no pressure term in the PDE (3.20), the rarefaction waves may appear. The stochastic density $r(t,x)$ can attain zero at some points. In the proposed stochastic Lax-Friedrichs, Lax-Wendroff, GForce and Godunov schemes the density cannot be equal to zero due to the CFL condition: $cfl < 1$. Nevertheless, we demonstrate in the present test, which can be interpreted as a vacuum test, that the mean density tends to zero. The investigated PDEs are given by eqs. (3.22) and (3.23).

PDF

The initial conditions at time $t = 0\,\mathrm{s}$ for the PDF transport eq. (3.2) is given by

$$\widetilde{f}_u(V; t=0, x) = H(x - x_c)\delta(V - V_0) + H(-(x - x_c))\delta(V),\ V_0 = 1\,\mathrm{m/s} \tag{A.45}$$

$$\overline{\rho}(t=0, x) = 1\,\mathrm{kg/m^3}. \tag{A.46}$$

The solution of the Cauchy problem (3.2), (A.45) and (A.46) is

$$\overline{\rho}\widetilde{f}_u(V; t, x) = H(x - x_c - V_0 t)\delta(V - V_0) + H(-(x - x_c))\delta(V),\ t > 0\,\mathrm{s}, \tag{A.47}$$

where the density is defined by

$$\overline{\rho}(t,x) = H(x - x_c - V_0 t) + H(-(x - x_c)) = \begin{cases} 1\,\mathrm{kg/m^3}, & \text{if } x < x_c \text{ and } x > V_0 t + x_c, \\ 0, & \text{if } x \in [x_c; x_c + V_0 t]. \end{cases} \tag{A.48}$$

The velocity is zero for any $x < x_c$, one for any $x > V_0 t + x_c$ and is undefined on the interval $x \in [x_c; x_c + V_0 t]$.

PDEs

The PDEs equivalent to the PDF eq. (3.2) are given by eqs. (3.20) and (3.22). The initial conditions for velocity and density are set according to the (A.45) and (A.46):

$$u(t=0, x) = V_0 H(x - x_c), \qquad r(t=0, x) = 1\,\mathrm{kg/m^3}. \tag{A.49}$$

Figure A.5 show initial profile of the velocity (left) and a solution of the Riemann problem at $t = T$ (right) of eqs. (3.20), (3.22) and (A.49). The yellow region signifies that the velocity is not defined while the density is zero.

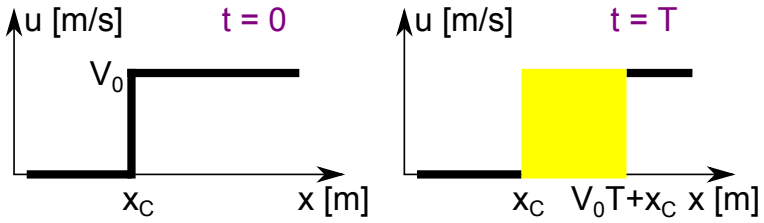

Figure A.5: Step: initial profile of the velocity (left); solution of the Riemann problem at $t = T$ (right)

Numerical solution

Calculations are performed on $L = 1\,\text{m}$ domain. At the initial time, the profile of velocity is a step centered at the middle of the domain $x_c = 0.5\,\text{m}$. The density equals to one and $V_0 = 1\,\text{m/s}$.

Spatial profiles. We consider spatial profiles of statistics at the time $t = 0.2\,\text{s}$, calculated with $N_x = 10^3$ points and $N_r = 10^4$ stochastic fields.

Figure A.6 shows the spatial profile of the mean density (left panel) and the Favre-averaged velocity (right panel). The mean density is very close to zero (its exact value is about 10^{-4}) on the interval $x \in [0.5\,\text{m}; 0.7\,\text{m}]$. It can never be equal to zero due to the CFL condition (3.58). The interpretation of values of stochastic velocity for each scheme is different in the region of vacuum. Thus, the stochastic Godunov method gives the value one for all velocity realization with the probability one. As a consequence, the Favre-averaged velocity is one on the interval $x \in [0.5\,\text{m}; 0.7\,\text{m}]$. For other stochastic schemes the probability to obtain the value zero for the velocity is much more than the probability to have one in the vacuum region. The probability to have zero for the velocity increases with time in the region of the vacuum. As a result, at time 0.1 s all profiles of stochastic velocity fields coincide. Right fig. A.6 shows the Favre-averaged velocity profiles for stochastic Lax-Friedrichs, Lax-Wendroff and GForce are close to each other. The mean velocity is zero on the interval $x \in [0.5\,\text{m}; 0.63\,\text{m}]$ and one on the interval $x \in [0.63\,\text{m}; 0.7\,\text{m}]$. Thus, stochastic numerical schemes interpret a vacuum state by the mean density closing to zero and by the mean velocity taking the values zero or one.

The density and velocity variance are presented in fig. A.7. Figure A.8 shows the velocity skewness and flatness. One can conclude that the stochastic Godunov method recovers better the theoretical solution for the density; contrariwise, the stochastic Lax-Friedrichs method gives the largest fluctuations in comparison with other schemes.

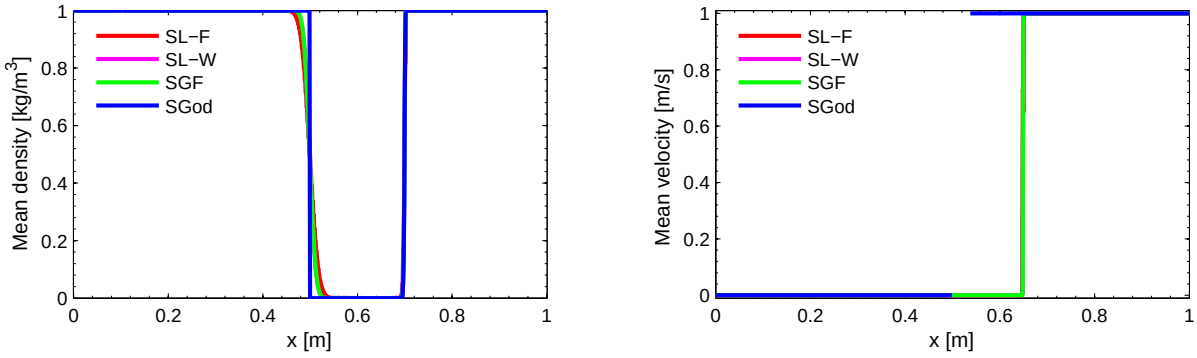

Figure A.6: Step: spatial profiles of mean density (left) and Favre-averaged velocity (right) at time $t = 0.2\,\mathrm{s}$. $N_r = 10^4$, $N_x = 10^3$.

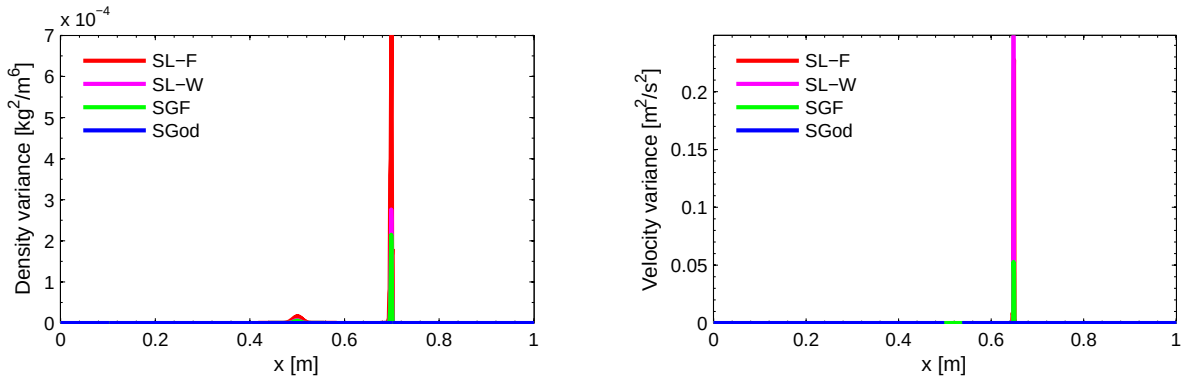

Figure A.7: Step: spatial profiles of density (left) and velocity (right) variance at time $t = 0.2\,\mathrm{s}$. $N_r = 10^4$, $N_x = 10^3$.

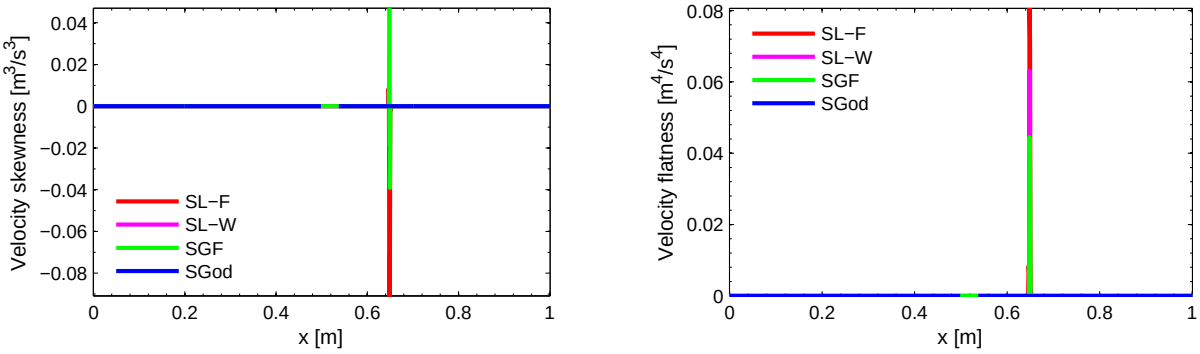

Figure A.8: Step: spatial profiles of velocity skewness (left) and flatness (right) at time $t = 0.2\,\mathrm{s}$. $N_r = 10^4$, $N_x = 10^3$.

A.5.2 Ramp velocity profile

This is the case when the velocity is multivalued. It takes three values with different probability. The purpose of this test is to check again the ability of the numerical methods to yield correct solution. The investigated PDEs are given by eqs. (3.22) and (3.23).

PDF

The initial conditions for eq. (3.2) are given by the following profiles:

$$\overline{\rho}(t=0,x)=\overline{\rho}_0, \qquad \widetilde{f_u}(V;t=0,x)=\delta\left(V-u_0(x)\right), \tag{A.50}$$

where

$$u_0(x)=V_0H(x_l-x)+V_0\left(\frac{x_r-x}{x_r-x_l}\right)H(x-x_l)H(x_r-x). \tag{A.51}$$

$$\overline{\rho}\widetilde{f_u}(V;t=0,x)=\overline{\rho}_0H(x_l-x)\delta(V-V_0)+\overline{\rho}_0\delta\left(V-V_0(x)\right)H(x-x_l)H(x_r-x)+\overline{\rho}_0H(x-x_r)\delta(V), \tag{A.52}$$

$$V_0(x)=V_0\frac{x_r-x}{x_r-x_l}. \tag{A.53}$$

The solution of eq. (3.9) for x is

$$x(t)=y+u_0(y)t=y+\left[H(x_l-y)+\left(\frac{x_r-y}{x_r-x_l}\right)H(y-x_l)H(x_r-y)\right]V_0t. \tag{A.54}$$

We can find from (A.54) y as the function of t and x, $y=y(t,x)$, if $t\neq\frac{x_r-x_l}{V_0}$. Substituting $y(t,x)$ into

$$F=\overline{\rho}_0\delta\left(V-u_0(y)\right), \tag{A.55}$$

we obtain

$$\overline{\rho}\widetilde{f_u}(V;t,x)=\overline{\rho}_0H(V_0t+x_l-x)\delta(V-V_0)+$$

$$\overline{\rho}_0\delta\left(V-V_t\right)\left(H(x-(x_l+V_0t))H(x_r-x)+H((x_l+V_0t)-x)H(x-x_r)\right)\frac{t_c}{|t_c-t|}+\overline{\rho}_0H(x-x_r)\delta(V), \tag{A.56}$$

where

$$V_t(t,x)=V_0\frac{x_r-x}{x_r-x_l-V_0t} \tag{A.57}$$

and

$$t_c=\frac{x_r-x_l}{V_0}. \tag{A.58}$$

We conclude from (A.56) that $t_c=\frac{x_r-x_l}{V_0}$ is a critical time. Before $t<t_c$ any point in space corresponds to a single Dirac delta function: $\delta(V-V_0)$ for $x<x_l+V_0t$, $\delta(V-V_t)$ for $x\in[x_l+V_0t;x_r]$ and $\delta(V)$ for $x>x_r$. After the time $t>t_c$, the interval $[x_r;x_l+V_0t]$ contains three Dirac delta functions.

Using the normalization condition of the PDF (3.6) we deduce that

- For $t<t_c=\frac{x_r-x_l}{V_0}$

$$\overline{\rho}(t,x) = \overline{\rho}_0 H(V_0 t + x_l - x) + \overline{\rho}_0 H(x - (x_l + V_0 t)) H(x_r - x) \frac{t_c}{t_c - t} + \overline{\rho}_0 H(x - x_r). \quad \text{(A.59)}$$

$$\widetilde{f}_u(V;t,x) = \frac{\overline{\rho}\widetilde{f}_u}{\overline{\rho}} =$$

$$\frac{H(V_0 t + x_l - x)\delta(V - V_0) + \delta(V - V_t)\, H(x - (x_l + V_0 t)) H(x_r - x) + H(x - x_r)\delta(V)}{H(V_0 t + x_l - x) + H(x - (x_l + V_0 t)) H(x_r - x) \frac{t_c}{t_c - t} + H(x - x_r)}. \quad \text{(A.60)}$$

- For $t > t_c = \frac{x_r - x_l}{V_0}$

$$\overline{\rho}(t,x) = \overline{\rho}_0 H(V_0 t + x_l - x) + \overline{\rho}_0 H(x_l + V_0 t - x) H(x - x_r) \frac{t_c}{t - t_c} + \overline{\rho}_0 H(x - x_r). \quad \text{(A.61)}$$

$$\widetilde{f}_u(V;t,x) =$$

$$\frac{H(V_0 t + x_l - x)\delta(V - V_0) + \delta(V - V_t)\, H((x_l + V_0 t) - x) H(x - x_r) \frac{t_c}{t - t_c} + H(x - x_r)\delta(V)}{H(V_0 t + x_l - x) + H(x_l + V_0 t - x) H(x - x_r) \frac{t_c}{t - t_c} + H(x - x_r)}. \quad \text{(A.62)}$$

It follows from the definition (3.5), when $n = 1$, that the Favre-averaged velocity is

$$\widetilde{u}(t,x) =$$

$$\frac{V_0 H(V_0 t + x_l - x) + V_t (H(x - (x_l + V_0 t)) H(x_r - x) + H((x_l + V_0 t) - x) H(x - x_r)) \frac{t_c}{|t_c - t|}}{H(V_0 t + x_l - x) + (H(x - (x_l + V_0 t)) H(x_r - x) + H((x_l + V_0 t) - x) H(x - x_r)) \frac{t_c}{|t_c - t|} + H(x - x_r)}. \quad \text{(A.63)}$$

The expressions for velocity moments of higher order are not written here.

PDEs

Accordingly to the initial conditions (A.50) and (A.51) for the PDF eq. (3.2), the density is $\overline{\rho}_0$ and the velocity profile is a ramp:

$$u_0(x) = \begin{cases} V_0, & \text{if } x < x_l, \\ V_0 \frac{x_r - x}{x_r - x_l}, & \text{if } x \in [x_l; x_r], \\ 0, & \text{if } x > x_r, \end{cases} \quad \text{(A.64)}$$

$$r_0(x) = \overline{\rho}_0. \quad \text{(A.65)}$$

The solution of eqs. (3.20) and (3.22) with given initial conditions (A.64) and (A.65) is presented in fig. A.9. Using the method of characteristics and formula (3.29), and assuming that the characteristics can cross, we deduce the following solutions:

- $0 < t < \frac{x_r - x_l}{V_0}$:

The solution is single-valued and it can be written as

$$r(t,x) = \begin{cases} \overline{\rho}_0, & \text{if } x < x_l + V_0 t, \\ \overline{\rho}_0 \frac{x_r - x_l}{x_r - (x_l + V_0 t)}, & \text{if } x \in [x_l + V_0 t; x_r], \\ \overline{\rho}_0, & \text{if } x > x_r. \end{cases} \tag{A.66}$$

$$u(t,x) = \begin{cases} V_0, & \text{if } x < x_l + V_0 t, \\ V_0 \frac{x_r - x}{x_r - (x_l + V_0 t)}, & \text{if } x \in [x_l + V_0 t; x_r], \\ 0, & \text{if } x > x_r. \end{cases} \tag{A.67}$$

- $t = t_c = \frac{x_r - x_l}{V_0}$:
  The velocity takes all values from zero to one and the density is a Dirac delta function at point $x = x_r$. For other values of x the solution is single-valued.

$$r(t,x) = \begin{cases} \overline{\rho}_0, & \text{if } x < x_r, \\ \overline{\rho}_0 \delta(x_r - x), & \text{if } x = x_r, \\ \overline{\rho}_0, & \text{if } x > x_r. \end{cases} \tag{A.68}$$

$$u(t,x) = \begin{cases} V_0, & \text{if } x < x_r, \\ [0; V_0], & \text{if } x = x_r, \\ 0, & \text{if } x > x_r. \end{cases} \tag{A.69}$$

- $t > \frac{x_r - x_l}{V_0}$:
  The system of eqs. (3.20) and (3.22) with the initial conditions (A.64) and (A.65) has three solutions (r_i, u_i), $i = 1, 2, 3$ on the interval $x \in [x_r; x_l + V_0 t]$. Outside the interval $[x_r; x_l + V_0 t]$, the solution is single-valued.

$$r(t,x) = \begin{cases} \overline{\rho}_0, & \text{if } x < x_r, \\ (r_1, r_2, r_3), & \text{if } x \in [x_r; x_l + V_0 t], \\ \overline{\rho}_0, & \text{if } x > x_l + V_0 t. \end{cases} \tag{A.70}$$

$$u(t,x) = \begin{cases} V_0, & \text{if } x < x_r, \\ (u_1, u_2, u_3), & \text{if } x \in [x_r; x_l + V_0 t], \\ 0, & \text{if } x > x_l + V_0 t. \end{cases} \tag{A.71}$$

where

$$(r_1,\ u_1) = (\overline{\rho}_0,\ V_0), \tag{A.72}$$

$$(r_2,\ u_2) = (\overline{\rho}_0,\ 0) \tag{A.73}$$

and

$$(r_3,\ u_3) = \left(\overline{\rho}_0 \frac{x_r - x_l}{-x_r + x_l + V_0 t},\ V_0 \frac{x - x_r}{x_l - x_r + V_0 t} \right). \tag{A.74}$$

In the strip $0 < t < \frac{x_r - x_l}{V_0}$ the mean density and the Favre-averaged velocity coincide with their solution (A.70) and (A.71) respectively. When the time is longer than $\frac{x_r - x_l}{V_0}$, the mean density $\overline{r} = \overline{\rho}$ is calculated as a sum of possible values of the density, i.e. the mean density is

$$\overline{r}(t,x) = \begin{cases} \overline{\rho}_0, & \text{if } x < x_r, \\ 2\overline{\rho}_0 + \overline{\rho}_0 \frac{x_r - x_l}{V_0 t - (x_r + x_l)}, & \text{if } x \in [x_r; x_l + V_0 t], \\ \overline{\rho}_0, & \text{if } x > x_l + V_0 t. \end{cases} \tag{A.75}$$

The Favre-averaged velocity is

$$\widetilde{u}(t,x) = \begin{cases} V_0, & \text{if } x < x_r, \\ V_0 \left(1 + \frac{(x_r - x_l)(x - x_r)}{(V_0 t - (x_r - x_l))^2}\right) \frac{V_0 t - (x_r - x_l)}{2V_0 t - (x_r - x_l)}, & \text{if } x \in [x_r; x_l + V_0 t], \\ 0, & \text{if } x > x_l + V_0 t. \end{cases} \tag{A.76}$$

The correspondence between $\widetilde{f}_u(V;t,x)$ from the transport PDF eqs. (3.2) and (A.50) and solution of PDEs (eqs. (3.20), (3.22), (A.64) and (A.65)) is following. If $t < t_c$, then

$$\widetilde{f}_u(V;t,x) = \frac{r(t,x)\delta(V - u(t,x))}{r(t,x)}. \tag{A.77}$$

The mean density is

$$\overline{\rho} = \overline{r} = r(t,x) \tag{A.78}$$

and the Favre-averaged velocity is

$$\widetilde{u} = u(t,x). \tag{A.79}$$

If $t > t_c$, then

$$\widetilde{f}_u(V;t,x) = \frac{r_1(t,x)\delta(V - u_1(t,x)) + r_2(t,x)\delta(V - u_2(t,x)) + r_3(t,x)\delta(V - u_3(t,x))}{r_1(t,x) + r_2(t,x) + r_3(t,x)}. \tag{A.80}$$

The mean density is

$$\overline{\rho} = \overline{r} = r_1(t,x) + r_2(t,x) + r_3(t,x) \tag{A.81}$$

and the Favre-averaged velocity is

$$\widetilde{u} = \frac{r_1(t,x)u_1(t,x) + r_2(t,x)u_2(t,x) + r_3(t,x)u_3(t,x)}{r_1(t,x) + r_2(t,x) + r_3(t,x)}. \tag{A.82}$$

Other moments can be calculated as

$$\widetilde{u'^n} = \frac{r_1(t,x)(u_1(t,x) - \widetilde{u})^n + r_2(t,x)(u_2(t,x) - \widetilde{u})^n + r_3(t,x)(u_3(t,x) - \widetilde{u})^n}{r_1(t,x) + r_2(t,x) + r_3(t,x)}. \tag{A.83}$$

Figure A.9 shows a temporal variation of the mean density $\overline{\rho} = \overline{r}$ and velocity and density profiles. During the time the graph of velocity "overturns". At time $t = \frac{x_r - x_l}{V_0}$ and at point $x = x_r$ the singularity appears. The mean density becomes a Dirac delta function. It accumulates here all mass coming from $t < \frac{x_r - x_l}{V_0}$. The velocity takes all values from 0 to V_0. After that the velocity flips and the density begins to spread from x_r to $x_l + V_0 t$.

As we can see from the analytical solution, the PDEs are equivalent to the PDF equation if all branches of density and velocity are taken into account.

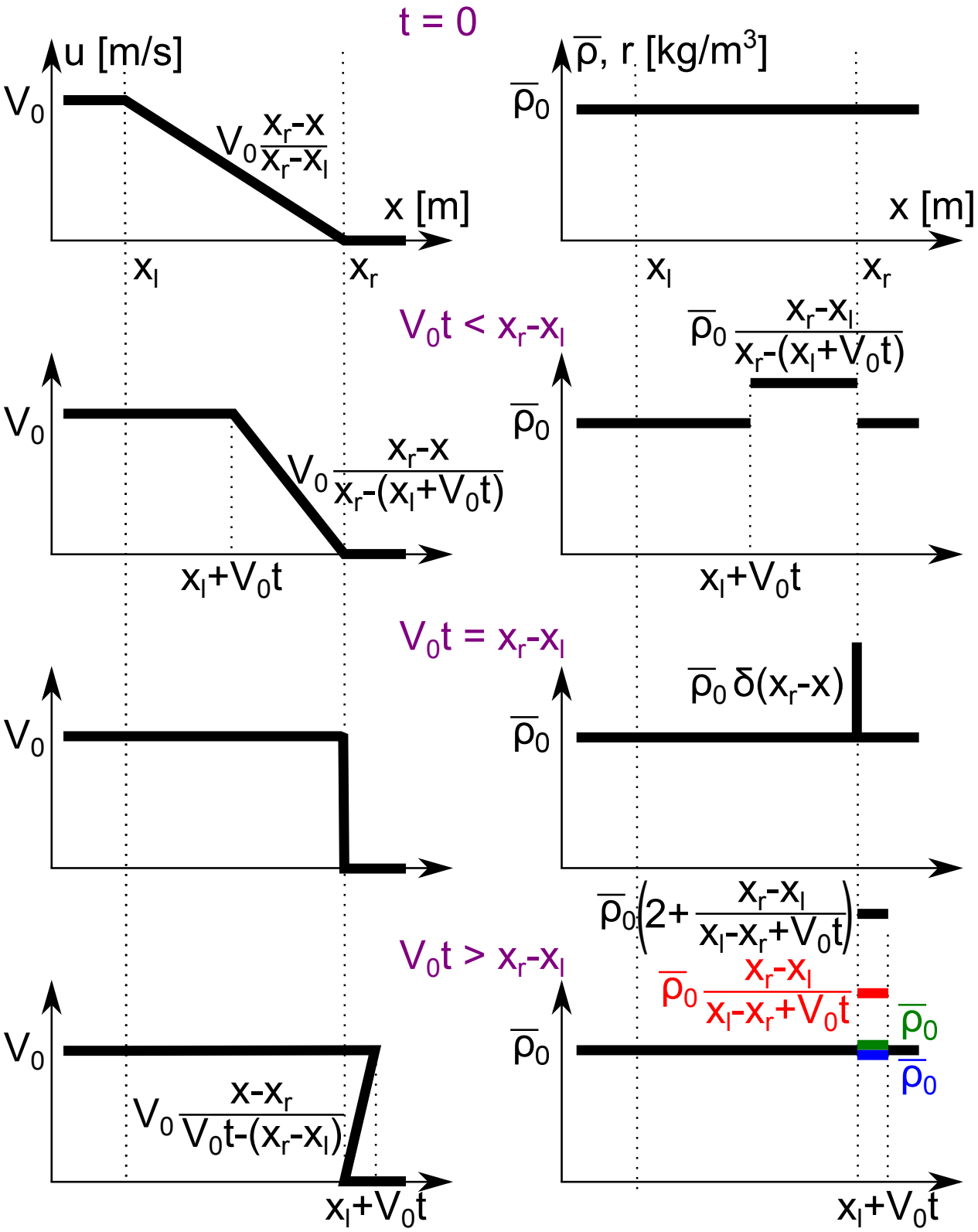

Figure A.9: Ramp: temporal variation of mean density and velocity profiles. Eulerian density r (red, green and blue curves in the right column) coincides with mean density $\overline{\rho}$ (black curve) for $t \leq \frac{x_r - x_l}{V_0}$, and differs in multivalued region for $t > \frac{x_r - x_l}{V_0}$.

Numerical solution

The computational domain has length $L = 1\,\mathrm{m}$. The left boundary of the ramp is located at $x_l = 0.25\,\mathrm{m}$ and the right at $x_r = 0.5\,\mathrm{m}$. V_0 is taken as $V_0 = 1\,\mathrm{m/s}$.

Spatial profiles. In order to illustrate the spatial profiles of the moments, we perform calculations with a number of stochastic fields $N_r = 10^4$ and with a number of cells $N_x = 5 \times 10^3$.

Numerical solutions of the PDEs are presented in fig. A.10 at time 0.1 s, where the analytical solution is still single-valued. It can be seen that before overlap the profiles of the mean density and the Favre-averaged velocity compared to the exact solution have a good agreement for any stochastic process.

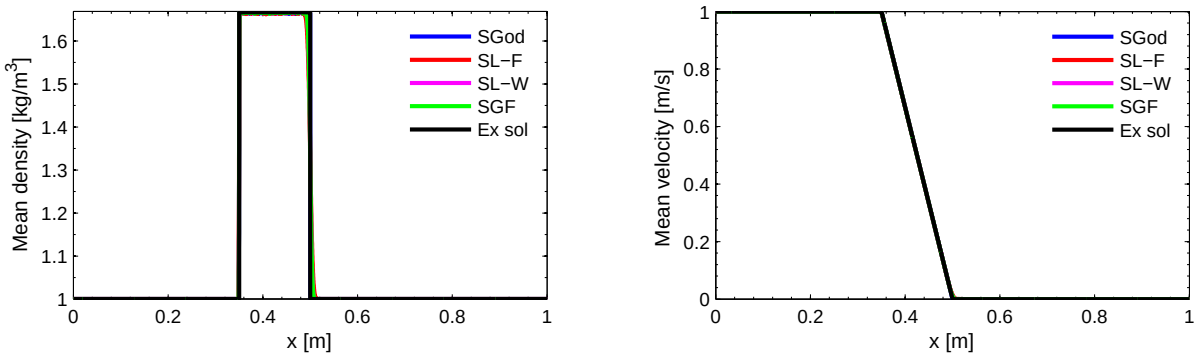

Figure A.10: Ramp: profiles of mean density (left) and velocity (right) at time 0.1 s. $N_r = 10^4$, $N_x = 5 \times 10^3$.

The left panel of fig. A.11 illustrates the density variance calculated by the stochastic GForce method with different number of stochastic fields. One can note that strong density fluctuations take place, even if the solution of problem is single-valued. In the interval $[0.35\,\mathrm{m}, 0.5\,\mathrm{m}]$ the density variance converges to the constant $0.09\,\mathrm{kg}^2/\mathrm{m}^6$. Outside of this interval, it is equal to zero. The right panel of fig. A.11 demonstrates the Favre velocity variance also at time 0.1 s, obtained with varied numbers of realizations by the stochastic GForce method. It is known that theoretically the Favre velocity variance is zero, numerically it fluctuates around the value $2.2500 \times 10^{-5}\,\mathrm{m}^2\mathrm{s}^{-2}$ at $x = 0.5\,\mathrm{m}$. The increase of the stochastic fields allows decreasing the velocity fluctuations, but at the same time for plotted fields $N_r = [100,\ 1100,\ 2100,\ 3100,\ 4100]$ the given profile is close to zero. The order $10^{-5}\mathrm{m}^2/\mathrm{s}^2$ for the Favre velocity variance is the consequence of the spatial error which starts to dominate for large N_r. We can conclude that before the overlap of solutions, there are no large fluctuations of velocity. The stochastic numerical schemes are in agreement with schemes satisfying the entropy increase condition. They give the same results.

A multivalued solution appears after $t \geq 0.25\,\mathrm{s}$. Figure A.12 shows the numerical solutions for the average density and velocity at time 0.3 s. The mean density fluctuates in the region of multivalued solution; while Favre-averaged velocity does not. One can also note that two spatial profiles are blurred near the point $x = 0.5\,\mathrm{m}$ where multivalued solution appears.

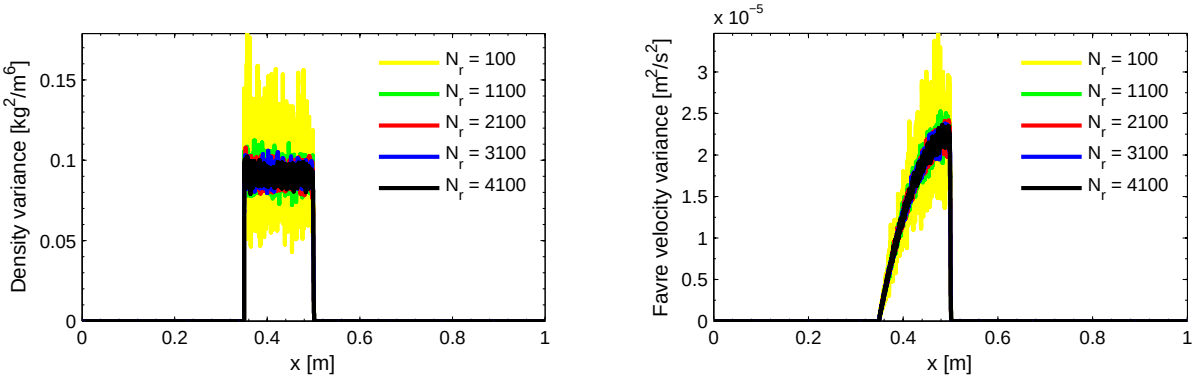

Figure A.11: Ramp: profiles of density variance (left) and velocity Favre variance (right) at time 0.1 s obtained with stochastic GForce method. $N_x = 5 \times 10^3$.

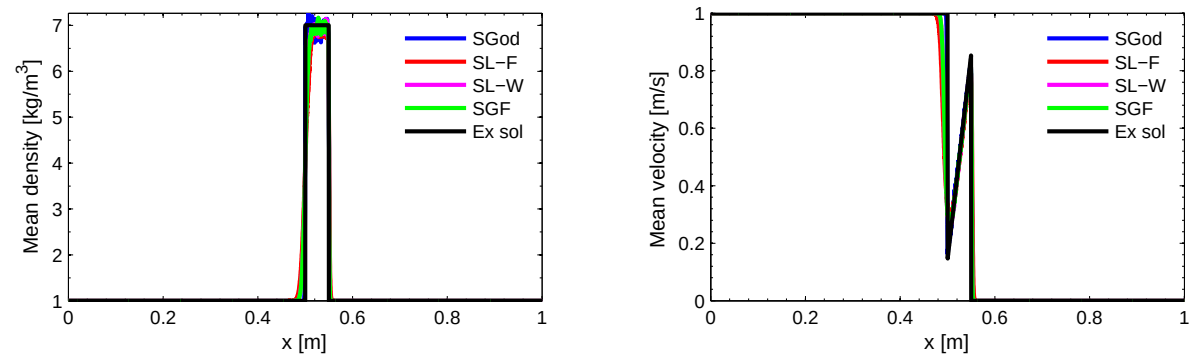

Figure A.12: Ramp: profiles of mean density (left) and velocity (right) at time 0.3 s. $N_r = 10^4$, $N_x = 5 \times 10^3$.

Two different realizations of the stochastic density and velocity fields at $t = 0.3$ s are presented in figs. A.13 and A.14. These profiles are part of the realizations set from which the presented above moments of density and velocity are computed. The density has large peaks, whereas the velocity can be either continuous in the interval greater than Δx if the solution is single or alternate different values in the region of multivalued solution.

At the time 0.4 s (figs. A.15 and A.16) the mean profiles of density, velocity and velocity variance begin to fluctuate significantly in comparison with profiles at 0.3 s. The largest fluctuations of the mean density are observed in the solution calculated with the stochastic Godunov method. Even if $N_r = 10^4$, numerical velocity variance gives 40% error at points $x = 0.5$ m and $x = 0.75$ m for four stochastic scheme. Despite of this fact, the numerical schemes still allow reconstructing statistics.

We examine the Favre-averaged PDF of the velocity when the system of the PDEs has three solutions. The considered time is 0.3 s, the spatial point is $x = 0.5249$ m. The analytical solution of the PDF equation or Eulerian PDEs in $t = 0.3$ s and $x = 0.5249$ m is the following. The velocity takes three values: $u_1 = 0$ m/s, $u_2 = 1$ m/s and $u_3 = 0.498$ m/s. The corresponding probabilities are $\frac{1}{7}$, $\frac{1}{7}$ and $\frac{5}{7}$ respectively (see the formula (A.62)). Numerical

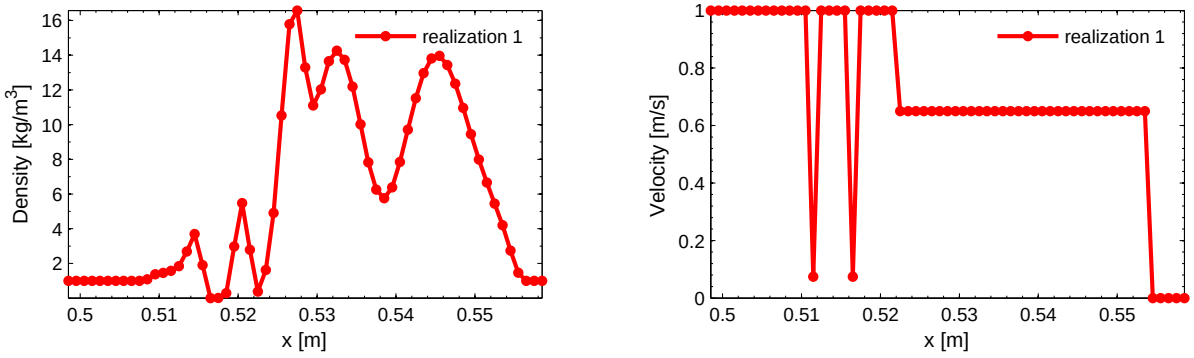

Figure A.13: Ramp: profiles of stochastic density (left) and velocity (right) at time 0.3 s; stochastic GForce method. $N_r = 10^4$, $N_x = 5 \times 10^3$.

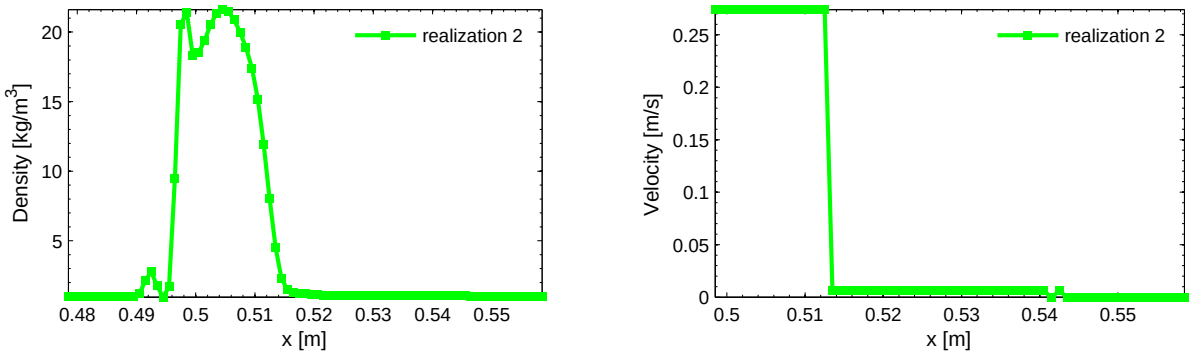

Figure A.14: Ramp: profiles of stochastic density (left) and velocity (right) at time 0.3 s; stochastic GForce method. $N_r = 10^4$, $N_x = 5 \times 10^3$.

Favre-averaged PDF is defined by the expression (2.94).

Left panels of figs. A.17 to A.20 show the weighted PDF of the velocity at point $x = 0.5249\,\mathrm{m}$. The profile of numerical PDF depends on the choice of histogram intervals and number of considered realizations. As we can see from right panels of figs. A.17 to A.20 the stochastic velocity takes all values on the interval $[0\,\mathrm{m/s}; 1\,\mathrm{m/s}]$. In particular, it takes mostly the values of $0\,\mathrm{m/s}$ and $1\,\mathrm{m/s}$. At the same time the conditional PDF of density for given velocities, presented in the right panel of fig. A.21 takes large values in the neighborhood of $0.5\,\mathrm{m/s}$ and very low values in $0\,\mathrm{m/s}$ and $1\,\mathrm{m/s}$. Due to such the conditional PDF, the probability of achieving $u_3 = 0.498\,\mathrm{m/s}$ is higher that of achieving $u_1 = 0\,\mathrm{m/s}$, $u_2 = 1\,\mathrm{m/s}$. The stochastic Godunov method gives the best weighted PDF in comparison with other stochastic schemes.

Left fig. A.21 demonstrates the distribution of the density. The stochastic Godunov method yields non-zero probability to attain high values of the density (there exists for instance a value exceeding $250\,\mathrm{kg/m^3}$ for given Δx and Δt).

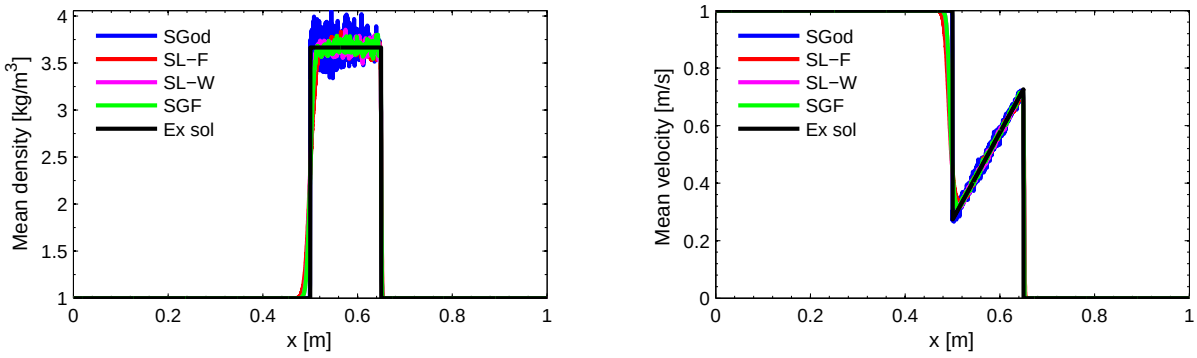

Figure A.15: Ramp: profiles of mean density (left) and velocity (right) at time 0.4 s. $N_r = 10^4$, $N_x = 5 \times 10^3$.

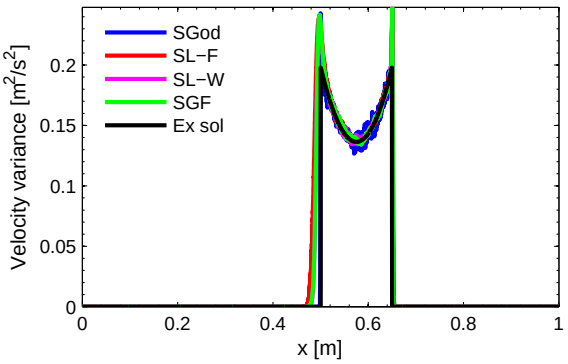

Figure A.16: Ramp: profiles of Favre variance of velocity at time 0.4 s. $N_r = 10^4$, $N_x = 5 \times 10^3$.

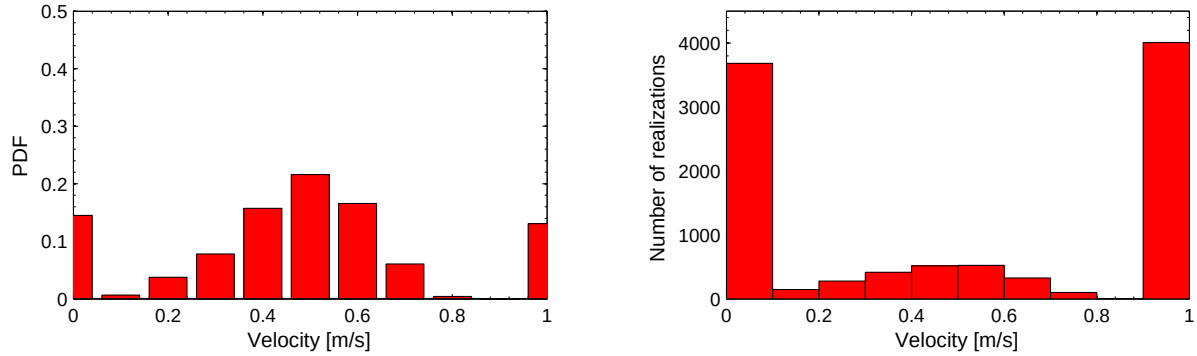

Figure A.17: Ramp: Favre-averaged PDF (left) and distribution of velocity (right) at $x = 0.5249$ m, $t = 0.3$ s. Stochastic Lax-Friedrichs method, $N_r = 10^4$, $N_x = 5 \times 10^3$.

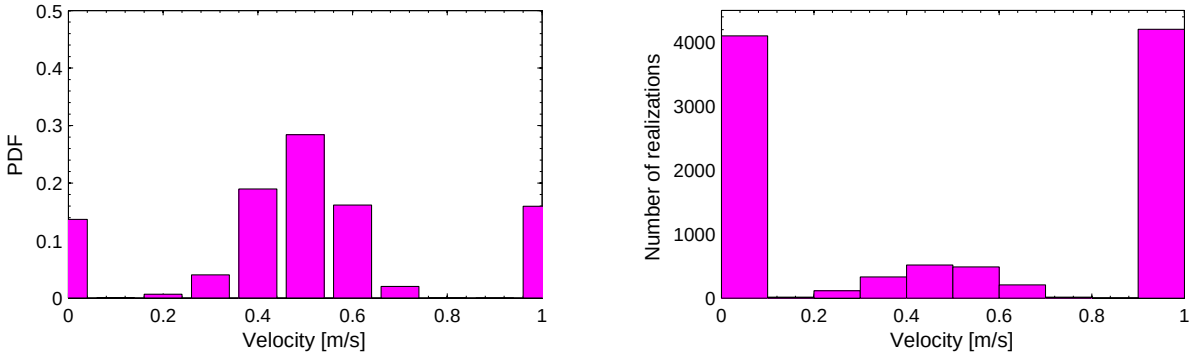

Figure A.18: Ramp: Favre-averaged PDF (left) and distribution of velocity (right) at $x = 0.5249\,\mathrm{m}$, $t = 0.3\,\mathrm{s}$. Stochastic Lax-Wendroff method, $N_r = 10^4$, $N_x = 5 \times 10^3$.

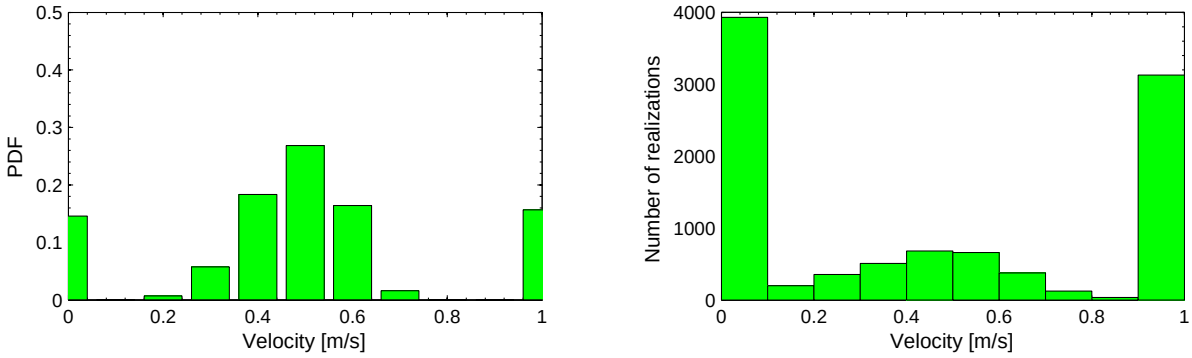

Figure A.19: Ramp: Favre-averaged PDF (left) and distribution of velocity (right) at $x = 0.5249\,\mathrm{m}$, $t = 0.3\,\mathrm{s}$. Stochastic GForce method, $N_r = 10^4$, $N_x = 5 \times 10^3$.

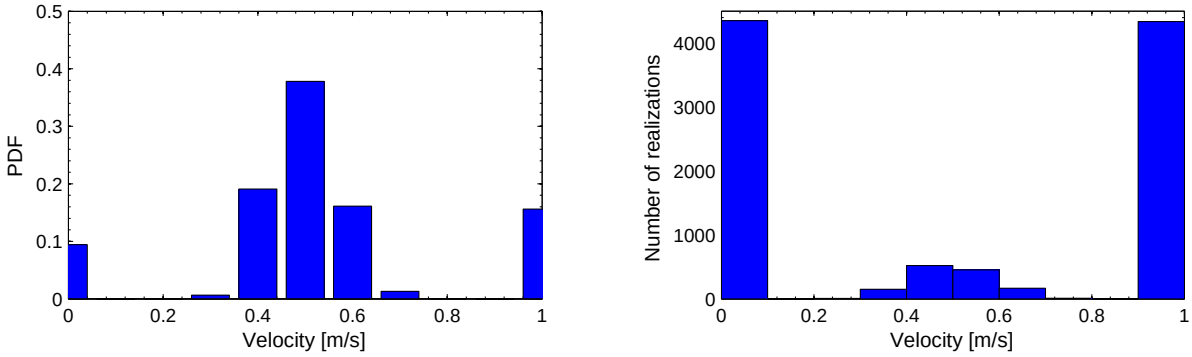

Figure A.20: Ramp: Favre-averaged PDF (left) and distribution of velocity (right) at $x = 0.5249\,\mathrm{m}$, $t = 0.3\,\mathrm{s}$. Stochastic Godunov method, $N_r = 10^4$, $N_x = 5 \times 10^3$.

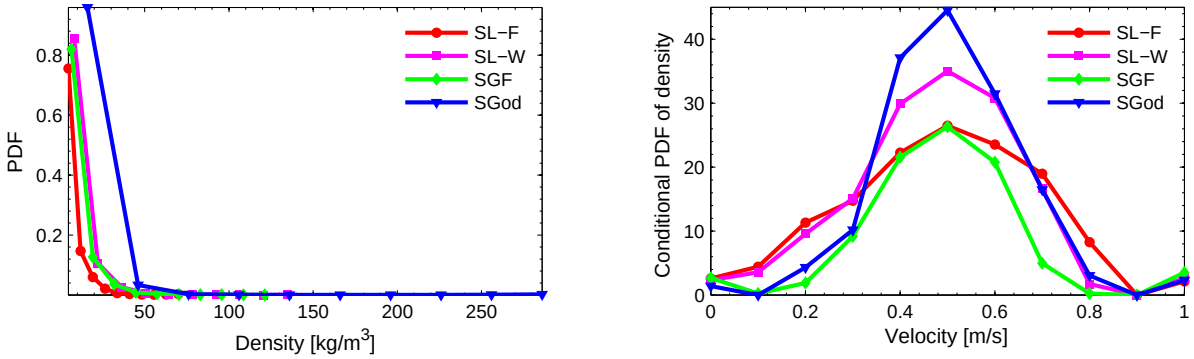

Figure A.21: Ramp: PDF of density (left) and conditional PDF of density for given velocities (right) obtained by different methods at time $t = 0.3\,\mathrm{s}$. $N_r = 10^4$, $N_x = 5 \times 10^3$.

Convergence. We consider the statistical convergence. Calculations are performed for a fixed number of cells $N_x = 10^5$. The number of stochastic fields is varied:

$$N_r = [100,\ 1100,\ 2100,\ 3100,\ 4100].$$

The reference solution is exact and given above. Figures A.22 and A.23 show the evolution of statistical convergence rates and coefficients for the mean density and the Favre-averaged velocity obtained by different numerical schemes before overlap. We observe that the convergence rates increase with time because both spatial and stochastic errors accumulate and do not allow observing convergence. Stochastic Godunov method gives the convergence rate around the theoretical value $N_r^{-0.5}$, whereas other methods yield about $N_r^{-0.35}$ for the mean density and $N_r^{-0.38}$ for the Favre-averaged velocity at time $t = 0.1\,\mathrm{s}$. The convergence coefficients also increase with the time. One can conclude that the stochastic Lax-Friedrichs method converges slower than others with respect to the theoretical solution.

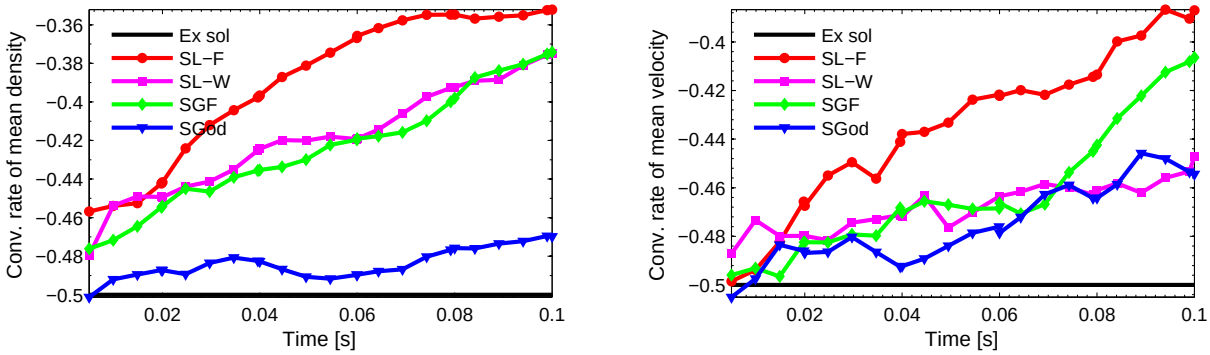

Figure A.22: Ramp: time evolution of statistical convergence rates for mean density (left) and Favre-averaged velocity (right). $N_x = 10^5$.

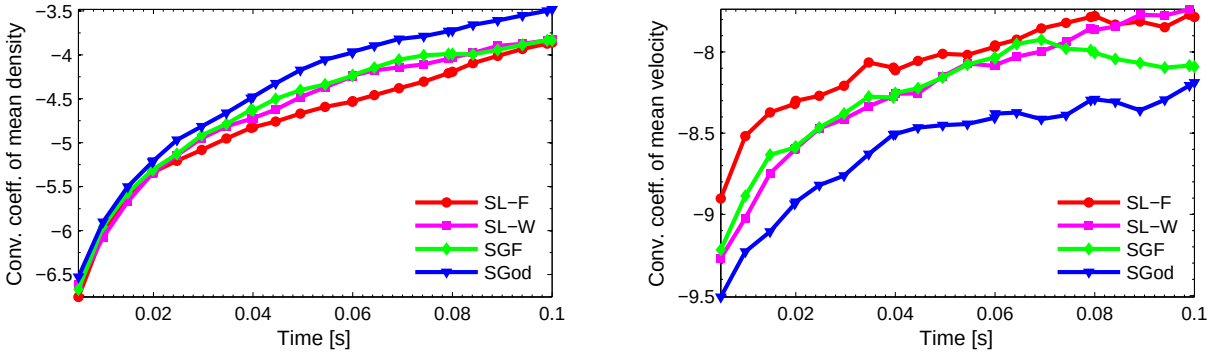

Figure A.23: Ramp: time evolution of statistical convergence coefficients for mean density (left) and Favre-averaged velocity (right). $N_x = 10^5$.

Finally, we check the spatial convergence. Calculations are performed with a fixed number of the stochastic fields $N_r = 10^7$. The number of grid cells is varied as:

$$N_x = [20,\ 40,\ 60,\ 80,\ 100].$$

Numerical solutions are compared with the exact solution. Figure A.24 shows the evolution of spatial errors for the mean density and for the Favre-averaged velocity as a function of $log(N_x)$ at time $t = 0.2\,\mathrm{s}$ (i.e. before the characteristics overlap). The errors are calculated for the stochastic Lax-Friedrichs method.

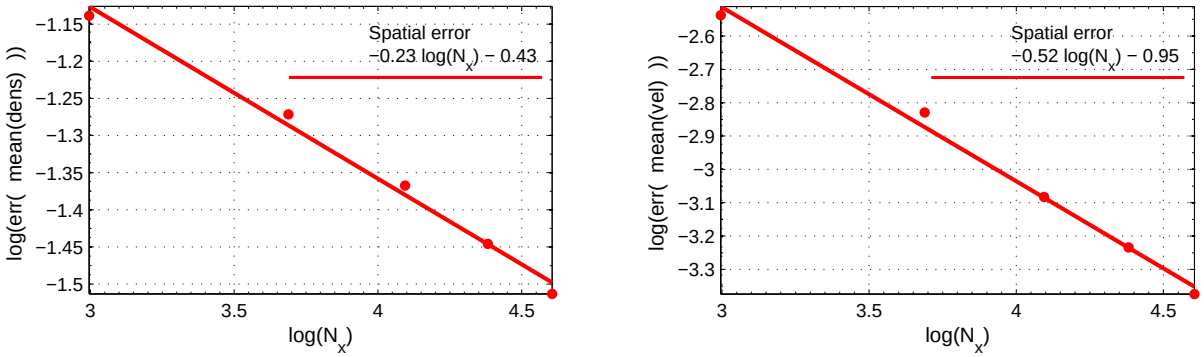

Figure A.24: Ramp: spatial convergence of mean density (left) and Favre-averaged velocity (right) at $t = 0.2\,\mathrm{s}$ on interval $[x_l; x_r + V_0 t]$, $V_0 = 1\,\mathrm{m/s}$, stochastic Lax-Friedrichs method. $N_r = 10^7$.

In the table A.1, the convergence spatial rate and convergence spatial coefficient are summarized for all the schemes. The order of convergence is about -0.5 for the averaged velocity and -0.3 for the mean density. The spatial convergence rate for the mean density is lower than the spatial convergence rate for the Favre-averaged velocity due to the numerical spatial derivative of the velocity which is proportional to $O(\frac{1}{\Delta x})$ and which is implicitly used in order to reconstruct the density.

	SLax-Friedrichs	SLax-Wendroff	SGForce	SGodunov
Favre-averaged velocity: rate (A)	-0.52	-0.54	-0.54	-0.41
Favre-averaged velocity: coeff (B)	-0.95	-1.26	-1.26	-2.36
Mean density: rate (A)	-0.23	-0.32	-0.32	-0.34
Mean density: coeff (B)	-0.43	-0.28	-0.28	-0.34

Table A.1: Ramp: approximation of spatial error of Favre-averaged velocity and mean density by $A \log(N_x) + B$ at time $t = 0.2\,\mathrm{s}$. $N_r = 10^7$.

A.5.3 Triangle velocity profile

Let us check the reconstruction of multivalued solution on the initial triangle velocity profile. This case corresponds to combination of the rarefication zone and three values of velocity. The investigated PDEs are given by eqs. (3.22) and (3.23).

PDF

The initial conditions for eq. (3.2) read

$$\overline{\rho}(t=0,x)=\overline{\rho}_0, \qquad \widetilde{f_u}(V;t=0,x)=\delta\left(V-u_0(x)\right), \tag{A.84}$$

where

$$u_0(x)=V_0\left(\frac{x-x_l}{x_c-x_l}\right)H(x-x_l)H(x_c-x)+V_0\left(\frac{x-x_r}{x_c-x_r}\right)H(x-x_c)H(x_r-x). \tag{A.85}$$

The initial condition for $\overline{\rho}\widetilde{f_u}$ is

$$\overline{\rho}\widetilde{f_u}(t=0,x)=$$
$$\overline{\rho}_0(H(x_l-x)+H(x-x_r))\delta(V)+\overline{\rho}_0\delta(V-V_1)H(x-x_l)H(x_c-x)+\overline{\rho}_0\delta(V-V_2)H(x-x_c)H(x_r-x), \tag{A.86}$$

where

$$V_1=V_0\left(\frac{x-x_l}{x_c-x_l}\right), \qquad V_2=V_0\left(\frac{x-x_r}{x_c-x_r}\right). \tag{A.87}$$

Accordingly to eq. (3.11), solutions for x and for $F=\overline{\rho}\widetilde{f_u}$ are

$$\begin{cases} x=y+\left[\left(\frac{y-x_l}{x_c-x_l}\right)H(y-x_l)H(x_c-y)+\left(\frac{y-x_r}{x_c-x_r}\right)H(y-x_c)H(x_r-y)\right]V_0t, \\ F=\overline{\rho}_0\delta\left(V-u_0(y)\right). \end{cases} \tag{A.88}$$

The variable y can be rewritten in terms of x and t. If the time $t\neq x_r-x_c$, we deduce that the solution of Cauchy problem (eqs. (3.2) and (A.86)) is

$$\overline{\rho}\widetilde{f_u}(t,x)=\overline{\rho}_0(H(x_l-x)+H(x-x_r))\delta(V)+$$
$$\overline{\rho}_0H(x-x_l)H(x_c+V_0t-x)\delta(V-V_{t_1})\frac{x_c-x_l}{x_c+V_0t-x_l}+$$
$$\overline{\rho}_0\left(H(x-x_c-V_0t)H(x_r-x)+H(x_c+V_0t-x)H(x-x_r)\right)\delta(V-V_{2t})\frac{t_c}{|t-t_c|}, \tag{A.89}$$

where

$$t_c=\frac{x_r-x_c}{V_0}, \qquad V_{t_1}=V_0\frac{x-x_l}{x_c-x_l+V_0t}, \qquad V_{t_2}=V_0\frac{x-x_r}{x_c-x_r+V_0t}. \tag{A.90}$$

As we can see from (A.89) there exists the critical time $t_c=\frac{x_r-x_c}{V_0}$. Before $t<t_c$ any point in space corresponds to a single Dirac delta function: $\delta(V)$ for $x\leq x_l$ and for $x\geq x_r$, $\delta(V-V_{t_1})$ for $x\in[x_l;x_c+V_0t]$ and $\delta(V-V_{t_2})$ for $x\in[x_c+V_0t;x_r]$. After the time t_c, the interval $[x_r;x_c+V_0t]$ is associated with three Dirac delta functions.

The mean density is

$$\overline{\rho} = \overline{\rho}_0(H(x_l - x) + H(x - x_r)) + \overline{\rho}_0 H(x - x_l)H(x_c + V_0 t - x)\frac{x_c - x_l}{x_c + V_0 t - x_l} +$$

$$\overline{\rho}_0 \left(H(x - x_c - V_0 t)H(x_r - x) + H(x_c + V_0 t - x)H(x - x_r)\right) \frac{t_c}{|t - t_c|}. \tag{A.91}$$

Using eqs. (A.89) and (A.91) we can find all moments of velocity.

PDEs

At the initial time the density is constant in space and it is

$$r_0(t = 0, x) = \overline{\rho}_0, \tag{A.92}$$

The profile of velocity is a triangle-shaped function:

$$u_0(t = 0, x) = \begin{cases} 0, & \text{if } x < x_l, \\ V_0 \frac{x - x_l}{x_c - x_l}, & \text{if } x_l \le x \le x_c, \\ V_0 \frac{x - x_r}{x_c - x_r}, & \text{if } x_c < x \le x_r. \\ 0, & \text{if } x > x_r, \end{cases} \tag{A.93}$$

The solution of the PDEs (3.20) and (3.22) with the initial conditions (A.92) and (A.93) can be found via the characteristics method. When the time $t < \frac{x_r - x_c}{V_0}$, the solution of this problem is single-valued, but when the time $t \ge \frac{x_r - x_c}{V_0}$ a multivalued solution appears.

- The solution of velocity when the time $t < \frac{x_r - x_c}{V_0}$ can be written as

$$u(t, x) = \begin{cases} 0, & \text{if } x < x_l, \\ V_0 \frac{x - x_l}{x_c - x_l + V_0 t}, & \text{if } x_l \le x \le x_c + V_0 t, \\ V_0 \frac{x - x_r}{x_c - x_r + V_0 t}, & \text{if } x_c + V_0 t < x \le x_r. \\ 0, & \text{if } x > x_r, \end{cases} \tag{A.94}$$

  The density is

$$r(t, x) = \begin{cases} \overline{\rho}_0, & \text{if } x < x_l, \\ \overline{\rho}_0 \frac{x_c - x_l}{x_c - x_l + V_0 t}, & \text{if } x_l \le x \le x_c + V_0 t, \\ \overline{\rho}_0 \frac{x_r - x_c}{x_r - x_c - V_0 t}, & \text{if } x_c + V_0 t < x \le x_r. \\ \overline{\rho}_0, & \text{if } x > x_r, \end{cases} \tag{A.95}$$

- At time $t = \frac{x_r - x_c}{V_0}$, the density is a Dirac delta function at point $x = x_r$ and the velocity takes any value from $[0; V_0]$ interval.

$$u(t, x) = \begin{cases} 0, & \text{if } x < x_l, \\ V_0 \frac{x - x_l}{x_c - x_l + V_0 t}, & \text{if } x_l \le x \le x_r, \\ [0; V_0], & \text{if } x = x_r. \\ 0, & \text{if } x > x_r, \end{cases} \tag{A.96}$$

$$r(t,x) = \begin{cases} \overline{\rho}_0, & \text{if } x < x_l, \\ \overline{\rho}_0 \frac{x_c - x_l}{x_c - x_l + t}, & \text{if } x_l \le x \le x_r, \\ \overline{\rho}_0 \delta(x - x_r), & \text{if } x = x_r. \\ \overline{\rho}_0, & \text{if } x > x_r, \end{cases} \tag{A.97}$$

- When the time is $t > \frac{x_r - x_c}{V_0}$, the velocity and density have three solutions:

$$u = \begin{cases} 0, & \text{if } x < x_l, \\ V_0 \frac{x - x_l}{x_c - x_l + V_0 t}, & \text{if } x_l \le x \le x_r, \\ (u_1,\ u_2,\ u_3) = \left(V_0 \frac{x - x_l}{x_c - x_l + V_0 t};\ 0;\ V_0 \frac{x - x_r}{x_c - x_r + V_0 t} \right), & \text{if } x_r < x \le x_c + V_0 t. \\ 0, & \text{if } x > x_r, \end{cases} \tag{A.98}$$

$$r(t,x) = \begin{cases} \overline{\rho}_0, & \text{if } x < x_l, \\ \overline{\rho}_0 \frac{x_c - x_l}{x_c - x_l + V_0 t}, & \text{if } x_l \le x \le x_r, \\ (r_1,\ r_2,\ r_3) = \left(\overline{\rho}_0 \frac{x_c - x_l}{x_c - x_l + V_0 t}; \overline{\rho}_0; \overline{\rho}_0 \frac{x_r - x_c}{x_c - x_r + V_0 t} \right), & \text{if } x_r < x \le x_c + V_0 t, \\ \overline{\rho}_0, & \text{if } x > x_c + V_0 t, \end{cases} \tag{A.99}$$

One can conclude that the solutions of the PDF eqs. (3.2) and (A.86) and the PDEs (3.20) and (3.22) with the initial conditions (A.92) and (A.93) are equivalent. The PDF is defined as

$$\widetilde{f}_u(V;t,x) = \frac{r(t,x)\delta(V - u(t,x))}{r(t,x)}, \tag{A.100}$$

if the solution of Eulerian PDEs is single-valued and as

$$\widetilde{f}_u(V;t,x) = \frac{r_1(t,x)\delta(V - u_1(t,x)) + r_2(t,x)\delta(V - u_2(t,x)) + r_3(t,x)\delta(V - u_3(t,x))}{r_1(t,x) + r_2(t,x) + r_3(t,x)} \tag{A.101}$$

for time $t > \frac{x_r - x_c}{V_0}$.

Figure A.25 shows temporal variation of the mean density and velocity profiles.

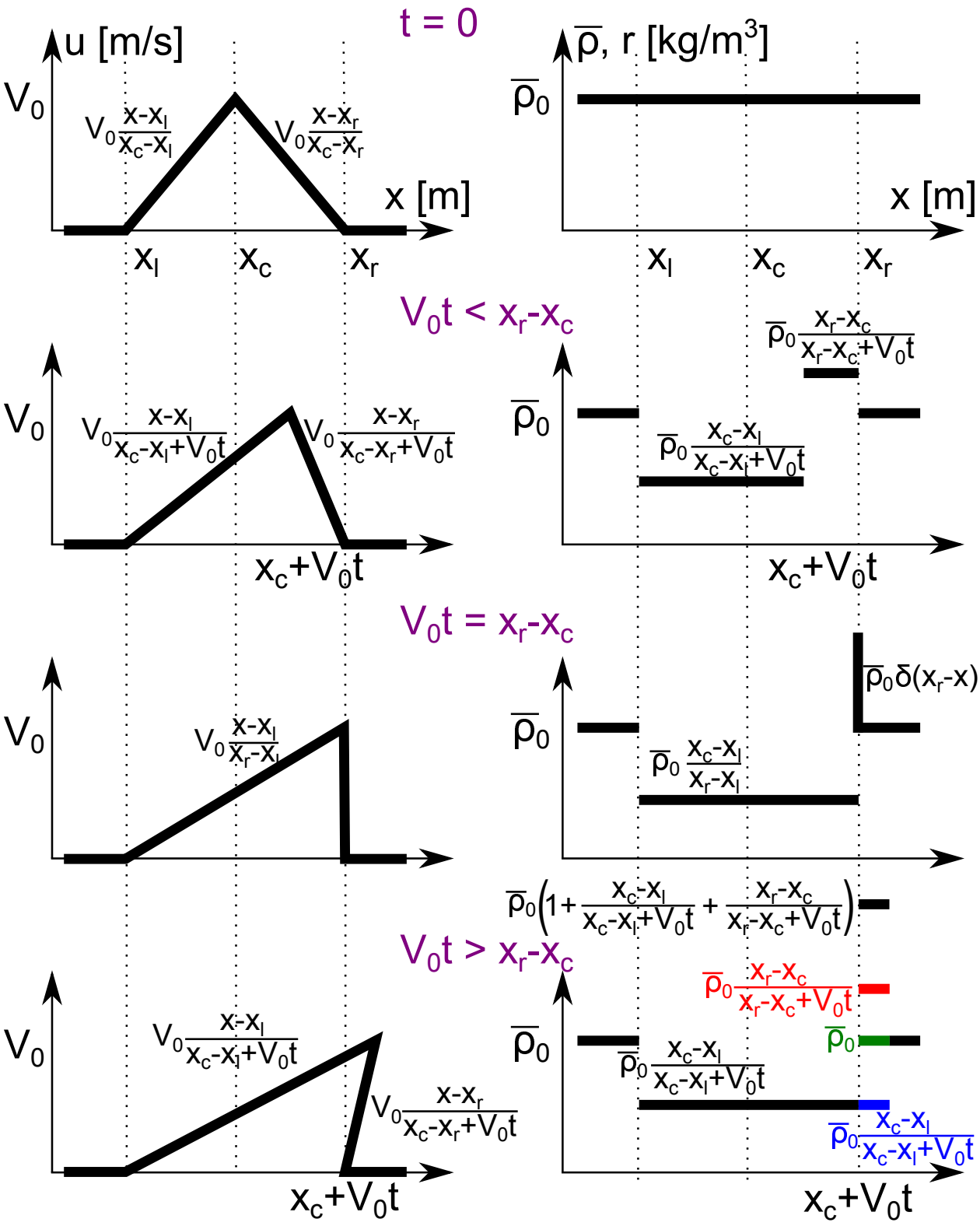

Figure A.25: Triangle: temporal variation of the mean density and velocity profiles. Eulerian density r (red, green and blue curves in the right column) coincides with mean density $\overline{\rho}$ (black curve) for $t < \frac{x_r - x_c}{V_0}$, and differs in multivalued region for $t \geq \frac{x_r - x_c}{V_0}$.

Numerical solution

Calculations are performed on $L = 1\,\text{m}$ domain. At the initial time, the profile of velocity is a triangle centered at the middle of the domain $x_c = 0.5\,\text{m}$, $x_l = 0.25\,\text{m}$ and $x_r = 0.75\,\text{m}$, $V_0 = 1\,\text{m/s}$ (fig. A.26).

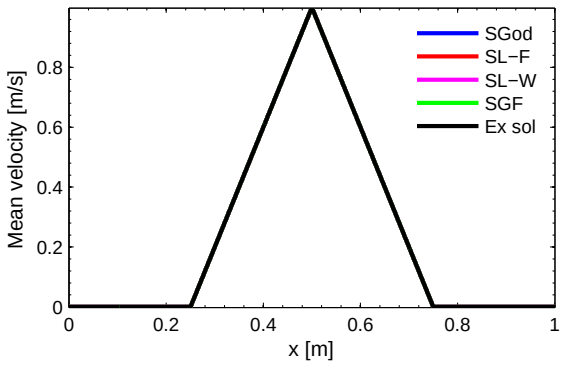

Figure A.26: Triangle: spatial initial profile of velocity. $N_r = 10^4$, $N_x = 5 \times 10^3$.

Spatial profiles. To illustrate the behavior of stochastic schemes we take $N_x = 5 \times 10^3$ and $N_r = 10^4$. In figs. A.27 to A.29 different statistics of density and velocity are presented before the overlap at time $t = 0.1\,\text{s}$. As for other numerical tests stochastic fluctuations appear, but their influence of statistics is negligible before overlap. Favre velocity variance, skewness and flatness stay close to zero containing some fluctuations due to the spatial error.

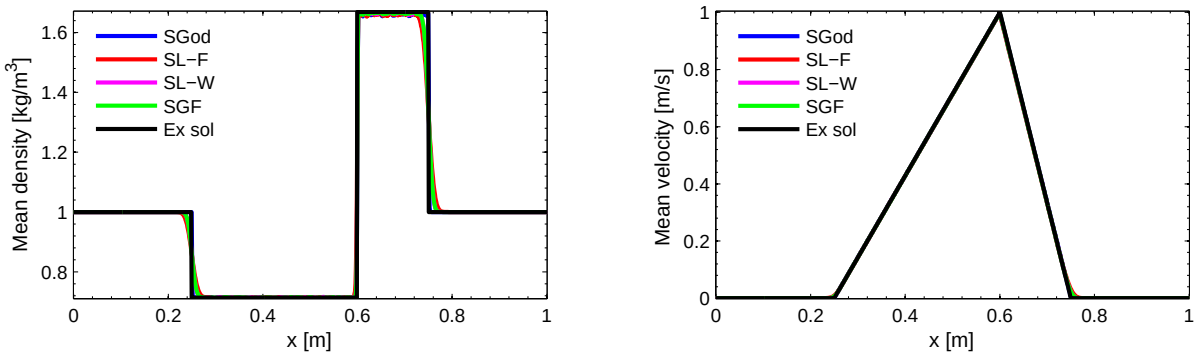

Figure A.27: Triangle: spatial profiles of mean density (left) and velocity (right) at time $t = 0.1\,\text{s}$. $N_r = 10^4$, $N_x = 5 \times 10^3$.

The averaged fields after overlap are shown in figs. A.30 to A.32. One can conclude that numerical schemes are able to find multivalued solution of the problem despite the numerical spatial diffusion and statistical error of stochastic schemes. One can note that in the region of multivalued solution $[0.75\,\text{m}; 0.9\,\text{m}]$ the density fluctuates for four stochastic schemes. The highest fluctuations appear for the solution calculated with stochastic Godunov scheme. In

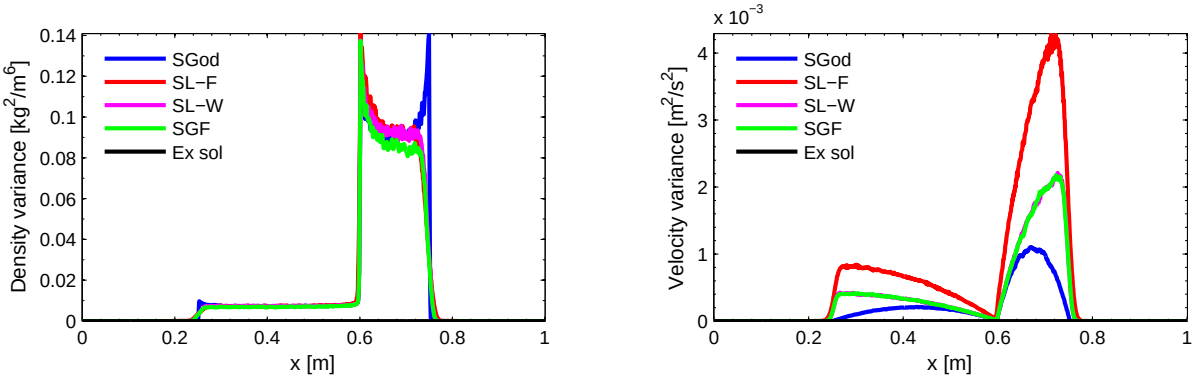

Figure A.28: Triangle: spatial profiles of density (left) and velocity (right) variance at time $t = 0.1\,\mathrm{s}$. $N_r = 10^4$, $N_x = 5 \times 10^3$.

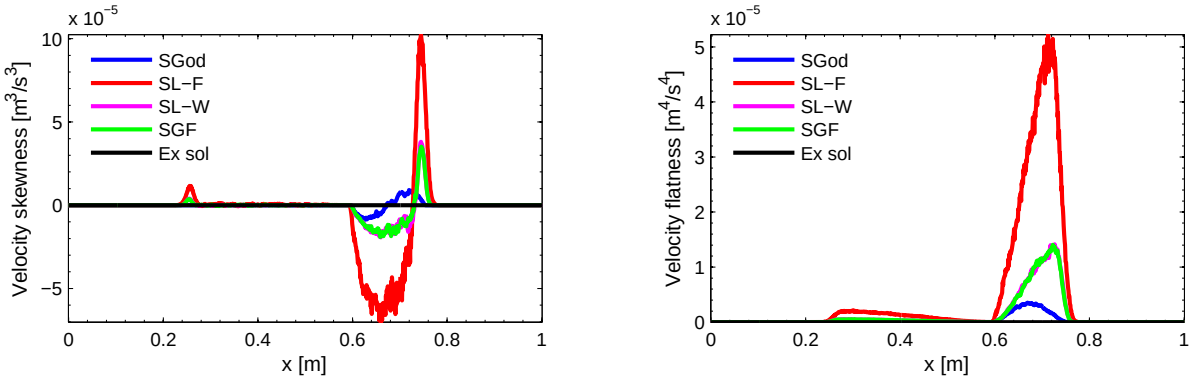

Figure A.29: Triangle: spatial profiles of velocity skewness (left) and flatness (right) at time $t = 0.1\,\mathrm{s}$. $N_r = 10^4$, $N_x = 5 \times 10^3$.

addition, the numerical diffusion smooths the profile of the mean density at points where the solution contains jumps: $x = 0.25\,\mathrm{m}$, $x = 0.75\,\mathrm{m}$ and $x = 0.9\,\mathrm{m}$. As velocity statistics are calculated from the density, the latter changes significantly statistics at these points.

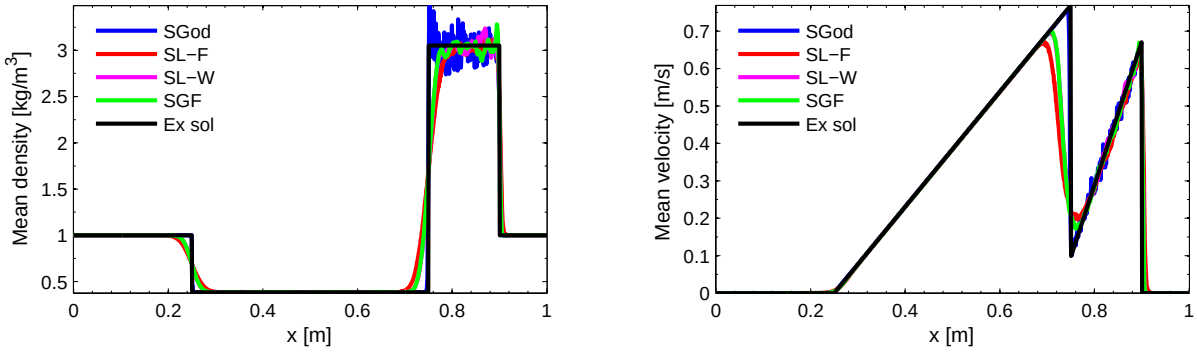

Figure A.30: Triangle: spatial profiles of mean density (left) and velocity (right) at time $t = 0.4\,\mathrm{s}$. $N_r = 10^4$, $N_x = 5 \times 10^3$.

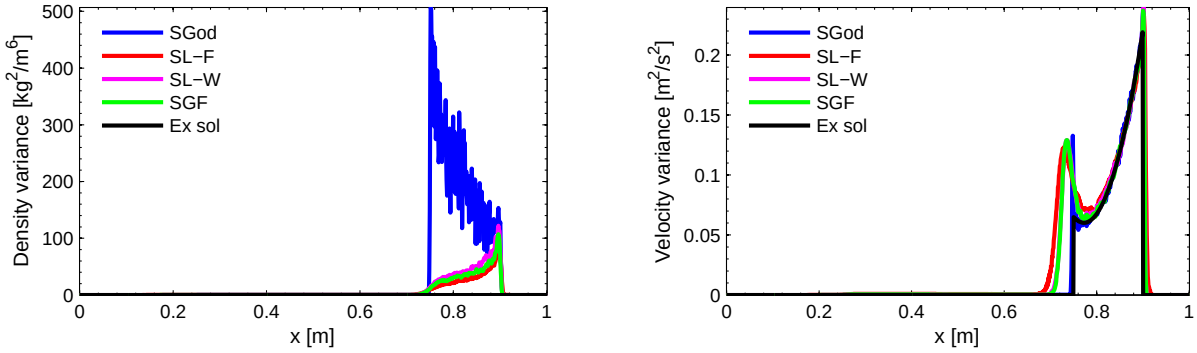

Figure A.31: Triangle: spatial profiles of density (left) and velocity (right) variance at time $t = 0.4\,\mathrm{s}$. $N_r = 10^4$, $N_x = 5 \times 10^3$.

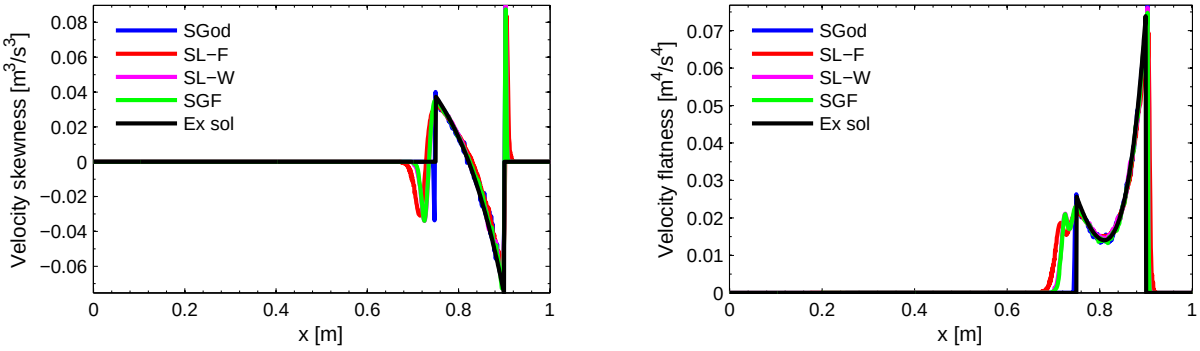

Figure A.32: Triangle: spatial profiles of velocity skewness (left) and flatness (right) at time $t = 0.4\,\mathrm{s}$. $N_r = 10^4$, $N_x = 5 \times 10^3$.

A.5.4 Hat velocity profile

The aim of this test is to check the stochastic numerical schemes when initial profiles of the density and the velocity are smooth functions. The investigated PDEs are given by eqs. (3.22) and (3.23).

PDEs

As in previous subsection the PDEs are eqs. (3.20) and (3.22). At the initial time, the profile of velocity is a smooth hat-like function centered at $x_c = 0.5\,\mathrm{m}$ the middle of the domain $D = [0\,\mathrm{m}; 1\,\mathrm{m}]$ with a length $L = 1\,\mathrm{m}$.

$$u_0(x) = \begin{cases} 0, & \text{if } x < 0.25\,\mathrm{m}, \\ V_0 exp(-(x - x_c)^2/L_0^2), & \text{if } 0.25\,\mathrm{m} \leq x \leq 0.75\,\mathrm{m}, \\ 0, & \text{if } x > 0.75\,\mathrm{m}, \end{cases} \tag{A.102}$$

where $V_0 = 1\,\mathrm{m/s}$ and $L_0 = 0.1\,\mathrm{m}$. The density is set identically to one. There is no analytical solution for this problem; as a consequence, only numerical solutions will be investigated.

Numerical solution

Spatial profiles. In order to reconstruct spatial profiles, the number of cells are imposed to $N_x = 10^3$ and the number of stochastic fields are set to $N_r = 10^4$. The considered time is $t = 0.1\,\mathrm{s}$.

Figure A.33 compares spatial profiles of the mean density and the Favre-averaged velocity calculated using different numerical schemes. The profiles of the mean density calculated with all the four methods coincide almost everywhere except the neighborhood of the point $x = 0.62\,\mathrm{m}$. The stochastic Lax-Friedrichs method gives the value of the mean density 20% smaller than other methods. The profiles of the Favre-averaged velocity are the same in all the cases.

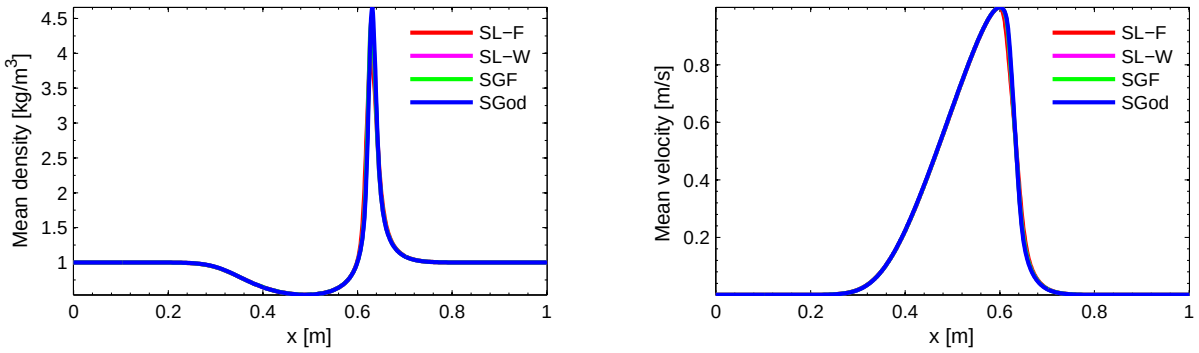

Figure A.33: Hat: spatial profiles of mean density (left) and velocity (right) at time $t = 0.1\,\mathrm{s}$. $N_r = 10^4$, $N_x = 10^3$.

Figures A.34 and A.35 represent the second and third statistics for the density and the velocity. The profiles obtained with the stochastic Lax-Wendroff and stochastic GForce schemes are very close to each other.

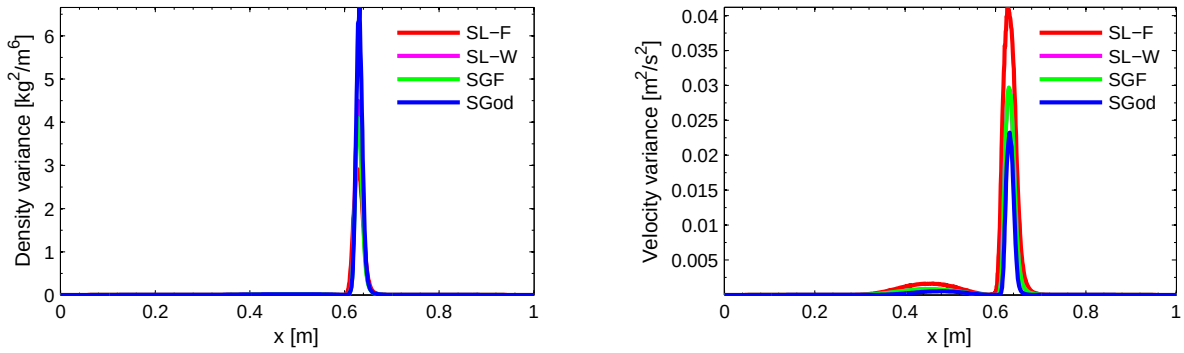

Figure A.34: Hat: spatial profiles of density (left) and velocity (right) variances at time $t = 0.1\,\mathrm{s}$. $N_r = 10^4$, $N_x = 10^3$.

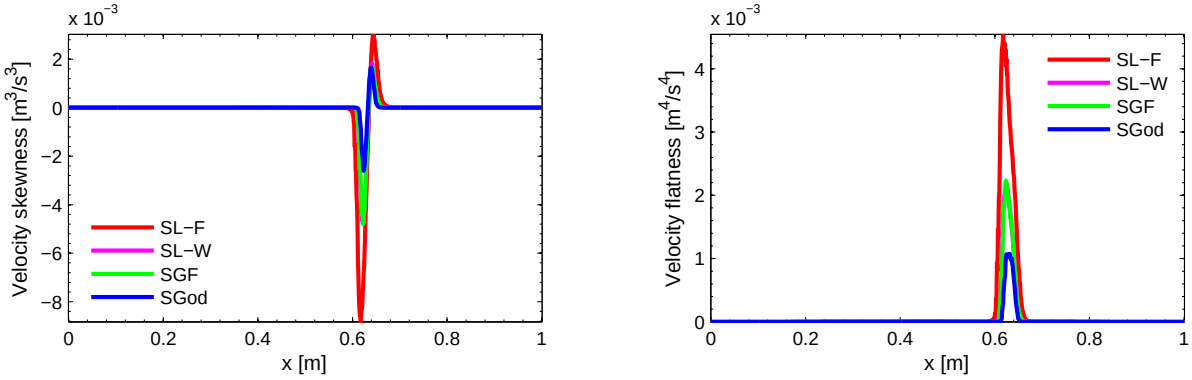

Figure A.35: Hat: spatial profiles of skewness(left) and flatness (right) of velocity at time $t = 0.1\,\mathrm{s}$. $N_r = 10^4$, $N_x = 10^3$.

Convergence. To assess the stochastic convergence of the numerical solutions we set $N_x = 10^4$ while the number of fields N_r varies from 20 to 80. The solution obtained with 1200 stochastic fields is taken as a reference solution to which other calculations are compared. Figures A.36 to A.39 show statistical convergence rates and coefficients of the hat problem. The order of convergence for the mean density, mean velocity and velocity variance is about -0.45 for all the numerical schemes. Other Favre statistics of the velocity slowly converge to the reference solutions, with the rate of about -0.3. The order of convergence of Favre-averaged statistics of the velocity (i.e. variance, skewness and flatness) decreases with time. It signifies that over the time the spatial error progressively extends its influence on the numerical solution.

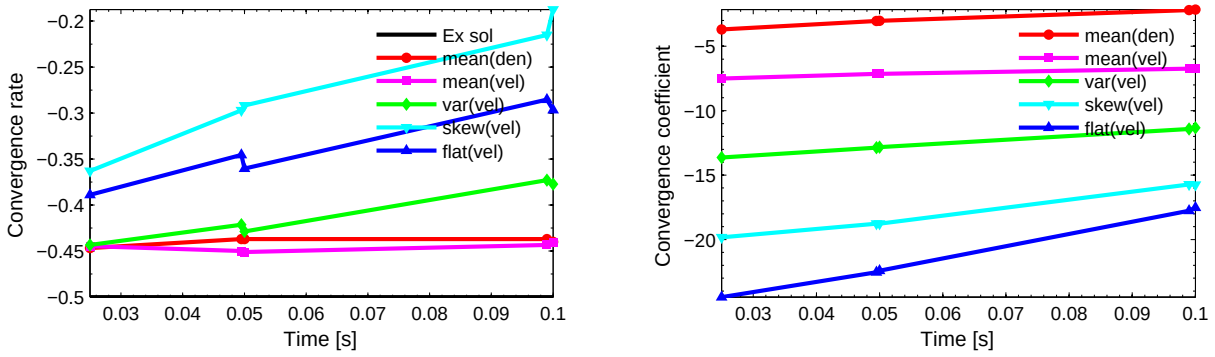

Figure A.36: Hat: time evolution of the statistical convergence rates (left) and coefficients (right) for moments of density and velocity; stochastic Godunov method. $N_x = 10^4$.

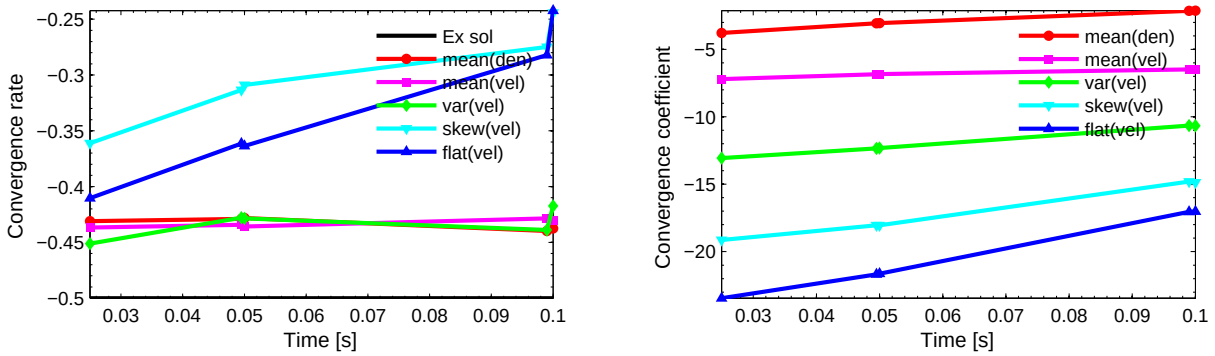

Figure A.37: Hat: time evolution of the statistical convergence rates (left) and coefficients (right) for moments of density and velocity; stochastic GForce method. $N_x = 10^4$.

The spatial convergence calculations are now performed with a fixed number of stochastic fields $N_r = 10^7$. The number of grid cells is varied from $N_x = 20$ to $N_x = 80$. The reference solution is obtained using $N_x = 100$. In figs. A.40 to A.42 the spatial convergence of statistics of the density and the velocity is presented. It can be seen that the order of convergence with respect to N_x slightly exceeds one. Such the behavior could be due to the approximate character of the chosen in this section reference solution.

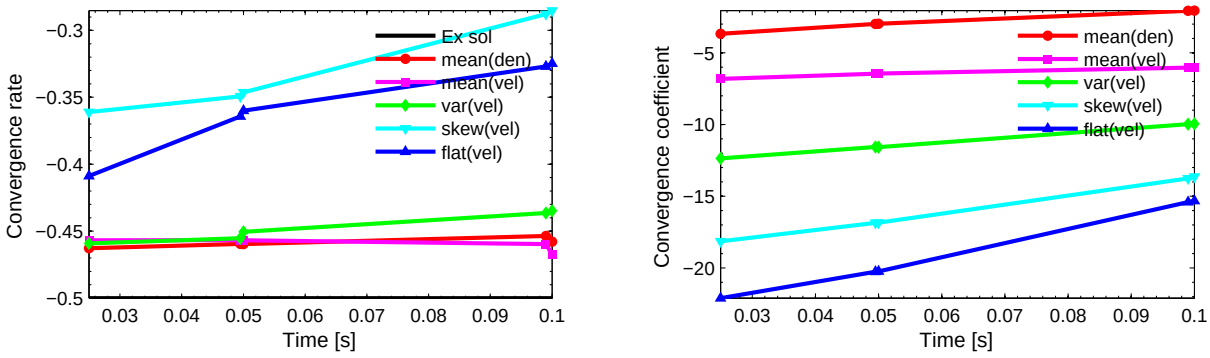

Figure A.38: Hat: time evolution of the statistical convergence rates (left) and coefficients (right) for moments of density and velocity; stochastic Lax-Friedrichs method. $N_x = 10^4$.

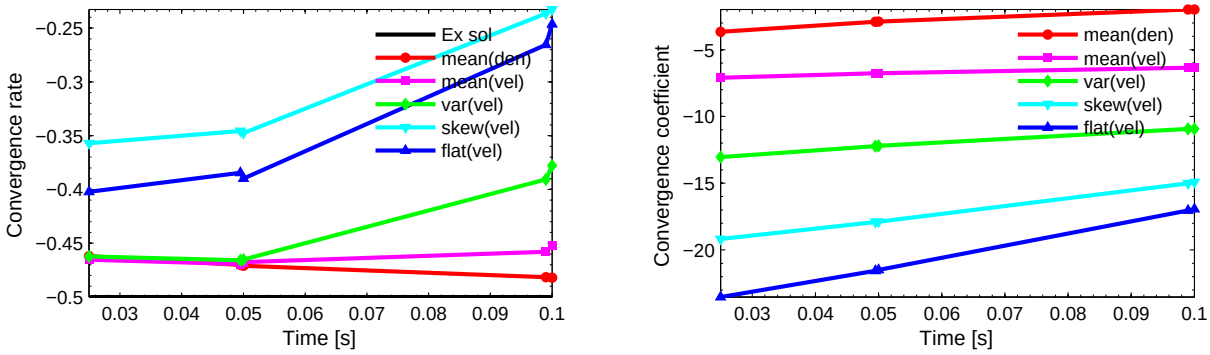

Figure A.39: Hat: time evolution of the statistical convergence rates (left) and coefficients (right) for moments of density and velocity; stochastic Lax-Wendroff method. $N_x = 10^4$.

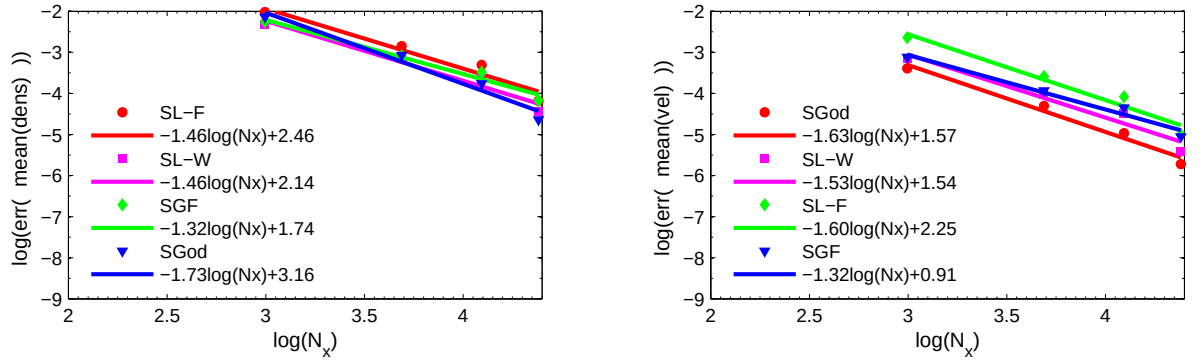

Figure A.40: Hat: spatial convergence of means density (left) and velocity (right) at time $t = 0.1\,\mathrm{s}$. $N_r = 10^7$.

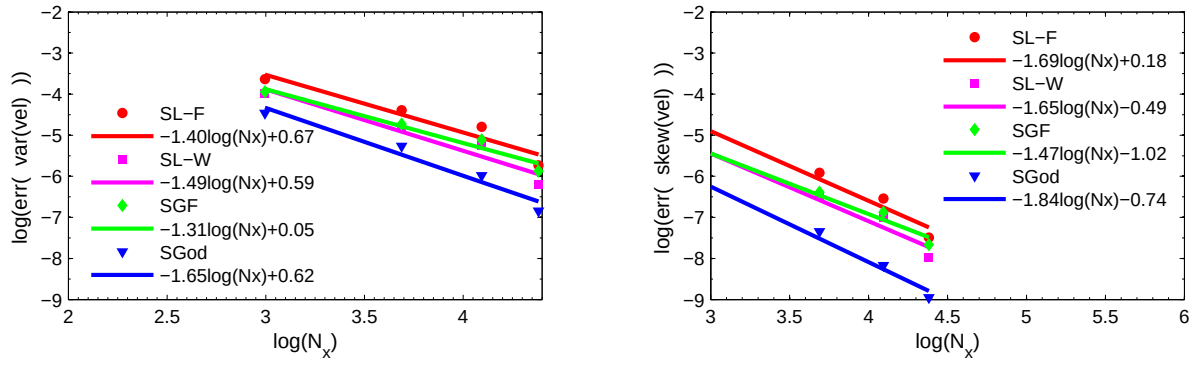

Figure A.41: Hat: spatial convergence of variance (left) and skewness (right) of velocity at time $t = 0.1\,\mathrm{s}$. $N_r = 10^7$.

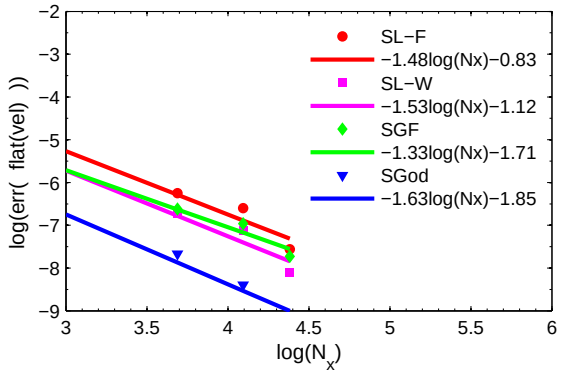

Figure A.42: Hat: spatial convergence of velocity flatness at time $t = 0.1\,\mathrm{s}$. $N_r = 10^7$.

A.5.5 Scheme non-dissipativity test

The solution of the PDF transport eq. (3.121) was not performed in the first test because of the numerical difficulties in solving the PDF equation in the region where $u' = 0$. Consequently, to compare solutions of the PDF eq. (3.121) and PDEs (3.127) and (3.128) we modified the initial fluctuating velocity profiles

Numerical solution

The initial fluctuating velocity profiles are

$$u'' = \sigma\xi \max\left(\sqrt{\exp\left(-\frac{x^2}{L^2}\right)}, 0.1\right), \tag{A.103}$$

where ξ is a normal Gaussian noise, $L = 0.1\,\mathrm{m}$ is a width of non-zero velocity domain and $\sigma = 1\,\mathrm{m/s}$ is a maximum standard deviation.

Obtained numerical solutions of the PDEs (3.127)-(3.128) are compared with the numerical solution of the PDF transport equation (3.121). The numerical modeling of velocity near points where the cut of velocity u'' by 0.1 is used is different in two approaches, due to the presence of Dirac delta function at this point. The solver of the PDF equation was written by R. Duclous in the framework of summer school in CIRM (Marseille). It is a direct numerical solver based on finite volume approximations [EmakoLetizia2014].

The calculation domain is $D = [-5\,\mathrm{m}; 5\,\mathrm{m}]$. In order to obtain a reference solution of the PDF equation (3.121), number of points in x is set to 512, number of points in V'' is 256. Minimum value of V'' is $-5\,\mathrm{m/s}$ and maximum value of V'' is $5\,\mathrm{m/s}$.

Spatial profiles. We demonstrate here spatial profiles of velocity variance (figs. A.43 and A.44), skewness (figs. A.45 and A.46), flatness (figs. A.48 and A.49) and mean density (figs. A.49 and A.50). The number of stochastic fields is large: $N_r = 10^7$ and the number of cells N_x varies. The considered time is $t = 0.2\,\mathrm{s}$. Based on these profiles the spatial convergence is calculated in the section "convergence". One can note that there is no difference between velocity statistics obtained from deterministic PDF equation and similar statistics calculated with any of the stochastic schemes.

The impact of statistical error is negligible: it is $O(\frac{1}{10^7}) \approx 3.1623 \times 10^{-4} O(1)$. Even if the exact constant is unknown, the statistical error is very small in comparison with the spatial error, because the decreasing of number of cells allows converging to expected values of statistics.

The observation of spatial error is the most straightforward for the mean density, since its theoretical value is simply one. For example, the stochastic Godunov scheme gives 2% of error for $N_x = 100$. For other schemes the error is approximately 0.2% for $N_x = 100$. The solution obtained with stochastic Lax-Friedrichs scheme coincides with the exact solution, because this scheme is linear.

Figures A.51 and A.52 illustrate the spatial profiles of the velocity variance for different numbers of realizations at time $t = 0.2\,\mathrm{s}$ with which the statistical convergence has been constructed ($N_x = 10^5$). One can note that $N_r = 1056$ allows recovering the second moment of velocity, whereas $N_r \leq 360$ is not sufficient to establish a spatial profile. The stochastic

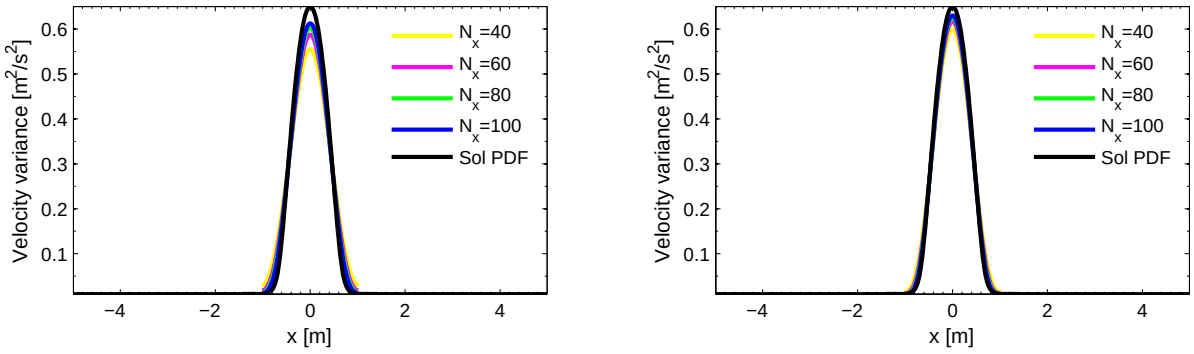

Figure A.43: Scheme non-dissipativity test: spatial profile of velocity variance at time $t = 0.2\,\mathrm{s}$. Left: stochastic Lax-Friedrichs method, right: stochastic Lax-Wendroff method. $N_r = 10^7$.

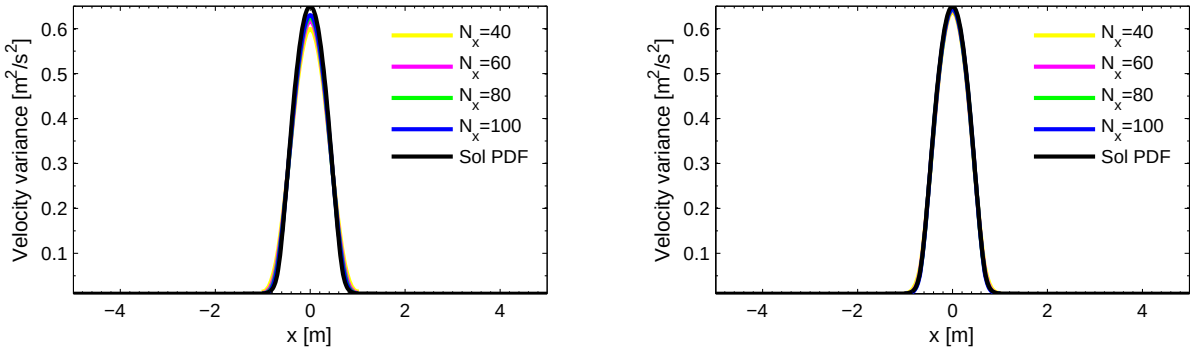

Figure A.44: Scheme non-dissipativity test: spatial profile of velocity variance at time $t = 0.2\,\mathrm{s}$. Left: stochastic GForce method, right: stochastic Godunov method. $N_r = 10^7$.

Godunov method does not give good agreement with theoretical velocity variance even with $N_r = 1056$, which is in fact related to a particular realization of noise sequence used in this calculation.

Figures A.53 and A.54 show spatial profiles of the mean density, velocity variance, skewness and flatness at time $t = 2\,\mathrm{s}$ calculated with $N_r = 9600$, $N_x = 1000$. Spatial statistics follow the statistics calculated using the PDF. In limit points of the spatial interval a small difference in solutions between the SPDEs and the PDF methods is present, as a consequence of Dirac delta function for velocity located in these points during PDF calculation.

Figures A.55 to A.62 represent several examples of the stochastic velocity and density fields at time $t = 2\,\mathrm{s}$ from which the presented earlier in figs. A.53 and A.54 statistics are obtained. As we can see on these figures, the velocity field has large jumps between two numerical neighbor points. In particular, when the velocity changes its sign, the stochastic Lax-Friedrichs scheme yields the multiple velocity jumps, because in this scheme the velocity at the middle point takes the left or the right value of velocity at the following time step. For other methods only a single large jump of velocity is observed at this point.

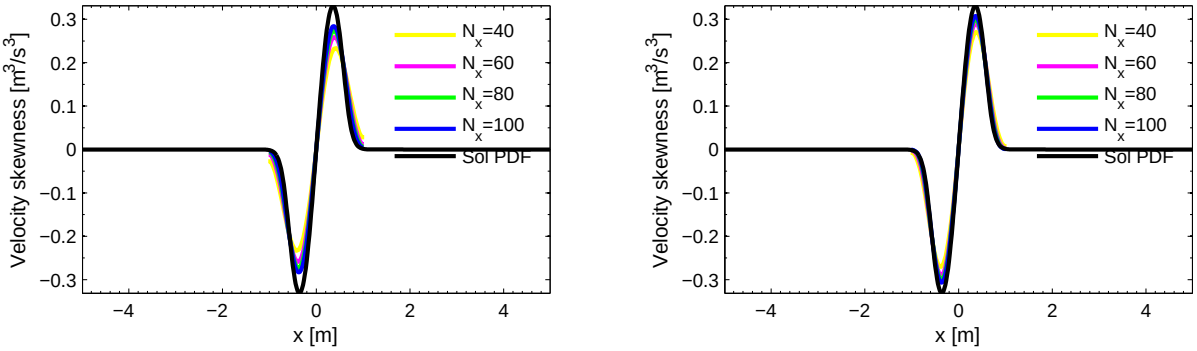

Figure A.45: Scheme non-dissipativity test: spatial convergence for velocity skewness at time $t = 0.2\,\mathrm{s}$. Left: stochastic Lax-Friedrichs method, right: stochastic Lax-Wendroff method. $N_r = 10^7$.

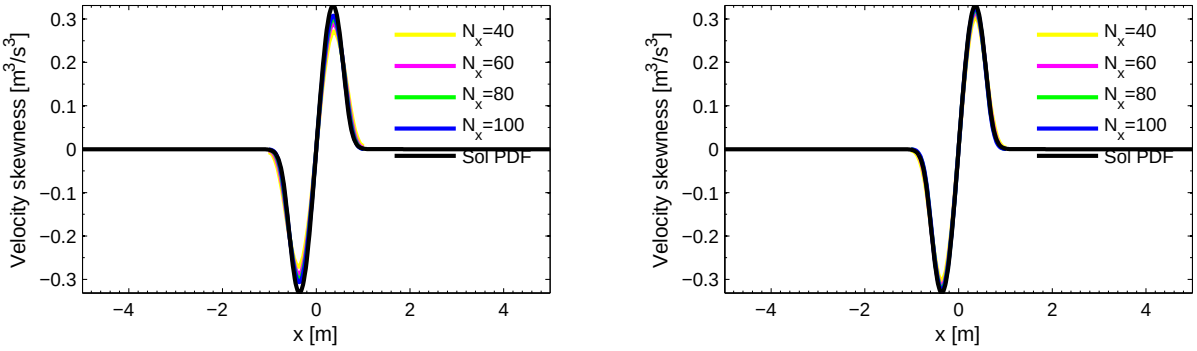

Figure A.46: Scheme non-dissipativity test: spatial profile of velocity skewness at time $t = 0.2\,\mathrm{s}$. Left: stochastic GForce method, right: stochastic Godunov method. $N_r = 10^7$.

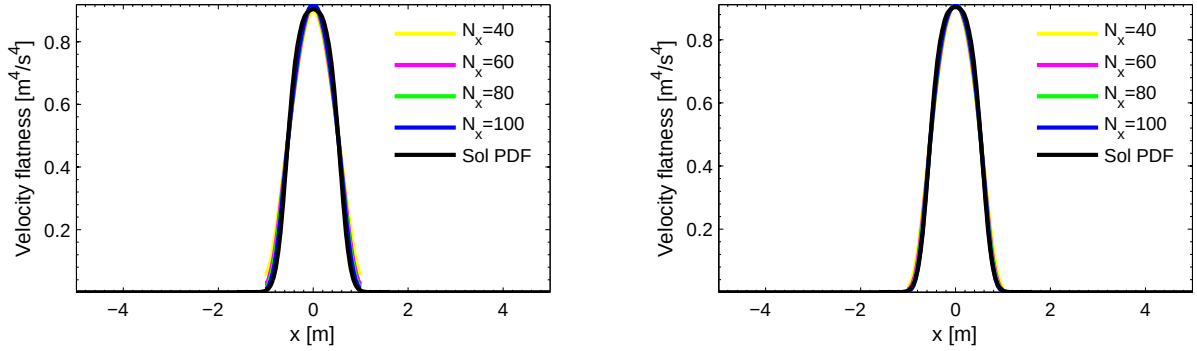

Figure A.47: Scheme non-dissipativity test: spatial profile of velocity flatness at time $t = 0.2\,\mathrm{s}$. Left: stochastic Lax-Friedrichs method, right: stochastic Lax-Wendroff method. $N_r = 10^7$.

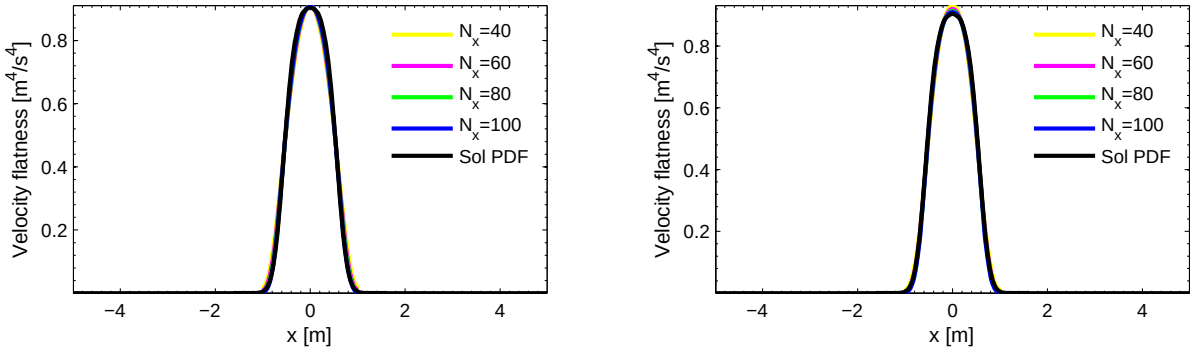

Figure A.48: Scheme non-dissipativity test: spatial profile of velocity flatness at time $t = 0.2\,\mathrm{s}$. Left: stochastic GForce method, right: stochastic Godunov method. $N_r = 10^7$.

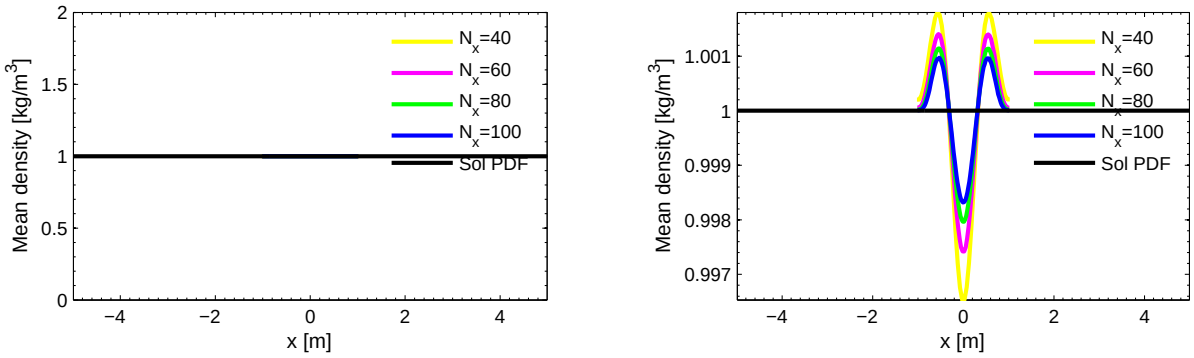

Figure A.49: Scheme non-dissipativity test: spatial profile of mean density at time $t = 0.2\,\mathrm{s}$. Left: stochastic Lax-Friedrihs method, right: stochastic Lax-Wendroff method. $N_r = 10^7$.

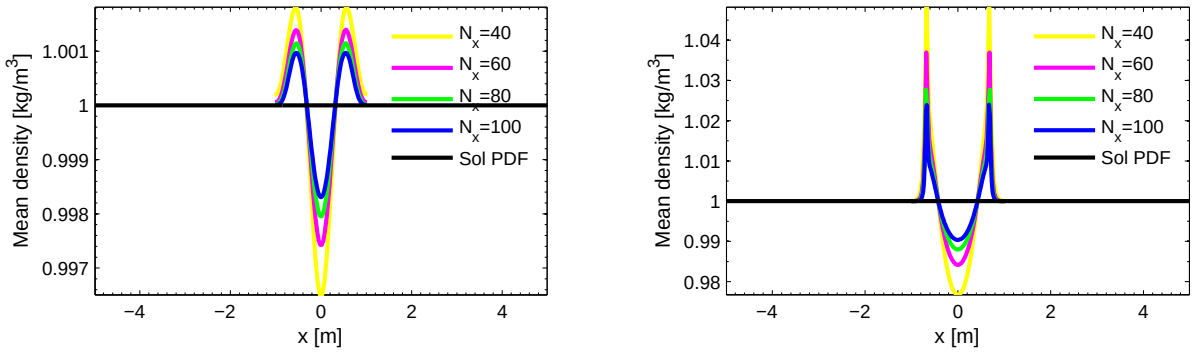

Figure A.50: Scheme non-dissipativity test: spatial profile of mean density at time $t = 0.2\,\mathrm{s}$. Left: stochastic GForce method, right: stochastic Godunov method. $N_r = 10^7$.

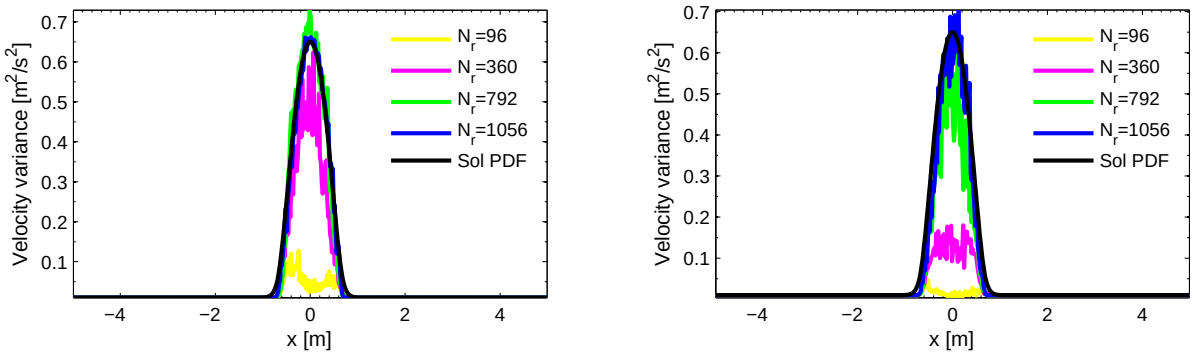

Figure A.51: Scheme non-dissipativity test: spatial convergence for velocity variance at time $t = 0.2\,\mathrm{s}$. Left: stochastic Lax-Friedrichs method, right: stochastic Lax-Wendroff method. $N_x = 10^5$.

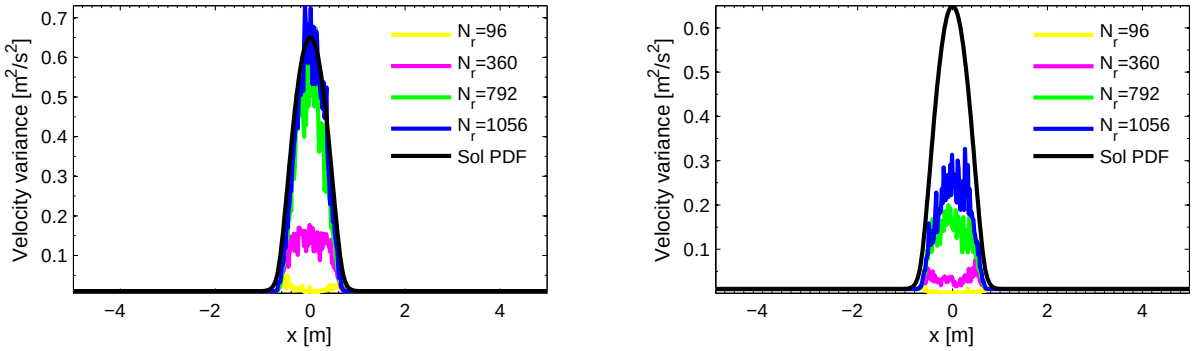

Figure A.52: Scheme non-dissipativity test: spatial profile of velocity variance at time $t = 0.2\,\mathrm{s}$. Left: stochastic GForce method, right: stochastic Godunov method. $N_x = 10^5$.

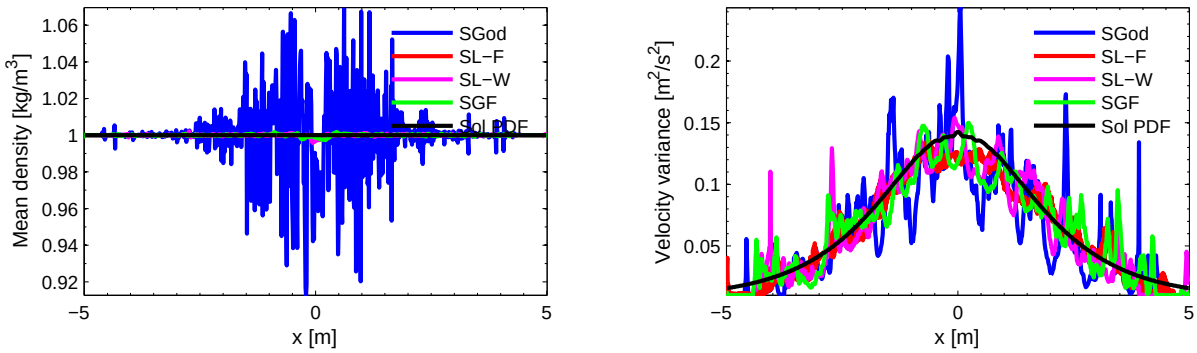

Figure A.53: Scheme non-dissipativity test: spatial profile of mean density (left) and velocity variance (right) at time $t = 2\,\mathrm{s}$. $N_r = 9600$, $N_x = 10^3$.

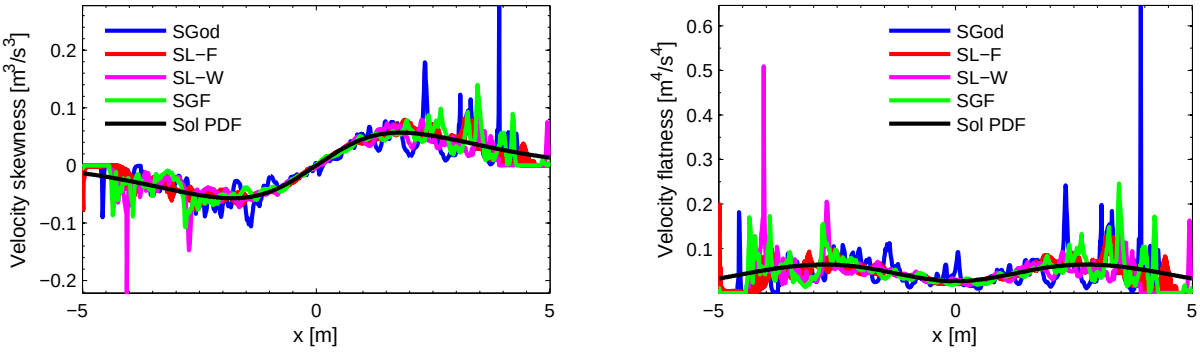

Figure A.54: Scheme non-dissipativity test: spatial profile of velocity skewness (left) and flatness (right) at time $t = 2\,\mathrm{s}$. $N_r = 9600$, $N_x = 10^3$.

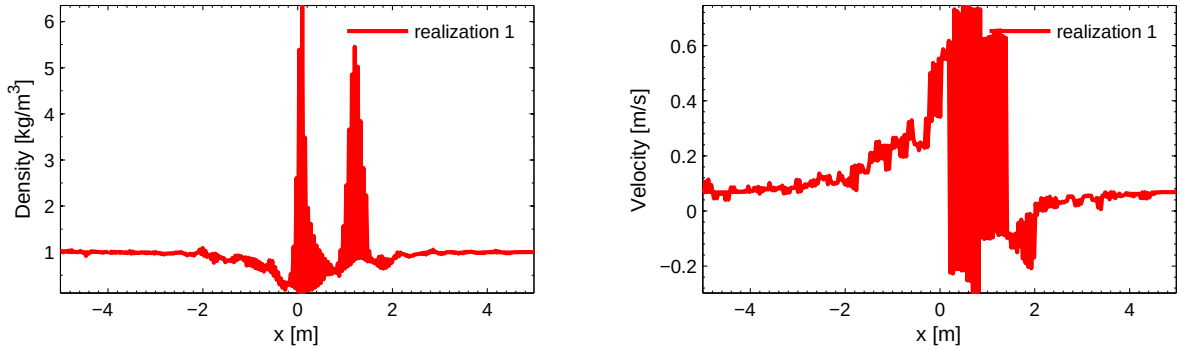

Figure A.55: Scheme non-dissipativity test: profiles of stochastic density (left) and velocity (right) at time $t = 2\,\mathrm{s}$, stochastic Lax-Friedrichs method. $N_r = 9600$, $N_x = 10^3$.

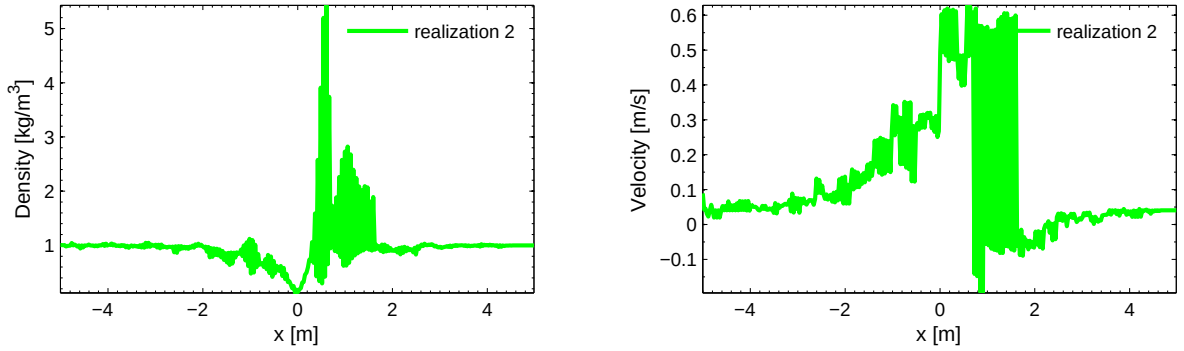

Figure A.56: Scheme non-dissipativity test: profiles of stochastic density (left) and velocity (right) at time $t = 2\,\mathrm{s}$, stochastic Lax-Friedrichs method. $N_r = 9600$, $N_x = 10^3$.

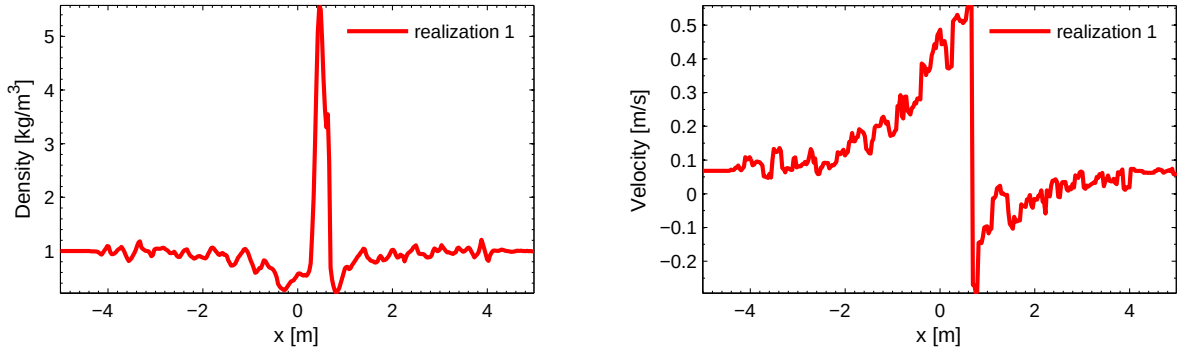

Figure A.57: Scheme non-dissipativity test: profiles of stochastic density (left) and velocity (right) at time $t = 2\,\mathrm{s}$, stochastic Lax-Wendroff method. $N_r = 9600$, $N_x = 10^3$.

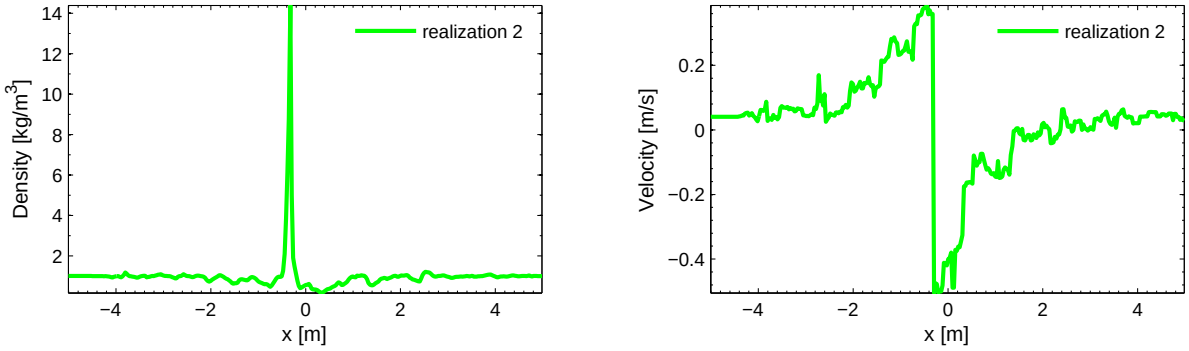

Figure A.58: Scheme non-dissipativity test: profiles of stochastic density (left) and velocity (right) at time $t = 2\,\mathrm{s}$, stochastic Lax-Wendroff method. $N_r = 9600$, $N_x = 10^3$.

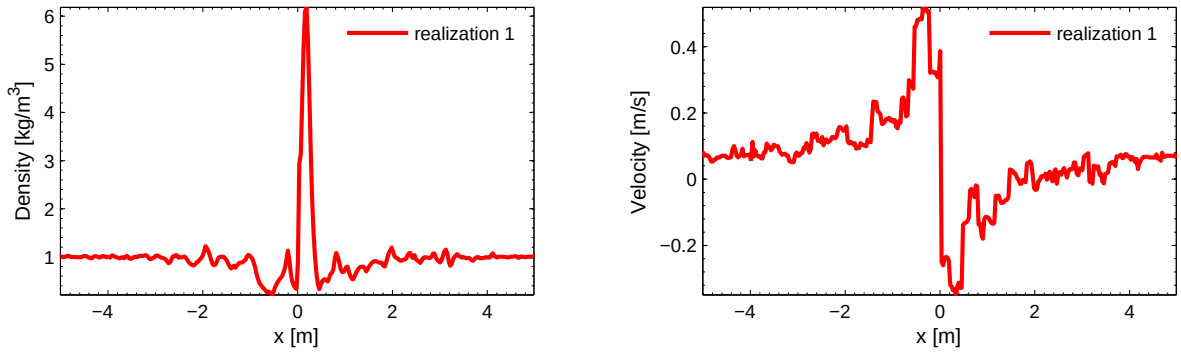

Figure A.59: Scheme non-dissipativity test: profiles of stochastic density (left) and velocity (right) at time $t = 2\,\mathrm{s}$, stochastic GForce method. $N_r = 9600$, $N_x = 10^3$.

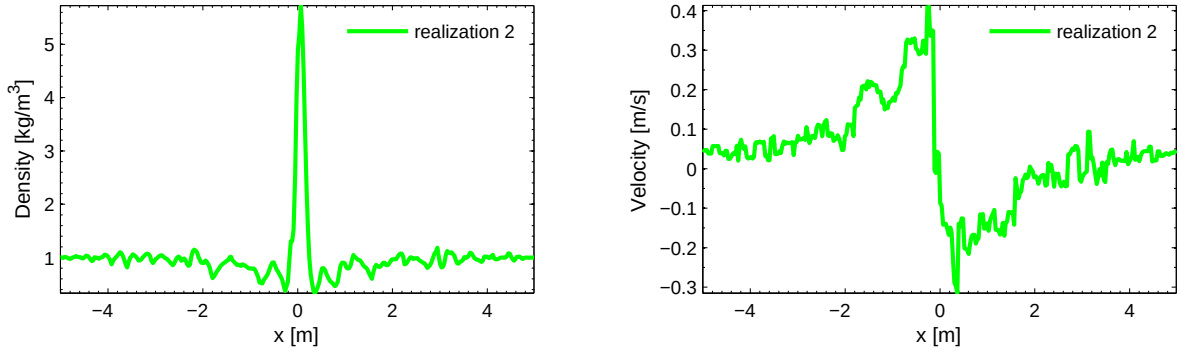

Figure A.60: Scheme non-dissipativity test: profiles of stochastic density (left) and velocity (right) at time $t = 2\,\mathrm{s}$, stochastic GForce method. $N_r = 9600$, $N_x = 10^3$.

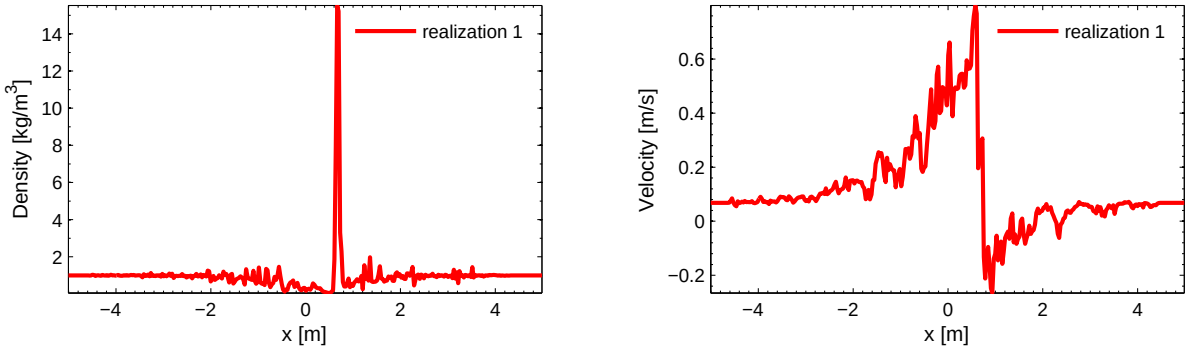

Figure A.61: Scheme non-dissipativity test: profiles of stochastic density (left) and velocity (right) at time $t = 2\,\mathrm{s}$, stochastic Godunov method. $N_r = 9600$, $N_x = 10^3$.

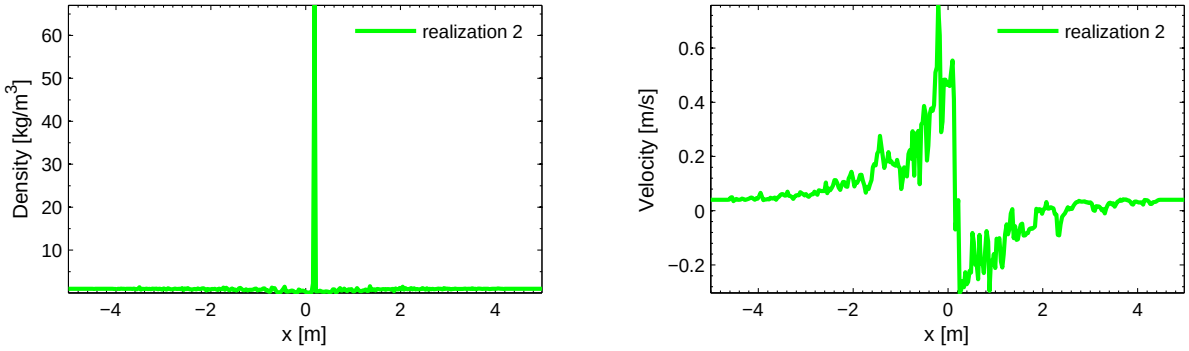

Figure A.62: Scheme non-dissipativity test: profiles of stochastic density (left) and velocity (right) at time $t = 2\,\mathrm{s}$, stochastic Godunov method. $N_r = 9600$, $N_x = 10^3$.

Convergence. To illustrate spatial convergence we perform calculations with a fixed number of stochastic fields $N_r = 10^7$ and we vary the number of cells N_x from 40 to 100. The length of the domain is shortened: $L = [-1\,\mathrm{m}; 1\,\mathrm{m}]$. The spatial error is calculated using the solution of the PDF transport equation. Figures A.63 and A.64 show that the spatial order of convergence is lower than -1 for the number of cells N_x. The convergence rate of $N_x^{-0.7}$ is observed for the mean density, velocity variance and skewness in three stochastic methods: Lax-Friedrichs, Lax-Wendroff and GForce. For these approaches $N_x^{-0.4}$ is the approximate convergence rate for the velocity flatness. The stochastic Godunov method converges slower than other methods.

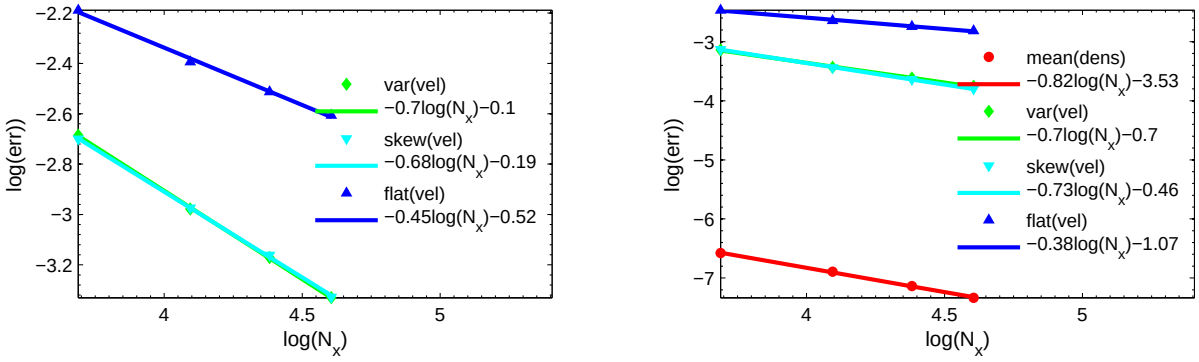

Figure A.63: Scheme non-dissipativity test: spatial convergence for velocity variance, skewness, flatness and mean density at time $t = 0.2\,\mathrm{s}$, left: stochastic Lax-Friedrichs method, right: stochastic Lax-Wendroff method. $N_r = 10^7$.

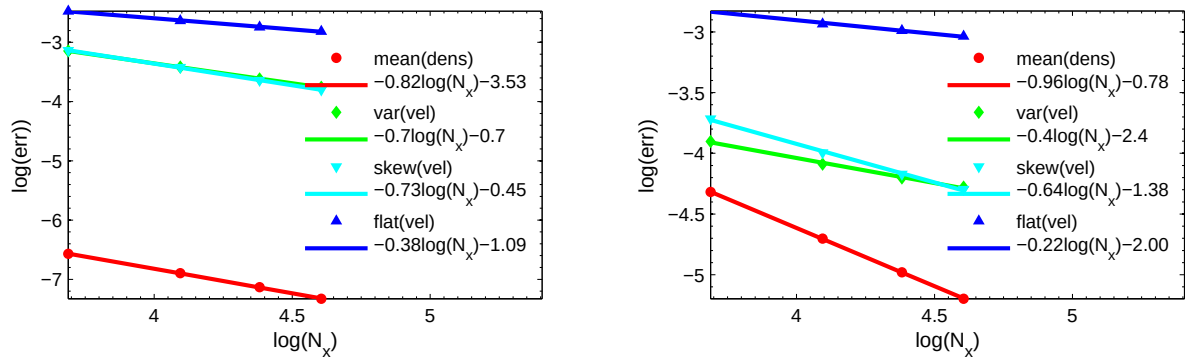

Figure A.64: Scheme non-dissipativity test: spatial convergence for velocity variance, skewness, flatness and mean density at time $t = 0.2\,\mathrm{s}$. Left: stochastic GForce method, right: stochastic Godunov method. $N_r = 10^7$.

In a second time we assess the stochastic convergence of the numerical solution. The number of cells is set to $N_x = 10^5$. The number of stochastic fields is varied from $N_r = 8$ to $N_r = 1056$. Statistical convergence of the mean density for four stochastic schemes is given in the table A.2. As we can see, the statistical convergence for the mean density for three

stochastic methods is about $N_r^{-0.275}$. Figures A.65 and A.66 show the statistical convergence of the first three Favre moments of the velocity at time $t = 0.2\,\mathrm{s}$. The stochastic Lax-Friedrichs, Lax-Wendroff and GForce schemes give good rate of the statistical convergence for the Favre velocity variance. The stochastic Godunov method converges slowly for all represented three Favre statistics of the velocity.

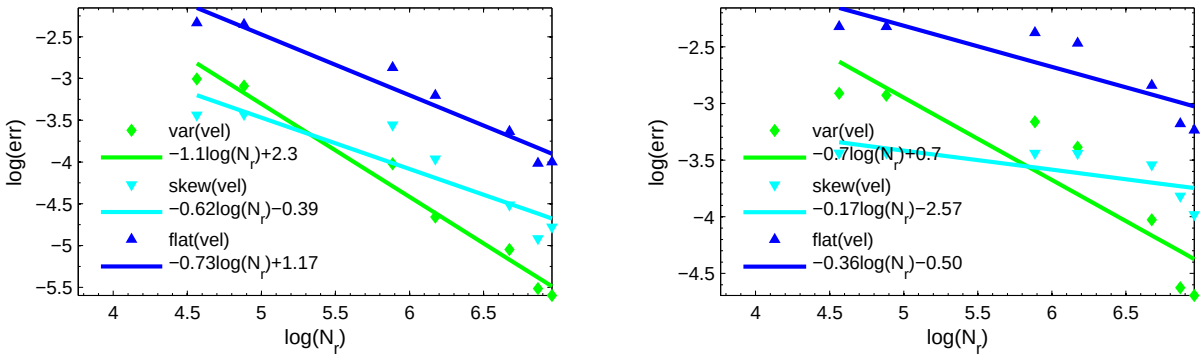

Figure A.65: Scheme non-dissipativity test: statistical convergence for velocity variance, skewness and flatness at time $t = 0.2\,\mathrm{s}$. Left: stochastic Lax-Friedrichs method, right: stochastic Lax-Wendroff method. $N_x = 10^5$.

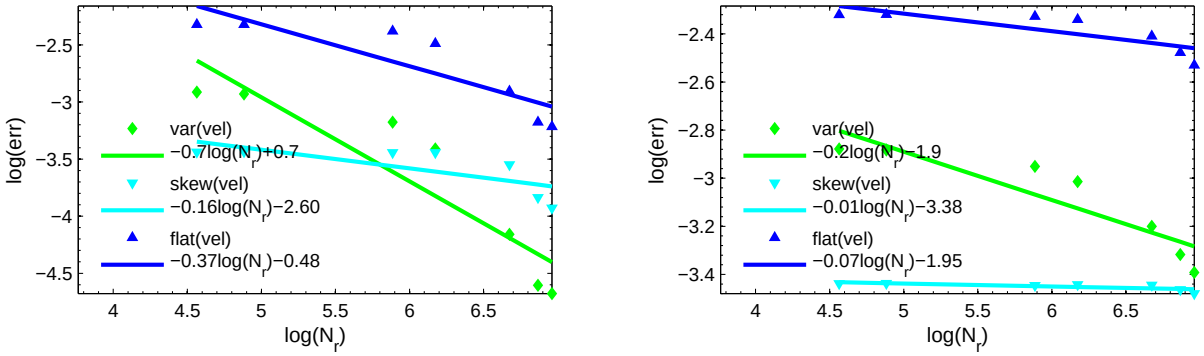

Figure A.66: Scheme non-dissipativity test: statistical convergence for velocity variance, skewness and flatness at time $t = 0.2\,\mathrm{s}$. Left: stochastic GForce method, right: stochastic Godunov method. $N_x = 10^5$.

Method	stochastic L-F	stochastic L-W	stochastic GF	stochastic God
Rate (A)	exact	-0.24	-0.31	-0.25
Coeff (B)	exact	-37.45	-36.62	-37.42

Table A.2: Scheme non-dissipativity test: approximation of statistical error of the mean density in logarithmic scale by $A\log(N_x) + B$ at time $t = 0.2\,\mathrm{s}$. $N_x = 10^5$.

A.6 Study of Langevin equation

The Ornstein-Uhlenbeck process has a long history in physics. Introduced in essence by Langevin in his famous 1908 paper on Brownian motion [Langevin1908], the process received a more thorough mathematical examination several decades later by Uhlenbeck and Ornstein [UhlenbeckOrnstein1930], Chandrasekhar [Chandrasekhar1943], and Wang and Uhlenbeck [WangUhlenbeck1945], and it is nowadays offered as a fairly standard textbook topic [Gardiner1985].

Let us consider in one-dimensional case a velocity u which evolves with time t according to a differential equation of the form

$$\begin{cases} du = -\omega u dt + \sqrt{2\omega\sigma^2} d\xi, \\ u(t_0) = u_0, \end{cases} \tag{A.104}$$

where ω is a characteristic turbulent frequency which does not depend on time, σ^2 is a velocity variance (it is also supposed to be a constant), $d\xi$ is a differential of standard Wiener process, $\overline{()}$ is a symbol of the mathematical average of all fields ξ. At initial time t_0, the velocity u_0 follows a Gaussian law with the mean $\overline{u_0}$ and the variance $\overline{u_0'^2}$, i.e.

$$u_0 = N\left(\overline{u_0}, \overline{u_0'^2}\right). \tag{A.105}$$

The analytical solution of the stochastic eqs. (A.104) and (A.105) is

$$u(t) = \exp(-\omega(t-t_0))u_0 + \sqrt{2\omega\sigma^2} \int_{t_0}^{t} \exp(-\omega(t-s)) d\xi, \ 0 \le s \le t. \tag{A.106}$$

$u(t)$ is a Gaussian variable with the mean $\exp(-\omega(t-t_0))\overline{u_0}$. Indeed taking the average of eq. (A.106) we deduce that

$$\overline{u(t)} = \exp(-\omega(t-t_0))\overline{u_0}, \tag{A.107}$$

because

$$\overline{\int_{t_0}^{t} \exp(-\omega(t-s)) d\xi} = 0. \tag{A.108}$$

Let us recall the Itô formula [Itô1944]. Consider a stochastic differential equation

$$dX(t) = f(t, X(t))dt + g(t, X(t))d\xi(t), \tag{A.109}$$

where $0 \le t \le T$ with $X(0)$ a random variable. Let be F a smooth function and f, g and F satisfy conditions of the Ito theorem, then

$$dF(t, X(t)) = \left(\frac{\partial F(t,X)}{\partial t} + f(t,X)\frac{\partial F(t,X)}{\partial x} + \frac{1}{2} g^2(t,X) \frac{\partial^2 F(t,X)}{\partial x^2} \right) dt + g(t,X)\frac{\partial F(t,X)}{\partial x} d\xi(t). \tag{A.110}$$

Using the Itô formula (A.110) the equation for v^2 can be written as

$$\begin{cases} du^2 = -2\omega(u^2 - \sigma^2)dt + 2u\sqrt{2\omega\sigma^2} d\xi, \\ u(t_0)^2 = u_0^2. \end{cases} \tag{A.111}$$

Whence

$$\begin{cases} d\overline{u^2} = -2\omega(\overline{u^2} - \sigma^2)dt, \\ \overline{u(t_0)^2} = \overline{u_0^2}. \end{cases} \tag{A.112}$$

$$d(\exp(2\omega t)\overline{u^2}) = 2\omega \exp(2\omega t)\sigma^2 dt, \tag{A.113}$$

$$\overline{u^2}(t) = \exp(-2\omega(t - t_0))\overline{u_0^2} + \sigma^2(1 - \exp(-2\omega(t - t_0))). \tag{A.114}$$

As $\overline{u'^2(t)} = \overline{u^2(t)} - (\overline{u(t)})^2$ we obtain

$$\overline{u'^2(t)} = \exp(-2\omega(t - t_0))\overline{u_0'^2} + \sigma^2(1 - \exp(-2\omega(t - t_0))). \tag{A.115}$$

When the time tends to infinity, the variance tends to σ^2. Thus we can conclude that $u(t)$ follows a Gaussian law with the mean

$$\exp(-\omega(t - t_0))\overline{u_0}$$

and the variance

$$\exp(-2\omega(t - t_0))\overline{u_0'^2} + \sigma^2(1 - \exp(-2\omega(t - t_0)))$$

By changing variables, $u(t)$ satisfies a recursive formula:

$$u(t + \Delta t) = \exp(-\omega\Delta t)u(t) + \sigma\sqrt{1 - \exp(-2\omega\Delta t)}\xi, \tag{A.116}$$

where $\xi = N(0, 1)$.

Let us consider a simple example of $u(t)$. Let be $\sigma = 1\,\mathrm{m/s}$, $\omega = 20\,\mathrm{Hz}$ and $u(t_0) = N(0, 1)$. Δt is set to $5 \times 10^{-4}\,\mathrm{s}$, a number of fields is $N_r = 10^4$. According to the eq. (A.116), $u(t)$ is a Gaussian variable with the mean 0 and the variance 1. Figures A.67 and A.68 compare variance, flatness and hyperflatness obtained numerically by the recurrent formula (A.116) against their theoretical values $1\,\mathrm{m^2/s^2}$, $3\,\mathrm{m^3/s^3}$ and $15\,\mathrm{m^4/s^4}$ respectively. There is a bias because the number of realizations is finite. The higher the moment is, the more realizations of the fields u are required to approximate the exact solution.

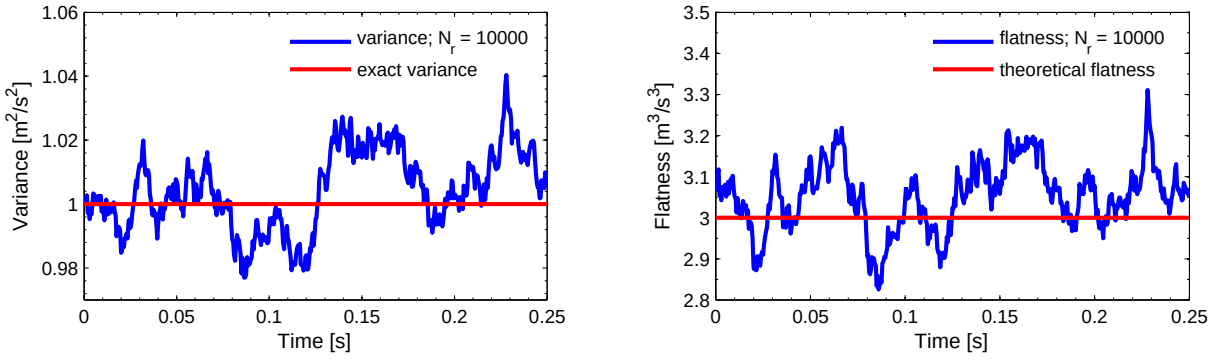

Figure A.67: Comparison of variance (left), flatness (right) with their theoretical values

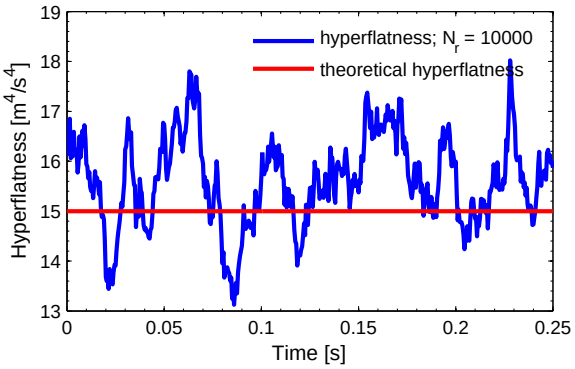

Figure A.68: Comparison of hyperflatness with its theoretical value

Appendix B

Dependence of solution on computational grid in reactive backward-facing step flow

B.1 Numerical setup

The 2D computational domain is presented in section 6.2.1. For this domain we consider several grids, denoted by $m1$, $m2$, $m3$, $m4$, $m5$. They contain 16068, 23990, 36956, 77030 and 106351 of inner cells respectively. Figure B.1 shows a close-up view of the step extremity of 2D grids. The grid $m3$ corresponds to fig. 6.4.

The physical models and boundary conditions are described in sections 6.2.2 and 6.3.1. In order to study the dependence of solution on computational grid, PFTC β-PDF 40-4 and TPaSR with geometrical fine structure residence time with $C_\omega = 10.5$ are investigated. The second order Runge-Kutta method with first order ODFI scheme is used.

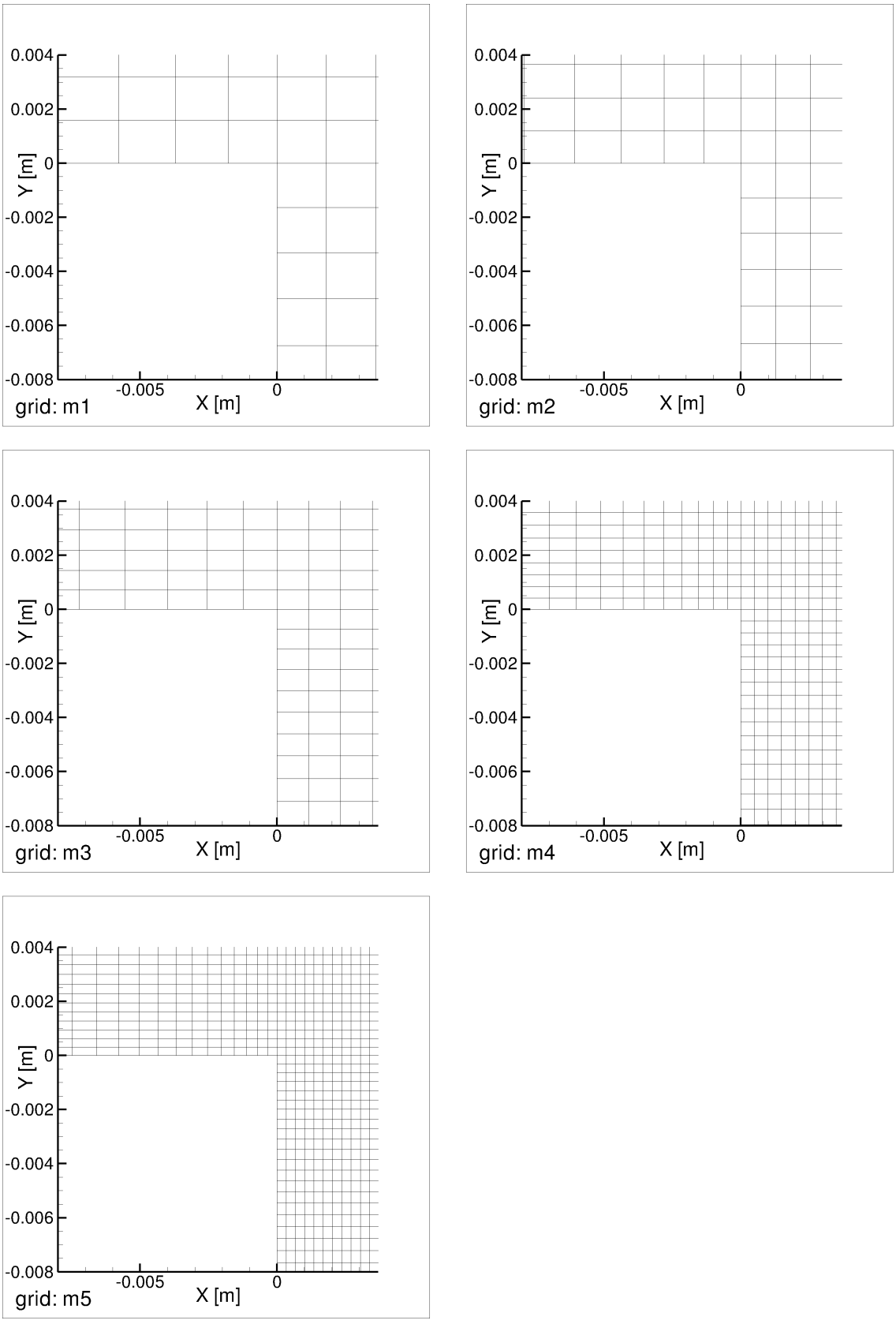

Figure B.1: 2D grids for backward-facing step flow; grids $m1$, $m2$, $m3$, $m4$, $m5$

B.2 Results

B.2.1 RANS/PFTC beta-PDF

The following test-cases are considered.

	Method	Boundary condition	Grid	Time step Δt
PFTC β-PDF 40-4	RK2 with 1st order ODFI sch.	nonhomogeneous	m1	8×10^{-7} s
PFTC β-PDF 40-4	RK2 with 1st order ODFI sch.	nonhomogeneous	m2	5×10^{-7} s
PFTC β-PDF 40-4	RK2 with 1st order ODFI sch.	nonhomogeneous	m3	4×10^{-7} s
PFTC β-PDF 40-4	RK2 with 1st order ODFI sch.	nonhomogeneous	m4	1×10^{-7} s
PFTC β-PDF 40-4	RK2 with 1st order ODFI sch.	nonhomogeneous	m5	1×10^{-7} s

Table B.1: Considered test-cases for RANS/PFTC β-PDF models in reactive backward-facing step flow

Figure B.2 demonstrates the effect of the grid resolution in the case of PFTC β-PDF 40-4 model, when the first order spatial scheme is used. With decreasing grid step solution better approaches the experimental temperature (see fig. B.2). The vertical profiles of Favre-averaged temperature calculated on the grid $m3$ are located between temperature profiles calculated on $m1$, $m2$ and on $m4$, $m5$, which are pairwise close to each other.

Figure B.3 illustrates the influence of the number of cells used in the simulation on the profiles of $\widetilde{u}_x$. The grid refinement allows decreasing the velocity values, e.g, for $X = 0.25\,\mathrm{m}$ the maximum of $\widetilde{u}_x$ on $m5$ grid decreases by 1.2162 times in comparison with the solution on $m1$ grid and in 1.1351 times in comparison with the solution on $m3$ grid, given that the experimental value is still 1.1563 times lower that the numerical solution on $m5$ grid.

Similarly to the streamwise velocity the transverse velocity converges to the experimental data with respect to the grid size. Figure B.4 illustrates five calculations on grids $m1$, $m2$, $m3$, $m4$ and $m5$ of the Favre-averaged transverse velocity $\widetilde{u}_y$. The converged result, approximately given by $m4$ and $m5$, is closer to the experimental solution than the calculations for coarser grids, but still remains significantly different for $0.25\,\mathrm{m} \leq X \leq 0.46\,\mathrm{m}$.

Concerning the dependence on the grid of RMS velocity fluctuations, similarly to the previous profiles, the refined $m5$ grid better approaches the measurement results that coarser $m1$, $m2$, $m3$ and $m4$ grids.

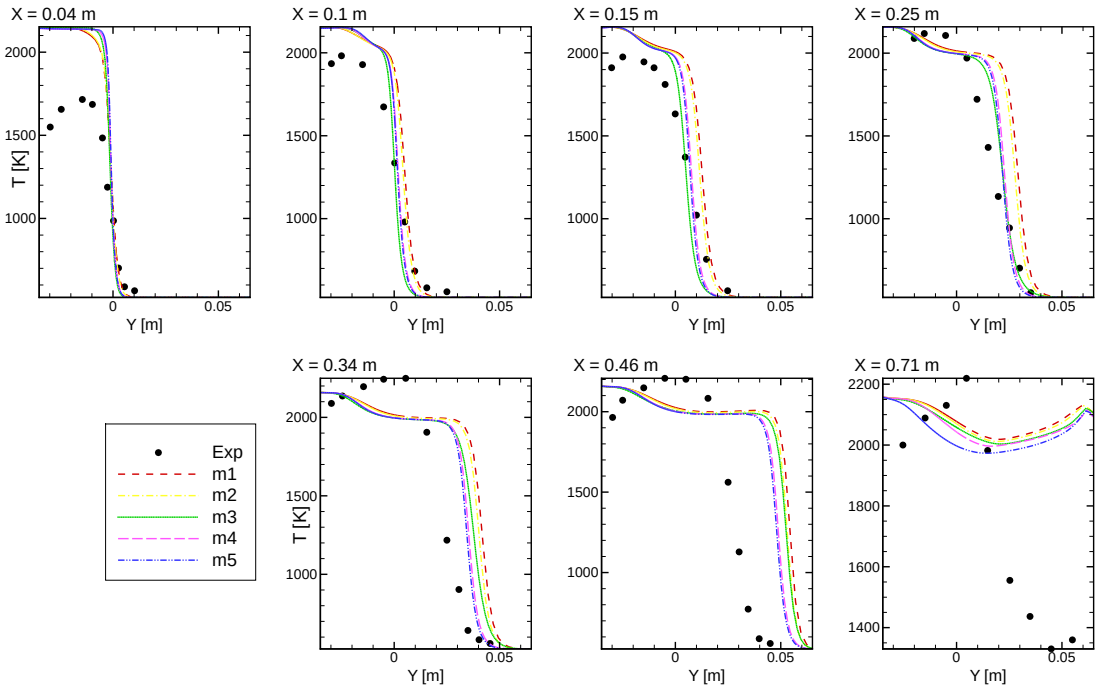

Figure B.2: Dependence of vertical profiles of Favre-averaged temperature $\widetilde{T}$ on computational grid in reactive backward facing step flow; RANS/PFTC β-PDF 40-4 with nonhomogeneous inlet profile

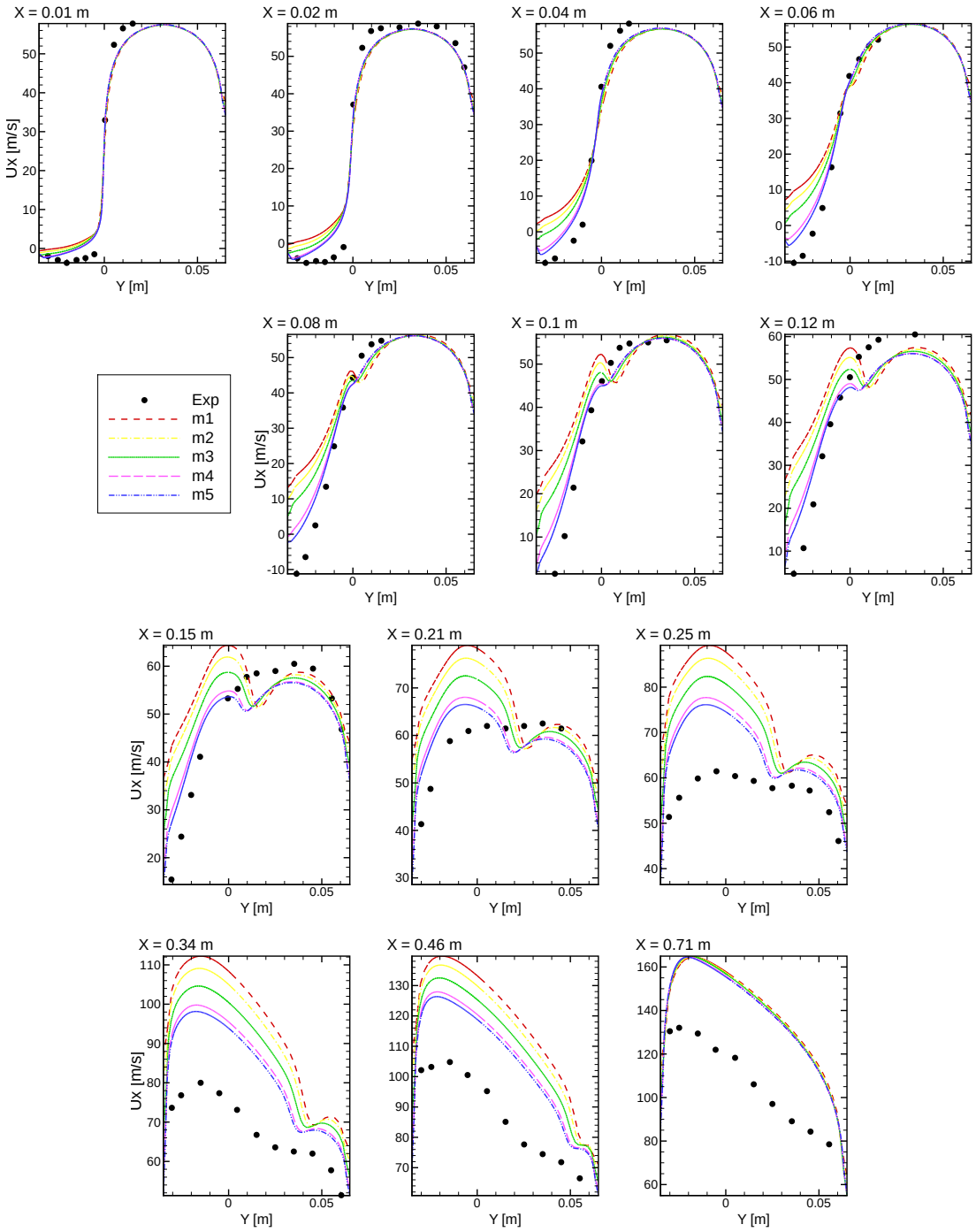

Figure B.3: Dependence of vertical profiles of Favre-averaged streamwise velocity $\widetilde{u}_x$ on computational grid in reactive backward-facing step flow; RANS/PFTC β-PDF 40-4

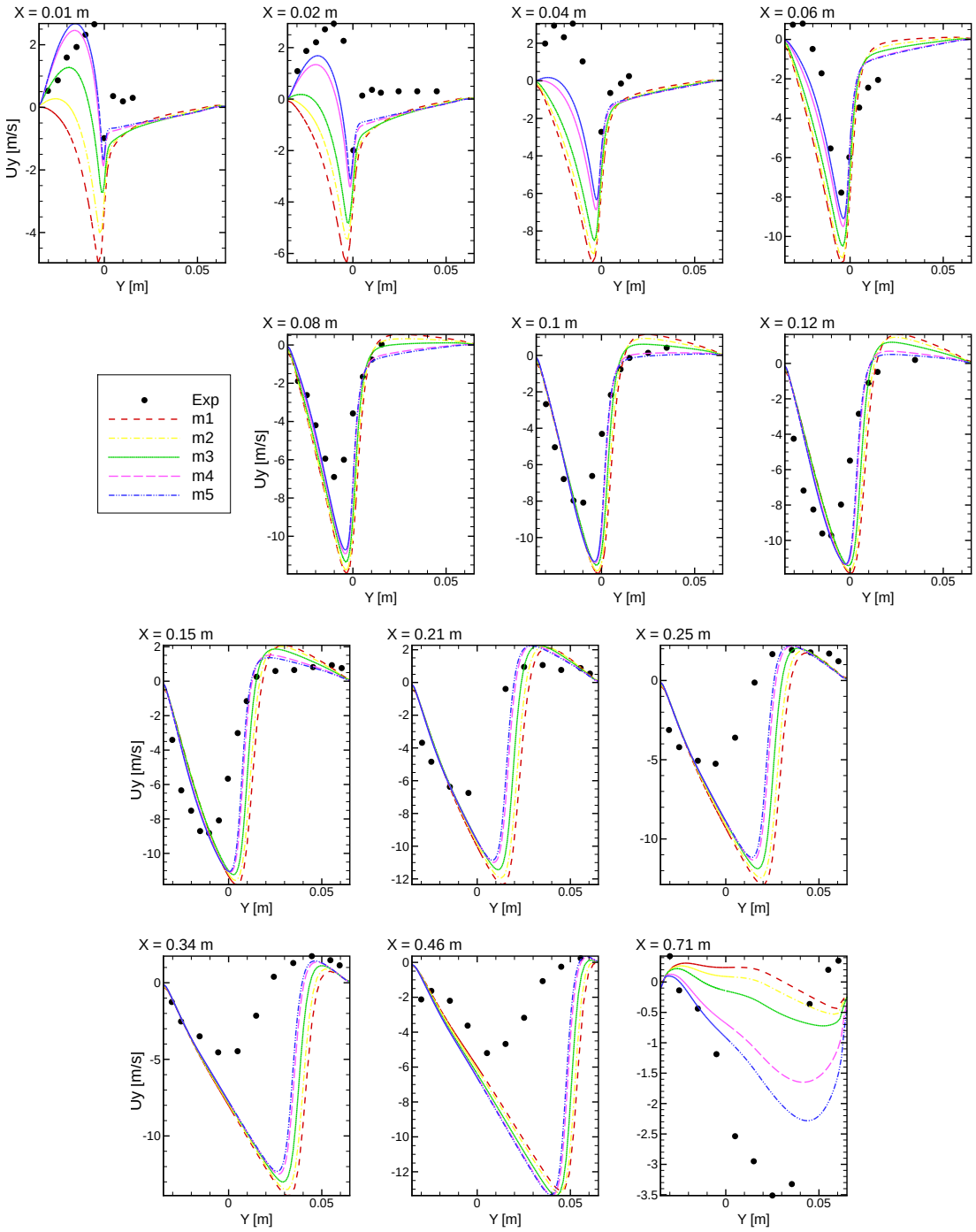

Figure B.4: Dependence of vertical profiles of the Favre-averaged transverse velocity $\widetilde{u}_y$ on computational grid in reactive backward-facing step flow; RANS/PFTC β-PDF 40-4

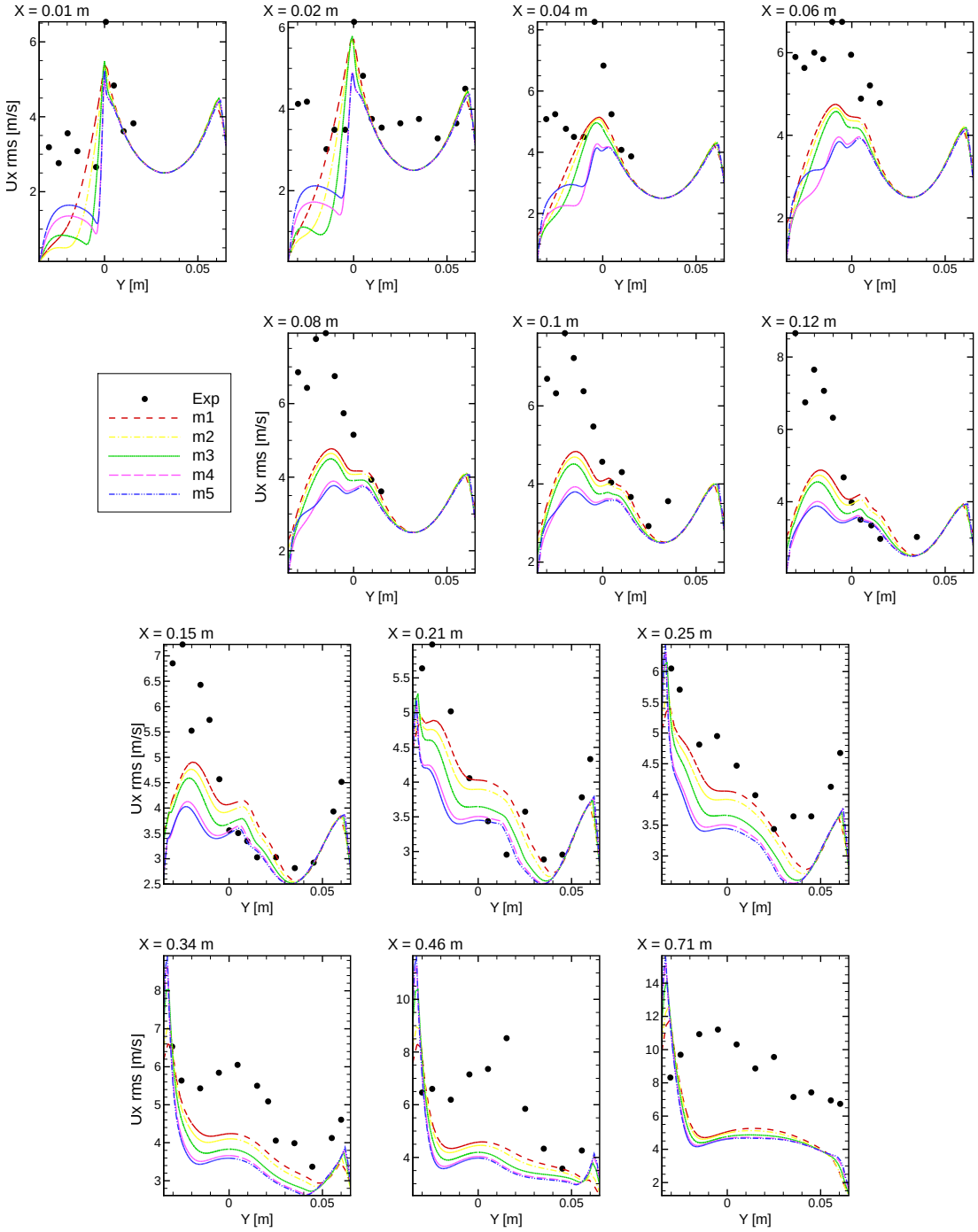

Figure B.5: Dependence of vertical profiles of u_x^{RMS} on computational grid in reactive backward-facing step flo; RANS/PFTC β-PDF

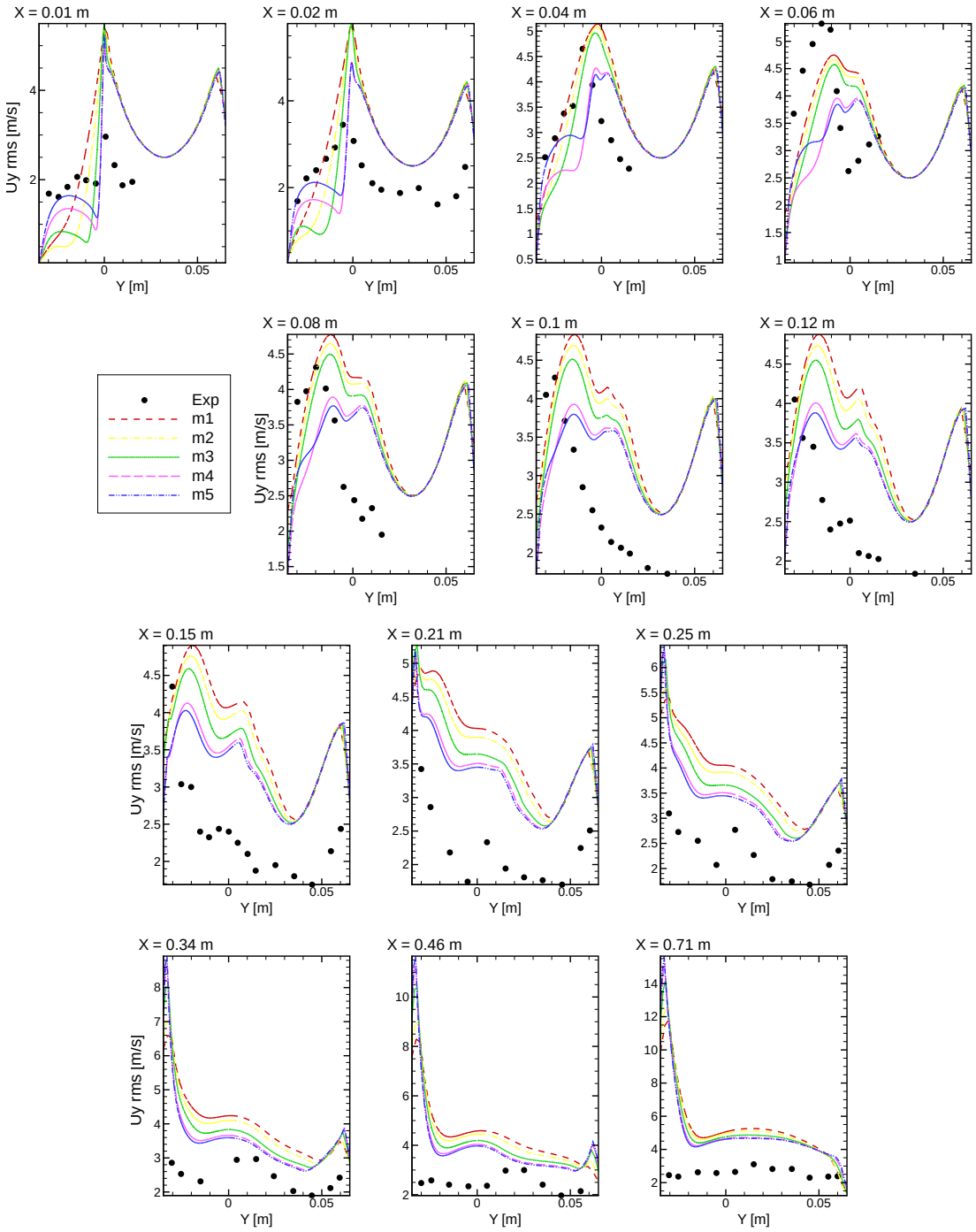

Figure B.6: Dependence of vertical profiles of u_y^{RMS} on computational grid in reactive backward-facing step flow; RANS/PFTC β-PDF

B.2.2 RANS/TPaSR

Table B.2 represents the test-cases under study.

Chemical model	Method	Boundary condition	Grid	Time step Δt
geom. $C_\omega = 10.5$	RK2 with 1st order ODFI sch.	nonhomogeneous	m1	8×10^{-7} s
geom. $C_\omega = 10.5$	RK2 with 1st order ODFI sch.	nonhomogeneous	m2	5×10^{-7} s
geom. $C_\omega = 10.5$	RK2 with 1st order ODFI sch.	nonhomogeneous	m3	4×10^{-7} s
geom. $C_\omega = 10.5$	RK2 with 1st order ODFI sch.	nonhomogeneous	m4	5×10^{-8} s

Table B.2: Considered test-cases for RANS/TPaSR approach in reactive backward-facing step flow. Following abbreviations are used in this section: "geom." - geometrical fine structure residence time, "kol." - Kolmogorov fine structure residence time and "magn." - Magnussen fine structure residence time.

The influence of the number of cells used in the simulation on the profiles of the Favre-averaged temperature $\widetilde{T}$ is presented in fig. B.7. On four considered grids the vertical profiles of the mean temperature remain close to each other.

The dependence of vertical profiles of Favre-averaged streamwise velocity $\widetilde{u}_x$ on computational grid is demonstrated in fig. B.8. In the lower part of step nose region the solution on the refined grid $m4$ better approximates the experimental data than the solutions on coarse grids. Only for $X = 0.21$ m the solution $\widetilde{u}_x$ on $m4$ underestimates the experimental profile whereas the solutions on grids $m1$, $m2$ and $m3$ remain in reasonable agreement.

The converged vertical profiles of transverse velocity with respect to the grid size ($m1$, $m2$, $m3$ and $m4$) are presented in fig. B.9. In the lower region of the step nose the solution on the refined grid $m4$ describes better the experimental data. The velocity becomes positive, while for the coarse grids the velocity is negative in this region. For $X \geq 0.71$ m the solution on the refined grid $m4$ overestimates experimental profile larger than solutions on the coarse grids.

The refined grid $m4$ allows decreasing RMS velocity values for u_x^{RMS} and u_y^{RMS} (see figs. B.10 and B.11).

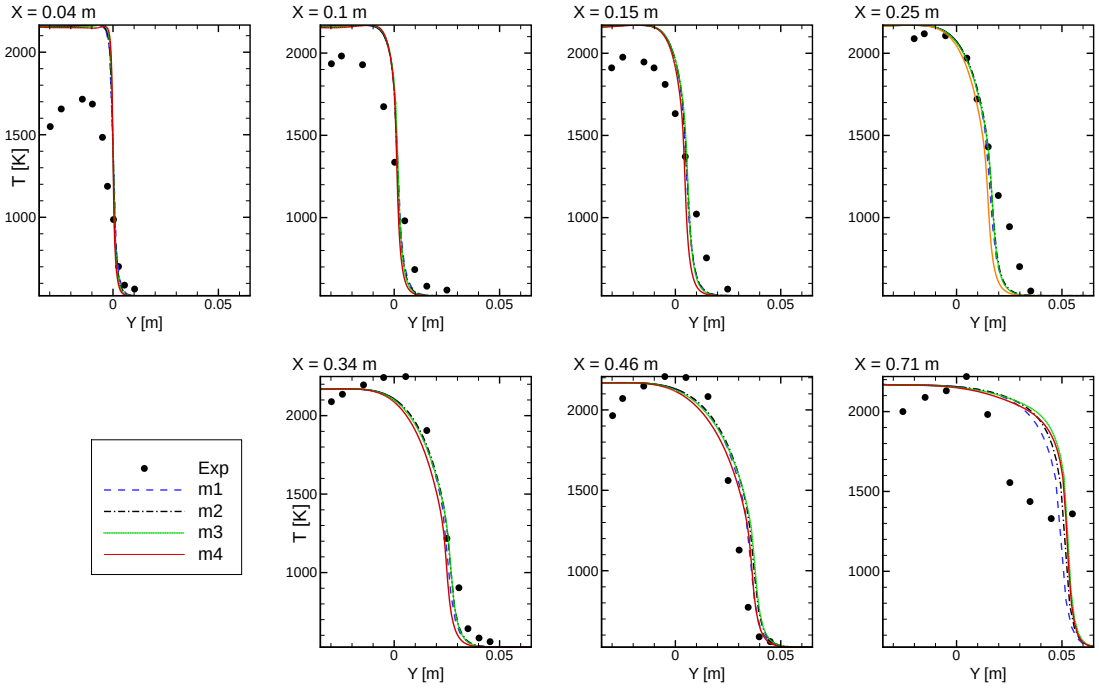

Figure B.7: Dependence of vertical profiles of Favre-averaged temperature $\widetilde{T}$ on computational grid in reactive backward-facing step flow; RANS/TPaSR

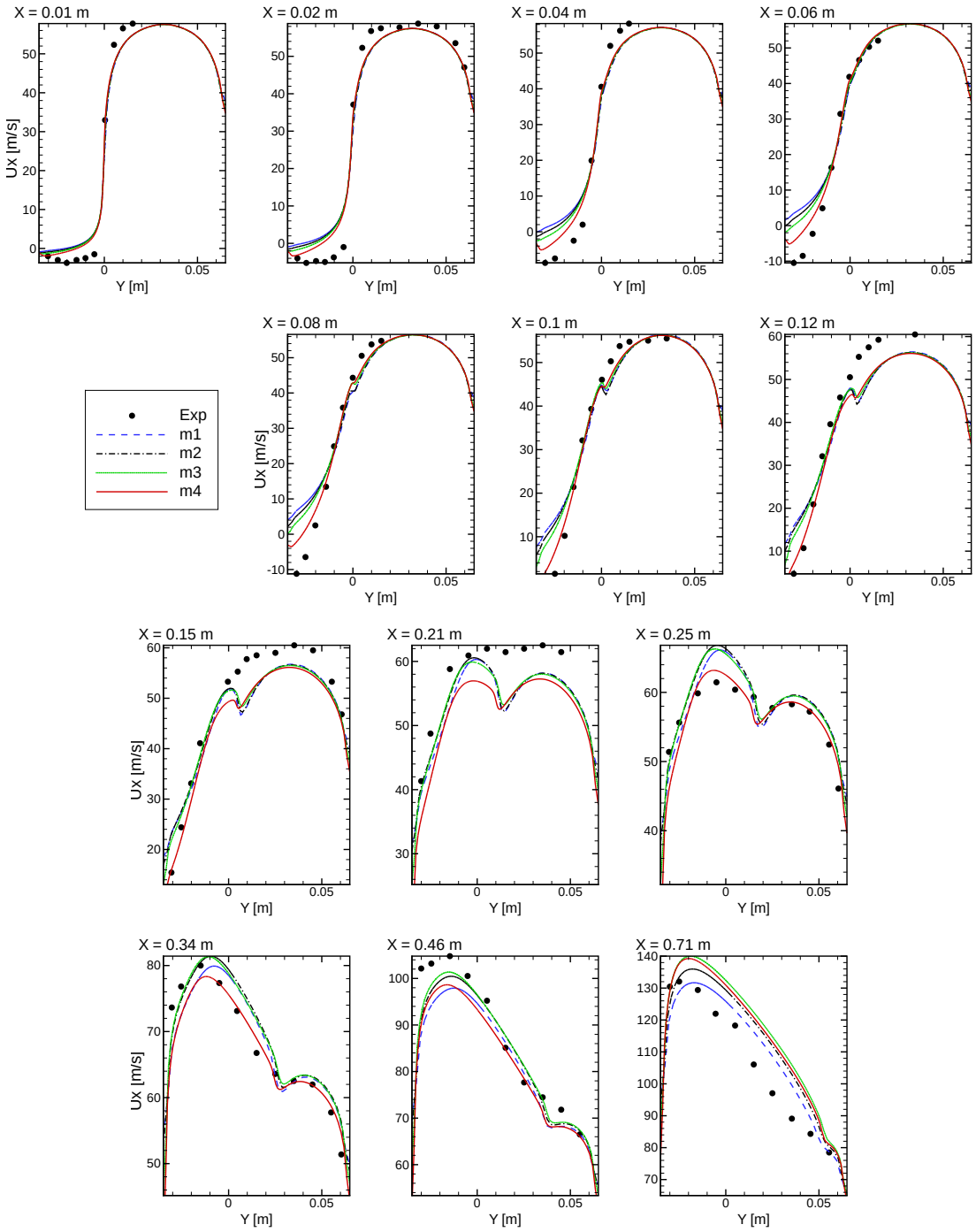

Figure B.8: Dependence of vertical profiles of Favre-averaged streamwise velocity $\widetilde{u}_x$ on computational grid in reactive backward-facing step flow; RANS/TPaSR

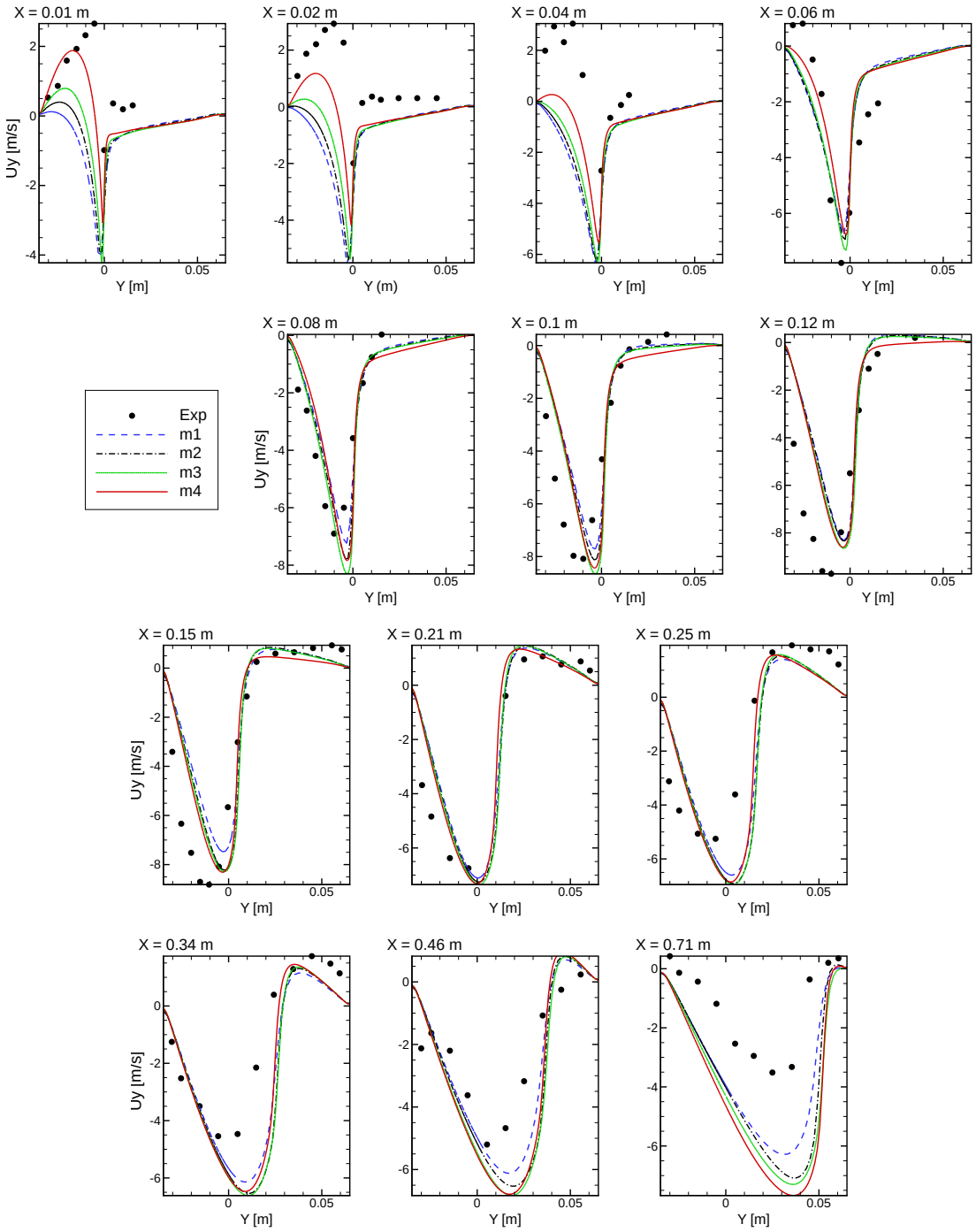

Figure B.9: Dependence of vertical profiles of of Favre-averaged transverse velocity $\widetilde{u}_y$ on computational grid in reactive backward-facing step flow; RANS/TPaSR

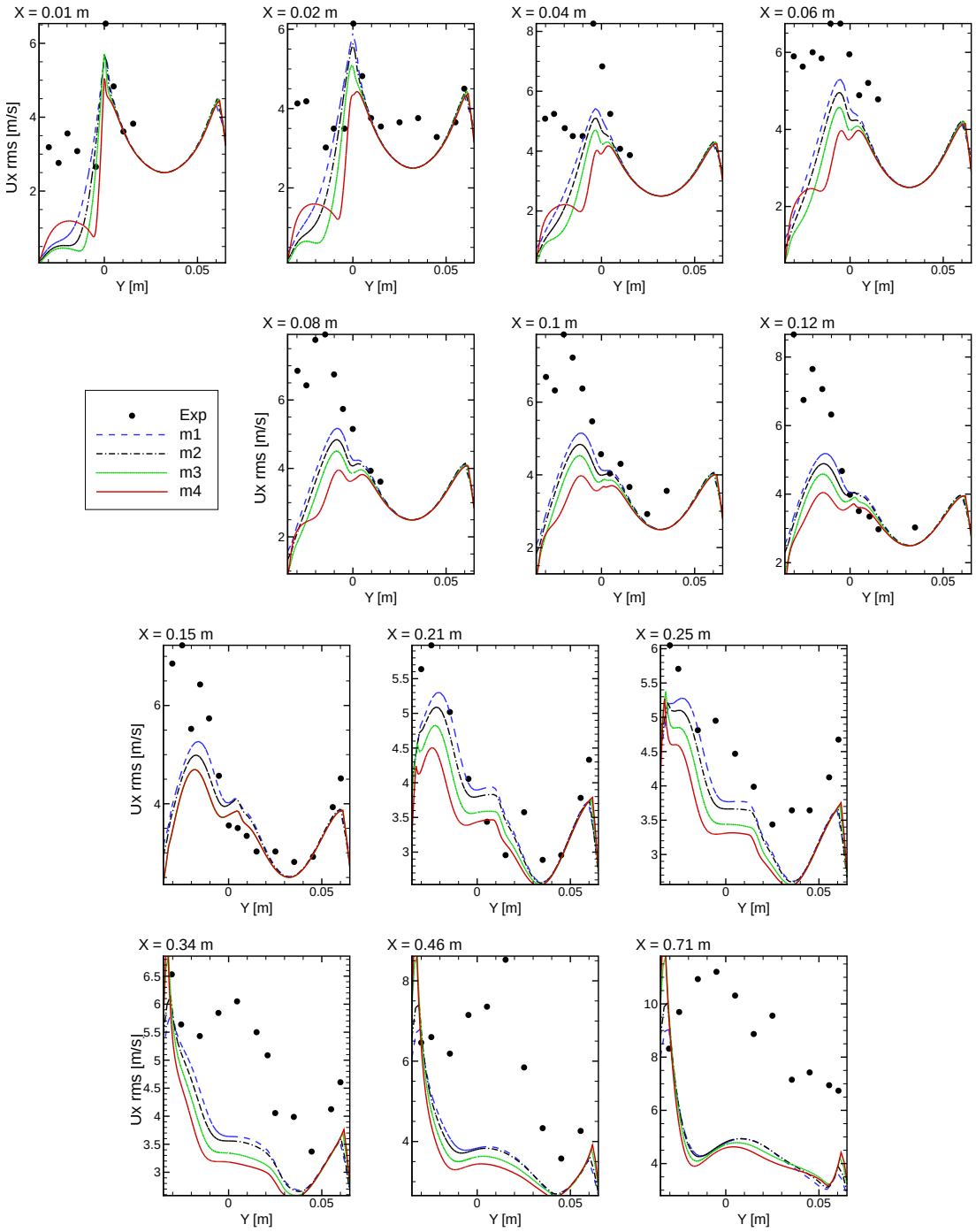

Figure B.10: Dependence of vertical profiles of u_x^{RMS} on computational grid in reactive backward-facing step flow; RANS/TPaSR

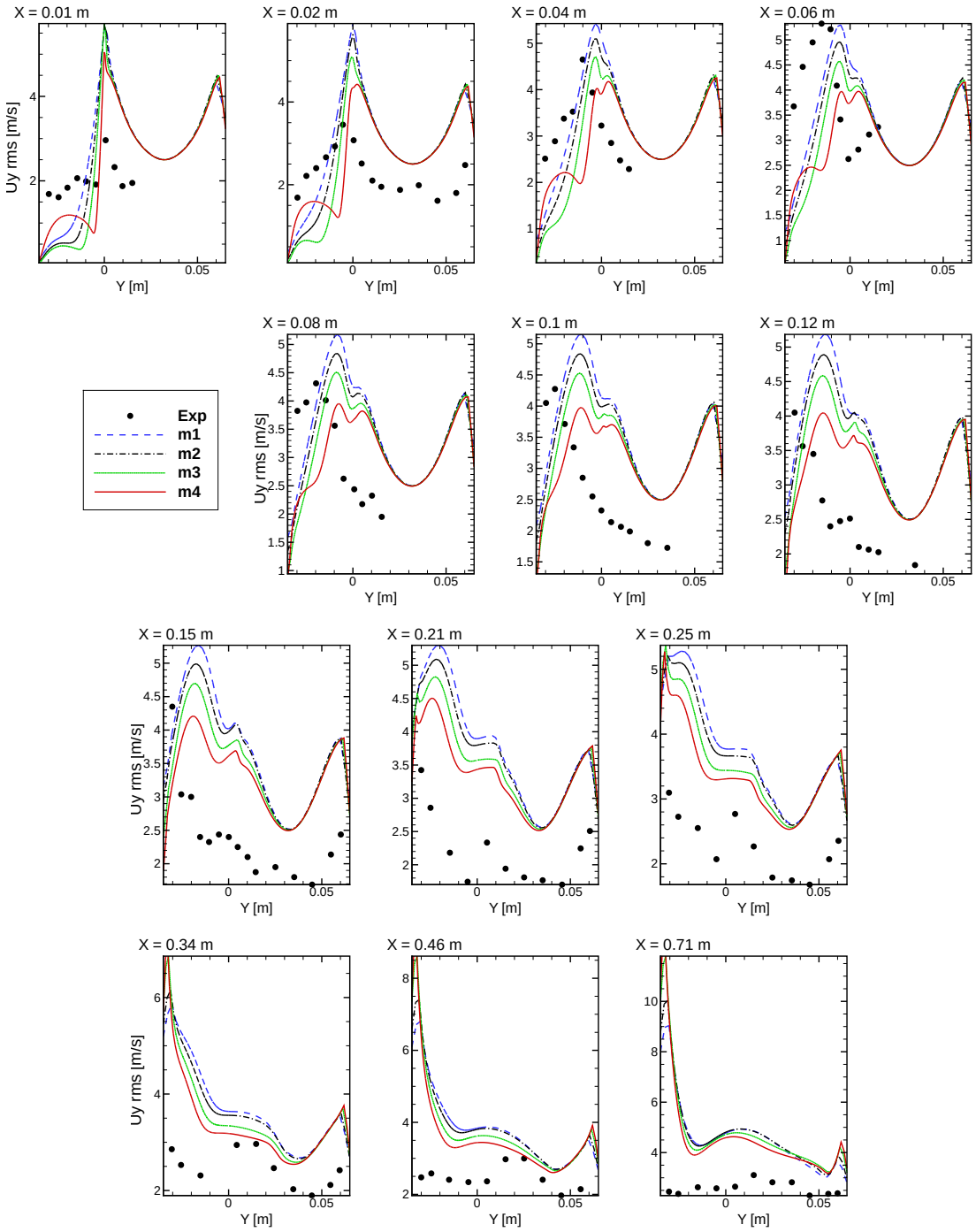

Figure B.11: Dependence of vertical profiles of u_y^{RMS} on computational grid in reactive backward-facing step flow; RANS/TPaSR

List of figures

2.1 Schematic presentation of two-point correlation measurements in a turbulent jet 25
2.2 The normalized axial two-point velocity correlation for homogeneous isotropic turbulence as a function of the distance r between the two points 26
2.3 Density spectrum of kinetic energy in logarithmic scale 26
2.4 Structure of a laminar premixed flame 28
2.5 Regime diagram for premixed turbulent combustion [Peters2000] 31
2.6 Structure of a laminar diffusion flame 32
2.7 Regimes of non-premixed turbulent combustion 34
2.8 β-PDF for different parameters a and b, defined in eq. (2.80) 43
2.9 Schematic computation cell based on EDC model [Magnussen1981] 52
2.10 Results from recent DNS of combustion at moderate Re_t and Da numbers from [TanahashiSato2008]. Figures show iso-surfaces of the heat-release (yellow) and vorticity (gray) from a planar flame in homogeneous isotropic turbulence at $Re_t \approx$ 515 and 141, $Da \approx 21$ and 5, and $Ka \approx 1.3$ and 2.8, respectively. 53
2.11 The dependence of the rates of heat release HR and of heat loses HT_{low}, HT_{cr}, HT_{int} and HT_{high} on the temperature for various heat transfer conditions 54
2.12 The dependence of the rates of heat release HR and of heat loses HT on the temperature; the case of self-ignition 55

3.1 Backward step: solution of eqs. (3.2), (3.12) and (3.13) 67
3.2 Backward step: initial profile of the velocity (left); solution of the PDF (3.2), (3.12) and (3.13) at $t = T$ (center); solution of the PDEs (3.20), (3.22) and (3.32) by any scheme with entropy increase condition at $t = T$ (right). 70
3.3 Backward step: spatial profiles of mean density (left) and density variance (right) at time $t = 0.1\,\mathrm{s}$. $N_r = 10^4$, $N_x = 10^3$. 84
3.4 Backward step: spatial profiles of Favre average (left) and Favre variance (right) of velocity at time $t = 0.1\,\mathrm{s}$. $N_r = 10^4$, $N_x = 10^3$. 85
3.5 Backward step: spatial profiles of Favre skewness (left) and flatness (right) of velocity at time $t = 0.1\,\mathrm{s}$. $N_r = 10^4$, $N_x = 10^3$. 85
3.6 Backward step: spatial profiles of one realization of density and velocity at time $t = 0.1\,\mathrm{s}$ obtained by stochastic Lax-Friedrichs method. $N_r = 10^4$, $N_x = 10^3$. 86
3.7 Backward step: spatial profiles of one realization of density and velocity at time $t = 0.1\,\mathrm{s}$ obtained by stochastic Lax-Wendroff method. $N_r = 10^4$, $N_x = 10^3$. 86
3.8 Backward step: spatial profiles of one realization of density and velocity at time $t = 0.1\,\mathrm{s}$ obtained by stochastic GForce method. $N_r = 10^4$, $N_x = 10^3$. 87

3.9 Backward step: spatial profiles of mean density (left) and density variance (right) at time $t = 0.1\,\mathrm{s}$ with mean correction of density (3.118). $N_r = 10^4$, $N_x = 10^3$. 87
3.10 Backward step: spatial profiles of Favre average (left) and Favre variance (right) of velocity at time $t = 0.1\,\mathrm{s}$ with mean correction of density (3.118). $N_r = 10^4$, $N_x = 10^3$. 88
3.11 Backward step: spatial profiles of Favre skewness (left) and flatness (right) of velocity at time $t = 0.1\,\mathrm{s}$ with mean correction of density (3.118). $N_r = 10^4$, $N_x = 10^3$. 88
3.12 Backward step: Favre-averaged PDF (left) and distribution of velocity (right) at $x = 0.5505\,\mathrm{m}$, $t = 0.1\,\mathrm{s}$. Stochastic Godunov method, $N_r = 10^4$, $N_x = 10^3$. 88
3.13 Backward step: Favre-averaged PDF (left) and distribution of velocity (right) at $x = 0.5505\,\mathrm{m}$, $t = 0.1\,\mathrm{s}$. Stochastic Lax-Friedrichs method, $N_r = 10^4$, $N_x = 10^3$. 89
3.14 Backward step: Favre-averaged PDF (left) and distribution of velocity (right) at $x = 0.5505\,\mathrm{m}$, $t = 0.1\,\mathrm{s}$. Stochastic Lax-Wendroff method, $N_r = 10^4$, $N_x = 10^3$. 89
3.15 Backward step: Favre-averaged PDF (left) and distribution of velocity (right) at $x = 0.5505\,\mathrm{m}$, $t = 0.1\,\mathrm{s}$. Stochastic GForce method, $N_r = 10^4$, $N_x = 10^3$. 89
3.16 Backward step: PDF of density (left) and conditional expectation of density for given velocities (right) at $x = 0.5505\,\mathrm{m}$, $t = 0.1\,\mathrm{s}$. $N_r = 10^4$, $N_x = 10^3$. 90
3.17 Backward step: time evolution of statistical convergence rates (left) and coefficients (right) for $0.5\,\mathrm{m} \le x \le 0.5\,\mathrm{m} + V_0 t$, $V_0 = 1\,\mathrm{m/s}$ (stochastic Lax-Friedrichs method). $N_x = 10^5$. 91
3.18 Backward step: time evolution of statistical convergence rates (left) and coefficients (right) for $0.5\,\mathrm{m} \le x \le 0.5\,\mathrm{m} + V_0 t$, $V_0 = 1\,\mathrm{m/s}$ (stochastic Lax-Wendroff method). $N_x = 10^5$. 92
3.19 Backward step: time evolution of statistical convergence rates (left) and coefficients (right) for $0.5\,\mathrm{m} \le x \le 0.5\,\mathrm{m} + V_0 t$, $V_0 = 1\,\mathrm{m/s}$ (stochastic GForce method). $N_x = 10^5$. 92
3.20 Backward step: time evolution of statistical convergence rates (left) and coefficients (right) for $0.5\,\mathrm{m} \le x \le 0.5\,\mathrm{m} + V_0 t$, $V_0 = 1\,\mathrm{m/s}$ (stochastic Godunov method). $N_x = 10^5$. 93
3.21 Backward step: time evolution of statistical convergence rates (left) and coefficients (right) for $0 \le x \le 0.5$ (stochastic Lax-Friedrichs method). $N_x = 10^5$. 93
3.22 Backward step: spatial error for mean density at $t = 0.2\,\mathrm{s}$ calculated by stochastic GForce method. $N_r = 10^7$. 94
3.23 Backward step: spatial error for the mean (left panel) and variance (right panel) of velocity at $t = 0.2\,\mathrm{s}$ calculated by stochastic GForce method. $N_r = 10^7$. 95
3.24 Scheme non-dissipativity test: initial spatial profile of velocity variance. $N_r = 10^4$, $N_x = 10^4$. 97
3.25 Scheme non-dissipativity test: evolution of integral on space of velocity variance (left) and spatial profile of velocity variance at different time calculated with stochastic Lax-Friedrichs scheme (right). $N_r = 10^4$, $N_x = 10^4$. 98
3.26 Scheme non-dissipativity test: spatial profile of velocity variance at $10t_c$. $N_r = 10^4$, $N_x = 10^4$. 99

3.27 Scheme non-dissipativity test: evolution of velocity variance at different time calculated with kinetic scheme (left), spatial profile of velocity variance at $2t_c$ (right). $N_r = 10^4$, $N_x = 10^4$. 99
3.28 Scheme non-dissipativity test: spatial profile of velocity variance at $4t_c$ (left) and at $10t_c$ (right). $N_r = 10^4$, $N_x = 10^4$. 100
3.29 Scheme non-dissipativity test: examples of stochastic density (left) and velocity (right) fields at $2t_c$ calculated with kinetic scheme. $N_r = 10^4$, $N_x = 10^4$. 100
3.30 Scheme non-dissipativity test: examples of stochastic density (left) and velocity (right) fields at $4t_c$ calculated with kinetic scheme. $N_r = 10^4$, $N_x = 10^4$. 101
3.31 Scheme non-dissipativity test: examples of stochastic density (left) and velocity (right) fields at $6t_c$ calculated with kinetic scheme. $N_r = 10^4$, $N_x = 10^4$. 101
3.32 Scheme non-dissipativity test: examples of stochastic density (left) and velocity (right) fields at $2t_c$ calculated with stochastic Lax-Friedrichs scheme. $N_r = 10^4$, $N_x = 10^4$. 102
3.33 Scheme non-dissipativity test: examples of stochastic density (left) and velocity (right) fields at $6t_c$ calculated with stochastic Lax-Friedrichs scheme. $N_r = 10^4$, $N_x = 10^4$. 102
3.34 Scheme non-dissipativity test: spatial profile of mean velocity at time $t = 1\,\mathrm{s}$. $N_r = 10^4$, $N_x = 10^4$. 103
3.35 Scheme non-dissipativity test: spatial profiles of mean density at time $t = 1\,\mathrm{s}$. $N_r = 10^4$, $N_x = 10^4$. 103
3.36 Scheme non-dissipativity test: spatial profile of the variance of density at time $t = 1\,\mathrm{s}$. $N_r = 10^4$, $N_x = 10^4$. 103
3.37 Scheme non-dissipativity test: spatial profiles of skewness and flatness of velocity at time $t = 1\,\mathrm{s}$. $N_r = 10^4$, $N_x = 10^4$. 104
3.38 Scheme non-dissipativity test: time evolution of the statistical convergence rates (left) and coefficients (right) for integral over space of velocity variance. $N_x = 10^5$. 105
3.39 Statistically homogeneous velocity fluctuations test: an example of $h(x)$ 108
3.40 Statistically homogeneous velocity fluctuations test: spatial profiles of mean density (left) and variance density (right) at $\tau = 2$. $N_r = 4800$, $N_x = 3 \times 10^4$ on $D = [-150; 150]$. 110
3.41 Statistically homogeneous velocity fluctuations test: spatial profiles of Favre velocity variance (left) and Favre velocity skewness (right) at $\tau = 2$. $N_r = 4800$, $N_x = 3 \times 10^4$ on $D = [-150; 150]$. 111
3.42 Statistically homogeneous velocity fluctuations test: spatial profiles of Favre velocity flatness at $\tau = 2$. $N_r = 4800$, $N_x = 3 \times 10^4$ on $D = [-150; 150]$. 111
3.43 Statistically homogeneous velocity fluctuations test: spatial profiles of mean density at $\tau \geq 8.5$. Left: stochastic Lax-Wendroff method; right: stochastic GForce method. $N_r = 4800$, $N_x = 3 \times 10^4$ on $D = [-150; 150]$. 112
3.44 Statistically homogeneous velocity fluctuations test: spatial profiles of mean density at $\tau \geq 8.5$. Left: stochastic Godunov method; right: kinetic scheme. $N_r = 4800$, $N_x = 3 \times 10^4$ on $D = [-150; 150]$. 113
3.45 Statistically homogeneous velocity fluctuations test: spatial profiles of density variance at $\tau \geq 8.5$. Left: stochastic Lax-Wendroff method; right: stochastic GForce method. $N_r = 4800$, $N_x = 3 \times 10^4$ on $D = [-150; 150]$. 113

3.46 Statistically homogeneous velocity fluctuations test: spatial profiles of density variance at $\tau \geq 8.5$. Left: stochastic Godunov method; right: kinetic scheme. $N_r = 4800$, $N_x = 3 \times 10^4$ on $D = [-150; 150]$. 114
3.47 Statistically homogeneous velocity fluctuations test: spatial profiles of velocity variance at $\tau \geq 8.5$. Left: stochastic Lax-Wendroff method; right: stochastic GForce method. $N_r = 4800$, $N_x = 3 \times 10^4$ on $D = [-150; 150]$. 114
3.48 Statistically homogeneous velocity fluctuations test: spatial profiles of velocity variance at $\tau \geq 8.5$. Left: stochastic Godunov method; right: kinetic scheme. $N_r = 4800$, $N_x = 3 \times 10^4$ on $D = [-150; 150]$. 115
3.49 Statistically homogeneous velocity fluctuations test: spatial profiles of velocity skewness at $\tau \geq 8.5$. Left: stochastic Lax-Wendroff method; right: stochastic GForce method. $N_r = 4800$, $N_x = 3 \times 10^4$ on $D = [-150; 150]$. 115
3.50 Statistically homogeneous velocity fluctuations test: spatial profiles of velocity skewness at $\tau \geq 8.5$. Left: stochastic Godunov method; right: kinetic scheme. $N_r = 4800$, $N_x = 3 \times 10^4$ on $D = [-150; 150]$. 116
3.51 Statistically homogeneous velocity fluctuations test: spatial profiles of velocity skewness at $\tau \geq 8.5$ calculated by kinetic scheme after normalization (3.168). $N_r = 4800$, $N_x = 3 \times 10^4$ on $D = [-150; 150]$. 116
3.52 Statistically homogeneous velocity fluctuations test: spatial profiles of velocity flatness at $\tau \geq 8.5$. Left: stochastic Lax-Wendroff method; right: stochastic GForce method. $N_r = 4800$, $N_x = 3 \times 10^4$ on $D = [-150; 150]$. 117
3.53 Statistically homogeneous velocity fluctuations test: spatial profiles of velocity flatness at $\tau \geq 8.5$. Left: stochastic Godunov method; right: kinetic scheme. $N_r = 4800$, $N_x = 3 \times 10^4$ on $D = [-150; 150]$. 117
3.54 Statistically homogeneous velocity fluctuations test: spatial profiles of velocity flatness at $\tau \geq 8.5$ calculated by kinetic scheme after normalization (3.168). $N_r = 4800$, $N_x = 3 \times 10^4$ on $D = [-150; 150]$. 118
3.55 Statistically homogeneous velocity fluctuations test: spatial profiles of velocity hyperskewness at $\tau \geq 8.5$. Left: stochastic Lax-Wendroff method; right: stochastic GForce method. $N_r = 4800$, $N_x = 3 \times 10^4$ on $D = [-150; 150]$. 118
3.56 Statistically homogeneous velocity fluctuations test: spatial profiles of velocity hyperskewness at $\tau \geq 8.5$. Left: stochastic Godunov method; right: kinetic scheme. $N_r = 4800$, $N_x = 3 \times 10^4$ on $D = [-150; 150]$. 119
3.57 Statistically homogeneous velocity fluctuations test: spatial profiles of velocity hyperskewness at $\tau \geq 8.5$ calculated by kinetic scheme after normalization (3.168). $N_r = 4800$, $N_x = 3 \times 10^4$ on $D = [-150; 150]$. 119
3.58 Statistically homogeneous velocity fluctuations test: spatial profiles of velocity hyperflatness at $\tau \geq 8.5$. Left: stochastic Lax-Wendroff method; right: stochastic GForce method. $N_r = 4800$, $N_x = 3 \times 10^4$ on $D = [-150; 150]$. 120
3.59 Statistically homogeneous velocity fluctuations test: spatial profiles of velocity hyperflatness at $\tau \geq 8.5$. Left: stochastic Godunov method; right: kinetic scheme. $N_r = 4800$, $N_x = 3 \times 10^4$ on $D = [-150; 150]$. 120
3.60 Statistically homogeneous velocity fluctuations test: spatial profiles of velocity hyperflatness at $\tau \geq 8.5$ calculated by kinetic scheme after normalization (3.168). $N_r = 4800$, $N_x = 3 \times 10^4$ on $D = [-150; 150]$. 120

3.61 Statistically homogeneous velocity fluctuations test: examples of stochastic density (left) and velocity (right) fields at $\tau = 0.5$ calculated with stochastic Godunov scheme. $N_r = 4800$, $N_x = 3 \times 10^4$ on $D = [-150; 150]$. 121
3.62 Statistically homogeneous velocity fluctuations test: examples of stochastic density (left) and velocity (right) fields at $\tau = 0.5$ calculated with kinetic scheme. $N_r = 4800$, $N_x = 3 \times 10^4$ on $D = [-150; 150]$. 121
3.63 Statistically homogeneous velocity fluctuations test: examples of stochastic density (left) and velocity (right) fields at $\tau = 1$ calculated with stochastic Godunov scheme. $N_r = 4800$, $N_x = 3 \times 10^4$ on $D = [-150; 150]$. 121
3.64 Statistically homogeneous velocity fluctuations test: examples of stochastic density (left) and velocity (right) fields at $\tau = 1$ calculated with kinetic scheme. $N_r = 4800$, $N_x = 3 \times 10^4$ on $D = [-150; 150]$. 122
3.65 Statistically homogeneous velocity fluctuations test: examples of stochastic density (left) and velocity (right) fields at $\tau = 1.5$ calculated with stochastic Godunov scheme. $N_r = 4800$, $N_x = 3 \times 10^4$ on $D = [-150; 150]$. 122
3.66 Statistically homogeneous velocity fluctuations test: examples of stochastic density (left) and velocity (right) fields at $\tau = 1.5$ calculated with kinetic scheme. $N_r = 4800$, $N_x = 3 \times 10^4$ on $D = [-150; 150]$. 122
3.67 Statistically homogeneous velocity fluctuations test: examples of stochastic density (left) and velocity (right) fields at $\tau = 2.5$ calculated with stochastic Godunov scheme. $N_r = 4800$, $N_x = 3 \times 10^4$ on $D = [-150; 150]$. 123
3.68 Statistically homogeneous velocity fluctuations test: examples of stochastic density (left) and velocity (right) fields at $\tau = 2.5$ calculated with kinetic scheme. $N_r = 4800$, $N_x = 3 \times 10^4$ on $D = [-150; 150]$. 123
3.69 Statistically homogeneous velocity fluctuations test: spatial profile of one realization of density (left) and its zoom (right) at $\tau = 2$; stochastic Lax-Friedrichs method. $N_r = 4800$, $N_x = 3 \times 10^4$ on $D = [-150; 150]$. 123
3.70 Statistically homogeneous velocity fluctuations test: spatial profile of one realization of velocity (left) and its zoom (right) at $\tau = 2$; stochastic Lax-Friedrichs method. $N_r = 4800$, $N_x = 3 \times 10^4$ on $D = [-150; 150]$. 124
3.71 Statistically homogeneous velocity fluctuations test: Favre PDF of velocity at time $\tau = 2$ (left) and $\tau = 8$ (right), $\zeta = 0.005$; stochastic Godunov method. $N_r = 4800$, $N_x = 3 \times 10^4$ on $D = [-150; 150]$. 124
3.72 Statistically homogeneous velocity fluctuations test: conditional expectations of density for given velocities at time $\tau = 2$ (left) and $\tau = 8$ (right), $\zeta = 0.005$; stochastic Godunov method. $N_r = 4800$, $N_x = 3 \times 10^4$ on $D = [-150; 150]$. 124
3.73 Statistically homogeneous velocity fluctuations test: time evolution of statistical convergence rate (left) and coefficient (right) of stochastic Godunov scheme. $N_x = 10^5$. 125
3.74 Statistically homogeneous velocity fluctuations test: time evolution of statistical convergence rate (left) and coefficient (right) of stochastic Lax-Wendroff scheme. $N_x = 10^5$. 126
3.75 Statistically homogeneous velocity fluctuations test: time evolution of statistical convergence rate (left) and coefficient (right) of stochastic Lax-Friedrichs scheme. $N_x = 10^5$. 126

3.76 Statistically homogeneous velocity fluctuations test: time evolution of statistical convergence rate (left) and coefficient (right) of stochastic GForce scheme. $N_x = 10^5$. 126
3.77 Model PDF eq. with non-zero RHS: transfer coefficient calculated with PDF 128
3.78 Comparison of transfer coefficient calculated using PDF (black line) and stochastic methods (colored lines). Left: $t = 1\,\mathrm{s}$, right: $t = 2\,\mathrm{s}$. $N_r = 2000$, $N_x = 612$. 129
3.79 Comparison of transfer coefficient calculated using PDF (black line) and stochastic methods (colored lines) for $t = 4\,\mathrm{s}$. $N_r = 2000$, $N_x = 612$. 129
3.80 Model PDF eq. with non-zero RHS: spatial profile of mean density at time 3 s; left: without mean velocity correction, right: with mean velocity correction. $N_r = 2000$, $N_x = 612$. 130
3.81 Model PDF eq. with non-zero RHS: spatial profile of Favre-averaged velocity at time 3 s; left: without mean velocity correction, right: with mean velocity correction. $N_r = 2000$, $N_x = 612$. 130
3.82 Model PDF eq. with non-zero RHS: spatial profile of Favre velocity variance at time 3 s; left: without mean velocity correction, right: with mean velocity correction. $N_r = 2000$, $N_x = 612$. 130
3.83 Model PDF eq. with non-zero RHS: spatial profile of Favre velocity skewness at time 3 s; left: without mean velocity correction, right: with mean velocity correction. $N_r = 2000$, $N_x = 612$. 131
3.84 Model PDF eq. with non-zero RHS: spatial profile of Favre velocity flatness at time 3 s; left: without mean velocity correction, right: with mean velocity correction. $N_r = 2000$, $N_x = 612$. 131
3.85 Model PDF eq. with non-zero RHS: spatial convergence of stochastic GForce (left) and stochastic Lax-Wendroff (right). $N_r = 10^6$. 132
3.86 Model PDF eq. with non-zero RHS: spatial convergence of stochastic Godunov method. $N_r = 10^6$. 132

4.1 Logarithmic spatial convergence of the semi-analytical method of the integration with the β-PDF. Left: convergence rate for $g(C) = C^{20}$, right: convergence rate for $g(Z, C) = Z^5 C^2$. The vector of 4 numbers corresponds to (p_1, q_1, p_2, q_2). 149
4.2 Production rate (left) and mass fraction (right) of CO_2; obtained from PFTC β-PDF table of the premixed flame CH_4/O_2, $\widetilde{Z} = 0.0455$, $\widetilde{Z''^2} = 0$, $N_c = 25$, $N_{VarC} = 15$ 150

6.1 Scheme of A3C test bench along with optimal diagnostics 156
6.2 Backward-facing step dimensions (the aspect ratio is preserved in this figure) and sensor point locations for convergence studies 157
6.3 Principal features of a backward step flow 157
6.4 2D grid for backward-facing step flow 158
6.5 Vertical profiles of Favre-averaged streamwise velocity $\widetilde{u}_x$ (left), $\frac{\sqrt{2/3k}}{\max(\widetilde{u}_x)}$ (center) and $\frac{l}{L_y}$ (right) at the inlet of A3C chamber 159
6.6 Discrepancy between the positive and negative sums of mass flow during 40 characteristic time in A3C chamber (converged solution); $k - l$ (BVM) model with nonhomogeneous inlet profiles 160

6.7 Errors of mean pressure $\overline{P}$ (left) and Favre-averaged temperature $\widetilde{T}$ (right) integrated over the computational domain of converged solution during 40 characteristic time in A3C chamber. $k-l$ (BVM) model with the nonhomogeneous inlet profiles 161
6.8 Recirculation regions in nonreactive backward-facing step flow; 2: $k-l$ (BVM) model with homogeneous inlet profiles, 3: $k-l$ (BVM) model with nonhomogeneous inlet profiles, 4: $k-\omega$ (BVM) model with homogeneous inlet profiles, 5: $k-\omega$ (EARSM) model with homogeneous inlet profiles 163
6.9 Vertical profiles of Favre-averaged streamwise velocity $\widetilde{u}_x$ in nonreactive backward-facing step flow; 1: experimental data, 2: $k-l$ (BVM) model with homogeneous inlet profiles, 3: $k-l$ (BVM) model with nonhomogeneous inlet profiles, 4: $k-\omega$ (BVM) model with homogeneous inlet profiles, 5: $k-\omega$ (EARSM) model with homogeneous inlet profiles 164
6.10 Vertical profiles of Favre-averaged transverse velocity $\widetilde{u}_y$ in nonreactive backward-facing step flow; 1: experimental data, 2: $k-l$ (BVM) model with homogeneous inlet profiles, 3: $k-l$ (BVM) model with nonhomogeneous inlet profiles, 4: $k-\omega$ (BVM) model with homogeneous inlet profiles, 5: $k-\omega$ (EARSM) model with homogeneous inlet profiles 165
6.11 Vertical profiles of u_x^{RMS} in nonreactive backward-facing step flow; 1: experimental data, 2: $k-l$ (BVM) model with homogeneous inlet profiles, 3: $k-l$ (BVM) model with nonhomogeneous inlet profiles, 4: $k-\omega$ (BVM) model with homogeneous inlet profiles, 5: $k-\omega$ (EARSM) model with homogeneous inlet profiles 166
6.12 Vertical profiles of u_y^{RMS} in nonreactive backward-facing step flow; 1: experimental data, 2: $k-l$ (BVM) model with homogeneous inlet profiles, 3: $k-l$ (BVM) model with nonhomogeneous inlet profiles, 4: $k-\omega$ (BVM) model with homogeneous inlet profiles, 5: $k-\omega$ (EARSM) model with homogeneous inlet profiles 167
6.13 Vertical profiles of turbulent frequency ω [Hz] in nonreactive backward-facing step flow; 2: $k-l$ (BVM) model with homogeneous inlet profiles, 3: $k-l$ (BVM) model with nonhomogeneous inlet profiles, 4: $k-\omega$ (BVM) model with homogeneous inlet profiles, 5: $k-\omega$ (EARSM) model with homogeneous inlet profiles 168
6.14 Two computational domains to evacuate acoustic waves; left: sudden enlargement, right: prolongation of domain 171
6.15 1500 K temperature isolines in reactive backward-facing step flow; RANS/quasi-laminar approaches; blue curve: PFTC noTCI with 2nd order spatial scheme; red curve: PFTC noTCI with 1st order spatial scheme 172
6.16 Vertical profiles of Favre-averaged temperature $\widetilde{T}$ in reactive backward-facing step flow; RANS/quasi-laminar approaches; blue curve: PFTC noTCI with 2nd order spatial scheme; black curve: PFTC noTCI with 1st order spatial scheme 173
6.17 Vertical profiles of Favre-averaged streamwise velocity $\widetilde{u}_x$ in reactive backward-facing step flow; RANS/quasi-laminar approaches; blue curve: PFTC noTCI with 2nd order spatial scheme; black curve: PFTC noTCI with 1st order spatial scheme 174
6.18 Vertical profiles of Favre-averaged transverse velocity $\widetilde{u}_y$ in reactive backward-facing step flow; RANS/quasi-laminar approaches; blue curve: PFTC noTCI with 2nd order spatial scheme; black curve: PFTC noTCI with 1st order spatial scheme 175

6.19 Vertical profiles of u_x^{RMS} in reactive backward-facing step flow; RANS/quasi-laminar approaches; blue curve: PFTC noTCI with 2nd order spatial scheme; black curve: PFTC noTCI with 1st order spatial scheme 176
6.20 Vertical profiles of u_y^{RMS} in reactive backward-facing step flow; RANS/quasi-laminar approaches; blue curve: PFTC noTCI with 2nd order spatial scheme; black curve: PFTC noTCI with 1st order spatial scheme 177
6.21 Vertical profiles of Favre-averaged temperature $\widetilde{T}$ in reactive backward-facing step flow; RANS/PFTC β-PDF 179
6.22 Field of Favre-averaged temperature $\widetilde{T}$ [K] in reactive backward-facing step flow; RANS/PFTC β-PDF 20-2 179
6.23 Field of Favre-averaged temperature $\widetilde{T}$ [K] in reactive backward-facing step flow; RANS/PFTC β-PDF 60-1 179
6.24 Vertical profiles of Favre variance of progress variable $\widetilde{C''^2}$ in reactive backward-facing step flow; RANS/PFTC β-PDF 180
6.25 Vertical profiles of Favre-averaged streamwise velocity $\widetilde{u}_x$ in reactive backward-facing step flow; RANS/PFTC β-PDF 182
6.26 Vertical profiles of Favre-averaged transverse velocity $\widetilde{u}_y$ in reactive backward-facing step flow; RANS/PFTC β-PDF 183
6.27 Vertical profiles of u_x^{RMS} in reactive backward-facing step flow; RANS/PFTC β-PDF 184
6.28 Vertical profiles of u_y^{RMS} in reactive backward-facing step flow; RANS/PFTC β-PDF 185
6.29 Vertical profiles of Favre-averaged temperature $\widetilde{T}$ in reactive backward-facing step flow; RANS/TPaSR 187
6.30 Vertical profiles of volume fraction γ^* of the fine structure and its equilibrium state γ_{eq}^* in reactive backward-facing step flow; RANS/TPaSR 188
6.31 Comparison of vertical profiles of Favre-averaged temperature $\widetilde{T}$ and temperature in fine structure region T^* in reactive backward-facing step flow; RANS/TPaSR 189
6.32 Field of Favre-averaged temperature $\widetilde{T}$ [K] in reactive backward-facing step flow; RANS/TPaSR 189
6.33 Isolines of temperature $\widetilde{T} = 1500\,\mathrm{K}$ in reactive backward-facing step flow; RANS 189
6.34 Vertical profiles of Favre-averaged streamwise velocity $\widetilde{u}_x$ in reactive backward-facing step flow; RANS/TPaSR 191
6.35 Vertical profiles of Favre-averaged transverse velocity $\widetilde{u}_y$ in reactive backward-facing step flow with homogeneous inlet profiles; RANS/TPaSR 192
6.36 Vertical profiles of u_x^{RMS} in reactive backward-facing step flow; RANS/TPaSR 193
6.37 Vertical profiles of Favre average of u_y^{RMS} in reactive backward-facing step flow; RANS/TPaSR 194
6.38 Extrusion of the bidimensional domain used for RANS calculations into a three-dimensional domain for LES 196
6.39 Slice of 3D grid at $Z = h$ for backward-facing step flow 196
6.40 Time-averaged profiles of streamwise velocity (left) and $\frac{2}{3}k$ (right); the averaged time is 0.21 s 198
6.41 Time evolution of inlet longitudinal and transverse velocity at different points 198
6.42 Vertical profiles of mean temperature $\langle\widetilde{T}\rangle$ in reactive backward-facing step flow; LES 200

6.43 Isolines of mean temperature $\langle\widetilde{T}\rangle = 1500\,\mathrm{K}$ in reactive backward-facing step flow; LES 201
6.44 Field of mean temperature $\langle\widetilde{T}\rangle$ [K] in reactive backward-facing step flow calculated with LES/QL RCM (OU); $Z = 0.035\,\mathrm{m}$ 202
6.45 Recirculation regions in reactive backward-facing step flow; LES 203
6.46 Vertical profiles of mean streamwise velocity $\langle\widetilde{u}_x\rangle$ in reactive backward-facing step flow; LES 205
6.47 Vertical profiles of mean transverse velocity $\langle\widetilde{u}_y\rangle$ in reactive backward-facing step flow; LES 206
6.48 Vertical profiles of $\langle\widetilde{Y}_{\mathrm{N}_2}\rangle$ in reactive backward-facing step flow; LES 208
6.49 Vertical profiles of $\langle\widetilde{Y}_{\mathrm{CO}}\rangle$ in reactive backward-facing step flow; LES 209
6.50 Vertical profiles of $\langle u_x^{RMS}\rangle$ in reactive backward-facing step flow; LES 211
6.51 Vertical profiles of $\langle u_y^{RMS}\rangle$ in reactive backward-facing step flow; LES 212
6.52 Spectra of pressure (left) and temperature (right) at point A in reactive backward-facing step flow; LES/PFTC β-PDF 214
6.53 Spectra of pressure (left) and temperature (right) at point B in reactive backward-facing step flow; LES/PFTC β-PDF 214
6.54 Spectra of pressure (left) and temperature (right) at point C in reactive backward-facing step flow; LES/PFTC β-PDF 215
6.55 Spectra of pressure (left) and temperature (right) at point D in reactive backward-facing step flow; LES/PFTC β-PDF 215
6.56 Spectra of pressure (left) and temperature (right) at point E in reactive backward-facing step flow; LES/PFTC β-PDF 215

A.1 Discretization of $[0, L]$ interval into N_x finite volumes 224
A.2 Piece-wise constant distribution of the solution at time t^n 224
A.3 Random choice method: solution is updated to t^n by random sampling of Riemann problem solution at I_i cell. The random sampling is represented by thick horizontal line. 225
A.4 RCM sampling of the RHS of the left Riemann problem solution with $0 \leq \theta^n \leq \frac{1}{2}$. Sampled state is assigned to the center of I_i cell. 225
A.5 Step: initial profile of the velocity (left); solution of the Riemann problem at $t = T$ (right) 232
A.6 Step: spatial profiles of mean density (left) and Favre-averaged velocity (right) at time $t = 0.2\,\mathrm{s}$. $N_r = 10^4$, $N_x = 10^3$. 233
A.7 Step: spatial profiles of density (left) and velocity (right) variance at time $t = 0.2\,\mathrm{s}$. $N_r = 10^4$, $N_x = 10^3$. 233
A.8 Step: spatial profiles of velocity skewness (left) and flatness (right) at time $t = 0.2\,\mathrm{s}$. $N_r = 10^4$, $N_x = 10^3$. 233
A.9 Ramp: temporal variation of mean density and velocity profiles. Eulerian density r (red, green and blue curves in the right column) coincides with mean density $\overline{\rho}$ (black curve) for $t \leq \frac{x_r - x_l}{V_0}$, and differs in multivalued region for $t > \frac{x_r - x_l}{V_0}$. 238
A.10 Ramp: profiles of mean density (left) and velocity (right) at time $0.1\,\mathrm{s}$. $N_r = 10^4$, $N_x = 5 \times 10^3$. 239

A.11 Ramp: profiles of density variance (left) and velocity Favre variance (right) at time 0.1 s obtained with stochastic GForce method. $N_x = 5 \times 10^3$. 240
A.12 Ramp: profiles of mean density (left) and velocity (right) at time 0.3 s. $N_r = 10^4$, $N_x = 5 \times 10^3$. 240
A.13 Ramp: profiles of stochastic density (left) and velocity (right) at time 0.3 s; stochastic GForce method. $N_r = 10^4$, $N_x = 5 \times 10^3$. 241
A.14 Ramp: profiles of stochastic density (left) and velocity (right) at time 0.3 s; stochastic GForce method. $N_r = 10^4$, $N_x = 5 \times 10^3$. 241
A.15 Ramp: profiles of mean density (left) and velocity (right) at time 0.4 s. $N_r = 10^4$, $N_x = 5 \times 10^3$. 242
A.16 Ramp: profiles of Favre variance of velocity at time 0.4 s. $N_r = 10^4$, $N_x = 5 \times 10^3$. 242
A.17 Ramp: Favre-averaged PDF (left) and distribution of velocity (right) at $x = 0.5249$ m, $t = 0.3$ s. Stochastic Lax-Friedrichs method, $N_r = 10^4$, $N_x = 5 \times 10^3$. 242
A.18 Ramp: Favre-averaged PDF (left) and distribution of velocity (right) at $x = 0.5249$ m, $t = 0.3$ s. Stochastic Lax-Wendroff method, $N_r = 10^4$, $N_x = 5 \times 10^3$. 243
A.19 Ramp: Favre-averaged PDF (left) and distribution of velocity (right) at $x = 0.5249$ m, $t = 0.3$ s. Stochastic GForce method, $N_r = 10^4$, $N_x = 5 \times 10^3$. 243
A.20 Ramp: Favre-averaged PDF (left) and distribution of velocity (right) at $x = 0.5249$ m, $t = 0.3$ s. Stochastic Godunov method, $N_r = 10^4$, $N_x = 5 \times 10^3$. 243
A.21 Ramp: PDF of density (left) and conditional PDF of density for given velocities (right) obtained by different methods at time $t = 0.3$ s. $N_r = 10^4$, $N_x = 5 \times 10^3$. 244
A.22 Ramp: time evolution of statistical convergence rates for mean density (left) and Favre-averaged velocity (right). $N_x = 10^5$. 245
A.23 Ramp: time evolution of statistical convergence coefficients for mean density (left) and Favre-averaged velocity (right). $N_x = 10^5$. 245
A.24 Ramp: spatial convergence of mean density (left) and Favre-averaged velocity (right) at $t = 0.2$ s on interval $[x_l; x_r + V_0 t]$, $V_0 = 1$ m/s, stochastic Lax-Friedrichs method. $N_r = 10^7$. 246
A.25 Triangle: temporal variation of the mean density and velocity profiles. Eulerian density r (red, green and blue curves in the right column) coincides with mean density $\overline{\rho}$ (black curve) for $t < \frac{x_r - x_c}{V_0}$, and differs in multivalued region for $t \geq \frac{x_r - x_c}{V_0}$. 250
A.26 Triangle: spatial initial profile of velocity. $N_r = 10^4$, $N_x = 5 \times 10^3$. 251
A.27 Triangle: spatial profiles of mean density (left) and velocity (right) at time $t = 0.1$ s. $N_r = 10^4$, $N_x = 5 \times 10^3$. 251
A.28 Triangle: spatial profiles of density (left) and velocity (right) variance at time $t = 0.1$ s. $N_r = 10^4$, $N_x = 5 \times 10^3$. 252
A.29 Triangle: spatial profiles of velocity skewness (left) and flatness (right) at time $t = 0.1$ s. $N_r = 10^4$, $N_x = 5 \times 10^3$. 252
A.30 Triangle: spatial profiles of mean density (left) and velocity (right) at time $t = 0.4$ s. $N_r = 10^4$, $N_x = 5 \times 10^3$. 253
A.31 Triangle: spatial profiles of density (left) and velocity (right) variance at time $t = 0.4$ s. $N_r = 10^4$, $N_x = 5 \times 10^3$. 253
A.32 Triangle: spatial profiles of velocity skewness (left) and flatness (right) at time $t = 0.4$ s. $N_r = 10^4$, $N_x = 5 \times 10^3$. 253

A.33 Hat: spatial profiles of mean density (left) and velocity (right) at time $t = 0.1\,\mathrm{s}$. $N_r = 10^4$, $N_x = 10^3$. 254
A.34 Hat: spatial profiles of density (left) and velocity (right) variances at time $t = 0.1\,\mathrm{s}$. $N_r = 10^4$, $N_x = 10^3$. 255
A.35 Hat: spatial profiles of skewness(left) and flatness (right) of velocity at time $t = 0.1\,\mathrm{s}$. $N_r = 10^4$, $N_x = 10^3$. 255
A.36 Hat: time evolution of the statistical convergence rates (left) and coefficients (right) for moments of density and velocity; stochastic Godunov method. $N_x = 10^4$. 256
A.37 Hat: time evolution of the statistical convergence rates (left) and coefficients (right) for moments of density and velocity; stochastic GForce method. $N_x = 10^4$. 256
A.38 Hat: time evolution of the statistical convergence rates (left) and coefficients (right) for moments of density and velocity; stochastic Lax-Friedrichs method. $N_x = 10^4$. 257
A.39 Hat: time evolution of the statistical convergence rates (left) and coefficients (right) for moments of density and velocity; stochastic Lax-Wendroff method. $N_x = 10^4$. 257
A.40 Hat: spatial convergence of means density (left) and velocity (right) at time $t = 0.1\,\mathrm{s}$. $N_r = 10^7$. 257
A.41 Hat: spatial convergence of variance (left) and skewness (right) of velocity at time $t = 0.1\,\mathrm{s}$. $N_r = 10^7$. 258
A.42 Hat: spatial convergence of velocity flatness at time $t = 0.1\,\mathrm{s}$. $N_r = 10^7$. 258
A.43 Scheme non-dissipativity test: spatial profile of velocity variance at time $t = 0.2\,\mathrm{s}$. Left: stochastic Lax-Friedrichs method, right: stochastic Lax-Wendroff method. $N_r = 10^7$. 260
A.44 Scheme non-dissipativity test: spatial profile of velocity variance at time $t = 0.2\,\mathrm{s}$. Left: stochastic GForce method, right: stochastic Godunov method. $N_r = 10^7$. 260
A.45 Scheme non-dissipativity test: spatial convergence for velocity skewness at time $t = 0.2\,\mathrm{s}$. Left: stochastic Lax-Friedrichs method, right: stochastic Lax-Wendroff method. $N_r = 10^7$. 261
A.46 Scheme non-dissipativity test: spatial profile of velocity skewness at time $t = 0.2\,\mathrm{s}$. Left: stochastic GForce method, right: stochastic Godunov method. $N_r = 10^7$. 261
A.47 Scheme non-dissipativity test: spatial profile of velocity flatness at time $t = 0.2\,\mathrm{s}$. Left: stochastic Lax-Friedrichs method, right: stochastic Lax-Wendroff method. $N_r = 10^7$. 261
A.48 Scheme non-dissipativity test: spatial profile of velocity flatness at time $t = 0.2\,\mathrm{s}$. Left: stochastic GForce method, right: stochastic Godunov method. $N_r = 10^7$. 262
A.49 Scheme non-dissipativity test: spatial profile of mean density at time $t = 0.2\,\mathrm{s}$. Left: stochastic Lax-Friedrihs method, right: stochastic Lax-Wendroff method. $N_r = 10^7$. 262
A.50 Scheme non-dissipativity test: spatial profile of mean density at time $t = 0.2\,\mathrm{s}$. Left: stochastic GForce method, right: stochastic Godunov method. $N_r = 10^7$. 262
A.51 Scheme non-dissipativity test: spatial convergence for velocity variance at time $t = 0.2\,\mathrm{s}$. Left: stochastic Lax-Friedrichs method, right: stochastic Lax-Wendroff method. $N_x = 10^5$. 263

A.52 Scheme non-dissipativity test: spatial profile of velocity variance at time $t = 0.2\,\mathrm{s}$. Left: stochastic GForce method, right: stochastic Godunov method. $N_x = 10^5$. 263
A.53 Scheme non-dissipativity test: spatial profile of mean density (left) and velocity variance (right) at time $t = 2\,\mathrm{s}$. $N_r = 9600$, $N_x = 10^3$. 263
A.54 Scheme non-dissipativity test: spatial profile of velocity skewness (left) and flatness (right) at time $t = 2\,\mathrm{s}$. $N_r = 9600$, $N_x = 10^3$. 264
A.55 Scheme non-dissipativity test: profiles of stochastic density (left) and velocity (right) at time $t = 2\,\mathrm{s}$, stochastic Lax-Friedrichs method. $N_r = 9600$, $N_x = 10^3$. 264
A.56 Scheme non-dissipativity test: profiles of stochastic density (left) and velocity (right) at time $t = 2\,\mathrm{s}$, stochastic Lax-Friedrichs method. $N_r = 9600$, $N_x = 10^3$. 264
A.57 Scheme non-dissipativity test: profiles of stochastic density (left) and velocity (right) at time $t = 2\,\mathrm{s}$, stochastic Lax-Wendroff method. $N_r = 9600$, $N_x = 10^3$. 265
A.58 Scheme non-dissipativity test: profiles of stochastic density (left) and velocity (right) at time $t = 2\,\mathrm{s}$, stochastic Lax-Wendroff method. $N_r = 9600$, $N_x = 10^3$. 265
A.59 Scheme non-dissipativity test: profiles of stochastic density (left) and velocity (right) at time $t = 2\,\mathrm{s}$, stochastic GForce method. $N_r = 9600$, $N_x = 10^3$. 265
A.60 Scheme non-dissipativity test: profiles of stochastic density (left) and velocity (right) at time $t = 2\,\mathrm{s}$, stochastic GForce method. $N_r = 9600$, $N_x = 10^3$. 266
A.61 Scheme non-dissipativity test: profiles of stochastic density (left) and velocity (right) at time $t = 2\,\mathrm{s}$, stochastic Godunov method. $N_r = 9600$, $N_x = 10^3$. 266
A.62 Scheme non-dissipativity test: profiles of stochastic density (left) and velocity (right) at time $t = 2\,\mathrm{s}$, stochastic Godunov method. $N_r = 9600$, $N_x = 10^3$. 266
A.63 Scheme non-dissipativity test: spatial convergence for velocity variance, skewness, flatness and mean density at time $t = 0.2\,\mathrm{s}$, left: stochastic Lax-Friedrichs method, right: stochastic Lax-Wendroff method. $N_r = 10^7$. 267
A.64 Scheme non-dissipativity test: spatial convergence for velocity variance, skewness, flatness and mean density at time $t = 0.2\,\mathrm{s}$. Left: stochastic GForce method, right: stochastic Godunov method. $N_r = 10^7$. 267
A.65 Scheme non-dissipativity test: statistical convergence for velocity variance, skewness and flatness at time $t = 0.2\,\mathrm{s}$. Left: stochastic Lax-Friedrichs method, right: stochastic Lax-Wendroff method. $N_x = 10^5$. 268
A.66 Scheme non-dissipativity test: statistical convergence for velocity variance, skewness and flatness at time $t = 0.2\,\mathrm{s}$. Left: stochastic GForce method, right: stochastic Godunov method. $N_x = 10^5$. 268
A.67 Comparison of variance (left), flatness (right) with their theoretical values 270
A.68 Comparison of hyperflatness with its theoretical value 271

B.1 2D grids for backward-facing step flow; grids $m1$, $m2$, $m3$, $m4$, $m5$ 274
B.2 Dependence of vertical profiles of Favre-averaged temperature $\widetilde{T}$ on computational grid in reactive backward facing step flow; RANS/PFTC β-PDF 40-4 with nonhomogeneous inlet profile 276
B.3 Dependence of vertical profiles of Favre-averaged streamwise velocity $\widetilde{u}_x$ on computational grid in reactive backward-facing step flow; RANS/PFTC β-PDF 40-4 277

B.4 Dependence of vertical profiles of the Favre-averaged transverse velocity $\widetilde{u}_y$ on computational grid in reactive backward-facing step flow; RANS/PFTC β-PDF 40-4 278
B.5 Dependence of vertical profiles of u_x^{RMS} on computational grid in reactive backward-facing step flo; RANS/PFTC β-PDF 279
B.6 Dependence of vertical profiles of u_y^{RMS} on computational grid in reactive backward-facing step flow; RANS/PFTC β-PDF 280
B.7 Dependence of vertical profiles of Favre-averaged temperature $\widetilde{T}$ on computational grid in reactive backward-facing step flow; RANS/TPaSR 282
B.8 Dependence of vertical profiles of Favre-averaged streamwise velocity $\widetilde{u}_x$ on computational grid in reactive backward-facing step flow; RANS/TPaSR 283
B.9 Dependence of vertical profiles of of Favre-averaged transverse velocity $\widetilde{u}_y$ on computational grid in reactive backward-facing step flow; RANS/TPaSR 284
B.10 Dependence of vertical profiles of u_x^{RMS} on computational grid in reactive backward-facing step flow; RANS/TPaSR 285
B.11 Dependence of vertical profiles of u_y^{RMS} on computational grid in reactive backward-facing step flow; RANS/TPaSR 286

List of tables

3.1 Coefficients in eq. (3.60) discretized with Lax-Friedrichs scheme 76
3.2 Coefficients in eq. (3.60) discretized with Godunov scheme 78
3.3 Backward step: spatial convergence of different methods. $N_r = 10^7$. The error on the interval i (as defined in eq. (3.120)) is approximated with $A_i log(N_x) + B_i$, with $i = 1, 2, 3$. 94

4.1 Source S_c in the transport equation of the Favre variance of progress variable $\widetilde{C''^2}$ 140
4.2 Dissipation term $2\overline{\rho}\widetilde{s_{\chi_c}}$ in the transport equation of the Favre variance of progress variable $\widetilde{C''^2}$ 141
4.3 Algebraic expressions for Favre progress variable variance 141

6.1 Position of sensor points in backward-facing step flow. Schematic distribution of these points is given in fig. 6.2. 162
6.2 Mean reattachment location X_r in nonreactive backward-facing step flow rescaled by the step height h. The last column shows the relative error of the numerical results with respect to the experimental value. 163
6.3 Considered test-cases for RANS/quasi-laminar models for reactive backward-facing step flow. Explicit second-order Runge Kutta method in time is denoted by RK2. 171
6.4 Considered test-cases for RANS/PFTC β-PDF models in reactive backward-facing step flow 178
6.5 Considered test-cases for RANS/TPaSR approach in reactive backward-facing step flow. Following abbreviations are used: "geom." - geometrical fine structure residence time, "kol." - Kolmogorov fine structure residence time and "magn." - Magnussen fine structure residence time. 186
6.6 Deviation of time-averaged velocity and velocity variance profiles from initial velocity profile in different norm; the averaged time is 0.21 s 198
6.7 Considered test-cases within LES for reactive backward-facing step flow 199
6.8 Flame contact point with the upper wall and its relative error in reactive backward-facing step flow 201
6.9 The mean reattachment location X_r in reactive backward-facing step flow. The last column shows the error of the numerical results with respect to the experimental value. LES. 203

A.1 Ramp: approximation of spatial error of Favre-averaged velocity and mean density by $A \log(N_x) + B$ at time $t = 0.2$ s. $N_r = 10^7$. 246

A.2 Scheme non-dissipativity test: approximation of statistical error of the mean density in logarithmic scale by $A\log(N_x) + B$ at time $t = 0.2\,\mathrm{s}$. $N_x = 10^5$. 268

B.1 Considered test-cases for RANS/PFTC β-PDF models in reactive backward-facing step flow 275

B.2 Considered test-cases for RANS/TPaSR approach in reactive backward-facing step flow. Following abbreviations are used in this section: "geom." - geometrical fine structure residence time, "kol." - Kolmogorov fine structure residence time and "magn." - Magnussen fine structure residence time. 281

Bibliography

[AbdelGayedBradley1989] R. Abdel-Gayed, D. Bradley, and F.-K. Lung. "Combustion regimes and the straining of turbulent premixed flames". In: *Combustion and Flame* 76.2 (1989), pp. 213–218 (cit. on p. 29).

[BarlowFrank1998] R. Barlow and J. Frank. "Effects of turbulence on species mass fractions in methane/air jet flames". In: *Symposium (International) on Combustion*. Vol. 27. 1. Elsevier. 1998, pp. 1087–1095 (cit. on p. 49).

[BatchelorTownsend1949] G. Batchelor and A. Townsend. "The nature of turbulent motion at large wave-numbers". In: *Proceedings of the Royal Society of London. Series A. Mathematical and Physical Sciences* 199.1057 (1949), pp. 238–255 (cit. on p. 52).

[BorghiDestriau1995] R. Borghi and M. Destriau. *La combustion et les flammes*. Editions OPHRYS, 1995 (cit. on pp. 29, 45).

[BouchutJin2003] F. Bouchut, S. Jin, and X. Li. "Numerical approximations of pressureless and isothermal gas dynamics". In: *SIAM Journal on Numerical Analysis* 41.1 (2003), pp. 135–158 (cit. on pp. 68, 83, 98).

[Bradbury1982] L. J. S. Bradbury. *Turbulent Shear Flows 3: Selected Papers from the Third International Symposium on Turbulent Shear Flows, the University of California, Davis, September 9-11, 1981*. Vol. 3. Not Avail, 1982 (cit. on p. 45).

[BurrageBurrage1996] K. Burrage and P. M. Burrage. "High strong order explicit Runge-Kutta methods for stochastic ordinary differential equationsp". In: *Applied Numerical Mathematics* 22.1 (1996), pp. 81–101 (cit. on p. 48).

[ButlerORourke1977] T. Butler and P. O'Rourke. "A numerical method for two dimensional unsteady reacting flows". In: *Symposium (International) on Combustion*. Vol. 16. 1. Elsevier. 1977, pp. 1503–1515 (cit. on p. 59).

[CabraMyhrvold2002] R. Cabra, T. Myhrvold, J. Chen, R. Dibble, A. Karpetis, and R. Barlow. "Simultaneous laser raman-rayleigh-lif measurements and numerical modeling results of a lifted turbulent H2 /N2 jet flame in a vitiated coflow". In: *Proceedings of the Combustion Institute* 29.2 (2002), pp. 1881–1888 (cit. on p. 49).

[CANTERA] CANTERA. *An object-oriented software toolkit for chemical kinetics, thermodynamics, and transport processes.* URL: `https://code.google.com/p/cantera/` (cit. on p. 142).

[Chandrasekhar1943] S. Chandrasekhar. "Stochastic problems in physics and astronomy". In: *Reviews of Modern Physics* 15.1 (1943), p. 1 (cit. on p. 269).

[CharletteMeneveau2002] F. Charlette, C. Meneveau, and D. Veynante. "A power-law flame wrinkling model for LES of premixed turbulent combustion Part II: Dynamic formulation". In: *Combustion and Flame* 131.1 (2002), pp. 181–197 (cit. on p. 59).

[ChechkinGoritsky2009] G. A. Chechkin, A. Y. Goritsky, and S. N. Kruzhkov. *Analytical and Numerical Aspects of Partial Differential Equations: Notes of a Lecture Series.* Walter de Gruyter, 2009 (cit. on p. 69).

[ChengLiu2003] L.-T. Cheng, H. Liu, S. Osher, et al. "Computational high-frequency wave propogation using the level-set method with applications to the semi-classical limit of the Schrödinger equations". In: *Communications in Mathematical Sciences* 1.3 (2003), pp. 593–621 (cit. on p. 64).

[ChevalierCourbet2005] P. Chevalier, B. Courbet, D. Dutoya, P. Klotz, E. Ruiz, J. Troyes, and P. Villedieu. "CEDRE: development and validation of a multiphysic computational software". In: *Proc. of the 1st European conf. for aerospace sciences.* 2005 (cit. on p. 158).

[Chomiak1970] J. Chomiak. "A possible propagation mechanism of turbulent flames at high Reynolds numbers". In: *Combustion and Flame* 15.3 (1970), pp. 319–321 (cit. on pp. 52, 56).

[Chomiak1979] J. Chomiak. "Basic considerations in the turbulent flame propagation in premixed gases". In: *Progress in Energy and Combustion Science* 5.3 (1979), pp. 207–221 (cit. on p. 56).

[Chung1969] P. M. Chung. "A simplified statistical model of turbulent, chemically reacting shear flows". In: *AIAA Journal* 7.10 (1969), pp. 1982–1991 (cit. on p. 44).

[ColinDucros2000] O. Colin, F. Ducros, D. Veynante, and T. Poinsot. "A thickened flame model for large eddy simulations of turbulent premixed combustion". In: *Physics of Fluids (1994-present)* 12.7 (2000), pp. 1843–1863 (cit. on pp. 59, 60).

[Courtois2005] R. Courtois. "Simulation aux grandes échelles de l'écoulement dans un chambre de combustion en forme de marche descendante". PhD thesis. Châtenay-Malabry, Ecole Centrale de Paris, 2005 (cit. on pp. 155, 170, 216).

[EmakoLetizia2014] C. Emako, V. Letizia, N. Petrova, R. Sainct, R. Duclous, and O. Soulard. "Diffusion limit of Langevin PDF models in weakly inhomogeneous turbulence". In: *CEMRACS* (2014) (cit. on pp. 5, 6, 20, 21, 64, 127, 219, 259).

[EngquistRunborg1999] B. Engquist and O. Runborg. *Multiphase computations in geometrical optics*. Springer, 1999 (cit. on p. 64).

[EngquistRunborg2003] B. Engquist and O. Runborg. "Computational high frequency wave propagation". In: *Acta numerica* 12 (2003), pp. 181–266 (cit. on p. 64).

[Fick1855] A. Fick. "V. On liquid diffusion". In: *The London, Edinburgh, and Dublin Philosophical Magazine and Journal of Science* 10.63 (1855), pp. 30–39 (cit. on p. 34).

[FlaschkaForest1980] H. Flaschka, M. Forest, and D. McLaughlin. "Multiphase averaging and the inverse spectral solution of the Korteweg-de Vries equation". In: *Communications on Pure and Applied Mathematics* 33.6 (1980), pp. 739–784 (cit. on p. 64).

[FomelSethian2002] S. Fomel and J. A. Sethian. "Fast-phase space computation of multiple arrivals". In: *Proceedings of the National Academy of Sciences* 99.11 (2002), pp. 7329–7334 (cit. on p. 64).

[Fox1975] R. L. Fox. "Multipoint distribution function hierarchy for compressible turbulent flow". In: *Physics of Fluids (1958-1988)* 18.10 (1975), pp. 1245–1248 (cit. on p. 45).

[Frost1960] V. Frost. "Mathematical model of turbulent combustion". In: *Proc. of the 3rd All-Union Symp. on Combust. Theory, Izd-vo AN SSSR, Moscow*. 1960, pp. 121–125 (cit. on p. 44).

[Frost1973] V. Frost. "Model of a turbulent diffusion flame". In: *Izv. Akad. Nauk SSSR, Energ. Transp* 6 (1973), p. 108 (cit. on p. 44).

[Frost1977] V. Frost. *Combustion and explosion*. Nauka, Moscow, 1977 (cit. on p. 44).

[Fureby2007] C. Fureby. "On LES and DES of wall bounded flows". In: *Ercoftac Bulletin* 72 (2007) (cit. on p. 56).

[Gardiner1985] C. W. Gardiner et al. *Handbook of stochastic methods*. Vol. 3. Springer Berlin, 1985 (cit. on p. 269).

[GermanoPiomelli1991] M. Germano, U. Piomelli, P. Moin, and W. H. Cabot. "A dynamic subgrid-scale eddy viscosity model". In: *Physics of Fluids A: Fluid Dynamics (1989-1993)* 3.7 (1991), pp. 1760–1765 (cit. on p. 41).

[Girimaji1991] S. Girimaji. "Assumed β-pdf model for turbulent mixing: Validation and extension to multiple scalar mixing". In: *Combustion Science and Technology* 78.4-6 (1991), pp. 177–196 (cit. on p. 43).

[GiviSirignano1984] P. Givi, W. Sirignano, and S. Pope. "Probability calculations for turbulent jet flows with mixing and reaction of NO and O3". In: *Combustion Science and Technology* 37.1-2 (1984), pp. 59–78 (cit. on p. 45).

[Glimm1965] J. Glimm. "Solutions in the large for nonlinear hyperbolic systems of equations". In: *Communications on Pure and Applied Mathematics* 18.4 (1965), pp. 697–715 (cit. on p. 72).

[Godunov1959] S. K. Godunov. "A difference method for numerical calculation of discontinuous solutions of the equations of hydrodynamics". In: *Matematicheskii Sbornik* 89.3 (1959), pp. 271–306 (cit. on p. 72).

[GranMagnussen1996] I. R. Gran and B. F. Magnussen. "A numerical study of a bluff-body stabilized diffusion flame. Part 2. Influence of combustion modeling and finite-rate chemistry". In: *Combustion Science and Technology* 119.1-6 (1996), pp. 191–217 (cit. on p. 52).

[Haworth2010] D. Haworth. "Progress in probability density function methods for turbulent reacting flows". In: *Progress in Energy and Combustion Science* 36.2 (2010), pp. 168–259 (cit. on p. 44).

[HaworthPope1986] D. Haworth and S. Pope. "A generalized Langevin model for turbulent flowss". In: *Physics of Fluids (1958-1988)* 29.2 (1986), pp. 387–405 (cit. on p. 49).

[Hill1976] J. C. Hill. "Homogeneous turbulent mixing with chemical reaction". In: *Annual Review of Fluid Mechanics* 8.1 (1976), pp. 135–161 (cit. on p. 45).

[Hoffmeister1980] M. Hoffmeister. "Turbulent Reacting Flows, Topics in Applied Physics". In: *ZAMM - Journal of Applied Mathematics and Mechanics / Zeitschrift fur Angewandte Mathematik und Mechanik* 62.2 (1980), pp. 139–139. DOI: 10.1002/zamm.19820620223 (cit. on p. 45).

[Ievlev1972] V. Ievlev. "Equations for finite-dimensional probability distributions of fluctuating quantities in turbulent flow". In: *Doklady Akademii Nauk SSSR* 208.5 (1972), pp. 1036–1038 (cit. on p. 45).

[Ievlev1975] V. Ievlev. "Turbulent flow of high-temperature continuum media". In: *Moscow Izdatelstvo Nauka* 208.5 (1975), pp. 1036–1038 (cit. on p. 45).

[Itô1944] K. Itô et al. "Stochastic integral". In: *Proceedings of the Imperial Academy* 20.8 (1944), pp. 519–524 (cit. on p. 269).

[IzardLehnasch2009] J.-F. Izard, G. Lehnasch, and A. Mura. "A Lagrangian Model of Combustion in High-Speed Flows: Application to Scramjet Conditions". In: *Combustion Science and Technology* 181.11 (2009), pp. 1372–1396 (cit. on p. 220).

[JanickaKolbe1978] J. Janicka, W. Kolbe, and W. Kollmann. "The solution of a pdf-transport equation for turbulent diffusion flames". In: *Proceedings of the 1978 Heat Transfer and Fluid Mechanics Institute*. 1978, p. 296 (cit. on p. 45).

[JennyPope2001] P. Jenny, S. Pope, M. Muradoglu, and D. Caughey. "A hybrid algorithm for the joint PDF equation of turbulent reactive flows". In: *Journal of Computational Physics* 166.2 (2001), pp. 218–252 (cit. on pp. 46, 49).

[JinLi2003] S. Jin and X. Li. "Multi-phase computations of the semiclassical limit of the Schrödinger equation and related problems: Whitham vs Wigner". In: *Physica D: Nonlinear Phenomena* 182.1 (2003), pp. 46–85 (cit. on p. 64).

[KarpovLipatnikov1994] V. P. Karpov, A. N. Lipatnikov, and V. L. Zimont. "A model of premixed turbulent combustion and its validation". In: *Archivum combustionis* 14.3 (1994), pp. 125–141 (cit. on p. 140).

[Kazantsev1968] A. Kazantsev. "Enhancement of a magnetic field by a conducting fluid". In: *Journal of Experimental and Theoretical Physics* 26.5 (1968), pp. 1031–1034 (cit. on p. 46).

[Kolmogorov1941] A. N. Kolmogorov. "The local structure of turbulence in incompressible viscous fluid for very large Reynolds numbers". In: *Dokl. Akad. Nauk SSSR*. Vol. 30. 4. 1941, pp. 299–303 (cit. on p. 25).

[Kraichnan2003] R. H. Kraichnan. "Small-Scale Structure of a Scalar Field Convected by Turbulence". In: *Physics of Fluids (1958-1988)* 11.5 (2003), pp. 945–953 (cit. on p. 46).

[KuoCorrsin1971] A. Y.-S. Kuo and S. Corrsin. "Experiments on internal intermittency and fine-structure distribution functions in fully turbulent fluid". In: *Journal of Fluid Mechanics* 50.02 (1971), pp. 285–319 (cit. on p. 52).

[KuoCorrsin1972] A. Y.-S. Kuo and S. Corrsin. "Experiment on the geometry of the fine-structure regions in fully turbulent fluid". In: *Journal of Fluid Mechanics* 56.03 (1972), pp. 447–479 (cit. on pp. 52, 53).

[KuznetsovSabelnikov1986] V. R. Kuznetsov and V. A. Sabelnikov. "Turbulence and combustion". In: *Moscow Izdatelstvo Nauka* 1 (1986) (cit. on p. 44).

[Kuznetsov1967] V. Kuznetsov. "On the probability density for the velocity difference at two points of a homogeneous isotropic turbulent flow". In: *Prikl. Mat. Mekh* 31 (1967) (cit. on p. 44).

[KuznetsovFrost1973] V. Kuznetsov and V. Frost. "Concentration probability distribution and intermittence in turbulent jets". In: *Fluid Dynamics* 8.2 (1973), pp. 223–228 (cit. on p. 44).

[LandenfeldSadiki2002] T. Landenfeld, A. Sadiki, and J. Janicka. "A turbulence-chemistry interaction model based on a multivariate presumed beta-pdf method for turbulent flames". In: *Flow, Turbulence and Combustion* 68.2 (2002), pp. 111–135 (cit. on p. 43).

[Langevin1908] P. Langevin. "Sur la théorie du mouvement brownien". In: *CR Acad. Sci. Paris* 146.530-533 (1908) (cit. on p. 269).

[LaxDavid Levermore1983] P. D. Lax and C. David Levermore. "The small dispersion limit of the Korteweg-de Vries equation. I". In: *Communications on Pure and Applied Mathematics* 36.3 (1983), pp. 253–290 (cit. on p. 64).

[LemonsLackman1995] D. Lemons, J. Lackman, M. Jones, and D. Winske. "Noise-induced instability in self-consistent Monte Carlo calculations". In: *Physical Review E* 52.6 (1995), p. 6855 (cit. on pp. 82, 112).

[LiWöhlbier2004] X. Li, J. G. Wöhlbier, S. Jin, and J. H. Booske. "Eulerian method for computing multivalued solutions of the Euler-Poisson equations and applications to wave breaking in klystrons". In: *Physical Review E* 70.1 (2004), p. 016502 (cit. on p. 64).

[LienLiu2009] F. Lien, H. Liu, E. Chui, and C. McCartney. "Development of an Analytical β-Function PDF Integration Algorithm for Simulation of Non-premixed Turbulent Combustion". In: *Flow, Turbulence and Combustion* 83.2 (2009), pp. 205–226 (cit. on pp. 20, 144, 219).

[LiuOsher2006] H. Liu, S. Osher, and R. Tsai. "Multi-valued solution and level set methods in computational high frequency wave propagation". In: *Commun. Comput. Phys* 1.5 (2006), pp. 765–804 (cit. on pp. 20, 50, 64).

[Lundgren1967] T. Lundgren. "Distribution functions in the statistical theory of turbulence". In: *Physics of Fluids (1958-1988)* 10.5 (1967), pp. 969–975 (cit. on p. 44).

[Lundgren1969] T. Lundgren. "Model equation for nonhomogeneous turbulence". In: *Physics of Fluids (1958-1988)* 12.3 (1969), pp. 485–497 (cit. on p. 45).

[Lyubimov1969] B. Lyubimov. "Lagrangian description of the dynamics of turbulent flow". In: *Doklady Akademii Nauk SSSR*. Vol. 184. 5. 1969, pp. 1069–1071 (cit. on p. 45).

[LyubimovUlinich1970] B. Lyubimov and F. Ulinich. "Statistical equations of turbulent flow in Lagrangian variables". In: 34.1 (1970), pp. 24–31 (cit. on p. 45).

[MagelSchnell1996] H.-C. Magel, U. Schnell, and K. R. Hein. "Simulation of detailed chemistry in a turbulent combustor flow". In: *Symposium (International) on Combustion*. Vol. 26. 1. Elsevier. 1996, pp. 67–74 (cit. on p. 52).

[Magnussen1981] B. Magnussen. "On the structure of turbulence and a generalized eddy dissipation concept for chemical reaction in turbulent flow". In: (1981) (cit. on p. 52).

[Magnussen2005] B. F. Magnussen. "The eddy dissipation concept a bridge between science and technology". In: *ECCOMAS thematic conference on computational combustion*. 2005, pp. 21–24 (cit. on p. 52).

[MagnussenHjertager1977] B. F. Magnussen and B. H. Hjertager. "On mathematical modeling of turbulent combustion with special emphasis on soot formation and combustion". In: *Symposium (International) on Combustion*. Vol. 16. 1. Elsevier. 1977, pp. 719–729 (cit. on p. 154).

[MagreMoreau1988] P. Magre, P. Moreau, G. Collin, R. Borghi, and M. Péalat. "Further studies by CARS of premixed turbulent combustion in a high velocity flow". In: *Combustion and Flame* 71.2 (1988), pp. 147–168 (cit. on pp. 5, 6, 21, 47, 155, 156, 169, 172, 195, 216, 220).

[MasriDibble1996] A. Masri, R. Dibble, and R. Barlow. "The structure of turbulent nonpremixed flames revealed by Raman-Rayleigh-LIF measurements". In: *Progress in Energy and Combustion Science* 22.4 (1996), pp. 307–362 (cit. on p. 49).

[MeierWeigand2007] W. Meier, P. Weigand, X. Duan, and R. Giezendanner-Thoben. "Detailed characterization of the dynamics of thermoacoustic pulsations in a lean premixed swirl flame". In: *Combustion and Flame* 150.1 (2007), pp. 2–26 (cit. on p. 139).

[MeneveauPoinsot1991] C. Meneveau and T. Poinsot. "Stretching and quenching of flamelets in premixed turbulent combustion". In: *Combustion and Flame* 86.4 (1991), pp. 311–332 (cit. on pp. 60, 141).

[MoinSquires1991] P. a. Moin, K. Squires, W. Cabot, and S. Lee. "A dynamic subgrid-scale model for compressible turbulence and scalar transport". In: *Physics of Fluids A: Fluid Dynamics (1989-1993)* 3.11 (1991), pp. 2746–2757 (cit. on p. 41).

[Monin1967a] A. Monin. "Equations for finite-dimensional probability distributions of turbulence fields". In: *Doklady Akademii Nauk SSSR* 177.5 (1967), p. 1036 (cit. on p. 44).

[Monin1967b] A. Monin. "Equations of turbulent motion". In: *Journal of Applied Mathematics and Mechanics* 31.6 (1967), pp. 1057–1068 (cit. on p. 44).

[MoreauLabbe1985] P. Moreau, J. Labbe, F. Dupoirieux, and R. Borghi. "Experimental and numerical study of a turbulent recirculation zone with combustion". In: *5th Symposium on Turbulent Shear Flows*. Vol. 1. 1985 (cit. on pp. 157, 162).

[Moule2013] Y. Moule. "Modélisation et Simulation de la Combustion dans les Écoulements Rapides. Applications aux Superstatoréacteurs." PhD thesis. Ecole Nationale Supérieure de Mécanique et d'Aérotechnique-Poitiers, 2013 (cit. on pp. 56, 58, 59).

[MouleSabelnikov2014] Y. Moule, V. Sabelnikov, and A. Mura. "Highly resolved numerical simulation of combustion in supersonic hydrogen-air coflowing jets". In: *Combustion and Flame* (2014) (cit. on pp. 58, 59).

[MuradogluJenny1999] M. Muradoglu, P. Jenny, S. B. Pope, and D. A. Caughey. "A consistent hybrid finite-volume/particle method for the PDF equations of turbulent reactive flows". In: *Journal of Computational Physics* 154.2 (1999), pp. 342–371 (cit. on p. 46).

[MuradogluPope2001] M. Muradoglu, S. B. Pope, and D. A. Caughey. "The hybrid method for the PDF equations of turbulent reactive flows: consistency conditions and correction algorithms". In: *Journal of Computational Physics* 172.2 (2001), pp. 841–878 (cit. on pp. 46, 49).

[NandulaPitz1996] S. Nandula, R. Pitz, R. Barlow, and G. Fiechtner. "Rayleigh/ Raman/ LIF measurements in a turbulent lean premixed combustor". In: *34 th Aerospace Sciences Meeting Exhibit,-Reno, NV*. 1996 (cit. on p. 139).

[NguyenPope1984] T. V. Nguyen and S. Pope. "Monte Carlo calculations of turbulent diffusion flames". In: *Combustion Science and Technology* 42.1-2 (1984), pp. 13–45 (cit. on p. 45).

[Novikov1968] E. Novikov. "Kinetic equations for a vortex field". In: *Soviet Physics Doklady*. Vol. 12. 1968, p. 1006 (cit. on p. 44).

[OsnesLangtangen1998] H. Osnes and H. P. Langtangen. "A study of some finite difference schemes for a unidirectional stochastic transport equation". In: *SIAM Journal on Scientific Computing* 19.3 (1998), pp. 799–812 (cit. on p. 46).

[Ourliac2009] M. Ourliac. "Utilisation d'une méthode eulérienne de résolution des équations PDF de scalaires turbulents pour la simulation de l'allumage d'une chambre de combustion cryotechnique". PhD thesis. PhD thesis, Université de Lyon, 2009 (cit. on pp. 45, 47, 81, 155, 162, 170).

[Peters1986] N. Peters. "Laminar Flamelet concept in turbulent combustion Twenty-First Symposium (International) on Combustion-The Combustion Institute 1231". In: (1986) (cit. on p. 29).

[Peters1999] N. Peters. "The turbulent burning velocity for large-scale and small-scale turbulence". In: *Journal of Fluid Mechanics* 384 (1999), pp. 107–132 (cit. on p. 140).

[Peters2000] N. Peters. *Turbulent combustion*. Cambridge university press, 2000 (cit. on pp. 24, 29, 31).

[PetrovaSabelnikov2013] N. Petrova and V. Sabelnikov. "Simulation of turbulent combustion in air-breathing chambers: extension of Eulerian Monte Carlo methods". In: *13th Onera-DLR Aerospace Symposium ODAS* (2013) (cit. on p. 21).

[Pitsch2005] H. Pitsch. "A consistent level set formulation for large-eddy simulation of premixed turbulent combustion". In: *Combustion and Flame* 143.4 (2005), pp. 587–598 (cit. on p. 140).

[PoinsotCandel1995] T. Poinsot, S. Candel, and A. Trouvé. "Applications of direct numerical simulation to premixed turbulent combustion". In: *Progress in Energy and Combustion Science* 21.6 (1995), pp. 531–576 (cit. on p. 23).

[PoinsotVeynante2005] T. Poinsot and D. Veynante. *Theoretical and numerical combustion*. 2005 (cit. on pp. 29, 32, 34).

[Pope1981] S. Pope. "Monte Carlo calculations of premixed turbulent flames". In: *Symposium (International) on Combustion*. Vol. 18. 1. Elsevier. 1981, pp. 1001–1010 (cit. on pp. 45, 72).

[Pope1985] S. Pope. "PDF methods for turbulent reactive flows". In: *Progress in Energy and Combustion Science* 11.2 (1985), pp. 119–192 (cit. on pp. 19, 45, 46, 63, 75).

[Pope1994] S. Pope. "Lagrangian PDF methods for turbulent flows". In: *Annual Review of Fluid Mechanics* 26.1 (1994), pp. 23–63 (cit. on pp. 41, 42).

[Pope2000] S. B. Pope. *Turbulent flows*. Cambridge university press, 2000 (cit. on pp. 19, 23, 27, 39, 46, 48).

[RemboldJenny2006] B. Rembold and P. Jenny. "A multiblock joint pdf finite-volume hybrid algorithm for the computation of turbulent flows in complex geometries". In: *Journal of Computational Physics* 220.1 (2006), pp. 59–87 (cit. on p. 46).

[RojdestvenskiiYanenko1978] B. Rojdestvenskii and N. Yanenko. *The Quasi-Linear Equations Systems*. "Nauka", Moscow, 1978 (cit. on p. 69).

[SabelnikovFureby2013] V. Sabelnikov and C. Fureby. "Extended LES-PaSR model for simulation of turbulent combustion". In: *Progress in Propulsion Physics*. Vol. 4. EDP Sciences. 2013, pp. 539–568 (cit. on pp. 5, 6, 21, 56, 58, 154).

[Sabelnikov1985] V. Sabelnikov. "Analysis of semiempirical hypotheses upon closure of the equation for concentration probability density (PDF)". In: *VINITI* 7212-85 (1985), p. 48 (cit. on p. 45).

[Sabelnikov1986] V. Sabelnikov. "Analysis of the models for concentration probability density in the theory of turbulent mixing and combustion". In: *Minsk, ITMO AN SSSR* (1986), pp. 12–29 (cit. on p. 45).

[SabelnikovSoulard2010] V. A. Sabelnikov and O. Soulard. "Eulerian (Field) Monte Carlo Methods for Solving PDF Transport Equations in Turbulent Reacting Flows". In: *Handbook of Combustion*. Wiley-VCH Verlag GmbH & Co. KGaA, 2010. DOI: 10.1002/9783527628148.hoc043 (cit. on pp. 20, 68).

[SabelnikovSoulard2005] V. Sabelnikov and O. Soulard. "Rapidly decorrelating velocity-field model as a tool for solving one-point Fokker-Planck equations for probability density functions of turbulent reactive scalars". In: *Physical Review E* 72.1 (2005), p. 016301 (cit. on pp. 20, 46).

[SabelnikovSoulard2006] V. Sabelnikov and O. Soulard. "White in time scalar advection model as a tool for solving joint composition PDF equations". In: *Flow, Turbulence and Combustion* 77.1-4 (2006), pp. 333–357 (cit. on pp. 20, 46).

[SainteRose2010] B. Sainte-Rose. "Simulations numériques d'écoulements réactifs massivement décollés par une approche hybride RANS/LES". PhD thesis. Ecole Centrale Paris, 2010 (cit. on pp. 155, 162, 170, 195, 213).

[SavitzkyGolay1964] A. Savitzky and M. J. Golay. "Smoothing and differentiation of data by simplified least squares procedures." In: *Analytical Chemistry* 36.8 (1964), pp. 1627–1639 (cit. on p. 128).

[Savre2010] J. Savre. "Simulation numérique instationnaire de la combustion turbulente au sein de foyers aéronautiques et prédiction des émissions polluantes". PhD thesis. Ecole Polytechnique, 2010 (cit. on pp. 20, 139, 219).

[Smagorinsky1963] J. Smagorinsky. "General circulation experiments with the primitive equations: I. The basic experiment*". In: *Monthly weather review* 91.3 (1963), pp. 99–164 (cit. on p. 41).

[SoulardSabelnikov2006] O. Soulard and V. Sabelnikov. "Eulerian Monte Carlo method for the joint velocity and mass-fraction probability density function in turbulent reactive gas flows". In: *Combustion, Explosion and Shock Waves* 42.6 (2006), pp. 753–762 (cit. on pp. 20, 47, 49, 50, 64, 68, 72).

[Soulard2005] O. Soulard. "Approches PDF pour la combustion turbulente, prise en compte d'un spectre d'échelles turbulentes dans la modélisation du micromélange et élaboration d'une méthode de Monte Carlo eulérienne". PhD thesis. Rouen, 2005 (cit. on pp. 45, 47, 155, 170).

[SparberMarkowich2003] C. Sparber, P. A. Markowich, and N. J. Mauser. "Wigner functions versus WKB-methods in multivalued geometrical optics". In: *Asymptotic Analysis* 33.2 (2003), pp. 153–187 (cit. on p. 64).

[SymesQian2003] W. W. Symes and J. Qian. "A slowness matching Eulerian method for multivalued solutions of eikonal equations". In: *Journal of Scientific Computing* 19.1-3 (2003), pp. 501–526 (cit. on p. 64).

[TanahashiFujimura2000] M. Tanahashi, M. Fujimura, and T. Miyauchi. "Coherent fine-scale eddies in turbulent premixed flames". In: *Proceedings of the Combustion Institute* 28.1 (2000), pp. 529–535 (cit. on p. 56).

[TanahashiSato2008] M. Tanahashi, M. Sato, M. Shimura, and T. Miyauchi. "DNS and combined laser diagnostics of turbulent combustion". In: *Journal of Thermal Science and Technology* 3 (2008), pp. 391–409 (cit. on pp. 53, 56).

[Tennekes2003] H. Tennekes. "Simple Model for the Small-Scale Structure of Turbulence". In: *Physics of Fluids (1958-1988)* 11.3 (2003), pp. 669–671 (cit. on p. 53).

[Toro1999] E. F. Toro. *Riemann solvers and numerical methods for fluid dynamics*. Vol. 16. Springer, 1999 (cit. on pp. 48, 83, 223).

[TrierSymes1991] J. van Trier and W. W. Symes. "Upwind finite-difference calculation of traveltimes". In: *Geophysics* 56.6 (1991), pp. 812–821 (cit. on p. 64).

[UhlenbeckOrnstein1930] G. E. Uhlenbeck and L. S. Ornstein. "On the theory of the Brownian motion". In: *Physical Review* 36.5 (1930), p. 823 (cit. on p. 269).

[Ulinich1968] F. Ulinich. "Statistical dynamics of a turbulent incompressible fluid (Statistical dynamics of turbulent incompressible fluid, discussing harmonic function in Navier-Stokes equation)". In: *Doklady Akademii Nauk SSSR*. Vol. 183. 1968, pp. 535–537 (cit. on p. 44).

[UlinichLyubimov1968] F. Ulinich and B. Lyubimov. "The statistical theory of turbulence in an incompressible fluid at high Reynolds numbers". In: *Journal of Experimental and Theoretical Physics* 55 (1968) (cit. on p. 44).

[Valiño1998] L. Valiño. "A field Monte Carlo formulation for calculating the probability density function of a single scalar in a turbulent flow". In: *Flow, Turbulence and Combustion* 60.2 (1998), pp. 157–172 (cit. on pp. 20, 46).

[VillermauxDevillon1972] J. Villermaux and J. Devillon. "Représentation de la coalescence et de la redispersion des domaines de ségrégation dans un fluide par un modèle d'interaction phénoménologique". In: *Proceedings of the 2nd International symposium on chemical reaction engineering*. 1972, pp. 1–13 (cit. on p. 45).

[ViswanathanWang2011] S. Viswanathan, H. Wang, and S. B. Pope. "Numerical implementation of mixing and molecular transport in LES/PDF studies of turbulent reacting flows". In: *Journal of Computational Physics* 230.17 (2011), pp. 6916–6957 (cit. on p. 46).

[Vulis1950] L. Vulis. "Thermodynamics of gas flows". In: *Gosenergoizdat, Moscow-Leningrad* (1950) (cit. on p. 54).

[WangPope2008] H. Wang and S. B. Pope. "Time-averaging strategies in the finite-volume/particle hybrid algorithm for the joint PDF equation of turbulent reactive flows". In: *Combustion Theory and Modelling* 12.3 (2008), pp. 529–544 (cit. on pp. 46, 49).

[WangUhlenbeck1945] M. C. Wang and G. E. Uhlenbeck. "On the theory of the Brownian motion II". In: *Reviews of Modern Physics* 17.2-3 (1945), pp. 323–342 (cit. on p. 269).

[Warnatz1984] J. Warnatz. "Rate coefficients in the C/H/O system". In: *Combustion chemistry*. Springer, 1984, pp. 197–360 (cit. on p. 44).

[WarnatzMaas2006] J. Warnatz, U. Maas, and R. W. Dibble. *Combustion: physical and chemical fundamentals, modeling and simulation, experiments, pollutant formation*. Springer, 2006 (cit. on p. 42).

[WernerDrummond1997] M. Werner and P. Drummond. "Robust algorithms for solving stochastic partial differential equations". In: *Journal of Computational Physics* 132.2 (1997), pp. 312–326 (cit. on p. 46).

[WestbrookDryer1981] C. K. Westbrook and F. L. Dryer. "Simplified reaction mechanisms for the oxidation of hydrocarbon fuels in flames". In: *Combustion Science and Technology* 27.1-2 (1981), pp. 31–43 (cit. on p. 170).

[Whitham2011] G. B. Whitham. *Linear and nonlinear waves*. Vol. 42. John Wiley & Sons, 2011 (cit. on p. 64).

[WoodwardPorter2000] P. R. Woodward, D. H. Porter, I. Sytine, S. Anderson, A. A. Mirin, B. Curtis, R. H. Cohen, W. P. Dannevik, A. M. Dimits, D. E. Eliason, et al. "Very High Resolution Simulations of Compressible, Turbulent Flows". In: *Computational Fluid Dynamics* (2000), pp. 3–15 (cit. on pp. 53, 56).

[ZeldovichFrankKamenetskii1938] Y. Zeldovich and D. Frank-Kamenetskii. "A theory of thermal propagation of flame". In: *Journal of Experimental and Theoretical Physics* 12.1 (1938), pp. 100–105 (cit. on p. 59).